

# Design and Properties of Lanthanoid Chelating Tags

Inauguraldissertation

zur

Erlangung der Würde eines Doktors der Philosophie

vorgelegt der

Philosophisch-Naturwissenschaftlichen Fakultät

der Universität Basel

von

Raphael Vogel

Basel 2023

Genehmigt von der Philosophisch-Naturwissenschaftlichen Fakultät:

auf Antrag von

Erstbetreuer: Prof. Dr. Daniel Häussinger

Zweitbetreuer: Prof. Dr. Edwin Charles Constable

Externer Experte: Prof. Dr. David Parker

Basel, den 21. Februar 2023

Prof. Dr. Marcel Mayor, Dekan

## Publications

- 1 Intrinsic anisotropy parameters of a series of lanthanoid complexes deliver new insights into the structure-magnetism relationship.  
R. Vogel, T. Müntener, D. Häussinger, *Chem*, **2021**, 7, 3144-3156.
- 2 Application of paramagnetic lanthanoid chelating tags in NMR spectroscopy and their use for the localization of ligands within biomacromolecules.  
D. Joss, R. Vogel, K. Zimmermann, D. Häussinger, *Comprehensive Coordination Chemistry III (Third Edition)*, **2021**, 617-645.
- 3 Highly Stable Silver(I) Complexes with Cyclen-Based Ligands Bearing Sulphide Arms: a Step Towards Silver-111 Labeled Radiopharmaceuticals.  
M. Tosato, M. Asti, M. Dalla Tiezza, L. Orian, D. Häussinger, R. Vogel, U. Köster, M. Jensen, A. Andrighetto, P. Pastore, V. Di Marco, *Inorganic Chemistry*, **2020**, 59, 10907-10919.
- 4 A tris(diisocyanide)chromium(0) complex is a luminescent analog of Fe(2,2'-bipyridine)<sub>3</sub><sup>2+</sup>.  
L. A. Büldt, X. Guo, R. Vogel, A. Prescimone, O. S. Wenger, *Journal of the American Chemical Society*, **2017**, 139, 985-992



## Acknowledgements

First of all, I would like to thank Prof. Dr. Daniel Häussinger for giving me the opportunity to perform my PhD in his group. I really enjoyed working with you for the last four and a half years and am very grateful for all that you taught me about NMR spectroscopy. Thank you for all the support and freedom you gave me during my PhD.

I would like to thank Prof. Dr. Edwin Charles Constable for accepting to co-supervise my thesis and with Prof. Dr. Catherin Housecroft for the helpful discussions during the group meetings.

I would like to thank Prof. Dr. David Parker for accepting to evaluate this thesis as an external expert.

For the fruitful collaboration on stable silver chelators I would like to thank Dr. Marianna Tosato and Prof. Dr. Valerio Dimarco.

For the proof reading of my thesis, I would like to thank David Vogel, Pascal Rieder, Thomas Müntener and Daniel Joss.

I would like to thank all the analytical, technical and administrative staff for their support. Dr Michael Pfeffer is acknowledged for the measurement of the HRMS samples.

The sciCORE facility is acknowledged for their support with the DFT geometry optimizations.

The Department of Chemistry of the University of Basel is acknowledge for their financial support

Special thanks go to all the students, Mirko Markovic, Andreas Mischler, Manon Millet and Annika Matt and the current and former Häussinger group members Dr. Thomas Müntener, Dr. Daniel Joss, Pascal Rieder, Leonie Bourgeois and Annika Matt with whom I had the pleasure of working together in the lab. I thank you all for the great time I could spend with you in and around the lab.

I would also like to thank all of the people from the chemistry department, which I got to know during my PhD, for all the pleasant times in and outside of the department. I refrain from listing names here but do sincerely hope that everyone I met during lunch, at the different social events or on other occasions feels mentioned here.

Last but not least I would like to thank my family and friends for their support throughout the years.

## Abstract

The work presented in this thesis is centred around the magnetic anisotropy of lanthanoids and how it can be harnessed for the study of bio macromolecules. Following the introduction about paramagnetic NMR spectroscopy, lanthanoids and lanthanoid chelating tags are three individual chapters regarding the properties, design and synthesis of lanthanoid chelating tags.

The first chapter comprises a published study concerning the anisotropy of the magnetic susceptibility exhibited by lanthanoid (III) ions within lanthanoid chelating tags (LCTs). LCTs are widely used to induce pseudocontact shifts (PCSs) or residual dipolar couplings (RDCs) on bio macromolecules. The size of the observed PCSs or RDCs is dependent on the anisotropy of the magnetic susceptibility of the lanthanoid (III) ion. The anisotropy of the magnetic susceptibility can be described by the anisotropy parameters, which are for LCTs commonly determined from PCS observed on a conjugated protein. Because the PCS observed on the protein are inevitably reduced by motional averaging, the anisotropy parameters determined from them describe always only a fraction of the anisotropy of the magnetic susceptibility a lanthanoid ion exhibits within an LCT. This study presents for the first time the intrinsic anisotropy parameters for the full lanthanoid series determined from shifts observed on the LCT itself. The strongly shifted proton spectra could no longer be assigned using conventional 2D-NMR assignment strategies, due to the extremely short T2 times. Instead, the 1D proton spectra were fully assigned using extensive, site-specific  $^2\text{H}$  and  $^{13}\text{C}$  labelling in combination with combinatorial methods. The full assignments were used to determine the anisotropy parameters, which deliver an upper limit for future PCS applications relying on this coordination polyhedron as well as new insights into future LCT designs. Surprisingly, we observed an, at least at room temperature, unprecedented correlation between the oblate or prolate f-electron distribution of the lanthanoid and the orientation of the main magnetic axis. Furthermore, a comparison of different ligands revealed that the size of the anisotropy parameters depends on the interaction between the ligand and the lanthanoid ion.

In the second chapter, the focus lies on the development of a new single-arm LCT, which could provide predictable anisotropy parameters. For current single-arm LCTs the averaging of the observed PCS on a conjugated protein is not only dependent on the LCT but also on the tagging site. Therefore, the averaging of the PCS is different for each tagging site, requiring the determination of the anisotropy parameters in each case. It would greatly ease the application of PCS NMR spectroscopy if a single-arm LCT would provide predictable anisotropy parameters. A priori knowledge of the anisotropy parameters would allow the choice of the

best-suited tagging site for a given application and facilitate the assignment of paramagnetic signals. Based on the insights gained from determining the intrinsic anisotropy parameters it was hypothesized that coaxiality between the rotation axis and z-axis of the tensor frame could provide predictable anisotropy parameters. The sought coaxiality can be achieved with a symmetric LCT that is tethered via a thioether to the protein. In order to develop a new LCT, two scaffolds were tested for their suitability as an LCT. The second scaffold provided a new symmetric LCT, which was successfully tethered to ubiquitin S57C. Determination of the anisotropy parameters and comparison to the estimated intrinsic anisotropy parameters showed that the PCS induced by the new LCT are barely affected by averaging. The current results were not sufficient to ascertain whether the new LCT is able to provide predictable anisotropy parameters but they hold great promise for further research.

The third chapter describes the synthesis of a new building block for DOTA-M8-based LCTs. DOTA-M8 provides excellent properties for the development of lanthanoid chelating tags but has the inherent problem that it is difficult to synthesize. The main challenge in the synthesis towards DOTA-M8 is the synthesis of M4-cyclen. In this chapter, a new cyclen building block is presented, which should be simpler to synthesize but still provides all the necessary properties for high performance LCTs. A convenient synthetic route towards the new building block was tested. The encountered obstacles revealed which changes would be necessary for the future success of the proposed synthetic strategy.



## Abbreviations

AIBN	Azobisisobutyronitrile
AcOH	Acetic acid
BMS	Borane dimethylsulfide
BnBr	Benzyl bromide
Boc	<i>tert</i> -Butyloxycarbonyl
<i>n</i> -BuLi	<i>n</i> -Butyllithium
Cbz	Benzyloxycarbonyl
COSY	Correlation spectroscopy
CPMG	Carr-Purcell-Meiboom-Gill
cryo-EM	Cryogenic electron microscopy
CS	Contact shift
CSA	Chemical shift anisotropy
DCM	Dichloromethane
DFT	Density functional theory
DIPEA	<i>N,N</i> -Diisopropylethylamine
DMAC	<i>N,N</i> -Dimethylacetamide
DMF	<i>N,N</i> -Dimethylformamide
DMSO	Dimethyl sulfoxide
DNA	Deoxyribonucleic acid
DOTA	2,2',2'',2'''-(1,4,7,10-Tetraazacyclododecane-1,4,7,10-tetrayl)tetraacetic acid
Et <sub>3</sub> N	Triethylamine
EtOH	Ethanol
GB1	Guanine nucleotide-binding protein subunit beta
GPCR	G protein-coupled receptor
GPS	Global positioning system
HATU	Hexafluorophosphate azabenzotriazole tetramethyl uronium
HMBC	Heteronuclear multiple bond correlation
HMQC	Heteronuclear multiple quantum correlation
HPLC	High-performance liquid chromatography
HPLC-MS	High-performance liquid chromatography-mass spectroscopy
IBX	2-Iodoxybenzoic acid
IPAP	In phase anti phase
LCT	Lanthanoid chelating tag

Ln	Lanthanoid
<i>m</i> -CPBA	<i>meta</i> -Chloroperoxybenzoic acid
MeCN	Acetonitrile
MeOH	Methanol
MRI	Magnetic resonance imaging
Ms	Methanesulfonyl
NBS	<i>N</i> -Bromosuccinimide
NMR	Nuclear magnetic resonance
NOE	Nuclear Overhauser effect
NOESY	Nuclear Overhauser enhancement and exchange spectroscopy
Nosyl	2-Nitrobenzenesulfonyl
NsCl	2-Nitrobenzenesulfonyl-chloride
PCS	Pseudocontact shift
Pd/C	Palladium on carbon
PDB	Protein data bank
PhSH	Thiophenol
PRE	Paramagnetic relaxation enhancement
PS	Paramagnetic shift
Py	Pyridine
Pypa	6,6'-(((Pyridine-2,6-diylbis(methylene)) bis ((carboxymethyl) azanediyl)) bis (methylene)) dipicolinic acid
RACS	Residual anisotropic chemical shift anisotropy
RDC	Residual dipolar coupling
SAP	Square antiprism
SMT	S-methylisothiourea sulfate
TCEP	Tris(2-carboxyethyl)phosphine
Terpy	Terpyridine
TFA	Trifluoroacetic acid
THF	Tetrahydrofuran
TSAP	Twisted square antiprism
TsCl	4-Toluenesulfonyl chloride
UTR	Unique tensor representation
VT-NMR	Variable temperature nuclear magnetic resonance
ZORA	Zeroth order regular approximation

## Table of contents

1.	Introduction	1
1.1	Paramagnetic NMR Spectroscopy	2
1.1.1	Paramagnetic Shift	3
1.1.1.1	Contact Shift	4
1.1.1.2	Pseudocontact Shift	5
1.1.1.3	Residual Anisotropic Chemical Shift	8
1.1.2	Paramagnetic Relaxation Enhancement	9
1.1.3	Residual Dipolar Coupling	10
1.2	Lanthanoids	11
1.3	Lanthanoid Chelating Tags	13
1.4	References	17
2.	Intrinsic anisotropy parameters of a series of lanthanoid complexes deliver new insights into the structure-magnetism relationship	21
2.1	Summary	24
2.2	Introduction	24
2.3	Results and Discussion	25
2.3.1	Structure of Ln-DOTA-M7FPy	25
2.3.2	NMR analysis and synthesis of isotopically labeled Ln-DOTA-M7FPy	26
2.3.3	Intrinsic anisotropy parameters	29
2.3.4	Ligand-field-like effects	30
2.3.5	Conclusions	32
2.4	Experimental Procedures	33
2.4.1	Resource availability	33
2.4.2	Tagging and anisotropy parameters fitting on ubiquitin	33
2.5	References	35
2.6	Supplemental information	37
2.6.1	Materials and Methods	37
2.6.2	Experimental Procedures and Characterization	39
2.6.3	Classified <sup>1</sup> H proton Shifts from Ln-DOTA-M7FPy ( <b>1</b> )	94
2.6.3.1	Early lanthanoids	94
2.6.3.2	Late lanthanoids	96
2.6.4	Determination of the final assignment of Ln-DOTA-M7FPy ( <b>1</b> )	99

2.6.5	Shift lists of the final assignments	102
2.6.5.1	Ln-DOTA-M7FPy ( <b>1</b> ) early lanthanoids	102
2.6.5.2	Ln-DOTA-M7FPy ( <b>1</b> ) late lanthanoids	103
2.6.5.3	Ln-DOTA-M8 ( <b>60</b> )	105
2.6.6	Full Tensors	107
2.6.7	Illustration of the reorientation of the main magnetic axis and the sign change	109
2.6.8	Correlation Graphs	111
2.6.8.1	Ln-DOTA-M7FPy ( <b>1</b> ) early lanthanoids	111
2.6.8.2	Ln-DOTA-M7FPy ( <b>1</b> ) late lanthanoids	112
2.6.8.3	Ln-DOTA-M8 ( <b>60</b> )	113
2.6.9	Anisotropy parameters from all possible assignments	114
2.6.9.1	Ln-DOTA-M7FPY ( <b>1</b> )	114
2.6.9.2	Ln-DOTA-M8 ( <b>60</b> )	127
2.6.10	pH-Values of all buffered samples	129
2.6.11	Shift ranges vs $\Delta\chi_{ax}$	129
2.6.12	Dysprosium spectrum with assignment	130
2.6.13	NMR spectra Ln-DOTA-M7FPy ( <b>1</b> )	131
2.6.14	Yb-DOTA-M7FPy <sup>1</sup> H-NMR spectra at different pH-values	164
2.6.15	NMR spectra Ln-DOTA-M8 ( <b>60</b> )	165
2.6.16	Selectively <sup>1</sup> H decoupled <sup>13</sup> C spectra	175
2.6.16.1	Ln-DOTA-M7FPy ( <b>1</b> )	175
2.6.16.2	Ln-DOTA-M8 ( <b>60</b> )	180
2.6.17	Overlaid spectra of the deuterium labelling schemes ( <b>2-5</b> )	182
2.6.18	<sup>15</sup> N <sup>1</sup> H HSQC spectra of ubiquitin S57C	236
2.6.19	Correlation Graphs ubiquitin S57C	242
2.6.20	PCSs from DOTA-M7FPy on ubiquitin S57C	246
2.6.21	RDCs from DOTA-M7FPy on ubiquitin S57C	254
2.6.22	References	256
3.	A new lanthanoid chelating tag – towards predictable anisotropy parameters	257
3.1	Aim of the project	259
3.2	Terpyridine based LCTs	261
3.2.1	Molecular design	261
3.2.2	Results and Discussion	262

3.2.2.1	Synthesis of the Ln-TerPyM4-Prototype complex	262
3.2.2.2	Properties of the Ln-TerPyM4-Prototype complex	264
3.2.2.3	Synthesis of Ln-TerPyM4-SO <sub>2</sub> -Me	266
3.2.2.4	Suitability of Ln-TerPyM4-SO <sub>2</sub> -Me as an LCT	268
3.3	Pypa Based LCTs	269
3.3.1	Molecular design	269
3.3.2	Results and Discussion	270
3.3.2.1	Synthesis of Ln-PypaM2-SO <sub>2</sub> -Ph	270
3.3.2.2	Suitability of Ln-PypaM2-SO <sub>2</sub> -Ph as an LCT	272
3.3.2.3	Ligand field like effects of Ln-PypaM2-SO <sub>2</sub> -Ph	273
3.3.2.4	Synthesis of Ln-PypaM2Cl <sub>2</sub> -SO <sub>2</sub> -Ph	274
3.3.2.5	Suitability of Ln-PypaM2Cl <sub>2</sub> -SO <sub>2</sub> -Ph as an LCT	276
3.4	Conclusion and Outlook	279
3.5	References	281
3.6	Supporting information	283
3.6.1	Materials and Methods	283
3.6.2	Experimental Procedures and Characterization	285
3.6.3	NMR Spectra TerPyM4	328
3.6.4	NMR Spectra PypaM2	331
3.6.5	Correlation Graph	347
3.6.6	Assignments and PCS on ubiquitin S57C	348
4.	Synthesis of a new cyclen building block for DOTA-based LCTs	353
4.1	Aim of the project	355
4.2	Retrosynthetic analysis	357
4.3	Results and Discussion	359
4.4	Conclusion and Outlook	361
4.5	References	362
4.6	Supporting information	363
4.6.1	Materials and Methods	363
4.6.2	Experimental Procedures and Characterization	364
4.6.3	<sup>1</sup> H and <sup>13</sup> C NMR Spectra	369



# 1. Introduction

Proteins are essential biomacromolecules for living organisms. Their functions and activities are often governed by interactions with other proteins and/or small molecules. Since they are therefore by design susceptible to interactions with other molecules and are involved in most biological processes they are optimal drug targets.<sup>[1,2]</sup> For the more rapid development of new and more target specific drugs it is essential to understand how proteins function.<sup>[3-6]</sup> The understanding of how proteins function is based on the knowledge of their structure and dynamics, as well as the protein-protein and protein-ligand interactions. Several techniques have been developed that provide insights into these aspects. X-ray crystallography<sup>[7]</sup> or cryogenic electron microscopy (cryo-EM)<sup>[8]</sup> for example readily provide information about the structures of proteins at an atomic level but are not well suited to provide information about solution dynamics and transient interactions of proteins as the proteins are analysed in the solid state. For the study of protein structures the recently reported artificial intelligence program AlphaFold<sup>[9]</sup> holds great promise as it is able to predict the structure based on the amino acid sequence with high accuracy. Solution dynamics and interactions are well accessible by methods such as fluorescence microscopy<sup>[10]</sup> or amide hydrogen exchange mass spectrometry<sup>[11]</sup>. The insights obtained by fluorescence microscopy or mass spectrometry are however not at an atomic resolution. High resolution NMR spectroscopy on the other hand offers structural information at an atomic resolution as well as information about protein dynamics and interactions.

Protein structure determination by NMR spectroscopy classically relies on restraints based on the nuclear Overhauser effect (NOE). The use of NOE restraints allowed the determination of the first protein structure by NMR spectroscopy<sup>[12]</sup>. However, NOE restraints are limited by the fact that they are only observable for strong interactions ( $K_d \leq 10 \mu\text{M}$ )<sup>[13]</sup> and are only observable over short distances (up to 5 Å)<sup>[14]</sup>. The distance limitation is a problem as it can complicate or prohibit the determination of the tertiary and quaternary structure of proteins. Therefore, long-range restraints are highly desirable for protein structure determination by NMR spectroscopy. An excellent possibility to obtain long range restraints is the use of paramagnetic effects.<sup>[15]</sup> For this reason, paramagnetic NMR spectroscopy has attracted a lot of interest in the last two decades. Besides the ability to provide long range restraints paramagnetic effects can also be used for the development of fascinating new methods such as PCS-CPMG<sup>[16]</sup>, which allows the structure determination of previously inaccessible excited state structures of proteins.

A prerequisite for the observation of paramagnetic effects is the presence of a paramagnetic centre. Since most proteins are diamagnetic it is necessary to introduce a paramagnetic centre to them in order to observe the desired paramagnetic effects. Most widely used as paramagnetic centres for protein NMR spectroscopy are lanthanoids. Lanthanoids are excellent paramagnetic centres due to their large magnetic anisotropies that allow the observation of pseudocontact shifts (PCSs) and residual dipolar couplings (RDCs). Because most proteins are naturally unable to host lanthanoid (III) ions artificial binders, so called lanthanoid chelating tags (LCTs), which can be site selectively conjugated to a protein of interest have been developed.<sup>[17]</sup> The size of the observed PCS or RDC is directly dependent on the size of the magnetic anisotropy, which can be described by the anisotropy parameters  $\Delta\chi_{ax}$  and  $\Delta\chi_{rh}$ . For LCTs, the anisotropy parameters are determined from PCSs observed on a conjugated protein. Because the LCT always has some motional flexibility in regard to the protein the PCSs observed on the protein are inevitably diminished by motional averaging. Therefore, the anisotropy parameters determined for LCTs never describe the full magnetic anisotropy a lanthanoid exhibits within a given LCT. Since the full magnetic anisotropy of lanthanoids remains unknown it is not possible to know how much potential is left for the development of new LCTs. This thesis is centred around the study of the magnetic anisotropy exhibited by lanthanoids within an LCT and the development of new LCTs using the knowledge obtained from studying the paramagnetic properties of lanthanoids.

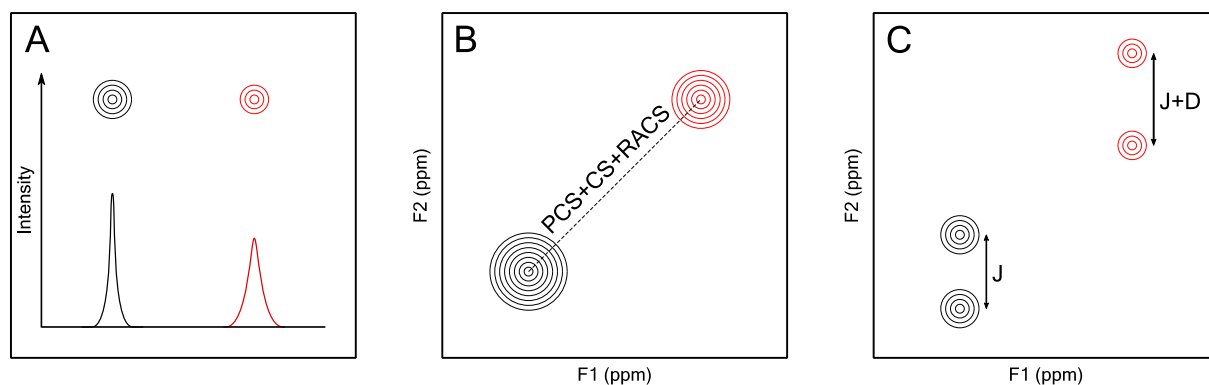
## 1.1 Paramagnetic NMR Spectroscopy

In general, all compounds that contain unpaired electrons exhibit paramagnetic behaviour. Measuring a paramagnetic compound by NMR spectroscopy can lead to the occurrence of several effects depending on the properties of the paramagnetic centre. The most pronounced are the paramagnetic shift (PS), the paramagnetic relaxation enhancement (PRE) and the residual dipolar coupling (RDC).<sup>[18]</sup> They affect the chemical shift, the relaxation and the J-coupling, respectively, of nuclei within the proximity of a paramagnetic centre (Fig. 1). Their influence on the resulting spectra can be used to generate valuable restraints in protein NMR spectroscopy<sup>[19]</sup> or to study the paramagnetic properties of lanthanide complexes<sup>[20]</sup>. Notably, only the paramagnetic shift and the PRE are of purely paramagnetic origin while RDC can also be observed in entirely diamagnetic samples.

Paramagnetic effects are often characterized as the difference of a signal property between a paramagnetic and a diamagnetic signal. The measurement of paramagnetic effects



thus requires a paramagnetic sample and a diamagnetic reference. The diamagnetic reference is required to eliminate influences on the chemical shift, the relaxation or the J-coupling, which originate from the presence of a paramagnetic metal or lanthanoid chelating tag but are not of paramagnetic origin.



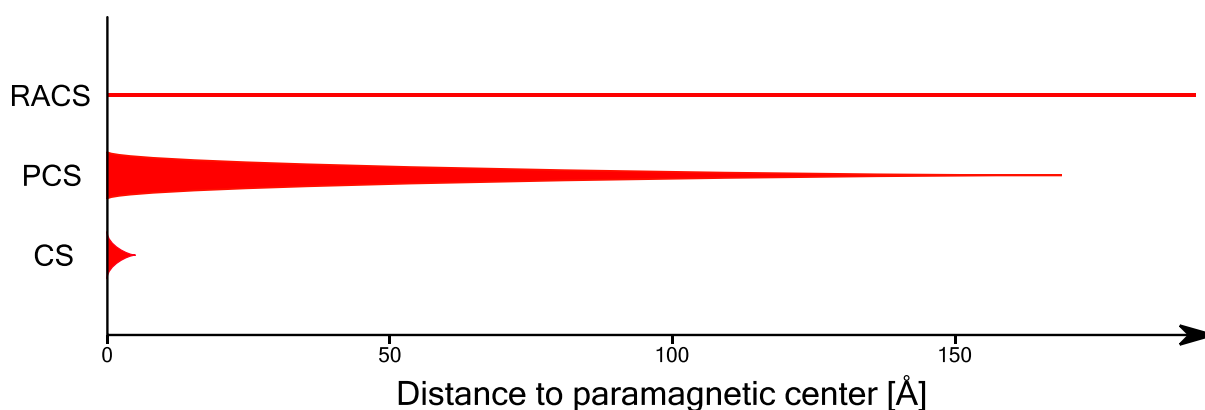
**Figure 1:** Schematic representation of the paramagnetic effects observable in NMR spectroscopy. Diamagnetic signals are black while the paramagnetic signals are red. A: Paramagnetic relaxation enhancement. B: Paramagnetic shift. C: Residual Dipolar Coupling. J denotes the observed coupling in a diamagnetic sample and D the difference observed due to the RDC in a paramagnetic sample. Figure reproduced from [21].

### 1.1.1 Paramagnetic Shift

Nuclei that are within the proximity of a paramagnetic centre experience an additional contribution to their chemical shift. Signals or spectra of paramagnetic compounds appear therefore to be shifted compared to their diamagnetic counterparts (Fig. 1B). While the paramagnetic shift is observed as a single effect it can receive contributions from up to three different effects. These are the contact shift (CS), the pseudocontact shift (PCS) and residual anisotropic chemical shift anisotropy (RACS). From the shift itself it is not possible to determine how much each effect contributes to the observed shift. The contribution of each component to the observed shift is dependent on the employed paramagnetic centre as well as the distance between the nuclei and the paramagnetic centre. For nuclei close (within a few bonds ( $\sim 4$ )) to the paramagnetic centre the contact shift and the PCS are mainly contributing to the observed shift. For nuclei with an intermediate distance to the paramagnetic centre that experience a sizeable shift ( $>0.2$  ppm) the shift is generally dominated by the PCS. The shift of nuclei, which are far away from the paramagnetic centre and show a significant chemical shift anisotropy, is often to a significant part caused by RACS (Fig. 2).<sup>[22]</sup>

The paramagnetic shift was in NMR spectroscopy first used to increase the chemical

shift range of 1D spectra of complicated small molecules by lanthanide shift reagents in order to simplify the analysis of their spectra. Lanthanide shift reagents were introduced at the end of the 1960s and found widespread application in NMR spectroscopy<sup>[23]</sup>. The development of modern 2D NMR spectroscopy marked the end of the extensive use of classical lanthanide shift reagents. Chiral lanthanide shift reagents are still in use as their induced paramagnetic shift can be used to determine the enantiomeric ratio of chiral molecules or their absolute stereochemistry<sup>[24–26]</sup>. Nowadays the paramagnetic shift and mainly the PCS are used in protein NMR spectroscopy to deliver valuable long-range restraints.



**Figure 2:** The red bands signify at what relative distance to the paramagnetic centre a contribution to the paramagnetic shift by either the contact shift (CS), the pseudocontact shift (PCS) or the residual anisotropic chemical shift (RACS) can be expected. The width of the band represents the relative size of the shift. The image is only a qualitative description.

### 1.1.1.1 Contact Shift

The contact or Fermi contact shift describes the through bond contribution to the paramagnetic shift. The contact shift arises from the presence of unpaired electron spin density from the paramagnetic centre on the measured nucleus and can be observed for all paramagnetic centres. Presence of unpaired electron spin density can be found on the measured nucleus due to direct spin delocalization and/or spin polarization through the bond network<sup>[27]</sup>. The size of any observed contact shift is directly proportional to the amount of unpaired electron spin density on a given nucleus often denoted by  $A$  which is the contact coupling constant. Because  $A$  diminishes with each additional bond between the paramagnetic centre and the measured nucleus, the contact shift usually effects only nuclei within a few bonds to the paramagnetic centre. The contact shift is generally stronger for transition metal complexes than lanthanoid complexes as the unpaired electrons from transition metals are directly involved in complex

bond formation while for lanthanoids the f-electrons are buried beneath the 5s and p orbitals. The unpaired electrons of lanthanoids do therefore not delocalize to bound ligands. Sutura *et al.*<sup>[28]</sup> have shown that for the determination of anisotropy parameters of lanthanoids from pseudocontact shifts of nuclei three bonds and farther away from the lanthanoid the contact shift can be neglected.

In protein NMR spectroscopy, contact shifts are of limited use as they only affect nuclei until a few bonds away from the paramagnetic centre. However, if the contact coupling constant  $A$  is a function of the dihedral angles of the bonds connecting the paramagnetic centre to its ligands they can be used to determine the geometry of the coordination sphere in metalloproteins<sup>[29–31]</sup>.

### 1.1.1.2 Pseudocontact Shift

The pseudocontact shift (PCS) describes the through-space contribution to the paramagnetic shift (Fig. 1B). The PCS results from a dipolar through-space interaction between the magnetic moment of the unpaired electrons and the magnetic moment of a given nucleus. The PCS can be described using equation (1), where  $\Delta pcs$  is the shift in ppm,  $x$ ,  $y$  and  $z$  are the coordinates of a given nucleus relative to the paramagnetic centre,  $r$  denotes the distance between a given nucleus and the paramagnetic centre and  $\Delta\chi_{ax}$  and  $\Delta\chi_{rh}$  are the anisotropy parameters, representing the anisotropic part of the magnetic susceptibility tensor  $\chi$ . The anisotropy parameters are related to the magnetic susceptibility tensor  $\chi$  through equations (2) and (3) where  $\tilde{\chi}_{xx}$ ,  $\tilde{\chi}_{yy}$  and  $\tilde{\chi}_{zz}$  represent the diagonal elements of the diagonalized matrix  $\tilde{\chi}$  of the magnetic susceptibility tensor  $\chi$ . The magnetic susceptibility tensor  $\chi$  can be obtained from equation (5) one of several different forms of the PCS equation. The derivation of the PCS equation as well as an extensive list of different forms of the equation can be found in literature<sup>[18]</sup>. Equation (1) is written in the principal frame of the magnetic susceptibility tensor  $\chi$ . Therefore, three Euler angles  $\alpha$ ,  $\beta$  and  $\gamma$  are additionally required to rotate the coordinates from the frame of the molecule or protein onto the frame of the  $\chi$  tensor.<sup>[27]</sup>

Equation (1) reveals two key properties of the PCS. (i) The PCS depends only on the anisotropic part of the magnetic susceptibility given by the anisotropy parameters  $\Delta\chi_{ax}$  and  $\Delta\chi_{rh}$ . Therefore, no shift can be observed if the magnetic susceptibility is isotropic and calculation of the PCS does not require knowledge of the full magnetic susceptibility tensor but only of its anisotropy. (ii) Besides the anisotropy parameters, the size of an observable PCS is dependent on the distance and the relative position of a given nucleus to the paramagnetic

centre. This spatial dependency makes the PCS a highly valuable restraint for protein structure elucidations by NMR spectroscopy.<sup>[19]</sup>

$$\delta_{pcs} = \frac{1}{12\pi r^3} \left[ \Delta\chi_{ax} \frac{2z^2 - x^2 - y^2}{r^2} + \frac{3}{2} \Delta\chi_{rh} \frac{x^2 - y^2}{r^2} \right] \quad (1)$$

$$\Delta\chi_{ax} = \tilde{\chi}_{zz} - \frac{\tilde{\chi}_{xx} + \tilde{\chi}_{yy}}{2} \quad (2)$$

$$\Delta\chi_{rh} = \tilde{\chi}_{xx} - \tilde{\chi}_{yy} \quad (3)$$

$$\chi = \begin{pmatrix} \chi_{xx} & \chi_{xy} & \chi_{xz} \\ \chi_{yx} & \chi_{yy} & \chi_{yz} \\ \chi_{zx} & \chi_{zy} & \chi_{zz} \end{pmatrix} \quad (4)$$

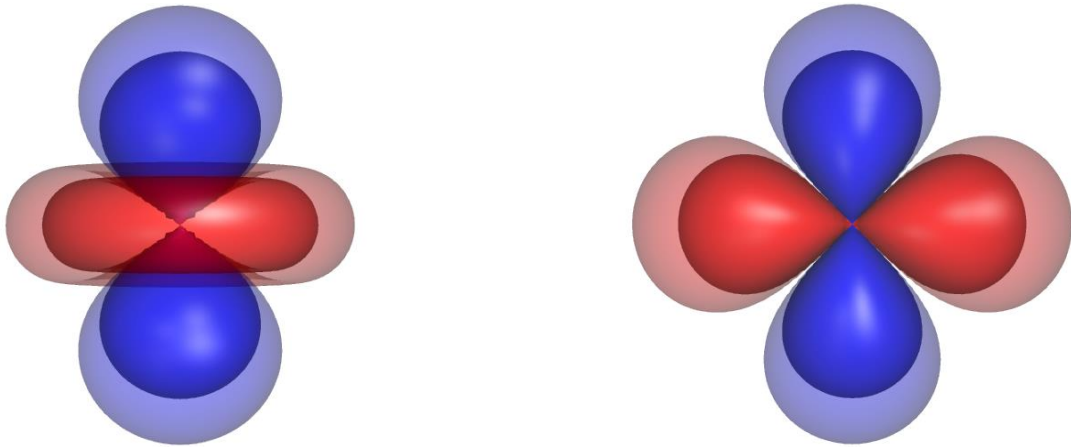
$$\delta_{pcs} = \frac{1}{4\pi r^3} \left[ (\chi_{zz} - \bar{\chi}) \frac{2z^2 - x^2 - y^2}{r^2} + (\chi_{xx} - \chi_{yy}) \frac{x^2 - y^2}{r^2} + \right. \\ \left. + \chi_{xy} \frac{2xy}{r^2} + \chi_{xz} \frac{2xz}{r^2} + \chi_{yz} \frac{2yz}{r^2} \right] \quad (5)$$

$$\bar{\chi} = \frac{\chi_{xx} + \chi_{yy} + \chi_{zz}}{3} \quad (6)$$

Calculation of PCSs using equation (1) is possible if the anisotropy parameters  $\Delta\chi_{ax}$  and  $\Delta\chi_{rh}$ , the coordinates  $x$ ,  $y$  and  $z$  of a given nucleus and the three Euler angles  $\alpha$ ,  $\beta$  and  $\gamma$  are known. Equation (1) can also be used to calculate the anisotropy parameters from known PCS if the structure on which the PCS are observed is known. Depending on whether the metal position is known either five or eight PCS are the required minimum to calculate  $\Delta\chi_{ax}$  and  $\Delta\chi_{rh}$ . Generally, the metal position is unknown for any spin label conjugated to a protein while for paramagnetic metal complexes the metal position is known. This originates from the fact that for the calculation of the anisotropy parameters on a protein the structure of the protein is used which does not include the location of the spin label and hence the position of the paramagnetic centre is unknown. For lanthanide complexes on the other hand the structure is usually obtained from a geometry optimization or crystal structure providing the metal position. It should be noted that equation (1) or any of the PCS equations cannot be used to directly determine the coordinates from a single set of PCS.<sup>[18]</sup> It is however possible to use three or more sufficiently different sets of PCS to locate individual atoms.<sup>[27]</sup>

PCSs allow the calculation of the anisotropy parameters and vice versa. Interestingly for a specific set of PCS several combinations of anisotropy parameters and Euler angles can be found that correctly reproduce the PCS. Therefore, the anisotropy parameters in combination with the Euler angles are usually reported using the unique tensor representation (UTR) defined by Schmitz *et al.*<sup>[32]</sup> The UTR guarantees that two different sets of anisotropy parameters and Euler angles, representing two different sets of PCSs, are comparable. If the UTR convention is applied  $\Delta\chi_{ax}$  and  $\Delta\chi_{rh}$  always show the same sign and  $\Delta\chi_{rh}$  is at most 2/3 of  $\Delta\chi_{ax}$ . The Euler angles follow in the UTR the ZYZ convention. For anisotropy parameters represented in UTR  $\Delta\chi_{ax}$  is proportional to the size of the observed PCS while  $\Delta\chi_{rh}$  determines the spatial dependence.

As an alternative to the anisotropy parameters and Euler angles the anisotropic part of the magnetic susceptibility can also be represented by isosurfaces (Fig. 3A) that depict at what distance and orientation to the paramagnetic centre a PCS of an arbitrary fixed value will be observed. The isosurfaces are usually coloured-coded based on the sign of the induced PCS.<sup>[33]</sup> For LCTs it is common to depict isosurfaces for two different PCS values (Fig. 3A).



**Figure 3:** Isosurfaces for fully axial and fully rhombic anisotropy parameters. The isosurfaces on the left represent the PCS for fully axial anisotropy parameters in UTR given by  $\Delta\chi_{rh} = 0$ . The isosurfaces on the right represent the PCS for fully rhombic anisotropy parameters in UTR given by  $\Delta\chi_{rh} = 3/2 \Delta\chi_{ax}$ . Red isosurfaces indicate a negative shift, blue isosurfaces indicate the corresponding positive shift. The isosurfaces indicate a positive or negative shift of 1/0.5 ppm (inner sphere/ outer sphere).

In contrast to the representation of the anisotropic part of the magnetic susceptibility by  $\Delta\chi_{ax}$  and  $\Delta\chi_{rh}$  the representation by isosurfaces is unambiguous. The isosurfaces can be calculated from the Euler angles and anisotropy parameters using equation (1). Since the isosurfaces are unambiguous, they are a good option to compare different sets of anisotropy parameters and Euler angles.

PCS can be used for several different applications in protein NMR spectroscopy ranging from structure determination to resonance assignment. PCS have been successfully applied for the in cell structure refinement of GB1 using only 2D NMR experiments<sup>[34]</sup> or the localization of different ligands within human carbonic anhydrase<sup>[35]</sup>. PCS can also be used to assign resonances in larger proteins where classical assignments strategies are no longer successful. Wu *et al.*<sup>[36]</sup> have recently developed a new method using this ability of PCS termed GPS by PCS to assign resonances of a G protein-coupled receptor (GPCR).

### 1.1.1.3 Residual Anisotropic Chemical Shift

The observed chemical shift of any given nucleus is a result of the interaction between the electronic environment around the nucleus, or chemical shielding and the external magnetic field. Since the chemical shielding is a tensor quantity and hence dependent on the orientation of the molecule relative to the external magnetic field the resulting chemical shift is anisotropic.<sup>[37]</sup> Since molecular tumbling leads to an equal population of all possible orientations in solution state NMR the observed shift for a given nucleus is the average shift over all possible orientations. For a partially aligned molecule some orientations are favoured leading to a different averaging of the chemical shift anisotropy (CSA). Signals of partially aligned molecules are therefore observed as slightly shifted to their unaligned counterparts. This shift is termed residual anisotropic chemical shift (RACS). For paramagnetic compounds RACS appear if the magnetic susceptibility is anisotropic and therefore able to cause alignment of the measured structure with the external magnetic field. The size of the observed RACS is dependent on the anisotropy parameters, the CSA of a given nucleus and the field strength of the external magnetic field. Compared to PCS, RACS have a much smaller magnitude for the same anisotropy parameters. However, they are distance independent and can for this reason contribute substantially to the observed shift of signals farther away from the paramagnetic centre (Fig 2). Generally, RACS have to be considered for the analysis of PCS on proteins in order to obtain a good correlation between calculated and experimental PCS. John *et al.*<sup>[22]</sup> have shown that for  $\Delta\chi_{ax} = 39.9$  and  $\Delta\chi_{rh} = 4.4$  at 18.8 T (800 MHz) RACS of up to nearly 0.2 ppm for <sup>15</sup>N can be observed. Programs used for the fitting of anisotropy parameters on proteins such as numbat<sup>[32]</sup> or paramagpy<sup>[38]</sup> are equipped with a function to automatically include a RACS correction into the fitting process. The nuclei least affected by RACS are protons due to their inherently small CSA. They are therefore best suited for the determination of the anisotropy parameters from PCS data.<sup>[22]</sup>

### 1.1.2 Paramagnetic Relaxation Enhancement

The paramagnetic relaxation enhancement (PRE) describes the increase in the relaxation rate observed for nuclei within the proximity of a paramagnetic centre caused by the presence of unpaired electron spins. Since the observation of the PRE depends on the presence of unpaired electrons, the effect is present for all paramagnetic centres. In NMR spectroscopy, the PRE leads to an increase in the linewidth of an observed signal and a decrease of its intensity (Fig. 1A).<sup>[39]</sup> The size of an observed PRE is often assumed to be only distance dependent with a distance proportionality of  $r^{-6}$  making it an isotropic effect. However, it was recently shown by Suturina *et al.* that this only holds for paramagnetic centres displaying an isotropic magnetic susceptibility and that the PRE becomes spatially dependent if the paramagnetic centre displays anisotropic magnetic susceptibility.<sup>[40]</sup> While the anisotropy of the PRE is not as pronounced as for the PCS it can, for small distance differences, lead to a stronger PRE for nuclei that are farther away from the paramagnetic centre than nuclei, which are slightly closer but show a different orientation to the paramagnetic centre. For larger distance differences between two nuclei, however it still holds that the nucleus, which is farther away from the paramagnetic centre, experiences a weaker PRE.

The main application of PRE is not found in NMR spectroscopy but in the closely related magnetic resonance imaging (MRI) of living organisms. Paramagnetic complexes like Gd-DOTA, which is commercially available as Dotarem, can be used to increase the relaxation rate of water molecules within specific organs. The increase in relaxation rate leads to better contrast in MRI images. Dotarem and similar complexes are therefore called contrast agents.<sup>[41]</sup> Similar to the application in MRI PREs can be used in protein NMR spectroscopy to probe the solvent accessibility of amino acid residues by the addition of soluble paramagnetic probes to the solution of a protein. This method is commonly referred to as solvent PRE or sPRE and is able to provide easy accessible information about protein structures and dynamics.<sup>[42]</sup> Additionally, like for other paramagnetic effects, PRE restraints, to study proteins or other biomacromolecules, can be derived from covalently attached paramagnetic probes. Due to the ease of application, PRE restraints have found widespread use in protein NMR spectroscopy.<sup>[39]</sup> The downside of PRE restraints is the limited amount of information they encode as they only provide distance and not spatial restraints. In protein NMR spectroscopy, PREs are generally induced using isotropic paramagnetic centres such as organic radicals,  $Mn^{2+}$  or  $Gd^{3+}$ . The advantage of using paramagnetic centres that display an isotropic magnetic susceptibility is that the only relevant observable paramagnetic effect on a conjugated biomacromolecule is the PRE. Using  $Gd^{3+}$  or  $Mn^{2+}$  as spin labels significant PREs up to 35 Å were observed.<sup>[39,43]</sup>

While it is possible to measure only the PRE it is not possible to measure other paramagnetic effects without the influence of the PRE. For the recording of PCS or RDC the influence of the PRE is an obstacle as it reduces the intensity of the observed signals and leads to line broadening. Signals close to the paramagnetic centre can even broaden beyond detection leading to complete bleaching of signals close to the paramagnetic centre. It is therefore of interest to use paramagnetic centres that provide large PCS or RDCs while at the same time cause as little PRE as possible. For the lanthanoids these properties are generally found for Terbium, Dysprosium and Thulium.<sup>[19]</sup>

For the measurement of paramagnetic complexes the PRE can be a significant issue. In a paramagnetic complex the nuclei of interest are much closer to the paramagnetic centre than on a spin labelled protein. For the nuclei close to the paramagnetic centre the PRE can be that severe that the magnetization lifetime is reduced below the duration of classical 2D NMR pulse sequences. Therefore, it is often only possible to record 1D NMR spectra of strongly paramagnetic complexes.

### 1.1.3 Residual Dipolar Coupling

The residual dipolar coupling (RDC) arises like RACS from partial alignment of the measured molecule to the external magnetic field. The coupling between two nuclei depends on the distance between them and the orientation of their bond vector relative to the external magnetic field. The coupling between two nuclei is strongest if the vector is parallel to the external magnetic field.<sup>[44]</sup> Without alignment, all orientations of the vector have the same probability and therefore the orientation dependency of the coupling is averaged out. If the molecule becomes partially aligned to the external magnetic field the movement of the vector is no longer isotropic leading to an increase or decrease of the observed coupling (Fig. 1C). The size of the observed RDC depends on the orientation of the bond vector relative to the alignment of the molecule to the external field.

For paramagnetic centres, the alignment is determined by the anisotropic part of the magnetic susceptibility. Therefore, RDCs can only be observed for paramagnetic centres, which display an anisotropic paramagnetic susceptibility. Paramagnetically induced RDCs can be described using equation (7) where  $\Delta\nu^{rdc}$  is the RDC in Hz,  $\Delta\chi_{ax}$  and  $\Delta\chi_{rh}$  are the anisotropy parameters,  $z_{AB}$ ,  $x_{AB}$  and  $y_{AB}$  described the orientation of the vector connecting the atoms A and B and  $r_{AB}$  describes the distance between the atoms A and B. The anisotropy parameters used in equation (7) are the same as the ones used in the PCS equation (1). As for the PCS the



equation describing the RDC originating from paramagnetic alignment can be written in several different forms.

$$\Delta\nu^{rdc} = \frac{1}{4\pi} \frac{B_0^2}{15kT} \frac{\gamma_A\gamma_B\hbar}{2\pi r_{AB}^3} \left[ \Delta\chi_{ax} \frac{2z_{AB}^2 - x_{AB}^2 - y_{AB}^2}{r_{AB}^2} + \frac{3}{2} \Delta\chi_{rh} \frac{x_{AB}^2 - y_{AB}^2}{r_{AB}^2} \right] \quad (7)$$

Other forms of the equation can be found in literature.<sup>[18]</sup> The biggest difference of equation (7) to the equation describing the PCS is the missing distance between the spin pair and the paramagnetic centre. RDCs are distance independent, which is an advantage of the RDCs compared to other restraints such as PREs or PCSs as they can always be observed over the whole molecular structure. Notably, is that the RDCs are dependent on the external magnetic field strength  $B_0$ . RDCs should for this reason always be reported with the field strength they have been measured at.

RDCs like PCS can be used to provide the anisotropy parameters of lanthanoids conjugated to a given protein. The fitting of anisotropy parameters on a protein from RDCs is possible with programs such as FANTEN<sup>[45]</sup> or paramagpy<sup>[38]</sup>. For a set of PCS and RDC from the same paramagnetic centre, the correlation between the calculated and experimental values is generally higher for PCSs than RDCs. It is therefore more common to determine the anisotropy parameters from PCSs than from RDCs.

As RDCs depend only on the partial alignment and not the paramagnetism itself different methods to achieve partial alignment can be used to record RDCs. Besides spin labelling with a paramagnetic centre the most common way to align proteins is the use of alignment media such as phages<sup>[46]</sup>, liquid crystals, DNA based media or collagen gel.<sup>[44]</sup> In protein NMR spectroscopy, RDCs can be used for structure refinement.<sup>[47]</sup> However, they are better suited for the determination of the relative orientation of secondary structure elements and to probe small structural changes due to ligand binding or mutations.<sup>[48]</sup>

## 1.2 Lanthanoids

The lanthanoids are a group of 15 elements referring to the elements from lanthanum to lutetium and are part of the rare earth elements. The lanthanoids are commonly treated as one group since they exhibit highly similar chemical properties. In aqueous solutions the lanthanoids are, due to the nature of the 4f-orbitals, predominately found in the 3+ oxidation state. The Ln(III) ions have the electron configuration  $[\text{Xe}]4f^n$  with n going from 0 (La) to 14

(Lu). The unique chemical similarity of the lanthanoid(III) ions originates from the fact that the 4f-orbitals are buried beneath the 5s and 5p orbitals. Due to the core like nature of the f-electrons they are not able to directly participate in any bonding interactions.<sup>[49]</sup>

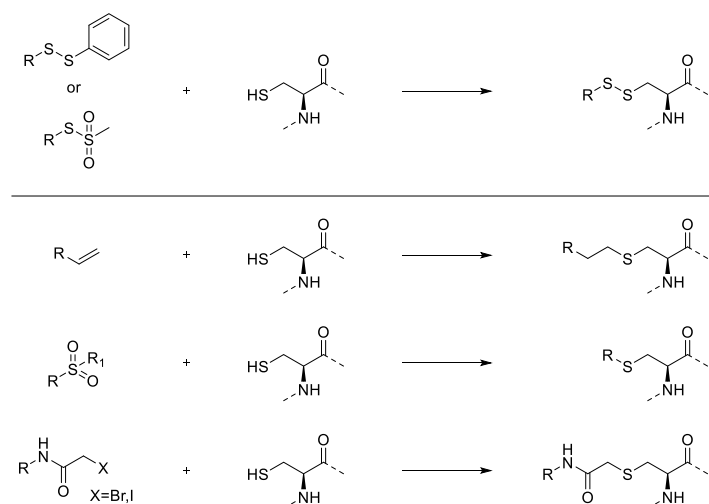
In difference to the transition metals and owed to the core like behaviour of the 4f-electrons the coordination chemistry of lanthanoid(III) ions is dominated by ligand steric effects rather than crystal field effects. Contrary to earlier beliefs lanthanoids show a wider range of coordination number than transition metals. For lanthanoids coordination numbers between 2 and 12 are known with the most common coordination numbers being 8 and 9. For small ligands the adopted coordination number is determined by how many ligands can be packed around the lanthanoid ion. The number is limited by the repulsion between the donor atoms in direct contact with the lanthanoid. These are so called first order effects. Lower coordination numbers are accessible through second order effects. Second order effects describe the steric crowding of bulky ligands with small donor atoms (N, O, C) to block the access of further ligands to the lanthanoid ion. Example of complexes where the coordination numbers are determined by first order effects are the lanthanide halides or the aqua ions such as  $\text{LnCl}_6^{3-}$  or  $[\text{Ln}(\text{H}_2\text{O})_9]^{3+}$ . For complexes such as  $\text{Ln}[\text{CH}(\text{SiMe}_3)_2]_3$  or  $[\text{Ln}\{\text{N}(\text{SiMe}_3)_2\}_3(\text{Ph}_3\text{PO})]$  the bulky ligands limit the coordination number due to second order effects. Generally, the later lanthanoids (Tb-Lu) show smaller coordination numbers than the earlier lanthanoids (La-Eu) due to their decreased size caused by the lanthanoid contraction. Because of the lanthanoid contraction the atomic and ionic radius decreases stronger than expected across the lanthanoid series. The ionic radii decrease steadily from 103 pm for lanthanum (III) to 86 pm for lutetium(III). The lanthanoid contraction results from the nature of the 4-f orbitals. Electrons residing in the 4-f orbitals are not very well able to shield the electrons in the 5s and 5p orbitals from the nucleus. The increasing positive charge of the nucleus going from La to Lu is therefore stronger than expected attracting the valence electrons. Additionally newly added electrons to the f-orbitals do not significantly increase the atomic or ionic radius as they are not added to a valence orbital.<sup>[49]</sup>

Apart from lanthanum (III) and lutetium (III) all lanthanoid (III) ions have unpaired electrons and are therefore paramagnetic. The paramagnetism of lanthanoids at room temperature is mainly governed by their ground state as excited states are not populated except for Sm(III) and Eu(III). For Eu (III) the paramagnetism is entirely determined by electrons populating excited states as the ground state of Eu is diamagnetic.<sup>[50]</sup> Unlike their chemical properties, the magnetic properties differ strongly from lanthanoid to lanthanoid. Except for gadolinium all lanthanoids exhibit an anisotropic magnetic susceptibility. A long-standing

dogma in lanthanoid chemistry was that the spectroscopic and magnetic properties are not or only weakly influenced by the ligands. Several recent publications<sup>[51–54]</sup> strongly challenge this suggesting that for lanthanoids ligand field like effects have a significant influence on the observed spectroscopic and magnetic properties. Because of their wide variety of paramagnetic properties lanthanoids have attracted a lot of interest for different applications such as single molecule magnets<sup>[55]</sup>, magnetic resonance imaging<sup>[56]</sup> or paramagnetic NMR spectroscopy<sup>[19]</sup>.

### 1.3 Lanthanoid Chelating Tags

Lanthanoids exhibit favourable paramagnetic properties for the application of paramagnetic protein NMR spectroscopy. The large magnetic anisotropy observed for lanthanoids makes them especially useful for the measurement of paramagnetic effects such as PCS or RDC, which are proportional to the anisotropy parameters. However, except for metalloproteins, which contain a suitable metal binding site for lanthanoid ions, lanthanoid ions cannot be directly attached to proteins. In order to be able to use lanthanoid ions as paramagnetic centres for the measurement of paramagnetic effects on a wide scope of proteins lanthanoid chelating tags (LCTs) have been developed. LCTs are small molecules, which show a high affinity for lanthanide ions and can be site selectively conjugated to a protein. Site selectivity

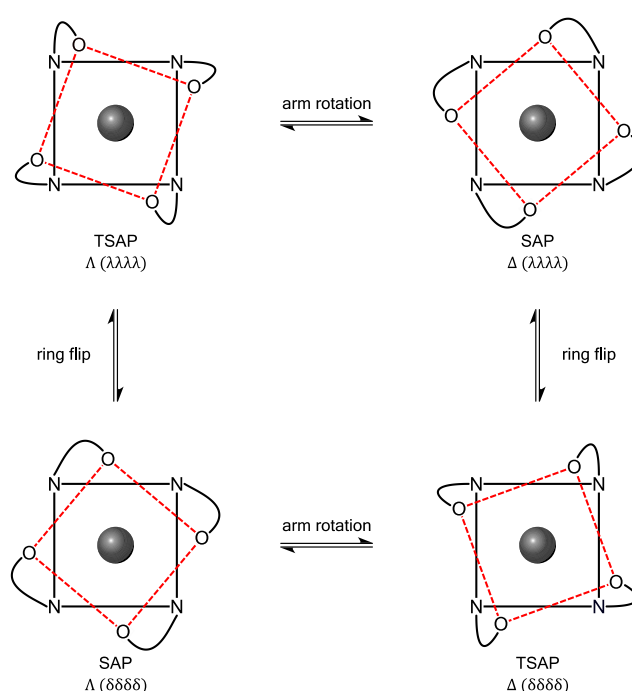


**Figure 3:** Reactive moieties for the site selective reaction with a cysteine residue.

is commonly achieved by addressing the specific reactivity of an amino acid. Most LCTs make use of the high nucleophilicity of the cysteine thiol group. Different reactive moieties have been developed that form either a disulphide or thioether linkage between the protein of interest and

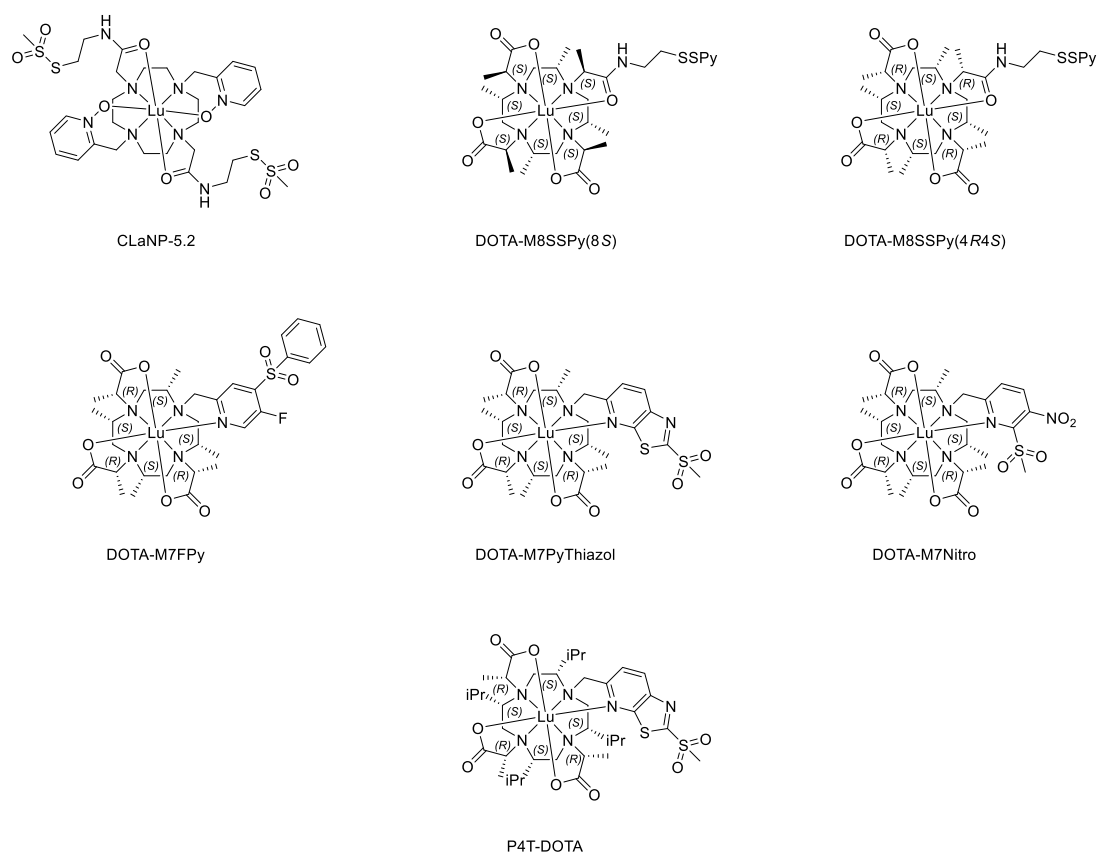
the LCT (Fig. 3).<sup>[57]</sup> Alternatively to cysteine the specific reactivity of unnatural amino acids can also be used to achieve site selective conjugation.<sup>[58,59]</sup> For the broad application of an LCT a reduction stable linkage such as a thioether is preferred as it allows the use of LCTs in a reductive environment. This is of interest for applications such as in cell NMR.<sup>[34]</sup> The use of a thioether linkage has further the advantage that it restricts the conformational motion between the paramagnetic centre and the protein leading potentially to less flexibility of the LCT relative to the protein.<sup>[60]</sup>

Besides the stability of the lanthanoid complex and the ability for site selective conjugation LCTs used for the application of PCS or RDC NMR spectroscopy have to fulfil two additional requirements: (i) the lanthanoid complex formed by the LCT should adopt only a single conformation. If an LCT can adopt multiple conformations that do not interconvert, on the NMR timescale, each of the adopted conformations will generate an individual set of PCSs and RDCs, while the fast interconversion, on the NMR time scale, between different conformations will lead to a reduction of the magnetic anisotropy. (ii) The flexibility of the LCT relative to the protein should be reduced as much as possible in order to limit the averaging of the observed PCS.<sup>[17]</sup>



**Figure 4:** Different conformations of Ln-DOTA. The pendant arms can rotate either clockwise ( $\Lambda$ ) or counter clockwise ( $\Delta$ ) and the ring can also display clockwise ( $\lambda\lambda\lambda\lambda$ ) or counter clockwise ( $\delta\delta\delta\delta$ ) helicity. The different rotations and helicities can be combined to form two diastereomers, the square antiprism (SAP) ( $\Delta(\lambda\lambda\lambda\lambda)$ ,  $\Lambda(\delta\delta\delta\delta)$ ) or the twisted square antiprism (TSAP) ( $\Lambda(\lambda\lambda\lambda\lambda)$  and  $\Delta(\delta\delta\delta\delta)$ ). Each diastereomer can form two enantiomers resulting in a total of four different conformations.<sup>[61]</sup>

Commonly, LCTs are developed based on existing multidentate chelators, for which it is known that they show a high affinity for lanthanoid ions. So far the most useful LCTs have been developed based on 2,2',2'',2'''-(1,4,7,10-Tetraazacyclododecane-1,4,7,10-tetrayl)tetraacetic acid (DOTA).<sup>[17,57,62]</sup> While DOTA provides a high affinity for lanthanoids the complexes formed with DOTA can adopt different conformations (Fig. 4). Two different approaches have been used to lock DOTA-based lanthanoid complexes into a single conformation. The first approach is to lock the formed lanthanoid complex into a single conformation by the introduction of stereogenic centres on either the cyclen ring and the



**Figure 5:** Chemical structures of different DOTA-based LCTs.

pendant arms<sup>[63]</sup> or only on the pendant arms<sup>[64]</sup>. Interestingly, the success of this approach can depend on the chosen chirality of the added substituents, exemplified by the case of DOTA M8SSPy (8S)<sup>[65]</sup> and DOTA M8SSPy (4R4S)<sup>[63]</sup> of which only the latter shows for all lanthanoids a single conformation. The second approach is the incorporation of specific pendant arms to force the formed lanthanoid complex into a single conformation. This approach was successfully applied with the use of pyridine *N*-oxide pendant arms in the development of CLaNP-5.2.<sup>[66,67]</sup>

The flexibility of an LCT relative to the conjugated protein can be influenced in several ways and depends not only on the LCT but also on the chosen tagging site on the protein. Changing half of the substituents, required to obtain only a single conformation, from methyl to isopropyl groups from DOTA-M7PyThiazol<sup>[60]</sup> to P4T-DOTA<sup>[68]</sup> lead to an increase of the observed PCS, which can be attributed to a reduced flexibility due to an increase in steric bulk. The largest influence on the flexibility originates from the tether between the protein and the LCT. Besides its length, the relative orientation of the attachment point to the protein has a great influence on the observed PCS on a conjugated protein. DOTA-M7FPy<sup>[60]</sup>, DOTA-M7PyThiazol<sup>[60]</sup> and DOTA-M7Nitro<sup>[43]</sup> each have a only a single rotatable bond between the lanthanoid and the protein but the observed PCS increase steadily across the three LCTs. This can be attributed to a different rotational motion which has a larger influence on the averaging of the PCS than translational motion. So far the only option to more or less fully suppress the flexibility of an LCT relative to a protein is the use of two instead of one attachment points.<sup>[69]</sup>

LCTs developed for PCS NMR spectroscopy are commonly compared based on the anisotropy parameters determined from PCS observed on a conjugated protein using programs such as numbat<sup>[32]</sup> or paramagpy<sup>[38]</sup>. Besides the correlation between the calculated and the experimental PCS the distance between the paramagnetic centre and the attachment point on the protein provide information on the quality of the determined anisotropy parameters. The anisotropy parameters determined from PCS observed on a conjugated protein are used to benchmark LCTs as this provides the necessary insight if an LCT can produce sizeable PCS or not. The drawback of the method is that the magnetic anisotropy exhibited by a lanthanoid within a given LCT remains unknown. It is therefore difficult to determine how well the motion of an LCT relative to a protein is suppressed and how much the size of the observed PCS could be increased with the further development of new LCTs.

## 1.4 References

- [1] A. L. Hopkins, C. R. Groom, *Nat. Rev. Drug Discov.* **2002**, *1*, 727–730.
- [2] P. Cohen, *Nat. Rev. Drug Discov.* **2002**, *1*, 309–315.
- [3] A. C. Anderson, *Chem. Biol.* **2003**, *10*, 787–797.
- [4] B. L. Staker, G. W. Buchko, P. J. Myler, *Physiol. Behav.* **2016**, *27*, 133–138.
- [5] Y. Lee, S. Basith, S. Choi, *J. Med. Chem.* **2018**, *61*, 1–46.
- [6] I. Shimada, T. Ueda, Y. Kofuku, M. T. Eddy, K. Wüthrich, *Nat. Rev. Drug Discov.* **2018**, *18*, 59–82.
- [7] Y. Shi, *Cell* **2014**, *159*, 995–1014.
- [8] E. Nogales, *Nat. Methods* **2016**, *24*, 24–27.
- [9] J. Jumper, R. Evans, A. Pritzel, T. Green, M. Figurnov, O. Ronneberger, K. Tunyasuvunakool, R. Bates, A. Žídek, A. Potapenko, et al., *Nature* **2021**, *596*, 583–589.
- [10] J. Lippincott-Schwartz, E. Snapp, A. Kenworthy, *Nat. Rev. Mol. Cell Biol.* **2001**, *2*, 444–456.
- [11] S. J. Eyles, I. A. Kaltashov, *Methods* **2004**, *34*, 88–99.
- [12] M. P. Williamson, T. F. Havel, K. Wüthrich, *J. Mol. Biol.* **1985**, *182*, 295–315.
- [13] E. R. P. Zuiderweg, *Biochemistry* **2002**, *41*, 1–7.
- [14] K. Wüthrich, *Angew. Chemie - Int. Ed.* **2003**, *42*, 3340–3363.
- [15] I. Bertini, A. Donaire, B. Jiménez, C. Luchinat, G. Parigi, M. Piccioli, L. Poggi, *J. Biomol. NMR* **2001**, *21*, 85–98.
- [16] J. B. Stiller, R. Otten, D. Häussinger, P. S. Rieder, D. L. Theobald, D. Kern, *Nature* **2022**, *603*, 528–535.
- [17] D. Joss, D. Häussinger, *Prog. Nucl. Magn. Reson. Spectrosc.* **2019**, *114–115*, 284–312.
- [18] I. Bertini, C. Luchinat, G. Parigi, *Prog. Nucl. Magn. Reson. Spectrosc.* **2002**, *40*, 249–273.
- [19] T. Müntener, D. Joss, D. Häussinger, S. Hiller, *Chem. Rev.* **2022**, *122*, 9422–9467.
- [20] Y. G. Gorbunova, A. G. Martynov, K. P. Birin, A. Y. Tsivadze, *Russ. J. Inorg. Chem.* **2021**, *66*, 202–216.
- [21] S. C. Chiliveri, M. V. Deshmukh, *J. Biosci.* **2016**, *41*, 787–803.
- [22] M. John, A. Y. Park, G. Pintacuda, N. E. Dixon, G. Otting, *J. Am. Chem. Soc.* **2005**, *127*, 17190–17191.
- [23] A. F. Cockerill, G. L. O. Davies, R. C. Harden, D. M. Rackham, *Chem. Rev.* **1973**, *73*, 553–588.
- [24] T. J. Wenzel, C. D. Chisholm, *Prog. Nucl. Magn. Reson. Spectrosc.* **2011**, *59*, 1–63.

- [25] H. L. Goering, J. N. Eikenberry, K. S. Gerald, *J. Am. Chem. Soc.* **1971**, *93*, 5913–5914.
- [26] R. R. Fraser, M. A. Petit, J. K. Saunders, *Chem. Commun.* **1971**, 1450–1451.
- [27] I. Bertini, C. Luchinat, G. Parigi, *Concepts Magn. Reson.* **2002**, *14*, 259–286.
- [28] E. Suturina, K. Mason, C. F. G. C. Geraldes, I. Kuprov, D. Parker, *Angew. Chemie Int. Ed.* **2017**, *56*, 12215–12218.
- [29] S. Jesus, G. Warmerdam, L. Bubacco, G. W. Canters, *Biochemistry* **1998**, *37*, 7378–7389.
- [30] N. V. Shokhirev, A. F. Walker, *J. Am. Chem. Soc.* **1998**, *120*, 981–990.
- [31] I. Bertini, S. Ciurli, A. Dikiy, R. Gasanov, C. Luchinat, G. Martini, N. Safarov, *J. Am. Chem. Soc.* **1999**, *121*, 2037–2046.
- [32] C. Schmitz, M. J. Stanton-Cook, X. C. Su, G. Otting, T. Huber, *J. Biomol. NMR* **2008**, *41*, 179–189.
- [33] C. Nitsche, G. Otting, *Prog. Nucl. Magn. Reson. Spectrosc.* **2017**, *98–99*, 20–49.
- [34] T. Müntener, D. Häussinger, P. Selenko, F. X. Theillet, *J. Phys. Chem. Lett.* **2016**, *7*, 2821–2825.
- [35] K. Zimmermann, D. Joss, T. Müntener, E. S. Nogueira, M. Schäfer, L. Knörr, F. W. Monnard, D. Häussinger, *Chem. Sci.* **2019**, *10*, 5064–5072.
- [36] F. Wu, P. S. Rieder, L. A. Abiko, P. Rößler, A. D. Gossert, D. Häussinger, S. Grzesiek, *J. Am. Chem. Soc.* **2022**, *144*, 21728–21740.
- [37] J. C. Facelli, *Concepts Magn. Reson. Part A Bridg. Educ. Res.* **2004**, *20*, 42–69.
- [38] H. W. Orton, T. Huber, G. Otting, *Magn. Reson.* **2020**, *1*, 1–12.
- [39] G. Marius Clore, J. Iwahara, *Chem. Rev.* **2009**, *109*, 4108–4139.
- [40] E. A. Suturina, K. Mason, C. F. G. C. Geraldes, N. F. Chilton, D. Parker, I. Kuprov, *Phys. Chem. Chem. Phys.* **2018**, *20*, 17676–17686.
- [41] J. Wahsner, E. M. Gale, A. Rodríguez-Rodríguez, P. Caravan, *Chem. Rev.* **2019**, *119*, 957–1057.
- [42] A. J. Lenard, F. A. A. Mulder, T. Madl, *Prog. Nucl. Magn. Reson. Spectrosc.* **2022**, *132–133*, 113–139.
- [43] D. Joss, F. Winter, D. Häussinger, *Chem. Commun.* **2020**, *56*, 12861–12864.
- [44] K. Chen, N. Tjandra, in *NMR Proteins Small Biomol.*, Springer-Verlag Berlin Heidelberg, **2012**, pp. 47–68.
- [45] M. Rinaldelli, A. Carlon, E. Ravera, G. Parigi, C. Luchinat, *J. Biomol. NMR* **2015**, *61*, 21–34.
- [46] M. R. Hansen, L. Mueller, A. Pardi, *Nat. Struct. Biol.* **1998**, *5*, 1065–1074.



- [47] A. Bax, *Protein Sci.* **2003**, *12*, 1–16.
- [48] A. Bax, A. Grishaev, *Curr. Opin. Struct. Biol.* **2005**, *15*, 563–570.
- [49] S. Cotton, *Lanthanide and Actinide Chemistry*, **2006**.
- [50] C. Housecroft, A. Sharpe, *Inorganic Chemistry*, Pearson, **2012**.
- [51] A. C. Harnden, E. A. Suturina, A. S. Batsanov, P. K. Senanayake, M. A. Fox, K. Mason, M. Vonci, E. J. L. McInnes, N. F. Chilton, D. Parker, *Angew. Chem. Int. Ed. Engl.* **2019**, *58*, 10290–10294.
- [52] D. Parker, E. A. Suturina, I. Kuprov, N. F. Chilton, *Acc. Chem. Res.* **2020**, *53*, 1520–1534.
- [53] K. Mason, A. C. Harnden, C. W. Patrick, A. W. J. Poh, A. S. Batsanov, E. A. Suturina, M. Vonci, E. J. L. McInnes, N. F. Chilton, D. Parker, *Chem. Commun.* **2018**, *54*, 8486–8489.
- [54] M. Vonci, K. Mason, E. A. Suturina, A. T. Frawley, S. G. Worswick, I. Kuprov, D. Parker, E. J. L. McInnes, N. F. Chilton, *J. Am. Chem. Soc.* **2017**, *139*, 14166–14172.
- [55] D. N. Woodruff, R. E. P. Winpenney, R. A. Layfield, *Chem. Rev.* **2013**, *113*, 5110–5148.
- [56] K.-L. N. A. Finney, A. C. Harnden, N. J. Rogers, P. K. Senanayake, A. M. Blamire, D. O. Hogain, D. Parker, *Chem. - A Eur. J.* **2017**, *23*, 7976–7989.
- [57] C. Nitsche, G. Otting, *Prog. Nucl. Magn. Reson. Spectrosc.* **2017**, *98–99*, 20–49.
- [58] C. T. Loh, K. Ozawa, K. L. Tuck, N. Barlow, T. Huber, G. Otting, B. Graham, *Bioconjug. Chem.* **2013**, *24*, 260–268.
- [59] I. D. Herath, C. Breen, S. H. Hewitt, T. R. Berki, A. F. Kassir, C. Dodson, M. Judd, S. Jabar, N. Cox, G. Otting, et al., *Chem. - A Eur. J.* **2021**, *27*, 13009–13023.
- [60] T. Müntener, J. Kottelat, A. Huber, D. Häussinger, *Bioconjug. Chem.* **2018**, *29*, 3344–3351.
- [61] A. C. L. Opina, M. Strickland, Y.-S. Lee, N. Tjandra, R. A. Byrd, R. E. Swenson, O. Vasalatiy, *Dalt. Trans.* **2016**, *45*, 4673–4687.
- [62] Q. Miao, C. Nitsche, H. Orton, M. Overhand, G. Otting, M. Ubbink, *Chem. Rev.* **2022**, *122*, 9571–9642.
- [63] D. Joss, R. M. Walliser, K. Zimmermann, D. Häussinger, *J. Biomol. NMR* **2018**, *72*, 29–38.
- [64] B. Graham, C. T. Loh, J. D. Swarbrick, P. Ung, J. Shin, H. Yagi, X. Jia, S. Chhabra, N. Barlow, G. Pintacuda, et al., *Bioconjug. Chem.* **2011**, *22*, 2118–2125.
- [65] D. Häussinger, J. R. Huang, S. Grzesiek, *J. Am. Chem. Soc.* **2009**, *131*, 14761–14767.
- [66] M. Polášek, J. Rudovský, P. Hermann, I. Lukeš, L. Vander Elst, R. N. Muller, *Chem.*

- Commun.* **2004**, *2*, 2602–2603.
- [67] P. H. J. Keizers, J. F. Desreux, M. Overhand, M. Ubbink, *J. Am. Chem. Soc.* **2007**, *129*, 9292–9293.
- [68] D. Joss, D. Häussinger, *Chem. Commun.* **2019**, *55*, 10543–10546.
- [69] P. H. J. Keizers, A. Saragliadis, Y. Hiruma, M. Overhand, M. Ubbink, *J. Am. Chem. Soc.* **2008**, *130*, 14802–14812.

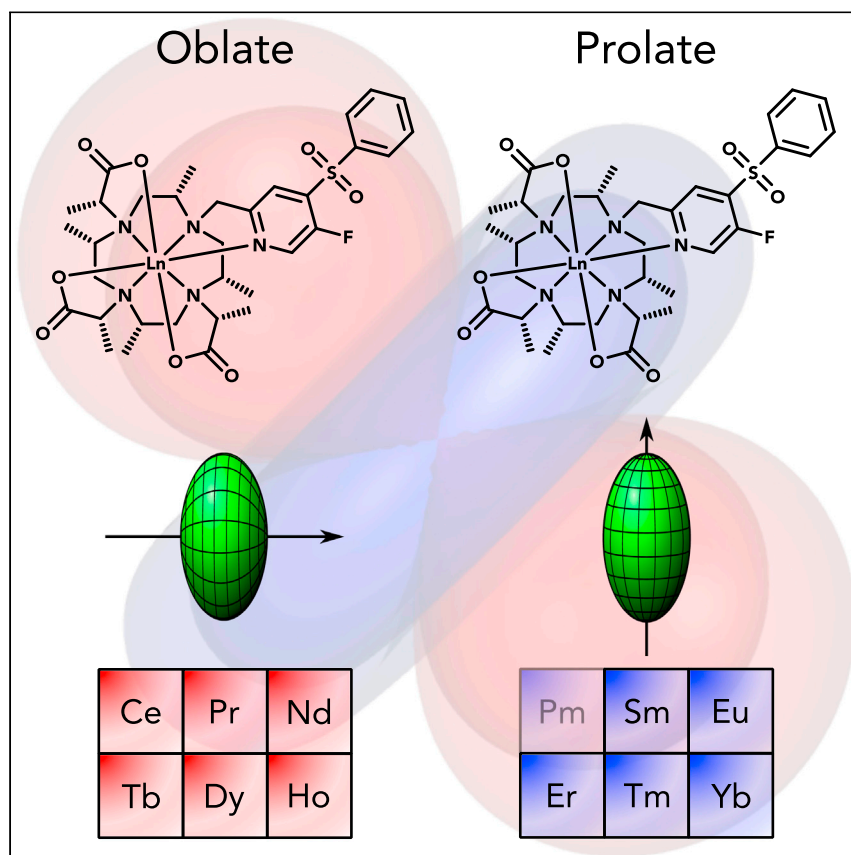
# Chapter I

2. Intrinsic anisotropy parameters of a series of lanthanoid complexes deliver new insights into the structure-magnetism relationship



## Article

# Intrinsic anisotropy parameters of a series of lanthanoid complexes deliver new insights into the structure-magnetism relationship



In contrast to other transition metals, lanthanoids are generally considered to display no significant ligand-field interaction with coordinating ligands. This interplay is regarded as omni-directional and merely electrostatic. An effort to determine intrinsic paramagnetic susceptibility parameters for a complete series of isostructural lanthanoid chelate complexes by site-specific isotope labeling and subsequent full assignment of  $^1\text{H-NMR}$  spectra yielded unexpected results: the orientation of the principal magnetic axis of the lanthanoid correlates with the ground state f-electron distribution, thus showing ligand-field-like effects at room temperature.

Raphael Vogel, Thomas Müntener, Daniel Häussinger

daniel.haeussinger@unibas.ch

### Highlights

Lanthanoids display ligand-field-like effects at room temperature

Anisotropic paramagnetic susceptibility parameters are reported for all lanthanoids

Site-specific isotope labels yield assignments of up to 1,400 ppm wide  $^1\text{H-NMR}$  spectra



## Article

# Intrinsic anisotropy parameters of a series of lanthanoid complexes deliver new insights into the structure-magnetism relationship

Raphael Vogel,<sup>1</sup> Thomas Müntener,<sup>1</sup> and Daniel Häussinger<sup>1,2,\*</sup>

## SUMMARY

Lanthanoid chelating tags (LCTs) are widely used for advanced paramagnetic NMR of biomacromolecules. The magnitude of their induced pseudocontact shifts (PCSs) and residual dipolar couplings (RDCs) depends critically on the anisotropy of the magnetic susceptibility tensor, which is usually determined by the resonances of the conjugated protein, inevitably reducing the effect by motional averaging. Here, for the first time, we present the intrinsic anisotropy parameters for the full lanthanoid series determined experimentally from resonances on the ligand itself. The strongly shifted proton spectra could only be assigned by extensive, site-specific isotope labeling. The extremely large anisotropies obtained deliver an upper limit for future PCS applications. To our great surprise, at least at room temperature, we observed an unprecedented correlation between the oblate or prolate f-electron distribution of the lanthanoid and the orientation of the main magnetic axis as well as the size of the magnetic anisotropy.

## INTRODUCTION

Lanthanoids and their rich structural chemistry have found wide-spread utilization in the last few decades.<sup>1</sup> The peculiar electronic properties of lanthanoids resulted in applications ranging from superconductivity<sup>2</sup> and laser devices<sup>3</sup> to single-molecule areas in spectroscopy<sup>4</sup> and magnetism.<sup>5</sup> Particularly fascinating, but not entirely understood, is the magnetism of the lanthanoids, which originates in their f-electronic structure.<sup>6</sup> Recently, lanthanoid single-molecule magnets were developed that show blocking temperatures up to liquid nitrogen temperature.<sup>7,8</sup> Especially, useful lanthanoid applications have been developed for nuclear magnetic resonance spectroscopy (NMR), starting with the classic "lanthanoid shift reagents"<sup>9</sup> up to the more recent field of paramagnetic biomolecular NMR spectroscopy. Trivalent lanthanoid cations can be tethered site-specifically to proteins using lanthanoid chelating tags (LCTs).<sup>10,11</sup> LCTs induce pseudo contactshifts (PCSs) for NMR investigations of protein structures, interactions, and dynamics.<sup>12,13</sup> The size of the PCS is proportional to the anisotropy parameters  $\Delta\chi_{ax}$  and  $\Delta\chi_{rh}$  of the magnetic susceptibility tensor of the lanthanoid ion (cf. Equation 1).<sup>14</sup> Not only do these anisotropy parameters play a crucial role for PCS NMR, they are also discussed in the context of single-molecule magnets<sup>5</sup> and low-temperature EPR spectra.<sup>15,16</sup> In general, the anisotropy parameters for different LCTs, and hence their performance, are determined from PCSs that are observed on the protein conjugated to the tag. The severe drawback of this method is that any flexibility in the linkage between the LCT and the protein will inevitably lead to an averaging of the anisotropy and, as a consequence, smaller  $\Delta\chi_{ax}$  and  $\Delta\chi_{rh}$ . Despite the continuous development of new LCTs<sup>17–21</sup> and their

## The bigger picture

Lanthanoid tri-cations are considered to be chemically indistinguishable. A general dogma on the 4 f-electrons states that they are shielded by the outer electrons such that they do not show ligand-field effects, nor contribute to directional bonding, but merely play a role as isotropic Coulomb clouds. Recently, research in the field of single-molecule magnetism and others has questioned this and demonstrated ligand-field effects for lanthanoids at low temperatures. Here, we present a complete series of isostructural lanthanoid complexes with a markedly non-symmetrical chelating ligand, designed for pseudocontact shift NMR spectroscopy. Unexpectedly, the orientation of the principal magnetic axis revealed a distinct correlation with the ground state f-electron distribution. We thus show, for the first time, a crucial interaction of the ligand field with the prolate or oblate f-electron distribution at room temperature, disproving the aforementioned dogma.

applications<sup>22,23</sup> in the last 2 decades, the precise anisotropy parameters of a LCT itself, i.e., without motional averaging due to the flexible attachment to the protein, have never been characterized so far. We would like to coin the term “intrinsic anisotropy parameters” for the anisotropy tensor that is determined on the tag itself, but of course, this “intrinsic” property is a function of temperature and the nature of the lanthanoid, among others.

PCS NMR spectroscopy conveniently provides the anisotropy parameters  $\Delta\chi_{ax}$  and  $\Delta\chi_{rh}$ , as well as the three Euler angles,  $\alpha$ ,  $\beta$ , and  $\gamma$ , if a 3D structural model of the lanthanoid complex and PCSs for at least five nuclei are available<sup>14</sup> (cf. Equation 1). The crucial, but especially in cases of strongly paramagnetic LCTs challenging task, is the assignment of the paramagnetically shifted set of resonances, as strong paramagnetic relaxation effects (PREs) prevent classical assignment strategies via two- or higher-dimensional NMR experiments. While axially

$$\delta_{PCS} = \frac{1}{12\pi r^3} \left[ \Delta\chi_{ax} \frac{2z^2 - x^2 - y^2}{r^2} + \frac{3}{2} \Delta\chi_{rh} \frac{x^2 - y^2}{r^2} \right] \quad (\text{Equation 1})$$

where  $\Delta\chi_{ax} = \chi_{zz} - \frac{\chi_{xx} + \chi_{yy}}{2}$  and  $\Delta\chi_{rh} = \chi_{xx} - \chi_{yy}$

symmetric tensors often allow the assignment of the paramagnetic spectra if several different lanthanoid metal data sets show similar trends,<sup>24,25</sup> rhombic tensors yield more complex spectra. An option for rhombic cases could be to choose the assignment based on the correlation coefficient obtained from iteratively fitting the anisotropy parameters for all possible combinations of assignments. In practice, however, the combinatorial space has to be restricted,<sup>26</sup> as it scales with the factorial of the number of signals.

Here, we present the first complete characterization of the intrinsic anisotropy parameters exhibited for the full stable lanthanoid series (La to Lu, but without Pm) of isostructural 1,4,7,10-tetraazacyclododecane-1,4,7,10-tetraacetic acid (DOTA)-based complexes with the rigid, high-affinity LCT DOTA-M7FPy.<sup>20</sup> The combinatorial space was restricted by using different selective <sup>2</sup>H and <sup>13</sup>C isotope labeling schemes of the LCT. The resulting intrinsic anisotropy parameters of Ln-DOTA-M7FPy are compared with  $\Delta\chi_{ax}$  and  $\Delta\chi_{rh}$  of a ubiquitin S57C construct conjugated to Ln-DOTA-M7FPy, and to an axial symmetric lanthanoid complex, Ln-DOTA-M8. This in-depth study allowed us to experimentally assign the <sup>1</sup>H-NMR spectra of a full series of lanthanoid complexes and provide an upper boundary for  $\Delta\chi_{ax}$  and  $\Delta\chi_{rh}$  of ideally rigid and non-flexible LCT conjugated to proteins.

Besides a new insight into the dynamic properties of the LCTs, we unexpectedly found a strong dependence of the orientation of the main magnetic axis on the ground state electron distribution of the lanthanoid<sup>27</sup> and the symmetry of the LCT (cf. Figure 1). Similar observations have been reported for lanthanoid complexes in solid state at 2 K.<sup>28</sup> Here, for the first time, we demonstrate that sufficiently non-symmetric ligands can deliver such ligand-field-like effects in solution and at room temperature as well.

## RESULTS AND DISCUSSION

### Structure of Ln-DOTA-M7FPy

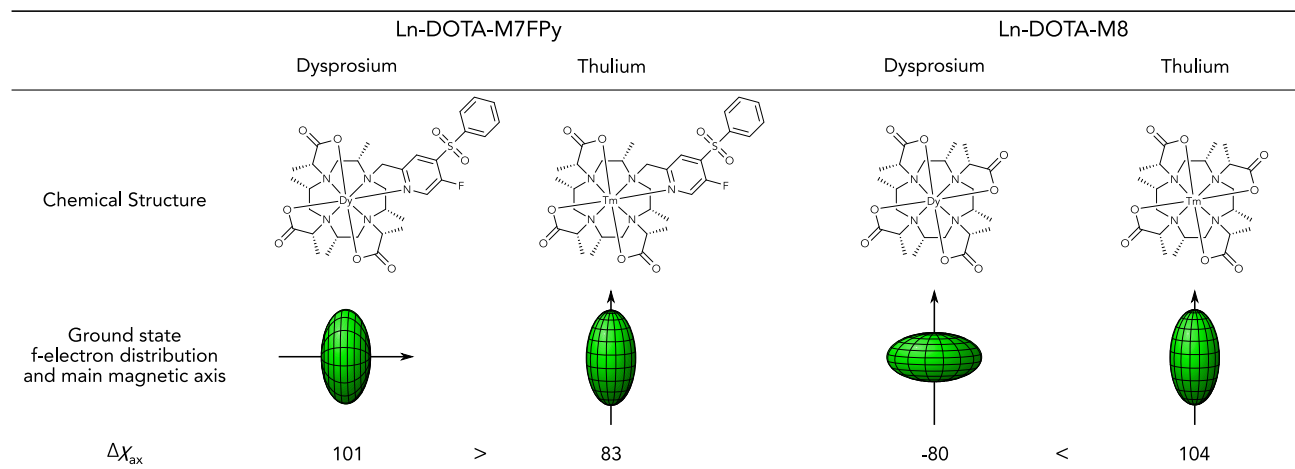
DOTA-based lanthanoid complexes provide the highest anisotropy parameters and, hence, the largest PCSs for structural biomolecular NMR applications. We have chosen the LCT DOTA-M7FPy for this attempt to unravel the intrinsic anisotropy parameters of the susceptibility tensors of all its lanthanoid complexes because it is a very

<sup>1</sup>Department of Chemistry, University of Basel, St. Johanns-Ring 19, 4056 Basel, Switzerland

<sup>2</sup>Lead contact

\*Correspondence:  
daniel.haeussinger@unibas.ch

<https://doi.org/10.1016/j.chempr.2021.08.011>



**Figure 1. Ligand-field-like effects**

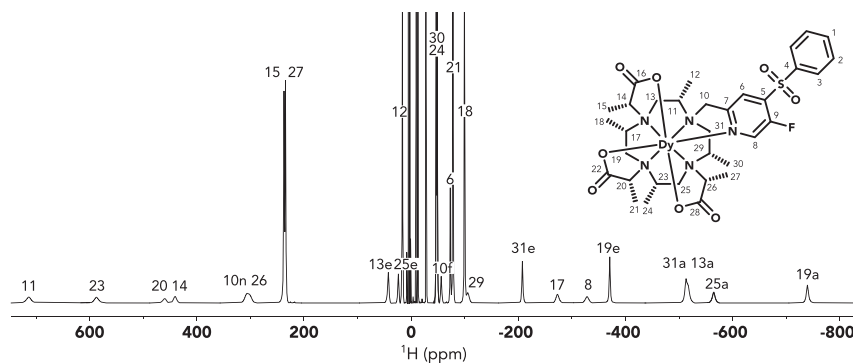
The ground state f-electron distribution is represented as a green ellipsoid and is approximately oblate for Dy and prolate for Tm.<sup>27</sup> The main magnetic axis is represented as a black arrow for all complexes; only in the combination of oblate Dy and the low symmetry ligand field of DOTA-M7FPy the main magnetic axis as well as the f-electron density are rotated by 90°. In the case of DOTA-M7FPy,  $\Delta\chi_{ax}$  is larger for the Dy than for the Tm complex, while the opposite is true for the highly symmetric ligand field of DOTA-M8.  $\Delta\chi_{ax}$  is reported in  $10^{-32}\text{m}^3$ .

rigid, high-affinity chelator that yields excellent PCSs. Ln-DOTA-M7FPy complexes display eleven stereogenic centers with defined stereochemistry (1R, 2S, 4S, 5S, 7S, 8S, 10S, 11S, 2'R, 2''R, 2'''R) and can adopt in principle four different conformers, however, due to the steric bulk introduced by the ligand design, solely the  $\Delta(\delta\delta\delta\delta)$  or square antiprism (SAP) conformer is formed. This can be safely assumed for both early and late lanthanoids, based on the NOE patterns observed for La-, Sm-, and Lu-DOTA-M7FPy (Figures S34, S51, and S83) and data in the literature.<sup>20,29,30</sup> The resulting  $C_1$ -symmetry turned out to be crucial for the magnetic properties of the lanthanoid complexes (see below). Even though the lanthanoid complexes display only  $C_1$ -symmetry, they contain a  $C_4$ -pseudosymmetric axis. The  $C_4$ -pseudosymmetry axis is normal to the cyclen-N4-plane going through the lanthanoid. While a rough estimation of  $\Delta\chi_{ax}$  is possible by assigning only the strongest PCS, a reliable determination of  $\Delta\chi_{rh}$  and of the orientation of the tensor also requires the careful assignment of the less strongly shifted resonances that vary tremendously for different lanthanoids. It was, therefore, of utmost importance to obtain trustworthy peak assignments for all Ln-DOTA-M7FPy complexes. The 3D structures of Ln-DOTA-M7FPy (Data S1) required to fit the anisotropy parameters were calculated using DFT geometry optimization (for details, see experimental procedures). As it is unclear whether a water molecule occupies the ninth coordination site, the structure was calculated for all four possible combinations of implicit and explicit water at the apical position. The best correlation coefficients were obtained for 8-fold coordination with implicit water.

### NMR analysis and synthesis of isotopically labeled Ln-DOTA-M7FPy

Ln-DOTA-M7FPy shows 29 resonances in the 1D proton spectra. From these signals, 26 can be used to fit the anisotropy parameters (Figure 2). The three resonances from the phenyl sulfone were excluded from the fitting process because the phenyl rotation induced large motional averaging of the PCS. We considered only the proton resonances as it was previously shown that they are not significantly affected by contact shifts.<sup>26</sup> Without restrictions,  $4 \cdot 10^{26}$  different assignments would be possible with 26 shifts. In order to restrict the combinatorial space to a manageable number, all 26 signals were classified using spectroscopic data. The proton NMR





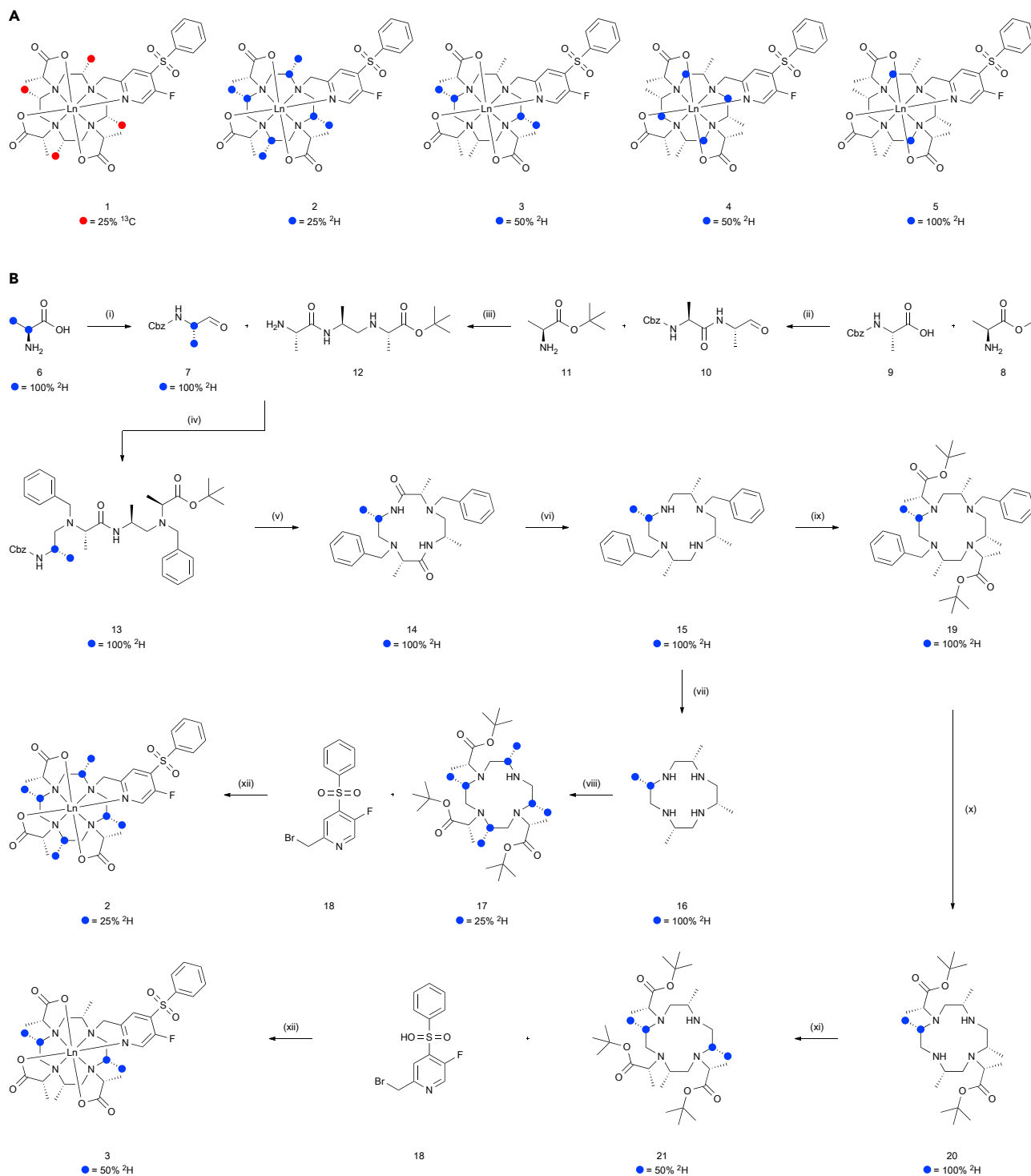
**Figure 2. Proton spectrum of Dy-DOTA-M7FPy**

$^1\text{H}$ -NMR spectrum of Dy-DOTA-M7FPy (20 mM) with assignment (for the central region of the spectrum, see [Figure S28](#)). The spectrum was recorded at 298 K in phosphate buffer (50 mM, pH = 6.0) at 600.13 MHz. The full spectrum was pieced together from 10 single spectra, each with a sweep width of 154 ppm. Abbreviations: a, axial; e, equatorial; n, near; f, far.

spectra of the diamagnetic (La, Lu) complexes, as well as the only weakly paramagnetic (Sm, Eu) compounds were assigned by classical 2D NMR (HSQC, HMBC, COSY, NOESY, or ROESY) spectroscopy. The stronger PREs in the cases of Ce, Pr, and Nd allowed only for the recording of COSY spectra. COSY correlations were still observable as the signal intensity profited from a paramagnetic contribution dampening the effect of the PRE.<sup>31,32</sup> Based on COSY correlations, all proton signals of Ce-, Pr-, and Nd-DOTA-M7FPy were classified ([supplemental information](#)) ([Tables S1–S3](#)).

For the late lanthanoids, no 2D NMR spectra were recorded as the magnetization lifetimes were extremely shortened by the much stronger PRE and did not allow for polarization transfer or dipolar interactions. Therefore, two different labeling schemes were employed that would in principle allow the classification of signals directly from the 1D spectra. The synthesis of the isotope labeled complexes was adapted from known synthetic strategies.<sup>20,33–35</sup> The isotope labels on the cyclen ring were either introduced by elongating the alanine based trimer **12** with an isotope enriched alanine derivative **7** ( $^2\text{H}$ ) ([Figure 3B](#)) or **27** ( $^{13}\text{C}$ ) ([Figure S2](#)) or by a reduction of macrocycle **47** with  $\text{LiAlD}_4$  ([Figure S4](#)). The alkylation of M4-cyclen (**16**, **34**, or **49**) ([Figures 3B](#) and [S2–S4](#)) or of the twice alkylated M4-cyclen (**20** or **54**) ([Figures 3B](#), [S2](#), and [S4](#)) leads to a scrambling of the isotope labels over four or two positions, respectively. If the isotopes were introduced through the labeled alanine **6** ( $^2\text{H}$ ) ([Figure 3B](#)) or **24** ( $^{13}\text{C}$ ) ([Figure S2](#)) an observed labeling of 50% or 25% at the respective positions was achieved ([1–3 Figure 3A](#)). The introduction of the isotope label at a later step in the synthesis by reduction of the macrocycle **44** with  $\text{LiAlD}_4$  ([Figure S4](#)) resulted in an observed labeling of 100% or 50% ([4 and 5 Figure 3A](#)), depending again on the order of the debenzylation and alkylation steps. Ln-DOTA-M7FPy (**1**) was synthesized for all lanthanoids (NMR spectra [Figures S30–S85](#)) apart from Pm; complexes **2** to **5** were only synthesized for the late lanthanoids Tb to Yb. Surprisingly, La-, Ce-, Pr-, and Nd-DOTA-M7FPy dissociated at pH < 3, with the highest rate of dissociation found for La and the lowest for Nd, thus following the trend in the ionic radii.

Carbon  $^{13}\text{C}$  labeling in combination with selectively  $^1\text{H}$  decoupled  $^{13}\text{C}$  spectra ([Figures S105–S109](#)) could be used to classify the cyclen methyl signals. Attempts to extend selective decoupling to classify other proton signals by labeling different



**Figure 3. Synthesis of labeled complexes**

(A) All labeling schemes used throughout this study. Blue dots mark positions that were labeled with deuterium  $^2\text{H}$ . Red dots mark positions that were labeled with carbon  $^{13}\text{C}$ .

(B) Exemplary synthetic route towards two (2 and 3) of the five labeled complexes 1–5: (i) (1)  $\text{LiAlH}_4$ , THF,  $0^\circ\text{--}5^\circ\text{C}$ ; (2) Cbz-Cl,  $\text{H}_2\text{O}$ , EtOAc,  $\text{Na}_2\text{CO}_3$ ; (3) IBX, EtOAc,  $77^\circ\text{C}$ . (ii) (1) T3P, DIPEA, EtOAc; (2)  $\text{NaBH}_4$ , MeOH,  $\text{H}_2\text{O}$ , THF,  $0^\circ\text{--}5^\circ\text{C}$ ; (3) IBX, MeCN,  $80^\circ\text{C}$ . (iii) (1)  $\text{NaBH}(\text{CH}_3\text{COO})_3$ , DCM; (2) Pd/C  $\text{H}_2$ , MeOH. (iv) (1)  $\text{NaBH}(\text{CH}_3\text{COO})_3$ , DCM; (2) BnBr, MeCN,  $45^\circ\text{C}$ . (v) (1) HBr, AcOH,  $40^\circ\text{C}$ ; (2) HATU, MeCN. (vi)  $\text{LiAlH}_4$ , DCM,  $-78^\circ\text{C}$ . (vii) Pd/C  $\text{H}_2$ , TFA,


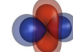
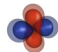


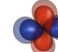
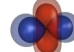
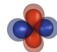



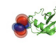
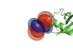
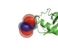
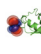
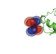
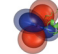
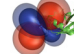
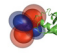
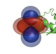
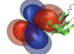
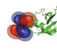
**Figure 3. Continued**

MeOH. (viii) OTf-Lac-O-t-Bu, K<sub>2</sub>CO<sub>3</sub>, DCM, MeCN. (ix) OTf-Lac-O-t-Bu, K<sub>2</sub>CO<sub>3</sub>, DCM, MeCN. (x) Pd(OH)<sub>2</sub>/C, NH<sub>4</sub>(HCOO), EtOH. (xi) OTf-Lac-O-t-Bu, K<sub>2</sub>CO<sub>3</sub>, DCM, MeCN. (xii) (1) K<sub>2</sub>CO<sub>3</sub>, MeCN; (2) HCl, MeCN, 80°C; (3) aq. NH<sub>4</sub>(CH<sub>3</sub>COO), Ln(III), 80°C. Below each labeled molecule, the observed labeling percentage is noted.

positions with <sup>13</sup>C were not successful as the intensity gain from the decoupling was no longer observable due to the stronger PRE. Deuterium labeling (spectra [Figures S113–S166](#)) on the other hand, which is less sensitive to PRE, allowed the classification of all proton signals for the late lanthanoids (for more details, see [supplemental information](#)) ([Tables S4–S7](#)). Four different deuterium labeling schemes were synthesized in order to sufficiently restrict the combinatorial space. Due to the late stage scrambling of the isotope labels, the amount of labeled material and the synthetic effort were greatly reduced. Careful control of the pH (50 mM phosphate buffer, pH 6.0, [Table S15](#)) and of the residual trifluoro acetic acid (TFA) from the HPLC purification was necessary to obtain reproducible chemical shifts ([Figure S86](#)).

**Intrinsic anisotropy parameters**

Classification of proton signals by either COSY spectra or labeling schemes reduced the possible assignments to a manageable number. The anisotropy parameters were therefore fitted for all possible remaining assignments ([Figures S13–S25](#)). Based on the spectroscopic data from Sm and Eu, we were able to show that the correct assignment is found among the ones that correlate best with the DFT structure. However, in two out of four simulations, it is not the one yielding the highest correlation coefficient. For the remaining lanthanoids, the anisotropy parameters could nonetheless be determined as they were highly conserved among the best correlated assignments. For Er, Tm, and Yb, the anisotropy parameters were determined unambiguously since only one set of anisotropy parameters was found, while for Ce, Pr, Nd, Tb, Dy, and Ho, two sets of anisotropy parameters were found, which had similar magnitude and rhombicity but show slightly differing orientation. For the further discussion, the set of anisotropy parameters that appears with overall higher correlation coefficients were chosen for the latter ones (for more details, see [supplemental information](#)) ([Figure S7](#), [Table S8](#)). The final anisotropy parameters of Ln-DOTA-M7FPy determined on the free tag (final assignment [Tables S9](#) and [S10](#), full tensors [Table S13](#)) and on the protein are depicted in [Figure 4](#). Uncertainties were determined using Monte Carlo simulations (for details, see [experimental procedures](#)). For most of the lanthanoids on ubiquitin, the uncertainty had to be estimated as the Monte Carlo simulation generated several sets of anisotropy parameters defining tensors of similar size but differing orientations. To avoid ambiguities, all anisotropy parameters are represented in the unique tensor representation (UTR).<sup>36</sup> The most striking result is the size of  $\Delta\chi_{ax}$  and  $\Delta\chi_{rh}$ —the intrinsic anisotropy parameters exceed by far the ones reported for typical LCT. Even the very recently published DOTA-M7-Nitro LCT,<sup>37</sup> which is unique in the size of its anisotropy parameters among LCT, has 5%–10% smaller values. A comparison between the anisotropy parameters on the free LCT and ubiquitin S57C shows that about 80% of the anisotropy is lost due to motional averaging of the protein tether.<sup>38,39</sup> The loss shows a slightly increasing trend going from Ce to Yb. There are two likely reasons for this trend: (1) The small magnitude of the observed PCS of the early lanthanoids makes them more susceptible to experimental errors, which result in an overestimation of the anisotropy parameters, or (2) The higher probability of the early lanthanoids to coordinate an additional donor at the ninth coordination site slightly reduces the motional averaging. It is noteworthy that the residual dipolar coupling (RDC)-derived  $\Delta\chi_{ax}$  parameters are very similar to the values obtained independently by PCSs. The

Free Tag (PCS)	Ce	Pr	Nd	Sm	Eu	Tb	Dy	Ho	Er	Tm	Yb
$\Delta\chi_{ax}$	3.3(0.04)	9.2(0.09)	4.2(0.05)	-0.76(0.008)	4.1(0.05)	62(0.7)	101(1)	40(0.4)	29(0.3)	83(0.9)	23(0.3)
$\Delta\chi_{rh}$	1.7(0.03)	2.3(0.07)	1.7(0.04)	-0.29(0.008)	2.4(0.05)	31(0.6)	24(0.8)	18(0.4)	8(0.3)	8(0.8)	8(0.2)
$\alpha$	67(0.6)	65(1)	63(0.7)	166(2)	163(1)	62(0.6)	62(1)	58(0.7)	158(2)	155(5)	151(1)
$\beta$	92(0.3)	90(0.3)	94(0.3)	168(0.4)	163(0.4)	92(0.3)	91(0.3)	93(0.3)	172(0.4)	176(0.3)	163(0.4)
$\gamma$	101(0.2)	106(0.2)	104(0.2)	11(1)	11(0.9)	101(0.3)	108(0.2)	104(0.3)	11(2)	8(4)	178(1)
											
On Protein (PCS)											
$\Delta\chi_{ax}$	-0.99(0.07) <sup>†</sup>	2.4(0.2) <sup>†</sup>	1.1(0.08) <sup>†</sup>	-0.76(0.05) <sup>†</sup>	0.84(0.06) <sup>†</sup>	-12(0.8)	-21(0.1)	6.6(0.5) <sup>†</sup>	5.1(0.2) <sup>†</sup>	-16(0.1)	-2.7(0.2) <sup>†</sup>
$\Delta\chi_{rh}$	-0.65(0.05) <sup>†</sup>	1.5(0.2) <sup>†</sup>	0.59(0.04) <sup>†</sup>	-0.46(0.03) <sup>†</sup>	0.53(0.04) <sup>†</sup>	-8(0.5)	-12(0.4)	4.2(0.3) <sup>†</sup>	0.52(0.1) <sup>†</sup>	-9(0.6)	-1.7(0.1) <sup>†</sup>
$\alpha$	79(3) <sup>†</sup>	144(3) <sup>†</sup>	153(3) <sup>†</sup>	92(3) <sup>†</sup>	156(3) <sup>†</sup>	131(1)	89(0.9)	136(3) <sup>†</sup>	1(3) <sup>†</sup>	64(0.5)	61(3) <sup>†</sup>
$\beta$	3(3) <sup>†</sup>	103(3) <sup>†</sup>	95(3) <sup>†</sup>	155(3) <sup>†</sup>	54(3) <sup>†</sup>	27(3)	36(0.4)	119(3) <sup>†</sup>	136(3) <sup>†</sup>	56(0.5)	40(3) <sup>†</sup>
$\gamma$	162(3) <sup>†</sup>	120(3) <sup>†</sup>	102(3) <sup>†</sup>	22(3) <sup>†</sup>	61(3) <sup>†</sup>	93(2)	127(2)	100(3) <sup>†</sup>	28(3) <sup>†</sup>	47(2)	49(3) <sup>†</sup>
											
$\frac{\Delta\chi_{ax}^{\text{On Protein}}}{\Delta\chi_{ax}^{\text{Free Tag}}} \%$	30%	26%	26%	100%	20%	19%	21%	16%	17%	19%	12%
On Protein (RDC)											
$\Delta\chi_{ax}$	-0.96(0.06) <sup>†</sup>	-4.0(0.2) <sup>†</sup>	2.0(0.1) <sup>†</sup>	-1.7(0.1) <sup>†</sup>	5.0(0.3) <sup>†</sup>	-13(0.7)	-18(0.5)	-8.1(0.5) <sup>†</sup>	3.4(0.2) <sup>†</sup>	-10(0.4)	-2.0(0.1) <sup>†</sup>
$\Delta\chi_{rh}$	-0.40(0.06) <sup>†</sup>	-1.8(0.3) <sup>†</sup>	1.1(0.2) <sup>†</sup>	-0.24(0.03) <sup>†</sup>	2.7(0.4) <sup>†</sup>	-4(0.4)	-3(0.4)	-1.4(0.2) <sup>†</sup>	2.1(0.3) <sup>†</sup>	-3(0.4)	-0.62(0.09) <sup>†</sup>
$\alpha$	101(5) <sup>†</sup>	71(5) <sup>†</sup>	147(5) <sup>†</sup>	90(5) <sup>†</sup>	151(5) <sup>†</sup>	103(2)	96(2)	100(5) <sup>†</sup>	136(5) <sup>†</sup>	48(1)	53(5) <sup>†</sup>
$\beta$	35(5) <sup>†</sup>	47(5) <sup>†</sup>	111(5) <sup>†</sup>	21(5) <sup>†</sup>	114(5) <sup>†</sup>	42(1)	42(1)	46(5) <sup>†</sup>	56(5) <sup>†</sup>	68(1)	60(5) <sup>†</sup>
$\gamma$	85(5) <sup>†</sup>	151(5) <sup>†</sup>	119(5) <sup>†</sup>	53(5) <sup>†</sup>	139(5) <sup>†</sup>	135(2)	142(4)	144(5) <sup>†</sup>	160(5) <sup>†</sup>	20(4)	170(5) <sup>†</sup>

†: Uncertainty was estimated based on the values from Tb, Dy and Tm

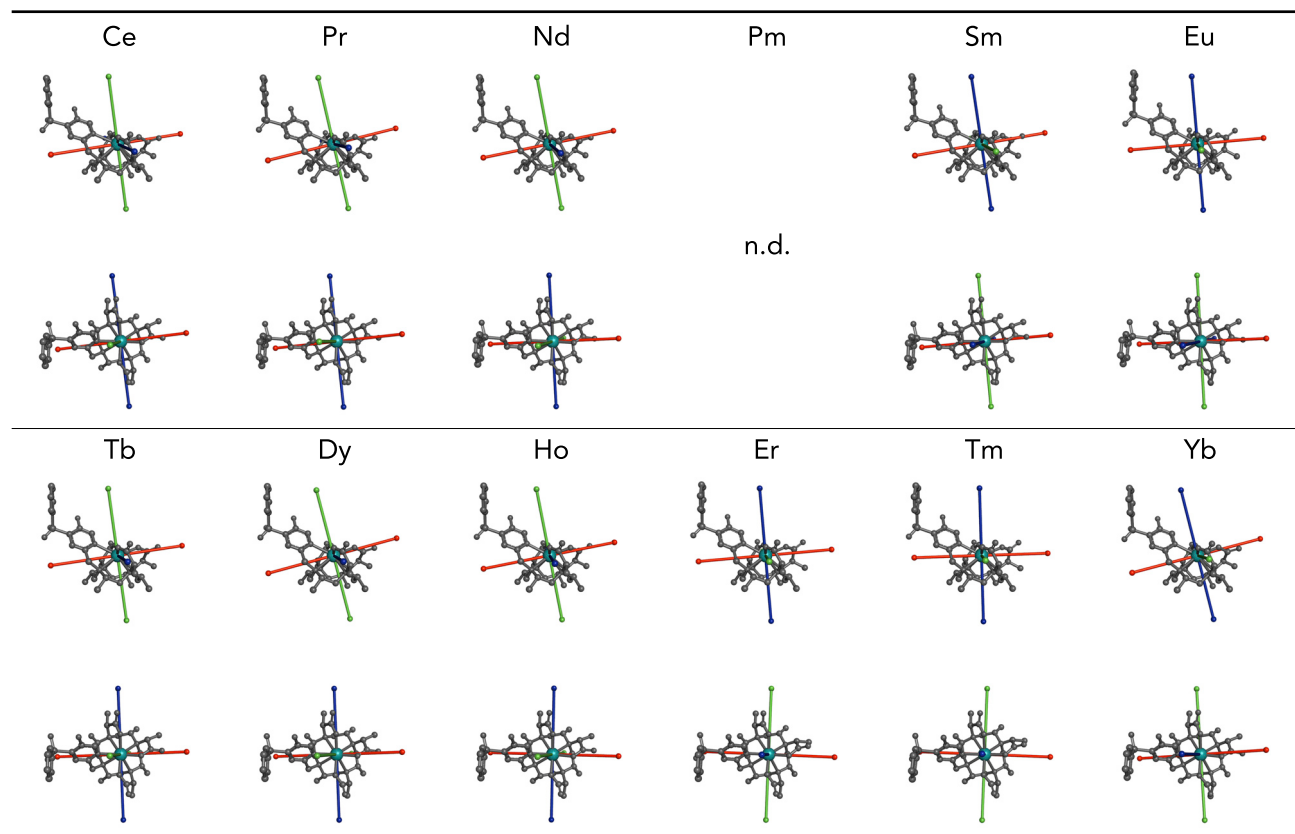
#### Figure 4. Anisotropy parameters of Ln-DOTA-M7FPy

PCS Anisotropy parameters  $\Delta\chi_{ax}$  and  $\Delta\chi_{rh}$  are reported in  $10^{-32} \text{ m}^3$ . All angles are reported in degrees. All standard deviations are given in parentheses. The molecular frame of the free tag is orientated so that the lanthanoid is at the origin, the z axis is perpendicular to the cyclen- $N_4$ -plane and the x axis is going in the direction of the nitrogen on which the pyridine linker is attached. Red isosurfaces indicate a negative shift, blue isosurfaces indicate the corresponding positive shift. On the free tag, the isosurfaces indicate a positive or negative shift of 0.2/0.1 ppm (inner sphere/ outer sphere) for the early lanthanoids (Ce-Eu) and 2/1 ppm (inner sphere/outer sphere) for the late lanthanoids (Tb-Yb). On the protein, the illustrations of the isosurfaces are magnified and indicate a positive or negative shift of 1/0.5 ppm (inner sphere/outer sphere) for all lanthanoids.

transfer of the full anisotropy potential to the protein by further rigidifying the attachment will result in the observation of significant and easy-to-detect PCSs in the range of 0.01 ppm for spins at a distance of up to 175 Å, thus opening a perspective for unique long-range restraints for structural work. In principle, the distance limit could be increased by enhancing the intrinsic anisotropy parameters, mainly  $\Delta\chi_{ax}$ . For Ln-DOTA-M7FPy, the largest  $\Delta\chi_{ax}$  is displayed by Dy and corresponds to a shift range of roughly 1,450 ppm. The size of  $\Delta\chi_{ax}$  throughout this study correlates in a first approximation to the observed shift range (Tables S16 and S17). Therefore, it is reasonable to assume that an increase or decrease in the intrinsic  $\Delta\chi_{ax}$  for future DOTA-type ligands should be reflected by an increase or decrease in the shift range of the free ligand, respectively.

#### Ligand-field-like effects

Most interestingly, however, is the absence of a change in the sign of  $\Delta\chi_{ax}$  and  $\Delta\chi_{rh}$ , within the lanthanoid series, which is in stark contrast to the findings in most other reported lanthanoid series,<sup>26,40,41</sup> as well as to Bleaney's theory.<sup>42</sup> Instead, the



**Figure 5. Orientation of the tensor frame**

Coordinate system axes defining the tensor frame from the anisotropy parameters. The axes are colored in blue (z axis), green (y axis) and red (x axis). The upper row depicts for each metal a side view of the twisted square antiprism of DOTA-M7FPy, while the lower row shows the line of vision orthogonal to the cyclen- $N_4$ -plane at the bottom of the antiprism. Hydrogens were omitted for clarity. The molecular frame of the free tag is orientated so that the lanthanoid is at the origin, the z axis is perpendicular to the cyclen- $N_4$ -plane and the x axis is going in the direction of the nitrogen on which the pyridine linker is attached.

main magnetic axis reorients itself depending on the f-electron ground state distribution being either oblate (Ce, Pr, Nd, Tb, Dy, Ho) or prolate (Sm, Eu, Er, Tm, Yb) (for more details on sign change and reorientation, see [Figure S9 supplemental information](#)). The additional sign change in the case of Sm, is most likely caused by interactions with excited manifolds. For the oblate lanthanoids (Ce, Pr, Nd, Tb, Dy, Ho), the main magnetic axis is perpendicular to the pseudo symmetry axis, while for the prolate lanthanoids (Sm, Eu, Er, Tm, Yb), the main magnetic axis is almost parallel to the pseudo symmetry axis with a small tilt ( $5^\circ$ – $15^\circ$ ) toward the pyridine (cf. [Figure 5](#)). For the late lanthanoids, a similar reorientation of the main magnetic axis was previously predicted to occur below  $40\text{ K}^{26}$  and reported for single-molecule magnets at low temperature (2 K). This unexpected preference for easy axis anisotropy for all late lanthanoids was attributed to a desymmetrization of the coordination polyhedron.<sup>28</sup> We could corroborate this rationale by comparing the anisotropy parameters of representative lanthanoids from each triad (Pr, Eu, Dy, Tm, see [Table S11](#) and [S12](#), [Figure S8](#), [supplemental information](#), full tensors [Table S14](#)) in the perfectly  $C_4$ -symmetric DOTA-M8 chelator, where we did not observe this alternating pattern, but rather a parallel orientation in all cases and a sign change for the tensor parameters between oblate (Pr, Dy) and prolate (Eu, Tm) lanthanoids. It is noteworthy, that earlier reports on non-methylated Na[Dy-DOTA] clearly showed, that even small disturbances of the axial symmetry by coordinating water at the ninth coordination site

**Table 1. Anisotropy parameters of DOTA-type LCTs**

Ligand	Lanthanoid		DOTA-M8-(4R4S)		DOTA-M8-(4R4S)-SSPy		DOTA-M7FPy		DOTA-M7PyThiazol		DOTA-M7-Nitro	
			Dy	Tm	Dy	Tm	Dy	Tm	Dy	Tm	Dy	Tm
Free ligand	$\Delta\chi_{ax}$		-80	104	-	-	101	83	-	-	-	-
		$\Delta\chi_{rh}$	-0	1	-	-	24	8	-	-	-	-
Ubi S57C	$\Delta\chi_{ax}$		-	-	-8.7	19.6	-21	-16	41.9	35.4	94.3	60.9
		$\Delta\chi_{rh}$	-	-	-4.1	3.0	-12	-9	26.1	11.3	10.7	12.3

Anisotropy parameters for different lanthanoid complexes determined either on the free ligand or ubiquitin S57C.  $\Delta\chi_{ax}$  and  $\Delta\chi_{rh}$  are reported in  $10^{-32}\text{m}^3$ . The anisotropy parameters of DOTA-M8-(4R4S)-SSPy,<sup>20</sup> DOTA-M7PyThiazol<sup>12</sup> and DOTA-M7-Nitro<sup>27</sup> are taken from previously published studies.

are sufficient to trigger a reorientation of the main magnetic axis at low temperature (2 K).<sup>43</sup> We suggest, based on our findings on Ln-DOTA-M7FPy and Ln-DOTA-M8, that in order to observe a similar reorientation at room temperature, the ligand scaffold itself needs to be profoundly asymmetric.

The second noteworthy result from the comparison between the anisotropy parameters of Ln-DOTA-M7FPy and Ln-DOTA-M8 is the modulation of  $\Delta\chi_{ax}$ . Compared to Ln-DOTA-M7FPy, the absolute size of  $\Delta\chi_{ax}$  for the prolate lanthanoids (Eu, Tm) increases by approximately 25%, while for the oblate lanthanoids (Pr, Dy),  $\Delta\chi_{ax}$  decreases by approx. 20% (Table S12). As a result, the largest anisotropy is displayed by Tm instead of Dy on DOTA-M8. Rinehart and Long recently proposed that the magnetic anisotropy of lanthanoid single-molecule magnets can be increased if the ligand field is matched to the f-electron ground state distribution.<sup>44</sup> The results obtained in this study as well as the anisotropy parameters determined for previously developed polymethylated DOTA-type LCTs indicate that at room temperature, different ligand fields also favor either the oblate or prolate lanthanoids. Whether the oblate or prolate lanthanoids are favored is indicated by the order of  $\Delta\chi_{ax}$  for Dy and Tm (Table 1). Polymethylated DOTA-type LCTs strongly resembling DOTA-M8 appear to favor a prolate f-electron ground state distribution while the DOTA-M7-pyridine-type ligands favor oblate lanthanoids.

The clear correlation between the oblate or prolate f-electron distribution and the modulation of  $\Delta\chi_{ax}$  as well as the main magnetic axis at room temperature suggest that the electronic structure of the lanthanoid might be crucial for the resulting paramagnetic properties. It should therefore also be possible at room temperature to tailor the ligand field toward the electronic structure of the lanthanoid in order to enhance the magnetic anisotropy. However, since the interaction between the ligand field and the oblate or prolate lanthanoids is significantly different, it is highly unlikely that one ligand accommodates all lanthanoids equally well. The proposed correlation between the electronic structure and the resulting anisotropy parameters stands in stark contrast to the long-accepted dogma that ligand-field effects play no significant role for lanthanoids at room temperature. It further poses the question of how crucial the interaction between the ligand molecular orbitals and the f-orbitals is and whether it has a directional component.

Unfortunately, there is currently no theoretical model that could account for our findings. A better understanding of the ligand-field effects at room temperature might allow to adapt and extend the description formulated by Rinehart and Long to the situation at room temperature for complexes with different degrees of symmetry.

## Conclusions

In summary, we experimentally determined the intrinsic anisotropy parameters for the full lanthanoid series on the rigid DOTA-M7FPy tag. Using selective isotope

labeling, we showed that the best correlated assignments represent the actual anisotropy parameters, but the assignment yielding the highest correlation coefficient is not necessarily the correct assignment. The first important finding was the size of  $\Delta\chi_{ax}$ , based on which we estimated that a completely immobilized Ln-DOTA-M7FPy could deliver PCS of 0.01 ppm up to 175 Å on a protein. The shift range of Ln-DOTA-M7FPy correlates approximately to the size of  $\Delta\chi_{ax}$ . Therefore, it should be possible to estimate  $\Delta\chi_{ax}$  of other DOTA-type lanthanoid complexes based on the values obtained for Ln-DOTA-M7FPy. To our great surprise, we observed a reorientation of the main magnetic axis instead of a sign change for the lanthanoid series depending on the oblate or prolate f-electron distribution of the lanthanoids. The comparison between the anisotropy parameters of Ln-DOTA-M7FPy and Ln-DOTA-M8 as well as anisotropy parameters from different tags further showed that the modulation of  $\Delta\chi_{ax}$  also correlates to the f-electron distribution. It is our hope that these results provide a basis for the tailoring of future lanthanoid complexes with enhanced paramagnetic properties. Furthermore, this study underlines that the quest for a comprehensive theory of the magnetic properties of lanthanoid compounds with ligand fields much larger than  $kT$  is of the utmost importance for the field. It also poses the question about the interaction between the ligand field and the lanthanoid f-electrons. Due to the different interactions between the ligand field and the either oblate or prolate lanthanoid, at least one member of the late two triads (oblate/prolate) should be investigated for new ligand scaffolds.

## EXPERIMENTAL PROCEDURES

### Resource availability

#### Lead contact

Further information and requests for resources should be directed to and will be fulfilled by the lead contact, Daniel Häussinger ([daniel.haessinger@unibas.ch](mailto:daniel.haessinger@unibas.ch)).

#### Materials availability

There are restrictions to the availability of all isotope labeled compounds because of limited lifetimes and costly starting materials.

#### Data and code availability

The code supporting the current study is available from the lead contact on request.

The published article includes all datasets generated or analyzed during this study.

### Tagging and anisotropy parameters fitting on ubiquitin

Ubiquitin S57C was tagged with all paramagnetic lanthanoids except Gd and Pm. As a diamagnetic reference, ubiquitin S57C was tagged with Lu. For all samples,  $^1\text{H}$   $^{15}\text{N}$  HSQC (Figures S167–S177) and IPAP spectra were recorded to determine the PCS and RDC anisotropy parameters. The IPAP spectra were processed using NMRPipe.<sup>45</sup> All signals were assigned using CcpNMR.<sup>46</sup> The PCS anisotropy parameters were fitted using Numbat<sup>36</sup> (correlation graphs Figures S178 and S179) while the RDC anisotropy parameters were fitted with Paramagpy<sup>47</sup> (correlation graphs Figures S180 and S181). The structure of ubiquitin for the calculations was obtained from the PDB library (PDB: 1UBI). For the fitting of the anisotropy parameters experienced by the protein, only the shifts of residues residing within secondary structure elements (PDB: 1UBQ) were used. The shifts from the  $\alpha$ -helix, on which the tag was attached, were excluded since attachment of the tag might lead to slight structural changes, which are not represented in the structure used to calculate the PCS. The metal position was determined by simultaneously fitting the anisotropy parameters

for Tb, Dy, Ho, and Tm. All other anisotropy parameters were calculated with the metal position ( $x = 21.826$ ,  $y = 12.804$ ,  $z = 8.288$ ) obtained from fitting Tb, Dy, Ho, and Tm. Uncertainties were determined for PCS using the integrated error analysis tool in Numbat<sup>36</sup> with the number of iterations set to 1,000 and the PCS subset set to 80%. For the RDC, the uncertainties were determined using the integrated error analysis tool in Paramagpy<sup>47</sup> with the number of iterations set to 1,000 and the sample fraction set to 80%.

### Anisotropy parameter fitting on Ln-DOTA-M7FPy and DOTA-M8

The required structures for the fitting of the anisotropy parameters were calculated with DFT geometry optimizations using the SARC2<sup>48</sup> basis set, which is optimized for lanthanoids and the BP86 functional.<sup>49,50</sup> To approximate the electronic structure of the lanthanoids, the zeroth order regular approximation (ZORA) was used. To account for solvent effects, the calculations were performed using the conductor-like polarizable continuum model (CPCM) as a solvent model. The calculations were performed with ORCA. An exemplary input file along with all calculated structures can be found in the supporting information. For the calculation of the PCS, La was taken as a diamagnetic reference for the early lanthanoids and Lu for the late lanthanoids. For the fitting of the anisotropy parameters on Ln-DOTA-M7FPy (correlation graphs Figures S10 and S11) and Ln-DOTA-M8 (correlation graphs Figure S12), a python program based on NUMBAT was used. We assumed that the methyl protons were in fast exchange. In order to account for the resulting methyl rotation, the PCS were calculated for all three proton positions and then averaged to obtain the final PCS of the methyl group. Uncertainties were calculated using a Monte Carlo simulation (1,000 iterations), where a random deviation of up to  $\pm 5\%$  was added to each shift.

### SUPPLEMENTAL INFORMATION

Supplemental information can be found online at <https://doi.org/10.1016/j.chempr.2021.08.011>.

### ACKNOWLEDGMENTS

We thank C.E. Housecroft, E.C. Constable, O.S. Wenger, S. Grzesiek, V. Köhler, P. Rieder, and D. Joss for helpful discussions. This work was supported by the Fondation Claude et Giuliana, Vaduz, Liechtenstein and the Department of Chemistry of the University of Basel. Calculations were performed at sciCORE (<http://scicore.unibas.ch/>) scientific computing centre at the University of Basel.

### AUTHOR CONTRIBUTIONS

Conceptualization, R.V., T.M., and D.H.; data curation, R.V. and T.M.; formal analysis, R.V.; investigation, R.V.; methodology, R.V. and D.H.; software, R.V., T.M.; validation, R.V., T.M., and D.H.; visualization, R.V.; writing—original draft, R.V. and D.H.; supervision, T.M. and D.H.; writing—review and editing, T.M.; funding acquisition, D.H.; project administration, D.H.; resources, D.H.

### DECLARATION OF INTERESTS

The authors declare no competing interests.

Received: April 20, 2021

Revised: July 9, 2021

Accepted: August 12, 2021

Published: September 8, 2021



## REFERENCES

- Levason, W. (2017). Chemistry and applications of the lanthanides. *Coord. Chem. Rev.* **340**, 1–298.
- Sun, W., Kuang, X., Keen, H.D.J., Lu, C., and Hermann, A. (2020). Second group of high-pressure high-temperature lanthanide polyydride superconductors. *Phys. Rev. B* **102**, 1–7.
- Bünzli, J.G. (2015). On the design of highly luminescent lanthanide complexes. *Coord. Chem. Rev.* **293–294**, 19–47.
- Zhou, J., Li, C., Li, D., Liu, X., Mu, Z., Gao, W., Qiu, J., and Deng, R. (2020). Single-molecule photoreaction quantitation through intraparticle-surface energy transfer (i-SET) spectroscopy. *Nat. Commun.* **11**, 4297.
- Woodruff, D.N., Winpenny, R.E.P., and Layfield, R.A. (2013). Lanthanide single-molecule magnets. *Chem. Rev.* **113**, 5110–5148.
- Parker, D., Suturina, E.A., Kuprov, I., and Chilton, N.F. (2020). How the ligand field in lanthanide coordination complexes determines magnetic susceptibility anisotropy, paramagnetic NMR shift, and relaxation behavior. *Acc. Chem. Res.* **53**, 1520–1534.
- Randall McClain, K.R., Gould, C.A., Chakarawet, K., Teat, S.J., Groshens, T.J., Long, J.R., and Harvey, B.G. (2018). High-temperature magnetic blocking and magneto-structural correlations in a series of dysprosium(III) metallocenium single-molecule magnets. *Chem. Sci.* **9**, 8492–8503.
- Guo, F.S., Day, B.M., Chen, Y.C., Tong, M.L., Mansikkamäki, A., and Layfield, R.A. (2018). Magnetic hysteresis up to 80 kelvin in a dysprosium metallocene single-molecule magnet. *Science* **362**, 1400–1403.
- Geraldes, C.F.G.C. (1993). Lanthanide shift reagents. *Methods Enzymol.* **227**, 43–78.
- Nitsche, C., and Otting, G. (2017). Pseudocontact shifts in biomolecular NMR using paramagnetic metal tags. *Prog. Nucl. Magn. Reson. Spectrosc.* **98–99**, 20–49.
- Joss, D., and Häussinger, D. (2019). Design and applications of lanthanide chelating tags for pseudocontact shift NMR spectroscopy with biomacromolecules. *Prog. Nucl. Magn. Reson. Spectrosc.* **114–115**, 284–312.
- Bertini, I., Luchinat, C., and Parigi, G. (2002). Paramagnetic constraints: an aid for quick solution structure determination of paramagnetic metalloproteins. *Concepts Magn. Reson.* **14**, 259–286.
- Brewer, K.D., Bacaj, T., Cavalli, A., Camilloni, C., Swarbrick, J.D., Liu, J., Zhou, A., Zhou, P., Barlow, N., Xu, J., et al. (2015). Dynamic binding mode of a Synaptotagmin-1-SNARE complex in solution. *Nat. Struct. Mol. Biol.* **22**, 555–564.
- Bertini, I., Luchinat, C., and Parigi, G. (2002). Magnetic susceptibility in paramagnetic NMR. *Prog. Nucl. Magn. Reson. Spectrosc.* **40**, 249–273.
- Pineda, E.M., Chilton, N.F., Marx, R., Dörfel, M., Sells, D.O., Neugebauer, P., Jiang, S.-D., Collison, D., van Slageren, J., McInnes, E.J.L., and Winpenny, R.E.P. (2014). Direct measurement of dysprosium(III) ...dysprosium(III) interactions in a single-molecule magnet. *Nat. Commun.* **5**, 1–7.
- Razzaghi, S., Brooks, E.K., Bordignon, E., Hubbell, W.L., Yulikov, M., and Jeschke, G. (2013). EPR relaxation-enhancement-based distance measurements on orthogonally spin-labeled T4-lysozyme. *Chembiochem* **14**, 1883–1890.
- Keizers, P.H.J., Saraglidis, A., Hiruma, Y., Overhand, M., and Ubbink, M. (2008). Design, synthesis, and evaluation of a lanthanide chelating protein probe: CLaNP-5 yields predictable paramagnetic effects independent of environment. *J. Am. Chem. Soc.* **130**, 14802–14812.
- Yang, F., Wang, X., Pan, B.B., and Su, X.C. (2016). Single-armed phenylsulfonated pyridine derivative of DOTA is rigid and stable paramagnetic tag in protein analysis. *Chem. Commun. (Camb)* **52**, 11535–11538.
- Joss, D., Bertrams, M., and Häussinger, D. (2019). A sterically overcrowded, isopropyl-substituted, lanthanide-chelating tag for protein pseudocontact shift NMR spectroscopy: synthesis of its macrocyclic scaffold and benchmarking on ubiquitin S57 C and hCA II S166 C. *Chem. Eur. J.* **25**, 11910–11917.
- Müntener, T., Kottelat, J., Huber, A., and Häussinger, D. (2018). New lanthanide chelating tags for PCS NMR spectroscopy with reduction stable, rigid linkers for fast and irreversible conjugation to proteins. *Bioconjug. Chem.* **29**, 3344–3351.
- Loh, C.T., Ozawa, K., Tuck, K.L., Barlow, N., Huber, T., Otting, G., and Graham, B. (2013). Lanthanide tags for site-specific ligation to an unnatural amino acid and generation of pseudocontact shifts in proteins. *Bioconjug. Chem.* **24**, 260–268.
- Gao, J., Liang, E., Ma, R., Li, F., Liu, Y., Liu, J., Jiang, L., Li, C., Dai, H., Wu, J., et al. (2017). Fluorine pseudocontact shifts used for characterizing the protein–ligand interaction mode in the limit of NMR intermediate exchange. *Angew. Chem. Int. Ed. Engl.* **56**, 12982–12986.
- Zimmermann, K., Joss, D., Müntener, T., Nogueira, E.S., Schäfer, M., Knörr, L., Monnard, F.W., and Häussinger, D. (2019). Localization of ligands within human carbonic anhydrase II using <sup>19</sup>F pseudocontact shift analysis. *Chem. Sci.* **10**, 5064–5072.
- Di Pietro, S., Piano, S.L., and Di Bari, L. (2011). Pseudocontact shifts in lanthanide complexes with variable crystal field parameters. *Coord. Chem. Rev.* **255**, 2810–2820.
- Hiller, M., Maier, M., Wadepohl, H., and Enders, M. (2016). Paramagnetic NMR analysis of substituted Biscyclooctatetraene lanthanide complexes. *Organometallics* **35**, 1916–1922.
- Suturina, E.A., Mason, K., Geraldes, C.F.G.C., Kuprov, I., and Parker, D. (2017). Beyond Bleaney's theory: experimental and theoretical analysis of periodic trends in lanthanide-induced chemical shift. *Angew. Chem. Int. Ed. Engl.* **56**, 12215–12218.
- Sievers, J. (1982). Asphericity of 4f-Shells in Their Hund's Rule Ground States. *Z. Physik B - Condensed Matter* **45**, 289–296.
- Boulon, M.E., Cucinotta, G., Luzon, J., Degl'Innocenti, C., Perfetti, M., Bernot, K., Calvez, G., Caneschi, A., and Sessoli, R. (2013). Magnetic anisotropy and spin-parity effect along the series of lanthanide complexes with DOTA. *Angew. Chem. Int. Ed. Engl.* **52**, 350–354.
- Opina, A.C.L., Strickland, M., Lee, Y.S., Tjandra, N., Swenson, R.E., and Vasalatiy, O. (2019). Comparison of solution properties of polymethylated DOTA-like lanthanide complexes with opposite chirality of the pendant arms. *Inorg. Chem.* **58**, 15788–15800.
- Joss, D., Walliser, R.M., Zimmermann, K., and Häussinger, D. (2018). Conformationally locked lanthanide chelating tags for convenient pseudocontact shift protein nuclear magnetic resonance spectroscopy. *J. Biomol. NMR* **72**, 29–38.
- Bertini, I., Piccioli, M., Tarchi, D., and Luchinat, C. (1994). COSY spectra of paramagnetic macromolecules: observability, scalar effects, cross-correlation effects, relaxation-allowed coherence transfer. *Concepts Magn. Reson.* **6**, 307–335.
- Bertini, I., Luchinat, C., and Tarchi, D. (1993). Are true scalar proton–proton connectivities ever measured in COSY spectra of paramagnetic macromolecules? *Chem. Phys. Lett.* **203**, 445–449.
- Müntener, T., Thommen, F., Joss, D., Kottelat, J., Prescimone, A., and Häussinger, D. (2019). Synthesis of chiral nine and twelve-membered cyclic polyamines from natural building blocks. *Chem. Commun. (Camb)* **55**, 4715–4718.
- Häussinger, D., Huang, J.R., and Grzesiek, S. (2009). DOTA-M8: an extremely rigid, high-affinity lanthanide chelating tag for PCS NMR spectroscopy. *J. Am. Chem. Soc.* **131**, 14761–14767.
- Müntener, T. (2019). Protein PCS NMR spectroscopy under physiological conditions: development of a new high yield cyclization method for rigidified DOTA-based tags with sulfhydryl-reactive activators forming a reductively stable linkage (PhD Thesis (University of Basel, Faculty of Science)).
- Schmitz, C., Stanton-Cook, M.J., Su, X.C., Otting, G., and Huber, T. (2008). Numbat: an interactive software tool for fitting deltachitensors to molecular coordinates using pseudocontact shifts. *J. Biomol. NMR* **41**, 179–189.
- Joss, D., Winter, F., and Häussinger, D. (2020). A novel, rationally designed lanthanoid chelating tag delivers large paramagnetic structural restraints for biomolecular NMR. *Chem. Commun. (Camb)* **56**, 12861–12864.
- Suturina, E.A., Häussinger, D., Zimmermann, K., Garbuio, L., Yulikov, M., Jeschke, G., and Kuprov, I. (2017). Model-free extraction of spin label position distributions from pseudocontact shift data. *Chem. Sci.* **8**, 2751–2757.

39. Shishmarev, D., and Otting, G. (2013). How reliable are pseudocontact shifts induced in proteins and ligands by mobile paramagnetic metal tags? A modelling study. *J. Biomol. NMR* *56*, 203–216.
40. Bertini, I., Janik, M.B.L., Lee, Y.M., Luchinat, C., and Rosato, A. (2001). Magnetic susceptibility tensor anisotropies for a lanthanide ion series in a fixed protein matrix. *J. Am. Chem. Soc.* *123*, 4181–4188.
41. Mironov, V.S., Galyametdinov, Y.G., Ceulemans, A., Görller-Walrand, C., and Binnemans, K. (2002). Room-temperature magnetic anisotropy of lanthanide complexes: a model study for various coordination polyhedra. *J. Chem. Phys.* *116*, 4673–4685.
42. Bleaney, B. (1972). Nuclear magnetic resonance shifts in solution due to lanthanide ions. *J. Magn. Reson.* *8*, 91–100.
43. Cucinotta, G., Perfetti, M., Luzon, J., Etienne, M., Car, P.E., Caneschi, A., Calvez, G., Bernot, K., and Sessoli, R. (2012). Magnetic anisotropy in a dysprosium/DOTA single-molecule magnet: Beyond simple magneto-structural correlations. *Angew. Chem. Int. Ed. Engl.* *51*, 1606–1610.
44. Rinehart, J.D., and Long, J.R. (2011). Exploiting single-ion anisotropy in the design of f-element single-molecule magnets. *Chem. Sci.* *2*, 2078–2085.
45. Delaglio, F., Grzesiek, S., Vuister, G.W., Zhu, G., Pfeifer, J., and Bax, A. (1995). NMRPipe: a multidimensional spectral processing system based on unix pipes. *J. Biomol. NMR* *6*, 277–293.
46. Vranken, W.F., Boucher, W., Stevens, T.J., Fogh, R.H., Pajon, A., Llinas, M., Ulrich, E.L., Markley, J.L., Ionides, J., and Laue, E.D. (2005). The CCPN data model for NMR spectroscopy: development of a software pipeline. *Proteins* *59*, 687–696.
47. Orton, H.W., Huber, T., and Otting, G. (2020). Paramagpy: software for fitting magnetic susceptibility tensors using paramagnetic effects measured in NMR spectra. *Magn. Reson.* *1*, 1–12.
48. Aravena, D., Neese, F., and Pantazis, D.A. (2016). Improved segmented all-electron relativistically contracted basis sets for the lanthanides. *J. Chem. Theory Comput.* *12*, 1148–1156.
49. Becke, A.D. (1988). Density-functional exchange-energy approximation with correct asymptotic behavior. *Phys. Rev. A Gen. Phys.* *38*, 3098–3100.
50. Perdew, J.P. (1986). Density-functional approximation for the correlation energy of the inhomogeneous electron gas. *Phys. Rev. B* *33*, 8822–8824.

## 2.6 Supplemental information

### 2.6.1 Materials and Methods

All chemicals were used as purchased without further purification if not stated otherwise.

All 400 MHz and 500 MHz NMR spectra were recorded on a Bruker Avance III NMR spectrometer operating at 400.13 MHz or 500.13 MHz proton frequency, respectively. The instruments were equipped with a direct observe 5-mm BBFO smart probe. All spectra were recorded at 298 K. All 600 MHz spectra were recorded either on a Bruker Avance III NMR spectrometer operating at 600.13 MHz proton frequency equipped with a direct observe 5-mm BBFO smart probe or indirect 5-mm BBI probe or a Bruker Avance III HD NMR spectrometer operating at 600.13 MHz proton frequency equipped with a cryogenic 5mm four-channel QCI probe (H/C/N/F). All spectra were recorded at 298 K. Ln-DOTA-M7FPy and Protein samples were measured in Shigemi micro cell tubes. For the ROESY experiments a mixing time of 25 ms was used. The  $^1\text{H}$  spectra of the strongly paramagnetic lanthanoids (Tb-Yb) were recorded in multiple spectra with a sweep width of 154 ppm. The spectra were baseline corrected and pieced together using MNova. For the recording of the single spectra of the strongly paramagnetic lanthanoids (Tb-Yb) the delay  $t_1$  and the acquisition were set to 0.5 seconds.

HR-ESI-MS spectra were measured on a Bruker MaXis 4G HiRes ESI Mass Spectrometer.

Analytical and preparative HPLC were performed on a Shimadzu LC20 HPLC-system equipped with a prominence UV/VIS detector, a FRC-10A fraction collector and a Shimadzu 2020 ESI-MS detector. For analytical HPLC a Reprosil-Pur 120 ODS-3, 3  $\mu\text{m}$  150x3 mm column was used. For preparative HPLC a Reprosil-Pur 120 ODS-3, 5  $\mu\text{m}$  150x20 mm column was used.

The methods use a binary gradient:

Solvent A: Water + 0.1% TFA.

Solvent B: 90% Acetonitrile + 10% water + 0.085% TFA.

Analytical method: Flow rate: 1.0 ml/min, oven temperature 40°C, UV set to 254 and 280 nm, gradient: 2 minutes at 5% B followed by a gradient over 4 min from 5% B to 100% B. These conditions were kept for 8 min followed by a gradient from 100% B to 5% B over 1 min. These conditions were kept constant for another 7 min, ESI-MS: positive mode 100-1500 m/z.

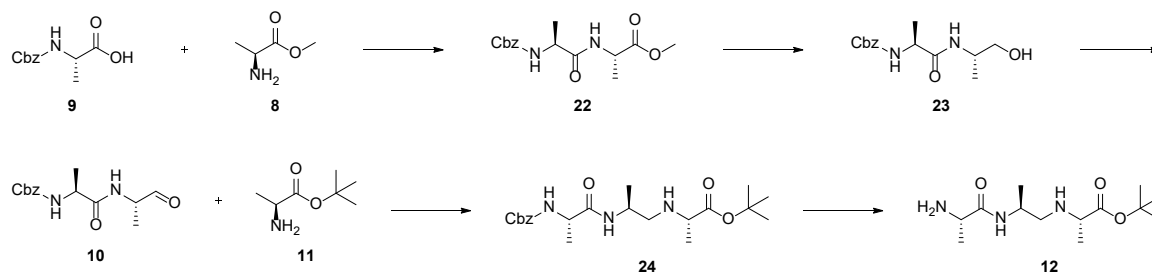
Preparative method: Flow rate: 9.0 ml/min, oven temperature 40°C, UV set to 254 and 280 nm, gradient: 2 min at 5% B followed by a gradient over 13 min from 5% B to 100% B. These conditions were kept for 7 min followed by a gradient from 100% B to 5% B over 1 min. These conditions were kept constant for another 2 min, ESI-MS: positive mode 100-1500 m/z. Fraction collector was set to the compound mass and a sample volume of 5-10 ml per fraction was collected.

For buffer exchange of proteins a Hettich Universal 320 R centrifuge at 6750 G in combination with Amicon Ultra-4 Centrifugal Filters Ultracel-3K from Merck Millipore were used.

For Tag purification and TFA removal by Sep-Pak column chromatography the same method was used. Sep-Pak cartridges (Sep-Pak® Vac RC (500 mg) C18 cartridges) were used in combination with a Bio-Rad Econo Pump equipped with a Bio-Rad Econo UV-Monitor. The Sep-Pak column was wetted with acetonitrile (20 ml) and then equilibrated with water (20 ml). Afterwards the product was loaded onto the column and washed with aq. phosphate buffer (pH = 7, 20 ml) and water (20 ml). The product was eluted with acetonitrile : water (1:1, 10 ml) and collected according to the UV signal.

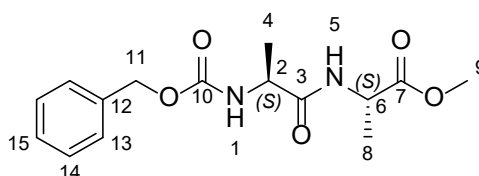
## 2.6.2 Experimental Procedures and Characterization

Experimental procedures are described the first time they were used. For the same compound with different isotope labelling only the characterization is reported. *tert*-Butyl (*S*)-2-(((trifluoromethyl)sulfonyl)oxy)propanoate (**35**) was synthesized according to H. Gsellinger<sup>1</sup>. 2-(Bromomethyl)-5-fluoro-4-(phenylsulfonyl) pyridine (**18**) was synthesized according to T. Müntener *et. al.*<sup>2</sup>.



**Figure S1:** Synthesis towards alanine trimer (**12**).

**Methyl ((benzyloxy)carbonyl)-*L*-alanyl-*L*-alaninate (**22**):** Methyl *L*-alaninate hydrochloride (42.7 g, 306 mmol, 1.0 eq.), ((benzyloxy)carbonyl)-*L*-alanine (68.3 g, 306 mmol, 1.0 eq.) and *N,N*-diisopropylethylamine (177 ml, 1.07 mol, 3.5 eq.) were suspended in ethyl acetate (500 ml). Propylphosphonic anhydride solution (50 wt. % in ethyl acetate, 214 g, 337 mmol, 1.1 eq.) was added dropwise and the mixture was stirred at 20-25°C for 18 h. The mixture was diluted with hydrochloric acid (2 M, 500 ml) and the layers were separated. The aqueous layer was extracted with ethyl acetate (200 ml). The combined organic layers were extracted with sat. aq. sodium hydrogen carbonate (500 ml) and brine (300 ml). The organic layer was dried over sodium sulphate and evaporated to dryness to yield methyl ((benzyloxy)carbonyl)-*L*-alanyl-*L*-alaninate (79.5 g, 258 mmol, 84%) as a white solid.



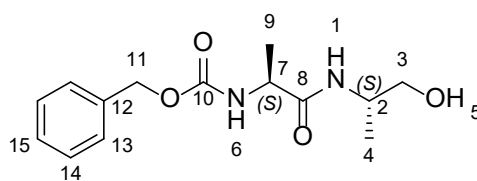
**<sup>1</sup>H-NMR (600 MHz, Chloroform-*d*)  $\delta$ :** 7.37-7.28 (m, 5H, H<sub>13,14,15</sub>), 6.65 (d, <sup>3</sup>*J*<sub>HH</sub> = 4.3 Hz, 1H, H<sub>5</sub>), 5.43 (d, <sup>3</sup>*J*<sub>HH</sub> = 6.2 Hz, 1H, H<sub>1</sub>), 5.10 (s, 2H, H<sub>11</sub>), 4.54 (qd, <sup>3</sup>*J*<sub>HH</sub> = 7.2 Hz,

$^3J_{\text{HH}} = 4.3$  Hz, 1H, H<sub>6</sub>), 4.25 (qd,  $^3J_{\text{HH}} = 7.2$  Hz,  $^3J_{\text{HH}} = 6.2$  Hz, 1H, H<sub>2</sub>), 3.73 (s, 3H, H<sub>9</sub>), 1.380 (d,  $^3J_{\text{HH}} = 7.2$  Hz, 3H, H<sub>8</sub>), 1.379 (s,  $^3J_{\text{HH}} = 7.2$  Hz, 3H, H<sub>4</sub>) ppm.

$^{13}\text{C}$  NMR (150 MHz, Chloroform-*d*)  $\delta$ : 173.32 (C<sub>7</sub>), 171.96 (C<sub>3</sub>), 155.94 (C<sub>10</sub>), 136.31 (C<sub>12</sub>), 128.67 (C<sub>14</sub>), 128.32 (C<sub>15</sub>), 128.19 (C<sub>13</sub>), 67.13 (C<sub>11</sub>), 52.63 (C<sub>9</sub>), 50.51 (C<sub>2</sub>), 48.18 (C<sub>6</sub>), 18.78 (C<sub>4</sub>), 18.37 (C<sub>8</sub>) ppm.

HR-ESI-MS: calcd. for [M+Na]<sup>+</sup> C<sub>15</sub>H<sub>20</sub>N<sub>2</sub>NaO<sub>5</sub> m/z= 331.1264 found m/z= 331.1265.

**Benzyl ((*S*)-1-(((*S*)-1-hydroxypropan-2-yl) amino) -1-oxopropan-2-yl) carbamate (23):** Methyl ((benzyloxy) carbonyl)-*L*-alanyl-*L*-alaninate (20.0 g, 64.9 mmol, 1.0 eq.) was dissolved in tetrahydrofuran (60 ml) and methanol (60 ml) and cooled to 0-5°C. A solution of sodium borohydride (15.3 g, 389 mmol, 6.0 eq.) in methanol : water 8:2 (225 ml) was added dropwise and the mixture was allowed to warm up to 20-25°C and was left stirring for 18 h. The pH was adjusted to 7 with hydrochloric acid (4 M). Volatile organic solvents were removed on the rotary evaporator. The white suspension was diluted with ethyl acetate (200 ml). The layers were separated and the aqueous layer was extracted with ethyl acetate (100 ml). The combined organic layers were extracted with sat. aq. sodium hydrogen carbonate (200 ml) and water (100 mL). The organic layer was dried over sodium sulphate and evaporated to dryness to yield benzyl ((*S*)-1-(((*S*)-1-hydroxypropan-2-yl)amino)-1-oxopropan-2-yl)carbamate (15.3 g, 54.6 mmol, 84%) as a white solid.

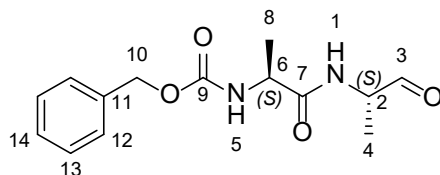


$^1\text{H}$ -NMR (600 MHz, Chloroform-*d*)  $\delta$ : 7.39-7.30 (m, 5H, H<sub>13,14,15</sub>), 6.17 (s, 1H, H<sub>1</sub>), 5.25 (s, 1H, H<sub>6</sub>), 5.11 (s, 2H, H<sub>11</sub>), 4.18 (qd,  $^3J_{\text{HH}} = 6.8$  Hz,  $^3J_{\text{HH}} = 6.2$  Hz, 1H, H<sub>7</sub>), 4.07-3.98 (m, 1H, H<sub>2</sub>), 3.73 (s, 1H, H<sub>3a</sub>), 3.53-3.45 (m, 1H, H<sub>3b</sub>), 1.38 (d,  $^3J_{\text{HH}} = 6.8$  Hz, 3H, H<sub>9</sub>), 1.14 (d,  $^3J_{\text{HH}} = 6.9$  Hz, 3H, H<sub>4</sub>) ppm.

**<sup>13</sup>C NMR (150 MHz, Chloroform-*d*)**  $\delta$ : 172.71 (C<sub>8</sub>), 156.16 (C<sub>10</sub>), 136.19 (C<sub>12</sub>), 128.74 (C<sub>14</sub>), 128.44 (C<sub>15</sub>), 128.32 (C<sub>13</sub>), 67.35 (C<sub>11</sub>), 66.82 (C<sub>3</sub>), 50.98 (C<sub>7</sub>), 47.94 (C<sub>2</sub>), 18.54 (C<sub>9</sub>), 16.97 (C<sub>4</sub>) ppm.

**HR-ESI-MS:** calcd. for [M+Na]<sup>+</sup> C<sub>14</sub>H<sub>20</sub>N<sub>2</sub>NaO<sub>4</sub> m/z= 303.1315 found m/z= 303.1317.

**Benzyl ((*S*)-1-oxo-1-(((*S*)-1-oxopropan-2-yl)amino)propan-2-yl)carbamate (10):** Benzyl ((*S*)-1-(((*S*)-1-hydroxypropan-2-yl)amino)-1-oxopropan-2-yl)carbamate (12.2 g, 43.5 mmol, 1.0 eq.) was dissolved in acetonitrile (200 ml). IBX (30.5 g, 109 mmol, 2.5 eq.) was added and the suspension was stirred at 80°C for 2 h. The reaction mixture was cooled to 20-25°C and diluted with ethyl acetate (600 ml). The suspension was filtered and the solvent was evaporated. The residue was redissolved in ethyl acetate (100 ml) and extracted with sat. aq. sodium hydrogen carbonate (100 ml) and water (100 ml). The organic layer was dried over sodium sulphate and evaporated to dryness to yield benzyl ((*S*)-1-oxo-1-(((*S*)-1-oxopropan-2-yl)amino)propan-2-yl)carbamate (11.2 g, 40.2 mmol, 93%) as a slightly yellow solid.



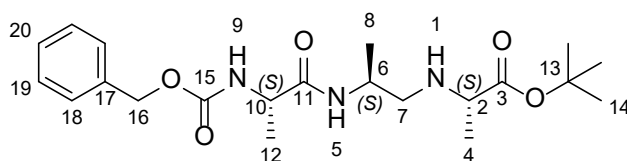
**<sup>1</sup>H-NMR (600 MHz, Chloroform-*d*)**  $\delta$ : 9.53 (s, 1H, H<sub>3</sub>), 7.39-7.30 (m, 5H, H<sub>12,13,14</sub>), 6.57 (s, 1H, H<sub>1</sub>), 5.24 (s, 1H, H<sub>5</sub>), 5.12 (s, 2H, H<sub>10</sub>), 4.47 (dq, <sup>3</sup>J<sub>HH</sub> = 7.0 Hz, <sup>3</sup>J<sub>HH</sub> = 6.6 Hz, 1H, H<sub>2</sub>), 4.32-4.23 (m, 1H, H<sub>6</sub>), 1.41 (d, <sup>3</sup>J<sub>HH</sub> = 7.0 Hz, 3H, H<sub>8</sub>), 1.35 (d, <sup>3</sup>J<sub>HH</sub> = 6.6 Hz, 3H, H<sub>4</sub>) ppm.

**<sup>13</sup>C NMR (150 MHz, Chloroform-*d*)**  $\delta$ : 198.69 (1 C, C<sub>3</sub>), 172.29 (1 C, C<sub>7</sub>), 155.94 (1 C, C<sub>9</sub>), 136.21 (1 C, C<sub>11</sub>), 128.73 (2 C, C<sub>13</sub>), 128.46 (1 C, C<sub>14</sub>), 128.30 (2 C, C<sub>12</sub>), 67.33 (1 C, C<sub>10</sub>), 54.71 (1 C, C<sub>2</sub>), 50.61 (1 C, C<sub>7</sub>), 18.60 (1 C, C<sub>8</sub>), 14.60 (1 C, C<sub>4</sub>) ppm.

**HR-ESI-MS:** calcd. for [M+H]<sup>+</sup> C<sub>14</sub>H<sub>19</sub>N<sub>2</sub>O<sub>4</sub> m/z= 279.1339 found m/z= 279.1334.

***tert*-Butyl ((*S*)-2-(((*S*)-2-(((benzyloxy)carbonyl)amino)propanamido)propyl)-*L*-alaninate (24):** Benzyl ((*S*)-1-oxo-1-(((*S*)-1-oxopropan-2-yl)amino)propan-2-yl)carbamate (11.2 g,

40.2 mmol, 1.0 eq.) was dissolved in methylene chloride (200 ml) and *tert*-butyl *L*-alaninate (5.84 g, 40.2 mmol, 1.0 eq.) was added. The solution was stirred at 20-25°C for 5 min followed by the addition of sodium triacetoxyborohydride (21.3 g, 101 mmol, 2.5 eq.). The suspension was stirred at 20-25°C for 4 h. The reaction mixture was extracted with sat. aq. sodium hydrogen carbonate (100 ml) and water (100 ml). The organic layer was dried over sodium sulphate and the solvent was evaporated. The crude product was purified by flash column chromatography (SiO<sub>2</sub>, ethyl acetate + 1% triethylamine, liquid deposit) to yield *tert*-butyl ((*S*)-2-((*S*)-2-(((benzyloxy)carbonyl)amino)propanamido)propyl)-*L*-alaninate (14.2 g, 34.8 mmol, 87%) as a colourless oil.



**<sup>1</sup>H-NMR (600 MHz, Chloroform-*d*)** δ: 7.38-7.28 (m, 5H, H<sub>18,19,20</sub>), 6.43 (s, 1H, H<sub>5</sub>), 5.44 (s, 1H, H<sub>9</sub>), 5.09 (s, 2H, H<sub>16</sub>), 4.25-4.16 (m, 1H, H<sub>10</sub>), 3.95-3.86 (m, 1H, H<sub>6</sub>), 3.20 (q, <sup>3</sup>*J*<sub>HH</sub> = 6.9 Hz, 1H, H<sub>2</sub>), 2.63 (dd, <sup>2</sup>*J*<sub>HH</sub> = 10.9 Hz, <sup>3</sup>*J*<sub>HH</sub> = 3.3 Hz, 1H, H<sub>7a</sub>), 2.53 (dd, <sup>2</sup>*J*<sub>HH</sub> = 10.9 Hz, <sup>3</sup>*J*<sub>HH</sub> = 4.3 Hz, 1H, H<sub>7b</sub>), 1.45 (s, 9H, H<sub>14</sub>), 1.38 (d, <sup>3</sup>*J*<sub>HH</sub> = 7.0 Hz, 3H, H<sub>12</sub>), 1.23 (d, <sup>3</sup>*J*<sub>HH</sub> = 7.2 Hz, 3H, H<sub>4</sub>), 1.14 (d, <sup>3</sup>*J*<sub>HH</sub> = 6.9 Hz, 3H, H<sub>8</sub>) ppm.

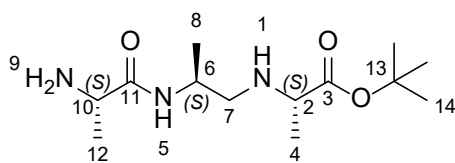
**<sup>13</sup>C NMR (150 MHz, Chloroform-*d*)** δ: 175.09 (C<sub>3</sub>), 171.81 (C<sub>11</sub>), 155.95 (C<sub>15</sub>), 136.48 (C<sub>17</sub>), 128.67 (C<sub>19</sub>), 128.30 (C<sub>20</sub>), 128.20 (C<sub>18</sub>), 81.23 (C<sub>13</sub>), 67.02 (C<sub>16</sub>), 57.38 (C<sub>2</sub>), 50.77 (C<sub>10</sub>), 52.00 (C<sub>7</sub>), 45.75 (C<sub>6</sub>), 28.22 (C<sub>14</sub>), 19.26 (C<sub>12</sub>), 18.56 (C<sub>8</sub>), 13.09 (C<sub>4</sub>) ppm.

**HR-ESI-MS:** calcd. for [M+H]<sup>+</sup> C<sub>21</sub>H<sub>34</sub>N<sub>3</sub>O<sub>5</sub> m/z= 408.2493 found m/z= 408.2500.

***tert*-Butyl ((*S*)-2-((*S*)-2-aminopropanamido)propyl)-*L*-alaninate (12):** *tert*-Butyl ((*S*)-2-((*S*)-2-(((benzyloxy) carbonyl)amino)propanamido)propyl)-*L*-alaninate (9.90 g, 24.3 mmol, 1.0 eq.) was dissolved in methanol (400 ml). Palladium on carbon (10%, 562 mg, 5.28 mmol, 0.22 eq.) was added and the suspension was stirred at 20-25°C under 1.0 bar of hydrogen for 20 h. The suspension was filtered through celite and the solvent was evaporated. The crude product was purified by flash column chromatography (SiO<sub>2</sub>, methylene chloride : ethanol



(8:2) + 2% triethylamine, liquid deposit) to yield *tert*-butyl ((*S*)-2-((*S*)-2-aminopropanamido)propyl)-*L*-alaninate (5.59 g, 20.4 mmol, 84%) as a slightly yellow oil.

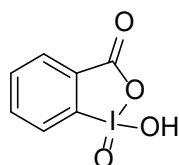


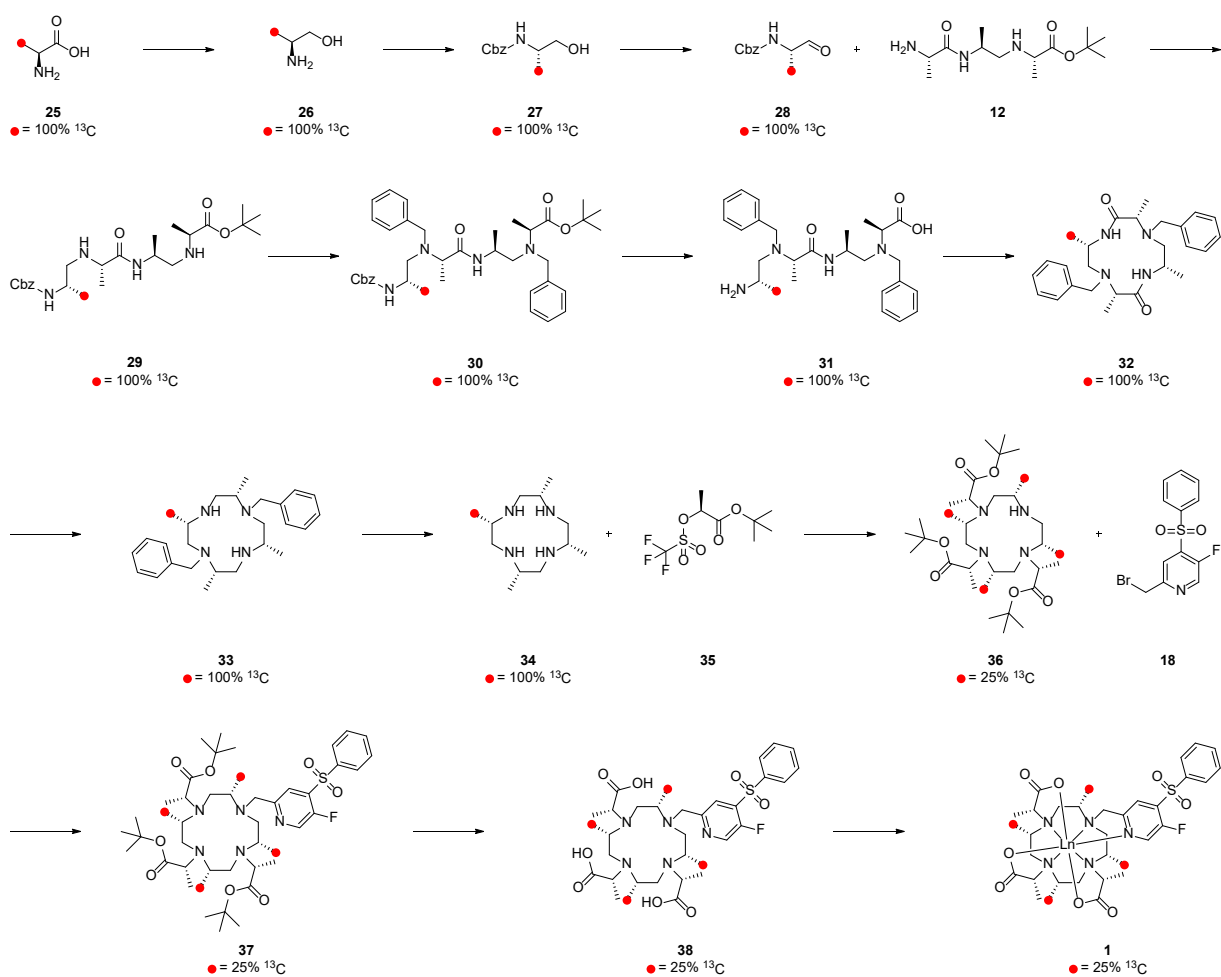
**<sup>1</sup>H-NMR (600 MHz, Chloroform-*d*)**  $\delta$ : 7.2 (s, 1H, H<sub>5</sub>), 4.00-3.90 (m, 1H, H<sub>6</sub>), 3.47 (q, <sup>3</sup>*J*<sub>HH</sub> = 7.0 Hz, 1H, H<sub>10</sub>), 3.20 (q, <sup>3</sup>*J*<sub>HH</sub> = 6.9 Hz, 1H, H<sub>2</sub>), 2.64 (dd, <sup>2</sup>*J*<sub>HH</sub> = 11.9 Hz, <sup>3</sup>*J*<sub>HH</sub> = 5.5 Hz, 1H, H<sub>7a</sub>), 2.54 (dd, <sup>2</sup>*J*<sub>HH</sub> = 11.9 Hz, <sup>3</sup>*J*<sub>HH</sub> = 3.3 Hz, 1H, H<sub>7b</sub>), 1.45 (s, 9H, H<sub>14</sub>), 1.31 (d, <sup>3</sup>*J*<sub>HH</sub> = 6.9 Hz, 3H, H<sub>12</sub>), 1.24 (d, <sup>3</sup>*J*<sub>HH</sub> = 7.0 Hz, 3H, H<sub>4</sub>), 1.16 (d, <sup>3</sup>*J*<sub>HH</sub> = 6.9 Hz, 3H, H<sub>8</sub>) ppm.

**<sup>13</sup>C NMR (150 MHz, Chloroform-*d*)**  $\delta$ : 175.35 (C<sub>11</sub>), 175.02 (C<sub>3</sub>), 80.96 (C<sub>13</sub>), 57.31 (C<sub>2</sub>), 52.43 (C<sub>7</sub>), 50.89 (C<sub>10</sub>), 44.89 (C<sub>6</sub>), 28.09 (C<sub>14</sub>), 21.78 (C<sub>12</sub>), 18.93 (C<sub>4</sub>), 18.68 (C<sub>8</sub>) ppm.

**HR-ESI-MS:** calcd. for [M+H]<sup>+</sup> C<sub>13</sub>H<sub>28</sub>N<sub>3</sub>O<sub>3</sub> *m/z* = 274.2125 found *m/z* = 274.2130.

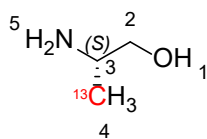
**2-Iodoxybenzoic acid:** Oxone (186 g, 606 mmol, 3.0 eq.) was dissolved in water (650 ml). Then 2-iodobenzoic acid (50.3 g, 203 mmol; 1.0 eq.) was added and the suspension was stirred at 80°C for 5.5 h. Afterwards the suspension was cooled to 0°C, the solid was filtered off and washed with water (400 ml) and acetone (500 ml) to yield 2-iodoxybenzoic acid (48.8 g, 174 mmol, 86%) as a white solid.





**Figure S2:** Synthesis towards Ln-DOTA-M7FPy (**1**) with carbon  $^{13}\text{C}$  labelled methyl groups on the basal cyclen ring. Red dots mark positions labelled with carbon  $^{13}\text{C}$ . Below each labelled molecule the observed labelling percentage is noted.

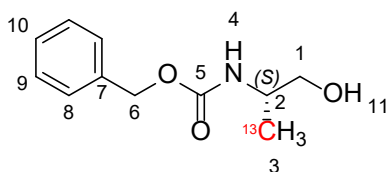
**(S)-2-Aminopropan-1-ol (26):** *L*-Alanine (500 mg, 5.61 mmol, 1.0 eq.) was suspended in dry tetrahydrofuran (30 ml) under an atmosphere of argon. The suspension was cooled to 0-5°C. Then lithium aluminium hydride (2.4 M in tetrahydrofuran, 4.7 ml, 11.2 mmol, 2.0 eq.) was added dropwise over 5 min. The suspension was kept at 0-5°C for 30 min. and then allowed to warm up to 20-25°C. The suspension was stirred at 20-25°C for 2 h. Afterwards the suspension was cooled to 0-5°C and sat. aq. sodium hydrogen carbonate (4.0 ml) was added slowly. The suspension was diluted with methylene chloride (20 ml) and sodium sulphate (13.0 g) was added. The suspension was filtered and the residue washed generously with methylene chloride (approx. 100 ml). The solvent was evaporated under reduced pressure (not for too long and not at too low pressure, the product is volatile). The product was obtained as a slightly yellow oil still containing some residual solvent. The product was directly used without further purification.



**<sup>1</sup>H NMR (500 MHz, Chloroform-*d*)**  $\delta$ : 3.54 (ddd, 1H,  $^2J_{\text{HH}} = 10.4$  Hz,  $^3J_{\text{HH}} = 4.1$  Hz,  $^3J_{\text{CH}} = 2.5$  Hz, H<sub>2a</sub>), 3.23 (ddd, 1H,  $^2J_{\text{HH}} = 10.4$  Hz,  $^3J_{\text{HH}} = 7.8$  Hz,  $^3J_{\text{CH}} = 2.5$  Hz, H<sub>2b</sub>), 3.01 (m, 1H, H<sub>3</sub>), 1.06 (dd,  $^1J_{\text{CH}} = 125.5$  Hz,  $^3J_{\text{HH}} = 6.6$  Hz, 3H, H<sub>3</sub>) ppm.

**HR-ESI-MS:** calcd. for [M+H]<sup>+</sup> C<sub>3</sub>H<sub>10</sub>NO  $m/z = 77.0790$  found 77.0791.

**Benzyl (*S*)-(1-hydroxypropan-2-yl)carbamate (27):** Sodium carbonate (1.85 g, 17.4 mmol, 3.1 eq.) was dissolved in water (9.5 ml). A solution of (*S*)-2-Aminopropan-1-ol (421 mg, 5.61 mmol, 1.0 eq.) in ethyl acetate (4.0 ml) was added. The biphasic mixture was stirred vigorously and benzyl chloroformate (986 mg, 5.78 mmol, 1.0 eq.) was added. The biphasic mixture was stirred at 20-25°C for 1 h. Then the solution was diluted with water (5.0 ml) and ethyl acetate (5.0 ml). The layers were separated and the aqueous layer was extracted with ethyl acetate (2\*10 ml). The combined organic layers were washed with water (10 ml), dried over sodium sulphate and the solvent was evaporated. The crude product was purified by flash column chromatography (SiO<sub>2</sub>, ethyl acetate : Cyclohexane (7:3), liquid deposit) to yield benzyl (*S*)-(1-hydroxypropan-2-yl)carbamate (665 mg, 3.18 mmol, 57%) as a colourless solid.



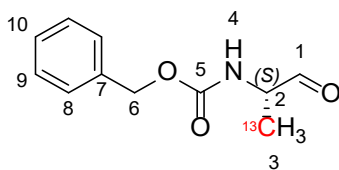
**<sup>1</sup>H NMR (500 MHz, Chloroform-*d*)**  $\delta$ : 9.56 (s, 1H, H<sub>1</sub>), 7.38 – 7.28 (m, 5H, H<sub>8,9,10</sub>), 5.09 (m, 2H, H<sub>6</sub>), 4.96 (m, 1H, H<sub>4</sub>), 3.83 (m, 1H, H<sub>2</sub>), 3.64 (m, 1H, H<sub>1a</sub>), 3.52 (m, 1H, H<sub>1b</sub>), 2.50 (s, 1H, H<sub>11</sub>), 1.16 (dd,  $^1J_{\text{CH}} = 127.1$  Hz,  $^3J_{\text{HH}} = 6.8$  Hz, 3H, H<sub>3</sub>) ppm.

**<sup>13</sup>C NMR (126 MHz, Chloroform-*d*)**  $\delta$ : 156.71 (C<sub>5</sub>), 136.48 (C<sub>7</sub>), 128.67 (C<sub>9</sub>), 128.30 (C<sub>10</sub>), 128.26 (C<sub>8</sub>), 66.98 (C<sub>6,1</sub>), 49.11 (d,  $^1J_{\text{CC}} = 37.2$  Hz, C<sub>2</sub>), 17.38 (C<sub>3</sub>) ppm.

**HR-ESI-MS:** calcd. for  $[M+Na]^+$   $C_{11}H_{15}NO_3Na$   $m/z = 233.0978$  found 233.0976.

$R_f = 0.31$  in Ethyl acetate : Cyclohexane (7:3).

**Benzyl (*S*)-(1-oxopropan-2-yl)carbamate (28):** Benzyl (*S*)-(1-hydroxypropan-2-yl)carbamate (1.01 g, 4.78 mmol, 1.0 eq.) was dissolved in ethyl acetate (20 ml). Argon was bubbled through the solution for 10 min. Then IBX (2.01 g, 7.17 mmol, 1.5 eq.) was added. The suspension was heated to 80°C for 2.6 h under an atmosphere of argon. When the suspension started refluxing dimethyl sulfoxide (1.1 ml, 1.21 g, 15.5 mmol, 3.2 eq.) was added. Afterwards the reaction was cooled to 0-5°C. The solid was filtered off and washed with ethyl acetate (25 ml). The filtrate was washed with sat. aq. sodium hydrogen carbonate (25 ml), water (25 ml) and brine (25 ml). The organic layer was dried over sodium sulphate and the solvent was evaporated under reduced pressure to yield benzyl (*S*)-(1-oxopropan-2-yl)carbamate (960 mg, 4.63 mmol, 97%) as a slightly yellow oil.



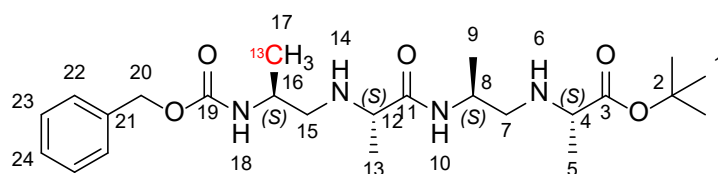
**$^1H$  NMR (500 MHz, Chloroform-*d*)**  $\delta$ : 9.56 (s, 1H, H<sub>1</sub>), 7.39 – 7.30 (m, 5H, H<sub>8,9,10</sub>), 5.40 (s, 1H, H<sub>4</sub>), 5.12 (s, 2H, H<sub>6</sub>), 4.31 (m, 1H, H<sub>2</sub>), 1.37 (dd,  $^1J_{CH} = 129.7$  Hz,  $^3J_{HH} = 7.5$  Hz, 3H, H<sub>3</sub>) ppm.

**$^{13}C$  NMR (126 MHz, Chloroform-*d*)**  $\delta$ : 199.07 (C<sub>1</sub>), 155.94 (C<sub>5</sub>), 136.27 (C<sub>7</sub>), 128.70 (C<sub>8</sub>), 128.40 (C<sub>9</sub>), 128.28 (C<sub>10</sub>), 67.21 (C<sub>6</sub>), 56.05 (d,  $^1J_{CC} = 36.1$  Hz, C<sub>2</sub>), 14.98 (C<sub>3</sub>) ppm.

**HR-ESI-MS:** calcd. for  $[M+Na]^+$   $C_{11}H_{13}NO_3Na$   $m/z = 231.0821$  found 231.0824.

***tert*-Butyl ((*S*)-2-((*S*)-2-(((*S*)-2-((benzyloxy)carbonyl)amino)propyl)amino)propanamido)propyl)-*L*-alaninate (29):** Benzyl (*S*)-(1-oxopropan-2-yl)carbamate (960 mg, 4.63 mmol, 1.0 eq.) and *tert*-butyl ((*S*)-2-((*S*)-2-aminopropanamido)propyl)-*L*-alaninate (1.26 g, 4.63 mmol, 1.0 eq.) were dissolved in methylene chloride (20 ml). Then sodium

triacetoxyborohydride (2.99 g, 14.1 mmol, 3.1 eq.) was added. The solution was stirred at 20-25°C for 18 h. Then sat. aq. sodium hydrogen carbonate (18 ml) was added. The layers were separated. The organic layer was washed with water (20 ml) and the combined aqueous layers were washed with methylene chloride (20 ml). The combined organic layers were washed with brine (20 ml) and dried over sodium sulphate. The solvent was evaporated under reduced pressure to yield *tert*-butyl ((*S*)-2-((*S*)-2-(((*S*)-2-(((benzyloxy) carbonyl) amino) propyl) amino) propanamido)propyl)-*L*-alaninate (2.11 g, 4.53 mmol, 98%) as a yellow oil.



**<sup>1</sup>H NMR (500 MHz, Chloroform-*d*)**  $\delta$ : 9.11-9.03 (m, 1H, H<sub>10</sub>), 7.38-7.27 (m, 5H, H<sub>22,23,24</sub>), 5.87-5.78 (m, 1H, H<sub>18</sub>), 5.15-5.09 (m, 1H, H<sub>20a</sub>), 5.02-4.92 (m, 1H, H<sub>20b</sub>), 4.42-4.29 (m, 1H, H<sub>8</sub>), 4.17-4.06 (m, 1H, H<sub>16</sub>), 4.03-3.94 (m, 1H, H<sub>12</sub>), 3.88-3.76 (m, 1H, H<sub>4</sub>), 3.37-3.25 (m, 1H, H<sub>7a</sub>), 3.24-3.15 (m, 1H, H<sub>15a</sub>), 3.06-2.99 (m, 1H, H<sub>15b</sub>), 2.96-2.87 (m, 1H, H<sub>7b</sub>), 1.56 (d, <sup>3</sup>*J*<sub>HH</sub> = 7.1 Hz, 3H, H<sub>5</sub>), 1.49 (d, <sup>3</sup>*J*<sub>HH</sub> = 7.1 Hz, 3H, H<sub>13</sub>), 1.46 (s, 9H, H<sub>1</sub>), 1.27 (d, <sup>3</sup>*J*<sub>HH</sub> = 7.1 Hz, 3H, H<sub>9</sub>), 1.24 (dd, <sup>1</sup>*J*<sub>CH</sub> = 129.0 Hz, <sup>3</sup>*J*<sub>HH</sub> = 7.1 Hz, 3H, H<sub>17</sub>) ppm.

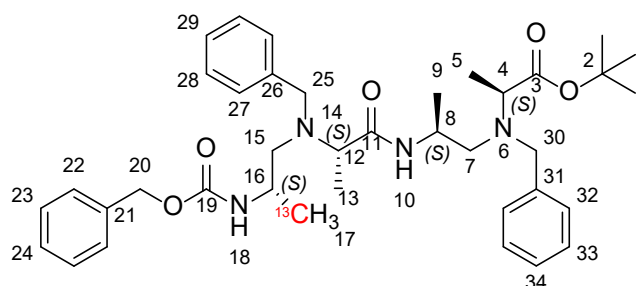
**<sup>13</sup>C NMR (126 MHz, Chloroform-*d*)**  $\delta$ : 170.16 (C<sub>11</sub>), 167.87 (C<sub>3</sub>), 157.10 (C<sub>19</sub>), 135.98 (C<sub>21</sub>), 128.66 (C<sub>22/23/24</sub>), 128.35 (C<sub>22/23/24</sub>), 127.95 (C<sub>22/23/24</sub>), 84.92 (C<sub>2</sub>), 67.33 (C<sub>20</sub>), 57.60 (C<sub>12</sub>), 56.81 (C<sub>4</sub>), 51.24 (C<sub>15</sub>), 50.09 (C<sub>7</sub>), 45.35 (C<sub>16</sub>), 44.96 (C<sub>8</sub>), 27.88 (C<sub>1</sub>), 18.82 (C<sub>17</sub>), 14.35 (C<sub>13</sub>), 14.31 (C<sub>5</sub>) ppm.

The C<sub>9</sub> shift cannot be identified since the signal is overlapped by the carbon <sup>13</sup>C signal of C<sub>17</sub>.

**HR-ESI-MS:** calcd. for [M+H]<sup>+</sup> C<sub>24</sub>H<sub>41</sub>N<sub>4</sub>O<sub>5</sub> *m/z* = 466.3105 found 466.3110.

***tert*-Butyl (5*S*,8*S*,11*S*,14*S*)-7,13-dibenzyl-5,8,11,14-tetramethyl-3,9-dioxo-1-phenyl-2-oxa-4,7,10,13 - tetraazapentadecan - 15 - oate (30):** *tert*-butyl ((*S*)-2-((*S*)-2-(((*S*)-2-(((benzyloxy) carbonyl)amino) propyl) amino)propanamido)propyl)-*L*-alaninate (2.09 g, 4.50 mmol, 1.0 eq.) was dissolved in acetonitrile (20 ml). Then potassium carbonate (2.49 g, 18.0 mmol, 4.0 eq.) and benzyl bromide (1.4 ml, 2.00 g, 11.7 mmol, 2.6 eq.) were added. The suspension was

heated to 45°C for 6.75 h. Then triethylamine (1.5 ml) was added and the suspension was heated for 1.25 h. Afterwards the suspension was cooled to 0-5°C and the solid was filtered off. The solvent was evaporated yielding a yellow oil. The oil was suspended in ethyl acetate and the precipitate was filtered off. The solvent was evaporated and the crude product was purified by flash column chromatography (SiO<sub>2</sub>, cyclohexane : ethyl acetate (7:3), liquid deposit) to yield *tert*-butyl (5*S*,8*S*,11*S*,14*S*) - 7,13 - dibenzyl - 5,8,11,14 - tetramethyl-3,9-dioxo-1-phenyl-2-oxa-4,7,10,13-tetraazapentadecan-15-oate (1.79 g, 2.77 mmol, 62%) as a colourless solid.



**<sup>1</sup>H NMR (500 MHz, Chloroform-*d*)**  $\delta$ : 7.40-7.16 (m, 15H, H<sub>22,23,24,27,28,29,32,33,34</sub>), 5.15-5.08 (m, 1H, H<sub>20a</sub>), 4.99-4.91 (m, 1H, H<sub>20b</sub>), 4.72-4.65 (m, 1H, H<sub>18</sub>), 4.04-3.95 (m, 1H, H<sub>8</sub>), 3.89-3.69 (m, 4H, H<sub>16,25a,30a,30b</sub>), 3.45-3.32 (m, 2H, H<sub>12,25b</sub>), 3.28 (q, 1H, <sup>3</sup>J<sub>HH</sub> = 7.36 Hz, H<sub>4</sub>) 2.70-2.64 (m, 1H, H<sub>7a</sub>), 2.62-2.55 (m, 1H, H<sub>7b</sub>), 2.52-2.46 (m, 1H, H<sub>15a</sub>), 2.34-2.24 (m, 1H, H<sub>15b</sub>), 1.44 (s, 9H, H<sub>1</sub>), 1.22-0.91 (m, 12H, H<sub>5,9,13,17</sub>) ppm.

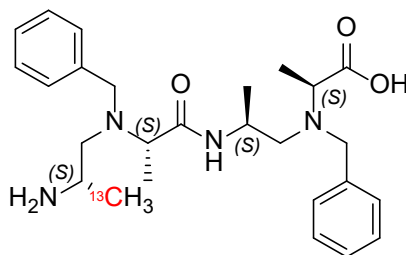
**<sup>13</sup>C NMR (126 MHz, Chloroform-*d*)**  $\delta$ : 173.42 (C<sub>3</sub>), 172.97 (C<sub>11</sub>), 156.47 (C<sub>19</sub>), 140.09 (C<sub>31</sub>), 139.26 (C<sub>26</sub>), 136.70 (C<sub>21</sub>), 129.09 (C<sub>22/23/24/27/28/29/32/33/34</sub>), 128.65 (C<sub>22/23/24/27/28/29/32/33/34</sub>), 128.60 (C<sub>22/23/24/27/28/29/32/33/34</sub>), 128.46 (C<sub>22/23/24/27/28/29/32/33/34</sub>), 128.30 (C<sub>22/23/24/27/28/29/32/33/34</sub>), 128.25 (C<sub>22/23/24/27/28/29/32/33/34</sub>), 128.19 (C<sub>22/23/24/27/28/29/32/33/34</sub>), 127.29 (C<sub>22/23/24/27/28/29/32/33/34</sub>), 126.93 (C<sub>22/23/24/27/28/29/32/33/34</sub>), 80.91 (C<sub>2</sub>), 66.65 (C<sub>20</sub>), 58.49 (C<sub>12</sub>), 57.78 (C<sub>4</sub>), 56.52 (C<sub>15</sub>), 56.39 (C<sub>30</sub>), 55.73 (C<sub>7</sub>), 54.91 (C<sub>25</sub>), 45.20 (d, <sup>1</sup>J<sub>CC</sub> = 37.0 Hz, C<sub>16</sub>), 44.31 (C<sub>8</sub>), 28.43 (C<sub>1</sub>), 19.53 (C<sub>17</sub>), 15.33 (C<sub>5</sub>), 8.34 (C<sub>13</sub>) ppm.

The C<sub>9</sub> shift cannot be identified since the signal is overlapped by the carbon <sup>13</sup>C signal of C<sub>17</sub>.

**HR-ESI-MS:** calcd. for [M+H]<sup>+</sup> C<sub>38</sub>H<sub>53</sub>N<sub>4</sub>O<sub>5</sub> m/z = 646.4044 found 646.4045.

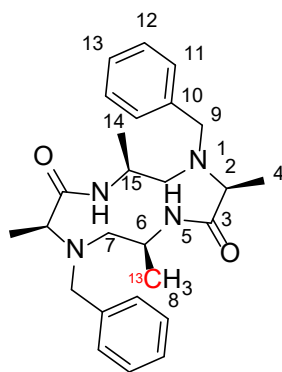
R<sub>f</sub> = 0.28 in Ethyl acetate : Cyclohexane (3:7).

***N*-((*S*)-2-((*S*)-2-(((*S*)-2-aminopropyl) (benzyl)amino) propanamido)propyl) -*N*-benzyl-*L*-alanine (**31**):** *tert*-butyl (5*S*,8*S*,11*S*,14*S*) -7,13 -dibenzyl -5,8,11,14 - tetramethyl -3,9-dioxo-1-phenyl-2-oxa-4,7,10,13-tetraazapentadecan-15-oate (1.79 g, 27.7 mmol, 1.0 eq.) was dissolved in hydrobromic acid (32% in acetic acid, 5.0 ml) and glacial acetic acid (5.0 ml). The solution was stirred at 40°C for 35 min. The solvent was evaporated under reduced pressure. The residue was dissolved in acetonitrile (10 ml) and conc. hydrochloric acid (0.50 ml) and the solvent was evaporated under reduced pressure. This process was repeated three times. Then the residue was dissolved in acetonitrile (10 ml) and the solvent was evaporated under reduced pressure. Afterwards the residue was dissolved in methanol (10 ml) and the solvent was evaporated under reduced pressure. The crude product was dried at 40°C under high vacuum for 72 h to yield *N*-((*S*)-2-((*S*)-2-(((*S*)-2-aminopropyl)(benzyl)amino) propanamido)propyl)-*N*-benzyl-*L*-alanine (1.90 g) as a beige foam. The product was obtained as hydrobromic and hydrochloric acid salt and was used without further purification.



**HR-ESI-MS:** calcd. for  $[M+H]^+$  C<sub>26</sub>H<sub>39</sub>N<sub>4</sub>O<sub>3</sub> m/z = 456.3050 found 456.3050.

**(3*S*,6*S*,9*S*,12*S*)-4,10-Dibenzyl-3,6,9,12-tetramethyl- 1,4,7,10 - tetraazacyclododecane - 2,8-dione (**32**):** *N*-((*S*)-2-((*S*)-2-(((*S*)-2-aminopropyl) (benzyl)amino) propanamido) propyl)-*N*-benzyl-*L*-alanine salts (1.62 g) were dissolved in acetonitrile (1.62 l) and *N,N*-diisopropylethylamine (3.0 ml, 2.35 g, 18.2 mmol, 5.0 eq.). Then HATU (1.35 g, 3.56 mmol, 1.0 eq.) was added. The solution was stirred at 20-25°C for 35 min. The solvent was evaporated and the crude product was purified by flash column chromatography (SiO<sub>2</sub>, cyclohexane : ethyl acetate (1:9) + 1% triethylamine, liquid deposit) to yield (3*S*,6*S*,9*S*,12*S*)-4,10-dibenzyl - 3,6,9,12- tetramethyl-1,4,7,10-tetraazacyclo dodecane- 2,8-dione (430 mg, 0.986 mmol, 40% (calculated over two steps)) as a white foam.



**$^1\text{H}$  NMR (500 MHz, Dimethylsulfoxide- $d_6$ )  $\delta$ :** 7.73 (d,  $^3J_{\text{HH}} = 5.00$  Hz, 2H, H<sub>5</sub>), 7.45-7.40 (m, 4H, H<sub>11</sub>), 7.33-7.25 (m, 6H, H<sub>12,13</sub>), 3.90 (d,  $^3J_{\text{HH}} = 13.5$  Hz, 2H, H<sub>9a</sub>), 3.57 (d,  $^3J_{\text{HH}} = 13.5$  Hz, 2H, H<sub>9b</sub>), 3.38-3.29 (m, 2H, H<sub>6,15</sub>), 3.20 (q,  $^3J_{\text{HH}} = 7.0$  Hz, 2H, H<sub>2</sub>), 2.81-2.73 (m, 2H, H<sub>7a</sub>), 2.32-2.26 (m, 2H, H<sub>7b</sub>), 1.15 (d,  $^3J_{\text{HH}} = 6.7$  Hz, 3H, H<sub>14</sub>), 1.15 (dd,  $^1J_{\text{CH}} = 127.0$  Hz,  $^3J_{\text{HH}} = 6.7$  Hz, 3H, H<sub>8</sub>), 1.15 (d,  $^3J_{\text{HH}} = 7.0$  Hz, 6H, H<sub>4</sub>) ppm.

**$^{13}\text{C}$  NMR (126 MHz, Dimethylsulfoxide- $d_6$ )  $\delta$ :** 172.13 (C<sub>3</sub>), 139.18 (C<sub>10</sub>), 129.03 (C<sub>11</sub>), 128.16 (C<sub>12</sub>), 127.10 (C<sub>13</sub>), 59.64 (C<sub>2</sub>), 56.85 (C<sub>9</sub>), 55.14 (C<sub>7</sub>), 44.07 (C<sub>15</sub>), 44.07 (d,  $^1J_{\text{CC}} = 37.2$  Hz, C<sub>6</sub>), 17.70 (C<sub>8,14</sub>), 8.54 (C<sub>4</sub>) ppm.

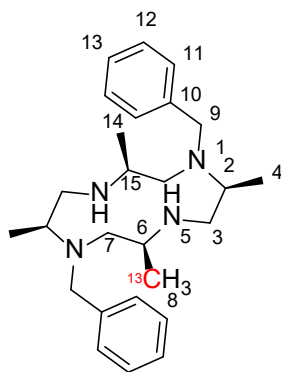
**HR-ESI-MS:** calcd. for  $[\text{M}+\text{H}]^+$  C<sub>26</sub>H<sub>37</sub>N<sub>4</sub>O<sub>2</sub>  $m/z = 438.2945$  found 438.2950.

R<sub>f</sub> = 0.3 in Ethyl acetate : Cyclohexane (9:1) + 1% Triethylamine.

**(2S,5S,8S,11S) -1,7-Dibenzyl- 2,5,8,11-tetramethyl- 1,4,7,10-tetraazacyclododecane (33):** (3S,6S,9S, 12S)-4,10-dibenzyl - 3,6,9,12 - tetramethyl - 1,4,7,10 - tetraazacyclo dodecane-2,8-dione (430 mg, 0.985 mmol, 1.0 eq.) was dissolved under argon in dry methylene chloride (11 ml). The solution was cooled to 0-5°C then trimethylsilyl chloride (589 mg, 0.692 ml, 5.42 mmol, 5.5 eq.) was added over 10 min. The solution was stirred at 0-5°C for 30 min. Afterwards lithium aluminium hydride (2 M in tetrahydrofuran, 1.4 ml, 2.80 mmol, 2.8 eq.) was added over 10 min. The solution was allowed to warm up to 20-25°C. The solution was stirred for 1 h then lithium aluminium hydride (2 M in tetrahydrofuran, 1.4 ml, 2.80 mmol, 2.8 eq.) was added. The solution was stirred for 2 h then lithium aluminium hydride (2M in tetrahydrofuran, 1.2 ml, 2.40 mmol, 2.4 eq.) was added. The suspension was stirred overnight. The suspension was cooled to 0-5°C and aq. potassium hydroxide (4 M, 3.0 ml) was added.



Then an excess of sodium sulphate was added and the suspension was filtered. The solvent was evaporated and the crude product was purified by flash column chromatography (SiO<sub>2</sub>, methylene chloride : ethanol (8:2) + 2% triethylamine, liquid deposit) to yield (2*S*,5*S*,8*S*,11*S*) - 1,7 - dibenzyl - 2,5,8,11-tetramethyl-1,4,7,10-tetraazacyclododecane (240 mg, 0.587 mmol, 60%) as a white solid.



**<sup>1</sup>H NMR (500 MHz, Chloroform-*d*)**  $\delta$ : 7.40-7.33 (m, 8H, H<sub>11,12</sub>), 7.28-7.24 (m, 2H, H<sub>13</sub>), 3.81 (d, <sup>3</sup>*J*<sub>HH</sub> = 13.1 Hz, 2H, H<sub>9a</sub>), 3.13-3.03 (m, 2H, H<sub>2</sub>), 3.02-2.75 (m, 8H, H<sub>3a,6,9b,5,15</sub>), 2.50-2.33 (m, 4H, H<sub>3b,7a</sub>), 2.30-2.18 (m, 2H, H<sub>7b</sub>), 0.91 (d, <sup>3</sup>*J*<sub>HH</sub> = 6.6 Hz, 6H, H<sub>4</sub>), 0.87 (dd, <sup>1</sup>*J*<sub>CH</sub> = 126.1 Hz, <sup>3</sup>*J*<sub>HH</sub> = 5.5 Hz, 3H, H<sub>8</sub>) 0.87 (d, <sup>3</sup>*J*<sub>HH</sub> = 5.5 Hz, 3H, H<sub>14</sub>) ppm.

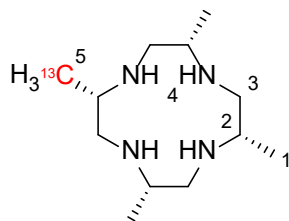
**<sup>13</sup>C NMR (126 MHz, Chloroform-*d*)**  $\delta$ : 139.94 (C<sub>10</sub>), 192.35 (C<sub>11</sub>), 128.5 (C<sub>12</sub>), 127.30 (C<sub>13</sub>), 56.64 (C<sub>7</sub>), 51.72 (C<sub>9</sub>), 50.05 (C<sub>2</sub>), 47.92 (C<sub>3</sub>), 46.51 (C<sub>15</sub>), 46.51 (d, <sup>1</sup>*J*<sub>CC</sub> = 37.2 Hz, C<sub>6</sub>), 18.19 (C<sub>8,14</sub>), 10.16 (C<sub>4</sub>) ppm.

**HR-ESI-MS:** calcd. for [M+H]<sup>+</sup> C<sub>26</sub>H<sub>41</sub>N<sub>4</sub> m/z = 410.3359 found 410.3356.

R<sub>f</sub> = 0.9 in Methylene chloride : Ethanol 8:2 + 2% Triethylamine

**(2*S*,5*S*,8*S*,11*S*) -2,5,8,11- Tetramethyl -1,4,7,10 -tetraazacyclododecane (34):** (2*S*,5*S*,8*S*,11*S*)-1,7-dibenzyl-2,5,8,11-tetramethyl-1,4,7,10-tetraazacyclododecane (155 mg, 0.379 mmol, 1.0 eq.) was dissolved in methanol (7.0 ml). Then palladium on carbon (10%, 16.1 mg, 0.0152 mmol, 0.040 eq.) and trifluoroacetic acid (0.15 ml) were added. The suspension was hydrogenated at 20-25°C under a pressure of 50 bar for 4 h. Reaction control with HPLC-MS showed only minor conversion. Therefore additional methanol (7.0 ml),

palladium on carbon (10%, 21.8 mg, 0.0206 mmol, 0.054 eq.) and trifluoroacetic acid (0.15 ml) were added and the suspension was hydrogenated at 20-25°C under a pressure of 50 bar for 20 h. Reaction control with HPLC-MS showed around 40% conversion. Then additional trifluoroacetic acid (0.15 ml) was added and the suspension was hydrogenated at 20-25°C under a pressure of 50 bar for 120 h. Afterwards the suspension was filtered over celite and the solvent was evaporated. The crude was dissolved in methylene chloride (10 ml) and extracted with aq. potassium hydroxide (4 M, 10 ml). The aqueous layer was washed with methylene chloride (10 ml) and the combined organic layers were dried over sodium sulphate. The solvent was evaporated to yield (2*S*,5*S*,8*S*,11*S*)-2,5,8,11-tetramethyl-1,4,7,10-tetraazacyclododecane (78.6 mg, 0.344 mmol, 91%) as a white solid.



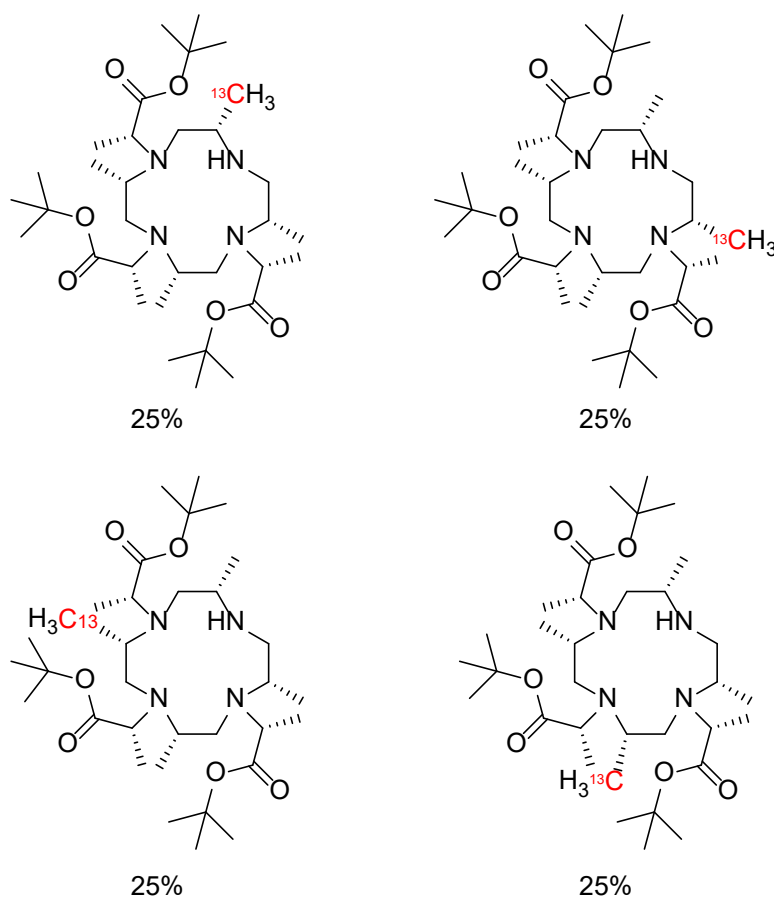
**<sup>1</sup>H NMR (500 MHz, Chloroform-*d*)**  $\delta$ : 2.69-2.60 (m, 8H, H<sub>2,3a</sub>), 2.42-2.34 (m, 4H, H<sub>3b</sub>), 2.20-2.07 (m, 4H, H<sub>4</sub>), 0.94 (dd, <sup>1</sup>*J*<sub>CH</sub> = 125.0 Hz, <sup>3</sup>*J*<sub>HH</sub> = 6.0 Hz, 3H, H<sub>5</sub>), 0.94 (dd, <sup>3</sup>*J*<sub>HH</sub> = 6.0 Hz, 9H, H<sub>1</sub>) ppm.

**<sup>13</sup>C NMR (126 MHz, Chloroform-*d*)**  $\delta$ : 52.36 (C<sub>3</sub>), 47.83 (C<sub>2</sub>), 47.83 (d, <sup>1</sup>*J*<sub>CC</sub> = 37.8 Hz, C<sub>5</sub>), 18.51 (C<sub>1</sub>) ppm.

**HR-ESI-MS:** calcd. for [M+H]<sup>+</sup> C<sub>12</sub>H<sub>29</sub>N<sub>4</sub> *m/z* = 230.2420 found 230.2422.

**Tri-*tert*-butyl 2,2',2''-((2*S*,5*S*,8*S*,11*S*)-2,5,8,11-tetramethyl-1,4,7,10-tetraazacyclododecane-1,4,7-triyl)(2*R*,2'*R*,2''*R*)-tripropionate (36):** (2*S*,5*S*,8*S*,11*S*)-2,5,8,11-tetramethyl-1,4,7,10-tetraazacyclo-dodecane (74.7 mg, 0.327 mmol, 1.0 eq.) was dissolved under an atmosphere of argon in dry methylene chloride (20 ml). Then potassium carbonate (130.7 mg, 0.943 mmol, 2.9 eq.), *tert*-butyl (*S*)-2-(((trifluoromethyl)sulfonyl)oxy)propanoate (202 mg, 0.726 mmol, 2.2 eq.) and dry acetonitrile (2.0 ml) were added. The suspension was stirred for

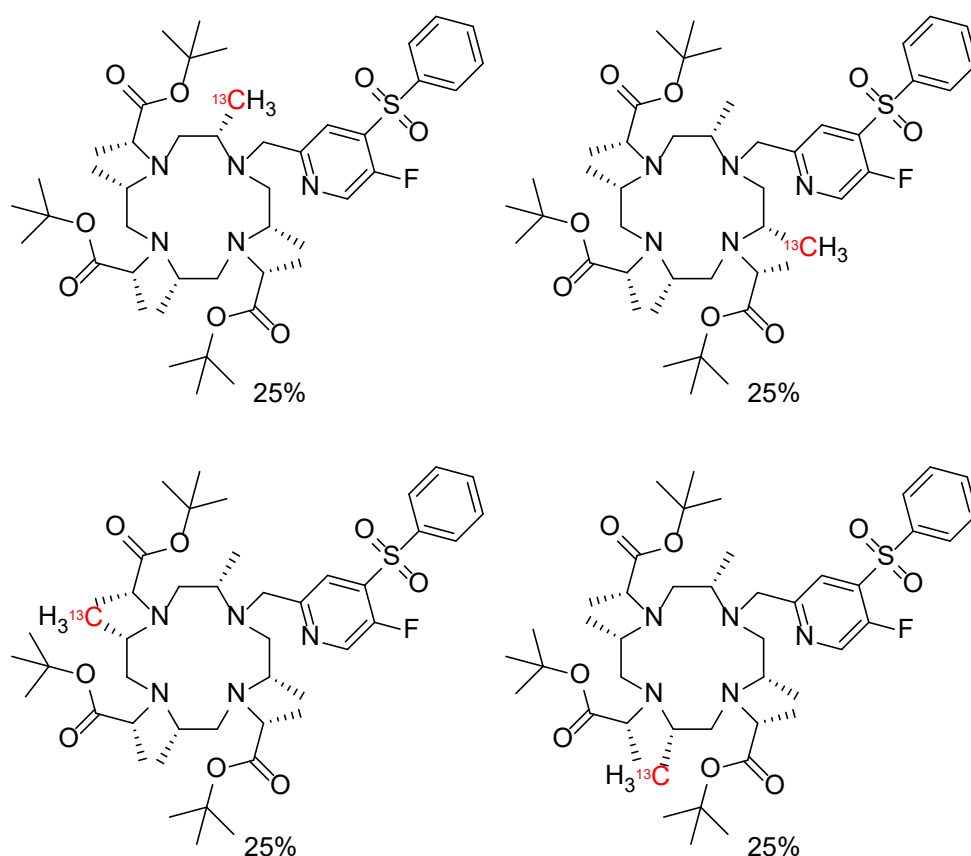
5.3 h. Reaction control with HPLC-MS showed mostly formation of the two times alkylated species, therefore additional *tert*-butyl (*S*)-2-(((trifluoromethyl)sulfonyl)oxy)propanoate (70.7 mg, 0.254 mmol, 0.8 eq.) was added. The suspension was stirred for 24 h. Then trimethylamine (0.50 ml) was added and the suspension was filtered. The solvent was evaporated and the residue was dissolved in acetonitrile (approx. 10 ml). The solution was concentrated to approx. 2 ml. The crude was purified by prep. HPLC to yield tri-*tert*-butyl 2,2',2''-((2*S*,5*S*,8*S*,11*S*) - 2,5,8,11 - tetramethyl - 1,4,7,10 - tetraazacyclododecane -1,4,7-triyl) (2*R*,2'*R*,2''*R*)-tri-propionate (200 mg, 0.327 mmol, 84%) as a yellow solid.



**HR-ESI-MS:** calcd. for  $[\text{M}+\text{H}]^+$   $\text{C}_{33}\text{H}_{64}\text{N}_4\text{O}_6$   $m/z = 614.4932$  found 614.4935.

**Tri-*tert*-butyl 2,2',2''-((2*S*,5*S*,8*S*,11*S*) -10- ((5-fluoro-4-(phenyl sulfonyl) pyridin-2-yl) methyl)-2,5,8,11-tetramethyl-1,4,7,10-tetraazacyclododecane-1,4,7-triyl)(2*R*,2'*R*,2''*R*)-tri propionate (37):** A flask under an atmosphere of argon was charged with tri-*tert*-butyl 2,2',2''-((2*S*,5*S*,8*S*,11*S*)-2,5,8,11-tetramethyl -1,4,7,10 - tetraazacyclododecane-1,4,7-triyl) (2*R*,2'*R*,2''*R*) - tripropionate (222 mg, 0.362 mmol, 1.0 eq.) and potassium carbonate (100 mg,

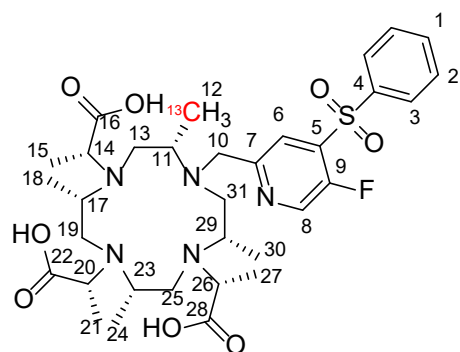
0.724 mmol, 2.0 eq.). Then a solution of 2-(bromomethyl)-5-fluoro-4-(phenylsulfonyl)pyridine (126 mg, 0.380 mmol, 1.1 eq.) in dry acetonitrile (7.0 ml) was added. The suspension was stirred overnight. The suspension was filtered and the solvent was evaporated. The crude was purified by prep. HPLC to yield tri-*tert*-butyl 2,2',2''-((2*S*,5*S*,8*S*,11*S*)-10-((5-fluoro-4-(phenylsulfonyl)pyridin-2-yl)methyl) - 2,5,8,11 - tetramethyl - 1,4,7,10 - tetraazacyclododecane-1,4,7-triyl)(2*R*,2'*R*,2''*R*)-tripropionate (272 mg, 0.316 mmol, 87%) as a yellow oil.



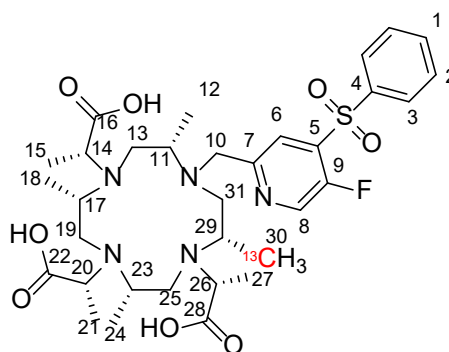
**HR-ESI-MS:** calcd. for  $[\text{M}+\text{H}]^+$   $\text{C}_{45}\text{H}_{73}\text{FN}_5\text{O}_8\text{S}$   $m/z = 863.5192$  found 863.5196.

**(2*R*,2'*R*,2''*R*)-2,2',2''-((2*S*,5*S*,8*S*,11*S*)-10-((5-Fluoro-4-(phenylsulfonyl)pyridin-2-yl)methyl)-2,5,8,11-tetramethyl-1,4,7,10-tetraazacyclododecane-1,4,7-triyl) tripropionic acid (38):** tri-*tert*-Butyl 2,2',2''-((2*S*,5*S*,8*S*,11*S*)-10-((5-fluoro-4-(phenylsulfonyl)pyridin-2-yl)methyl) - 2,5,8,11 - tetramethyl - 1,4,7,10 - tetraazacyclododecane-1,4,7-triyl)(2*R*,2'*R*,2''*R*)-tripropionate (272 mg, 0.315 mmol, 1.0 eq.) was dissolved in acetonitrile (10 ml) and aq. hydrochloric acid (1 M, 30 ml). The solution was heated to 80°C for 3.6 h. The reaction mixture

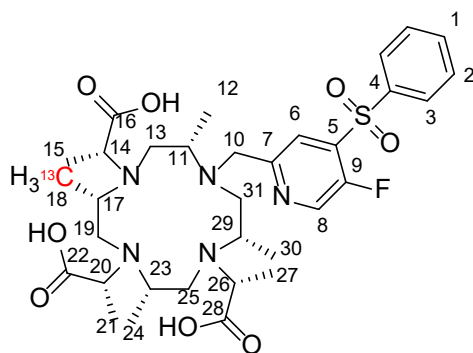
was concentrated and directly purified by prep. HPCL to yield (2*R*,2'*R*,2''*R*)-2,2',2''-((2*S*,5*S*,8*S*,11*S*)-10-((5-fluoro-4-(phenylsulfonyl)pyridin-2-yl)methyl)-2,5,8,11-tetramethyl-1,4,7,10-tetraazacyclododecane-1,4,7-triyl)tripropionic acid (121 mg, 0.175 mmol, 55%) as a white solid.



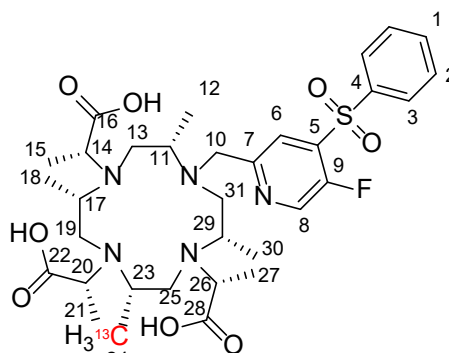
25%



25%



25%



25%

**<sup>1</sup>H NMR (500 MHz, Acetonitrile-*d*<sub>3</sub>) δ:** 8.68 (s, 1H, H<sub>8</sub>), 8.19 (d, <sup>4</sup>J<sub>HF</sub> = 5.3 Hz, 1H, H<sub>6</sub>), 8.02 (d, <sup>3</sup>J<sub>HH</sub> = 8.1 Hz, 2H, H<sub>3</sub>), 7.81 – 7.74 (m, 1H, H<sub>1</sub>), 7.66 (m, 2H, H<sub>2</sub>), 4.70 (d, <sup>2</sup>J<sub>HH</sub> = 15.5 Hz, 1H, H<sub>10a</sub>), 4.61 (d, <sup>2</sup>J<sub>HH</sub> = 15.5 Hz, 1H, H<sub>10b</sub>), 4.19 (q, <sup>3</sup>J<sub>HH</sub> = 7.3 Hz, 1H, H<sub>20</sub>), 3.95-3.76 (m, 3H, H<sub>11,23,29</sub>), 3.71 (q, <sup>3</sup>J<sub>HH</sub> = 7.0 Hz, 1H, H<sub>26</sub>), 3.47 (q, <sup>3</sup>J<sub>HH</sub> = 7.0 Hz, 1H, H<sub>14</sub>), 3.22 (m, 1H, H<sub>17</sub>), 3.11 – 2.73 (m, 8H, H<sub>13a,b,19a,b,25a,b,31a,b</sub>), 1.58 (d, <sup>3</sup>J<sub>HH</sub> = 7.3 Hz, 3H, H<sub>21</sub>), 1.38 (d, <sup>3</sup>J<sub>HH</sub> = 7.2 Hz, 3H, H<sub>15</sub>), 1.33 (d, <sup>3</sup>J<sub>HH</sub> = 6.8 Hz, 3H, H<sub>27</sub>), 1.29 (dd, <sup>1</sup>J<sub>CH</sub> = 128.0 Hz, <sup>3</sup>J<sub>HH</sub> = 6.4 Hz, 3H, H<sub>24</sub>), 1.15 (dd, <sup>1</sup>J<sub>CH</sub> = 128.0 Hz, <sup>3</sup>J<sub>HH</sub> = 6.5 Hz, 3H, H<sub>30</sub>), 1.12 (dd, <sup>1</sup>J<sub>CH</sub> = 128.0 Hz, <sup>3</sup>J<sub>HH</sub> = 6.7 Hz, 3H, H<sub>18</sub>), 1.06 (dd, <sup>1</sup>J<sub>CH</sub> = 128.0 Hz, <sup>3</sup>J<sub>HH</sub> = 6.5 Hz, 3H, H<sub>12</sub>) ppm.

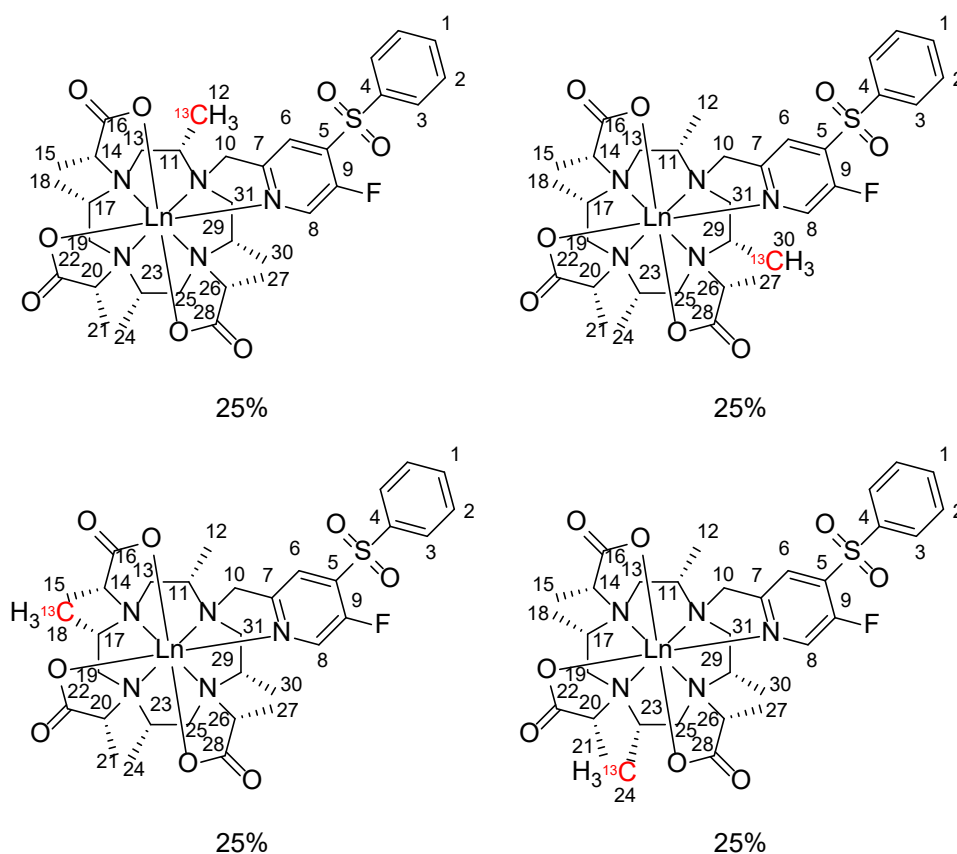
**<sup>13</sup>C NMR (126 MHz, Acetonitrile-*d*<sub>3</sub>) δ:** 176.47 (C<sub>16</sub>), 173.83 (C<sub>28</sub>), 171.85 (C<sub>22</sub>), 155.71 (C<sub>9</sub>), 149.05 (C<sub>7</sub>), 141.76 (C<sub>8</sub>), 139.85 (C<sub>4</sub>), 138.42 (C<sub>5</sub>), 136.18 (C<sub>1</sub>), 130.87 (C<sub>2</sub>), 129.40 (C<sub>3</sub>), 125.74 (C<sub>6</sub>), 65.56 (C<sub>20</sub>), 61.76 (C<sub>23</sub>), 61.45 (C<sub>14</sub>), 59.65 (C<sub>11</sub>), 56.89 (C<sub>17</sub>), 56.88 (C<sub>10</sub>), 56.42

(C<sub>26</sub>), 50.16 (C<sub>31</sub>), 49.67 (C<sub>29</sub>) 48.00 (C<sub>19</sub>), 47.46 (C<sub>25</sub>), 45.82 (C<sub>13</sub>), 16.09 (C<sub>27</sub>), 14.79 (C<sub>15</sub>), 14.69 (C<sub>18</sub>), 13.84 (C<sub>21</sub>), 13.83 (C<sub>30</sub>), 12.77 (C<sub>12</sub>), 12.67 (C<sub>24</sub>) ppm.

<sup>19</sup>F NMR (471 MHz, Acetonitrile-*d*<sub>3</sub>) δ: -123.86 ppm.

HR-ESI-MS: calcd. for [M+H]<sup>+</sup> C<sub>33</sub>H<sub>48</sub>FN<sub>5</sub>O<sub>8</sub>S m/z = 695.3314 found 695.3315.

**Ln-DOTA-M7FPy (1) general procedure:** (2*R*,2'*R*,2''*R*) -2,2',2'' -((2*S*,5*S*,8*S*,11*S*) -10- ((5 - fluoro-4-(phenylsulfonyl)pyridin-2-yl)methyl) -2,5,8,11 – tetramethyl -1,4,7,10- tetraazacyclo dodecane-1,4,7-triyl) tripropionic acid (1.0 eq.) was dissolved in aq. ammonium acetat (100 mM, 8.0 ml). The solution was heated to 80°C then La(NO<sub>3</sub>)<sub>3</sub> \* 6H<sub>2</sub>O, Ce(Cl)<sub>3</sub> \* 7H<sub>2</sub>O, Pr(NO<sub>3</sub>)<sub>3</sub> \* 5H<sub>2</sub>O, Nd(Cl)<sub>3</sub> \* 6H<sub>2</sub>O, Sm(Cl)<sub>3</sub> \* 6H<sub>2</sub>O, Eu(OTf)<sub>3</sub>, Gd(OTf)<sub>3</sub>, Tb(Cl)<sub>3</sub> \* 6H<sub>2</sub>O, Dy(OTf)<sub>3</sub>, Ho(OTf)<sub>3</sub>, Er(Cl)<sub>3</sub> \* 6H<sub>2</sub>O, Tm(OTf)<sub>3</sub>, Yb(NO<sub>3</sub>)<sub>3</sub> \* 5H<sub>2</sub>O or Lu(OTf)<sub>3</sub> (2.1 eq.) was added, respectively. The solution was stirred overnight. Then the solution was cooled to 20- 25°C and directly purified by prep. HPLC (Sm-Lu) or by Sep-Pak column chromatography (supporting info S3) (La-Nd) to yield the desired tag.



[La(DOTA-M7FPy)] 62% yield as a white solid.

**<sup>1</sup>H NMR (600 MHz, Deuterium Oxide, 50 mM Phosphate Buffer pH=6.0) δ:** 8.56 (m, 1H, H<sub>8</sub>), 8.17 (d, <sup>4</sup>J<sub>HF</sub> = 5.4 Hz, 1H, H<sub>6</sub>), 8.07 (m, 2H, H<sub>3</sub>), 7.84 (m, 1H, H<sub>1</sub>), 7.70 (m, 2H, H<sub>2</sub>), 4.38 (d, <sup>2</sup>J<sub>HH</sub> = 16.1 Hz, 1H, H<sub>10a</sub>), 4.32 (d, <sup>2</sup>J<sub>HH</sub> = 16.1 Hz, 1H, H<sub>10b</sub>), 3.81-3.73 (m, 2H, H<sub>14,20</sub>), 3.46 (m, 1H, H<sub>31(axial)</sub>), 3.31-3.20 (m, 2H, H<sub>11,17</sub>), 3.17 – 3.01 (m, 4H, H<sub>13(axial),19(axial),25(axial),23</sub>), 2.92 (q, <sup>3</sup>J<sub>HH</sub> = 7.2 Hz, 1H, H<sub>26</sub>), 2.74 (d, <sup>2</sup>J<sub>HH</sub> = 14.9 Hz, 1H, H<sub>13(equatorial)</sub>), 2.66 (d, <sup>2</sup>J<sub>HH</sub> = 14.9 Hz, 1H, H<sub>19(equatorial)</sub>), 2.51 (d, <sup>2</sup>J<sub>HH</sub> = 14.1 Hz, 1H, H<sub>25(equatorial)</sub>), 2.47 (d, <sup>2</sup>J<sub>HH</sub> = 14.5 Hz, 1H, H<sub>31(equatorial)</sub>), 2.15 (m, 1H, H<sub>29</sub>), 1.44 (d, <sup>3</sup>J<sub>HH</sub> = 7.4 Hz, 3H, H<sub>15</sub>), 1.41 (d, <sup>3</sup>J<sub>HH</sub> = 7.4 Hz, 3H, H<sub>21</sub>), 1.26 (d, <sup>3</sup>J<sub>HH</sub> = 7.2 Hz, 3H, H<sub>27</sub>), 1.15 (dd, <sup>1</sup>J<sub>CH</sub> = 128 Hz, <sup>3</sup>J<sub>HH</sub> = 6.7 Hz, 3H, H<sub>12</sub>), 1.13 (dd, <sup>1</sup>J<sub>CH</sub> = 128 Hz, <sup>3</sup>J<sub>HH</sub> = 6.7 Hz, 6H, H<sub>18,24</sub>), 0.88 (dd, <sup>1</sup>J<sub>CH</sub> = 128 Hz, <sup>3</sup>J<sub>HH</sub> = 6.7 Hz, 3H, H<sub>30</sub>) ppm.

**<sup>13</sup>C NMR (150.9 MHz, Deuterium Oxide, 50 mM Phosphate Buffer pH=6.0) δ:** 183.58 (C<sub>16</sub>), 183.53 (C<sub>28</sub>), 182.59 (C<sub>22</sub>), 157.61 (C<sub>7</sub>), 154.29 (C<sub>9</sub>), 139.69 (C<sub>8</sub>), 138.57 (C<sub>5</sub>) 136.89 (C<sub>4</sub>) 135.91 (C<sub>1</sub>), 130.02 (C<sub>2</sub>), 128.49 (C<sub>3</sub>), 122.39 (C<sub>6</sub>), 66.80 (C<sub>26</sub>), 66.57 (C<sub>14</sub>), 66.28 (C<sub>20</sub>), 63.51 (C<sub>10</sub>), 61.60 (C<sub>29</sub>), 60.40 (C<sub>11</sub>), 60.20 (C<sub>17</sub>), 60.13 (C<sub>23</sub>), 54.90 (C<sub>31</sub>), 45.91 (C<sub>19</sub>), 45.88 (C<sub>25</sub>), 45.13 (C<sub>13</sub>), 14.06 (C<sub>27</sub>), 13.97 (C<sub>15</sub>), 13.79 (C<sub>24</sub>), 13.05 (C<sub>21</sub>), 12.98 (C<sub>18</sub>), 12.41 (C<sub>30</sub>), 9.71 (C<sub>12</sub>) ppm.

**<sup>19</sup>F NMR (565 MHz, Deuterium Oxide, 50 mM Phosphate Buffer pH=6.0) δ:** -122.94 ppm.

**HR-ESI-MS:** calcd. for [M+Na]<sup>+</sup> C<sub>33</sub>H<sub>45</sub>FLaN<sub>5</sub>NaO<sub>8</sub>S m/z = 853.1962 found 853.1967.

[Ce(DOTA-M7FPy)] 63% yield as a yellow solid.

**<sup>19</sup>F NMR (565 MHz, Deuterium Oxide, 50 mM Phosphate Buffer pH=6.0) δ:** -126.04 ppm.

**HR-ESI-MS:** calcd. for [M+Na]<sup>+</sup> C<sub>33</sub>H<sub>45</sub>FCeN<sub>5</sub>NaO<sub>8</sub>S m/z = 854.1953 found 854.1946.

[Pr(DOTA-M7FPy)] 72% yield as a slightly green solid.

**<sup>19</sup>F NMR (565 MHz, Deuterium Oxide, 50 mM Phosphate Buffer pH=6.0) δ:** -131.41 ppm.

**HR-ESI-MS:** calcd. for  $[M+Na]^+$  C<sub>33</sub>H<sub>45</sub>FPrN<sub>5</sub>NaO<sub>8</sub>S m/z = 855.1975 found 855.1977.

[Nd(DOTA-M7FPy)] 65% yield as a slightly yellow solid.

**<sup>19</sup>F NMR (565 MHz, Deuterium Oxide, 50 mM Phosphate Buffer pH=6.0) δ:** -126.43 ppm.

**HR-ESI-MS:** calcd. for  $[M+Na]^+$  C<sub>33</sub>H<sub>45</sub>FNdN<sub>5</sub>NaO<sub>8</sub>S m/z = 856.1976 found 856.1979.

[Sm(DOTA-M7FPy)] 43% yield as a white solid.

**<sup>1</sup>H NMR (500 MHz, Deuterium Oxide, 50 mM Phosphate Buffer pH=6.0) δ:** 8.64 (d, <sup>4</sup>J<sub>HF</sub> = 5.16 Hz, 1H, H<sub>6</sub>), 8.07 (d, <sup>2</sup>J<sub>HH</sub> = 16.3 Hz, 1H, H<sub>10a</sub>), 8.03 (d, <sup>3</sup>J<sub>HH</sub> = 7.9 Hz, 2H, H<sub>3</sub>), 7.76 (m, 2H, H<sub>1,14</sub>), 7.62 (m, 2H, H<sub>2</sub>), 7.47 (s, 1H, H<sub>11</sub>), 7.19 (m, 1H, H<sub>20</sub>), 6.89 (m, 1H, H<sub>26</sub>), 5.72 (d, <sup>2</sup>J<sub>HH</sub> = 16.3 Hz, 1H, H<sub>10b</sub>), 5.43 (m, 2H, H<sub>23</sub>), 5.23 (s, 1H, H<sub>8</sub>), 4.79 (m, 1H, H<sub>29</sub>), 3.31 (s, 1H, H<sub>17</sub>), 2.74 (d, <sup>3</sup>J<sub>HH</sub> = 7.0 Hz, 3H, H<sub>15</sub>), 2.54 (d, <sup>3</sup>J<sub>HH</sub> = 7.0 Hz, 3H, H<sub>27</sub>), 2.02 (d, <sup>2</sup>J<sub>HH</sub> = 14.8 Hz, 1H, H<sub>31(equatorial)</sub>), 1.78 (d, <sup>2</sup>J<sub>HH</sub> = 15.6 Hz, 1H, H<sub>13(equatorial)</sub>), 1.55 (d, <sup>3</sup>J<sub>HH</sub> = 6.7 Hz, 3H, H<sub>21</sub>), 1.44 (d, <sup>2</sup>J<sub>HH</sub> = 15.9 Hz, 1H, H<sub>25(equatorial)</sub>), 1.23 (dd, <sup>1</sup>J<sub>CH</sub> = 127 Hz, <sup>3</sup>J<sub>HH</sub> = 6.0 Hz, 3H, H<sub>12</sub>), 0.80 (dd, <sup>1</sup>J<sub>CH</sub> = 128 Hz, <sup>3</sup>J<sub>HH</sub> = 6.4 Hz, 3H, H<sub>30</sub>), 0.22 (dd, <sup>1</sup>J<sub>CH</sub> = 127 Hz, <sup>3</sup>J<sub>HH</sub> = 6.6 Hz, 3H, H<sub>18</sub>), 0.20 (dd, <sup>1</sup>J<sub>CH</sub> = 127 Hz, <sup>3</sup>J<sub>HH</sub> = 6.0 Hz, 3H, H<sub>24</sub>), -0.30 (d, <sup>2</sup>J<sub>HH</sub> = 15.4 Hz, 1H, H<sub>19(equatorial)</sub>), -0.90 (m, 1H, H<sub>31(axial)</sub>), -3.33 (m, 1H, H<sub>13(axial)</sub>), -3.99 (m, 1H, H<sub>25(axial)</sub>), -4.68 (m, 1H, H<sub>19(axial)</sub>) ppm.

**<sup>13</sup>C NMR (126 MHz, Deuterium Oxide, 50 mM Phosphate Buffer pH=6.0) δ:** 195.23 (C<sub>16</sub>), 194.55 (C<sub>28</sub>), 189.57 (C<sub>22</sub>), 161.52 (C<sub>7</sub>), 152.25 (C<sub>9</sub>), 138.85 (C<sub>5</sub>), 138.79 (C<sub>8</sub>), 136.79 (C<sub>4</sub>), 135.84 (C<sub>1</sub>), 129.92 (C<sub>2</sub>), 128.42 (C<sub>3</sub>), 121.34 (C<sub>6</sub>), 73.08 (C<sub>26</sub>), 73.08 (C<sub>14</sub>), 69.90 (C<sub>10</sub>), 69.36 (C<sub>20</sub>), 63.63 (C<sub>11</sub>), 63.29 (C<sub>29</sub>), 59.88 (C<sub>23</sub>), 58.81 (C<sub>17</sub>), 55.61 (C<sub>31</sub>), 44.87 (C<sub>25</sub>), 44.52 (C<sub>13</sub>), 40.98 (C<sub>19</sub>), 14.84 (C<sub>27</sub>), 14.74 (C<sub>15</sub>), 12.62 (C<sub>21</sub>), 11.68 (C<sub>30</sub>), 11.68 (C<sub>24</sub>), 10.94 (C<sub>18</sub>), 9.13 (C<sub>12</sub>) ppm.

**<sup>19</sup>F NMR (471 MHz, Deuterium Oxide, 50 mM Phosphate Buffer pH=6.0) δ:** -124.10 ppm.

**HR-ESI-MS:** calcd. for  $[M+Na]^+$  C<sub>33</sub>H<sub>45</sub>FSmN<sub>5</sub>NaO<sub>8</sub>S m/z = 866.2096 found 866.2103.



[Eu(DOTA-M7FPy)] 75% yield as a white solid.

**<sup>1</sup>H NMR (600 MHz, Deuterium Oxide, 50 mM Phosphate Buffer pH=6.0) δ:** 45.80 (s, 1H, H<sub>19(axial)</sub>), 38.22 (s, 1H, H<sub>25(axial)</sub>), 35.18 (s, 1H, H<sub>13(axial)</sub>), 24.82 (s, 1H, H<sub>31(axial)</sub>), 22.37 (s, 1H, H<sub>8</sub>), 11.12 (s, 1H, H<sub>19(equatorial)</sub>), 9.07 (d, <sup>3</sup>J<sub>HH</sub> = 7.5 Hz, 2H, H<sub>3</sub>), 8.52 (m, 1H, H<sub>1</sub>), 8.47 (m, 2H, H<sub>2</sub>), 8.42 (s, 1H, H<sub>17</sub>), 7.35 (d, <sup>1</sup>J<sub>CH</sub> = 128 Hz, 3H, H<sub>18</sub>), 6.48 (d, <sup>1</sup>J<sub>CH</sub> = 128 Hz, 3H, H<sub>24</sub>), 5.96 (s, 1H, H<sub>6</sub>), 2.94 (s, 3H, H<sub>21</sub>), 1.56 (d, <sup>1</sup>J<sub>CH</sub> = 128 Hz, 3H, H<sub>30</sub>), 0.93 (s, 1H, H<sub>25(equatorial)</sub>), 0.40 (d, <sup>1</sup>J<sub>CH</sub> = 128 Hz, 3H, H<sub>12</sub>), -1.70 (s, 1H, H<sub>13(equatorial)</sub>), -3.80 (s, 1H, H<sub>31(equatorial)</sub>), -6.83 (s, 3H, H<sub>15</sub>), -7.23 (s, 3H, H<sub>27</sub>), -7.57 (s, 1H, H<sub>29</sub>), -12.02 (s, 1H, H<sub>10a</sub>), -13.44 (s, 1H, H<sub>10b</sub>), -13.69 (s, 1H, H<sub>20</sub>), -15.23 (s, 1H, H<sub>23</sub>), -18.47 (s, 1H, H<sub>14</sub>), -19.19 (s, 1H, H<sub>26</sub>), -26.42 (s, 1H, H<sub>11</sub>) ppm.

**<sup>19</sup>F NMR (565 MHz, Deuterium Oxide, 50 mM Phosphate Buffer pH=6.0) δ:** -123.32 ppm.

**HR-ESI-MS:** calcd. for [M+Na]<sup>+</sup> C<sub>33</sub>H<sub>45</sub>FEuN<sub>5</sub>NaO<sub>8</sub>S m/z = 867.2112 found 867.2107.

[Gd(DOTA-M7FPy)] 69% yield as a white solid.

**HR-ESI-MS:** calcd. for [M+Na]<sup>+</sup> C<sub>33</sub>H<sub>45</sub>FGdN<sub>5</sub>NaO<sub>8</sub>S m/z = 872.2145 found 872.2137.

[Tb(DOTA-M7FPy)] 68% yield as a white solid.

**<sup>19</sup>F NMR (565 MHz, Deuterium Oxide, 50 mM Phosphate Buffer pH=6.0) δ:** -194.36 ppm.

**HR-ESI-MS:** calcd. for [M+Na]<sup>+</sup> C<sub>33</sub>H<sub>45</sub>FTbN<sub>5</sub>NaO<sub>8</sub>S m/z = 873.2152 found 873.2155.

[Dy(DOTA-M7FPy)] 41% yield as a white solid.

**<sup>19</sup>F NMR (565 MHz, Deuterium Oxide, 50 mM Phosphate Buffer pH=6.0) δ:** -232.80 ppm.

**HR-ESI-MS:** calcd. for [M+Na]<sup>+</sup> C<sub>33</sub>H<sub>45</sub>FDyN<sub>5</sub>NaO<sub>8</sub>S m/z = 878.2196 found 878.2198.

[Ho(DOTA-M7FPy)] 80% yield as a pink solid.

**<sup>19</sup>F NMR (565 MHz, Deuterium Oxide, 50 mM Phosphate Buffer pH=6.0) δ:** -176.24 ppm.

**HR-ESI-MS:** calcd. for  $[M+Na]^+$  C<sub>33</sub>H<sub>45</sub>FHoN<sub>5</sub>NaO<sub>8</sub>S m/z = 879.2202 found 879.2207.

[Er(DOTA-M7FPy)] 82% yield as a white solid.

**<sup>19</sup>F NMR (565 MHz, Deuterium Oxide, 50 mM Phosphate Buffer pH=6.0) δ:** -95.63 ppm.

**HR-ESI-MS:** calcd. for  $[M+Na]^+$  C<sub>33</sub>H<sub>45</sub>FErN<sub>5</sub>NaO<sub>8</sub>S m/z = 880.2201 found 880.2204.

[Tm(DOTA-M7FPy)] 78% yield as a white solid.

**<sup>19</sup>F NMR (565 MHz, Deuterium Oxide, 50 mM Phosphate Buffer pH=6.0) δ:** -51.48 ppm.

**HR-ESI-MS:** calcd. for  $[M+Na]^+$  C<sub>33</sub>H<sub>45</sub>FTmN<sub>5</sub>NaO<sub>8</sub>S m/z = 883.2241 found 883.2240.

[Yb(DOTA-M7FPy)] 13% yield as a white solid.

**<sup>19</sup>F NMR (565 MHz, Deuterium Oxide, 50 mM Phosphate Buffer pH=6.0) δ:** -89.33 ppm.

**HR-ESI-MS:** calcd. for  $[M+Na]^+$  C<sub>33</sub>H<sub>45</sub>FYbN<sub>5</sub>NaO<sub>8</sub>S m/z = 888.2290 found 888.2300.

[Lu(DOTA-M7FPy)] 80% as a white solid.

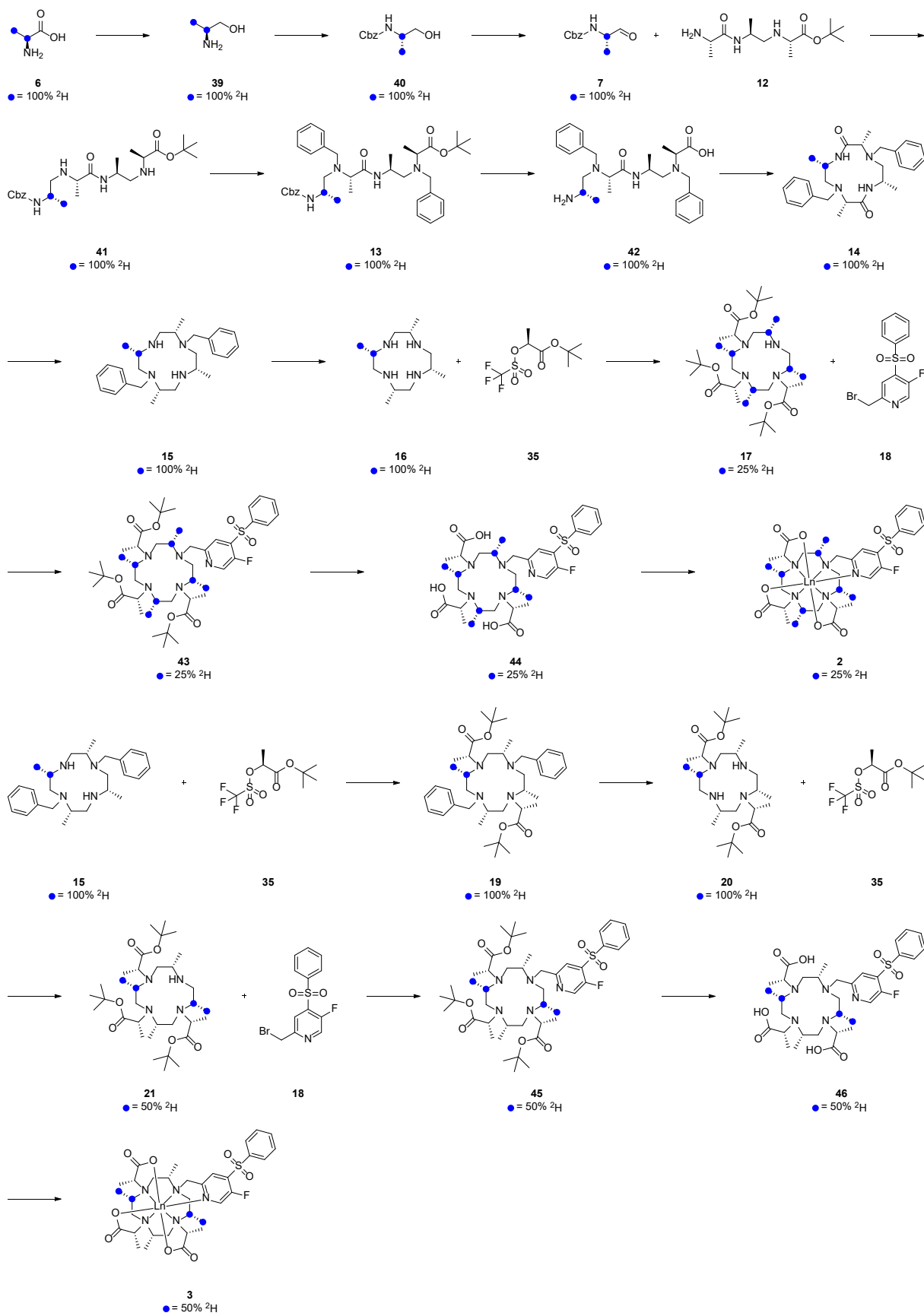
**<sup>1</sup>H NMR (600 MHz, Deuterium Oxide, 50 mM Phosphate Buffer pH=6.0) δ:** 8.47 (d, <sup>2</sup>J<sub>HF</sub> = 2.4 Hz, 1H, H<sub>8</sub>), 8.16 (d, <sup>4</sup>J<sub>HF</sub> = 5.4 Hz, 1H, H<sub>6</sub>), 8.07 (m, 2H, H<sub>3</sub>), 7.84 (m, 1H, H<sub>1</sub>), 7.70 (m, 2H, H<sub>2</sub>), 4.65 (d, <sup>2</sup>J<sub>HH</sub> = 17.9 Hz, 1H, H<sub>10a</sub>), 4.46 (d, <sup>2</sup>J<sub>HH</sub> = 17.9 Hz, 1H, H<sub>10b</sub>), 3.83-3.77 (m, 2H, H<sub>14,20</sub>), 3.45 (m, 1H, H<sub>31(axial)</sub>), 3.16 (m, 1H, H<sub>11</sub>) 3.13-3.00 (m, 5H, H<sub>13(axial),17,19(axial),23,25(axial)</sub>), 2.98 (q, <sup>3</sup>J<sub>HH</sub> = 6.7 Hz, 1H, H<sub>26</sub>), 2.84 (d, <sup>2</sup>J<sub>HH</sub> = 15.5 Hz, 1H, H<sub>13(equatorial)</sub>), 2.76 – 2.69 (m, 2H, H<sub>25(equatorial),29</sub>), 2.66 – 2.59 (m, 2H, H<sub>19(equatorial),31(equatorial)</sub>), 1.46 (d, <sup>3</sup>J<sub>HH</sub> = 7.0 Hz, 6H, H<sub>15,21</sub>), 1.28 (d, <sup>3</sup>J<sub>HH</sub> = 7.1 Hz, 3H, H<sub>27</sub>), 1.23 (dd, <sup>1</sup>J<sub>HC</sub> = 128 Hz, <sup>3</sup>J<sub>HH</sub> = 6.2 Hz, 3H, H<sub>12</sub>), 1.19 (dd, <sup>1</sup>J<sub>CH</sub> = 128 Hz, <sup>3</sup>J<sub>HH</sub> = 6.4 Hz, 3H, H<sub>18</sub>), 1.18 (dd, <sup>1</sup>J<sub>CH</sub> = 128 Hz, <sup>3</sup>J<sub>HH</sub> = 6.7 Hz, 3H, H<sub>24</sub>), 1.00 (dd, <sup>1</sup>J<sub>CH</sub> = 128 Hz, <sup>3</sup>J<sub>HH</sub> = 6.7 Hz, 3H, H<sub>30</sub>) ppm.

**<sup>13</sup>C NMR (150.9 MHz, Deuterium Oxide, 50 mM Phosphate Buffer pH=6.0) δ:** 183.19 (C<sub>16</sub>), 183.02 (C<sub>28</sub>), 182.91 (C<sub>22</sub>), 157.61 (C<sub>7</sub>), 154.43 (C<sub>9</sub>), 138.96 (C<sub>8</sub>), 138.92 (C<sub>5</sub>), 136.69 (C<sub>4</sub>), 135.99 (C<sub>1</sub>), 129.03 (C<sub>2</sub>), 128.57 (C<sub>3</sub>), 122.02 (C<sub>6</sub>), 67.45 (C<sub>14</sub>), 67.34 (C<sub>20</sub>), 66.94 (C<sub>26</sub>), 64.87 (C<sub>10</sub>), 61.53 (C<sub>11</sub>), 60.75 (C<sub>29</sub>), 60.82 (C<sub>17</sub>), 60.69 (C<sub>23</sub>), 55.32 (C<sub>31</sub>), 46.21 (C<sub>25</sub>), 45.86 (C<sub>19</sub>), 45.25 (C<sub>13</sub>), 13.42 (C<sub>15</sub>), 13.28 (C<sub>27</sub>), 13.26 (C<sub>21</sub>), 13.05 (C<sub>24</sub>), 12.76 (C<sub>18</sub>), 12.59 (C<sub>30</sub>), 10.22 (C<sub>12</sub>) ppm.

**<sup>19</sup>F NMR (565 MHz, Deuterium Oxide, 50 mM Phosphate Buffer pH=6.0) δ:** -122.73 ppm.

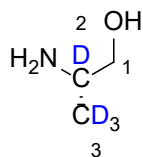
**HR-ESI-MS:** calcd. for [M+Na]<sup>+</sup> C<sub>33</sub>H<sub>45</sub>FLuN<sub>5</sub>NaO<sub>8</sub>S m/z = 889.2306 found 889.2315.

**Protein Tagging:** To a solution of Ubiquitin S57C (62.5 μl, 1 mM in 10 mM phosphate, 1 mM TCEP, pH = 7.00) a phosphate buffer (237.5 μl, 10 mM phosphate 2 mM TCEP, pH = 7.00) was added. The solution was incubated in the fridge overnight to reduce disulphides. The buffer was exchanged by ultrafiltration (4x) (Amicon Ultra-4 Centrifugal Filters Ultracel-3K, Millipore) to a phosphate buffer (450 μM TCEP, 10 mM phosphate, pH = 7.00). For all samples except Lu the Ubiquitin S57C concentration was adjusted to 150 μM (300 μl). For Lu the concentration was adjusted to 450 μM (300 μl). To all samples a 6-fold excess of Ln-DOTA-M7FPy (**1**) loaded with Ce, Pr, Nd, Sm, Eu, Tb, Dy, Ho, Er, Tm, Yb, or Lu was added, respectively, and the sample was shaken for 18 h at 22°C. The reaction progress was monitored by HPLC-MS. The buffer was exchanged by ultrafiltration (4x) (Amicon Ultra-4 Centrifugal Filters Ultracel-3K, Millipore) to a phosphate buffer (10 mM phosphate, pH = 6.00). The final solution was concentrated to 250 μl, the filter unit was washed with 40 μl phosphate buffer (10 mM phosphate, pH = 6.00) and deuterium oxide (15 μl) was added.



**Figure S3:** Synthesis towards Ln-DOTA-M7FPy (**2&3**) with deuterium labelled methyl groups and  $\text{H}_\alpha$  proton on the basal cyclen ring. Blue dots mark positions labelled with deuterium  $^2\text{H}$ . Below each labelled molecule the observed labelling percentage is noted.

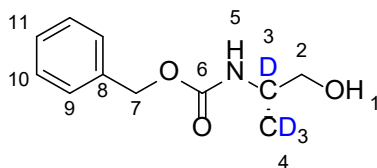
**(S)-2-Aminopropan-1-ol (39):**



**<sup>1</sup>H NMR (500 MHz, Chloroform-*d*)**  $\delta$ : 3.51 (d,  $^2J_{\text{HH}} = 10.6$  Hz, 1H, H<sub>1</sub>), 3.21 (d,  $^2J_{\text{HH}} = 10.6$  Hz, 1H, H<sub>i</sub>).

**HR-ESI-MS:** calcd. for [M+Na]<sup>+</sup> C<sub>3</sub>H<sub>5</sub>D<sub>4</sub>NONa  $m/z = 102.0827$  found 102.0826.

**Benzyl (S)-(1-hydroxypropan-2-yl)carbamate (40):**

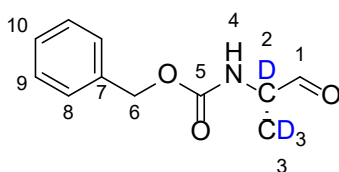


**<sup>1</sup>H NMR (500 MHz, Chloroform-*d*)**  $\delta$ : 7.40-7.28 (m, 5H, H<sub>9,10,11</sub>), 5.10 (s, 2H, H<sub>7</sub>), 4.92 (s, 1H, H<sub>5</sub>), 3.65 (d,  $^2J_{\text{HH}} = 10.1$  Hz, 1H, H<sub>2a</sub>), 3.51 (d,  $^2J_{\text{HH}} = 10.1$  Hz, 1H, H<sub>2b</sub>) 2.39 (s, 1H, H<sub>1</sub>).

**<sup>13</sup>C NMR (126 MHz, Chloroform-*d*)**  $\delta$ : 156.72 (C<sub>6</sub>), 136.50 (C<sub>8</sub>), 128.68 (C<sub>9/10/11</sub>), 128.31 (C<sub>9/10/11</sub>), 128.26 (C<sub>9/10/11</sub>), 66.99 (C<sub>7,2</sub>) ppm.

**HR-ESI-MS:** calcd. for [M+Na]<sup>+</sup> C<sub>11</sub>H<sub>11</sub>D<sub>4</sub>NO<sub>3</sub>Na  $m/z = 236.1195$  found 236.1194.

**Benzyl (S)-(1-oxopropan-2-yl)carbamate (7):**

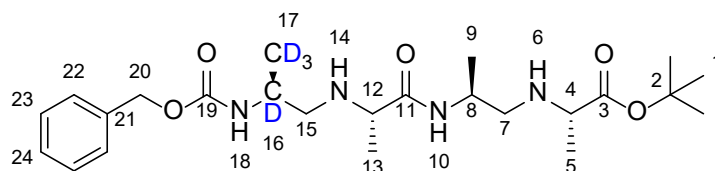


**<sup>1</sup>H NMR (500 MHz, Chloroform-*d*)**  $\delta$ : 9.57 (s, 1H, H<sub>1</sub>), 7.38-7.28 (m, 5H, H<sub>8,9,10</sub>), 5.40 (s, 1H, H<sub>4</sub>), 5.12 (s, 2H, H<sub>6</sub>) ppm.

**<sup>13</sup>C NMR (126 MHz, Chloroform-*d*)**  $\delta$ : 199.26 (C<sub>1</sub>), 155.95 (C<sub>5</sub>), 136.07 (C<sub>7</sub>), 128.70 (C<sub>8/9/10</sub>), 128.40 (C<sub>8/9/10</sub>), 128.28 (C<sub>8/9/10</sub>), 67.19 (C<sub>6</sub>) ppm.

**HR-ESI-MS**: calcd. for [M+Na]<sup>+</sup> C<sub>11</sub>H<sub>9</sub>D<sub>4</sub>NO<sub>3</sub>Na m/z = 234.1039 found 234.1038.

***tert*-Butyl ((*S*)-2-((*S*)-2-(((*S*)-2-(((benzyloxy)carbonyl)amino)propyl)amino)propanamido) propyl)-*L*-alaninate (41):**

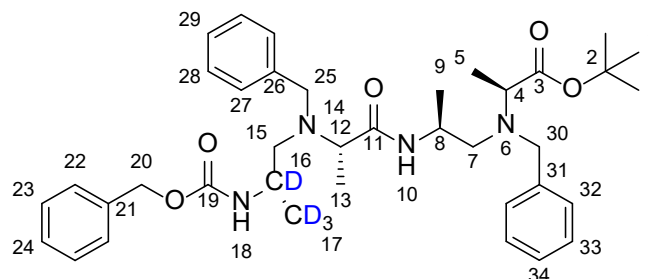


**<sup>1</sup>H NMR (500 MHz, Chloroform-*d*)**  $\delta$ : 7.38-7.27 (m, 5H, H<sub>22,23,24</sub>), 5.47 (s, 1H, H<sub>18</sub>), 5.08 (m, 2H, H<sub>20</sub>), 3.95 (m, 1H, H<sub>8</sub>), 3.15 (q, <sup>3</sup>J<sub>HH</sub> = 7.2 Hz, 1H, H<sub>4</sub>), 3.07 (q, <sup>3</sup>J<sub>HH</sub> = 7.2 Hz, 1H, H<sub>12</sub>), 2.76 (m, 1H, H<sub>15a</sub>), 2.66 (dd, <sup>2</sup>J<sub>HH</sub> = 11.8 Hz, <sup>3</sup>J<sub>HH</sub> = 4.8 Hz, 1H, H<sub>7a</sub>), 2.58 (m, 1H, H<sub>15b</sub>), 2.44 (dd, <sup>2</sup>J<sub>HH</sub> = 11.8 Hz, <sup>3</sup>J<sub>HH</sub> = 7.4 Hz, 1H, H<sub>7b</sub>), 1.43 (s, 9H, H<sub>1</sub>), 1.26 (d, <sup>3</sup>J<sub>HH</sub> = 7.0 Hz, 3H, H<sub>13</sub>), 1.19 (d, <sup>3</sup>J<sub>HH</sub> = 7.0 Hz, 3H, H<sub>5</sub>), 1.11 (d, <sup>3</sup>J<sub>HH</sub> = 6.6 Hz, 3H, H<sub>9</sub>) ppm.

**<sup>13</sup>C NMR (126 MHz, Chloroform-*d*)**  $\delta$ : 173.87 (C<sub>3</sub>), 173.65 (C<sub>11</sub>), 155.02 (C<sub>19</sub>), 135.62 (C<sub>21</sub>), 127.49 (C<sub>22/23/24</sub>), 127.14 (C<sub>22/23/24</sub>), 127.08 (C<sub>22/23/24</sub>), 79.96 (C<sub>2</sub>), 65.51 (C<sub>20</sub>), 58.07 (C<sub>12</sub>), 56.12 (C<sub>4</sub>), 52.74 (C<sub>15</sub>), 51.34 (C<sub>7</sub>), 43.73 (C<sub>8</sub>), 27.05 (C<sub>1</sub>), 19.00 (C<sub>13</sub>), 17.80 (C<sub>5,9</sub>) ppm.

**HR-ESI-MS**: calcd. for [M+H]<sup>+</sup> C<sub>24</sub>H<sub>37</sub>D<sub>4</sub>N<sub>4</sub>O<sub>5</sub> m/z = 469.3323 found 469.3323.

***tert*-Butyl (5*S*,8*S*,11*S*,14*S*)-7,13-dibenzyl-5,8,11,14-tetramethyl-3,9-dioxo-1-phenyl-2-oxa-4,7,10,13 - tetraazapentadecan-15-oate (13):**

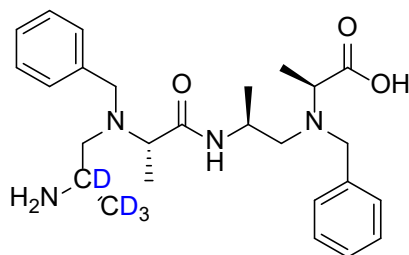


**<sup>1</sup>H NMR (500 MHz, Chloroform-*d*)**  $\delta$ : 7.40-7.16 (m, 15H, H<sub>22,23,24,27,28,29,32,33,34</sub>), 5.13 (d, <sup>2</sup>*J*<sub>HH</sub> = 12.2 Hz, 1H, H<sub>20a</sub>), 4.96 (d, <sup>2</sup>*J*<sub>HH</sub> = 12.2 Hz, 1H, H<sub>20b</sub>), 4.69 (s, 1H, H<sub>18</sub>), 4.00 (m, 1H, H<sub>8</sub>), 3.86 (d, <sup>2</sup>*J*<sub>HH</sub> = 14.5 Hz, 1H, H<sub>30a</sub>), 3.76-3.68 (m, 2H, H<sub>30b,25a</sub>), 3.43-3.35 (m, 2H, H<sub>25b,12</sub>), 3.29 (q, <sup>3</sup>*J*<sub>HH</sub> = 7.0 Hz, 1H, H<sub>4</sub>), 2.68 (dd, <sup>2</sup>*J*<sub>HH</sub> = 13.1 Hz, <sup>3</sup>*J*<sub>HH</sub> = 5.7 Hz, 1H, H<sub>7a</sub>), 2.60 (dd, <sup>2</sup>*J*<sub>HH</sub> = 13.1 Hz, <sup>3</sup>*J*<sub>HH</sub> = 7.8 Hz, 1H, H<sub>7b</sub>), 2.49 (m, 1H, H<sub>15a</sub>), 2.29 (m, 1H, H<sub>15b</sub>), 1.45 (s, 9H, H<sub>1</sub>), 1.21 (d, <sup>3</sup>*J*<sub>HH</sub> = 7.0 Hz, 1H, H<sub>13</sub>), 1.20-1.14 (m, 6H, H<sub>5,9</sub>) ppm.

**<sup>13</sup>C NMR (126 MHz, Chloroform-*d*)**  $\delta$ : 173.43 (C<sub>3</sub>), 172.98 (C<sub>11</sub>), 156.47 (C<sub>19</sub>), 140.07 (C<sub>31</sub>), 139.24 (C<sub>26</sub>), 136.68 (C<sub>21</sub>), 129.09 (C<sub>22/23/24/27/28/29/32/33/34</sub>), 128.65 (C<sub>22/23/24/27/28/29/32/33/34</sub>), 128.60 (C<sub>22/23/24/27/28/29/32/33/34</sub>), 128.45 (C<sub>22/23/24/27/28/29/32/33/34</sub>), 128.30 (C<sub>22/23/24/27/28/29/32/33/34</sub>), 128.26 (C<sub>22/23/24/27/28/29/32/33/34</sub>), 128.20 (C<sub>22/23/24/27/28/29/32/33/34</sub>), 127.29 (C<sub>22/23/24/27/28/29/32/33/34</sub>), 126.94 (C<sub>22/23/24/27/28/29/32/33/34</sub>), 80.90 (C<sub>2</sub>), 66.63 (C<sub>20</sub>), 58.45 (C<sub>12</sub>), 57.74 (C<sub>4</sub>), 56.36 (C<sub>15,30</sub>), 55.69 (C<sub>7</sub>), 54.86 (C<sub>15</sub>), 44.28 (C<sub>8</sub>), 28.41 (C<sub>1</sub>), 19.18 (C<sub>9</sub>), 15.29 (C<sub>5</sub>), 8.28 (C<sub>13</sub>) ppm.

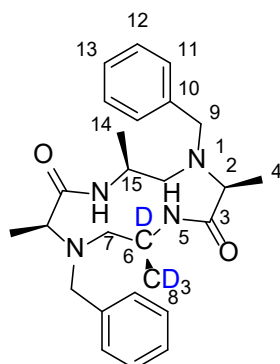
**HR-ESI-MS:** calcd. for [M+H]<sup>+</sup> C<sub>38</sub>H<sub>49</sub>D<sub>4</sub>N<sub>4</sub>O<sub>5</sub> *m/z* = 649.4262 found 649.4254.

***N*-((*S*)-2-((*S*)-2-(((*S*)-2-aminopropyl) (benzyl)amino) propanamido)propyl) -*N*-benzyl-*L*-alanine (42):**



**HR-ESI-MS:** calcd. for  $[M+H]^+$  C<sub>26</sub>H<sub>35</sub>D<sub>4</sub>N<sub>4</sub>O<sub>3</sub> m/z = 459.3268 found 459.3271.

**(3*S*,6*S*,9*S*,12*S*)-4,10-Dibenzyl-3,6,9,12-tetramethyl- 1,4,7,10-tetraazacyclododecane-2,8-dione (14):**



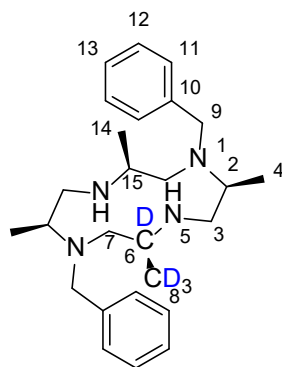
**<sup>1</sup>H NMR (500 MHz, Dimethylsulfoxide-*d*<sub>6</sub>)**  $\delta$ : 7.75-7.70 (m, 2H, H<sub>5</sub>), 7.46-7.41 (m, 4H, H<sub>11</sub>), 7.34-7.25 (m, 6H, H<sub>12,13</sub>), 3.93-3.87 (m, 2H, H<sub>9a</sub>), 3.61-3.53 (m, 2H, H<sub>9b</sub>), 3.36-3.28 (m, 1H, H<sub>15</sub>), 3.24-3.17 (m, 2H, H<sub>2</sub>), 2.81-2.74 (m, 2H, H<sub>7a</sub>), 2.33-2.26 (m, 2H, H<sub>7b</sub>), 1.15 (d, <sup>3</sup>J<sub>HH</sub> = 6.60 Hz, 3H, H<sub>14</sub>), 1.05 (d, <sup>3</sup>J<sub>HH</sub> = 6.98 Hz, 6H, H<sub>4</sub>) ppm.

**<sup>13</sup>C NMR (126 MHz, Dimethylsulfoxide-*d*<sub>6</sub>)**  $\delta$ : 172.15 (C<sub>3</sub>), 139.19 (C<sub>10</sub>), 129.04 (C<sub>11/12/13</sub>), 128.16 (C<sub>11/12/13</sub>), 127.09 (C<sub>11/12/13</sub>), 59.57 (C<sub>2</sub>), 56.79 (C<sub>9</sub>), 55.13 (C<sub>7</sub>), 44.10 (C<sub>15</sub>), 17.68 (C<sub>14</sub>), 8.51 (C<sub>4</sub>) ppm.

**HR-ESI-MS:** calcd. for  $[M+H]^+$  C<sub>26</sub>H<sub>33</sub>D<sub>4</sub>N<sub>4</sub>O<sub>2</sub> m/z = 441.3162 found 441.3159.



**(2*S*,5*S*,8*S*,11*S*)-1,7-Dibenzyl-2,5,8,11-tetramethyl-1,4,7,10-tetraazacyclododecane (15):**

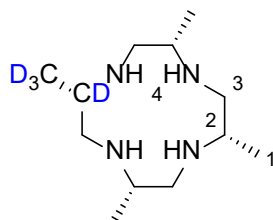


**<sup>1</sup>H NMR (500 MHz, Chloroform-*d*)**  $\delta$ : 7.40-7.24 (m, 10H, H<sub>11,12,13</sub>), 3.81 (d, <sup>2</sup>*J*<sub>HH</sub> = 13.08 Hz, 2H, H<sub>9a</sub>), 3.14-3.03 (m, 2H, H<sub>2</sub>), 3.03-2.90 (m, 2H, H<sub>9b</sub>), 2.88-2.76 (m, 3H, H<sub>15,3a</sub>), 2.49-2.34 (m, 4H, H<sub>3b,7a</sub>), 2.31-2.10 (m, 2H, H<sub>7a</sub>), 0.90 (d, <sup>3</sup>*J*<sub>HH</sub> = 6.36 Hz, 6H, H<sub>4</sub>), 0.87 (d, <sup>3</sup>*J*<sub>HH</sub> = 5.98 Hz, 3H, H<sub>14</sub>) ppm.

**<sup>13</sup>C NMR (126 MHz, Chloroform-*d*)**  $\delta$ : 139.95 (C<sub>10</sub>), 129.32 (C<sub>11/12/13</sub>), 128.49 (C<sub>11/12/13</sub>), 127.28 (C<sub>11/12/13</sub>), 56.64 (C<sub>7</sub>), 51.72 (C<sub>9</sub>), 50.06 (C<sub>2</sub>), 47.94 (C<sub>3</sub>), 46.52 (C<sub>15</sub>), 18.80 (C<sub>8</sub>), 10.13 (C<sub>4</sub>) ppm.

**HR-ESI-MS:** calcd. for [M+H]<sup>+</sup> C<sub>26</sub>H<sub>37</sub>D<sub>4</sub>N<sub>4</sub> *m/z* = 413.3577 found 413.3578.

**(2*S*,5*S*,8*S*,11*S*)-2,5,8,11-Tetramethyl-1,4,7,10-tetraazacyclododecane (16):**

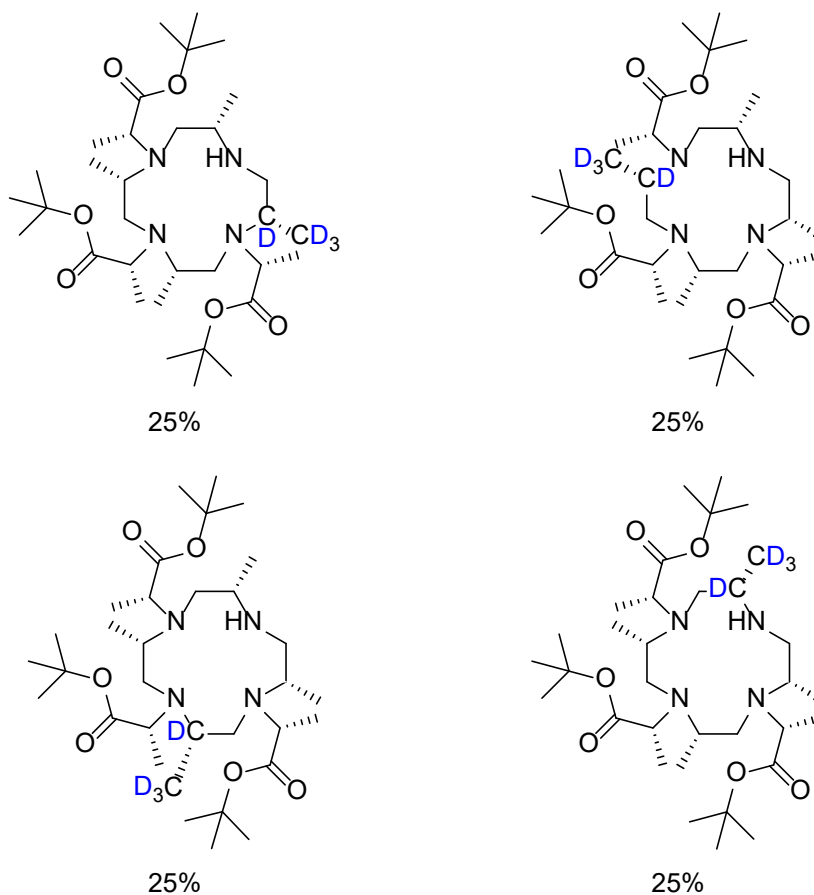


**<sup>1</sup>H NMR (500 MHz, Chloroform-*d*)**  $\delta$ : 2.71-2.59 (m, 7H, H<sub>2,3a</sub>), 2.42-2.33 (m, 4H, H<sub>3b</sub>), 0.94 (d, <sup>3</sup>*J*<sub>HH</sub> = 5.89 Hz, 9H, H<sub>1</sub>) ppm.

**<sup>13</sup>C NMR (126 MHz, Chloroform-*d*)**  $\delta$ : 52.44 (C<sub>3</sub>), 47.83 (C<sub>2</sub>), 18.54 (C<sub>1</sub>) ppm.

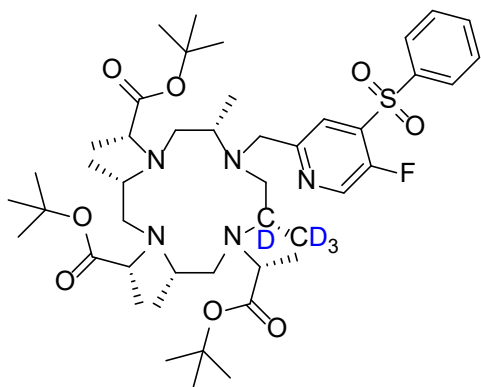
**HR-ESI-MS:** calcd. for  $[M+H]^+$   $C_{12}H_{25}D_4N_4$   $m/z = 233.2638$  found 233.2638.

**Tri-*tert*-butyl 2,2',2''- ((2*S*,5*S*,8*S*,11*S*) -2,5,8,11 -tetramethyl -1,4,7,10 - tetraazacyclododecane-1,4,7-triyl)(2*R*,2'*R*,2''*R*)-tripropionate (17):**

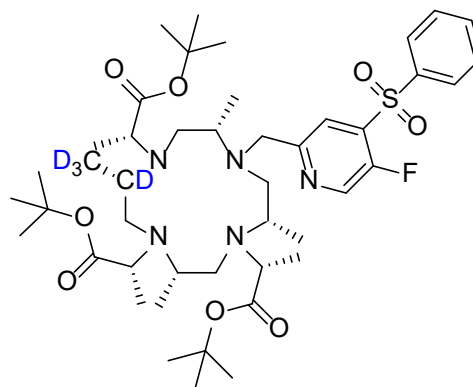


**HR-ESI-MS:** calcd. for  $[M+H]^+$   $C_{33}H_{61}D_4N_4O_6$   $m/z = 617.5150$  found 617.5143.

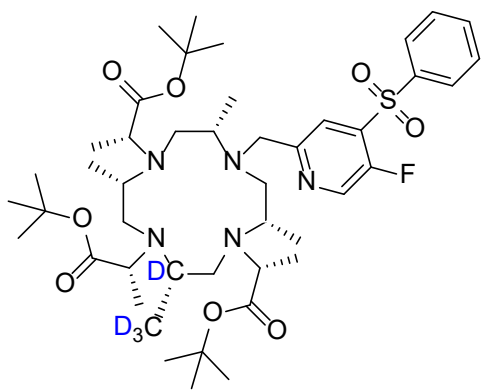
**Tri-*tert*-butyl 2,2',2''-((2*S*,5*S*,8*S*,11*S*) -10- ((5-fluoro-4-(phenyl sulfonyl) pyridin-2-yl) methyl)-2,5,8,11- tetramethyl-1,4,7,10-tetraazacyclododecane-1,4,7-triyl)(2*R*,2'*R*,2''*R*)-tri propionate (43):**



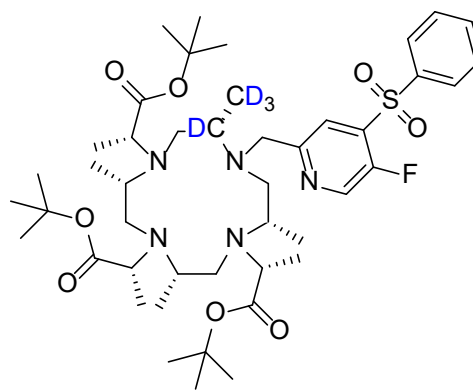
25%



25%



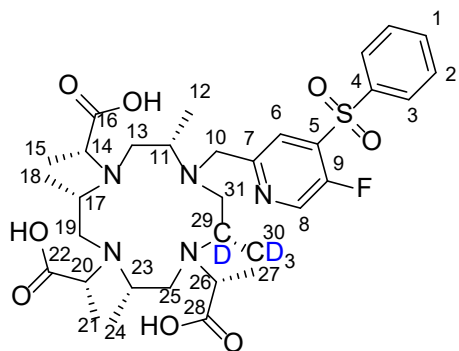
25%



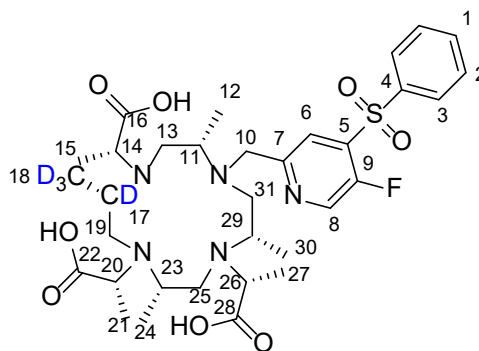
25%

**HR-ESI-MS:** calcd. for [M+H]<sup>+</sup> C<sub>45</sub>H<sub>69</sub>D<sub>4</sub>FN<sub>5</sub>O<sub>8</sub>S m/z = 866.5409 found 866.5398.

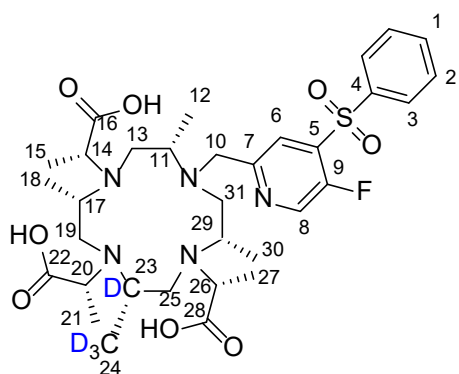
**(2*R*,2'*R*,2''*R*)-2,2',2''-((2*S*,5*S*,8*S*,11*S*)-10-((5-Fluoro-4-(phenylsulfonyl)pyridin-2-yl)methyl)-2,5,8,11-tetramethyl-1,4,7,10-tetraazacyclododecane-1,4,7-triyl) tripropionic acid (44):**



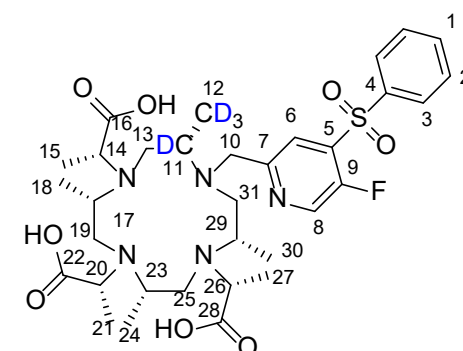
25%



25%



25%



25%

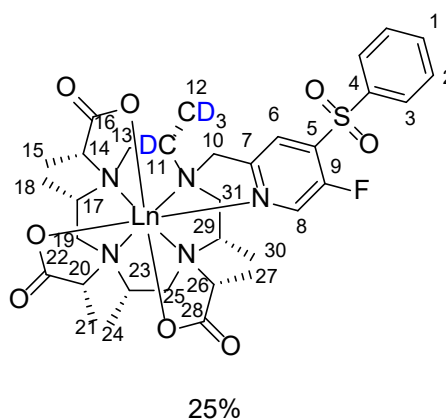
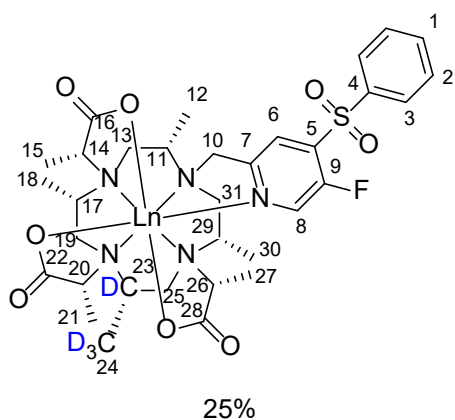
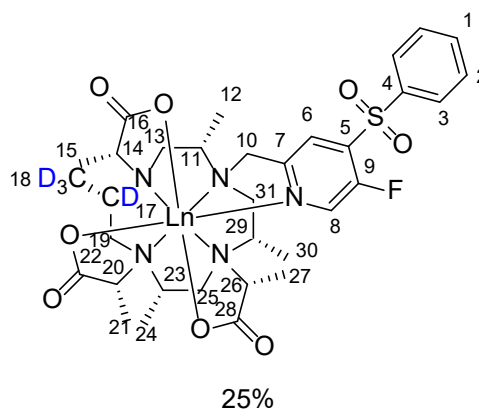
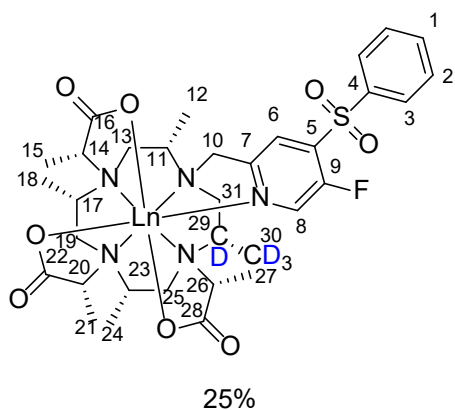
**<sup>1</sup>H NMR (500 MHz, Acetonitrile-*d*<sub>3</sub>)**  $\delta$ : 8.68 (s, 1H, H<sub>8</sub>), 8.19 (d, <sup>4</sup>*J*<sub>HF</sub> = 5.0 Hz, 1H, H<sub>6</sub>), 8.02 (d, <sup>3</sup>*J*<sub>HH</sub> = 8.0 Hz, 2H, H<sub>3</sub>), 7.78 (m, 1H, H<sub>1</sub>), 7.66 (m, 2H, H<sub>2</sub>), 4.69 (d, <sup>2</sup>*J*<sub>HH</sub> = 15.2 Hz 1H, H<sub>10a</sub>), 4.61 (d, <sup>2</sup>*J*<sub>HH</sub> = 15.2 Hz 1H, H<sub>10b</sub>), 4.15 (m, 1H, H<sub>20</sub>), 3.94-3.84 (m, 1.5H, H<sub>23,29</sub>), 3.80 (m, 0.75H, H<sub>11</sub>), 3.73 (m, 1H, H<sub>26</sub>), 3.47 (m, 1H, H<sub>14</sub>), 3.25 (m, 0.75H, H<sub>17</sub>), 3.12-2.78 (m, 8H, H<sub>13a,13b,19a,19b,25a,25b,31a,31b</sub>), 1.56 (d, <sup>3</sup>*J*<sub>HH</sub> = 7.8 Hz, 3H, H<sub>21</sub>), 1.37 (d, <sup>3</sup>*J*<sub>HH</sub> = 7.2 Hz, 3H, H<sub>15</sub>), 1.33 (d, <sup>3</sup>*J*<sub>HH</sub> = 6.6 Hz, 3H, H<sub>27</sub>), 1.28 (d, <sup>3</sup>*J*<sub>HH</sub> = 6.6 Hz, 2.25H, H<sub>24</sub>), 1.16 (d, <sup>3</sup>*J*<sub>HH</sub> = 6.6 Hz, 2.25H, H<sub>30</sub>), 1.12 (d, <sup>3</sup>*J*<sub>HH</sub> = 6.6 Hz, 2.25H, H<sub>18</sub>), 1.04 (d, <sup>3</sup>*J*<sub>HH</sub> = 6.6 Hz, 2.25H, H<sub>12</sub>), ppm.

**<sup>13</sup>C NMR (152 MHz, Acetonitrile-*d*<sub>3</sub>)**  $\delta$ : 176.25 (C<sub>16</sub>), 173.89 (C<sub>28</sub>), 171.96 (C<sub>22</sub>), 155.62 (C<sub>9</sub>), 149.12 (C<sub>7</sub>), 141.68 (C<sub>8</sub>), 139.93 (C<sub>4</sub>), 138.27 (C<sub>5</sub>), 136.21 (C<sub>1</sub>), 130.87 (C<sub>2</sub>), 129.44 (C<sub>3</sub>), 125.68 (C<sub>6</sub>), 65.39 (C<sub>20</sub>), 61.62 (C<sub>23</sub>), 61.50 (C<sub>14</sub>), 59.45 (C<sub>11</sub>), 56.94 (C<sub>17</sub>), 56.80 (C<sub>26</sub>), 56.77 (C<sub>10</sub>), 50.10 (C<sub>31</sub>), 49.91 (C<sub>29</sub>), 47.96 (C<sub>19</sub>), 47.53 (C<sub>25</sub>), 45.84 (C<sub>13</sub>), 16.23 (C<sub>27</sub>), 14.74 (C<sub>15</sub>), 14.65 (C<sub>18</sub>), 13.95 (C<sub>21</sub>), 13.80 (C<sub>30</sub>), 12.84 (C<sub>12</sub>), 12.73 (C<sub>24</sub>) ppm.

$^{19}\text{F}$  NMR (471 MHz, Acetonitrile- $d_3$ )  $\delta$ : -124.44 ppm.

HR-ESI-MS: calcd. for  $[\text{M}+\text{H}]^+$   $\text{C}_{33}\text{H}_45\text{D}_4\text{FN}_5\text{O}_8\text{S}$   $m/z = 698.3531$  found 698.3517.

Ln-DOTA-M7FPy (2):



$[\text{Tb}(\text{DOTA-M7FPy})]$  83% yield as a white solid.

$^{19}\text{F}$  NMR (565 MHz, Deuterium Oxide, 50 mM Phosphate Buffer pH=6.0)  $\delta$ : -193.97 ppm.

HR-ESI-MS: calcd. for  $[\text{M}+\text{Na}]^+$   $\text{C}_{33}\text{H}_{41}\text{D}_4\text{FTbN}_5\text{NaO}_8\text{S}$   $m/z = 876.2370$  found 876.2359.

$[\text{Dy}(\text{DOTA-M7FPy})]$  93% yield as a white solid.

$^{19}\text{F}$  NMR (565 MHz, Deuterium Oxide, 50 mM Phosphate Buffer pH=6.0)  $\delta$ : -232.61 ppm.

**HR-ESI-MS:** calcd. for  $[M+Na]^+$   $C_{33}H_{41}D_4FDyN_5NaO_8S$   $m/z = 881.2414$  found 881.2406.

[Ho(DOTA-M7FPy)] 63% yield as a pink solid.

**$^{19}F$  NMR (565 MHz, Deuterium Oxide, 50 mM Phosphate Buffer pH=6.0)  $\delta$ :** -176.08 ppm.

**HR-ESI-MS:** calcd. for  $[M+Na]^+$   $C_{33}H_{41}D_4FHoN_5NaO_8S$   $m/z = 882.2419$  found 882.2418.

[Er(DOTA-M7FPy)] 75% yield as a white solid.

**$^{19}F$  NMR (565 MHz, Deuterium Oxide, 50 mM Phosphate Buffer pH=6.0)  $\delta$ :** -95.91 ppm.

**HR-ESI-MS:** calcd. for  $[M+Na]^+$   $C_{33}H_{41}D_4FErN_5NaO_8S$   $m/z = 883.2419$  found 883.2407.

[Tm(DOTA-M7FPy)] 87% yield as a white solid.

**$^{19}F$  NMR (565 MHz, Deuterium Oxide, 50 mM Phosphate Buffer pH=6.0)  $\delta$ :** -53.66 ppm.

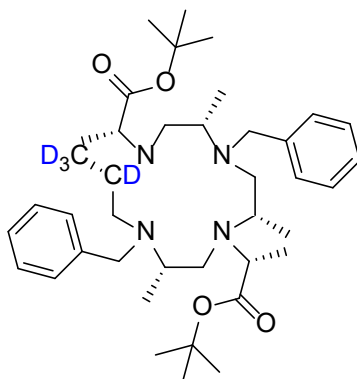
**HR-ESI-MS:** calcd. for  $[M+Na]^+$   $C_{33}H_{41}D_4FTmN_5NaO_8S$   $m/z = 886.2458$  found 886.2441.

[Yb(DOTA-M7FPy)] 72% yield as a white solid.

**$^{19}F$  NMR (565 MHz, Deuterium Oxide, 50 mM Phosphate Buffer pH=6.0)  $\delta$ :** -89.01 ppm.

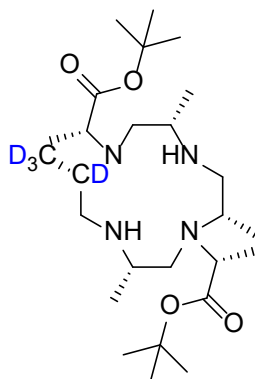
**HR-ESI-MS:** calcd. for  $[M+Na]^+$   $C_{33}H_{41}D_4FYbN_5NaO_8S$   $m/z = 891.2508$  found 891.2492.

**Di-*tert*-butyl 2,2'- ((2*S*,5*S*,8*S*,11*S*) -4,10 -dibenzyl- 2,5,8,11 -tetramethyl-1,4,7,10-tetraazacyclododecane-1,7-diyl)(2*R*,2'*R*)-dipropionate (19):** (2*S*,5*S*,8*S*,11*S*)-1,7-Dibenzyl-2,5,8,11-tetramethyl-1,4,7,10-tetra-azacyclododecane (225 mg, 0.551 mmol, 1.0 eq.) was dissolved under argon in dry methylene chloride (20 ml). Then potassium carbonate (228 mg, 1.65 mmol, 3.0 eq.), *tert*-butyl (*S*)-2-(((trifluoromethyl) sulfonyl)oxy)propanoate (330 mg, 1.19 mmol, 2.2 eq.) and dry acetonitrile (10 ml) were added. The suspension was stirred for 24 h. Then triethylamine (0.50 ml) was added and the suspension was filtered. The solvent was evaporated and the crude was purified by prep. HPLC to yield di-*tert*-butyl 2,2'- ((2*S*,5*S*,8*S*,11*S*) -4,10-dibenzyl-2,5,8,11- tetramethyl- 1,4,7,10-tetraazacyclododecane-1, 7-diyl) (2*R*,2'*R*)-dipropionate (200 mg, 0.327 mmol, 84%) as a colourless solid.



**HR-ESI-MS:** calcd. for  $[M+H]^+$   $C_{40}H_{61}D_4N_4O_4$   $m/z = 669.5251$  found 669.5252.

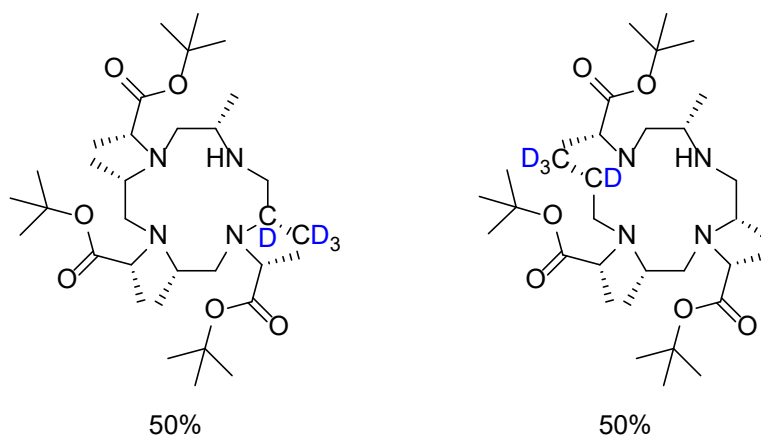
**Di-*tert*-butyl 2,2'-((2*S*,5*S*,8*S*,11*S*)-2,5,8,11-tetramethyl-1,4,7,10-tetraazacyclododecane-1,7-diyl)(2*R*, 2'*R*)-dipropionate (20):** di-*tert*-butyl 2,2'-((2*S*,5*S*,8*S*,11*S*)-4,10-dibenzyl-2,5,8,11-tetramethyl-1,4,7,10-tetra azacyclododecane-1, 7-diyl)(2*R*,2'*R*)-dipropionate (325 mg, 0.489 mmol, 1.0 eq.) and palladium hydroxide on carbon (20 wt. % loading, 112 mg) was suspended in ethanol (45 ml). The solution was heated to 88°C. When a temperature of 72°C was reached ammonium formate (308 mg, 4.88 mmol, 10 eq) was added. The suspension was heated to 88°C for 3.5 h. Then the suspension was cooled to 20-25°C, filtered over celite and the solvent was evaporated. The crude was purified by prep. HPLC to yield di-*tert*-butyl 2,2'-((2*S*,5*S*,8*S*,11*S*)- 2,5,8,11 -tetramethyl -1,4,7,10-tetraazacyclododecane-1,7-diyl)(2*R*,2'*R*)-dipropionate (203 mg, 0.419 mmol, 86%) as a colourless solid.



**HR-ESI-MS:** calcd. for  $[M+H]^+$   $C_{26}H_{49}D_4N_4O_4$   $m/z = 489.4312$  found 489.4315.

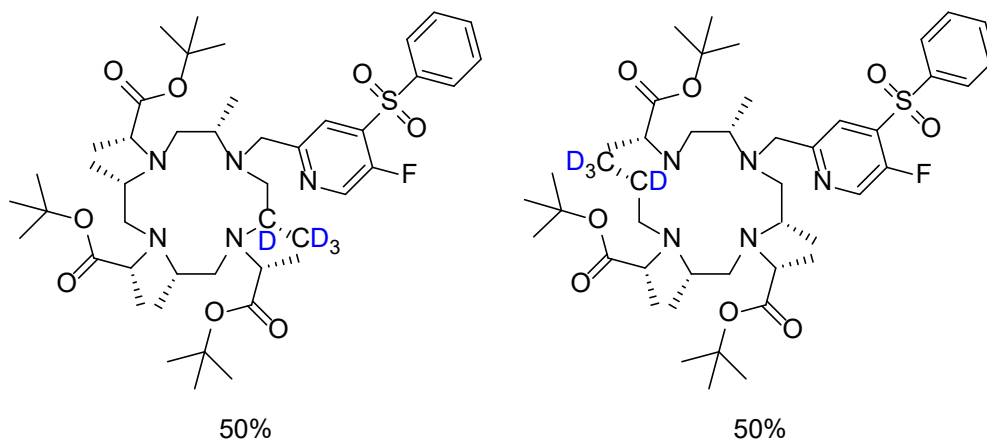


**Tri-*tert*-butyl 2,2',2''- ((2*S*,5*S*,8*S*,11*S*) -2,5,8,11 -tetramethyl -1,4,7,10 -tetraazacyclododecane-1,4,7-triyl)(2*R*,2'*R*,2''*R*)-tripropionate (21):** di-*tert*-butyl 2,2'-((2*S*,5*S*,8*S*,11*S*)- 2,5,8,11 -tetramethyl -1,4,7,10-tetraazacyclododecane-1,7-diyl)(2*R*,2'*R*)-dipropionate (200 mg, 0.413 mmol, 1.0 eq) was dissolved in methylene chloride (40 ml). Then potassium carbonate (571 mg, 6.24 mmol, 15 eq.), *tert*-butyl (*S*)-2-(((trifluoromethyl)sulfonyl)oxy)propanoate (58.0 mg, 0.208 mmol, 0.51 eq.) and dry acetonitrile (0.5 ml) were added. The suspension was stirred for 24 h. Reaction control with HPLC-MS showed nearly no formation of the four times alkylated species, therefore additional *tert*-butyl (*S*)-2-(((trifluoromethyl)sulfonyl)oxy)propanoate (23.0 mg, 0.0827 mmol, 0.20 eq.) was added. The suspension was stirred for 15 h. Then trimethylamine (0.50 ml) was added and the suspension was filtered. The solvent was evaporated and the crude was purified by prep. HPLC to yield tri-*tert*-butyl 2, 2',2''- ((2*S*,5*S*,8*S*,11*S*) -2,5,8,11-tetramethyl-1,4,7,10-tetraazacyclododecane-1,4,7-triyl) (2*R*,2'*R*,2''*R*)-tripropionate (106 mg, 0.173 mmol, 42%) as a colourless oil.



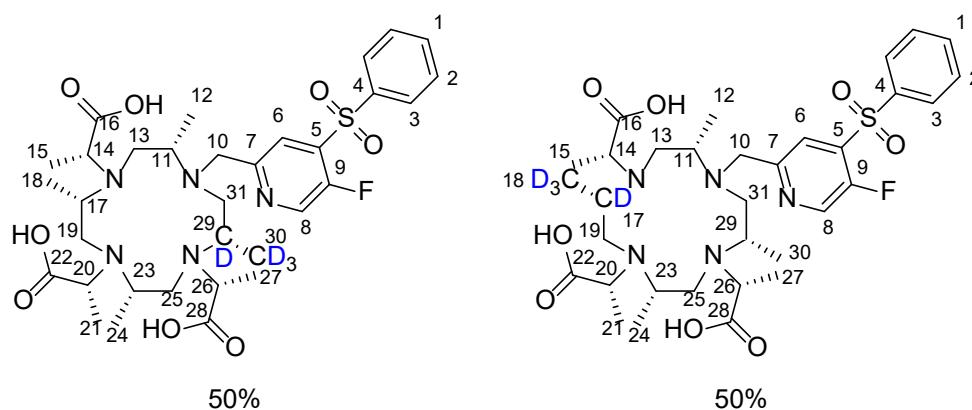
**HR-ESI-MS:** calcd. for  $[M+H]^+$   $C_{33}H_{61}D_4N_4O_6$   $m/z = 617.5150$  found 617.5160.

**Tri-*tert*-butyl 2,2',2''-((2*S*,5*S*,8*S*,11*S*) -10- ((5-fluoro-4-(phenyl sulfonyl) pyridin-2-yl) methyl)-2,5,8,11- tetramethyl-1,4,7,10-tetraazacyclododecane-1,4,7-triyl)(2*R*,2'*R*,2''*R*)-tri propionate (45):**



**HR-ESI-MS:** calcd. for  $[M+H]^+$   $C_{45}H_{69}D_4FN_5O_8S$   $m/z = 866.5409$  found 866.5403.

**(2*R*,2'*R*,2''*R*)-2,2',2''-((2*S*,5*S*,8*S*,11*S*) -10- ((5- Fluoro -4- (phenylsulfonyl) pyridin-2-yl) methyl)- 2,5,8,11-tetramethyl-1,4,7,10-tetraazacyclododecane-1,4,7-triyl) tripropionic acid (46):**



**$^1H$  NMR (500 MHz, Acetonitrile- $d_3$ )  $\delta$ :** 8.68 (s, 1H, H<sub>8</sub>), 8.21 (d,  $^4J_{HF} = 3.0$  Hz, 1H, H<sub>6</sub>), 8.03 (d,  $^3J_{HH} = 7.4$  Hz, 2H, H<sub>3</sub>), 7.78 (m, 1H, H<sub>1</sub>), 7.66 (m, 2H, H<sub>2</sub>), 4.73 (d,  $^2J_{HH} = 14.8$  Hz 1H, H<sub>10a</sub>), 4.63 (d,  $^2J_{HH} = 14.8$  Hz 1H, H<sub>10b</sub>), 4.33 (m, 1H, H<sub>20</sub>), 3.94 (m, 1H, H<sub>23</sub>), 3.89-3.79 (m, 1.5H, H<sub>11,29</sub>), 3.68 (m, 1H, H<sub>26</sub>), 3.46 (m, 1H, H<sub>14</sub>), 3.29-3.14 (m, 2.5H, H<sub>17,19a,31</sub>), 3.09-2.81

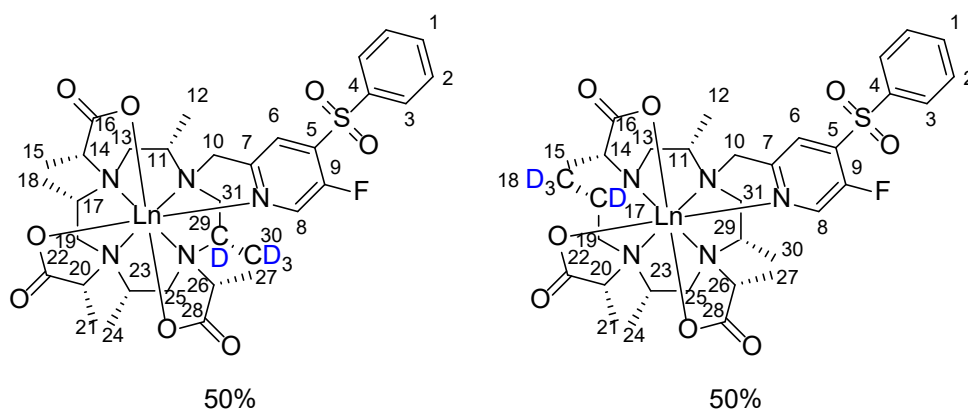
(m, 6H, H<sub>13a,13b,19b,25a,25b,31b</sub>), 1.62 (d, <sup>3</sup>J<sub>HH</sub> = 6.9 Hz, 3H, H<sub>21</sub>), 1.38 (d, <sup>3</sup>J<sub>HH</sub> = 6.6 Hz, 3H, H<sub>15</sub>), 1.35-1.26 (m, 6H, H<sub>24,27</sub>), 1.19-1.05 (m, 6H, H<sub>12,18,30</sub>) ppm.

<sup>13</sup>C NMR (152 MHz, Acetonitrile-*d*<sub>3</sub>) δ: 175.51 (C<sub>16</sub>), 172.84 (C<sub>28</sub>), 170.59 (C<sub>22</sub>), 154.73 (C<sub>9</sub>), 147.96 (C<sub>7</sub>), 140.8 (C<sub>8</sub>), 138.90 (C<sub>4</sub>), 137.47 (C<sub>5</sub>), 135.24 (C<sub>1</sub>), 129.93 (C<sub>2</sub>), 128.41 (C<sub>3</sub>), 124.82 (C<sub>6</sub>), 64.31 (C<sub>20</sub>), 61.42 (C<sub>23</sub>), 59.81 (C<sub>14</sub>), 58.86 (C<sub>11</sub>), 55.94 (C<sub>10</sub>), 55.57 (C<sub>17</sub>), 55.01 (C<sub>26</sub>), 49.38 (C<sub>31</sub>), 48.59 (C<sub>29</sub>), 47.25 (C<sub>19</sub>), 46.40 (C<sub>25</sub>), 44.88 (C<sub>13</sub>), 14.99 (C<sub>27</sub>), 13.99 (C<sub>15</sub>), 13.67 (C<sub>18</sub>), 12.90 (C<sub>30</sub>), 12.84 (C<sub>21</sub>), 11.67 (C<sub>12</sub>), 11.63 (C<sub>24</sub>) ppm.

<sup>19</sup>F NMR (471 MHz, Acetonitrile-*d*<sub>3</sub>) δ: -123.88 ppm.

HR-ESI-MS: calcd. for [M+H]<sup>+</sup> C<sub>33</sub>H<sub>45</sub>D<sub>4</sub>FN<sub>5</sub>O<sub>8</sub>S m/z = 698.3531 found 698.3530.

Ln-DOTA-M7FPy (3):



[Tb(DOTA-M7FPy)] 66% yield as a white solid.

<sup>19</sup>F NMR (565 MHz, Deuterium Oxide, 50 mM Phosphate Buffer pH=6.0) δ: -193.99 ppm.

HR-ESI-MS: calcd. for [M+H]<sup>+</sup> C<sub>33</sub>H<sub>42</sub>D<sub>4</sub>FTbN<sub>5</sub>O<sub>8</sub>S m/z = 854.2550 found 854.2547.

[Dy(DOTA-M7FPy)] 84% yield as a white solid.

<sup>19</sup>F NMR (565 MHz, Deuterium Oxide, 50 mM Phosphate Buffer pH=6.0) δ: -232.67 ppm.

HR-ESI-MS: calcd. for [M+Na]<sup>+</sup> C<sub>33</sub>H<sub>41</sub>D<sub>4</sub>FDyN<sub>5</sub>NaO<sub>8</sub>S m/z = 881.2414 found 881.2399.

[Ho(DOTA-M7FPy)] 67% yield as a pink solid.

**<sup>19</sup>F NMR (565 MHz, Deuterium Oxide, 50 mM Phosphate Buffer pH=6.0) δ: -176.07 ppm.**

**HR-ESI-MS:** calcd. for [M+Na]<sup>+</sup> C<sub>33</sub>H<sub>41</sub>D<sub>4</sub>FHoN<sub>5</sub>NaO<sub>8</sub>S m/z = 882.2419 found 882.2415.

[Er(DOTA-M7FPy)] 64% yield as a white solid.

**<sup>19</sup>F NMR (565 MHz, Deuterium Oxide, 50 mM Phosphate Buffer pH=6.0) δ: -95.95 ppm.**

**HR-ESI-MS:** calcd. for [M+Na]<sup>+</sup> C<sub>33</sub>H<sub>41</sub>D<sub>4</sub>FErN<sub>5</sub>NaO<sub>8</sub>S m/z = 883.2419 found 883.2414.

[Tm(DOTA-M7FPy)] 83% yield as a white solid.

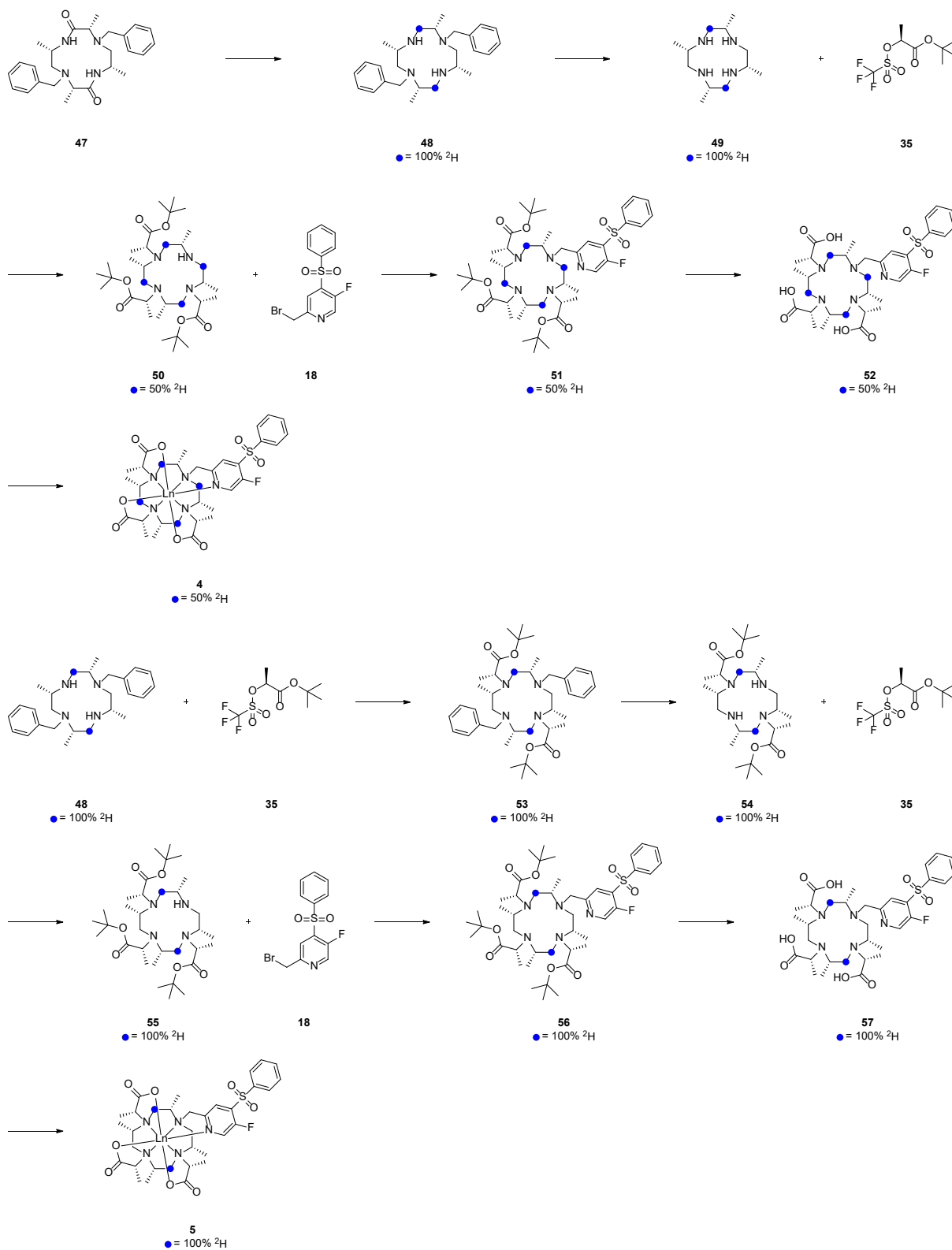
**<sup>19</sup>F NMR (565 MHz, Deuterium Oxide, 50 mM Phosphate Buffer pH=6.0) δ: -53.52 ppm.**

**HR-ESI-MS:** calcd. for [M+Na]<sup>+</sup> C<sub>33</sub>H<sub>41</sub>D<sub>4</sub>FTmN<sub>5</sub>NaO<sub>8</sub>S m/z = 886.2458 found 886.2458.

[Yb(DOTA-M7FPy)] 77% yield as a white solid.

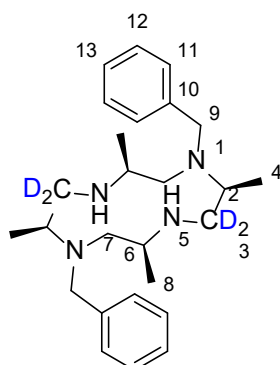
**<sup>19</sup>F NMR (565 MHz, Deuterium Oxide, 50 mM Phosphate Buffer pH=6.0) δ: -88.94 ppm.**

**HR-ESI-MS:** calcd. for [M+Na]<sup>+</sup> C<sub>33</sub>H<sub>41</sub>D<sub>4</sub>FYbN<sub>5</sub>NaO<sub>8</sub>S m/z = 891.2508 found 891.2492.



**Figure S4:** Synthesis towards Ln-DOTA-M7FPy (**4&5**) with deuterium labelled axial and equatorial methylene protons on the basal cyclen ring. Blue dots mark positions labelled with deuterium  $^2\text{H}$ . Below each labelled molecule, the observed labelling percentage is noted.

**(2*S*,5*S*,8*S*,11*S*)-1,7-Dibenzyl-2,5,8,11-tetramethyl-1,4,7,10-tetraazacyclododecane (48):** (3*S*,6*S*,9*S*,12*S*)-4,10-dibenzyl-3,6,9,12-tetramethyl-1,4,7,10-tetraazacyclododecane-2,8-dione (502 mg, 1.15 mmol, 1.0 eq.) was dissolved under argon in dry methylene chloride (20 ml). The solution was cooled to 0-5°C then trimethylsilyl chloride (687 mg, 0.81 ml, 6.33 mmol, 5.5 eq.) was added over 8 min. The solution was stirred at 0-5°C for 30 min. Afterwards lithium aluminium deuteride (1 M in tetrahydrofuran, 9.0 ml, 9.00 mmol, 7.8 eq.) was added over 10 min. the solution was stirred at 0-5° for 30 min. Then the solution was allowed to warm up to 20-25°C. The suspension was stirred for 19 h Afterwards the suspension was cooled to 0-5°C and aq.(D<sub>2</sub>O) potassium deuteroxide (4M, 1.2 ml) was added. Then an excess of sodium sulphate was added and the suspension was filtered. The solvent was evaporated and the crude was purified by flash column chromatography (SiO<sub>2</sub>, methylene chloride : ethanol 8:2 + 2% triethylamine, liquid deposit) to yield (2*S*,5*S*,8*S*,11*S*)-1,7-dibenzyl-2,5,8,11-tetramethyl-1,4,7,10-tetraazacyclododecane (298 mg, 0.729 mmol, 63%) as an orange brown solid.

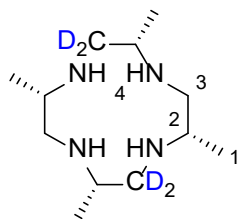


**<sup>1</sup>H NMR (500 MHz, Chloroform-*d*)**  $\delta$ : 7.40-7.24 (m, 10H, H<sub>11,12,13</sub>), 3.81 (d, <sup>2</sup>*J*<sub>HH</sub> = 13.1 Hz, 2H, H<sub>9a</sub>), 3.08 (m, 2H, H<sub>2</sub>), 2.98 (d, <sup>2</sup>*J*<sub>HH</sub> = 13.1 Hz, 2H, H<sub>9b</sub>), 2.93 (m, 2H, H<sub>5</sub>), 2.84 (m, 2H, H<sub>6</sub>), 2.45 (m, 2H, H<sub>7a</sub>), 2.24 (m, 2H, H<sub>7b</sub>) 0.90 (d, <sup>3</sup>*J*<sub>HH</sub> = 6.6 Hz, 6H, H<sub>4</sub>), 0.87 (d, <sup>3</sup>*J*<sub>HH</sub> = 5.5 Hz, 3H, H<sub>8</sub>) ppm.

**<sup>13</sup>C NMR (126 MHz, Chloroform-*d*)**  $\delta$ : 139.94 (C<sub>10</sub>), 129.31 (C<sub>11/12/13</sub>), 128.48 (C<sub>11/12/13</sub>), 127.26 (C<sub>11/12/13</sub>), 56.64 (C<sub>7</sub>), 51.73 (C<sub>9</sub>), 49.88 (C<sub>2</sub>), 46.47, 18.82 (C<sub>8</sub>), 10.10 (C<sub>4</sub>) ppm.

**HR-ESI-MS:** calcd. for [M+H]<sup>+</sup> C<sub>26</sub>H<sub>37</sub>D<sub>4</sub>N<sub>4</sub> m/z = 413.3577 found 413.3578.

**(2*S*,5*S*,8*S*,11*S*)-2,5,8,11-Tetramethyl-1,4,7,10-tetraazacyclododecane (49):**



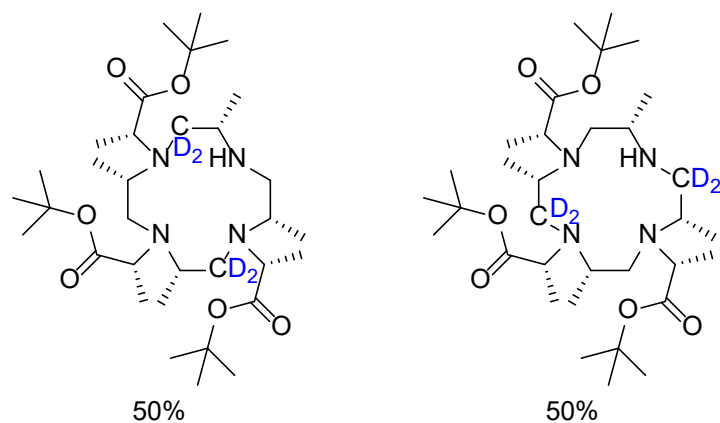
**<sup>1</sup>H NMR (500 MHz, Chloroform-*d*)**  $\delta$ : 2.72-2.58 (m, 6H, H<sub>2,3a</sub>), 2.37 (m, 2H, H<sub>3b</sub>), 2.08 (m, 2H, H<sub>4</sub>) 0.94 (d, <sup>3</sup>*J*<sub>HH</sub> = 5.8 Hz, 12H, H<sub>1</sub>) ppm.

**<sup>13</sup>C NMR (126 MHz, Chloroform-*d*)**  $\delta$ : 52.40(C<sub>3</sub>), 47.74 (C<sub>2</sub>), 47.65 (C<sub>2</sub>), 18.53 (C<sub>1</sub>), 18.49(C<sub>1</sub>) ppm.

For C<sub>2</sub> and C<sub>1</sub> two carbon shifts are observed due to the isotope shift caused by the deuterium.

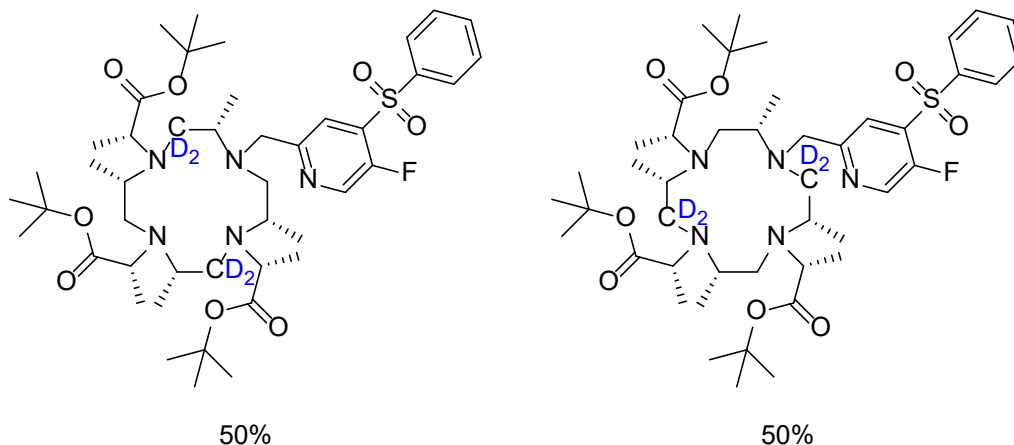
**HR-ESI-MS:** calcd. for [M+H]<sup>+</sup> C<sub>12</sub>H<sub>25</sub>D<sub>4</sub>N<sub>4</sub> *m/z* = 233.2638 found 233.2642.

**Tri-*tert*-butyl 2,2',2''-((2*S*,5*S*,8*S*,11*S*)-2,5,8,11-tetramethyl-1,4,7,10-tetraazacyclododecane-1,4,7-triyl)(2*R*,2'*R*,2''*R*)-tripropionate (50):**



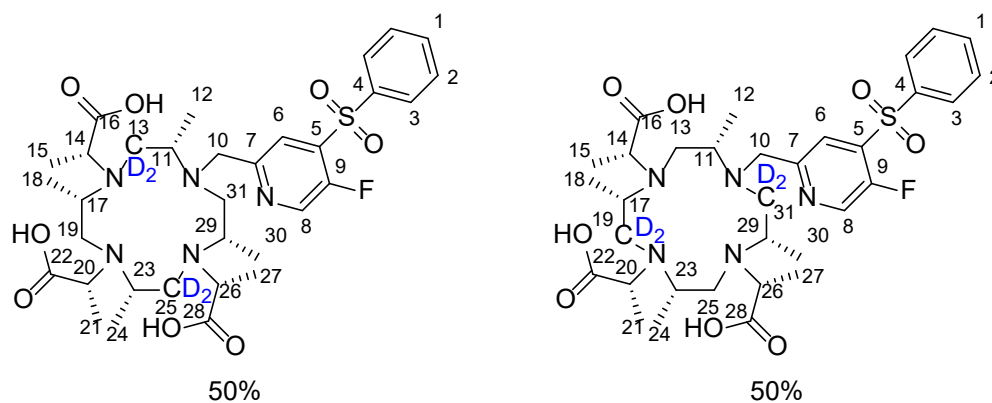
**HR-ESI-MS:** calcd. for [M+H]<sup>+</sup> C<sub>33</sub>H<sub>61</sub>D<sub>4</sub>N<sub>4</sub>O<sub>6</sub> *m/z* = 617.5150 found 617.5154.

**Tri-*tert*-butyl 2,2',2''-((2*S*,5*S*,8*S*,11*S*) -10- ((5-fluoro-4-(phenyl sulfonyl) pyridin-2-yl) methyl)-2,5,8,11- tetramethyl-1,4,7,10-tetraazacyclododecane-1,4,7-triyl)(2*R*,2'*R*,2''*R*)-tri propionate (51):**



**HR-ESI-MS:** calcd. for  $[M+H]^+$  C<sub>45</sub>H<sub>69</sub>D<sub>4</sub>FN<sub>5</sub>O<sub>8</sub>S m/z = 866.5409 found 866.5412.

**(2*R*,2'*R*,2''*R*)-2,2',2''-((2*S*,5*S*,8*S*,11*S*) -10- ((5- Fluoro -4- (phenylsulfonyl) pyridin-2-yl) methyl)- 2,5,8,11-tetramethyl-1,4,7,10-tetraazacyclododecane-1,4,7-triyl) tripropionic acid (52):**



**<sup>1</sup>H NMR (500 MHz, Acetonitrile-*d*<sub>3</sub>)**  $\delta$ : 8.68 (s, 1H, H<sub>8</sub>), 8.18 (m, 1H, H<sub>6</sub>), 8.02 (d, <sup>3</sup>J<sub>HH</sub> = 8.00 Hz, 2H, H<sub>3</sub>), 7.78 (m, 1H, H<sub>1</sub>), 7.66 (m, 2H, H<sub>2</sub>), 4.69 (m, 1H, H<sub>10a</sub>), 4.61 (m, H<sub>10b</sub>), 4.17 (m, 1H, H<sub>20</sub>), 3.96-3.84 (m, 2H, H<sub>23,29</sub>), 3.80 (m, 1H, H<sub>11</sub>), 3.73 (m, 1H, H<sub>26</sub>), 3.47 (m, 1H, H<sub>14</sub>), 3.23 (m, 1H, H<sub>17</sub>), 3.12-2.98 (m, 2H, H<sub>19a,31a</sub>), 3.16-2.81 (m, 4H,



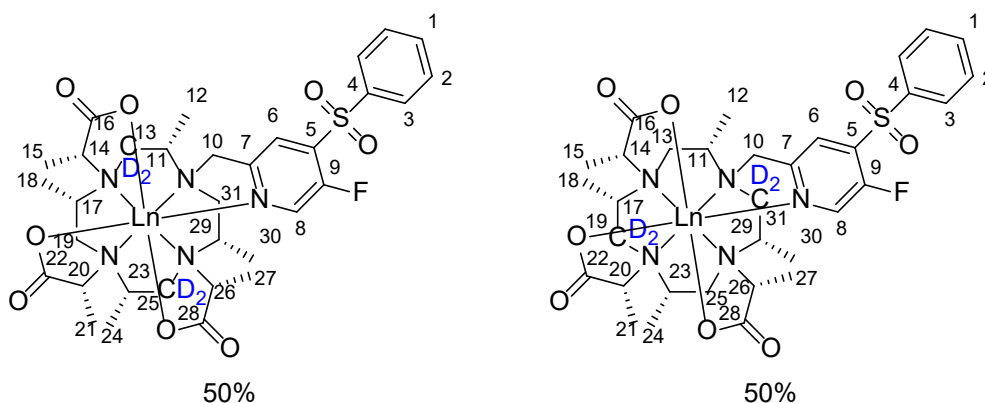
H<sub>13a,13b,19a,19b,25a,25b,31a,31b</sub>), 1.57 (m, 3H, H<sub>21</sub>), 1.37 (m, 3H, H<sub>15</sub>), 1.33 (m, 3H, H<sub>27</sub>), 1.28 (m, 3H, H<sub>24</sub>), 1.15 (m, 3H, H<sub>30</sub>), 1.12 (m, 3H, H<sub>18</sub>), 1.05 (m, 3H, H<sub>12</sub>), ppm.

<sup>13</sup>C NMR (152 MHz, Acetonitrile-*d*<sub>3</sub>) δ: 176.25 (C<sub>16</sub>), 173.87 (C<sub>28</sub>), 171.91 (C<sub>22</sub>), 155.67 (C<sub>9</sub>), 149.22 (C<sub>7</sub>), 141.73 (C<sub>8</sub>), 139.75 (C<sub>4</sub>), 138.53 (C<sub>5</sub>), 136.18 (C<sub>1</sub>), 130.83 (C<sub>2</sub>), 129.35 (C<sub>3</sub>), 125.65 (C<sub>6</sub>), 65.32 (C<sub>20</sub>), 61.45 (C<sub>14</sub>), 61.28 (C<sub>23</sub>), 59.36 (C<sub>11</sub>), 56.76 (C<sub>17</sub>), 56.76 (C<sub>26</sub>), 56.72 (C<sub>10</sub>), 50.15 (C<sub>31</sub>), 49.75 (C<sub>29</sub>), 47.99 (C<sub>19</sub>), 47.52 (C<sub>25</sub>), 45.96 (C<sub>13</sub>), 16.18 (C<sub>27</sub>), 14.73 (C<sub>15</sub>), 14.62 (C<sub>18</sub>), 13.90 (C<sub>21</sub>), 13.74 (C<sub>30</sub>), 12.73 (C<sub>12</sub>), 12.68 (C<sub>24</sub>) ppm.

<sup>19</sup>F NMR (471 MHz, Acetonitrile-*d*<sub>3</sub>) δ: -123.32

HR-ESI-MS: calcd. for [M+H]<sup>+</sup> C<sub>33</sub>H<sub>45</sub>D<sub>4</sub>FN<sub>5</sub>O<sub>8</sub>S m/z = 698.3531 found 698.3536.

#### Ln-DOTA-M7FPy (4):



[Tb(DOTA-M7FPy)] 61% yield as a white solid.

<sup>19</sup>F NMR (565 MHz, Deuterium Oxide, 50 mM Phosphate Buffer pH=6.0) δ: -194.15 ppm.

HR-ESI-MS: calcd. for [M+Na]<sup>+</sup> C<sub>33</sub>H<sub>41</sub>D<sub>4</sub>FTbN<sub>5</sub>NaO<sub>8</sub>S m/z = 876.2370 found 876.2371.

[Dy(DOTA-M7FPy)] 63% yield as a white solid.

<sup>19</sup>F NMR (565 MHz, Deuterium Oxide, 50 mM Phosphate Buffer pH=6.0) δ: -232.74 ppm.

**HR-ESI-MS:** calcd. for  $[M+Na]^+$   $C_{33}H_{41}D_4FDyN_5NaO_8S$   $m/z = 881.2414$  found 881.2410.

[Ho(DOTA-M7FPy)] 56% yield as a pink solid.

**$^{19}F$  NMR (565 MHz, Deuterium Oxide, 50 mM Phosphate Buffer pH=6.0)  $\delta$ :** -176.05 ppm.

**HR-ESI-MS:** calcd. for  $[M+Na]^+$   $C_{33}H_{41}D_4FHoN_5NaO_8S$   $m/z = 882.2419$  found 882.2419.

[Er(DOTA-M7FPy)] 51% yield as a white solid.

**$^{19}F$  NMR (565 MHz, Deuterium Oxide, 50 mM Phosphate Buffer pH=6.0)  $\delta$ :** -95.91 ppm.

**HR-ESI-MS:** calcd. for  $[M+Na]^+$   $C_{33}H_{41}D_4FErN_5NaO_8S$   $m/z = 883.2419$  found 883.2406.

[Tm(DOTA-M7FPy)] 62% yield as a white solid.

**$^{19}F$  NMR (565 MHz, Deuterium Oxide, 50 mM Phosphate Buffer pH=6.0)  $\delta$ :** -53.05 ppm.

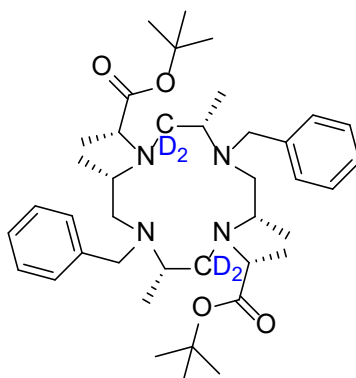
**HR-ESI-MS:** calcd. for  $[M+Na]^+$   $C_{33}H_{41}D_4FTmN_5NaO_8S$   $m/z = 886.2458$  found 886.2458.

[Yb(DOTA-M7FPy)] 66% yield as a white solid.

**$^{19}F$  NMR (565 MHz, Deuterium Oxide, 50 mM Phosphate Buffer pH=6.0)  $\delta$ :** -88.89 ppm.

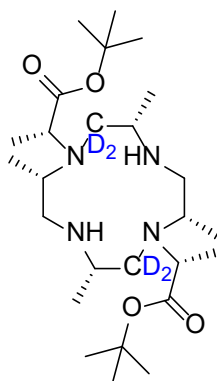
**HR-ESI-MS:** calcd. for  $[M+Na]^+$   $C_{33}H_{41}D_4FYbN_5NaO_8S$   $m/z = 891.2508$  found 891.2503.

**Di-*tert*-butyl 2,2'-((2*S*,5*S*,8*S*,11*S*)-4,10-dibenzyl-2,5,8,11-tetramethyl-1,4,7,10-tetraazacyclododecane-1,7-diyl)(2*R*,2'*R*)-dipropionate (53):**



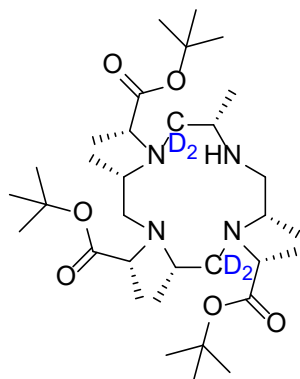
**HR-ESI-MS:** calcd. for  $[M+H]^+$   $C_{40}H_{60}D_4N_4O_4$   $m/z = 669.5251$  found 669.5256.

**Di-*tert*-butyl 2,2'-((2*S*,5*S*,8*S*,11*S*)-2,5,8,11-tetramethyl-1,4,7,10-tetraazacyclododecane-1,7-diyl)(2*R*,2'*R*)-dipropionate (54):**



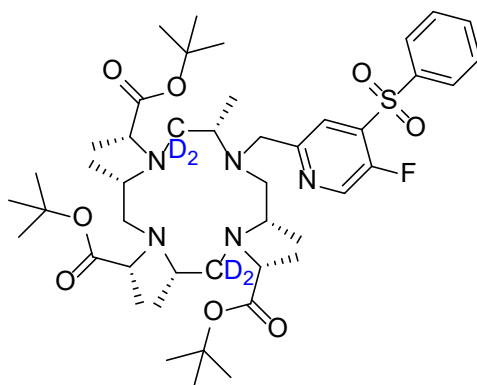
**HR-ESI-MS:** calcd. for  $[M+H]^+$   $C_{26}H_{49}D_4N_4O_4$   $m/z = 489.4312$  found 489.4307.

**Tri-*tert*-butyl 2,2',2''-((2*S*,5*S*,8*S*,11*S*)-2,5,8,11-tetramethyl-1,4,7,10-tetraazacyclododecane-1,4,7-triyl)(2*R*,2'*R*,2''*R*)-tripropionate (55):**



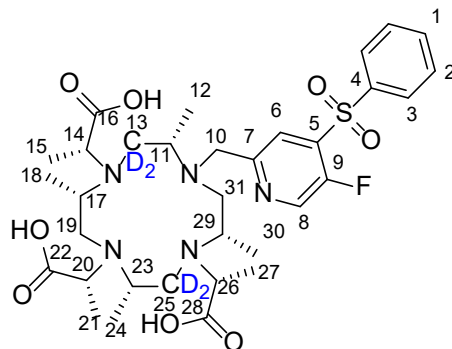
**HR-ESI-MS:** calcd. for  $[M+H]^+$   $C_{33}H_{61}D_4N_4O_6$   $m/z = 617.5150$  found 617.5154.

**Tri-*tert*-butyl 2,2',2''-((2*S*,5*S*,8*S*,11*S*)-10-((5-fluoro-4-(phenyl sulfonyl) pyridin-2-yl)methyl)-2,5,8,11-tetramethyl-1,4,7,10-tetraazacyclododecane-1,4,7-triyl)(2*R*,2'*R*,2''*R*)-tripropionate (56):**



**HR-ESI-MS:** calcd. for  $[M+H]^+$   $C_{45}H_{69}D_4FN_5O_8S$   $m/z = 866.5409$  found 866.5403.

**(2*R*,2'*R*,2''*R*)-2,2',2''-((2*S*,5*S*,8*S*,11*S*) -10- ((5- Fluoro -4- (phenylsulfonyl) pyridin-2-yl) methyl)- 2,5,8,11-tetramethyl-1,4,7,10-tetraazacyclododecane-1,4,7-triyl) tripropionic acid (57):**



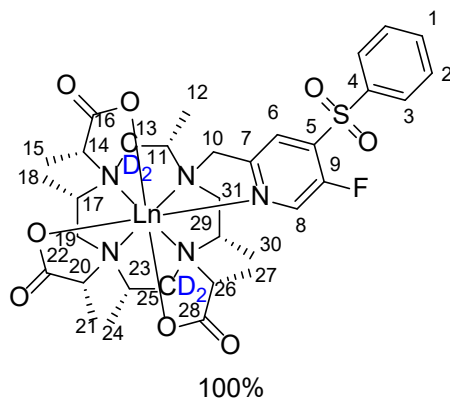
**<sup>1</sup>H NMR (500 MHz, Acetonitrile-*d*<sub>3</sub>) δ:** 8.68 (s, 1H, H<sub>8</sub>), 8.18 (d, <sup>4</sup>*J*<sub>HF</sub> = 5 Hz, 1H, H<sub>6</sub>), 8.02 (d, <sup>3</sup>*J*<sub>HH</sub> = 8.0 Hz, 2H, H<sub>3</sub>), 7.77 (m, 1H, H<sub>1</sub>), 7.65 (m, 2H, H<sub>2</sub>), 4.68 (d, <sup>2</sup>*J*<sub>HH</sub> = 15.6 Hz, 1H, H<sub>10a</sub>), 4.60 (d, <sup>2</sup>*J*<sub>HH</sub> = 15.4 Hz, 1H, H<sub>10b</sub>), 4.20 (m, 1H, H<sub>20</sub>), 3.93-3.84 (m, 2H, H<sub>23,29</sub>), 3.81 (q, <sup>3</sup>*J*<sub>HH</sub> = 6.5 Hz, 1H, H<sub>11</sub>), 3.73 (m, 1H, H<sub>26</sub>), 3.48 (m, 1H, H<sub>14</sub>), 3.22 (m, 1H, H<sub>17</sub>), 3.12-2.98 (m, 2H, H<sub>19a,31a</sub>), 2.96-2.81 (m, 2H, H<sub>19b,31b</sub>), 1.58 (d, <sup>3</sup>*J*<sub>HH</sub> = 7.2 Hz, 3H, H<sub>21</sub>), 1.38 (d, <sup>3</sup>*J*<sub>HH</sub> = 6.9 Hz, 3H, H<sub>15</sub>), 1.34 (d, <sup>3</sup>*J*<sub>HH</sub> = 6.6 Hz, 3H, H<sub>27</sub>), 1.28 (d, <sup>3</sup>*J*<sub>HH</sub> = 6.3 Hz, 3H, H<sub>24</sub>), 1.15 (d, <sup>3</sup>*J*<sub>HH</sub> = 6.6 Hz, 3H, H<sub>30</sub>), 1.12 (d, <sup>3</sup>*J*<sub>HH</sub> = 6.6 Hz, 3H, H<sub>18</sub>), 1.06 (d, <sup>3</sup>*J*<sub>HH</sub> = 5.6 Hz, 3H, H<sub>12</sub>), ppm.

**<sup>13</sup>C NMR (152 MHz, Acetonitrile-*d*<sub>3</sub>) δ:** 176.49 (C<sub>16</sub>), 173.76 (C<sub>28</sub>), 171.84 (C<sub>22</sub>), 155.54 (C<sub>9</sub>), 149.11 (C<sub>7</sub>), 141.69 (C<sub>8</sub>), 139.81 (C<sub>4</sub>), 138.38 (C<sub>5</sub>), 136.08 (C<sub>1</sub>), 130.78 (C<sub>2</sub>), 129.31 (C<sub>3</sub>), 125.65 (C<sub>6</sub>), 65.46 (C<sub>20</sub>), 61.68 (C<sub>23</sub>), 61.37 (C<sub>14</sub>), 59.48 (C<sub>11</sub>), 57.03 (C<sub>17</sub>), 56.82 (C<sub>10</sub>), 56.30 (C<sub>26</sub>), 50.12 (C<sub>31</sub>), 49.66 (C<sub>29</sub>), 47.91 (C<sub>19</sub>), 46.84 (C<sub>25</sub>), 45.16 (C<sub>13</sub>), 15.99 (C<sub>27</sub>), 14.67 (C<sub>15</sub>), 14.55 (C<sub>18</sub>), 13.74 (C<sub>21</sub>), 13.73 (C<sub>30</sub>), 12.60 (C<sub>12</sub>), 12.55 (C<sub>24</sub>) ppm.

**<sup>19</sup>F NMR (471 MHz, Acetonitrile-*d*<sub>3</sub>) δ:** -123.20 ppm

**HR-ESI-MS:** calcd. for [M+H]<sup>+</sup> C<sub>33</sub>H<sub>45</sub>D<sub>4</sub>FN<sub>5</sub>O<sub>8</sub>S m/z = 698.3531 found 698.3521.

**Ln-DOTA-M7FPy (5):**



[Tb(DOTA-M7FPy)] 96% yield as a white solid.

**<sup>19</sup>F NMR (565 MHz, Deuterium Oxide, 50 mM Phosphate Buffer pH=6.0) δ: -193.82 ppm.**

**HR-ESI-MS:** calcd. for [M+Na]<sup>+</sup> C<sub>33</sub>H<sub>41</sub>D<sub>4</sub>FTbN<sub>5</sub>NaO<sub>8</sub>S m/z = 876.2370 found 876.2370.

[Dy(DOTA-M7FPy)] 86% yield as a white solid.

**<sup>19</sup>F NMR (565 MHz, Deuterium Oxide, 50 mM Phosphate Buffer pH=6.0) δ: -232.61 ppm.**

**HR-ESI-MS:** calcd. for [M+Na]<sup>+</sup> C<sub>33</sub>H<sub>41</sub>D<sub>4</sub>FDyN<sub>5</sub>NaO<sub>8</sub>S m/z = 881.2414 found 881.2425.

[Ho(DOTA-M7FPy)] 73% yield as a pink solid.

**<sup>19</sup>F NMR (565 MHz, Deuterium Oxide, 50 mM Phosphate Buffer pH=6.0) δ: -175.98 ppm.**

**HR-ESI-MS:** calcd. for [M+Na]<sup>+</sup> C<sub>33</sub>H<sub>41</sub>D<sub>4</sub>FHoN<sub>5</sub>NaO<sub>8</sub>S m/z = 882.2419 found 882.2404.

[Er(DOTA-M7FPy)] 68% yield as a white solid.

**<sup>19</sup>F NMR (565 MHz, Deuterium Oxide, 50 mM Phosphate Buffer pH=6.0) δ: -95.98 ppm.**

**HR-ESI-MS:** calcd. for [M+Na]<sup>+</sup> C<sub>33</sub>H<sub>41</sub>D<sub>4</sub>FErN<sub>5</sub>NaO<sub>8</sub>S m/z = 883.2419 found 883.2433.

[Tm(DOTA-M7FPy)] 80% yield as a white solid.

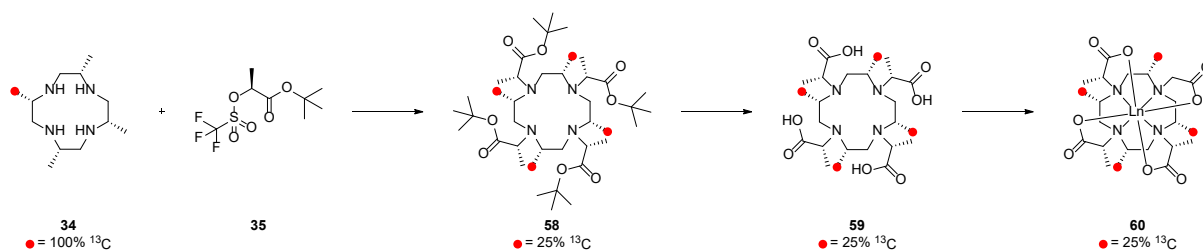
**$^{19}\text{F}$  NMR (565 MHz, Deuterium Oxide, 50 mM Phosphate Buffer pH=6.0)  $\delta$ : -53.44 ppm.**

**HR-ESI-MS:** calcd. for  $[\text{M}+\text{Na}]^+$   $\text{C}_{33}\text{H}_{41}\text{D}_4\text{FTmN}_5\text{NaO}_8\text{S}$   $m/z = 886.2458$  found 886.2444.

[Yb(DOTA-M7FPy)] 84% yield as a white solid.

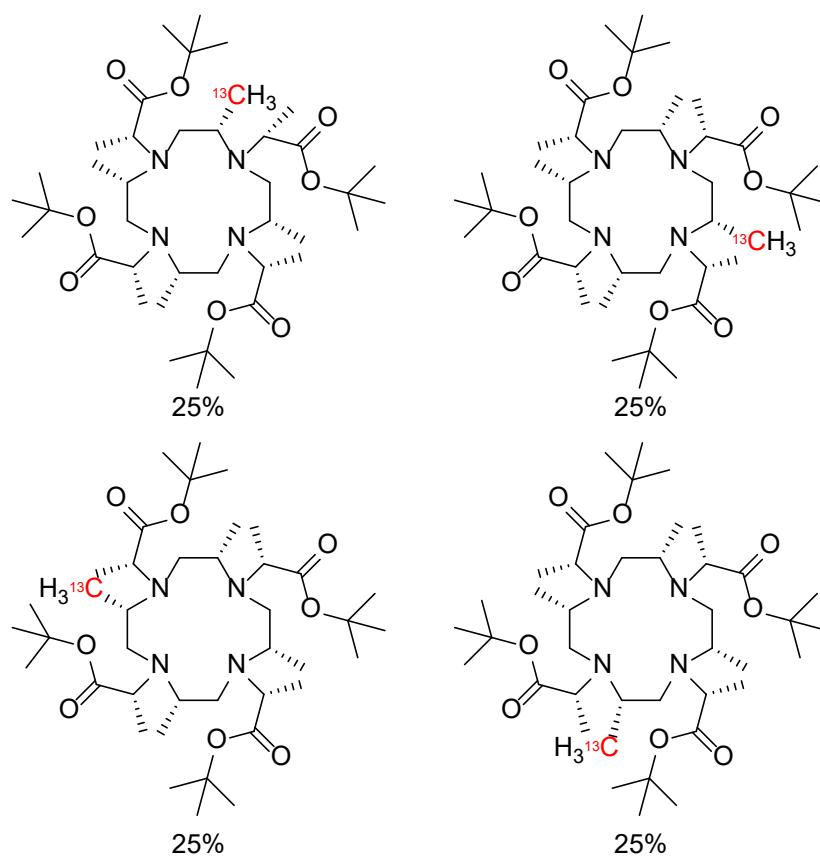
**$^{19}\text{F}$  NMR (565 MHz, Deuterium Oxide, 50 mM Phosphate Buffer pH=6.0)  $\delta$ : -89.07 ppm.**

**HR-ESI-MS:** calcd. for  $[\text{M}+\text{Na}]^+$   $\text{C}_{33}\text{H}_{41}\text{D}_4\text{FYbN}_5\text{NaO}_8\text{S}$   $m/z = 891.2508$  found 891.2516.



**Figure S5:** Synthesis towards Ln-DOTA-M8 (**60**) with carbon  $^{13}\text{C}$  labelled methyl groups on the basal cyclen ring. Red dots mark positions labelled with carbon  $^{13}\text{C}$ . Below each labelled molecule, the observed labelling percentage is noted.

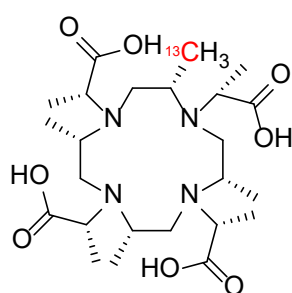
**Tetra-*tert*-butyl 2,2',2'',2'''-((2*S*,5*S*,8*S*,11*S*)-2,5,8-trimethyl-11-(methyl- $^{13}\text{C}$ )-1,4,7,10-tetraazacyclo-dodecane-1,4,7,10-tetrayl)(2*R*,2'*R*,2''*R*,2'''*R*)-tetrapropionate (**58**):** Tetra-*tert*-butyl 2,2', 2'',2'''-((2*S*,5*S*, 8*S*, 11*S*) -2,5,8- trimethyl-11- (methyl- $^{13}\text{C}$ ) -1,4,7,10-tetraazacyclo- dodecane- 1,4,7,10-tetrayl) (2*R*,2'*R*,2''*R*,2'''*R*) -tetrapropionate was isolated as a by product from the three-fold-alkylation of (2*S*,5*S*,8*S*,11*S*)-2,5,8,11-tetramethyl-1,4,7,10-tetraazacyclododecane (SI page 15). The product was obtained, combined from several reactions, as a slightly yellow solid (110 mg, 0.148 mmol).



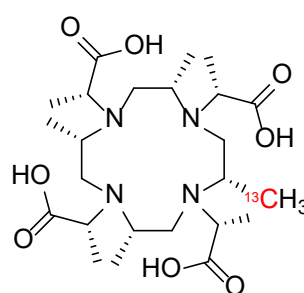
**HR-ESI-MS:** calcd. for  $[\text{M}+\text{Na}]^+$   $\text{C}_{40}\text{H}_{77}\text{N}_4\text{O}_8$   $m/z = 742.5769$  found 742.5777.



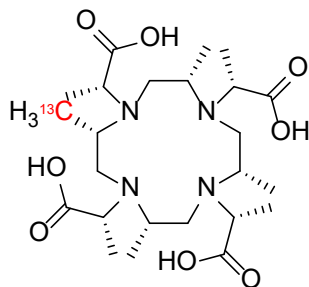
**(2*R*,2'*R*,2''*R*,2'''*R*)-2,2',2'',2'''-((2*S*,5*S*,8*S*,11*S*)-2,5,8-trimethyl-11-(methyl-<sup>13</sup>C)-1,4,7,10-tetraazacyclo dodecane-1,4,7,10-tetrayl)tetrapropionic acid (59):** Tetra-*tert*-butyl 2,2',2'',2'''-((2*S*,5*S*,8*S*,11*S*)-2,5,8-trimethyl-11-(methyl-<sup>13</sup>C)-1,4,7,10-tetraazacyclo dodecane-1,4,7,10-tetrayl) (2*R*,2'*R*,2''*R*,2'''*R*)-tetra propionate (110 mg, 0.148 mmol, 1.0 eq.) was dissolved in acetonitrile (10 ml) and aq. hydrochloric acid (1 M, 20 ml) was added. The solution was heated to 80°C for 8 h. Afterwards the solution was cooled to 20-25°C. The solvent was evaporated. The crude was purified by prep. HPLC to yield (2*R*,2'*R*,2''*R*,2'''*R*)-2,2',2'',2'''-((2*S*,5*S*,8*S*,11*S*)-2,5,8- trimethyl-11- (methyl-<sup>13</sup>C)- 1,4,7,10 –tetraaza cyclododecane-1,4,7, 10-tetrayl)tetrapropionic acid (57.0 mg, 0.110 mmol, 75%) as a colourless solid.



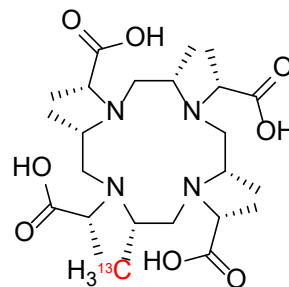
25%



25%



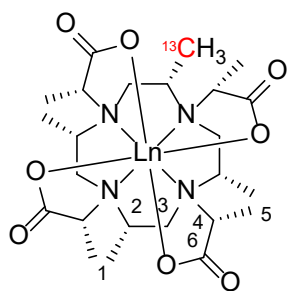
25%



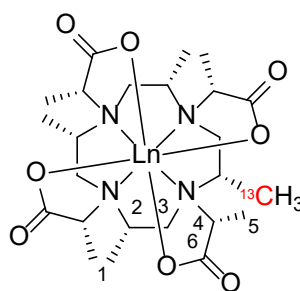
25%

**HR-ESI-MS:** calcd. for  $[M+Na]^+$  C<sub>24</sub>H<sub>45</sub>N<sub>4</sub>O<sub>8</sub> m/z = 518.3265 found 518.3270.

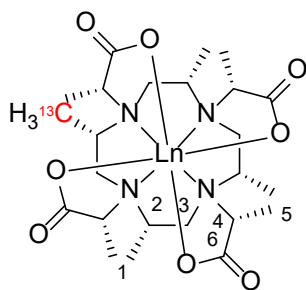
**Ln-DOTA-M8 (60) general procedure:** (2*R*,2'*R*,2''*R*,2'''*R*)-2,2',2'',2'''-((2*S*,5*S*,8*S*,11*S*)-2,5,8-trimethyl-11- (methyl-<sup>13</sup>C)- 1,4,7,10 -tetraazacyclododecane-1,4,7, 10-tetrayl)tetrapropionic acid (1.0 eq.) was dissolved in aq. ammonium acetat (100 mM, 8.0 ml). The solution was heated to 80°C then La(NO<sub>3</sub>)<sub>3</sub> \* 6H<sub>2</sub>O, Pr(NO<sub>3</sub>)<sub>3</sub> \* 5H<sub>2</sub>O, Eu(OTf)<sub>3</sub>, Dy(OTf)<sub>3</sub>, Tm(OTf)<sub>3</sub> or Lu(OTf)<sub>3</sub> (1.1 eq.) was added respectively. The solution was stirred overnight. Then the solution was cooled to 20-25°C and directly purified by prep. HPLC.



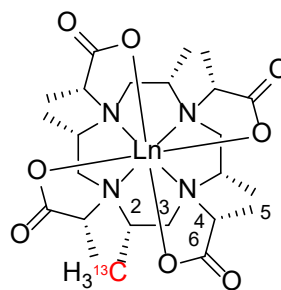
25%



25%



25%



25%

[La(DOTA-M8)] 58% yield as a white solid.

**<sup>1</sup>H NMR (500.13 MHz, Deuterium Oxide, 50 mM Phosphate Buffer pH=6.0) δ:** 3.84 (q, <sup>3</sup>J<sub>HH</sub> = 7.2 Hz, 4H, H<sub>4</sub>), 3.17 (m, 4H, H<sub>2</sub>), 3.08 (m, 4H, H<sub>3ax.</sub>), 2.60 (d, <sup>2</sup>J<sub>HH</sub> = 15.4 Hz, 4H, H<sub>3eq.</sub>), 1.42 (d, <sup>3</sup>J<sub>HH</sub> = 7.2 Hz, 12H, H<sub>5</sub>), 1.13 (dd, <sup>2</sup>J<sub>CH</sub> = 127.5 Hz, <sup>3</sup>J<sub>HH</sub> = 6.6 Hz, 12H, H<sub>1</sub>) ppm.

**<sup>13</sup>C NMR (125.76 MHz, Deuterium Oxide, 50 mM Phosphate Buffer pH=6.0) δ:** 182.97 (C<sub>6</sub>), 66.00 (C<sub>4</sub>), 60.04 (C<sub>2</sub>), 45.57 (C<sub>3</sub>), 13.15 (C<sub>5</sub>), 13.10 (C<sub>1</sub>) ppm.

**HR-ESI-MS:** calcd. for [M+H+Na]<sup>+</sup> C<sub>24</sub>H<sub>41</sub>LaN<sub>4</sub>O<sub>8</sub>Na m/z = 676.1914 found 676.1923.

[Pr(DOTA-M8)] 73% yield as a white slightly green solid.

**<sup>1</sup>H NMR (500.13 MHz, Deuterium Oxide, 50 mM Phosphate Buffer pH=6.0) δ:** 37.85 (s, 4H, H<sub>4</sub>), 24.49 (s, 4H, H<sub>2</sub>), 9.46 (s, 12H, H<sub>5</sub>), -3.97 (d, <sup>2</sup>J<sub>CH</sub> = 126.7 Hz, 12H, H<sub>1</sub>), -7.60 (s, 4H, H<sub>3eq.</sub>), -57.46 (s, 4H, H<sub>3ax.</sub>) ppm.

**HR-ESI-MS:** calcd. for [M+H+Na]<sup>+</sup> C<sub>24</sub>H<sub>41</sub>PrN<sub>4</sub>O<sub>8</sub>Na m/z = 678.1927 found 678.1939.

[Eu(DOTA-M8)] 73% yield as a white slightly green solid.

**<sup>1</sup>H NMR (500.13 MHz, Deuterium Oxide, 50 mM Phosphate Buffer pH=6.0) δ:** 47.17 (s, 4H, H<sub>3ax.</sub>), 4.82 (d, <sup>2</sup>J<sub>CH</sub> = 127.1 Hz, 12H, H<sub>1</sub>), 4.42 (s, 4H, H<sub>3eq.</sub>), -4.60 (s, 12H, H<sub>5</sub>), -14.18 (s, 4H, H<sub>2</sub>), , -23.04 (s, 4H, H<sub>4</sub>) ppm.

**HR-ESI-MS:** calcd. for [M+2Na]<sup>+</sup> C<sub>24</sub>H<sub>40</sub>EuN<sub>4</sub>O<sub>8</sub>Na<sub>2</sub> m/z = 712.1884 found 712.1890.

[Dy(DOTA-M8)] 86% yield as a white solid.

**HR-ESI-MS:** calcd. for [M+2Na]<sup>+</sup> C<sub>24</sub>H<sub>40</sub>DyN<sub>4</sub>O<sub>8</sub>Na<sub>2</sub> m/z = 723.1967 found 723.1971.

[Tm(DOTA-M8)] 42% yield as a white solid.

**HR-ESI-MS:** calcd. for [M+H+Na]<sup>+</sup> C<sub>24</sub>H<sub>41</sub>TmN<sub>4</sub>O<sub>8</sub>Na m/z = 706.2192 found 706.2192.

[Lu(DOTA-M8)] 56% yield as a white solid.

**<sup>1</sup>H NMR (500.13 MHz, Deuterium Oxide, 50 mM Phosphate Buffer pH=6.0) δ:** 3.75 (q, <sup>3</sup>J<sub>HH</sub> = 7.3 Hz, 4H, H<sub>4</sub>), 3.04 (m, 4H, H<sub>2</sub>), 3.01 (m, 4H, H<sub>3ax.</sub>), 2.67 (d, <sup>2</sup>J<sub>HH</sub> = 12.8 Hz, 4H, H<sub>3eq.</sub>), 1.45 (d, <sup>3</sup>J<sub>HH</sub> = 7.3 Hz, 12H, H<sub>5</sub>), 1.18 (dd, <sup>2</sup>J<sub>CH</sub> = 127.5 Hz, <sup>3</sup>J<sub>HH</sub> = 5.8 Hz, 12H, H<sub>1</sub>) ppm.

**<sup>13</sup>C NMR (125.76 MHz, Deuterium Oxide, 50 mM Phosphate Buffer pH=6.0) δ:** 183.04 (C<sub>6</sub>), 66.94 (C<sub>4</sub>), 60.50 (C<sub>2</sub>), 45.64 (C<sub>3</sub>), 13.10 (C<sub>5</sub>), 12.53 (C<sub>1</sub>) ppm.

**HR-ESI-MS:** calcd. for [M+H+Na]<sup>+</sup> C<sub>24</sub>H<sub>41</sub>LuN<sub>4</sub>O<sub>8</sub>Na m/z = 712.2258 found 712.2262.

## 2.6.3 Classified <sup>1</sup>H proton Shifts from Ln-DOTA-M7FPy (1)

### 2.6.3.1 Early lanthanoids

The proton spectra of Sm- and Eu-DOTA-M7FPy were fully assigned by classical 2D NMR (HSQC, HMBC, COSY, NOESY, ROESY) spectroscopy. For the remaining three early lanthanoids only COSY correlations could be observed. Based on the correlations from the COSY spectra and the PRE it was possible to directly assign the protons 6, 8, 10f and 10n (SI Fig S6). Due to the pseudosymmetric nature of Ln-DOTA-M7FPy all remaining signals, relevant for the determination of the anisotropy parameters (the phenyl protons 1, 2 and 3 were not used due to motional averaging), belonged either to one of the three identical spin systems on the lactate side arms or one of the four identical spin systems on the basal cyclen ring. Using the COSY correlations it was possible to group all signals based on their belonging to a spin system and to classify each signal within a spin system by its respective type (eg. H<sub>α</sub>-proton) (SI Table S2 and S3). The classification in combination with two sets of identical spin systems had the advantage that it made it possible to iterate spin systems instead of individual signals leading to a great reduction in the number of possible combinations and a generated a larger error for a wrongful assignment. The total number of possible assignments for the early lanthanoids can be calculated by a multiplication of the factorial of the number of identical spin systems on the lactate side arms and the basal cyclen ring giving a total of 3!\*4! = 144 possible combinations.

**Table S1:** Directly assigned <sup>1</sup>H proton shifts of Ln-DOTA-M7FPy from the early lanthanoids.

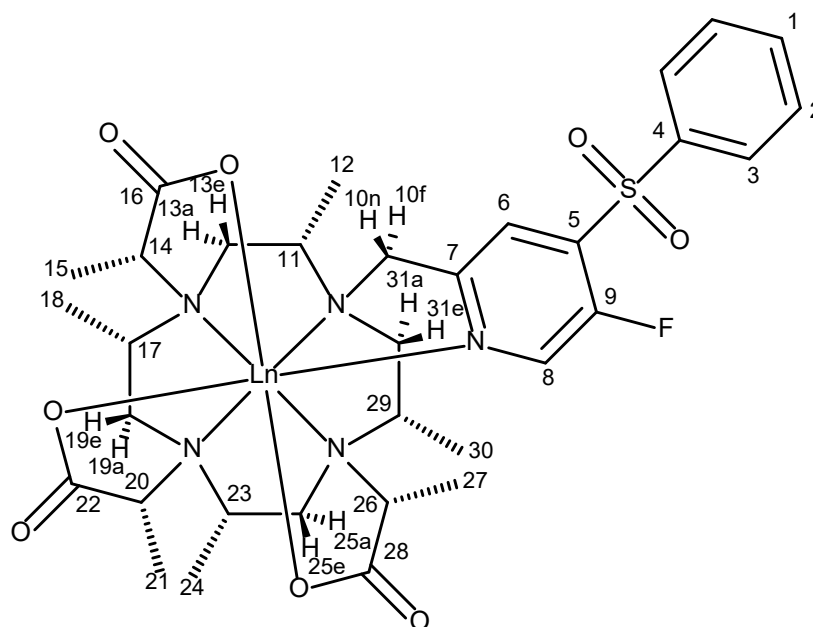
	Ce	Pr	Nd	Sm	Eu
6	8.17	0.78	7.04	8.64	5.96
8	0.39	-3.16	-1.76	5.23	22.37
10f	5.73	0.82	9.55	5.72	-12.02
10n	13.88	24.13	17.6	8.07	-13.44

**Table S2:** Classified <sup>1</sup>H proton shifts within the Spin systems on the lactate side arms of Ln-DOTA-M7FPy from the early lanthanoids.

	Ce	Pr	Nd	Sm	Eu
1					
Methyl-protons	8.79	23.58	11.38	2.74	-6.83
H <sub>α</sub> -proton	21.86	48.85	23.83	7.76	-18.47
2					
Methyl-protons	-0.43	-7.62	-1.35	1.55	2.94
H <sub>α</sub> -proton	11.59	21.53	15.85	7.19	-13.69
3					
Methyl-protons	8.31	23.00	10.34	2.54	-7.23
H <sub>α</sub> -proton	20.12	45.55	21.90	6.89	-19.19

**Table S3:** Classified  $^1\text{H}$  proton shifts within the Spin systems on the basal cyclen ring of Ln-DOTA-M7FPy from the early lanthanoids.

1	Ce	Pr	Nd	Sm	Eu
Methyl-protons	0.7	1.16	1.63	1.23	0.40
$\text{H}_\alpha$ -proton	23.37	46.30	33.79	7.47	-26.42
Equatorial-methylene-proton	1.85	8.53	7.47	1.78	-1.70
Axial-methylene-proton	-20.53	-45.99	-22.58	-3.33	35.18
2					
Methyl-protons	-2.16	-7.73	-3.32	0.22	7.35
$\text{H}_\alpha$ -proton	0.18	-20.10	-4.64	3.31	8.42
Equatorial-methylene-proton	-8.86	-27.98	-8.01	-0.30	11.12
Axial-methylene-proton	-25.97	-64.61	-31.73	-4.68	45.80
3					
Methyl-protons	-2.22	-4.98	-2.60	0.20	6.48
$\text{H}_\alpha$ -proton	17.55	52.34	24.56	5.43	-15.23
Equatorial-methylene-proton	-0.71	4.23	2.55	1.44	0.93
Axial-methylene-proton	-23.71	-51.60	-28.00	-3.99	38.22
4					
Methyl-protons	-0.48	-3.16	-1.51	0.80	1.56
$\text{H}_\alpha$ -proton	5.42	-5.56	1.32	4.79	-7.57
Equatorial-methylene-proton	-2.57	-13.33	-0.01	2.02	-3.80
Axial-methylene-proton	-16.32	-43.07	-19.64	-0.90	24.82



**Figure S6:** Structure of Ln-DOTA-M7FPy with atom numbers. The methylene protons on the basal cyclen ring are separated into axial (a) and equatorial (e) protons. From the methylene protons on the pyridine linker one is significantly closer to the paramagnetic centre than the other. Based on their distance to the paramagnetic centre these protons are termed far (f) and near (n).

### 2.6.3.2 Late lanthanoids

For the late lanthanoid complexes signals were classified using different isotope labelling schemes. Carbon  $^{13}\text{C}$  labelling (main text Fig. 3 1) in combination with selective  $^1\text{H}$  decoupled  $^{13}\text{C}$  spectra (Si Fig. S105-S109) allowed the classification of the cyclen methyl proton signals (12, 18, 24, 30 see Fig. S6). For Yb the cyclen methyl proton signals (12, 18, 24, 30 see Fig. S6) were classified based on the clearly visible  $^1J_{\text{CH}}$  coupling in the  $^1\text{H}$  NMR spectrum. The selective decoupling relied on the intensity increase of the decoupled signal compared to the coupled signals. Attempts to extend selective decoupling to classify other proton signals by labelling different positions with  $^{13}\text{C}$  (eg. the cyclen  $\text{C}_\alpha$  carbons (11, 17, 23, 29 see Fig. S6) were not successful. The intensity gain from the decoupling was no longer significant because of the stronger PRE. Changing to deuterium labelling, however, enabled also the classification of signals, which were strongly affected by PRE. The deuterium labelling was observed as a direct reduction of the signal intensity in the 1D proton NMR spectra. For the sample concentrations applied (~20 mM) a deuterium labelling of 25% was still sufficient for the unambiguous detection of intensity differences in strongly paramagnetic lanthanoid complexes. Using four different deuterium labelling schemes (main text Fig. 3 2-5) all proton signals from the basal cyclen ring were classified by their type (eg. methyl proton, axial methylene proton, etc.) and their pseudo symmetric position (Si Table S4). The classification of pseudosymmetric positions was possible due to the use of two different labelling schemes for the same type of protons where once all four positions were labelled and once only two (main text Fig. 3 2-5). The axial and equatorial protons as well as the  $\text{H}_\alpha$ -Protons and the methyl protons were labelled at the same time because their signals could be differentiated by the PRE. The differentiation of signals from protons of a different type by PRE is only possible if the distance difference is significant. Otherwise, the anisotropic nature of the PRE can lead to a wrongful assignment<sup>3</sup>. Since the methyl protons showed characteristic signals with a narrow linewidth and a higher integral the remaining three methyl signals were classified as the lactate side arm methyl protons (Si Table S5). From the remaining seven shifts two were assigned based on their PRE to the positions 6 and 10f (Si Table S6). It was possible to assign these two protons by PRE as each of their distances to the paramagnetic centre was significantly different from the other remaining positions. To further reduce the number of possible assignments we assumed that from the remaining five signals the signal which shifted into the same direction as the axial protons belonged to position 8 (Si Table S6). This assumption was based on the fact that for all of the early lanthanoids the signal from position 8 shifted into the same direction as the axial protons. The four remaining signals couldn't be any further differentiated and were therefore

classified by the remaining positions (Si Table S7). The total number of assignments for the late lanthanoids can be calculated by the multiplication of the factorials of each classified group of signals giving a total of  $2! \cdot 2! \cdot 2! \cdot 2! \cdot 2! \cdot 2! \cdot 2! \cdot 2! \cdot 3! \cdot 4! = 36864$  possible combinations. For Ho and Er one H<sub>α</sub>-proton was overlapped by a signal which was less affected by PRE and the shift could therefore not be classified using the isotope labelling. For these two lanthanoids the anisotropy parameters of all possible combinations were fitted using only one shift for the positions 17 and 29. This approach lead to no reduction in the total number of possible combinations. To the final assignment, the shift was added by approximating it to the shift of the closest signal where the calculated shifts should have been as this is most likely the signal overlapping the shift from the H<sub>α</sub>-proton. The approximated shifts are marked in red (Si Table S10).

**Table S4:** Classified <sup>1</sup>H proton shifts on the basal cyclen ring of Ln-DOTA-M7FPy from the late lanthanoids. The numbers (SI Fig. S6) represent the possible positions to which the shift could be assigned.

Methyl-protons	Tb	Dy	Ho	Er	Tm	Yb
18 / 30	-70.73	-46.91	-46.59	42.24	68.99	32.44
18 / 30	-28.22	-99.49	-17.88	4.29	24.06	-3.76
12 / 24	6.48	-48.44	15.02	25.78	67.05	26.04
12 / 24	-45.34	16.35	-32.28	4.45	15.18	-7.63
H <sub>α</sub> -Protons						
17 / 29	26.43	-105.71	-86.81	-90.09	-215.24	-2.44
17 / 29	-103.37	-273.04	-	-	-322.86	-92.07
11 / 23	351.23	713.71	322.06	-177.52	-322.86	-87.52
11 / 23	448.23	587.59	227.63	-151.98	-405.94	-137.91
Equatorial-methylene-protons						
19 / 31	-121.60	-207.51	-65.01	96.26	177.40	-11.10
19 / 31	-253.63	-370.64	-170.39	15.36	41.30	84.44
13 / 25	-31.76	23.84	-16.73	13.15	104.37	21.85
13 / 25	-21.65	42.59	15.07	33.41	95.86	17.83
Axial-methylene-protons						
19 / 31	-563.30	-513.11	-226.45	196.72	792.40	252.37
19 / 31	-382.82	-739.56	-367.96	312.00	589.88	116.66
13 / 25	-438.95	-516.36	-257.30	274.41	768.30	190.63
13 / 25	-474.56	-564.77	-300.28	256.20	731.69	189.08

**Table S5:** Classified <sup>1</sup>H proton shifts on the lactate side arms of Ln-DOTA-M7FPy from the late lanthanoids. The numbers (SI Fig. S6) represent the possible positions to which the shift could be assigned.

Methyl-protons	Tb	Dy	Ho	Er	Tm	Yb
15 / 21 / 27	143.91	-78.00	98.97	-7.78	-122.76	-6.60
15 / 21 / 27	143.84	237.32	93.81	-51.99	-81.28	-35.46
15 / 21 / 27	-22.80	234.59	-19.20	-60.04	-124.59	-38.34

**Table S6:** Directly assigned <sup>1</sup>H proton shifts of Ln-DOTA-M7FPy from the late lanthanoids.

	Tb	Dy	Ho	Er	Tm	Yb
6	-9.12	-72.96	-9.16	-11.36	-86.84	-5.26
10f	9.54	-56.08	11.95	-65.22	-211.74	-56.71
8	-244.7	-328.28	-166.81	185.63	488.09	179.52

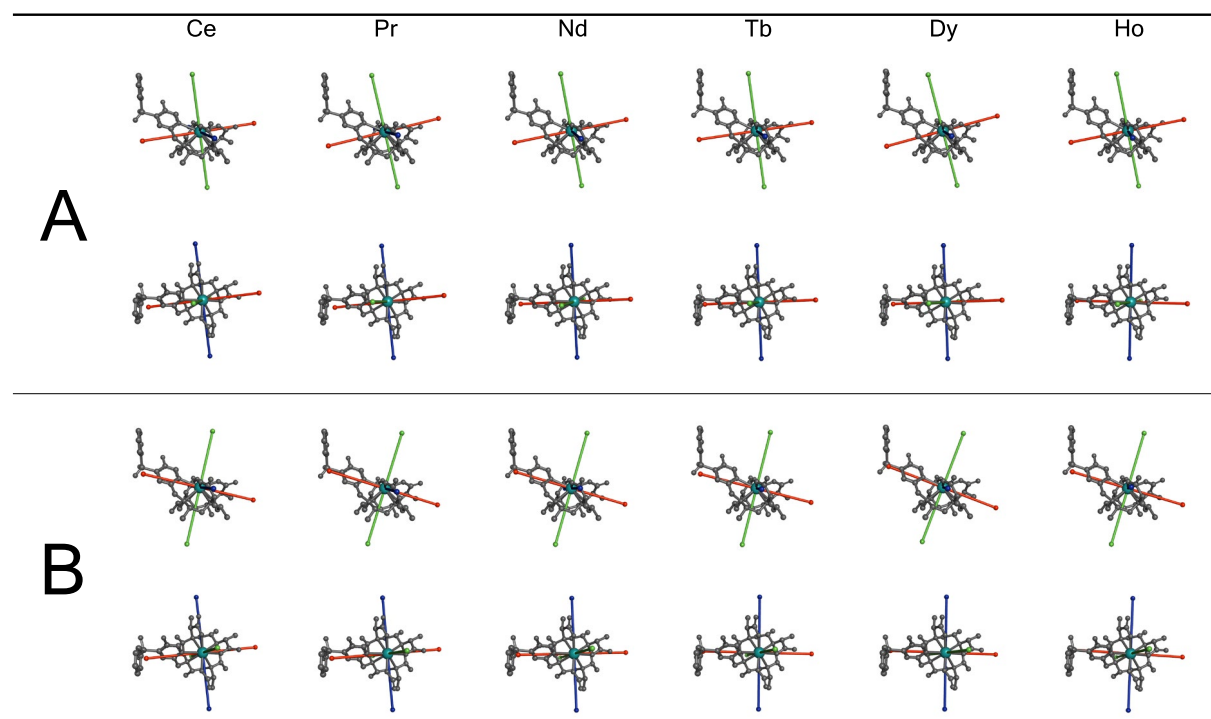
**Table S7:** Classification of the remaining unassigned protons from Ln-DOTA-M7FPy of the late lanthanoids. The numbers (SI Fig. S6) represent the possible positions to which the shift could be assigned.

Remaining-protons	Tb	Dy	Ho	Er	Tm	Yb
14 / 20 / 26 / 10n	325.95	440.69	204.14	-156.54	-398.67	-103.16
14 / 20 / 26 / 10n	315.79	459.69	196.16	-155.32	-407.75	-107.56
14 / 20 / 26 / 10n	267.49	301.94	177.67	-149.14	-429.16	-108.16
14 / 20 / 26 / 10n	252.67	306.41	172.72	-140.44	-432.07	-97.96




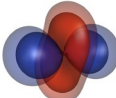
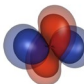
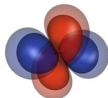
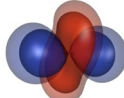
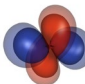
## 2.6.4 Determination of the final assignment of Ln-DOTA-M7FPy (1)

Classification of the signals led to a reduction of the possible assignments for all lanthanoids to a manageable number. For Ce, Pr and Nd the restrictions from the spin systems, further termed COSY restrictions, gave a total of 144 assignments (Si pages 93 and 94) and for Tb, Dy, Ho, Er, Tm and Yb the restrictions obtained based on the labelling schemes further termed labelling restrictions, gave a total of 36864 assignments (Si pages 95-97). Therefore, the anisotropy parameters were fitted, for all lanthanoids, for all possible assignments (Si pages 113-125). For Sm and Eu the COSY and labelling restrictions were simulated based on the full assignment obtained by classical 2D NMR spectroscopy. The obtained assignments and their anisotropy parameters were ordered, for all lanthanoids separately, from highest to lowest correlation coefficient between the calculated and experimental PCS. By first analysing the results from Sm and Eu we were able to check if the actual assignment is represented by the highest correlation coefficient. For Sm two assignments were found among all possible assignments



**Figure S7:** Coordination axis defining the tensor frame of the two differing orientations found for the oblate lanthanoids (Ce-Nd, Tb-Ho) among the best correlated assignments. The axes are coloured in blue (z-axis), red (x-axis) and green (y-axis). Panel A shows orientation A. Panel B shows orientation B. For each orientation the upper row depicts a side view of the twisted square antiprism of DOTA-M7FPy, while the lower row shows the line of vision orthogonal to the cyclen-N<sub>4</sub>-plane at the bottom of the antiprism. Hydrogens were omitted for clarity. The best correlated assignment showing orientation A for each lanthanoid was found, among all assignments order from highest to lowest correlation coefficient, at the following position: Ce 1<sup>st</sup> (0.9876), Pr 1<sup>st</sup> (0.9838), Nd 1<sup>st</sup> (0.9747), Tb 1<sup>st</sup> (0.9935), Dy 1<sup>st</sup> (0.9921), and Ho 1<sup>st</sup> (0.9945). The best correlated assignment showing orientation B for each lanthanoid was found, among all assignments order from highest to lowest correlation coefficient, at the following position: Ce 3<sup>rd</sup> (0.9824), Pr 3<sup>rd</sup> (0.9803), Nd 3<sup>rd</sup> (0.9653), Tb 9<sup>th</sup> (0.9930), Dy 13<sup>th</sup> (0.9917) and Ho 67<sup>th</sup> (0.9918). The correlation coefficient of each assignment is remarked in parentheses.

(36864) with the labelling restrictions that showed a higher correlation coefficient than the actual assignment and none among the possible assignments (144) from the COSY restrictions. For Eu 60 assignments were found among all possible assignments (36864) with the labelling restrictions that showed a higher correlation coefficient than the actual assignment and also none among the possible assignments (144) from the COSY restrictions. It appears that the probability of generating an assignment with a correlation coefficient higher than the actual assignment depends on the overall deviation of the observed shifts from linearity as the highest correlation coefficients for Sm were around 0.99 while they were around 0.94 for Eu. From the simulations, it was concluded that with the COSY restrictions the actual assignment is represented by the highest correlation coefficient while the labelling restriction yield the actual assignment amongst the best correlated assignments but it might not be the one showing the highest correlation coefficient. Fortunately, the anisotropy parameters from the best correlated assignments of the late lanthanoids (Tb-Yb), where the labelling restrictions were applied, were highly conserved. For Er, Tm and Yb only a single set of very similar anisotropy parameters was found for the best correlated assignments while for Tb, Dy and Ho two sets of anisotropy parameters were found among the best correlated assignments. For Er, Tm and Yb this meant that any of the best correlated assignments could be used as the final assignment and the obtained anisotropy parameters would be basically the same. We decided to use the one with the highest correlation coefficient. For Tb, Dy and Ho on the other hand all of the best correlated assignments yielded anisotropy parameters of a similar size and rhombicity but depending on which assignment was chosen the tensor frame could adopt one of two orientations (see Fig. S7, the orientations will further be termed orientation A and B). Therefore, we had to decide which of the two orientations the actual tensor frame would adopt and chose based on this assumption the final assignment. Based on two reasons we assumed that the tensor frame of Tb, Dy and Ho would adopt orientation A. The first was that the assignments, where the tensor frame adopts orientation A, showed for Tb, Dy and Ho higher correlation coefficients than the assignments that defined a tensor frame of orientation B. The second reason was that the anisotropy parameters from Ce, Pr and Nd, which were determined by the highest correlation coefficient, also defined a tensor frame of orientation A. We assumed that Tb, Dy and Ho would adopt the same orientation as Ce, Pr and Nd since the tensor frame for all prolate lanthanoids (Sm, Eu, Er, Tm and Yb) showed a similar orientation (main text Fig. 5) and it appeared reasonable that the same was true for the oblate lanthanoids (Ce, Pr, Nd, Tb, Dy and Ho). Interestingly, anisotropy parameters defining a tensor frame of orientation B were also found for Ce, Pr and Nd but also for assignments with a lower correlation coefficient. For

	Ce	Pr	Nd	Tb	Dy	Ho
$\Delta\chi_{ax}$	3.4(0.04)	9.3(0.09)	4.1(0.05)	62(0.7)	98(1)	41(0.4)
$\Delta\chi_{rh}$	1.8(0.03)	2.4(0.08)	1.8(0.04)	33(0.6)	29(0.9)	19(0.4)
$\alpha$	66(0.5)	64(1)	62(0.6)	59(0.6)	58(0.8)	57(0.6)
$\beta$	88(0.3)	90(0.2)	87(0.3)	88(0.3)	88(0.3)	86(0.3)
$\gamma$	79(0.2)	75(0.2)	76(0.2)	78(0.3)	72(0.2)	76(0.3)
						

**Table S8:** PCS anisotropy parameters on DOTA-M7FPy for the oblate lanthanoids (Ce-Nd & Tb-Ho) from the best correlated assignment yielding orientation B. The anisotropy parameters  $\Delta\chi_{ax}$  and  $\Delta\chi_{rh}$  are reported in  $10^{-32}\text{m}^3$ . All angles are reported in degree. The molecular frame of the free tag is orientated so that the lanthanoid is at the origin, the z-axis is perpendicular to cyclen- $\text{N}_4$ -plane and the x-axis is going in the direction of the nitrogen on which the pyridine linker is attached. Red isosurfaces indicate a negative shift, blue isosurfaces indicate the corresponding positive shift. The isosurfaces indicate a positive or negative shift of 0.2/0.1 ppm (inner sphere/ outer sphere) for the early lanthanoids (Ce-Nd) and 2/1 ppm (inner sphere/outer sphere) for the late lanthanoids (Tb-Ho). In parentheses, the standard deviation is remarked.

completeness sake, we determined the anisotropy parameters for both orientations. In both cases, the assignment with the highest correlation coefficient was used to determine the anisotropy parameters. The anisotropy parameters defining a tensor frame of orientation A are depicted in figure 4 in the main text and the ones defining a tensor frame of orientation B in table S8.

In conclusion, the assignment yielding the highest correlation coefficient was chosen as the final assignment used to determine the anisotropy parameters for all lanthanoids (Ce, Pr, Nd, Tb, Dy, Ho, Er, Tm, Yb) where classical 2D NMR spectroscopy could no longer be used to determine the assignment. For the prolate lanthnaoids the anisotropy parameters were determined unambiguously while for the oblate lanthanoids a small possibility remains that the tensor frame could adopt orientation B. However all of the observation about ligand field like effects described in the main text would also apply for orientation B.

## 2.6.5 Shift lists of the final assignments

### 2.6.5.1 Ln-DOTA-M7FPy (1) early lanthanoids

**Table S9:** Shift list in ppm of Ln-DOTA-M7FPy (1) (early lanthanoids) from the final assignment recorded at 298 K.

Ce		Pr		Nd		Sm		Eu	
Position	Shift	Position	Shift	Position	Shift	Position	Shift	Position	Shift
11	23.37	11	64.3	11	33.79	6	8.64	19a	45.8
14	21.86	23	52.34	23	24.56	10n	8.07	25a	38.22
26	20.12	14	48.85	14	23.83	3	8.03	13a	35.18
23	17.55	26	45.55	26	21.9	14	7.76	31a	24.82
10n	13.88	10n	24.13	10n	17.6	1	7.76	8	22.37
20	11.59	15	23.58	20	15.85	2	7.62	19e	11.12
15	8.79	27	23	15	11.38	11	7.47	3	9.07
27	8.31	20	21.53	27	10.34	20	7.19	1	8.52
6	7.66	13e	8.53	10f	9.55	26	6.89	2	8.47
1	7.5	1	6.55	13e	7.47	10f	5.72	17	8.42
3	7.5	2	6.11	1	7.27	23	5.43	18	7.35
2	7.3	3	5.02	6	7.04	8	5.23	24	6.48
10f	5.73	25e	4.23	2	7.03	29	4.79	6	5.96
29	5.42	12	1.16	3	6.95	17	3.31	21	2.94
13e	1.85	10f	0.82	25e	2.55	15	2.74	30	1.56
12	0.7	6	0.78	12	1.63	27	2.54	25e	0.93
8	0.39	30	-3.16	29	1.32	31e	2.02	12	0.4
17	0.18	24	-4.98	31e	-0.01	13e	1.78	13e	-1.7
21	-0.43	29	-5.56	21	-1.35	21	1.55	31e	-3.8
30	-0.48	21	-7.62	30	-1.51	25e	1.44	15	-6.83
25e	-0.71	18	-7.73	8	-1.76	12	1.23	27	-7.23
18	-2.16	31e	-13.33	24	-2.6	30	0.8	29	-7.57
24	-2.22	8	-16.13	18	-3.32	18	0.22	10f	-12.02
31e	-2.57	17	-20.1	17	-4.64	24	0.2	10n	-13.44
19e	-8.86	19e	-27.98	19e	-8.01	19e	-0.3	20	-13.69
31a	-16.32	31a	-43.07	31a	-19.64	31a	-0.9	23	-15.23
13a	-20.53	13a	-45.99	13a	-22.58	13a	-3.33	14	-18.47
25a	-23.71	25a	-51.6	25a	-28	25a	-3.99	26	-19.19
19a	-25.97	19a	-64.61	19a	-31.73	19a	-4.68	11	-26.42

### 2.6.5.2 Ln-DOTA-M7FPy (1) late lanthanoids

**Table S10a:** Shift list in ppm of Ln-DOTA-M7FPy (late lanthanoids Tb-Ho) from the final assignment recorded at 298 K. The shifts marked in red were not observed but approximated from fitting the anisotropy parameters.

Tb		Dy		Ho	
Position	Shift	Position	Shift	Position	Shift
11	448.95	11	713.71	11	322.06
23	351.23	23	587.59	23	227.36
14	325.95	20	459.69	14	204.14
20	315.79	14	440.59	20	196.16
26	267.49	10n	306.41	26	177.67
10n	252.67	26	301.94	10n	172.72
15	143.91	15	237.32	15	98.97
27	143.84	27	234.59	27	93.81
29	26.43	13e	42.59	13e	15.07
10f	9.54	25e	23.84	12	15.02
12	6.48	12	16.35	10f	11.95
1	-2.19	1	-9.12	1	0.11
2	-3.23	3	-12.21	3	-0.89
3	-8.29	2	-27.82	2	-5.38
6	-9.12	30	-46.91	29	-9.00
13e	-21.65	24	-48.44	6	-9.16
21	-22.8	10f	-56.08	25e	-16.73
30	-28.22	6	-72.96	30	-17.88
25e	-31.76	21	-78	21	-19.2
24	-45.34	18	-99.49	24	-32.28
18	-70.73	29	-105.71	18	-46.59
17	-103.37	31e	-207.51	31e	-65.01
31e	-121.6	17	-273.04	17	-86.81
8	-244.7	8	-328.28	8	-166.81
19e	-253.63	19e	-370.64	19e	-170.39
31a	-382.82	31a	-513.11	31a	-226.45
13a	-438.95	13a	-516.36	13a	-257.3
25a	-474.56	25a	-564.77	25a	-300.28
19a	-563.3	19a	-739.56	19a	-367.96

**Table S10b:** Shift list in ppm of Ln-DOTA-M7FPy (late lanthanoids Er-Yb) from the final assignment recorded at 298 K. The shifts marked in red were not observed but approximated from fitting the anisotropy parameters.

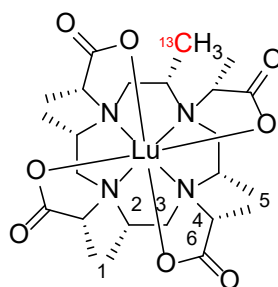
Er		Tm		Yb	
Position	Shift	Position	Shift	Position	Shift
19a	312	19a	792.4	19a	252.37
13a	274.41	25a	768.3	25a	190.63
25a	256.2	13a	731.69	13a	189.08
31a	196.72	31a	589.88	8	179.52
8	185.63	8	488.09	31a	116.66
19e	96.26	19e	177.44	19e	85.44
18	42.24	25e	104.35	18	32.44
13e	33.41	13e	95.87	24	26.04
24	25.78	18	68.99	25e	21.85
17	25.00	24	67.05	13e	17.83
31e	15.36	31e	41.28	3	13.1
25e	13.15	30	24.06	2	12.02
2	12.96	1	16.69	1	11.99
1	12.23	2	15.5	17	-2.44
3	12.23	12	15.18	30	-3.76
12	4.45	3	10.1	6	-5.26
30	4.29	21	-81.28	21	-6.6
21	-7.78	6	-86.48	12	-7.63
6	-11.36	27	-122.76	31e	-11.1
15	-51.99	15	-124.59	15	-35.46
27	-60.04	10f	-211.74	27	-38.34
10f	-65.22	17	-215.24	10f	-56.71
29	-90.09	29	-322.86	23	-87.52
10n	-140.44	23	-322.86	29	-92.07
26	-149.14	10n	-398.67	10n	-97.96
23	-151.98	11	-405.94	26	-103.16
20	-155.32	26	-407.75	20	-107.56
14	-156.54	20	-429.16	14	-108.16
11	-177.52	14	-432.07	11	-137.91

### 2.6.5.3 Ln-DOTA-M8 (60)

**Table S11:** Shift list in ppm of Ln-DOTA-M8 (60) from the final assignment recorded at 298 K.

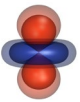
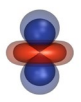
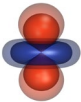
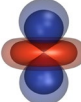
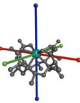
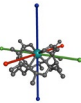
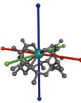
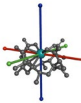
Pr		Eu		Dy		Tm	
Position	Shift	Position	Shift	Position	Shift	Position	Shift
4	37.85	3a	47.17	4	415.92	3a	915.08
2	24.49	1	4.82	2	272.46	3e	130.08
5	9.46	3e	4.42	5	101.97	1	53.54
1	-3.97	5	-4.60	1	-47.53	5	-140.67
3e	-7.60	2	-14.18	3e	-127.80	2	-408.40
3a	-57.46	4	-23.04	3a	-682.84	4	-527.53

The shifts of Pr and Eu were fully assigned by NMR spectroscopy. For Dy and Tm the  $^{13}\text{C}$  methyl (1, Si Fig. S8) signal was assigned using selective decoupled  $^{13}\text{C}$  NMR spectroscopy (Si Fig. S107 and S108). The remaining methyl signal, which could be identified by the linewidth and intensity, was assigned to the sidearm methyl (5, Si Fig. S8). The remaining four shifts were assigned by fitting the anisotropy parameters for all possible combinations ( $4! = 24$ ). The final assignment was determined based on the best correlation coefficient. In both cases, a second assignment with a high correlation coefficient was found showing near identical anisotropy parameters. The anisotropy parameters from all possible combinations are depicted in the Si on page 126 and 127. The final anisotropy parameters are shown in table S12 in the Si.



**Figure S8:** Ln-DOTA-M8 with atom numbers. The methylene protons on the basal cyclen ring are separated into axial (a) and equatorial (e) protons.

**Table S12:** Anisotropy parameters determined on Ln-DOTA-M8 and comparison between  $\Delta\chi_{Ax(DOTA-M8)}$  and  $\Delta\chi_{Ax(DOTA-M7FPy)}$ .  $\Delta\chi_{Ax}$  and  $\Delta\chi_{Rh}$  are reported in  $10^{-32}m^3$ . Angles are reported in degree. The molecular frame of the free tag is orientated so that the lanthanoid is at the origin, the z-axis is perpendicular to cyclen-N<sub>4</sub>-plane and the x-axis is going in the direction of one of the four cyclen nitrogens. Red isosurfaces indicate a negative shift, blue isosurfaces indicate the corresponding positive shift. The isosurfaces indicate a positive or negative shift of 0.2/0.1 ppm (inner sphere/ outer sphere) for Pr and Eu and 2/1 ppm (inner sphere/outer sphere) for Dy and Tm. The axes are coloured in blue (z-axis), red (x-axis) and green (y-axis). Due to the fully axial nature of the tensor the x- and y-axis are no longer unambiguously defined. In parentheses, the standard deviation is remarked. Hydrogens were omitted for clarity.

Lanthanoid	Pr	Eu	Dy	Tm
$\Delta\chi_{ax}$	-7.2(0.2)	5.2(0.1)	-80(2)	104(2)
$\Delta\chi_{rh}$	-0(0.00005)	0(0.0004)	-0(0.007)	1(0.05)
$\alpha$	180(0.00001)	180(2)	0(0.00008)	180(5)
$\beta$	180(0.01)	180(0.0003)	0(0.02)	0(0.04)
$\gamma$	90(0.00001)	0(0.00002)	90(0.0001)	90(6)
				
				
$\frac{\Delta\chi_{ax}^{Ln-DOTA-M8}}{\Delta\chi_{ax}^{Ln-DOTA-M7FPy}}$ %	78%	127%	79%	125%



### 2.6.8 Full Tensors

Full Tensor of Ln-DOTA-M7FPy and Ln-DOTA-M8 were determined by fitting the final assignment to equation (S1). The anisotropy parameters  $\Delta\chi_{ax}$  and  $\Delta\chi_{rh}$  can be obtained from the full tensors by first diagonalizing the matrix then calculate  $\Delta\chi_{ax}$  and  $\Delta\chi_{rh}$  from the trace of the diagonal matrix using the relations from equation (1) in the main text and finally transforming the obtained values to UTR.

$$\delta_{pcs} = \frac{1}{4\pi r^3} \left[ (\chi_{zz} - \bar{\chi}) \frac{2z^2 - x^2 - y^2}{r^2} + (\chi_{xx} - \chi_{yy}) \frac{x^2 - y^2}{r^2} + \chi_{xy} \frac{2xy}{r^2} + \chi_{xz} \frac{2xz}{r^2} + \chi_{yz} \frac{2yz}{r^2} \right] \quad (S1)$$

$$\text{here } \bar{\chi} = \frac{\chi_{xx} + \chi_{yy} + \chi_{zz}}{3}$$

**Table S13:** Full Tensors of Ln-DOTA-M7FPy.

Ce	Tb
$\chi = \begin{bmatrix} 0.060 & 0.91 & -0.35 \\ 0.91 & 1.8 & -0.020 \\ -0.35 & -0.020 & -1.9 \end{bmatrix}$	$\chi = \begin{bmatrix} 4.1 & 20 & -5.9 \\ 20 & 31 & 0.90 \\ -5.9 & 0.90 & -35 \end{bmatrix}$
Pr	Dy
$\chi = \begin{bmatrix} -0.64 & 3.1 & -0.52 \\ 3.1 & 4.7 & 0.34 \\ -0.52 & 0.34 & -4.1 \end{bmatrix}$	$\chi = \begin{bmatrix} -3.3 & 38 & -7.3 \\ 38 & 47 & 1.1 \\ -7.3 & 1.1 & -44 \end{bmatrix}$
Nd	Ho
$\chi = \begin{bmatrix} 0.063 & 1.4 & -0.49 \\ 1.4 & 2.1 & -0.086 \\ -0.49 & -0.086 & -2.1 \end{bmatrix}$	$\chi = \begin{bmatrix} 3.3 & 14 & -5.0 \\ 14 & 18 & 0.21 \\ -5.0 & 0.21 & -21 \end{bmatrix}$
Pm	Er
n.d.	$\chi = \begin{bmatrix} -7.5 & -4.9 & 3.7 \\ -4.9 & -12 & -1.5 \\ 3.7 & -1.5 & 19 \end{bmatrix}$

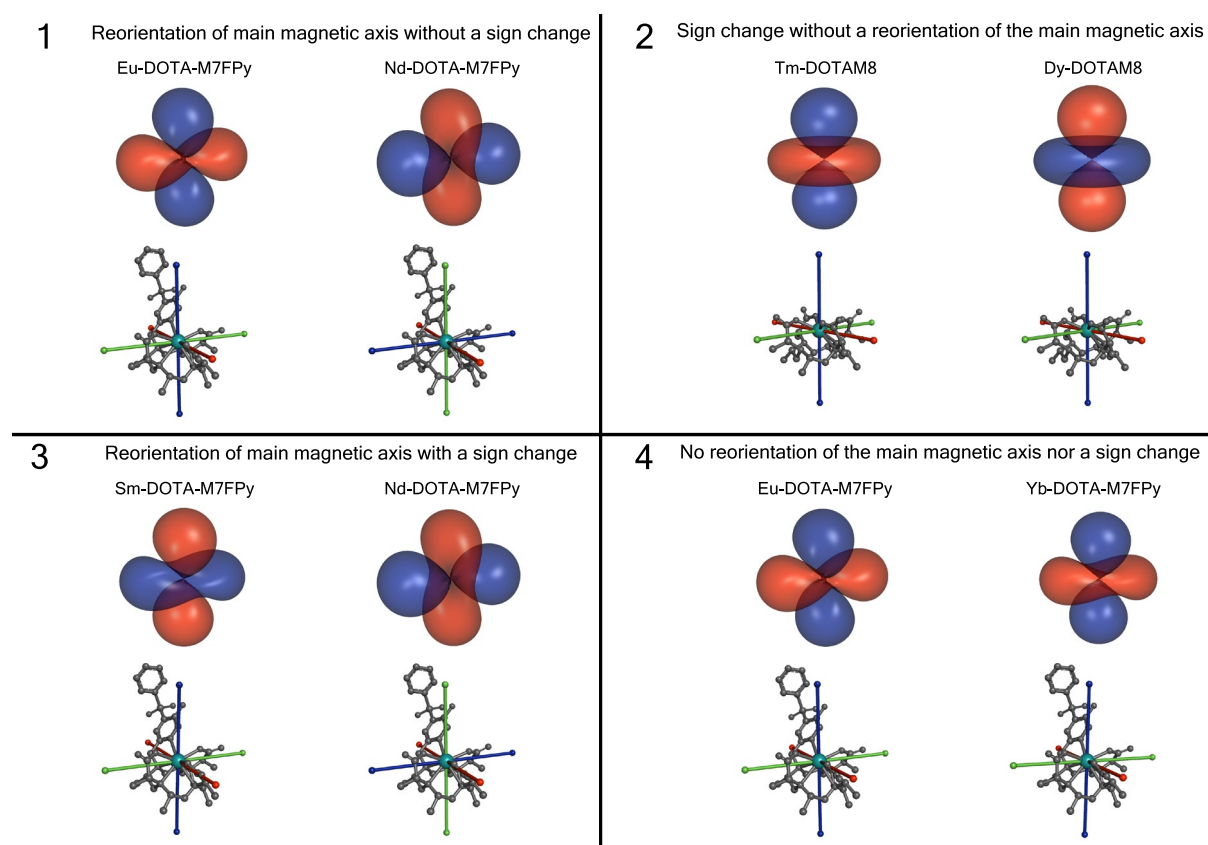
Sm	Tm
$\chi = \begin{bmatrix} 0.13 & 0.12 & -0.13 \\ 0.12 & 0.35 & 0.021 \\ -0.13 & 0.021 & -0.50 \end{bmatrix}$	$\chi = \begin{bmatrix} -26 & -4.1 & 5.6 \\ -4.1 & -29 & -2.5 \\ 5.6 & -2.5 & 55 \end{bmatrix}$
Eu	Yb
$\chi = \begin{bmatrix} -0.47 & -1.0 & 0.83 \\ -1.0 & -2.0 & -0.12 \\ 0.83 & -0.12 & 2.5 \end{bmatrix}$	$\chi = \begin{bmatrix} -4.3 & -4.0 & 4.8 \\ -4.0 & -9.8 & -2.7 \\ 4.8 & -2.7 & 14 \end{bmatrix}$

**Table S14:** Full Tensors of Ln-DOTA-M8.

Pr	Dy
$\chi = \begin{bmatrix} 2.4 & 0.0010 & -0.0026 \\ 0.0010 & 2.4 & -0.0036 \\ -0.0026 & -0.0036 & -4.8 \end{bmatrix}$	$\chi = \begin{bmatrix} 27 & 0.038 & -0.061 \\ 0.038 & 26 & -0.018 \\ -0.061 & -0.018 & -53 \end{bmatrix}$
Eu	Tm
$\chi = \begin{bmatrix} -1.8 & -0.016 & -0.0025 \\ -0.016 & -1.7 & -0.00069 \\ -0.0025 & -0.00069 & 3.5 \end{bmatrix}$	$\chi = \begin{bmatrix} -35 & 0.23 & -0.068 \\ 0.23 & -34 & 0.74 \\ -0.068 & 0.74 & 69 \end{bmatrix}$

## 2.6.7 Illustration of the reorientation of the main magnetic axis and the sign change

It is not trivial to distinguish the various possibilities of changes in a given set of anisotropy parameters and there is a probably infinite number of tensors that result in the very same PCS and, hence, also the same isosurfaces. Not all authors in the literature stick to the UTR convention which makes a comparison even more difficult in some cases. We, therefore, wish to briefly discuss the various cases on a graphical example, depicting the changes on the isosurfaces and the corresponding reorientation of the magnetic axes in the molecular frame of the tag.



**Figure S9:** The four panels depict the four combinations of a sign change of  $\Delta\chi_{ax}$  and  $\Delta\chi_{rh}$  and the reorientation of the main magnetic axis. In each panel it is remarked which combination is depicted and suitable isosurfaces and tensor coordinate frames visualize the change. The depicted axes show the coordinate frame of the tensor. The axes are coloured in blue (z-axis), red (x-axis) and green (y-axis). The molecular frame is orientated so that the lanthanoid is at the origin, the z-axis is perpendicular to cyclen- $N_4$ -plane and the x-axis is going in the direction of the nitrogen on which the pyridine is attached (Ln-DOTA-M7FPy (panel 1, 3 and 4)) or one of the four cyclen nitrogens (Ln-DOTA-M8 (panel 2)). Red isosurfaces indicate a negative shift, blue isosurfaces indicate the corresponding positive shift. The view onto the isosurfaces and the tensor frame is for all four panels from the same angle the magnification differs however for the different isosurfaces. Hydrogens were omitted for clarity.

Each panel contains two sets of anisotropy parameters and describes their relation to each other. The main magnetic or z-axis is always represented by a blue axis in the coordinate system and has the same orientation as the dumb-bell like lobe of the isosurfaces. On the left side of each panel, the z-axis is orthogonal to the plane formed by the four nitrogen atoms of the ligand. In

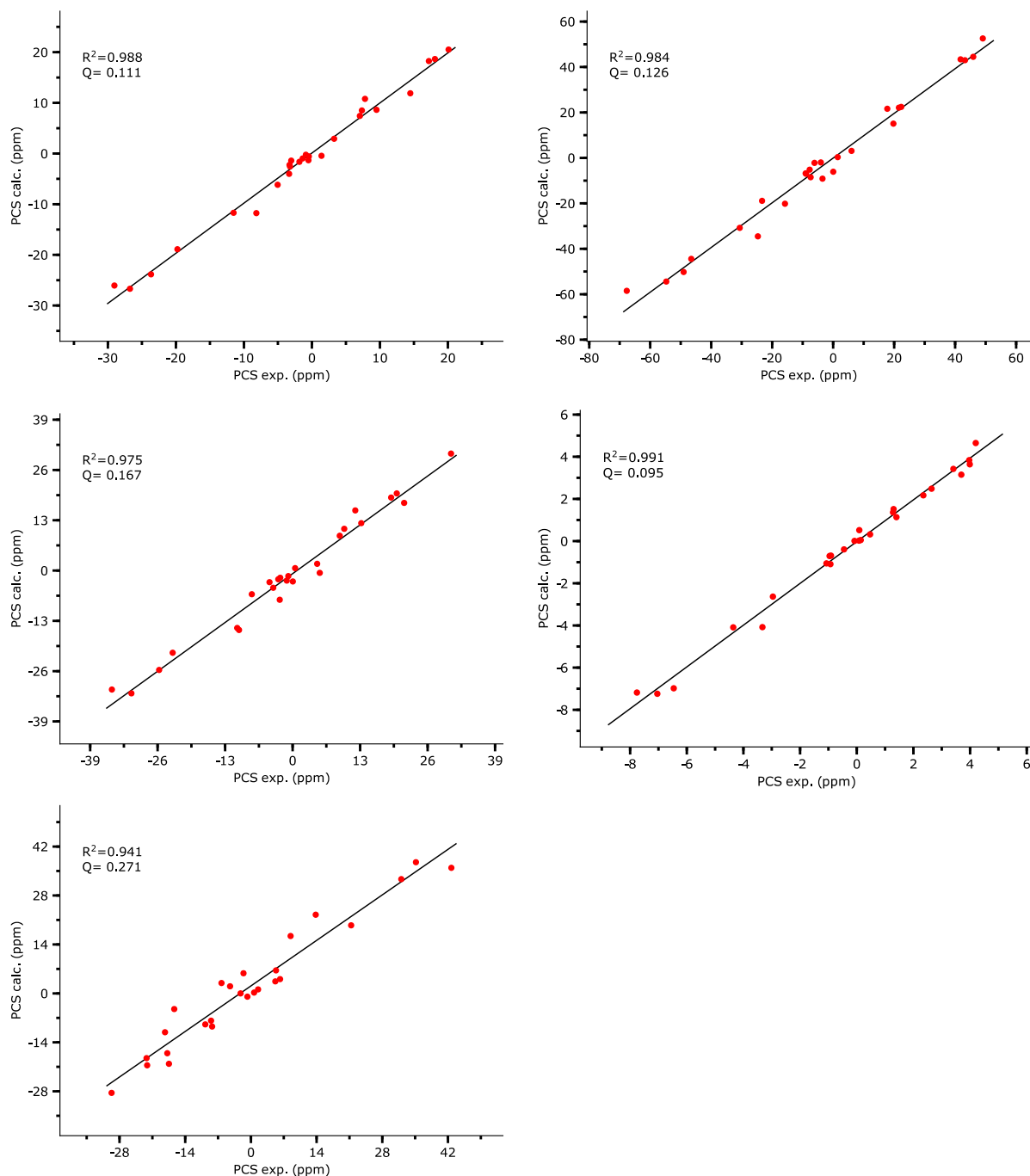
panel 1, left side, the isosurface for this lobe is blue, indicating positive shifts and in panel 1, right side after the reorientation of the z-axis this lobe is still blue, so a reorientation without sign change has occurred.

In sharp contrast to this, panel 2 describes a sign change without reorientation, so the magnetic axes are unchanged but the signs of the dumb-bell like lobe and the torus like lobe have interchanged. The shape of the torus depends on the rhombicity and can be perfectly round for an axial system or severely distorted in strongly rhombic systems.

Panel three depicts a reorientation of the axes and a simultaneous sign change, whereas the last panel shows only slight changes in the sizes of the axial and rhombic anisotropy parameters, but neither axes reorientation nor a sign change.

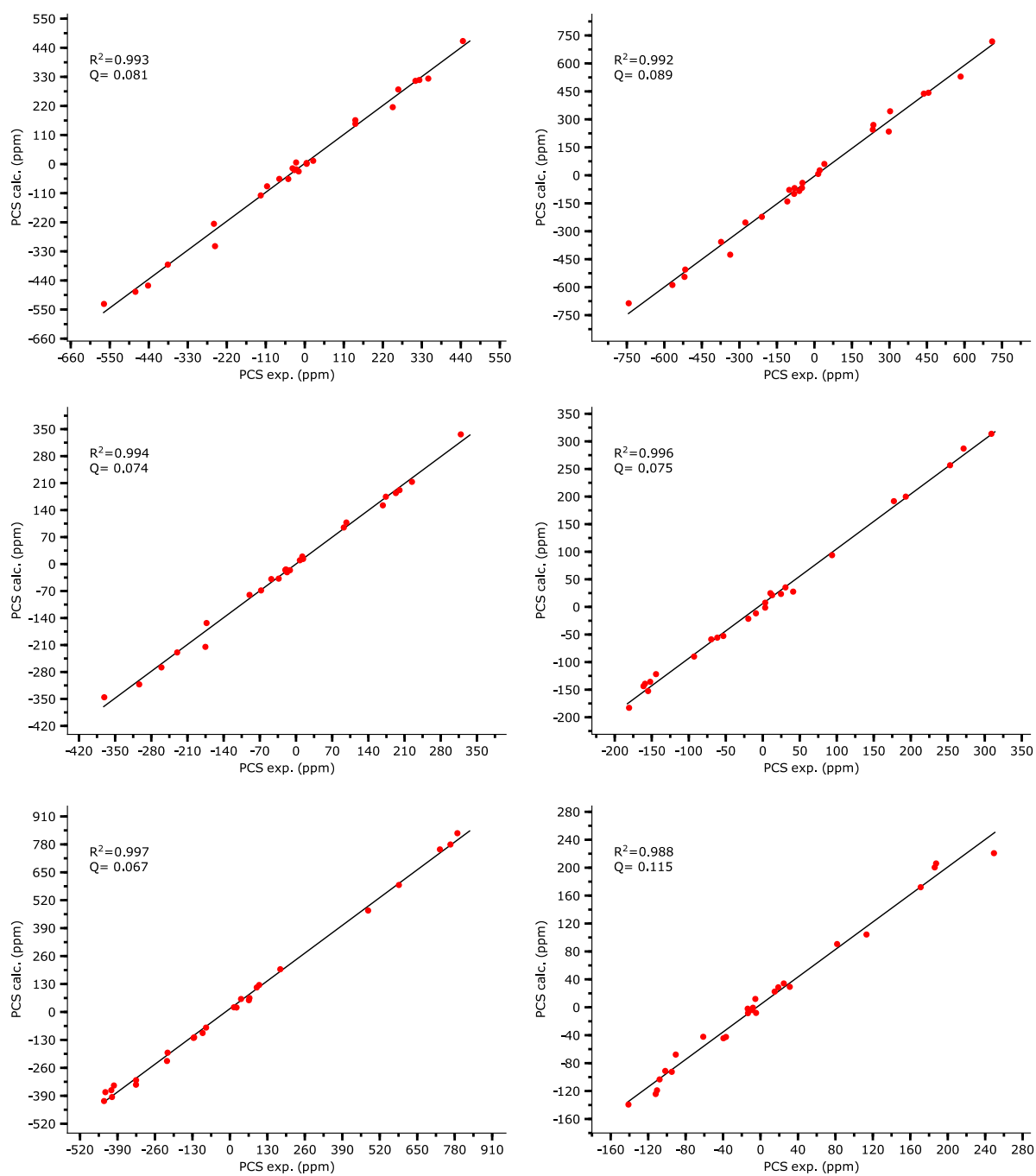
## 2.6.8 Correlation Graphs

### 2.6.8.1 Ln-DOTA-M7FPy (1) early lanthanoids



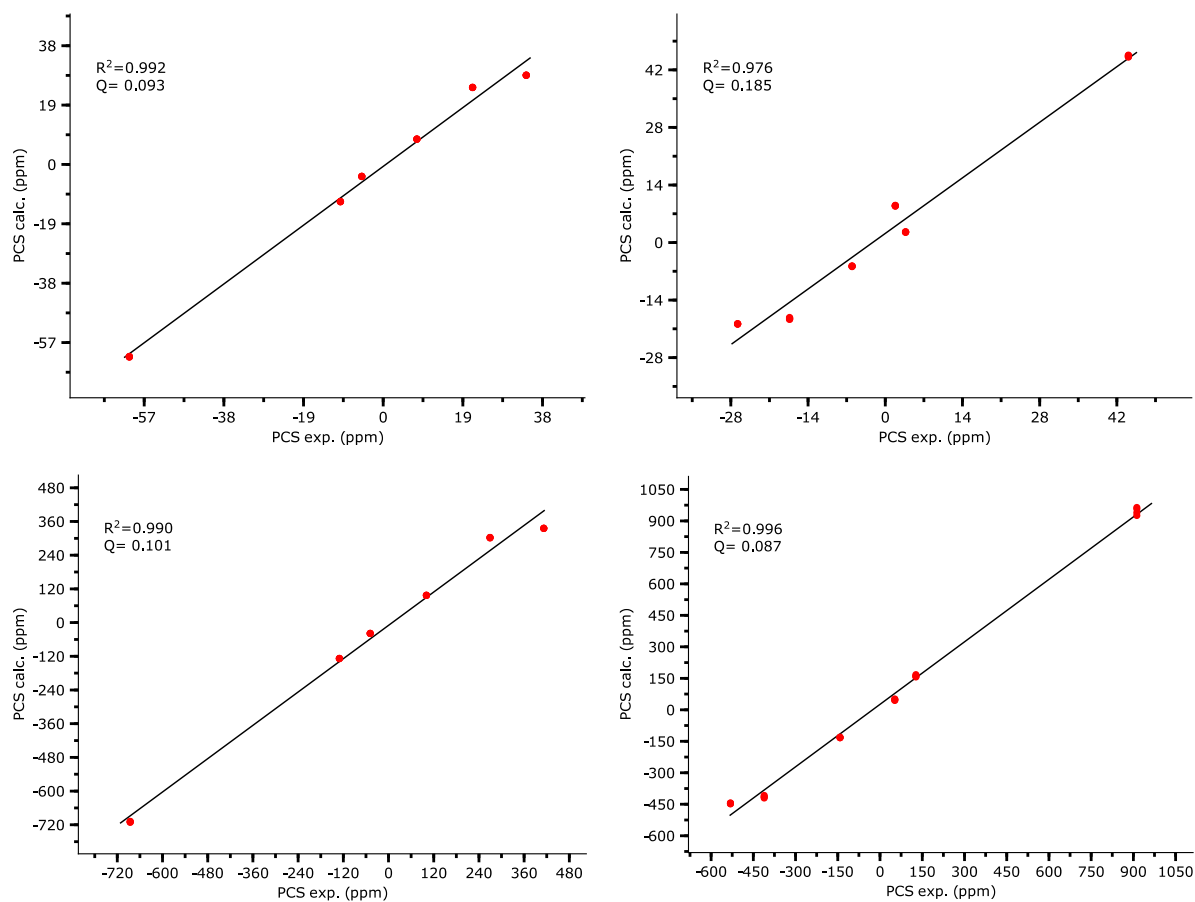
**Figure S10:** Correlation graphs between calculated and experimental PCS on Ln-DOTA-M7FPy. Top left Ce. Top right Pr. Middle left Nd. Middle right Sm. Bottom left Eu.

## 2.6.8.2 Ln-DOTA-M7FPy (1) late lanthanoids



**Figure S11:** Correlation graphs between calculated and experimental PCS on Ln-DOTA-M7FPy. Top left Tb. Top right Dy. Middle left Ho. Middle right Er. Bottom left Tm. Bottom right Yb.

### 2.6.8.3 Ln-DOTA-M8 (60)

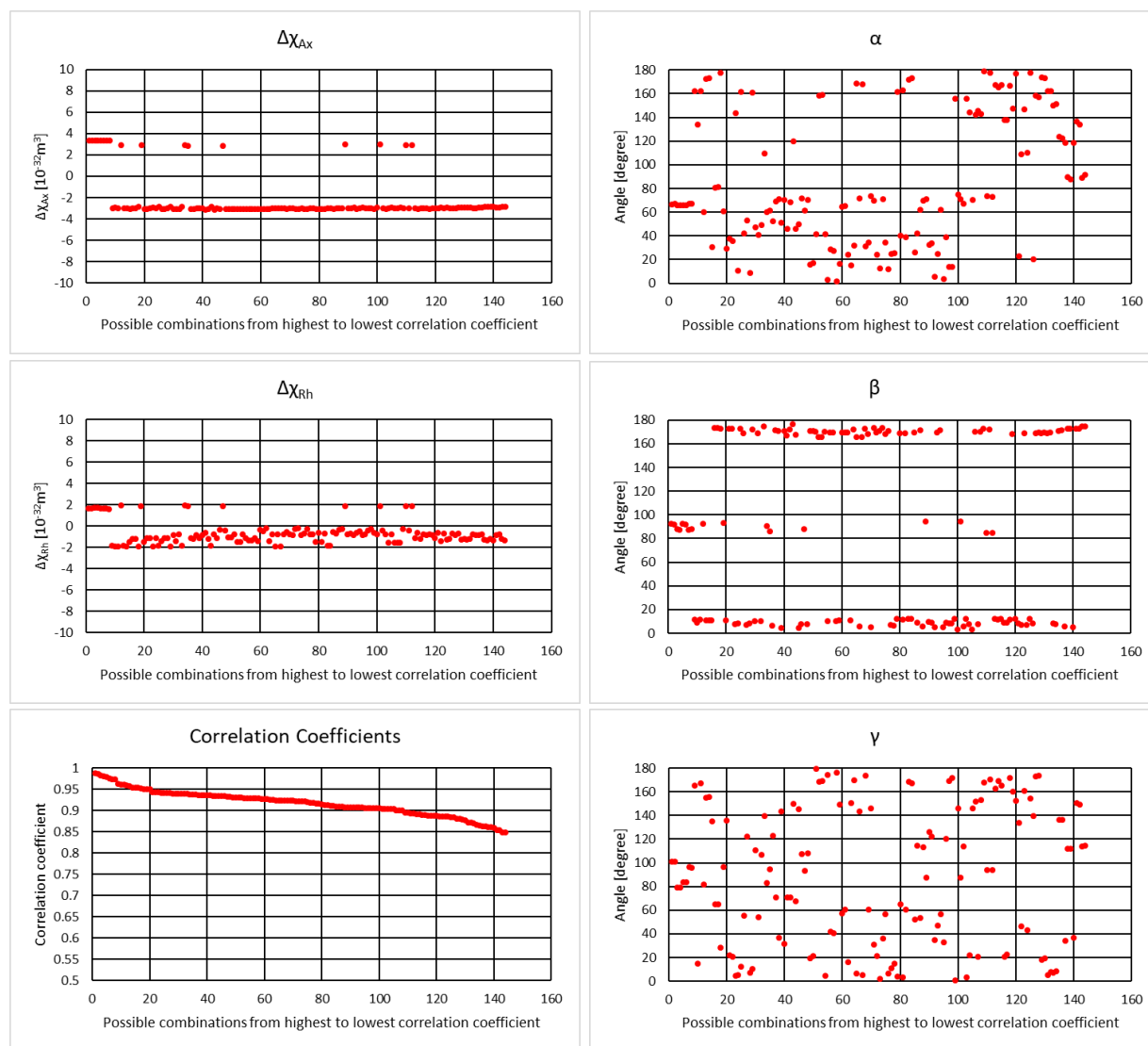


**Figure S12:** Correlation graphs between calculated and experimental PCS on Ln-DOTA-M8. Top left Pr. Top right Eu. Bottom left Dy. Bottom right Tm.

## 2.6.10 Anisotropy parameters of all possible assignments

### 2.6.10.1 Ln-DOTA-M7FPY (1)

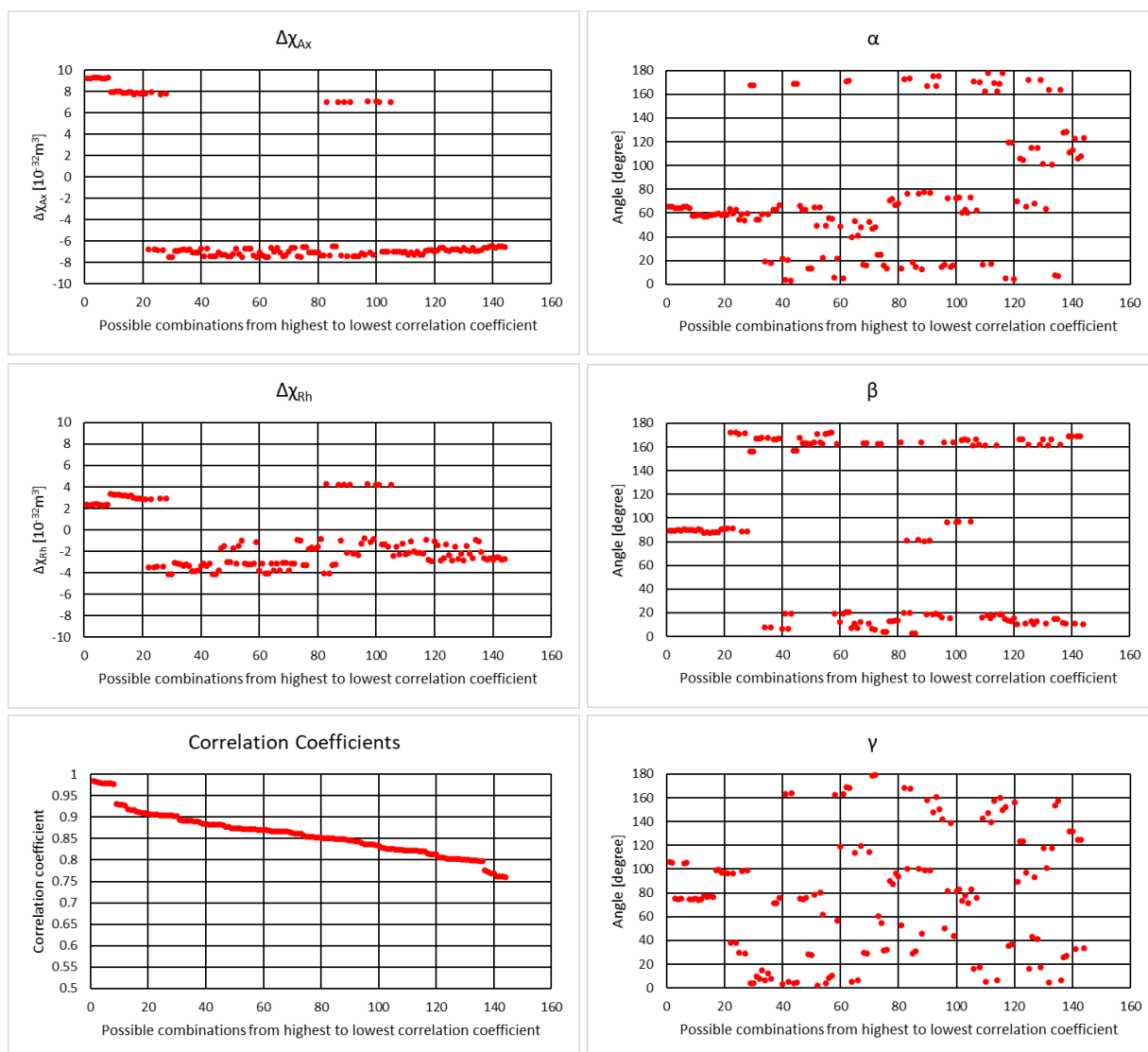
Ce-DOTA-M7FPy:



**Figure S13:** The anisotropy parameters and the correlation coefficient of all 144 possible assignments for Ce-DOTA-M7FPy were plotted separately from highest to lowest correlation coefficient. The anisotropy parameters and correlation coefficient of a given assignment are therefore spread over all six graphs and can be found at an equal position (e.g. position one represents in all graphs the assignment yielding the highest correlation coefficient). The anisotropy parameters were plotted separately to show their individual variance over all possible assignments.

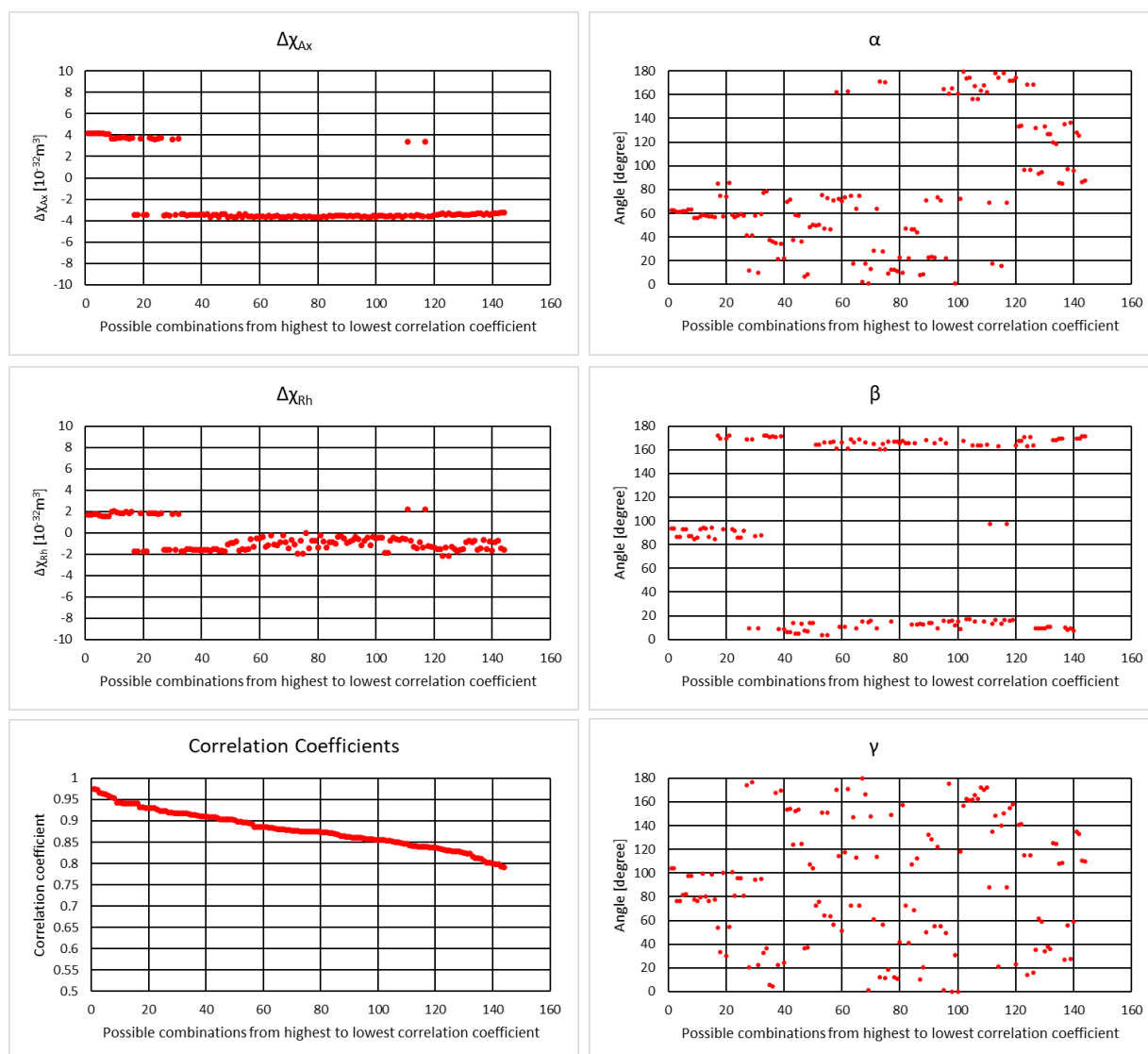


Pr-DOTA-M7FPy:



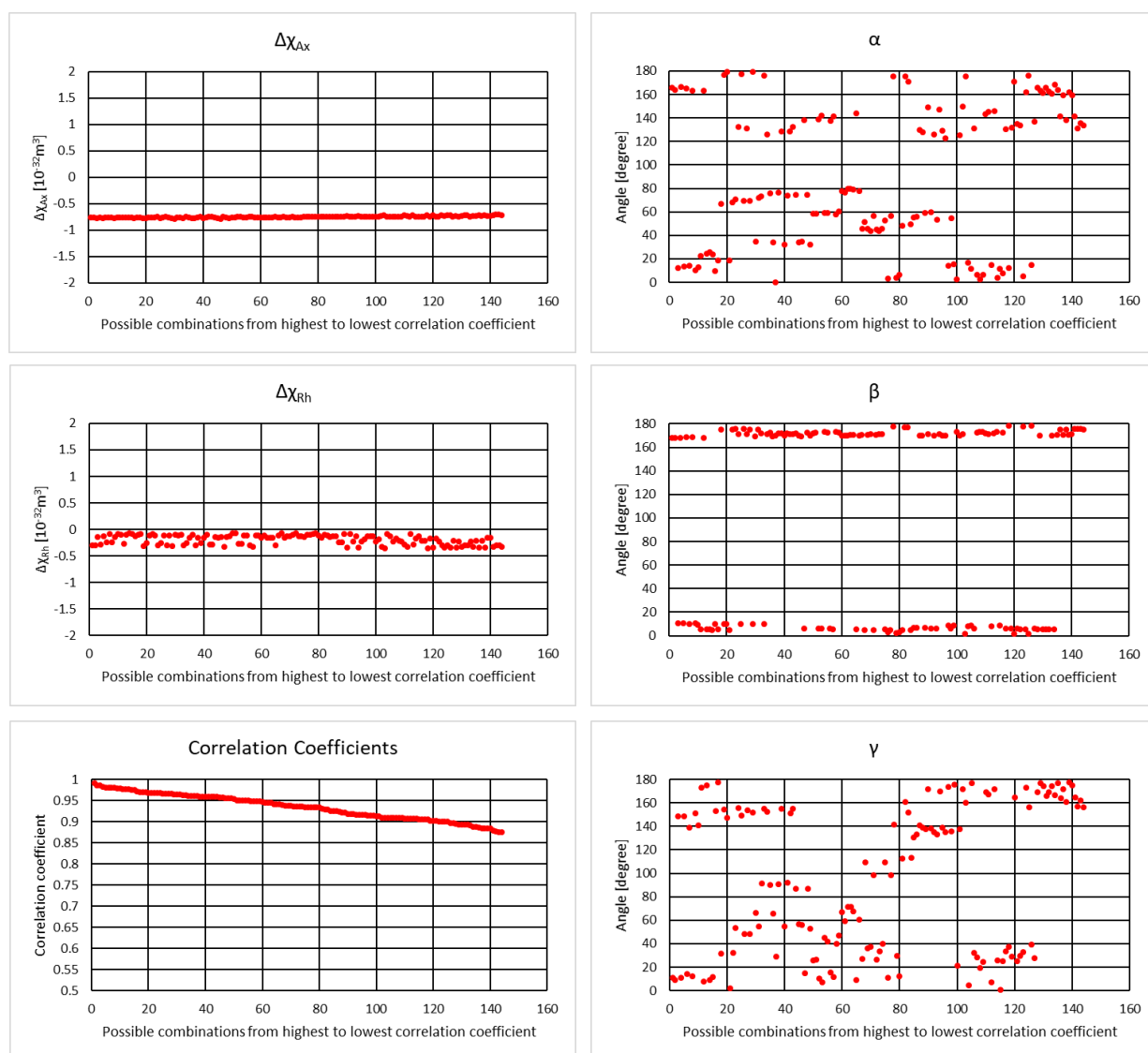
**Figure S14:** The anisotropy parameters and the correlation coefficient of all 144 possible assignments for Pr-DOTA-M7FPy were plotted separately from highest to lowest correlation coefficient. The anisotropy parameters and correlation coefficient of a given assignment are therefore spread over all six graphs and can be found at an equal position (e.g. position one represents in all graphs the assignment yielding the highest correlation coefficient). The anisotropy parameters were plotted separately to show their individual variance over all possible assignments.

## Nd-DOTA-M7FPy:



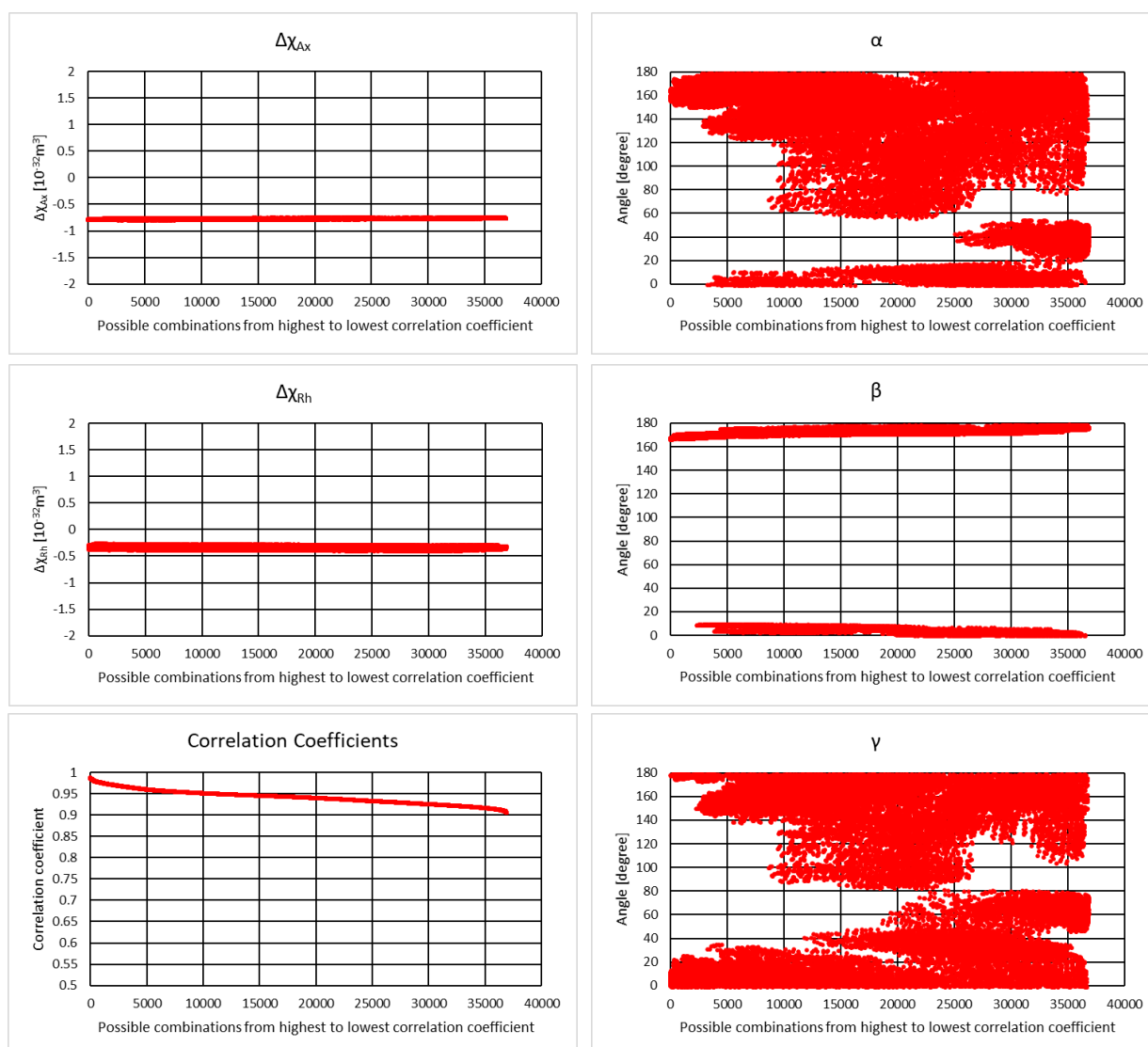
**Figure S15:** The anisotropy parameters and the correlation coefficient of all 144 possible assignments for Nd-DOTA-M7FPy were plotted separately from highest to lowest correlation coefficient. The anisotropy parameters and correlation coefficient of a given assignment are therefore spread over all six graphs and can be found at an equal position (e.g. position one represents in all graphs the assignment yielding the highest correlation coefficient). The anisotropy parameters were plotted separately to show their individual variance over all possible assignments.

## Sm-DOTA-M7FPy:



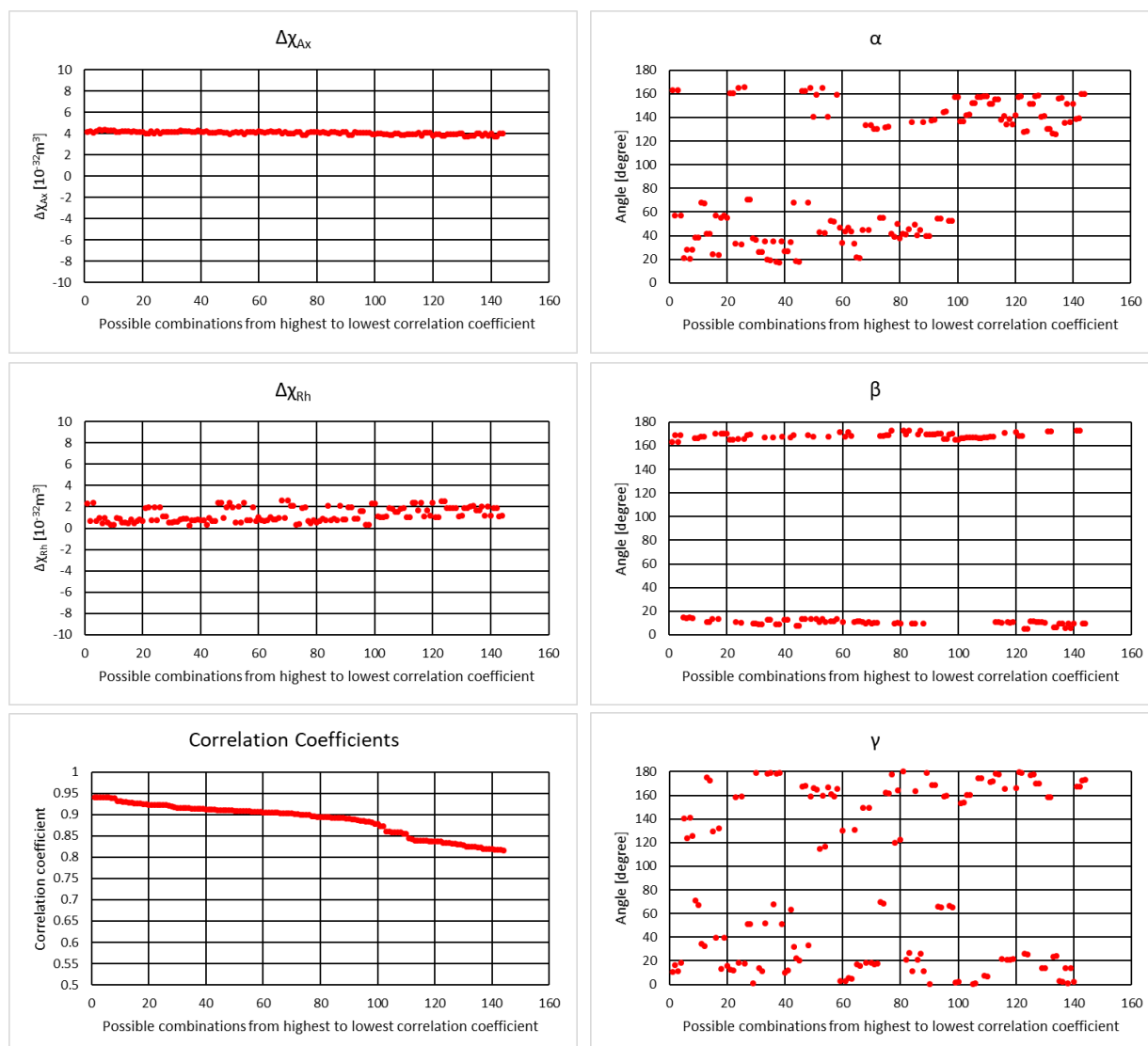
**Figure S16:** The anisotropy parameters and the correlation coefficient of all 144 possible assignments for Sm-DOTA-M7FPy were plotted separately from highest to lowest correlation coefficient. The anisotropy parameters and correlation coefficient of a given assignment are therefore spread over all six graphs and can be found at an equal position (e.g. position one represents in all graphs the assignment yielding the highest correlation coefficient). The anisotropy parameters were plotted separately to show their individual variance over all possible assignments.

## Sm-DOTA-M7FPy:



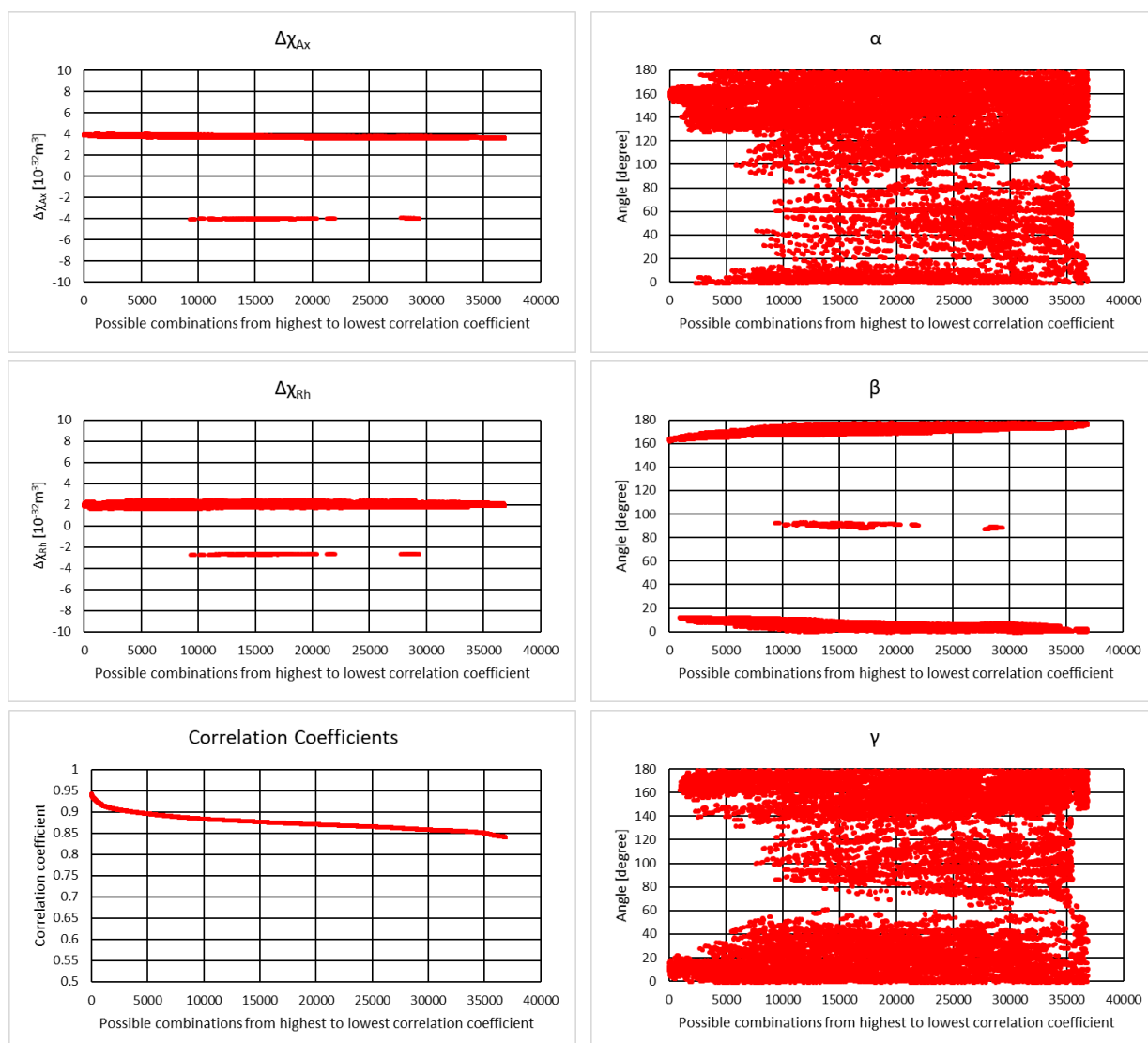
**Figure S17:** The anisotropy parameters and the correlation coefficient of all 36864 possible assignments for Sm-DOTA-M7FPy were plotted separately from highest to lowest correlation coefficient. The anisotropy parameters and correlation coefficient of a given assignment are therefore spread over all six graphs and can be found at an equal position (e.g. position one represents in all graphs the assignment yielding the highest correlation coefficient). The anisotropy parameters were plotted separately to show their individual variance over all possible assignments.

## Eu-DOTA-M7FPy:



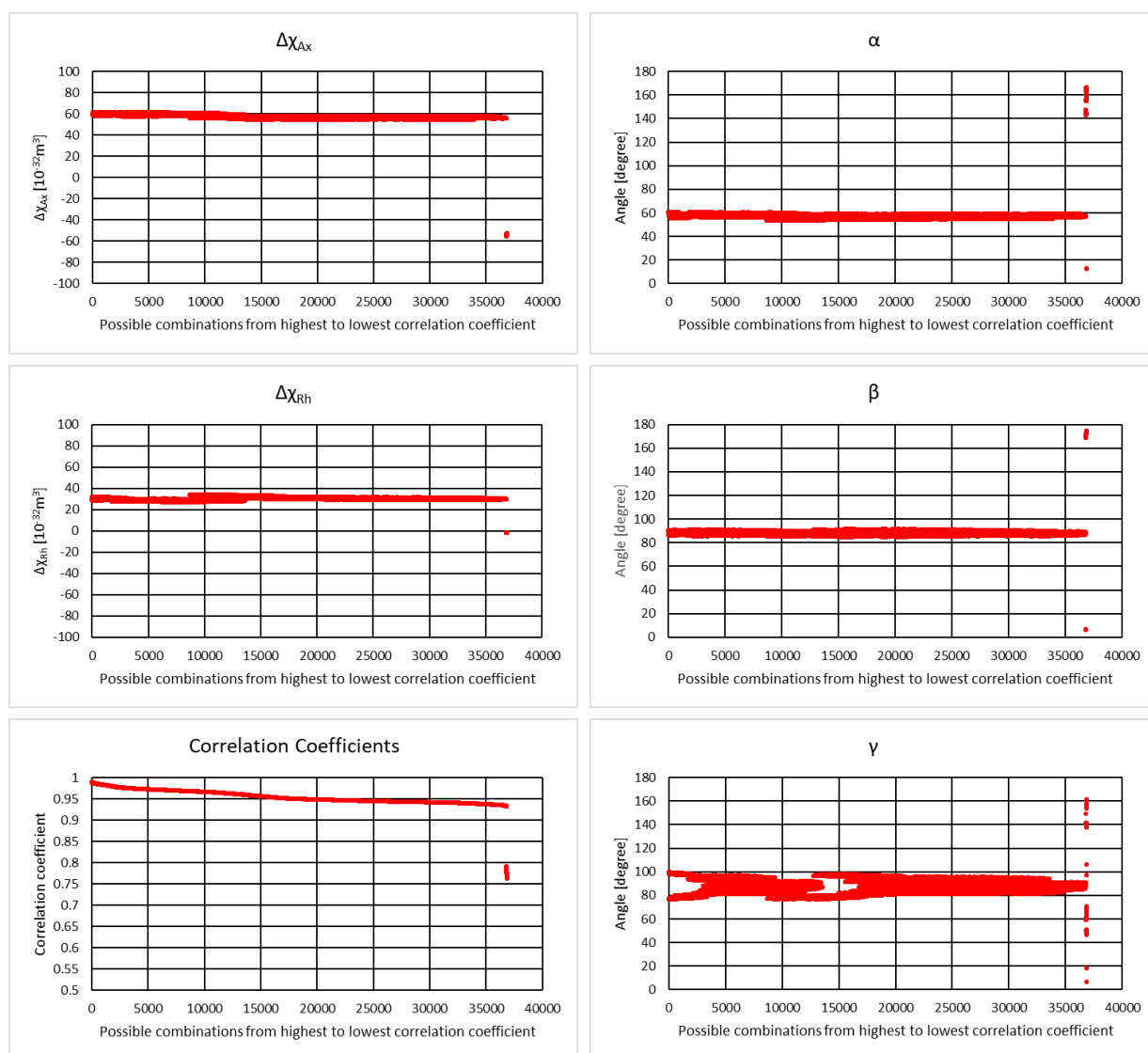
**Figure S18:** The anisotropy parameters and the correlation coefficient of all 144 possible assignments for Eu-DOTA-M7FPy were plotted separately from highest to lowest correlation coefficient. The anisotropy parameters and correlation coefficient of a given assignment are therefore spread over all six graphs and can be found at an equal position (e.g. position one represents in all graphs the assignment yielding the highest correlation coefficient). The anisotropy parameters were plotted separately to show their individual variance over all possible assignments.

## Eu-DOTA-M7FPy:



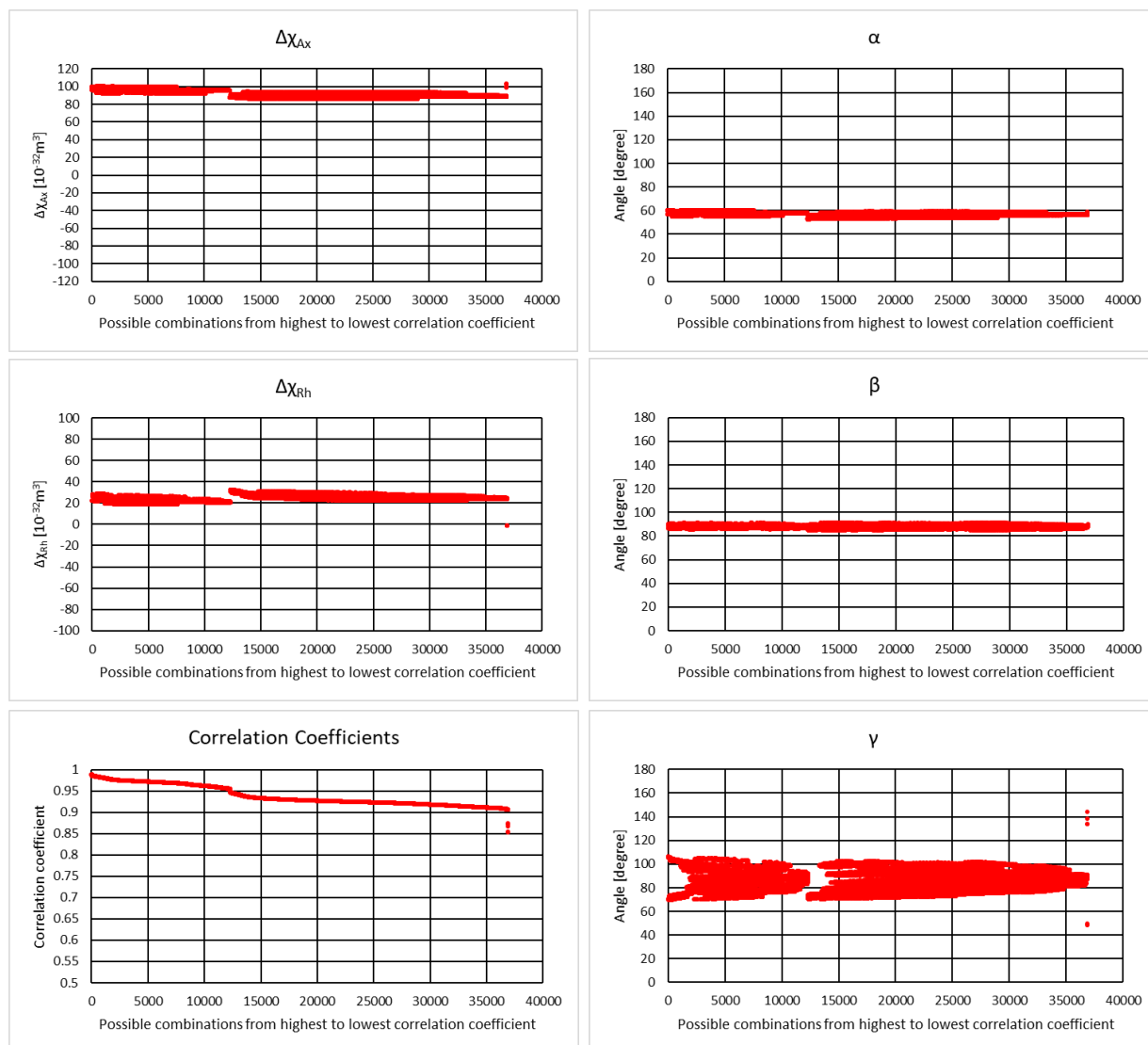
**Figure S19:** The anisotropy parameters and the correlation coefficient of all 36864 possible assignments for Eu-DOTA-M7FPy were plotted separately from highest to lowest correlation coefficient. The anisotropy parameters and correlation coefficient of a given assignment are therefore spread over all six graphs and can be found at an equal position (e.g. position one represents in all graphs the assignment yielding the highest correlation coefficient). The anisotropy parameters were plotted separately to show their individual variance over all possible assignments.

Tb-DOTA-M7FPy:



**Figure S20:** The anisotropy parameters and the correlation coefficient of all 36864 possible assignments for Tb-DOTA-M7FPy were plotted separately from highest to lowest correlation coefficient. The anisotropy parameters and correlation coefficient of a given assignment are therefore spread over all six graphs and can be found at an equal position (e.g. position one represents in all graphs the assignment yielding the highest correlation coefficient). The anisotropy parameters were plotted separately to show their individual variance over all possible assignments.

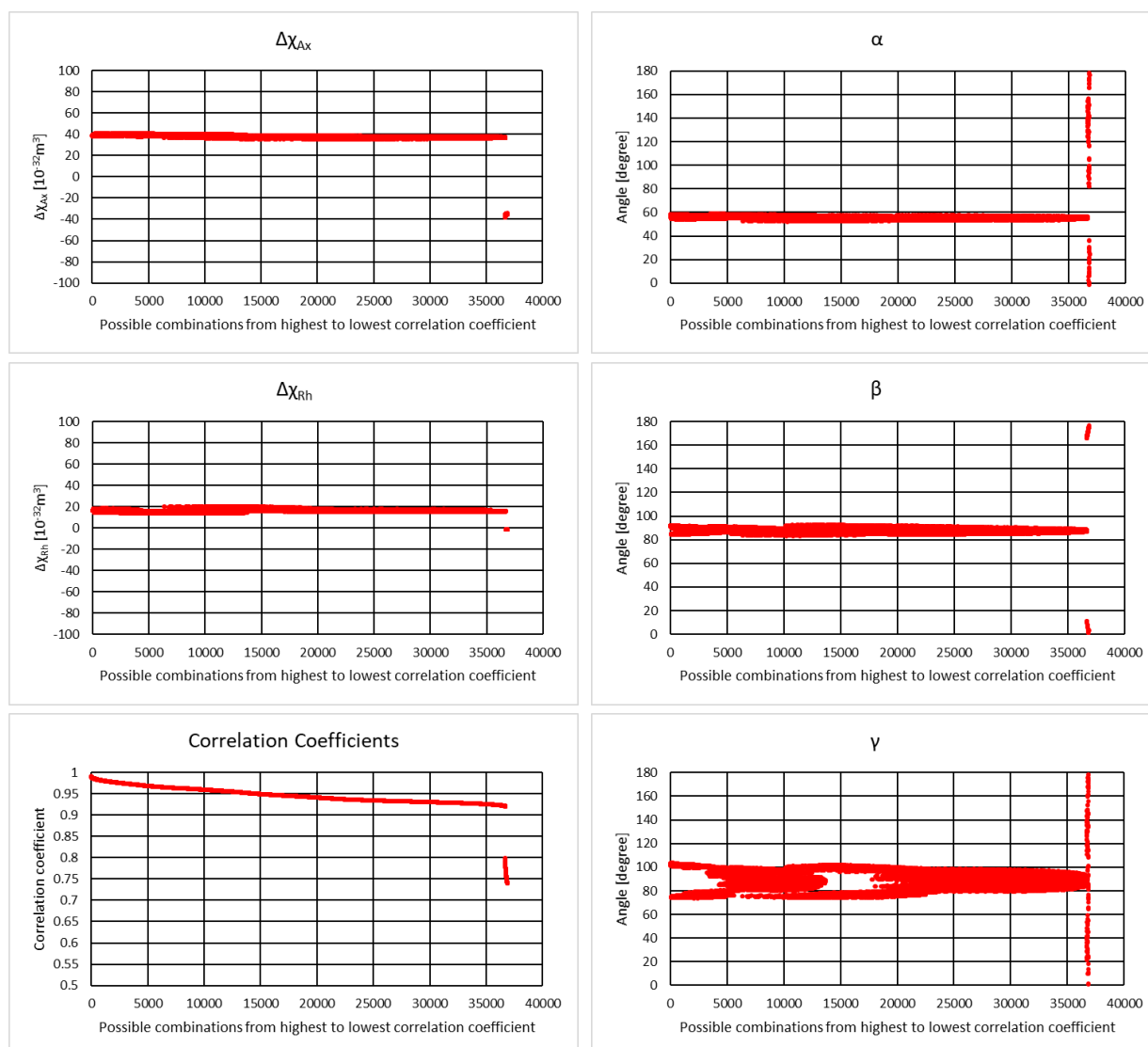
## Dy-DOTA-M7FPy:



**Figure S21:** The anisotropy parameters and the correlation coefficient of all 36864 possible assignments for Dy-DOTA-M7FPy were plotted separately from highest to lowest correlation coefficient. The anisotropy parameters and correlation coefficient of a given assignment are therefore spread over all six graphs and can be found at an equal position (e.g. position one represents in all graphs the assignment yielding the highest correlation coefficient). The anisotropy parameters were plotted separately to show their individual variance over all possible assignments.

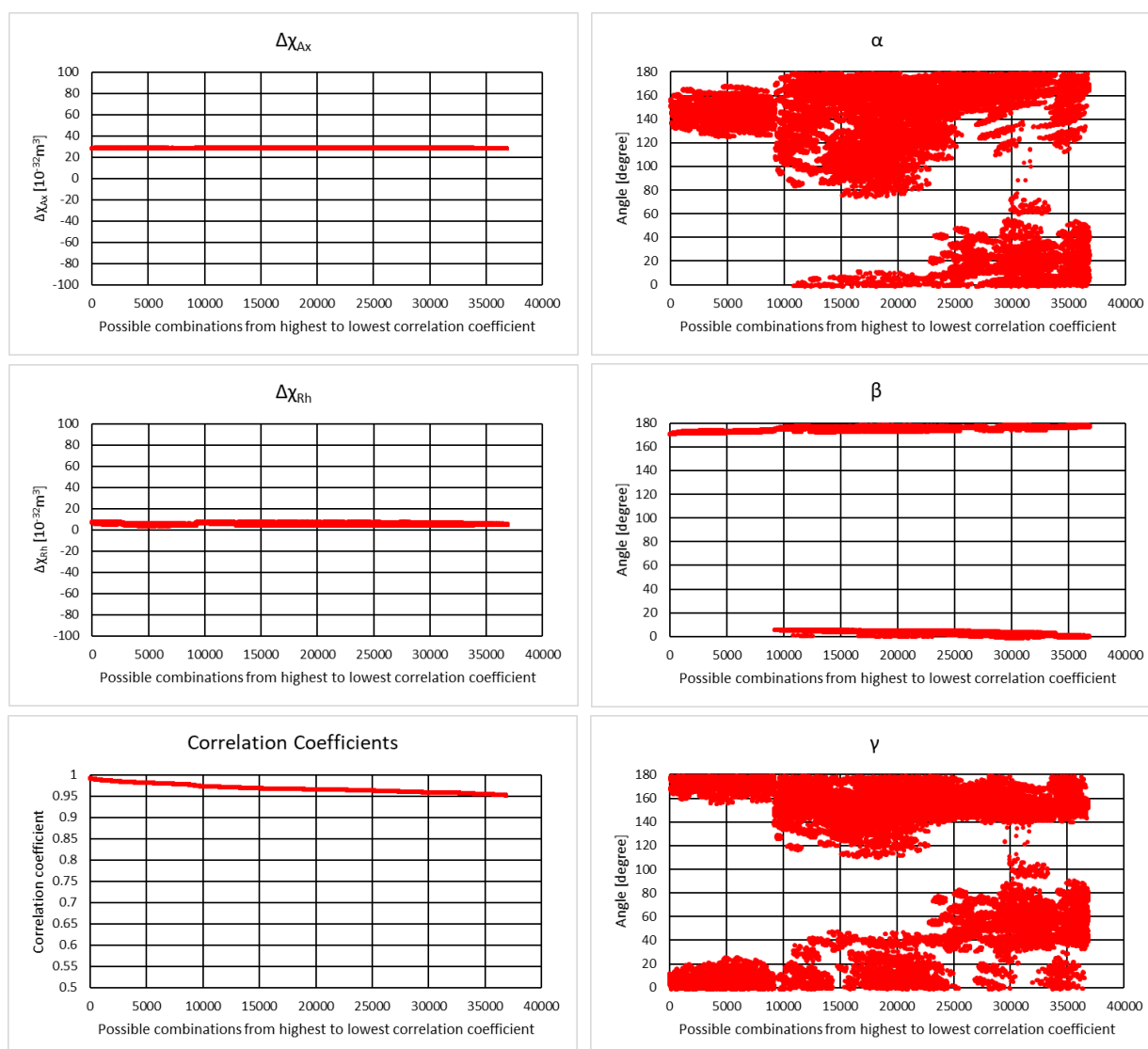


## Ho-DOTA-M7FPy:



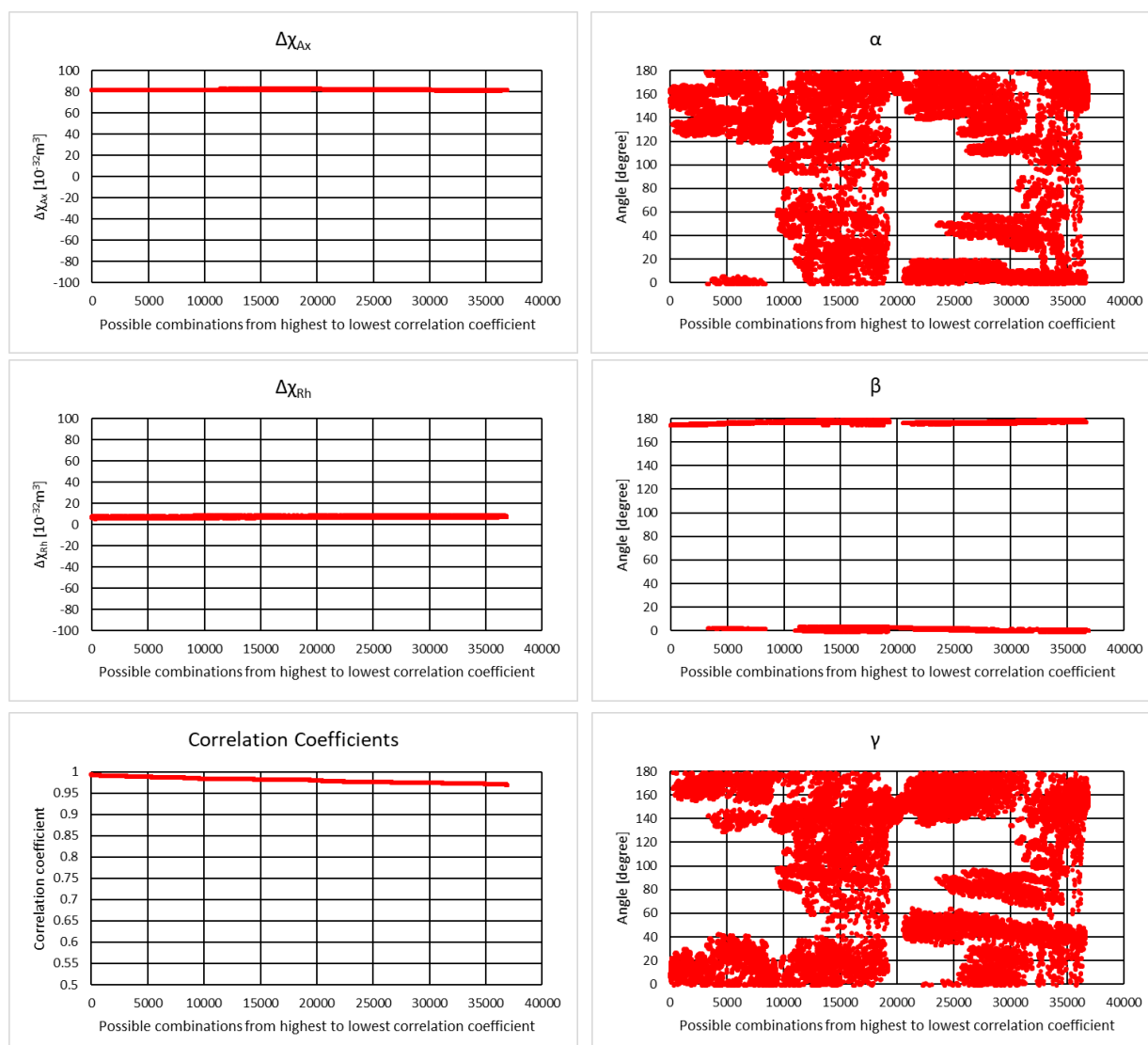
**Figure S22:** The anisotropy parameters and the correlation coefficient of all 36864 possible assignments for Ho-DOTA-M7FPy were plotted separately from highest to lowest correlation coefficient. The anisotropy parameters and correlation coefficient of a given assignment are therefore spread over all six graphs and can be found at an equal position (e.g. position one represents in all graphs the assignment yielding the highest correlation coefficient). The anisotropy parameters were plotted separately to show their individual variance over all possible assignments.

## Er-DOTA-M7FPy:



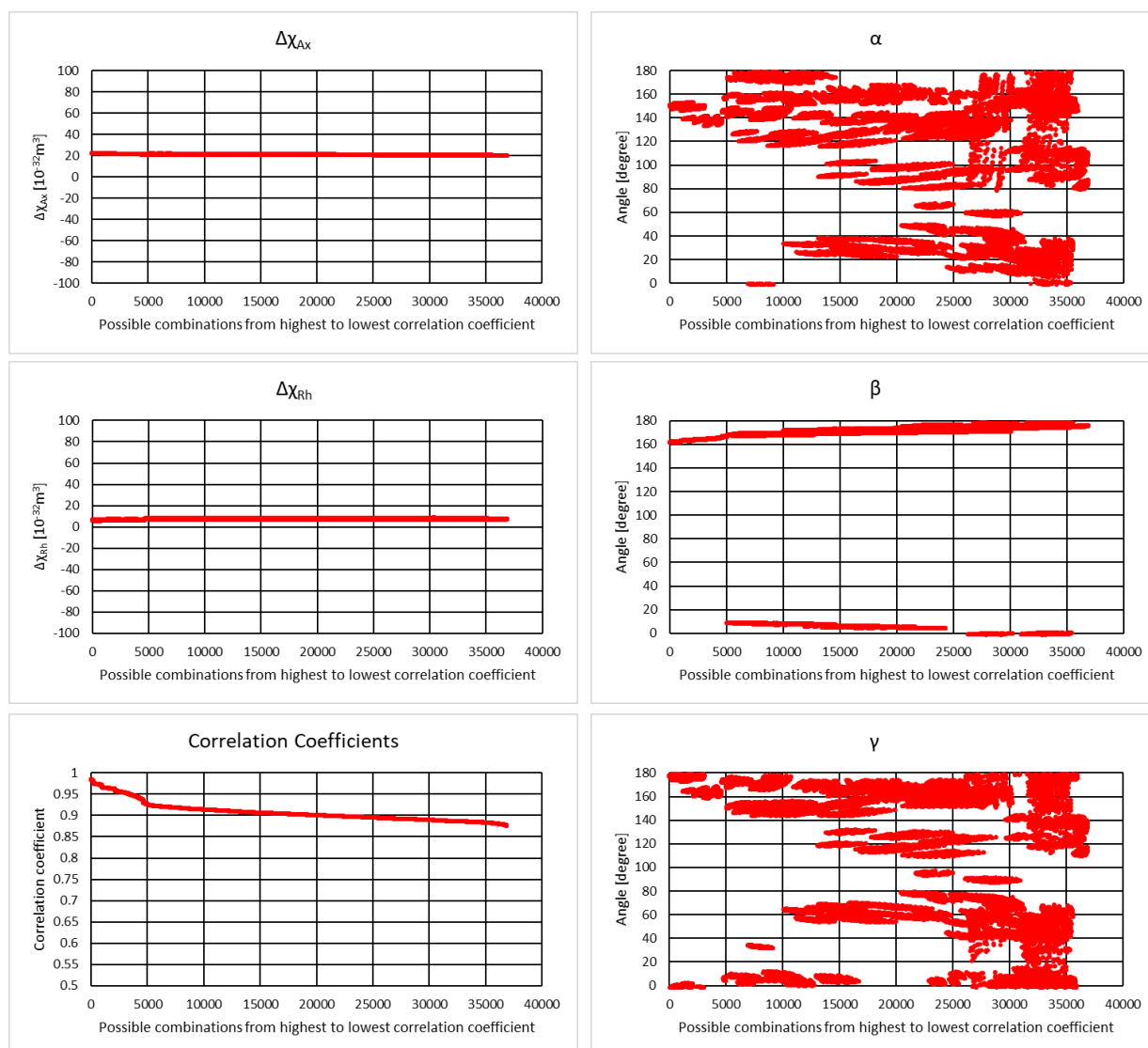
**Figure S23:** The anisotropy parameters and the correlation coefficient of all 36864 possible assignments for Er-DOTA-M7FPy were plotted separately from highest to lowest correlation coefficient. The anisotropy parameters and correlation coefficient of a given assignment are therefore spread over all six graphs and can be found at an equal position (e.g. position one represents in all graphs the assignment yielding the highest correlation coefficient). The anisotropy parameters were plotted separately to show their individual variance over all possible assignments.

## Tm-DOTA-M7FPy:



**Figure S24:** The anisotropy parameters and the correlation coefficient of all 36864 possible assignments for Tm-DOTA-M7FPy were plotted separately from highest to lowest correlation coefficient. The anisotropy parameters and correlation coefficient of a given assignment are therefore spread over all six graphs and can be found at an equal position (e.g. position one represents in all graphs the assignment yielding the highest correlation coefficient). The anisotropy parameters were plotted separately to show their individual variance over all possible assignments.

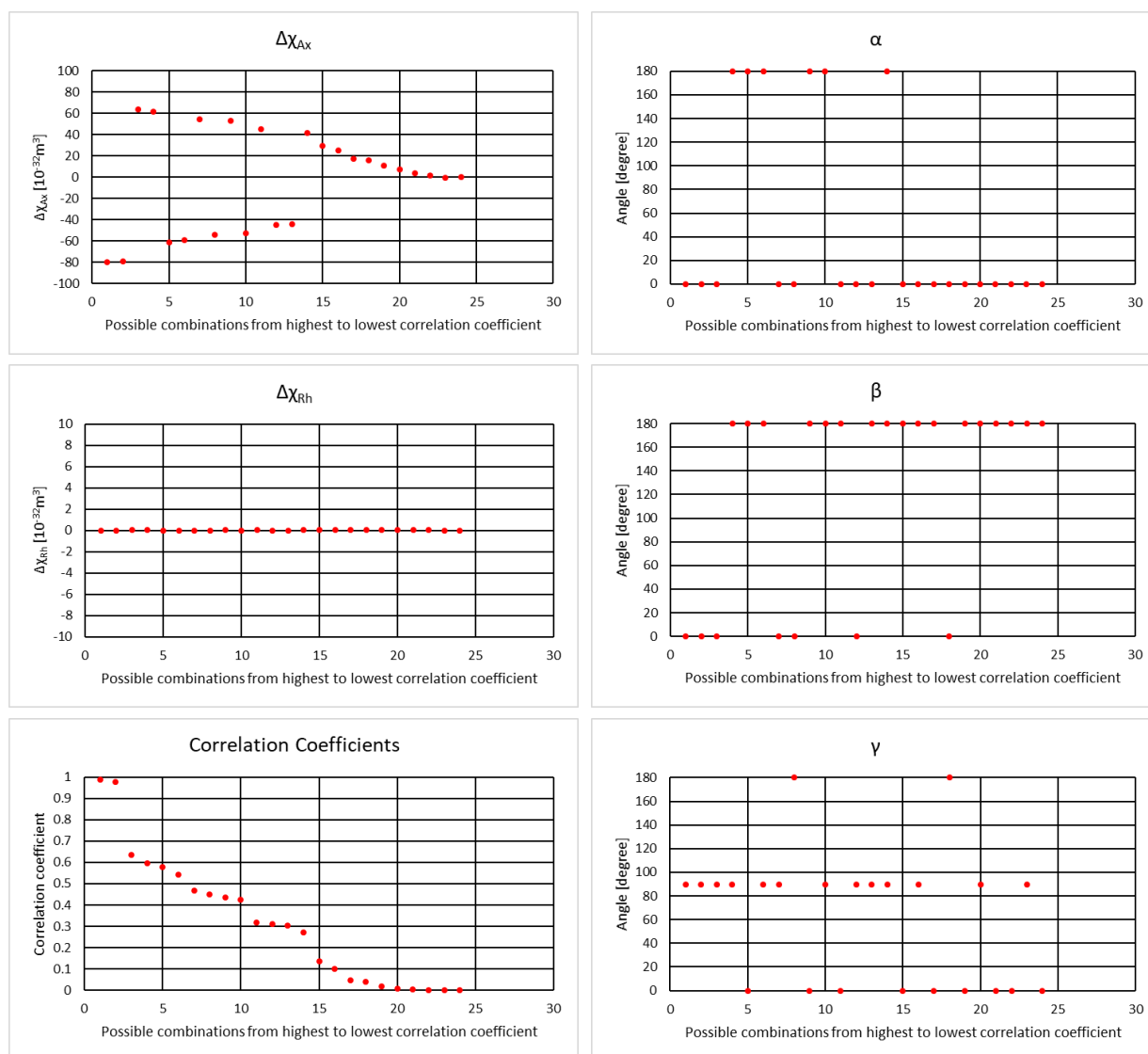
Yb-DOTA-M7FPy:



**Figure S25:** The anisotropy parameters and the correlation coefficient of all 36864 possible assignments for Yb-DOTA-M7FPy were plotted separately from highest to lowest correlation coefficient. The anisotropy parameters and correlation coefficient of a given assignment are therefore spread over all six graphs and can be found at an equal position (e.g. position one represents in all graphs the assignment yielding the highest correlation coefficient). The anisotropy parameters were plotted separately to show their individual variance over all possible assignments.

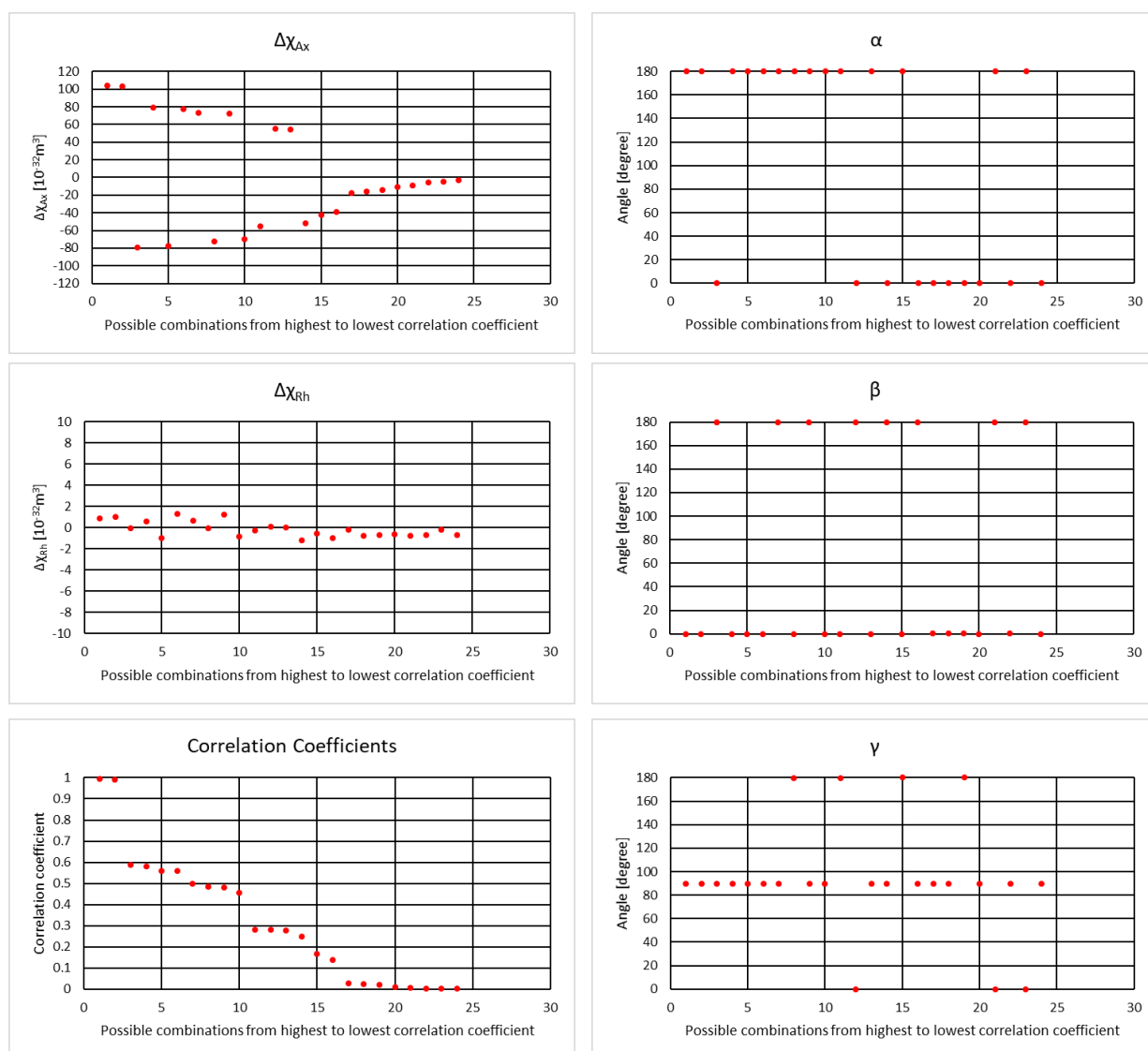
## 2.6.9.2 Ln-DOTA-M8 (60)

Dy-DOTA-M8:



**Figure S26:** The anisotropy parameters and the correlation coefficient of all 24 possible assignments for Dy-DOTA-M8 were plotted separately from highest to lowest correlation coefficient. The anisotropy parameters and correlation coefficient of a given assignment are therefore spread over all six graphs and can be found at an equal position (e.g. position one represents in all graphs the assignment yielding the highest correlation coefficient). The anisotropy parameters were plotted separately to show their individual variance over all possible assignments.

## Tm-DOTA-M8:

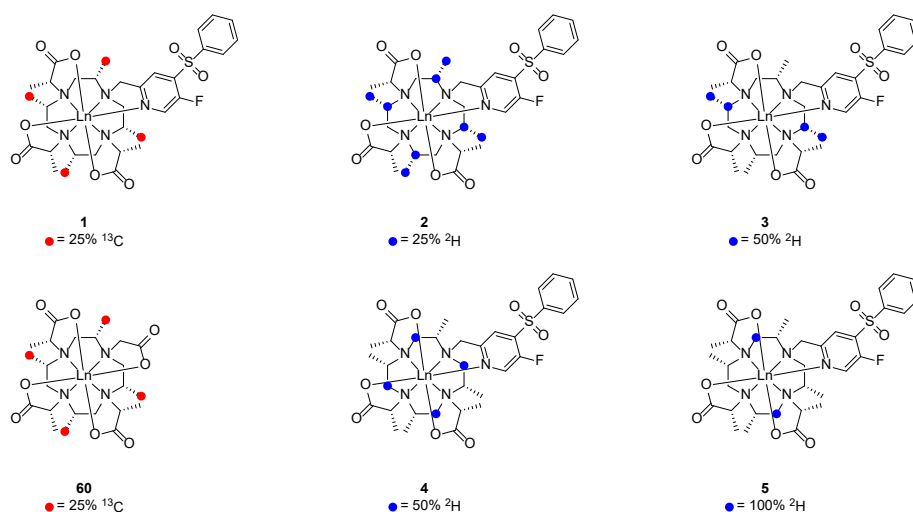


**Figure S27:** The anisotropy parameters and the correlation coefficient of all 24 possible assignments for Tm-DOTA-M8 were plotted separately from highest to lowest correlation coefficient. The anisotropy parameters and correlation coefficient of a given assignment are therefore spread over all six graphs and can be found at an equal position (e.g. position one represents in all graphs the assignment yielding the highest correlation coefficient). The anisotropy parameters were plotted separately to show their individual variance over all possible assignments.

## 2.6.10 pH-Values of all buffered samples

**Table S15:** pH-Values of all samples measured in 50 mM phosphate buffer recorded after the measurement. The numbers in the first row indicate the labelling scheme (see Fig. S28 below). All pH values were determined in D<sub>2</sub>O.

	La	Ce	Pr	Nd	Sm	Eu	Tb	Dy	Ho	Er	Tm	Yb	Lu
<b>1</b>	6.055	5.975	6.021	5.903	6.044	6.026	6.025	6.027	6.014	6.026	6.033	5.856	5.978
<b>2</b>	-	-	-	-	-	-	-	5.985	6.058	6.049	5.900	6.049	6.070
<b>3</b>	-	-	-	-	-	-	-	5.993	6.057	6.053	5.659	6.048	6.056
<b>4</b>	-	-	-	-	-	-	-	6.026	6.065	6.047	5.780	6.052	6.054
<b>5</b>	-	-	-	-	-	-	-	5.979	6.050	6.053	6.016	6.056	6.055
<b>60</b>	6.026	-	6.017	-	-	6.028	-	6.036	-	-	6.053	-	6.044



**Figure S28:** All labelled Ln-DOTA-type complexes used throughout this study. The numbers below the structures indicate the observed labelling.

## 2.6.11 Shift ranges vs $\Delta\chi_{Ax}$

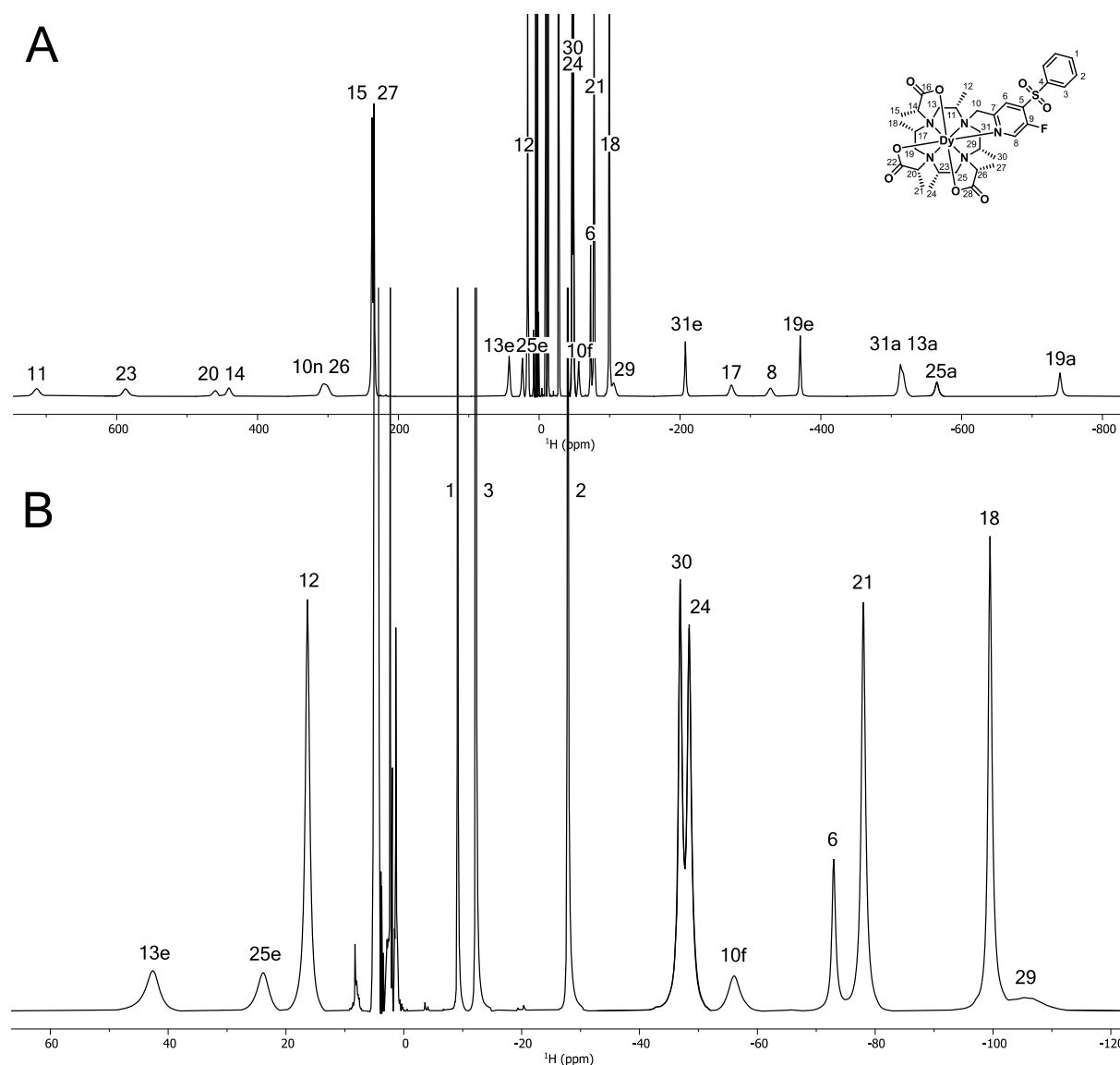
**Table S16:** <sup>1</sup>H-NMR spectra shift range in ppm and  $\Delta\chi_{Ax}$  of Ln-DOTA-M7FPy

	Ce	Pr	Nd	Sm	Eu	Tb	Dy	Ho	Er	Tm	Yb
<b>Shift Range</b>	49.34	128.9	65.52	13.32	72.22	1012	1453	690.0	489.5	1225	390.3
<b><math>\Delta\chi_{Ax}</math></b>	3.3	9.1	4.1	-0.76	4.1	61.8	100.5	40.1	29.8	83.0	23.5

**Table S17:** <sup>1</sup>H-NMR spectra shift range in ppm and  $\Delta\chi_{Ax}$  of Ln-DOTA-M8

	Ce	Pr	Nd	Sm	Eu	Tb	Dy	Ho	Er	Tm	Yb
<b>Shift Range</b>	-	95.31	-	-	70.21	-	1099	-	-	1442	-
<b><math>\Delta\chi_{Ax}</math></b>	-	-7.2	-	-	5.2	-	-79.8	-	-	103.6	-

## 2.6.12 Dysprosium spectrum with assignment



**Figure S29:** **A:** Full Spectrum of Dy-DOTA-M7FPy with assignment. The full spectrum was pieced together from single spectra with a sweep width of 154 ppm. The spectra were recorded at 298 K in phosphate buffer (50 mM, pH = 6.05) at 600.13 MHz. The methylene protons on the basal cyclen ring are separated into axial (a) and equatorial (e) protons. From the methylene protons on the pyridine linker one is significantly closer to the paramagnetic centre than the other. Based on their distance to the paramagnetic centre these protons are termed far (f) and near (n). **B:** Cut-out of the middle of the Dy-DOTA-M7FPy spectrum.



## 2.6.13 NMR spectra of Ln-DOTA-M7FPy (1)

La-DOTA-M7FPy

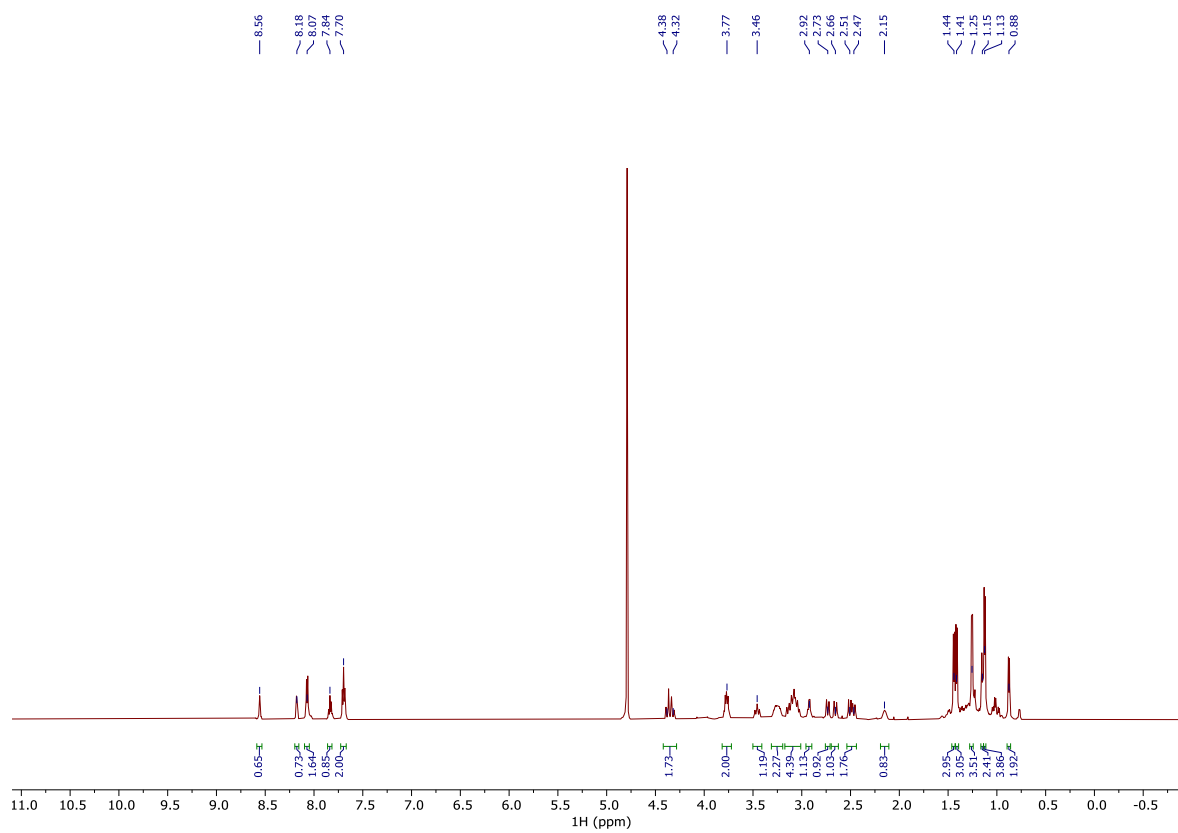
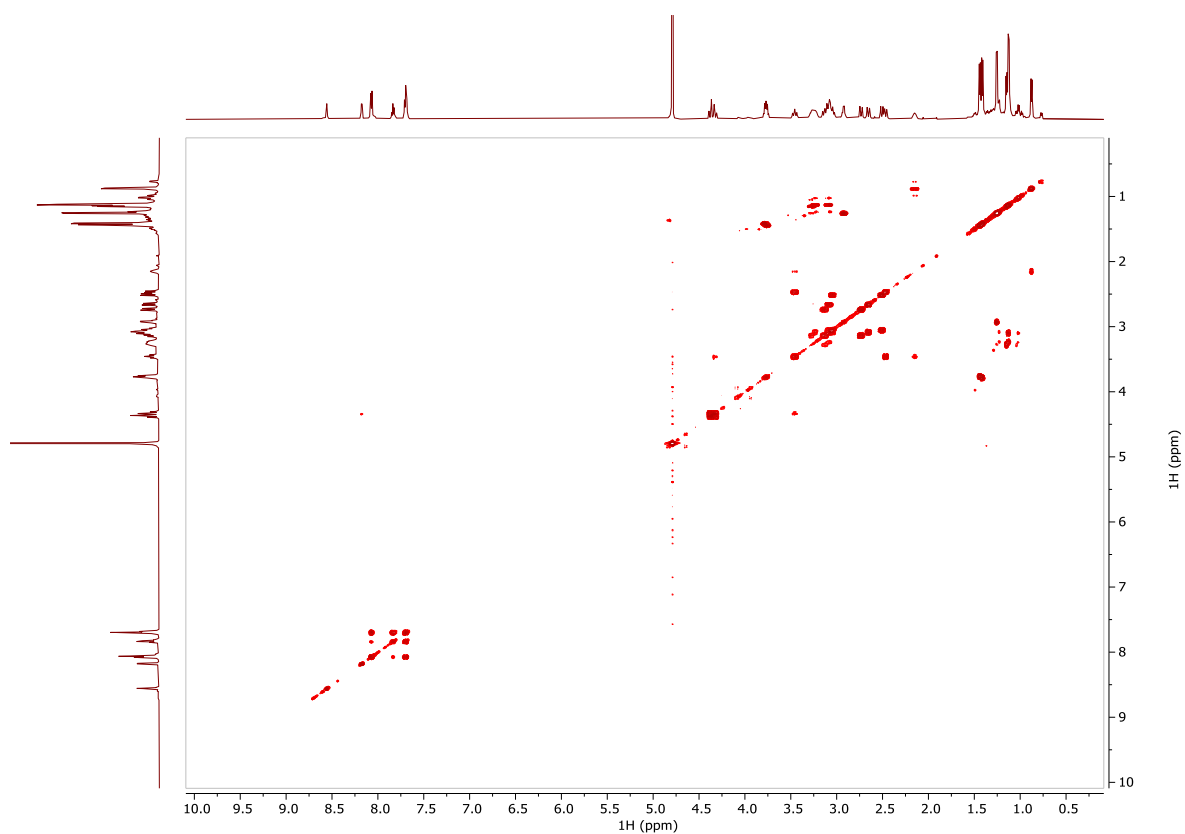
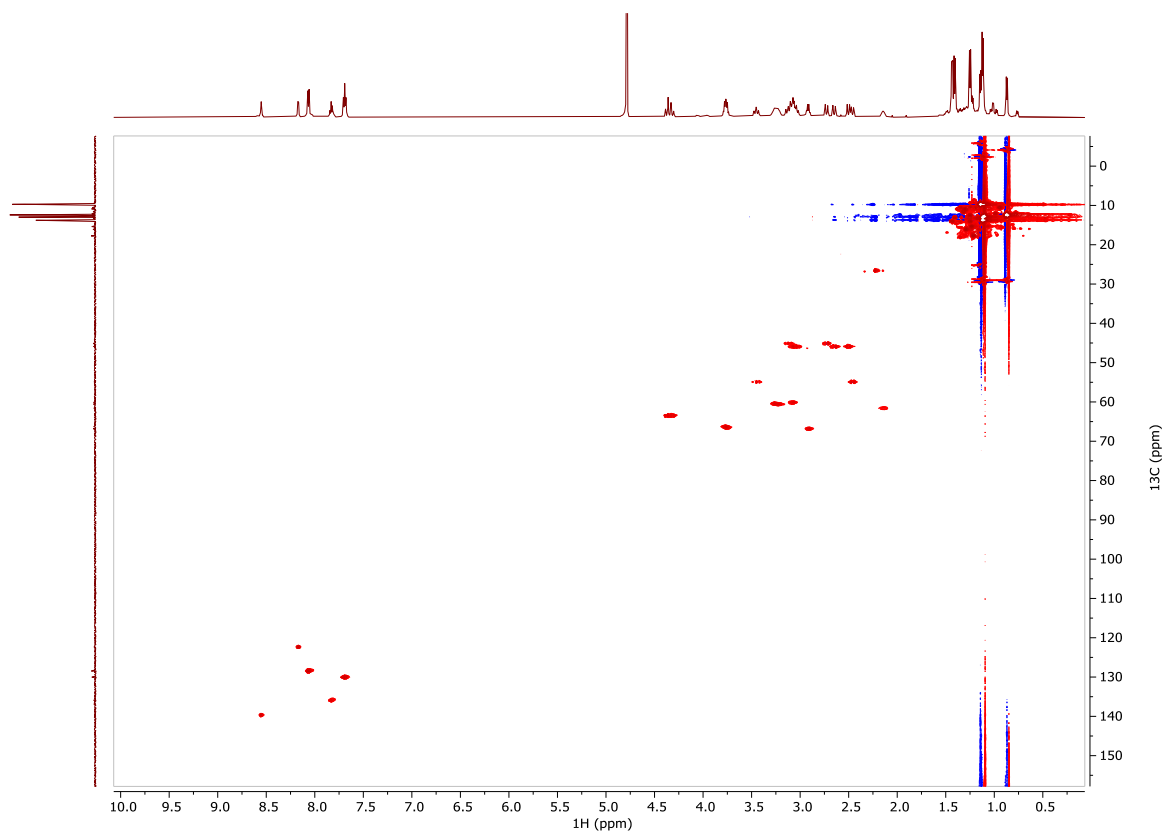


Figure S30:  $^1\text{H}$  NMR spectrum of La-DOTA-M7FPy.



**Figure S31:**  $^1\text{H}$   $^1\text{H}$  COSY spectrum of La-DOTA-M7FPy.



**Figure S32:**  $^1\text{H}$   $^{13}\text{C}$  HMQC spectrum of La-DOTA-M7FPy.

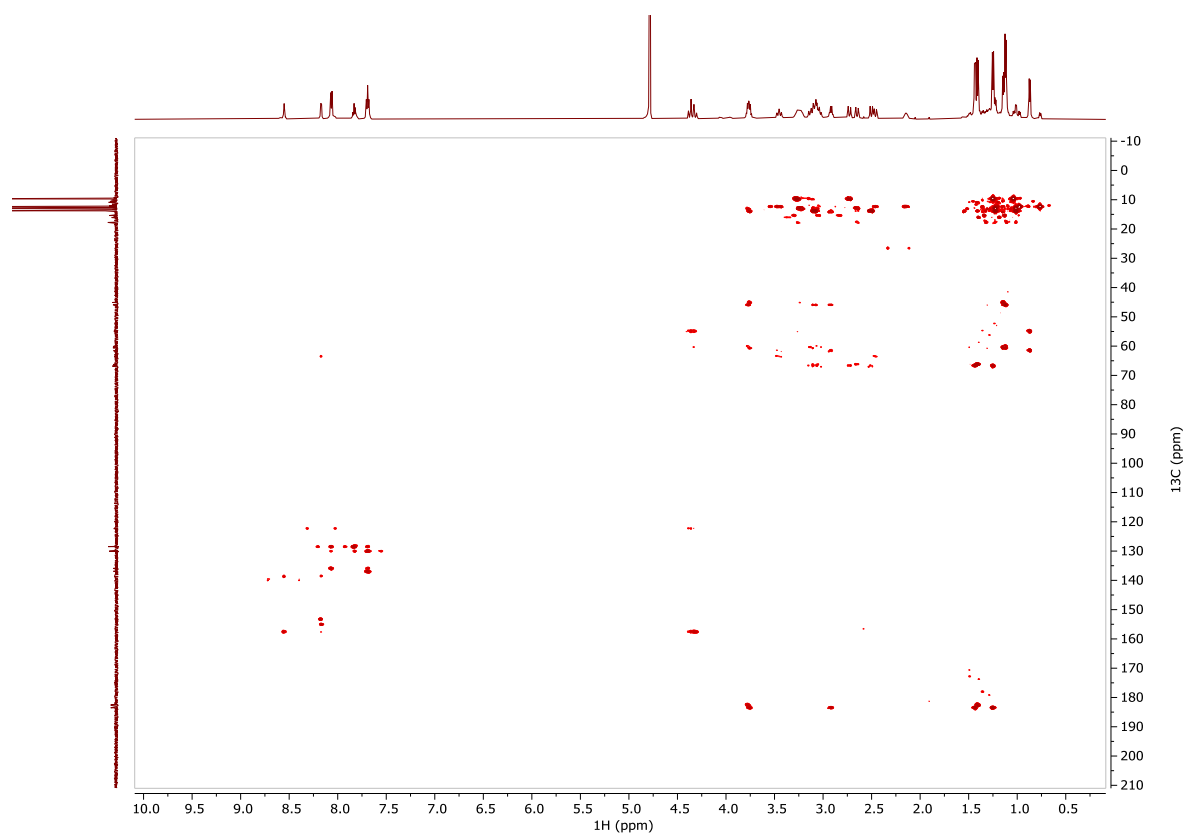


Figure S33:  $^1\text{H}$   $^{13}\text{C}$  HMBC spectrum of La-DOTA-M7FPy.

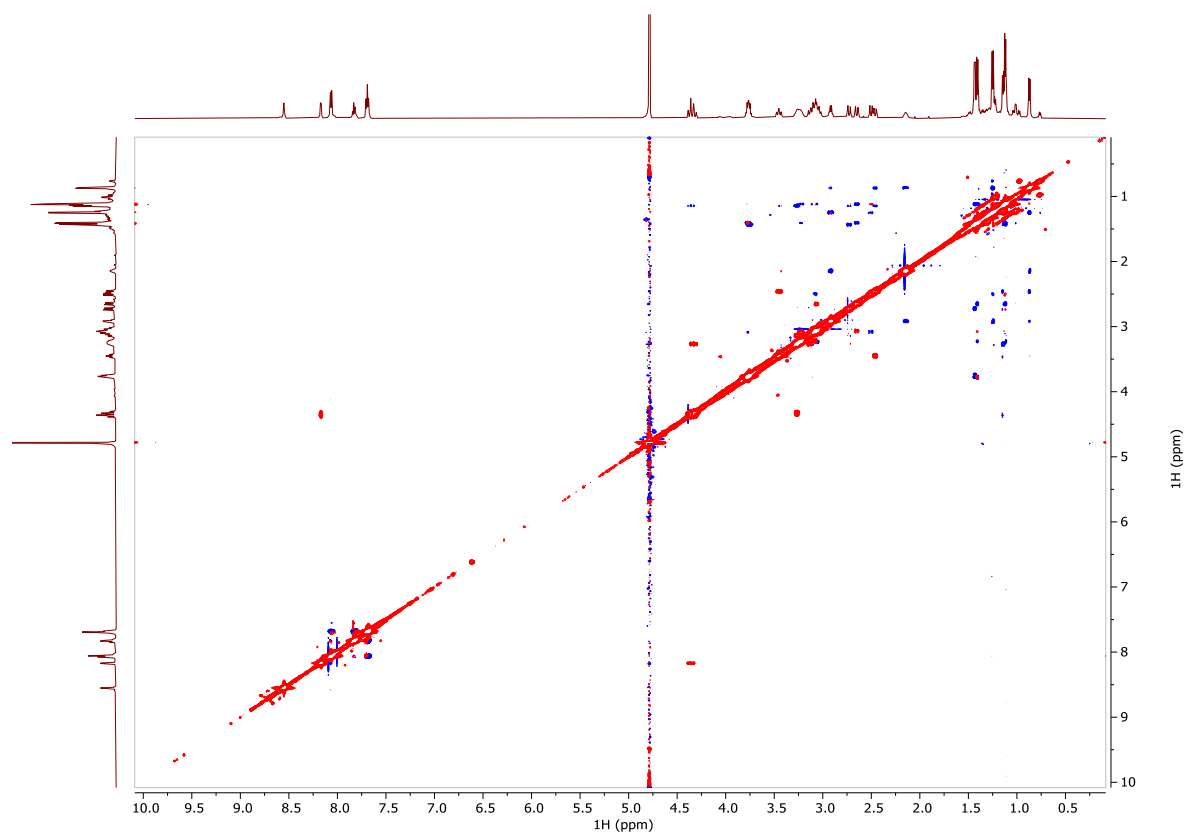


Figure S34:  $^1\text{H}$   $^1\text{H}$  NOESY spectrum of La-DOTA-M7FPy.

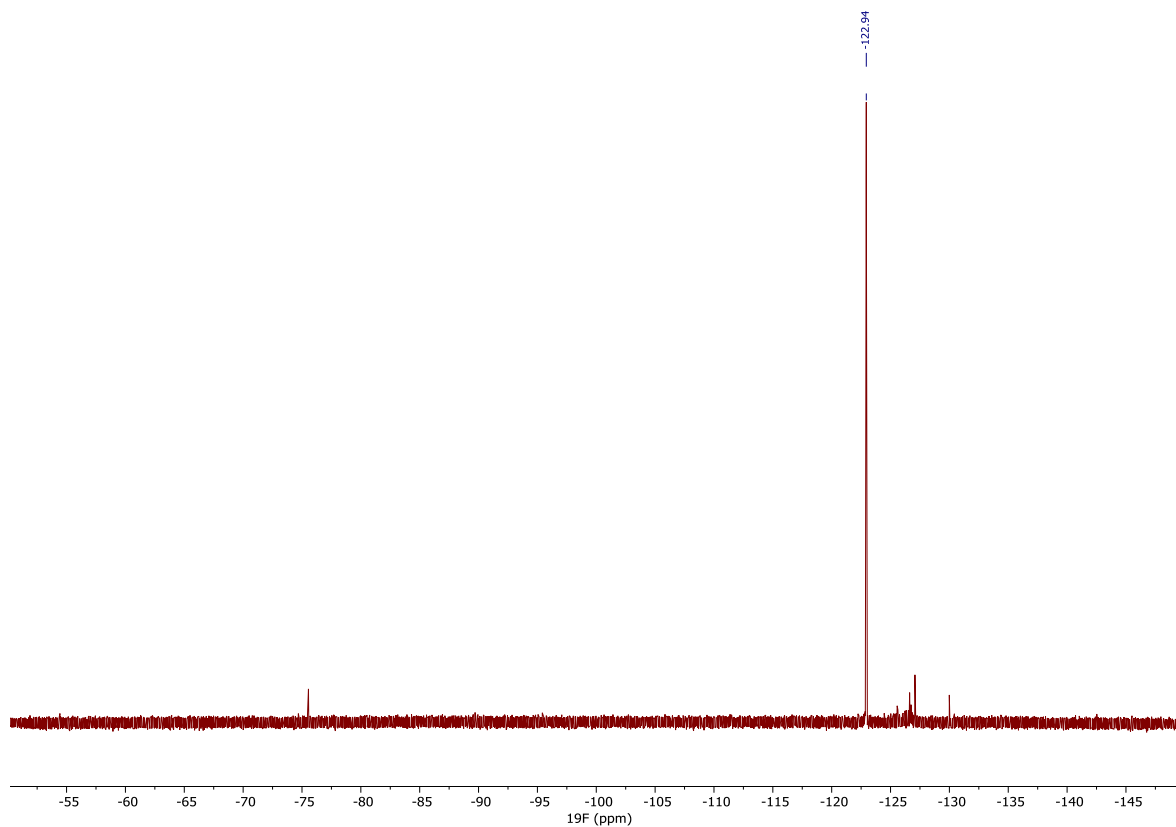


Figure S35:  $^{19}\text{F}\{^1\text{H}\}$  NMR spectrum of La-DOTA-M7FPy.

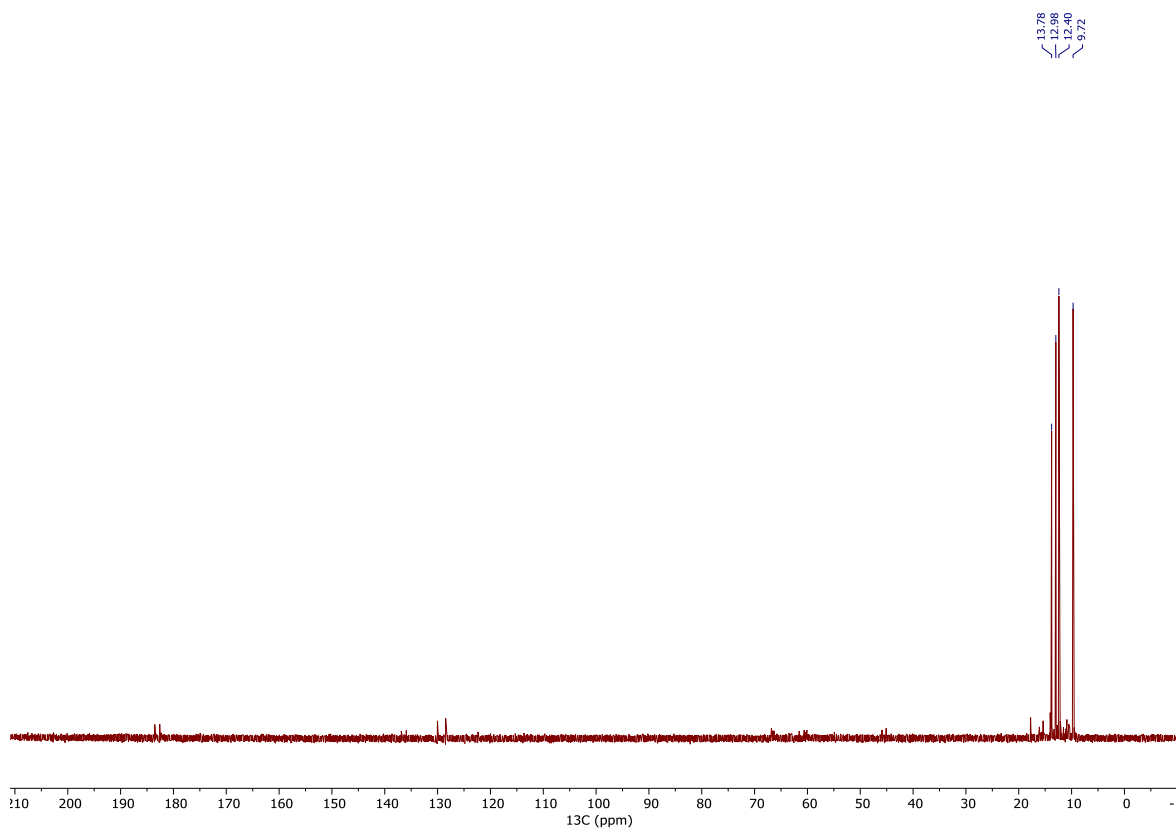


Figure S36:  $^{13}\text{C}\{^1\text{H}\}$  NMR spectrum of La-DOTA-M7FPy.

# Ce-DOTA-M7FPy

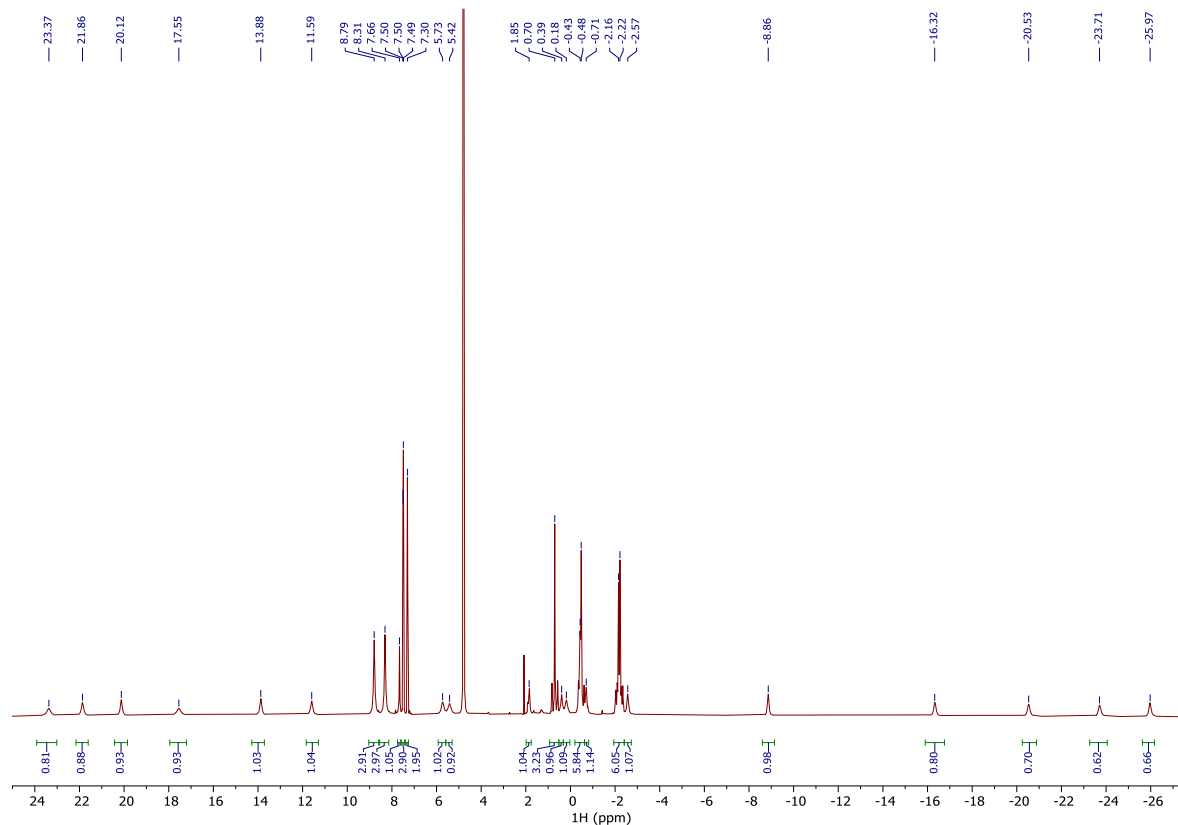


Figure S37:  $^1\text{H}$  NMR spectrum of Ce-DOTA-M7FPy.

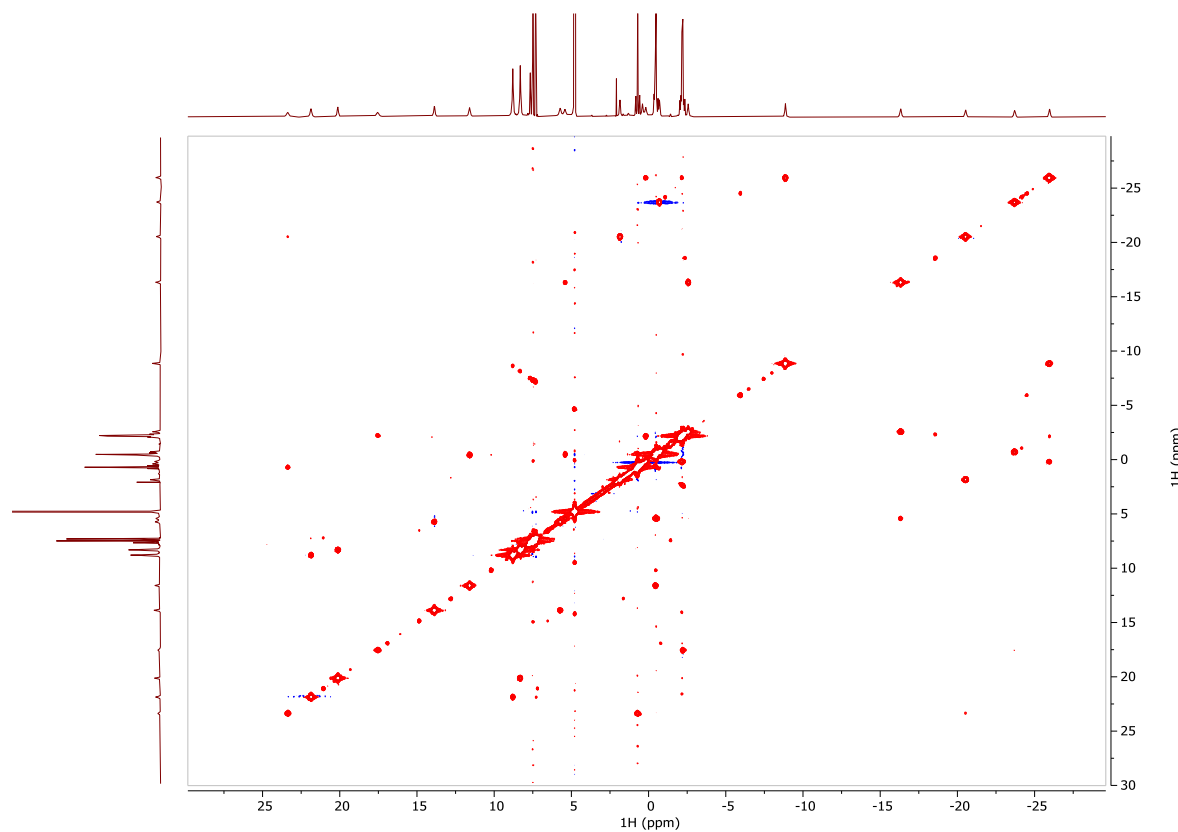
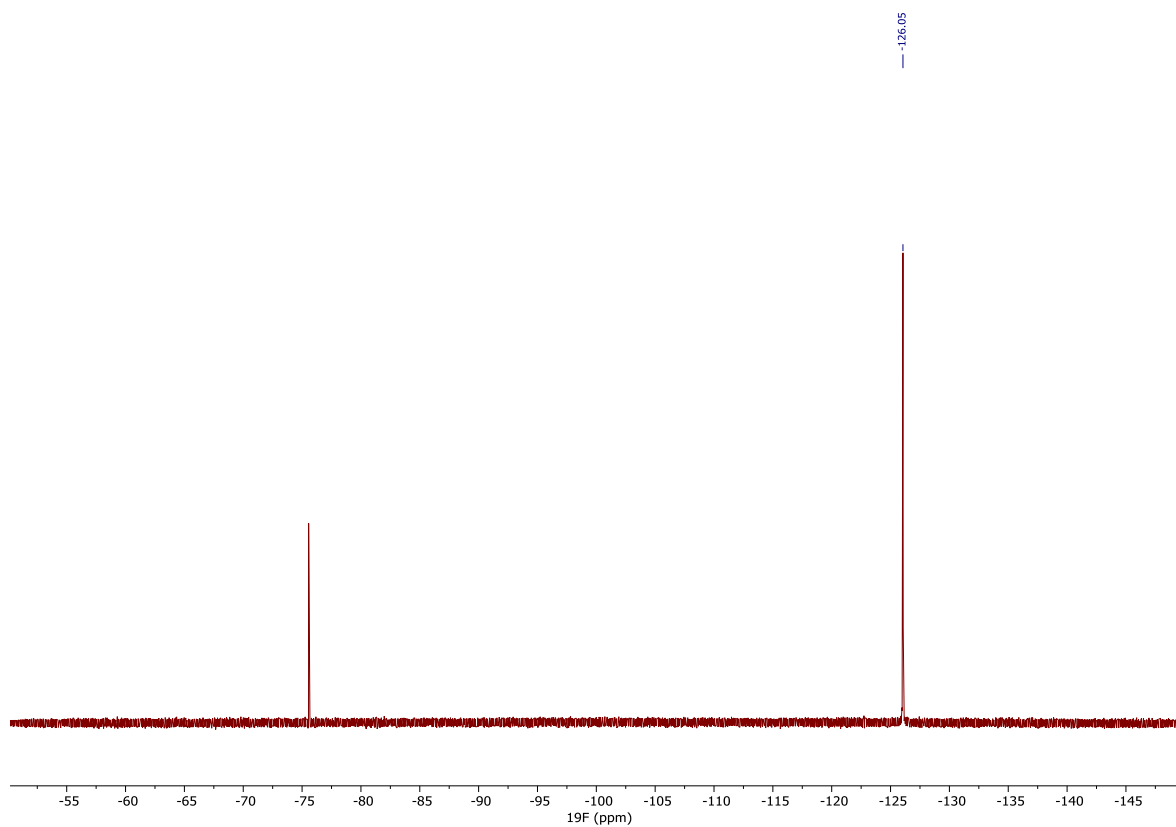
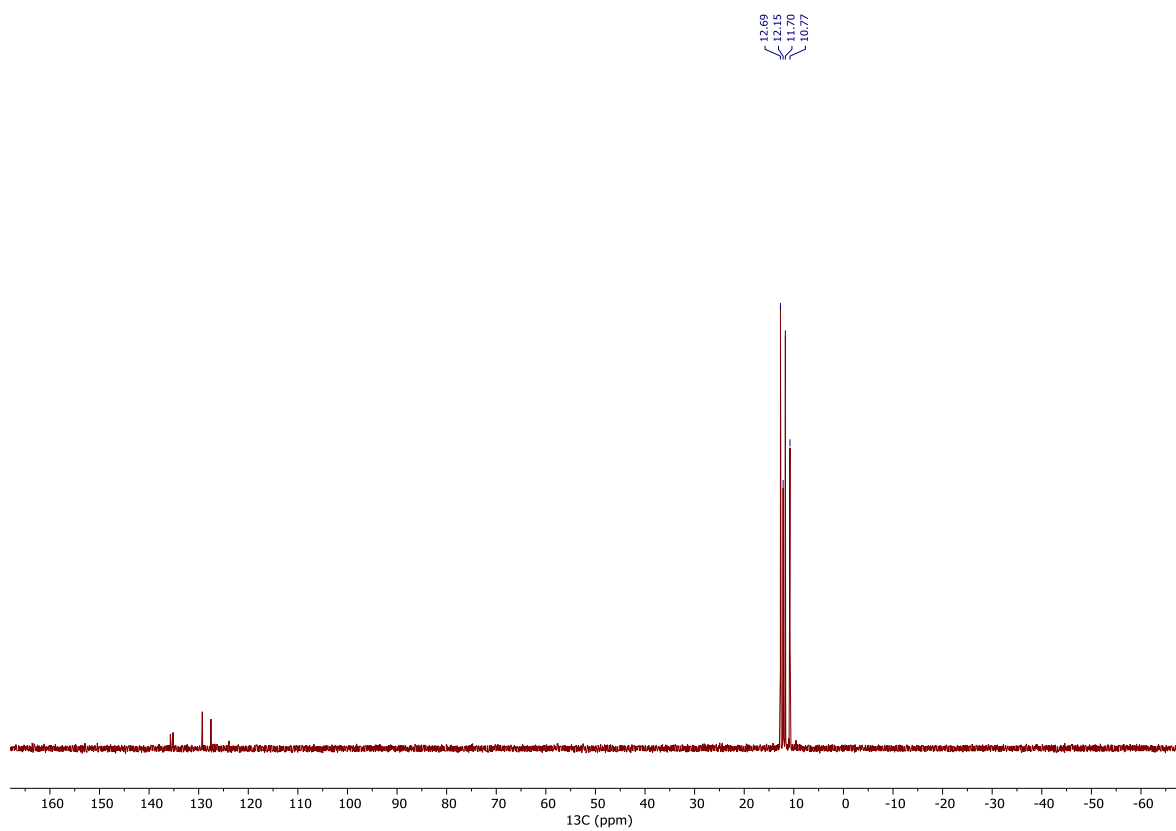


Figure S38:  $^1\text{H}$   $^1\text{H}$  COSY spectrum of Ce-DOTA-M7FPy.



**Figure S39:**  $^{19}\text{F}\{^1\text{H}\}$  NMR spectrum of Ce-DOTA-M7FPy.



**Figure S40:**  $^{13}\text{C}\{^1\text{H}\}$  NMR spectrum of Ce-DOTA-M7FPy.

# Pr-DOTA-M7FPy

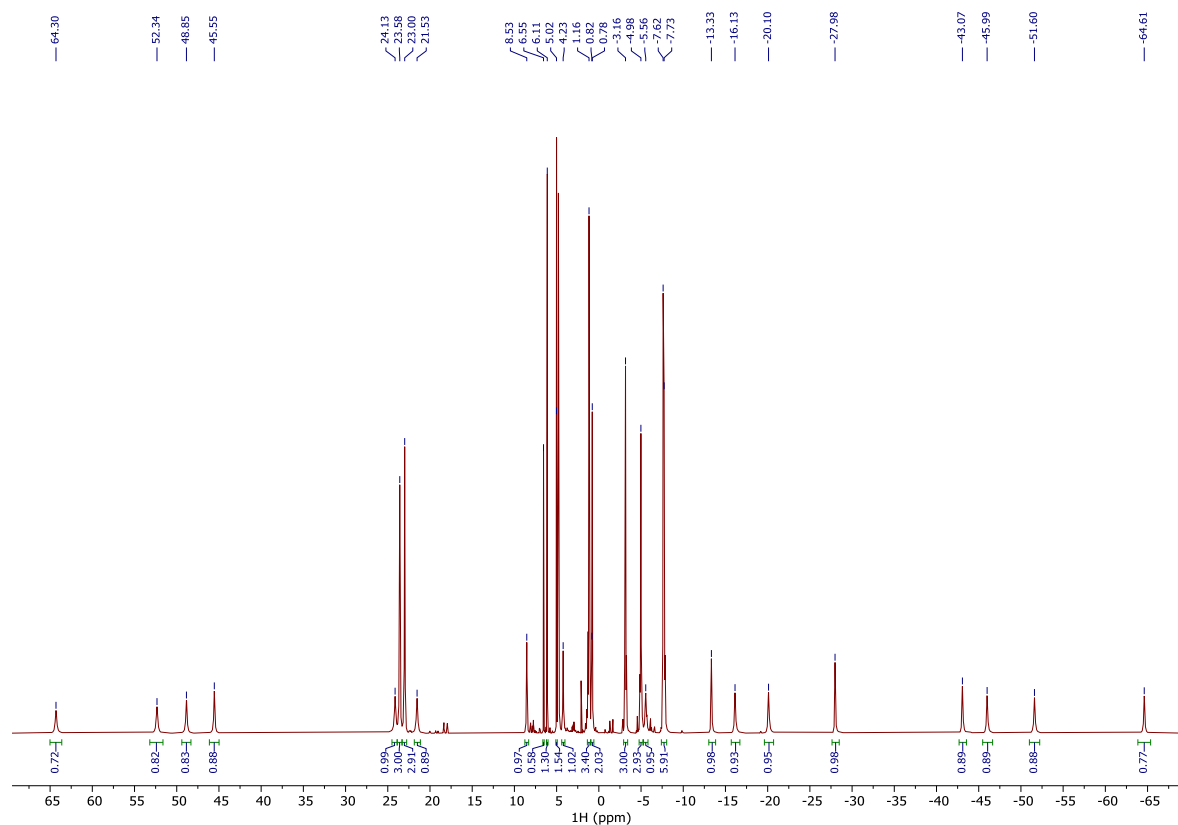


Figure S41:  $^1\text{H}$  NMR spectrum of Pr-DOTA-M7FPy.

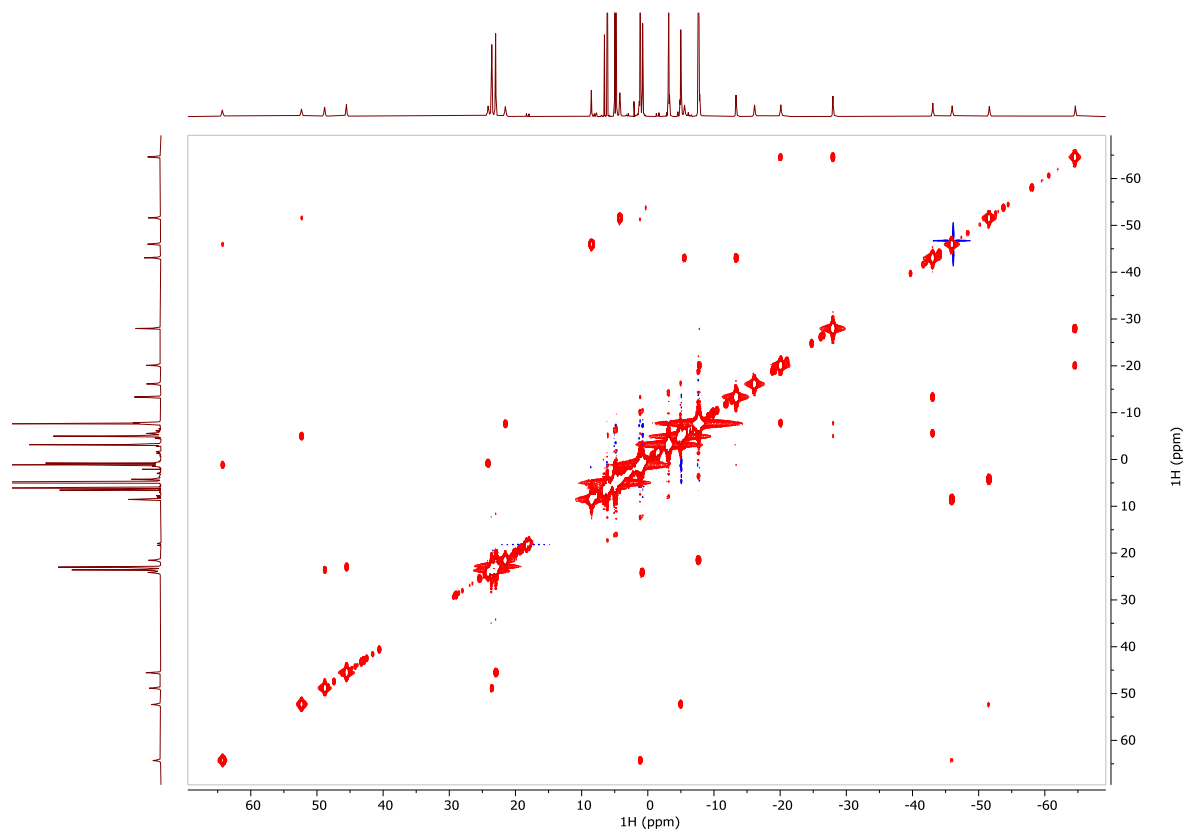


Figure S42:  $^1\text{H}$   $^1\text{H}$  COSY spectrum of Pr-DOTA-M7FPy.

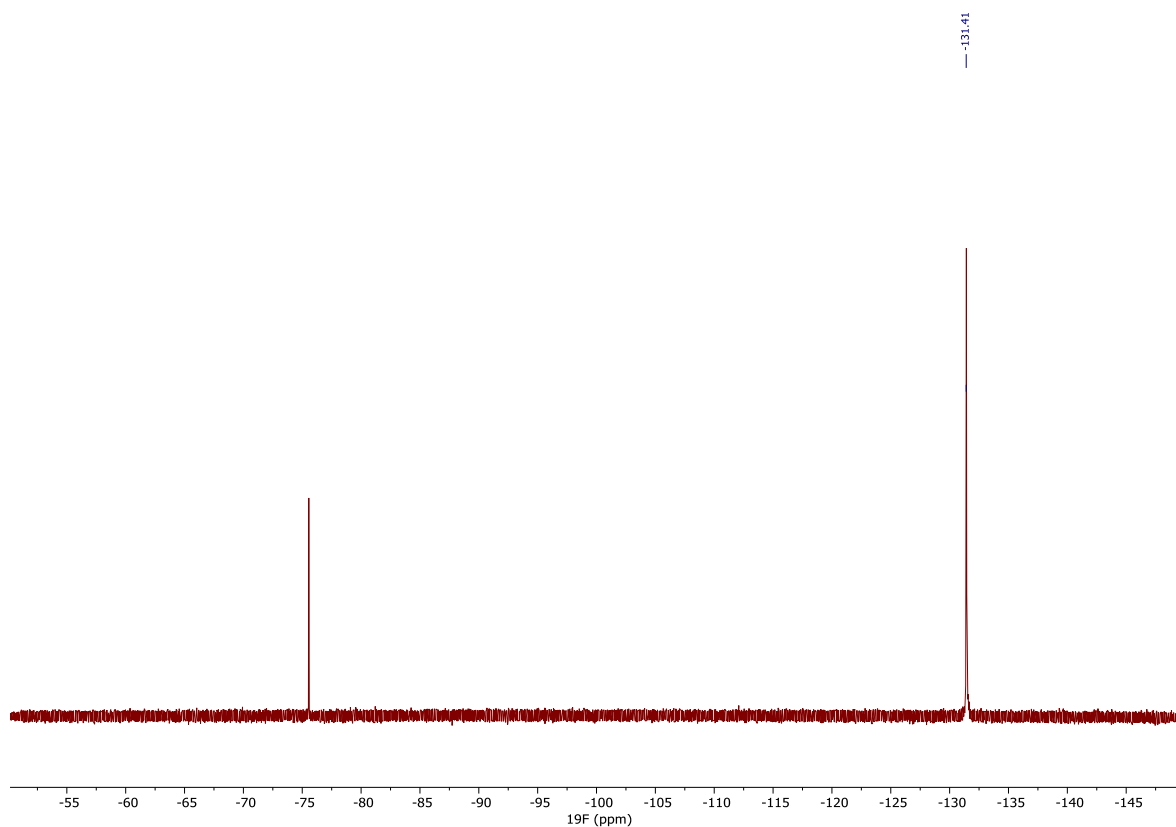


Figure S43:  $^{19}\text{F}\{^1\text{H}\}$  NMR spectrum of Pr-DOTA-M7FPy.

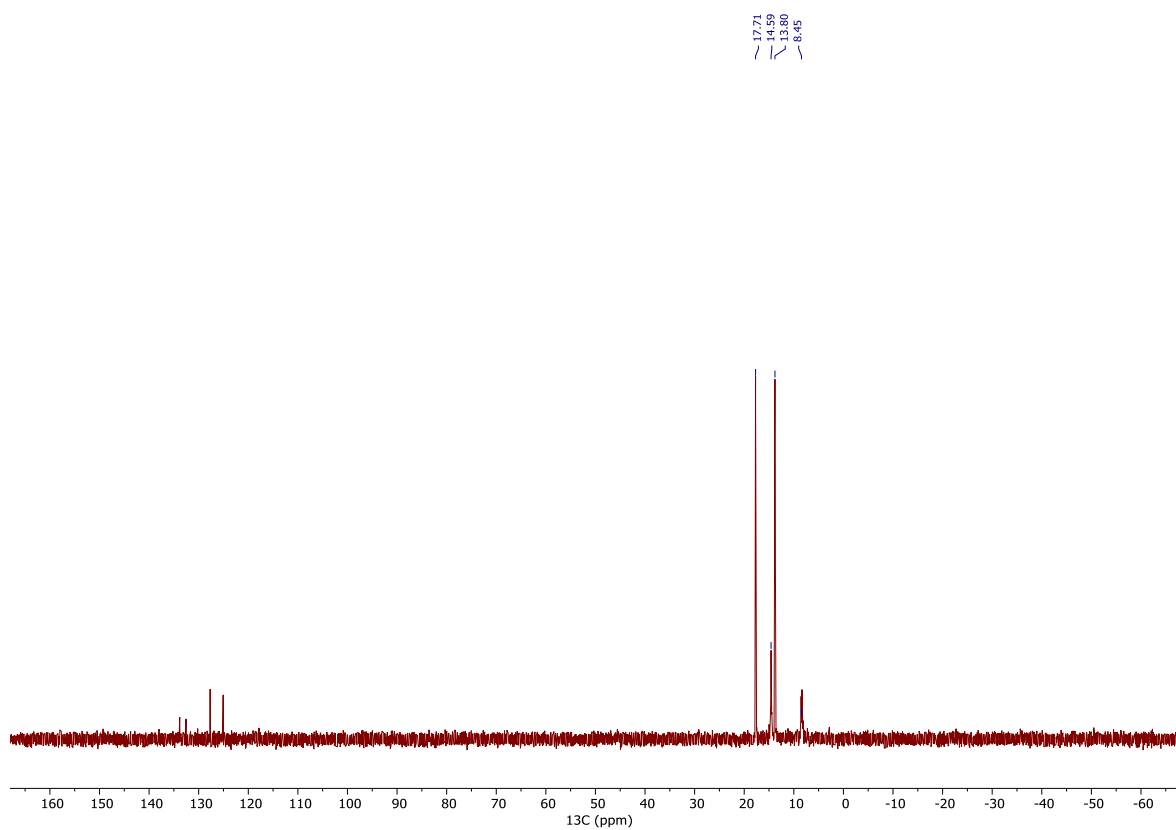


Figure S44:  $^{13}\text{C}\{^1\text{H}\}$  NMR spectrum of Pr-DOTA-M7FPy.



# Nd-DOTA-M7FPy

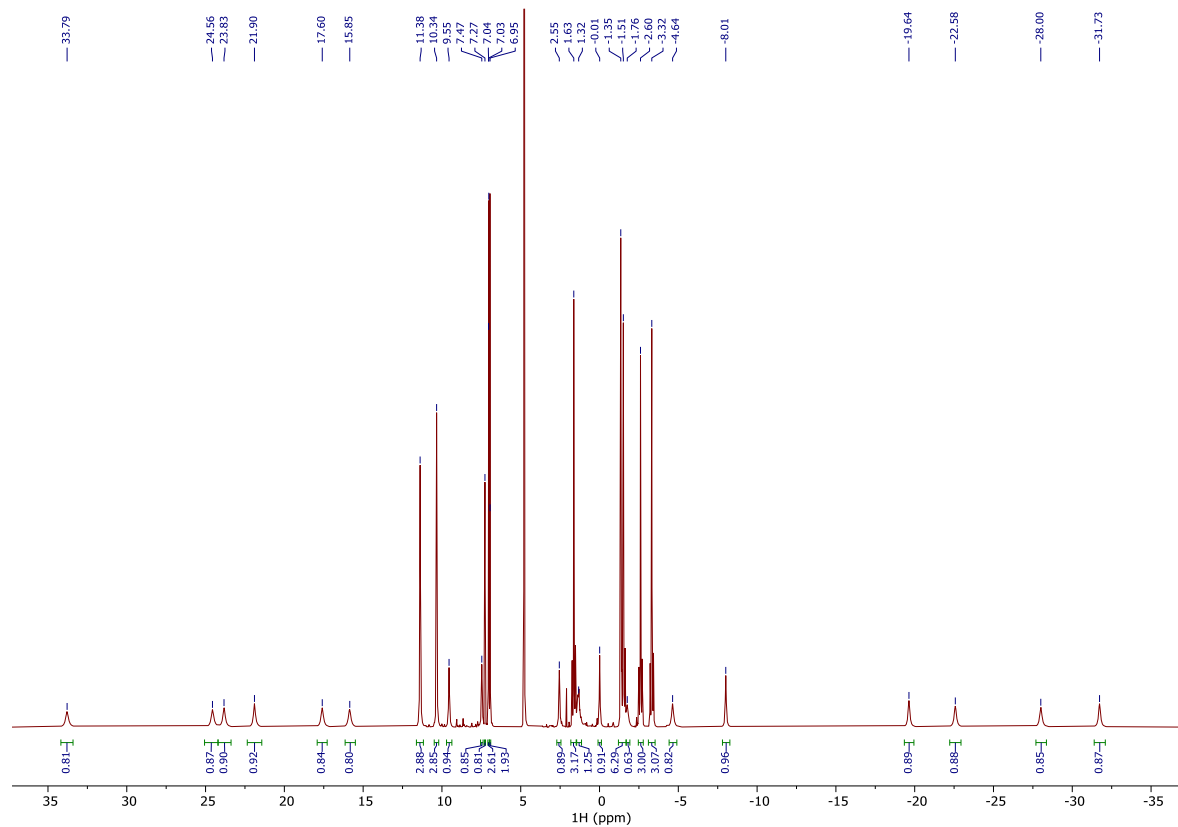


Figure S45:  $^1\text{H}$  NMR spectrum of Nd-DOTA-M7FPy.

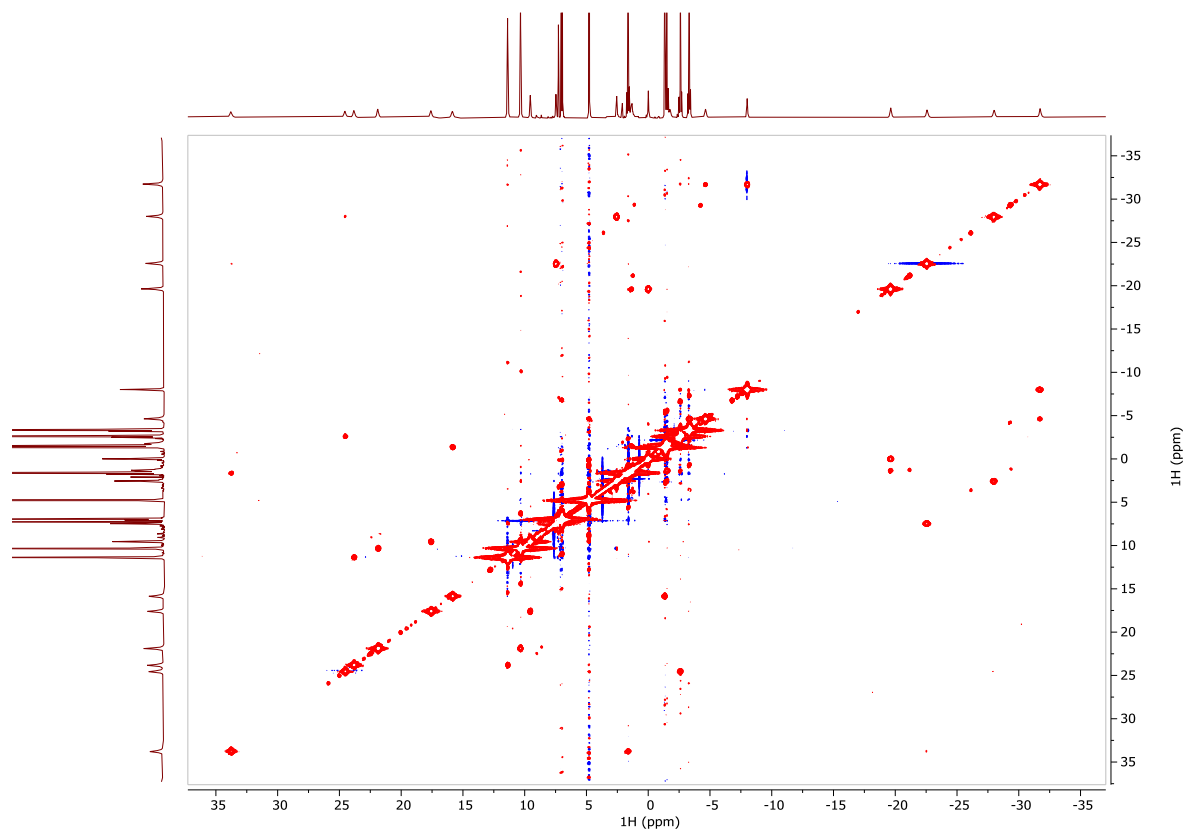
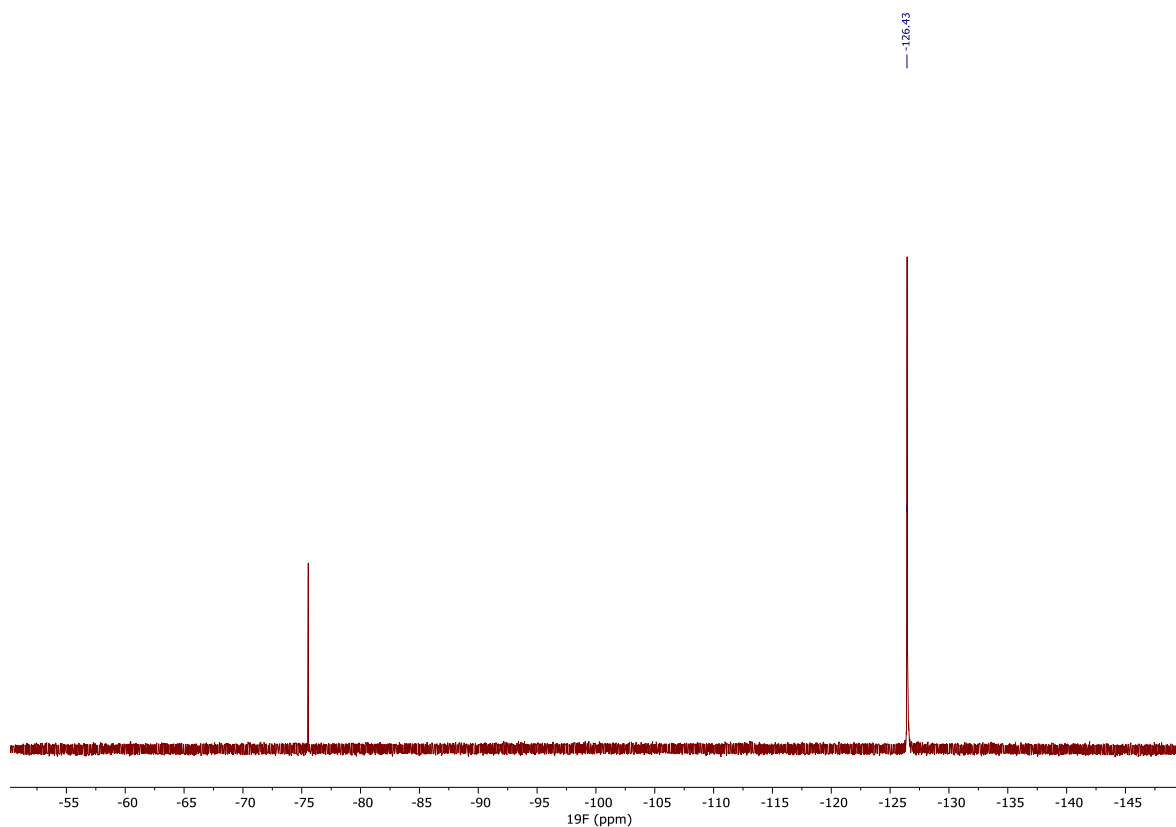
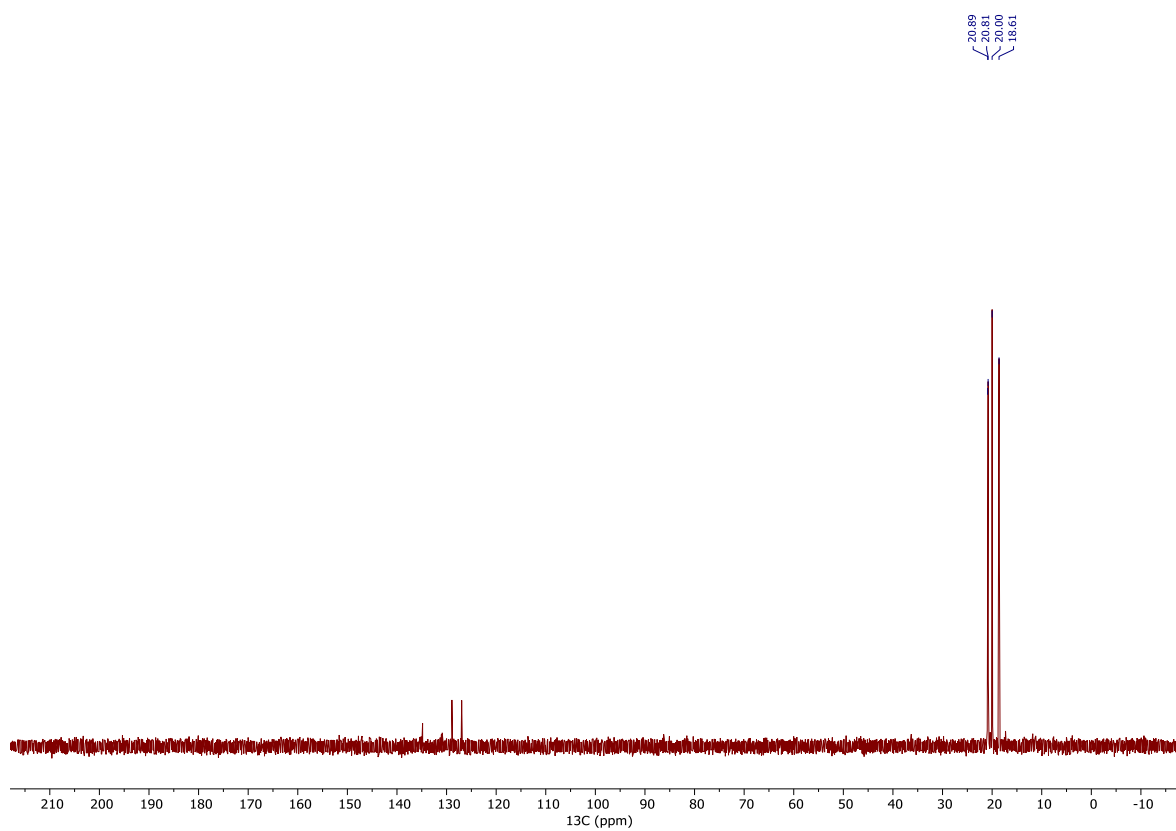


Figure S46:  $^1\text{H}$   $^1\text{H}$  COSY spectrum of Nd-DOTA-M7FPy.



**Figure S47:**  $^{19}\text{F}\{^1\text{H}\}$  NMR spectrum of Nd-DOTA-M7FPy.



**Figure S48:**  $^{13}\text{C}\{^1\text{H}\}$  NMR spectrum of Nd-DOTA-M7FPy.

# Sm-DOTA-M7FPy

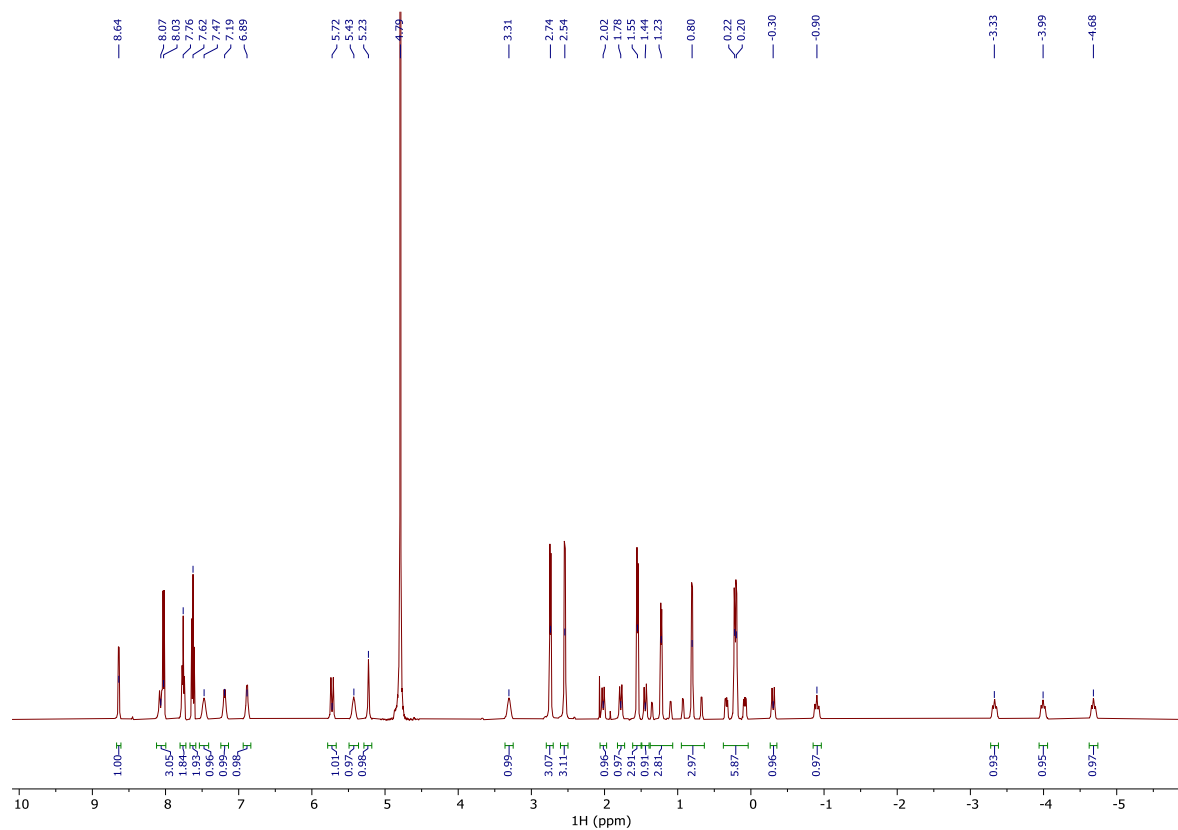


Figure S49:  $^1\text{H}$  NMR spectrum of Sm-DOTA-M7FPy.

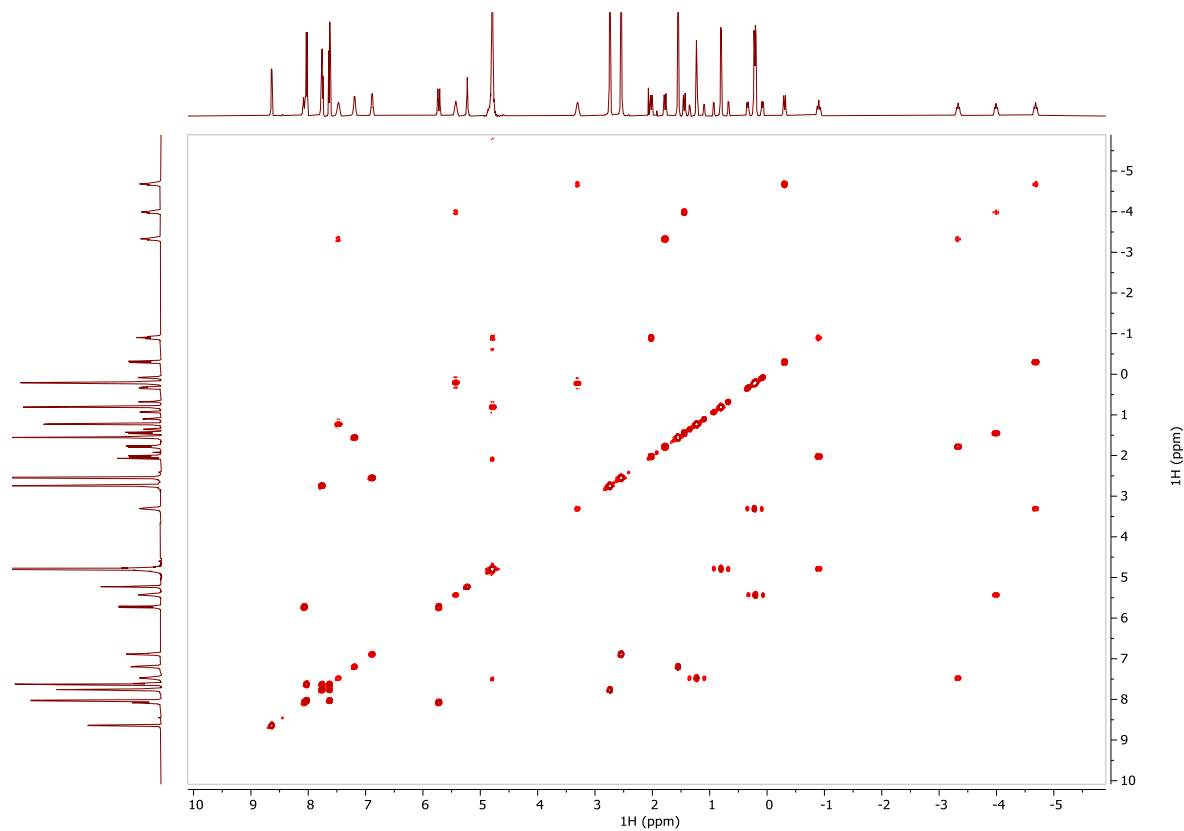
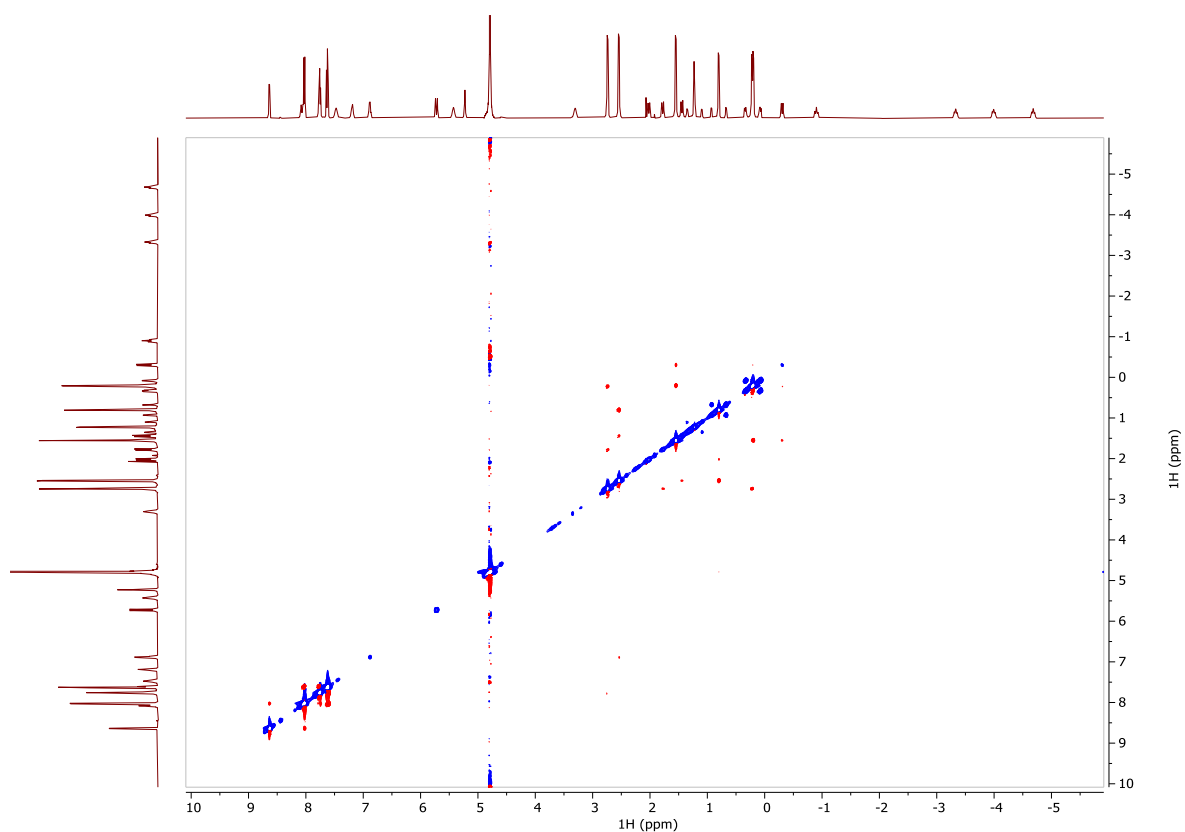
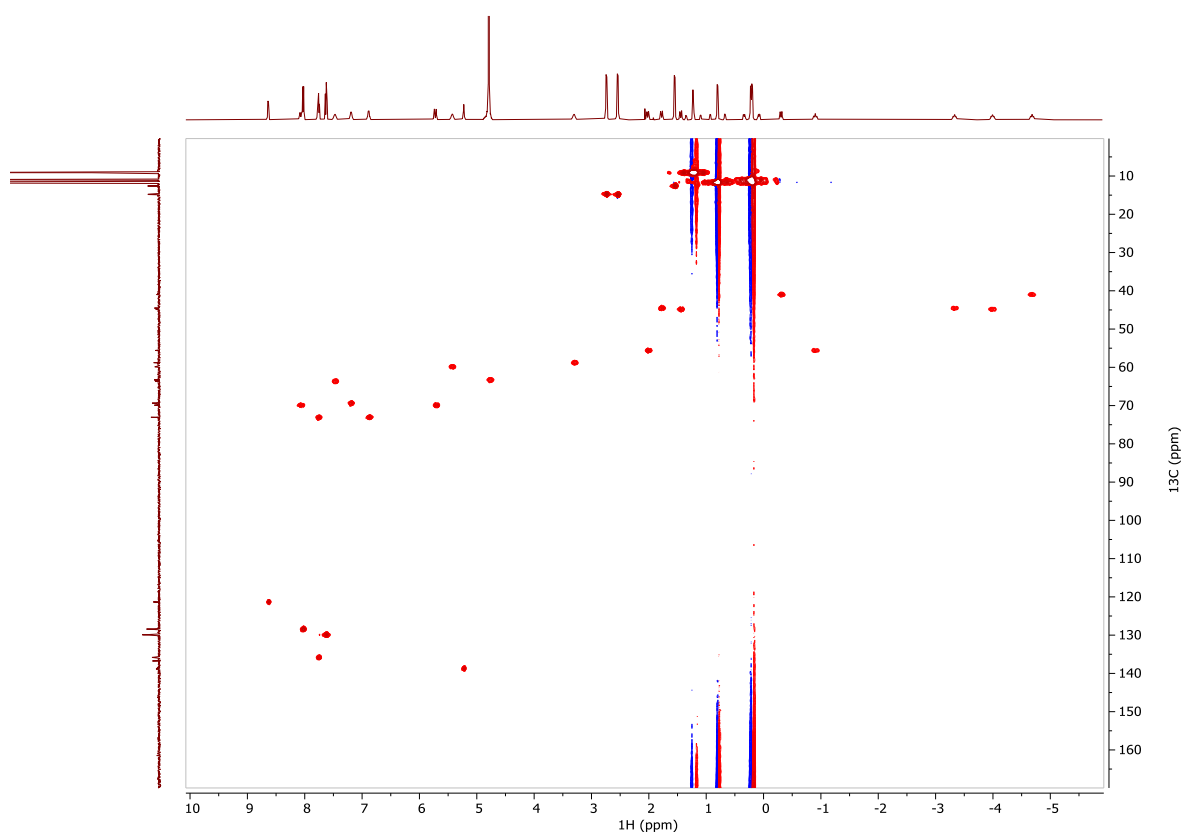


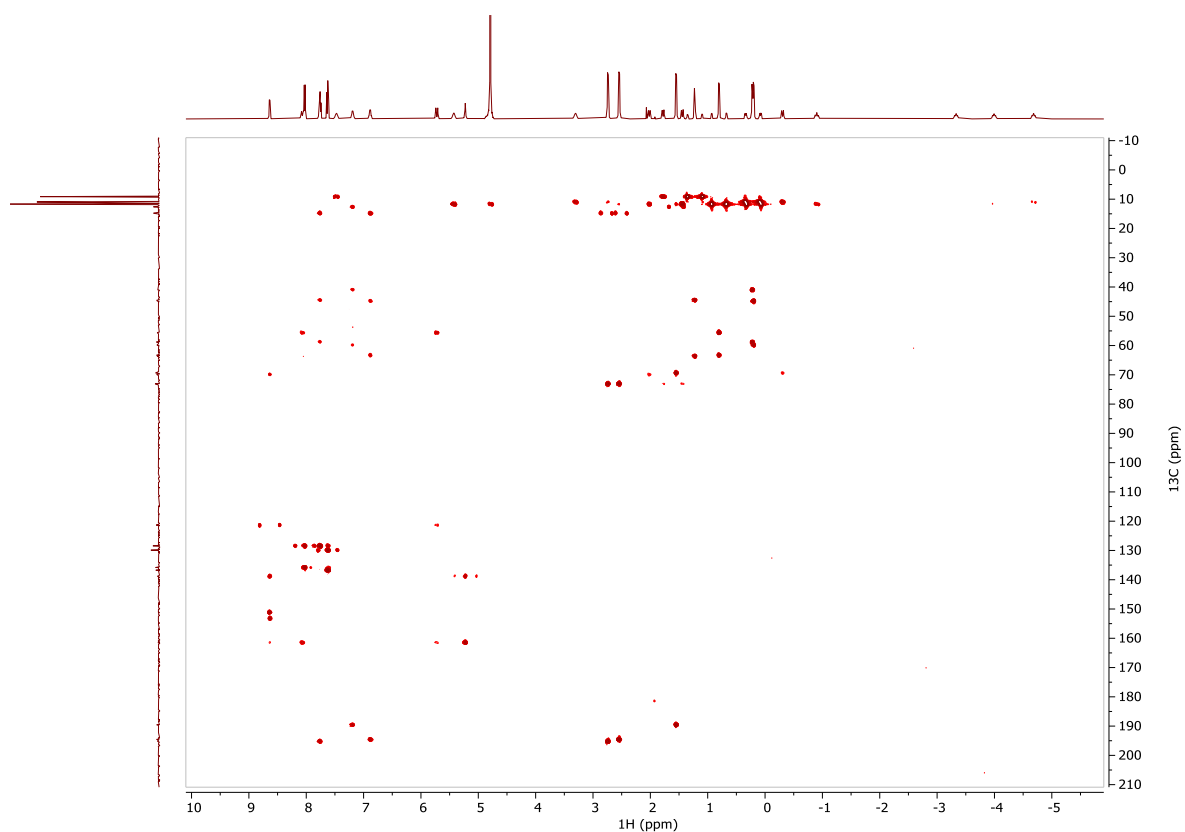
Figure S50:  $^1\text{H}$   $^1\text{H}$  COSY spectrum of Sm-DOTA-M7FPy.



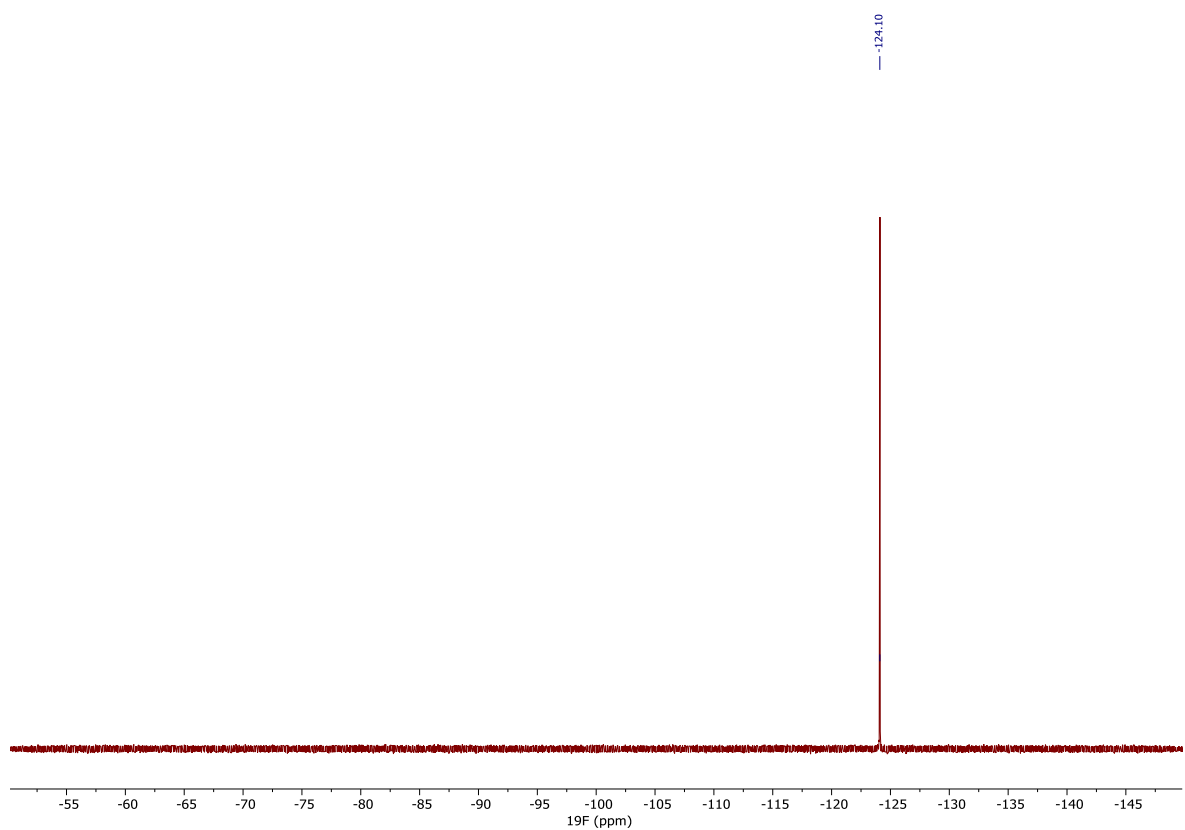
**Figure S51:**  $^1\text{H}$   $^1\text{H}$  NOESY spectrum of Sm-DOTA-M7FPy.



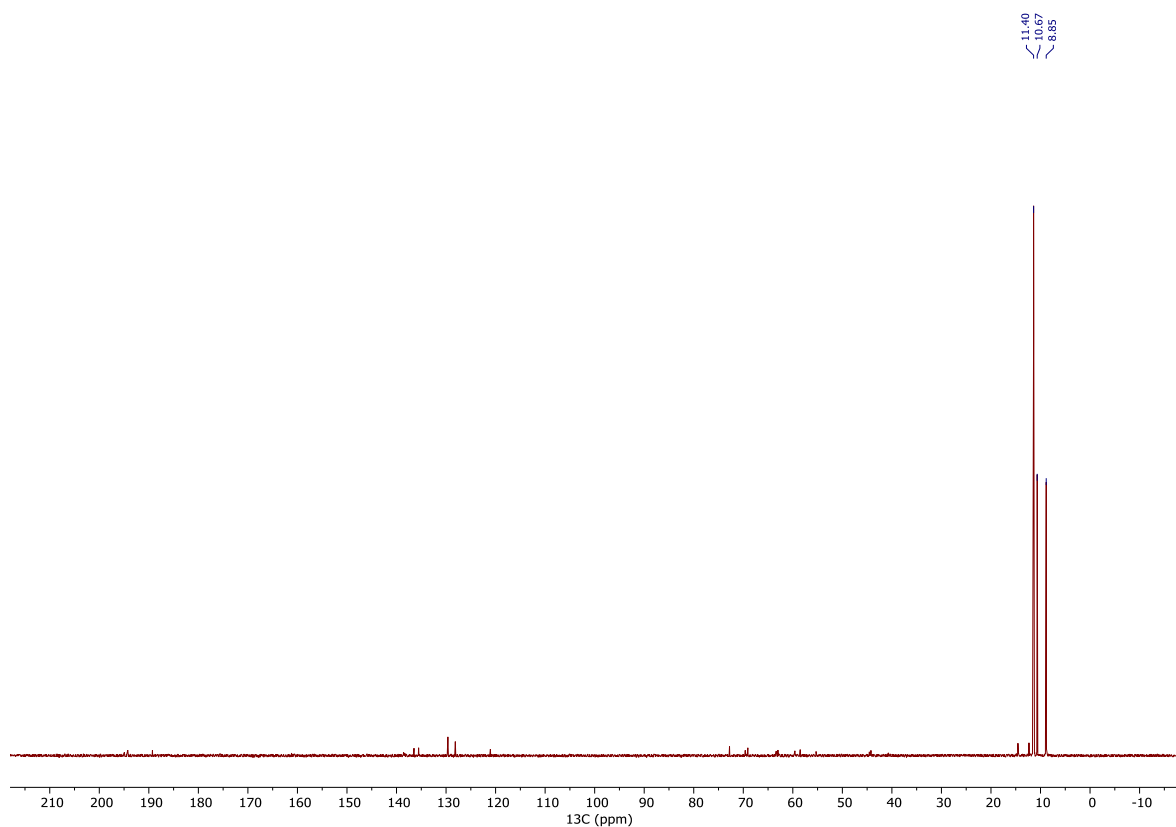
**Figure S52:**  $^1\text{H}$   $^{13}\text{C}$  HMQC spectrum of Sm-DOTA-M7FPy.



**Figure S53:**  $^1\text{H}$   $^{13}\text{C}$  HMBC spectrum of Sm-DOTA-M7FPy.



**Figure S54:**  $^{19}\text{F}\{^1\text{H}\}$  NMR spectrum of Sm-DOTA-M7FPy.



**Figure S55:**  $^{13}\text{C}\{^1\text{H}\}$  NMR spectrum of Sm-DOTA-M7FPy.

# Eu-DOTA-M7FPy

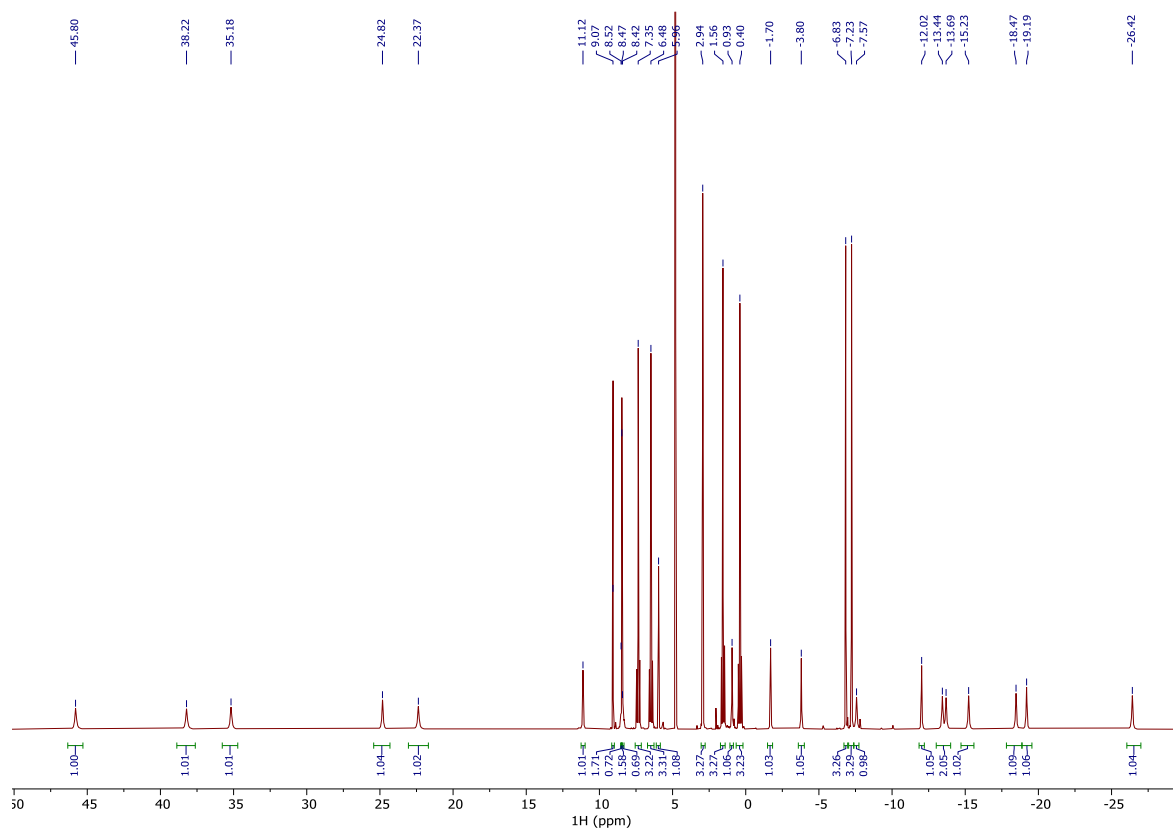


Figure S56:  $^1\text{H}$  NMR spectrum of Eu-DOTA-M7FPy.

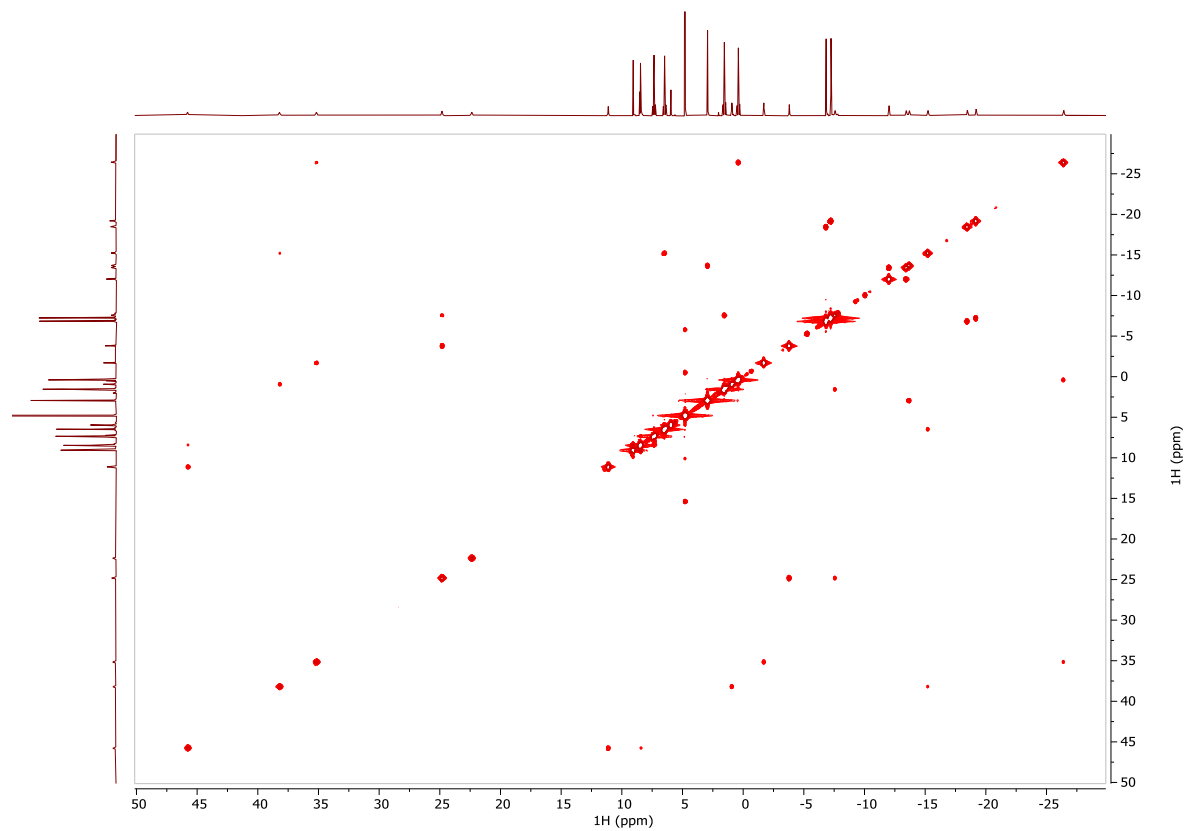


Figure S57:  $^1\text{H}$   $^1\text{H}$  COSY spectrum of Eu-DOTA-M7FPy.

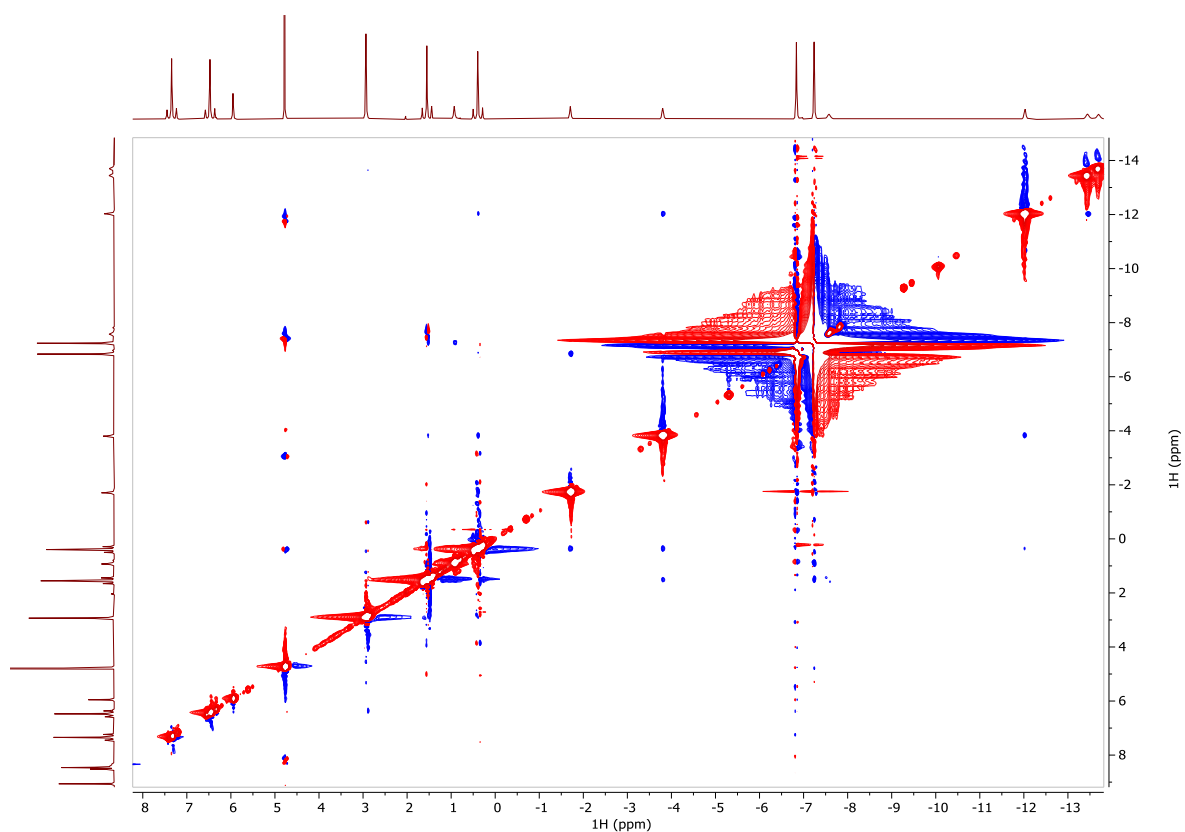


Figure S58:  $^1\text{H}$   $^1\text{H}$  ROESY spectrum of Eu-DOTA-M7FPy.

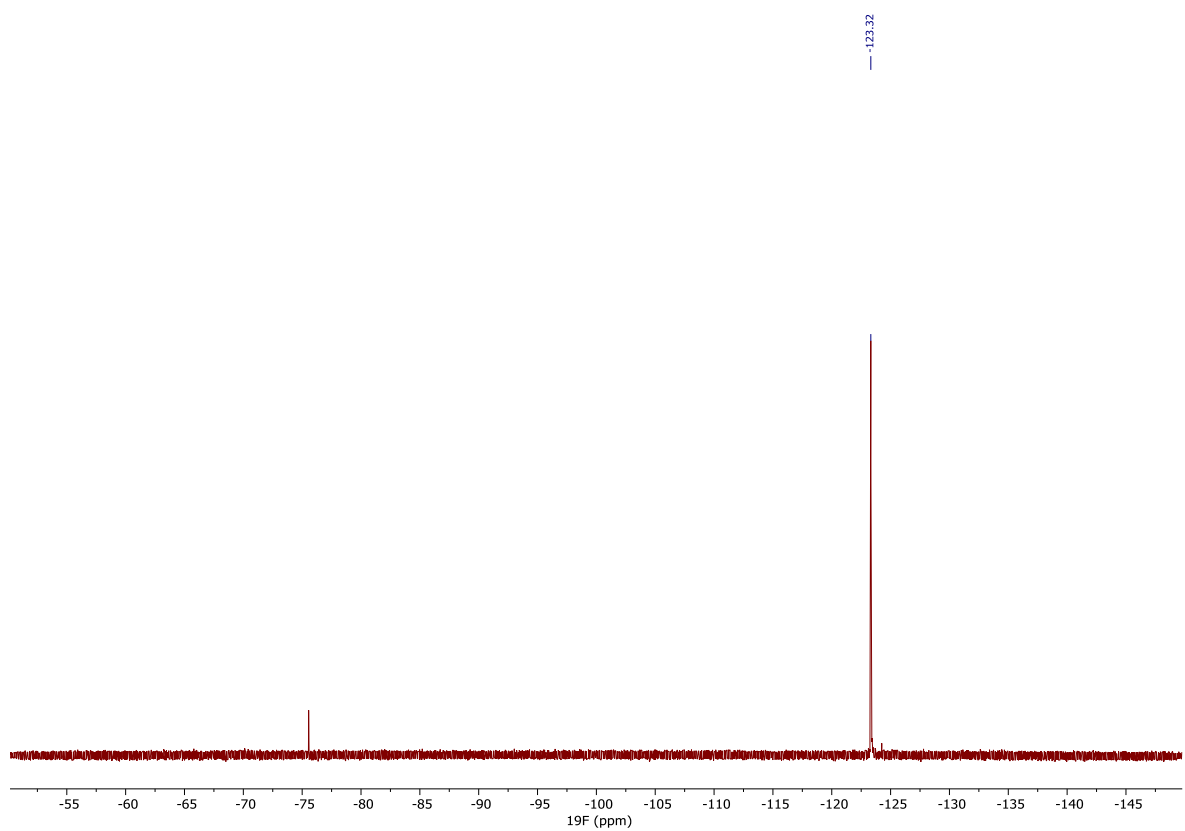
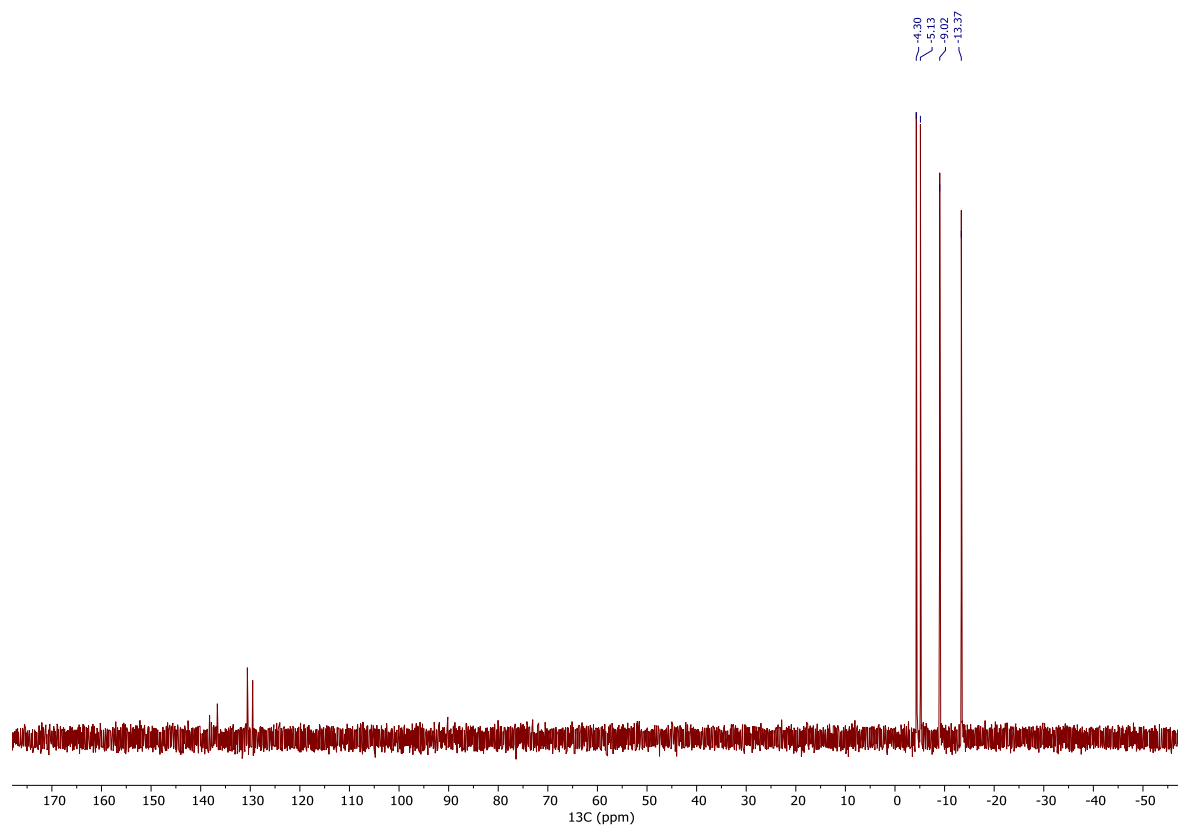


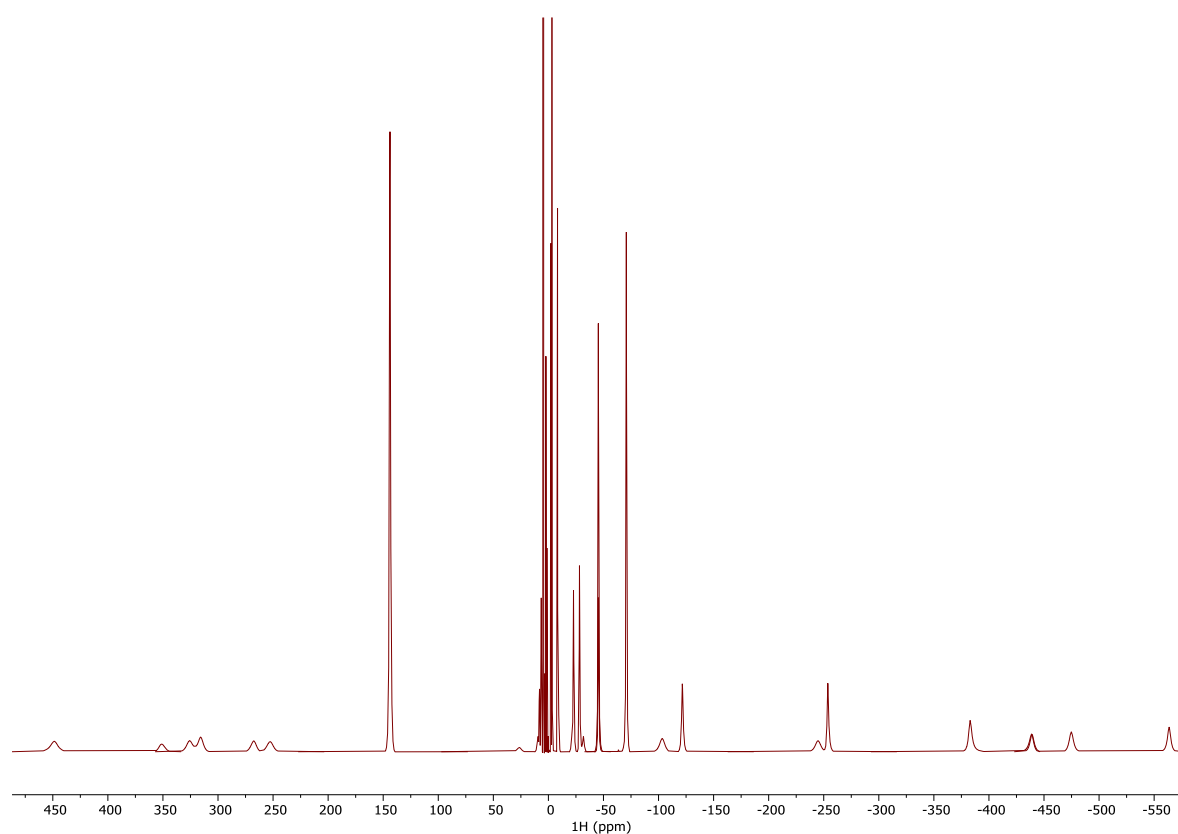
Figure S59:  $^{19}\text{F}\{^1\text{H}\}$  NMR spectrum of Eu-DOTA-M7FPy.





**Figure S60:**  $^{13}\text{C}\{^1\text{H}\}$  NMR spectrum of Eu-DOTA-M7FPy.

Tb-DOTA-M7FPy



**Figure S61:**  $^1\text{H}$  NMR spectrum of Tb-DOTA-M7FPy pieced together from multiple spectra with a sweep width of 154 ppm.

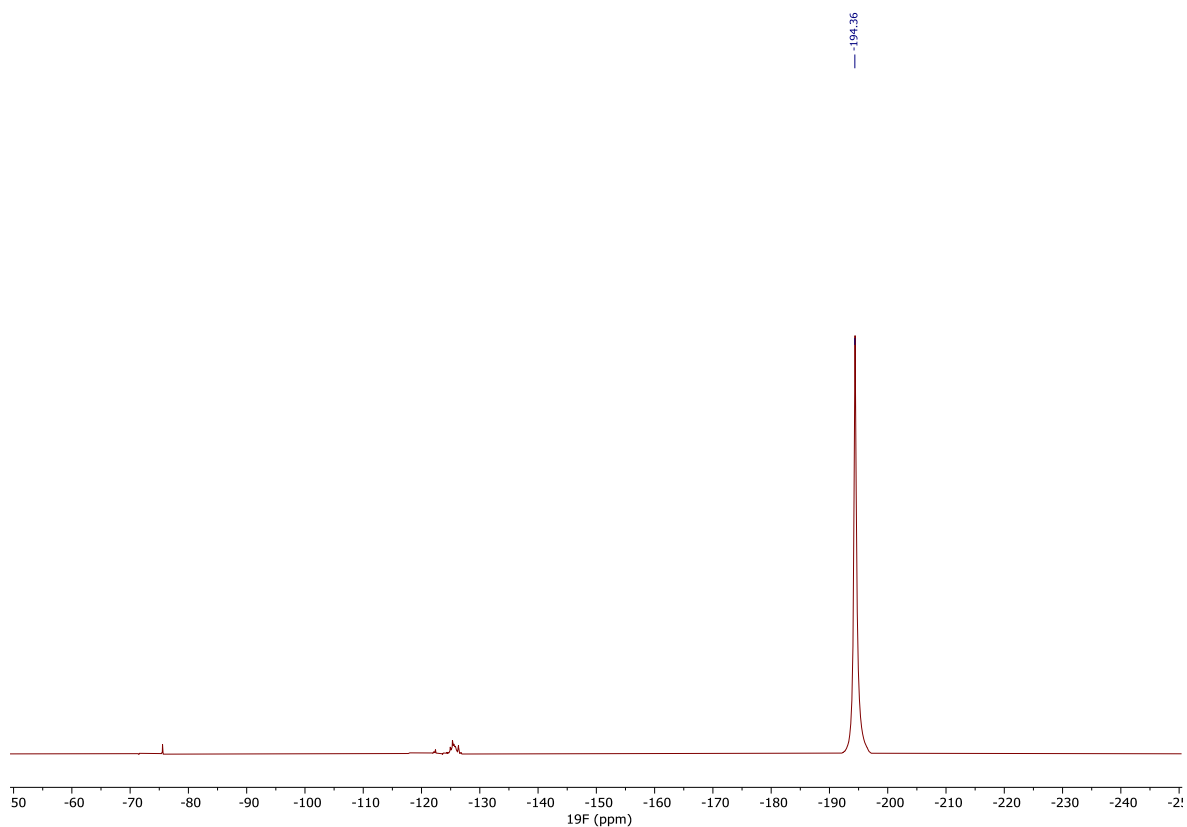


Figure S62:  $^{19}\text{F}\{^1\text{H}\}$  NMR spectrum of Tb-DOTA-M7FPy.

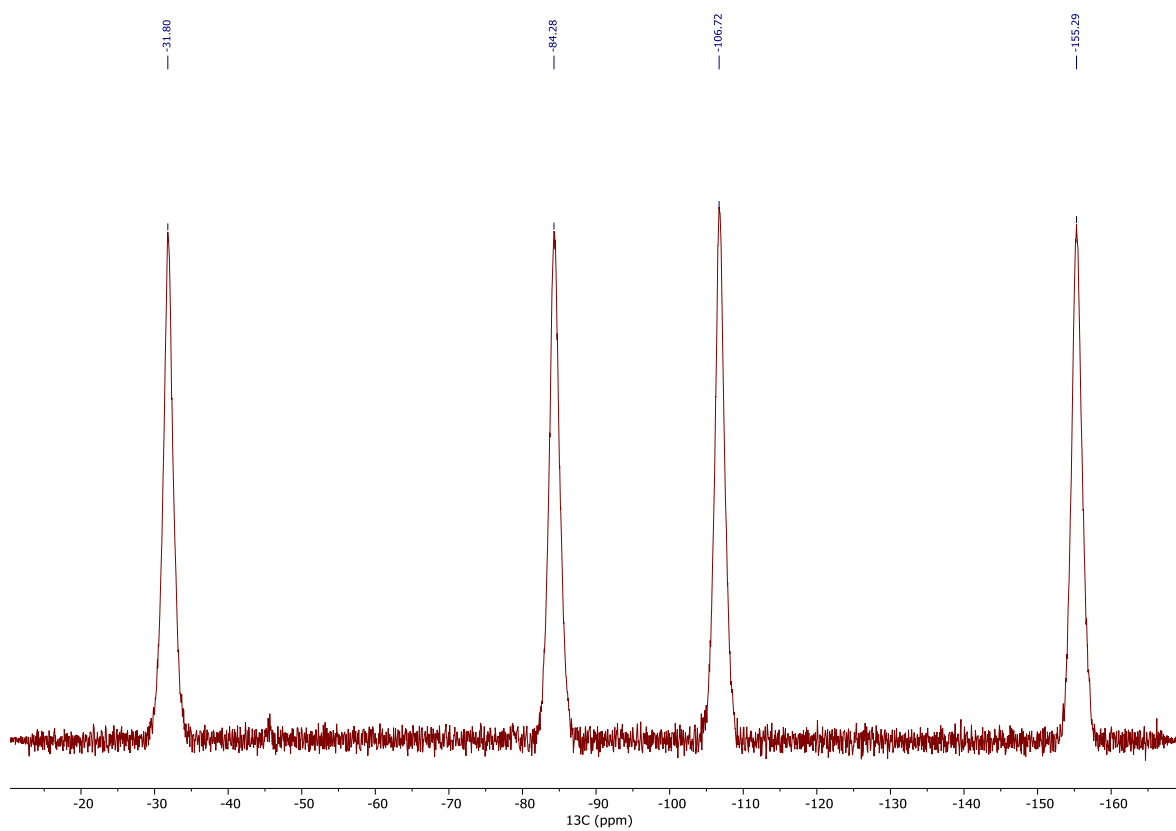
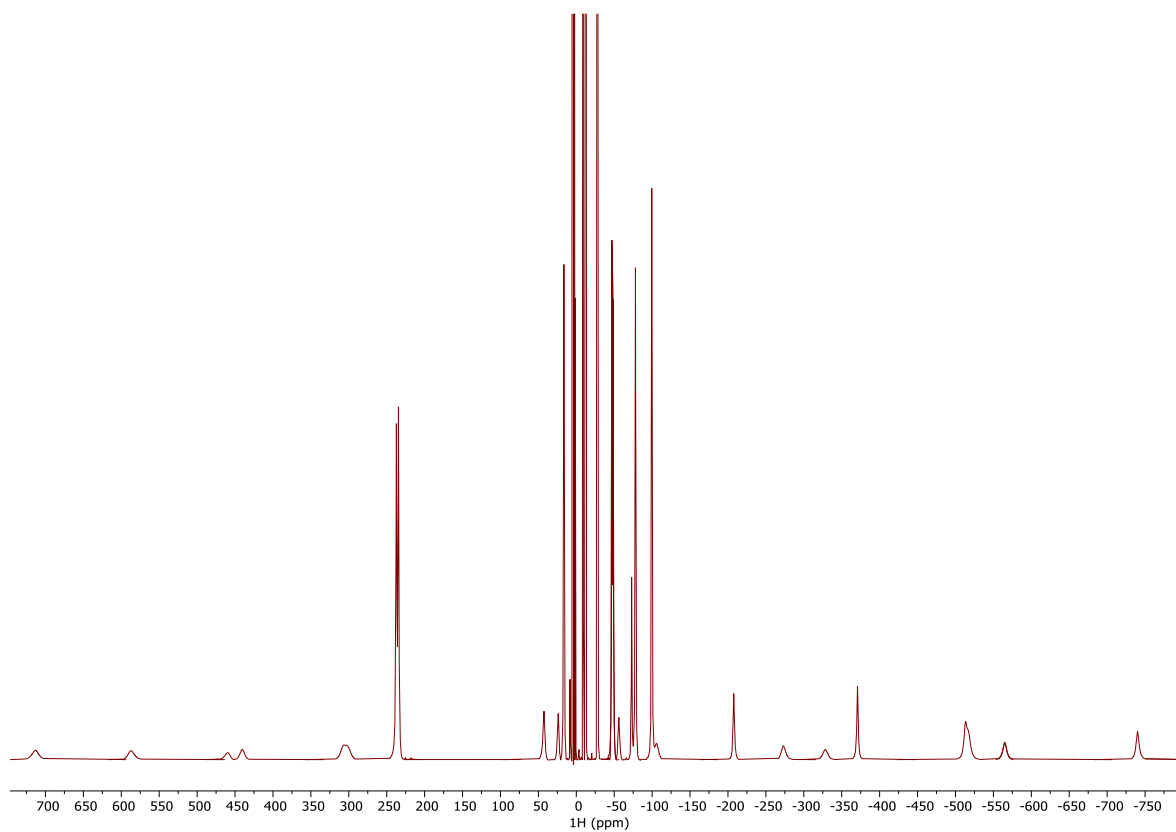


Figure S63:  $^{13}\text{C}$  NMR spectrum of Tb-DOTA-M7FPy.

Dy-DOTA-M7FPy



**Figure S64:** <sup>1</sup>H NMR spectrum of Dy-DOTA-M7FPy pieced together from multiple spectra with a sweep width of 154 ppm.



Figure S65:  $^{19}\text{F}\{^1\text{H}\}$  NMR spectrum of Dy-DOTA-M7FPy.

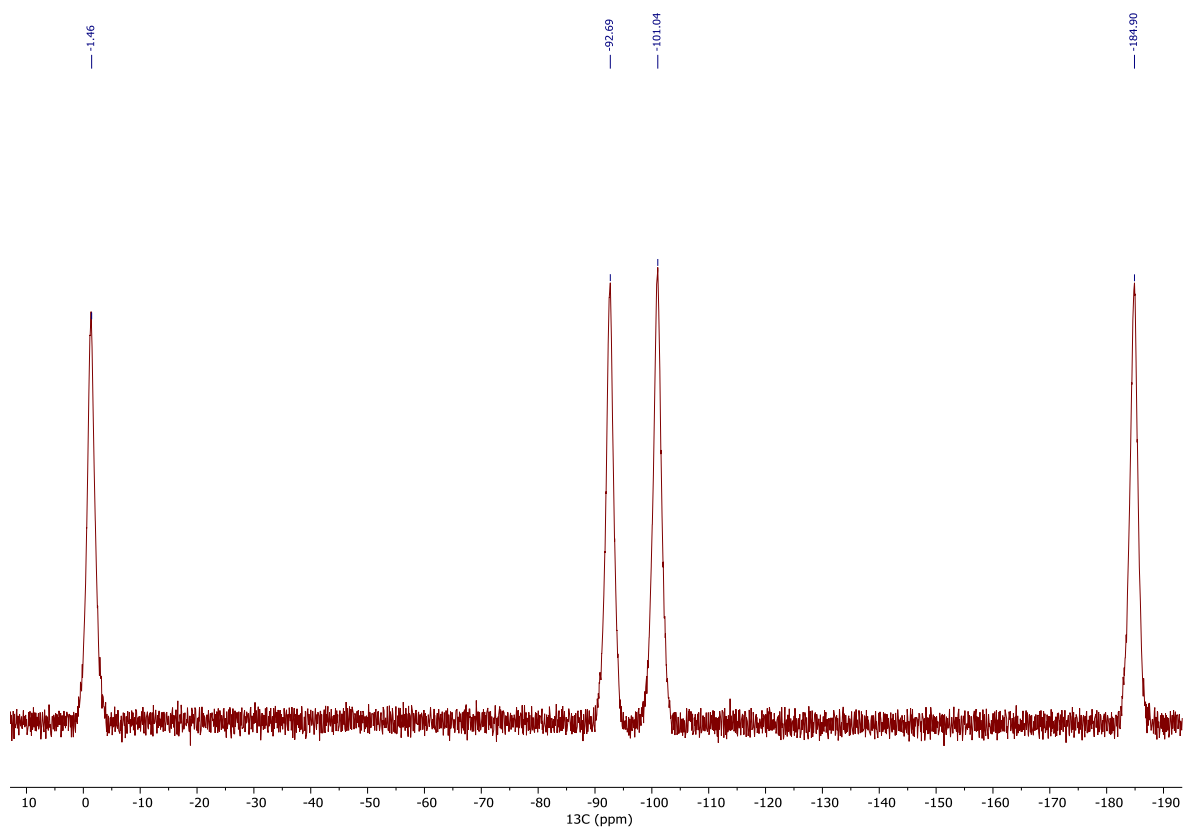
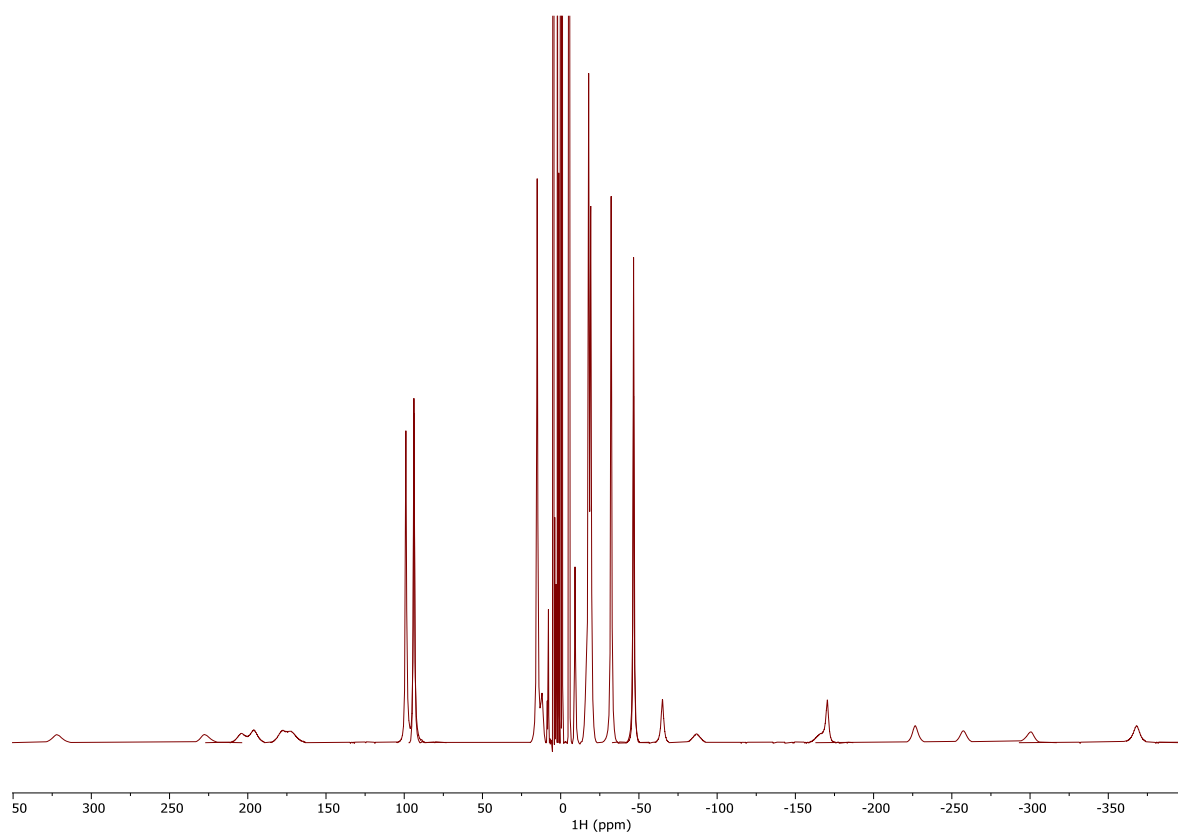
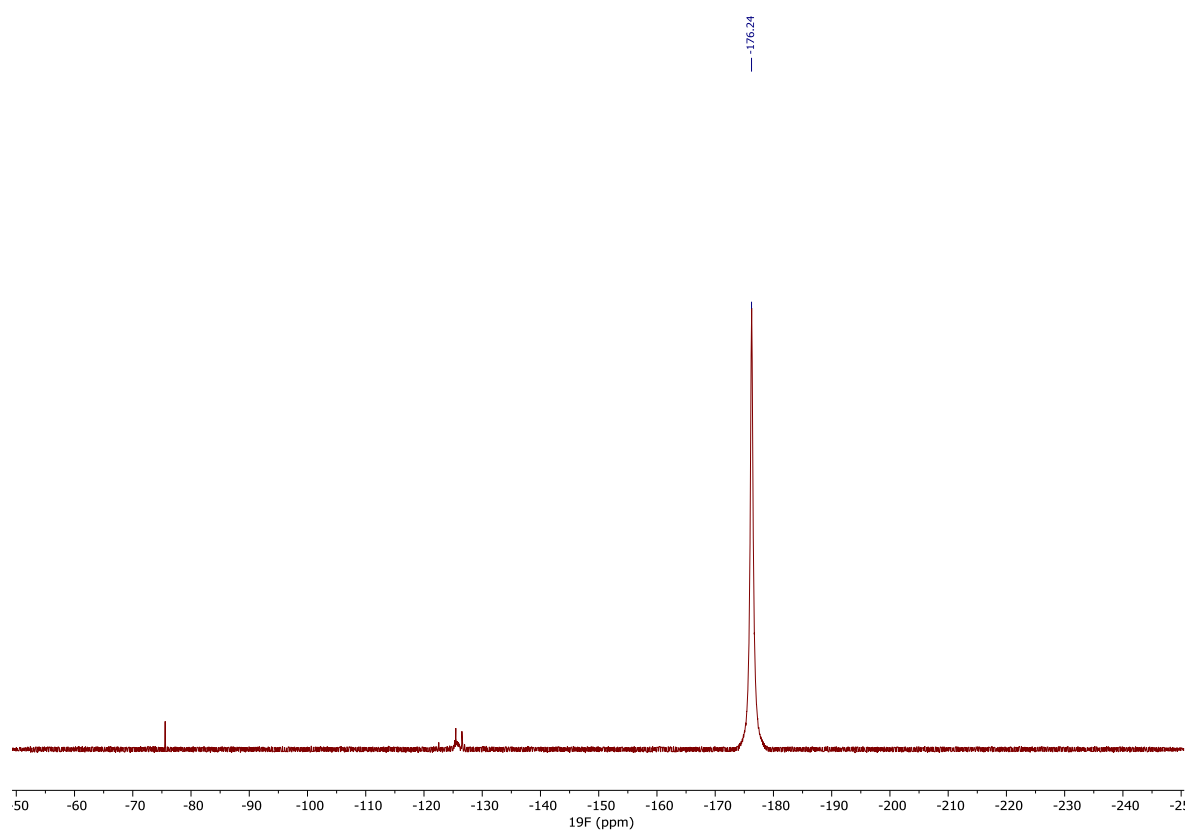


Figure S66:  $^{13}\text{C}$  NMR spectrum of Dy-DOTA-M7FPy.

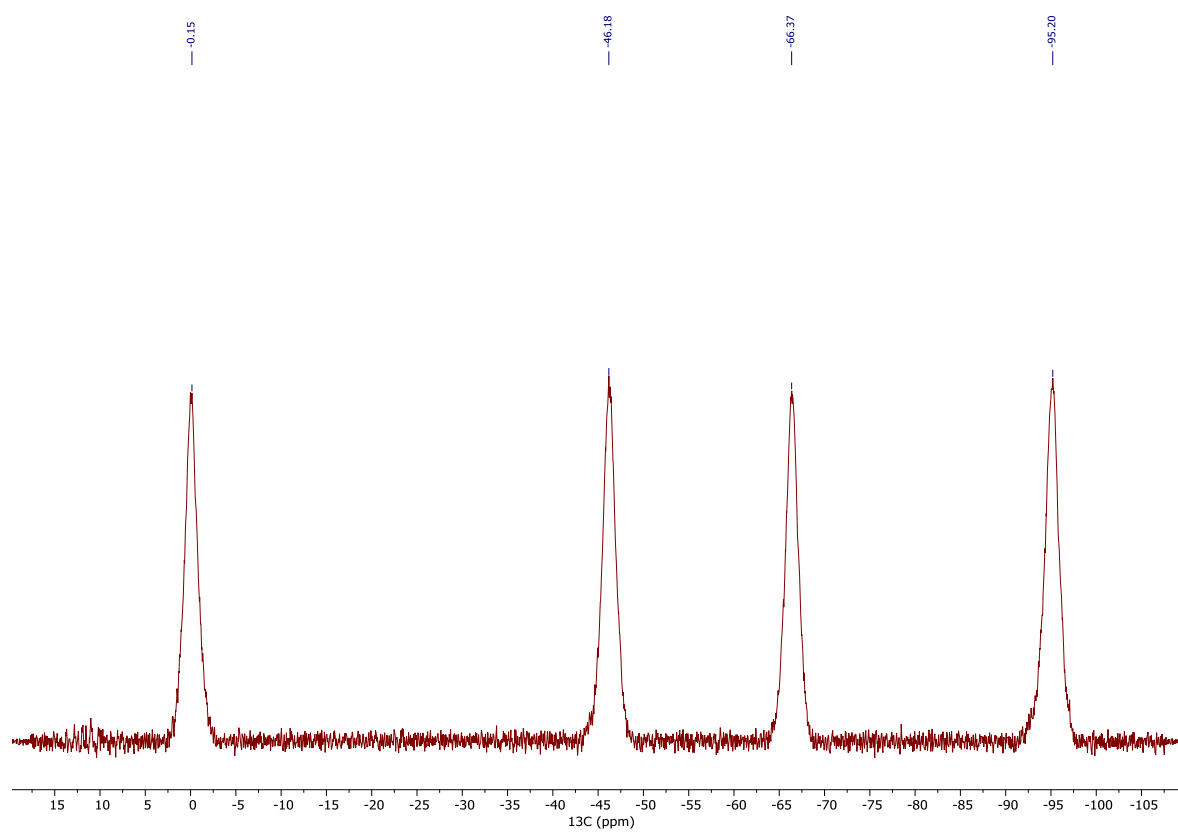
Ho-DOTA-M7FPy



**Figure S67:**  $^1\text{H}$  NMR spectrum of Ho-DOTA-M7FPy pieced together from multiple spectra with a sweep width of 154 ppm.

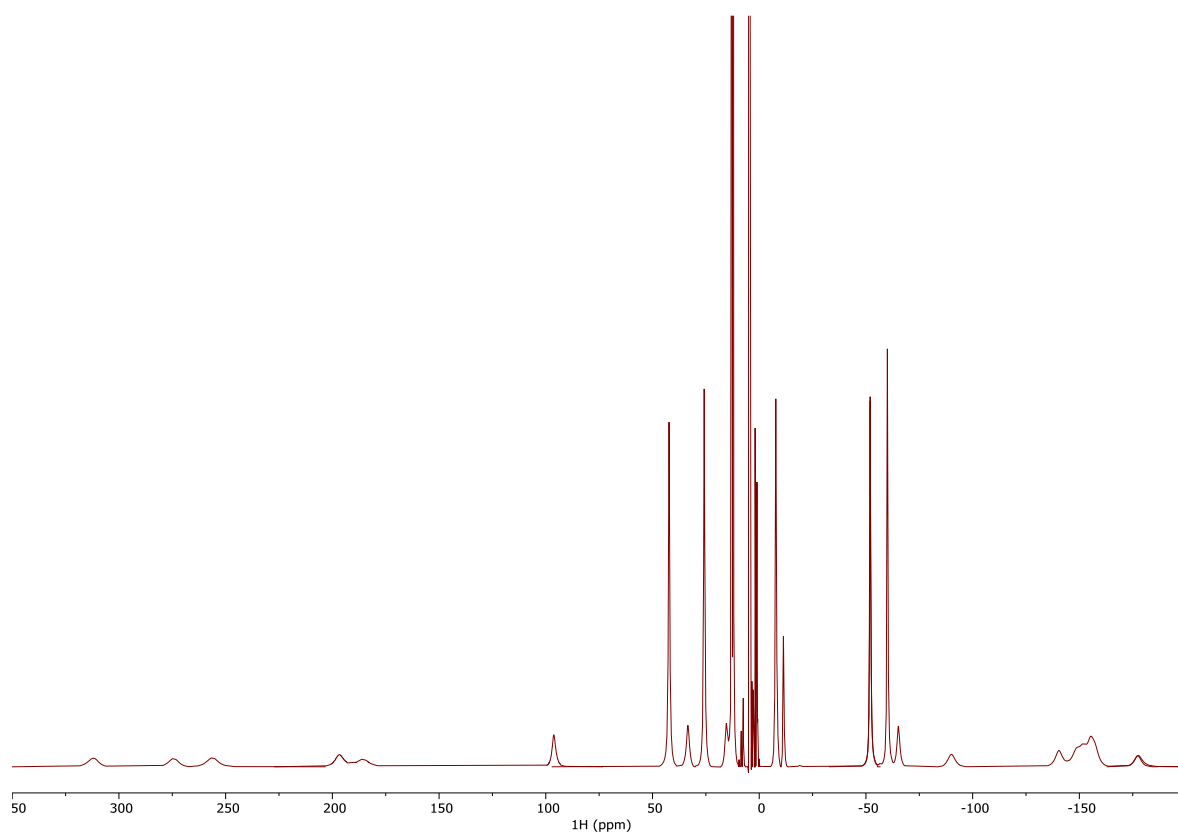


**Figure S68:**  $^{19}\text{F}\{^1\text{H}\}$  NMR spectrum of Ho-DOTA-M7FPy.



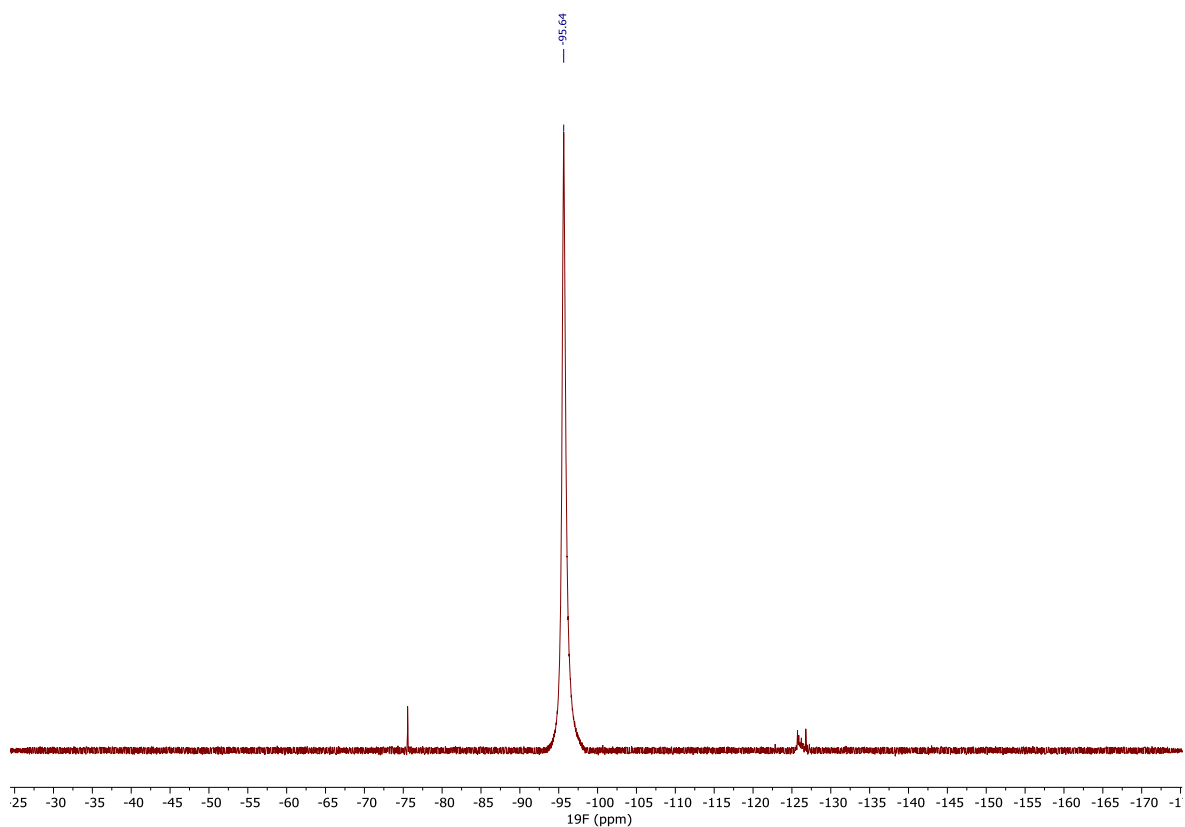
**Figure S69:**  $^{13}\text{C}$  NMR spectrum of Ho-DOTA-M7FPy.

Er-DOTA-M7FPy

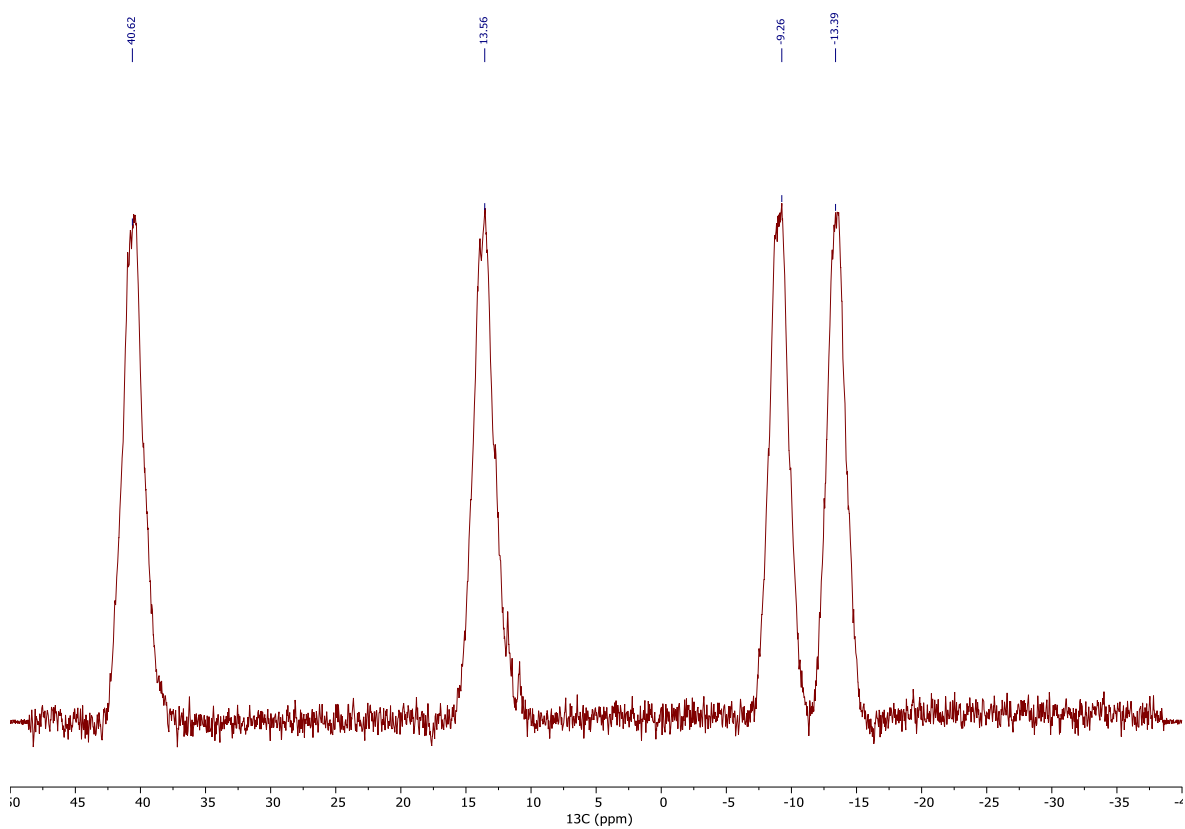


**Figure S70:**  $^1\text{H}$  NMR spectrum of Er-DOTA-M7FPy pieced together from multiple spectra with a sweep width of 154 ppm.



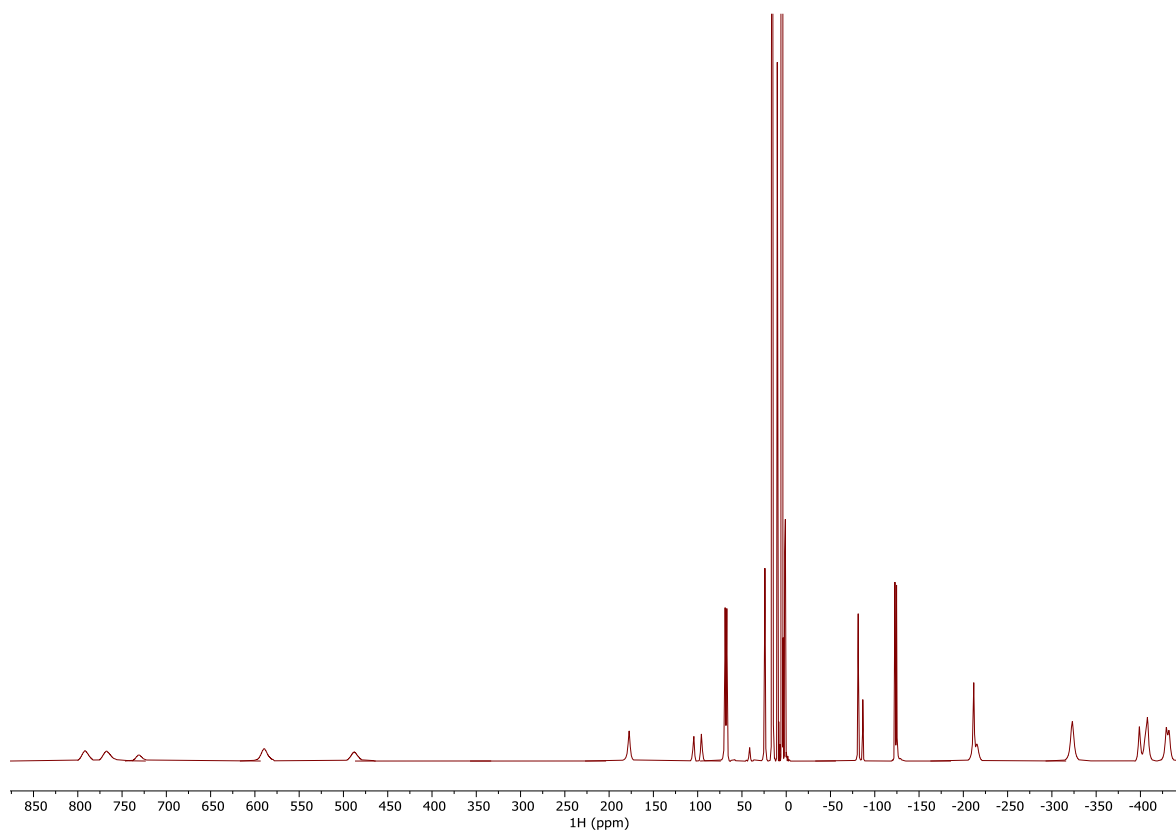


**Figure S71:**  $^{19}\text{F}\{^1\text{H}\}$  NMR spectrum of Er-DOTA-M7FPy.



**Figure S72:**  $^{13}\text{C}$  NMR spectrum of Er-DOTA-M7FPy.

Tm-DOTA-M7FPy



**Figure S73:** <sup>1</sup>H NMR spectrum of Tm-DOTA-M7FPy pieced together from multiple spectra with a sweep width of 154 ppm.

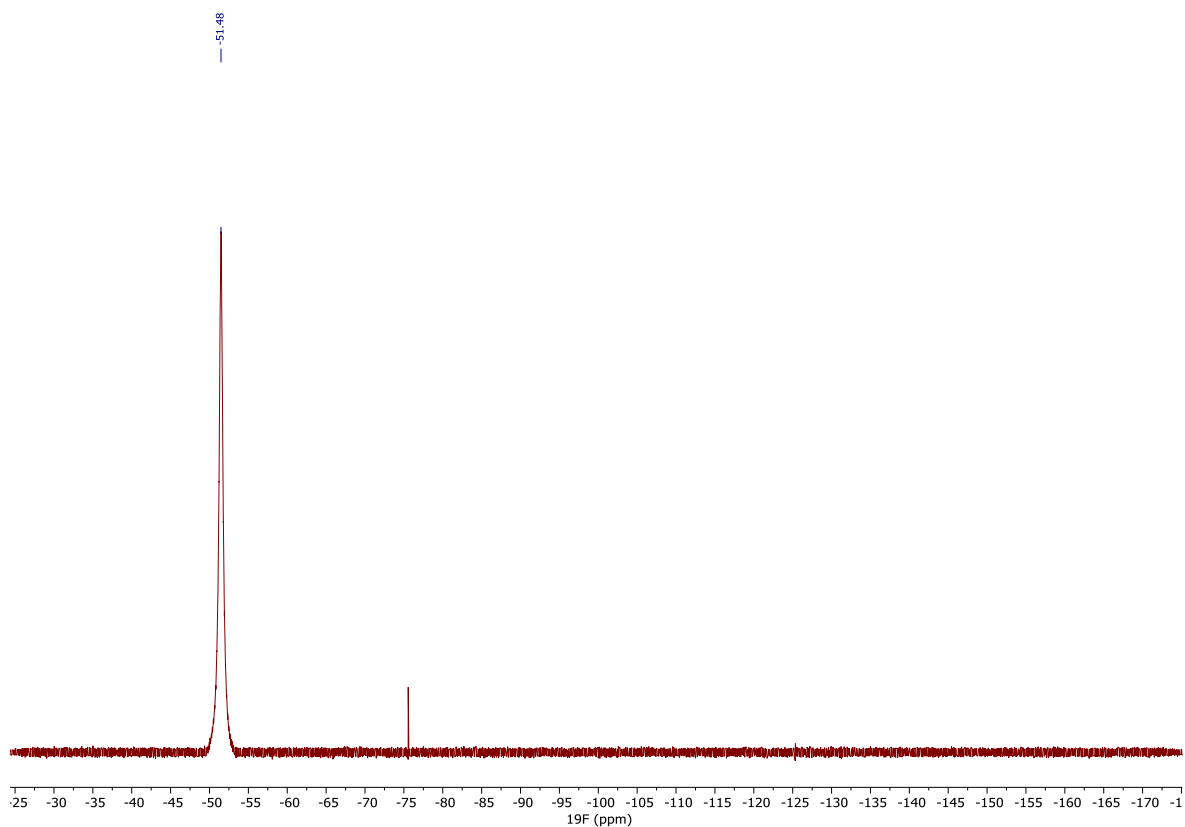


Figure S74:  $^{19}\text{F}\{^1\text{H}\}$  NMR spectrum of Tm-DOTA-M7FPy.

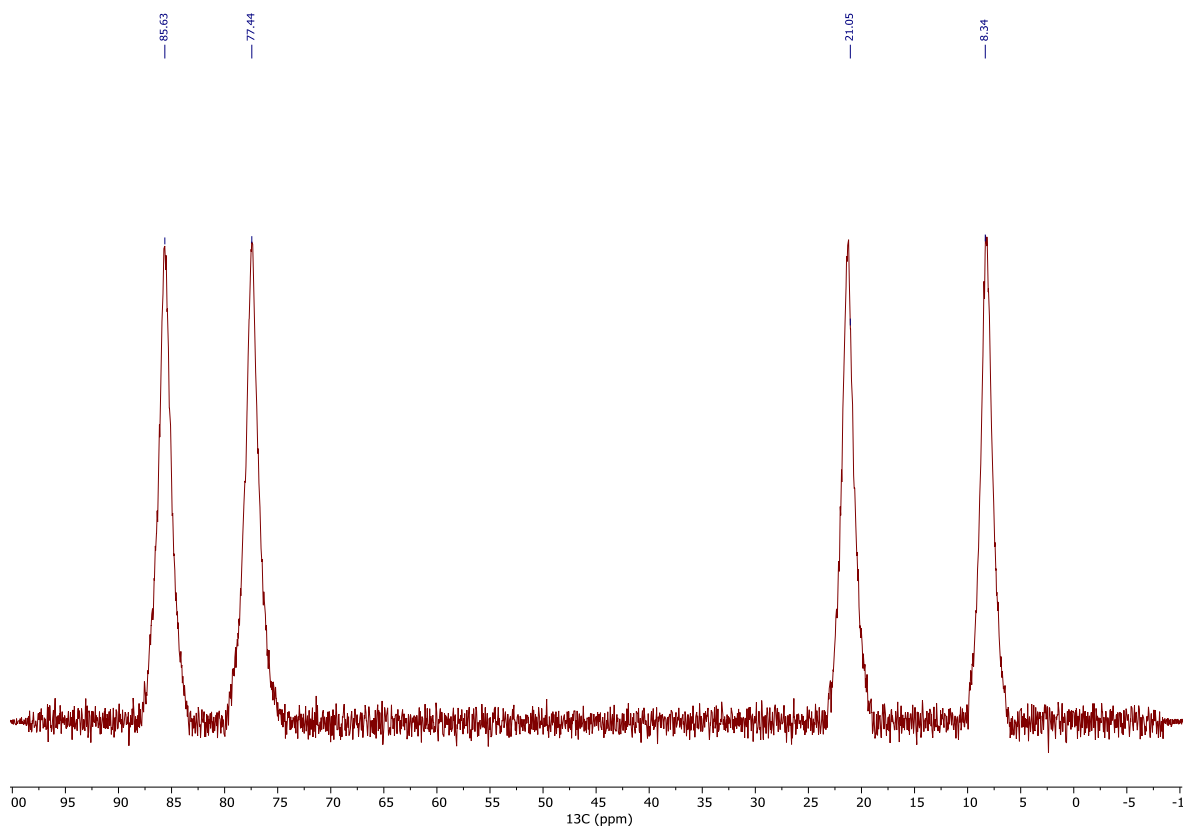
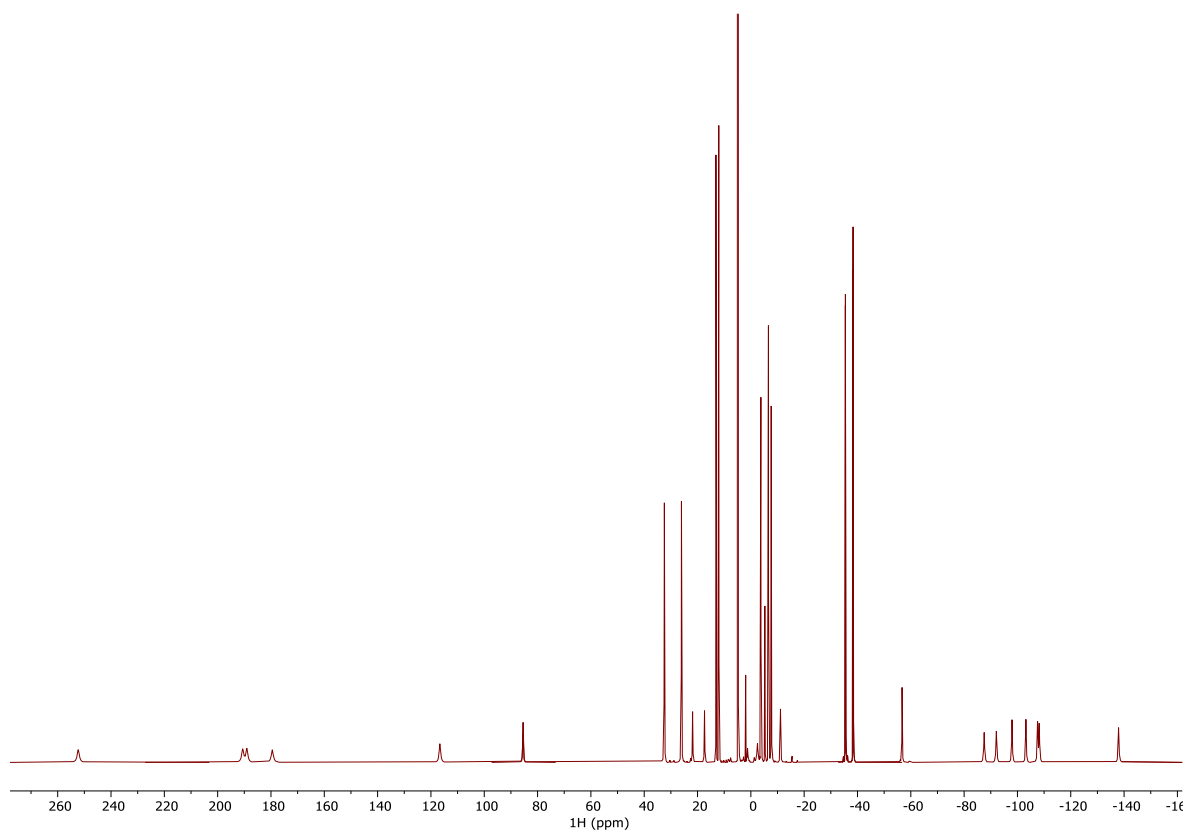
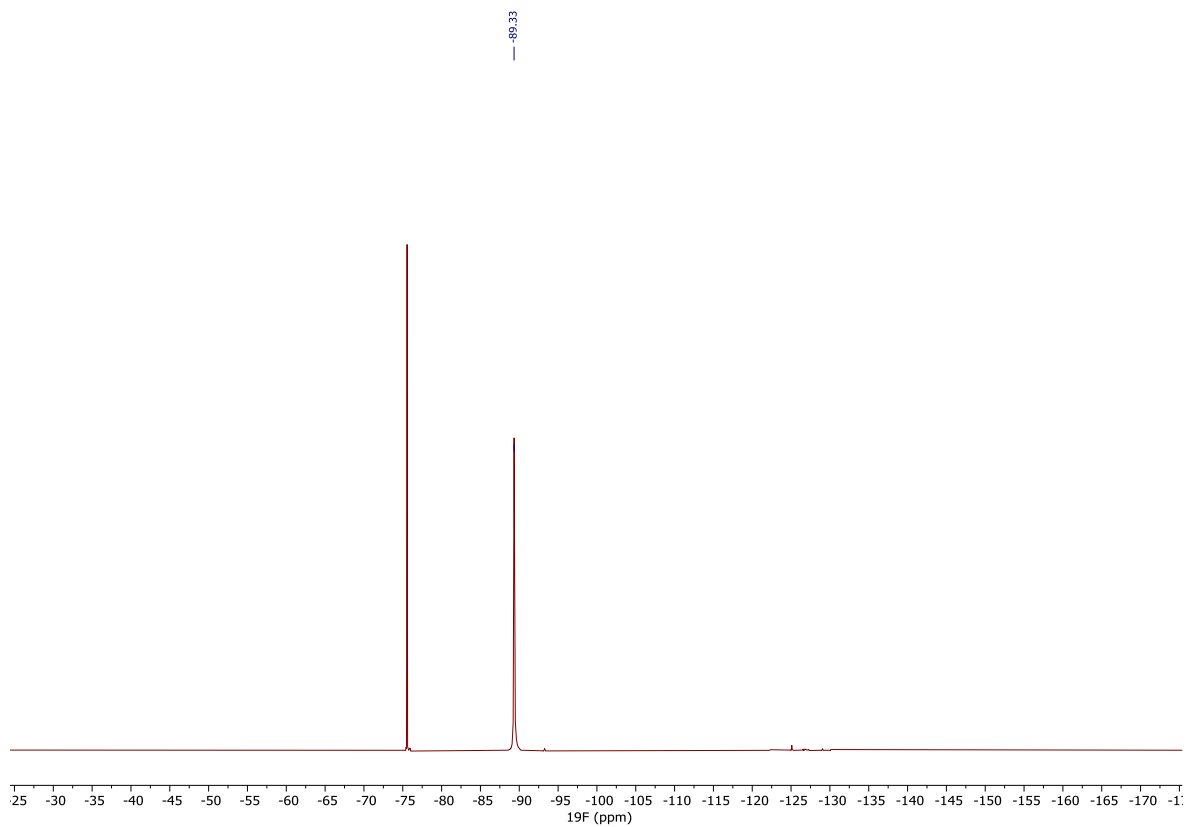


Figure S75:  $^{13}\text{C}$  NMR spectrum of Tm-DOTA-M7FPy.

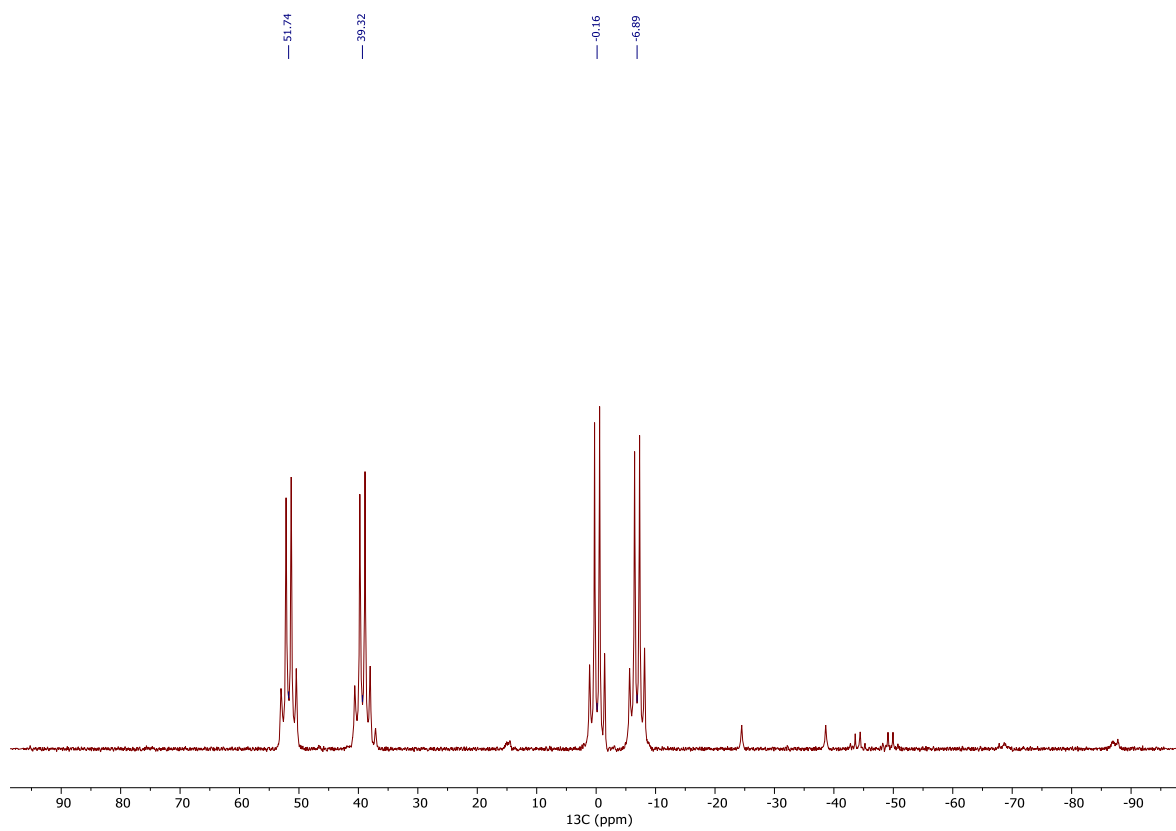
Yb-DOTA-M7FPy



**Figure S76:** <sup>1</sup>H NMR spectrum of Yb-DOTA-M7FPy pieced together from multiple spectra with a sweep width of 154 ppm.



**Figure S77:**  $^{19}\text{F}\{^1\text{H}\}$  NMR spectrum of Yb-DOTA-M7FPy.



**Figure S78:**  $^{13}\text{C}$  NMR spectrum of Yb-DOTA-M7FPy.

# Lu-DOTA-M7FPy

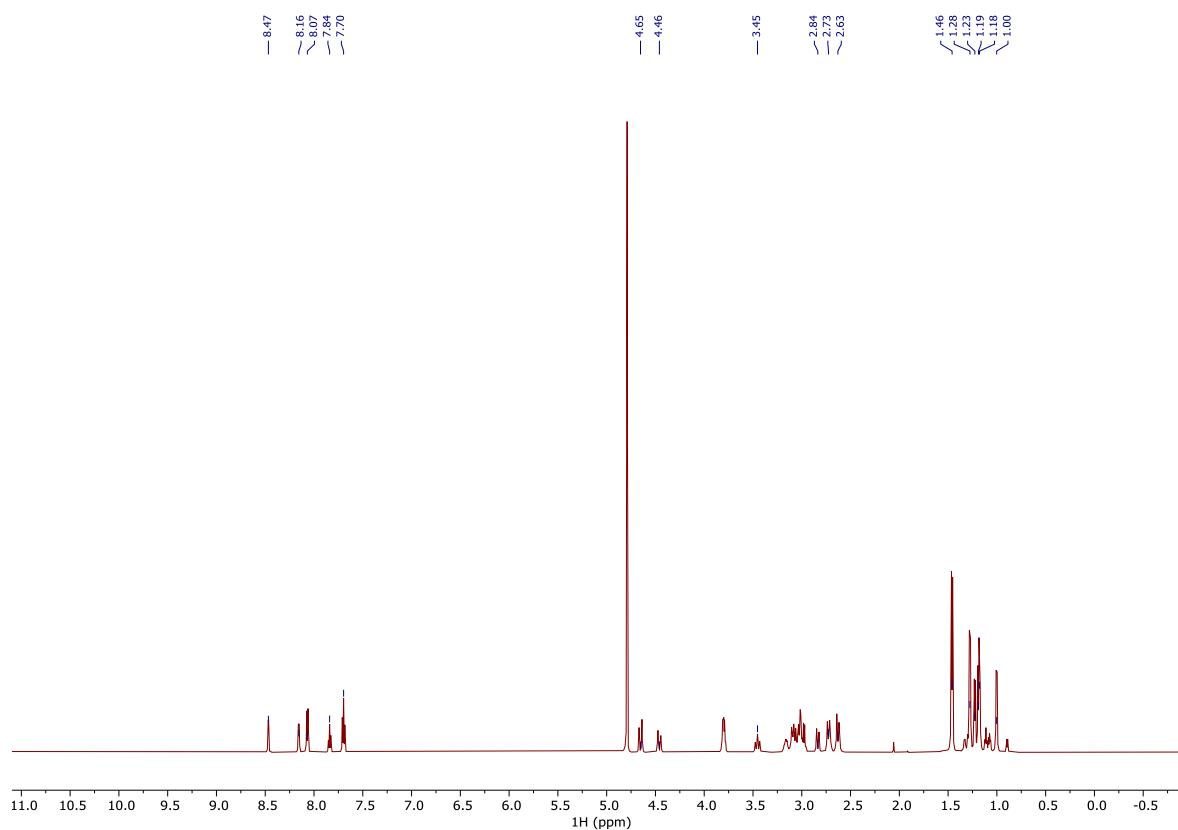


Figure S79:  $^1\text{H}$  NMR spectrum of Lu-DOTA-M7FPy.

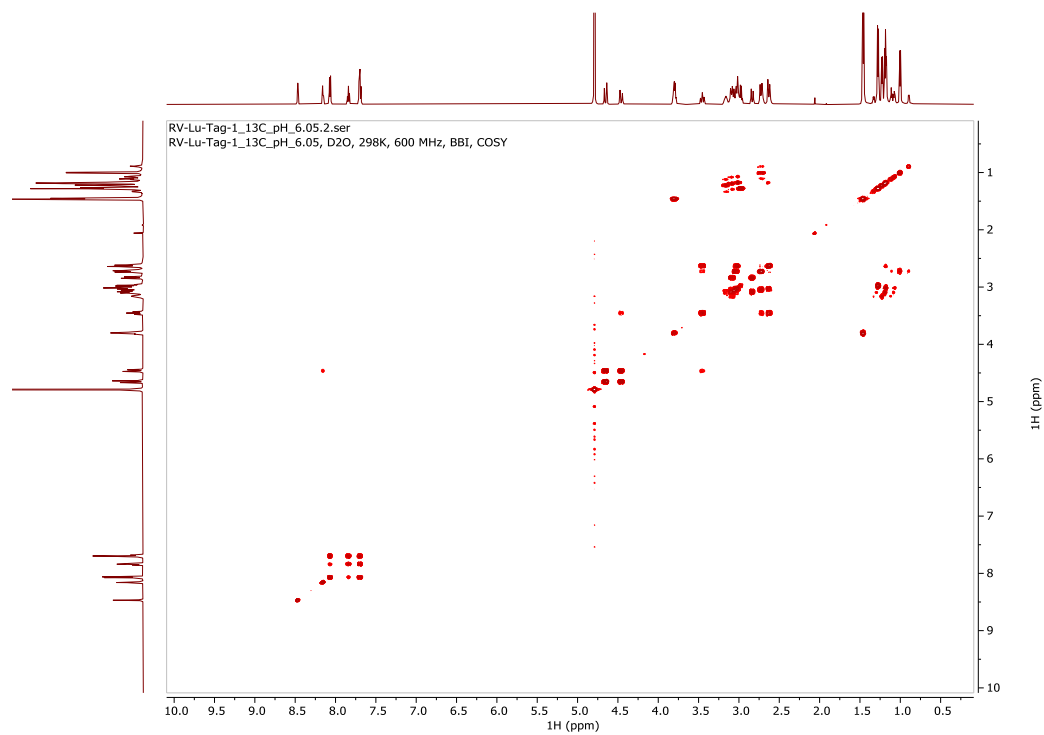
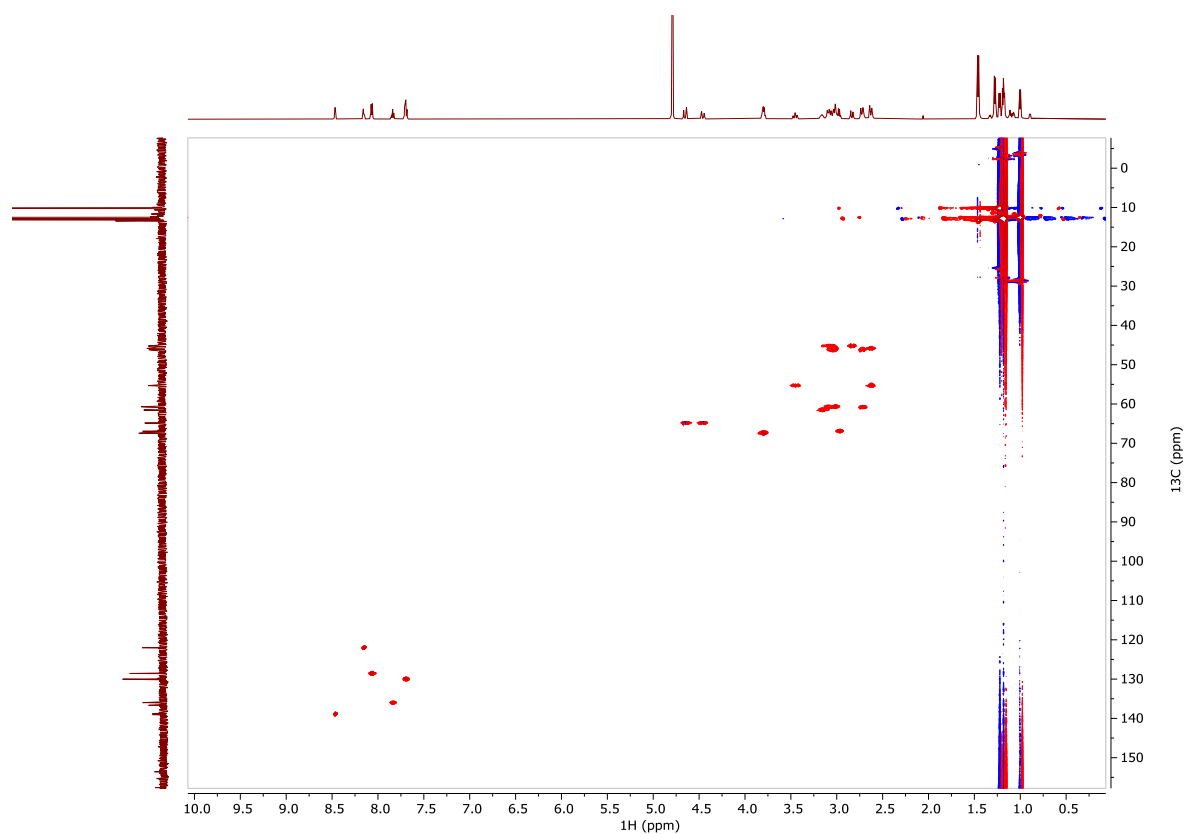
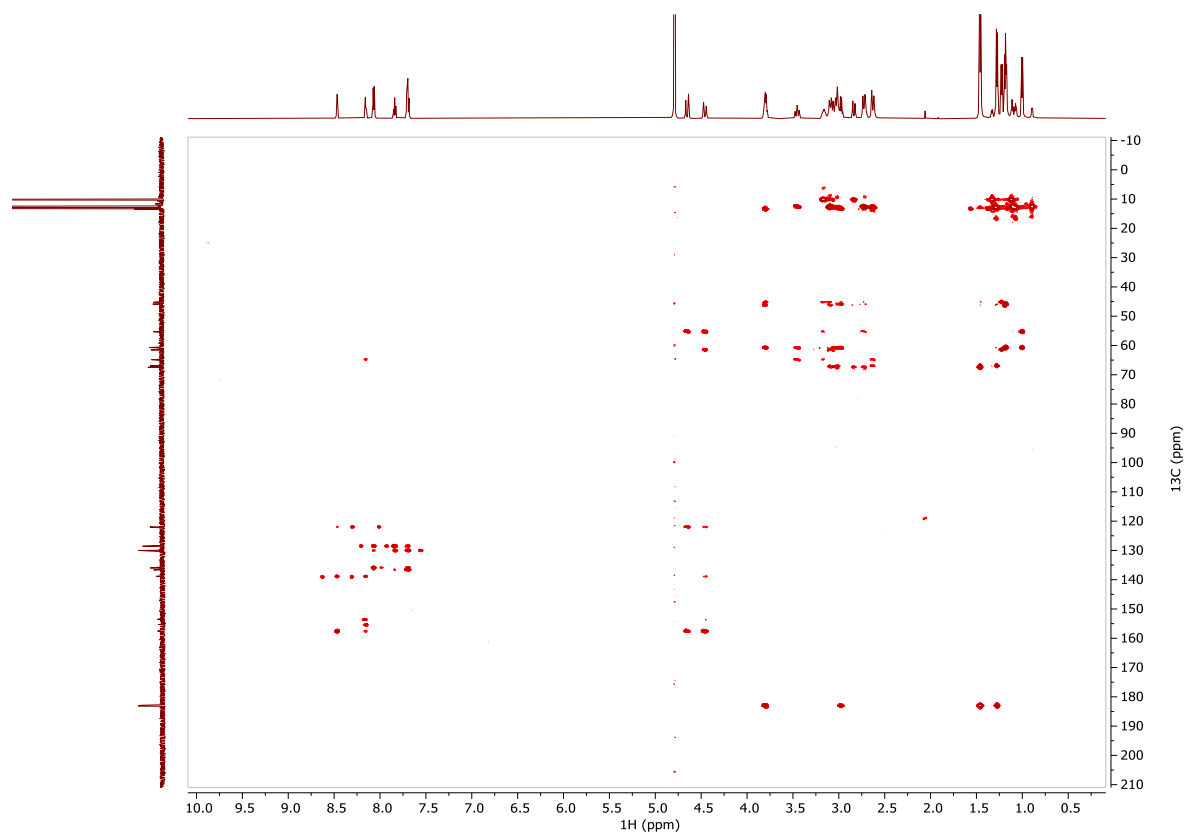


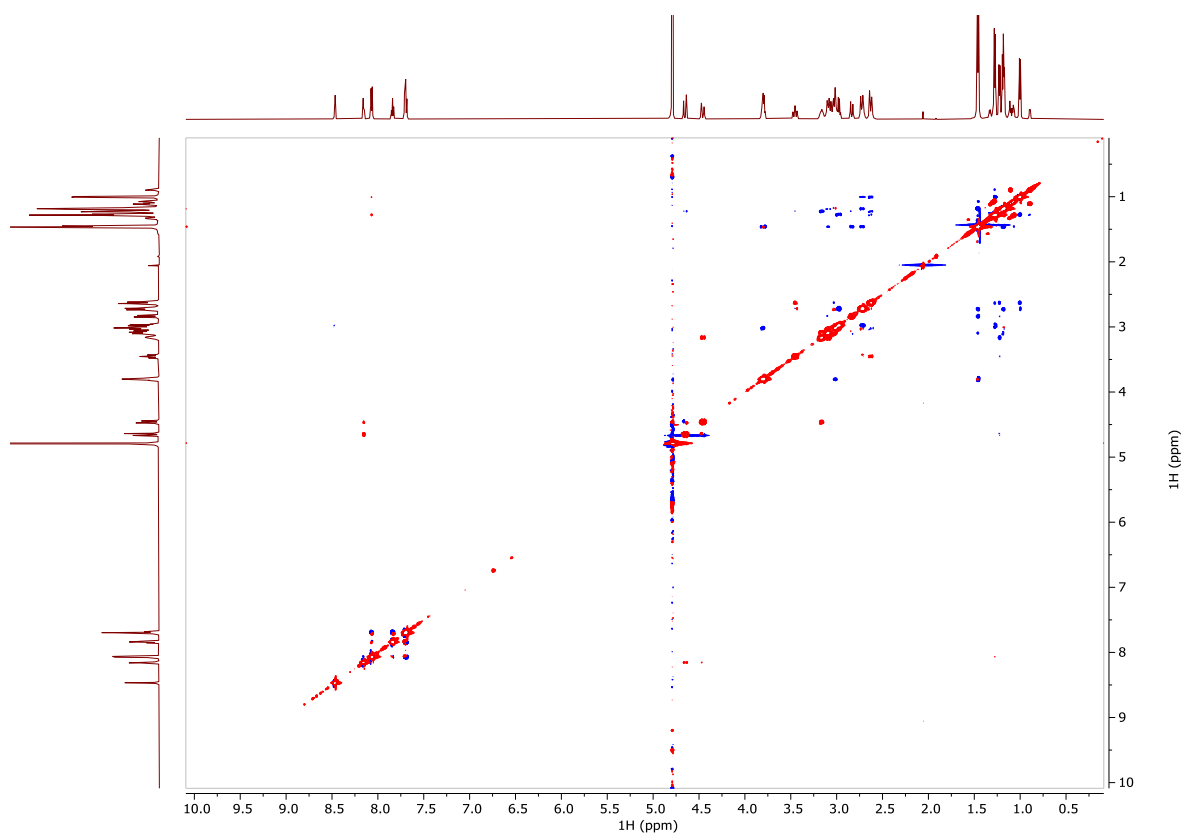
Figure S80:  $^1\text{H}$   $^1\text{H}$  COSY spectrum of Lu-DOTA-M7FPy.



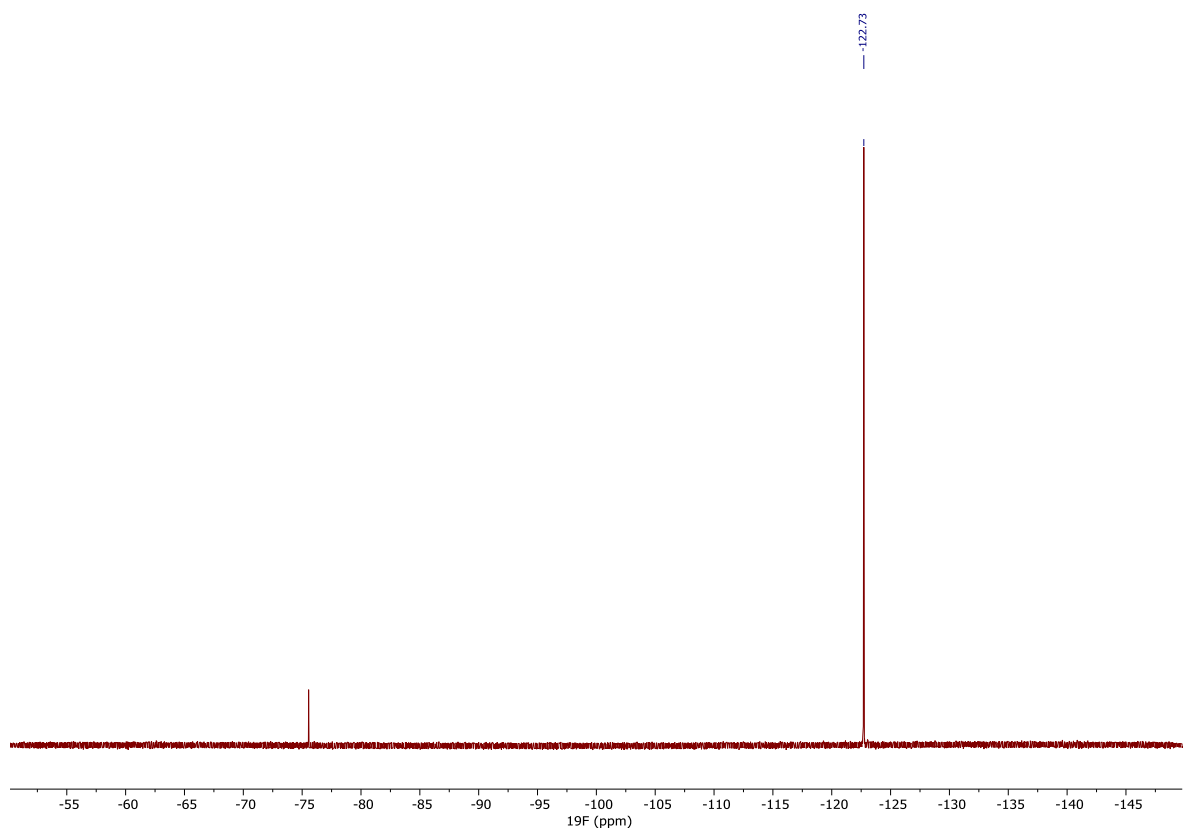
**Figure S81:**  $^1\text{H}$   $^{13}\text{C}$  HMQC spectrum of Lu-DOTA-M7FPy.



**Figure S82:**  $^1\text{H}$   $^{13}\text{C}$  HMBC spectrum of Lu-DOTA-M7FPy.

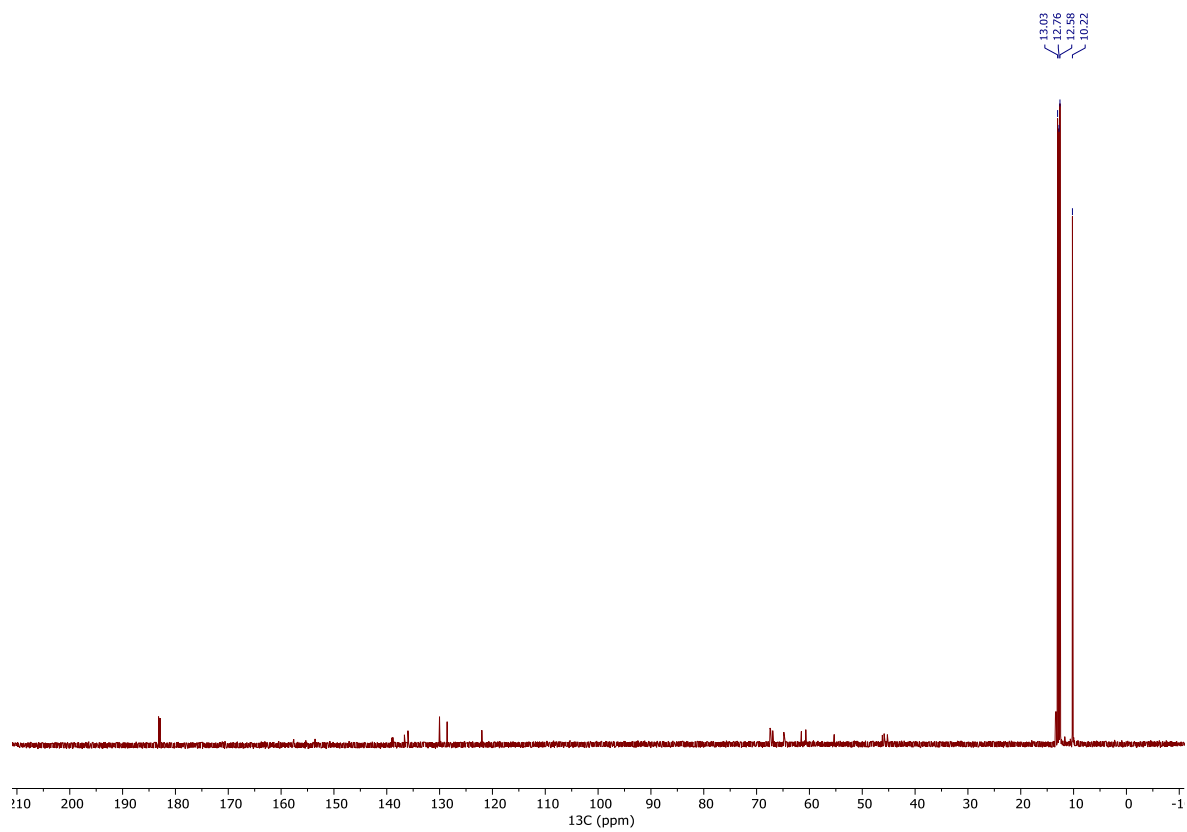


**Figure S83:**  $^1\text{H}$   $^1\text{H}$  NOESY spectrum of Lu-DOTA-M7FPy.



**Figure S84:**  $^{19}\text{F}\{^1\text{H}\}$  NMR spectrum of Lu-DOTA-M7FPy.





**Figure S85:**  $^{13}\text{C}\{^1\text{H}\}$  NMR spectrum of Lu-DOTA-M7FPy.

## 2.6.14 Yb-DOTA-M7FPy $^1\text{H}$ -NMR spectra at different pH-values



**Figure S86:** Stacked upper and lower range of the Yb-DOTA-M7FPy spectrum. The spectra were recorded at different pH values (blue pH = 1.2, green pH = 1.6, red pH = 6.1, black pH = 6.5) and containing different ions. Blue and green contained TFA. For red the TFA was removed by Sep-Pak column chromatography and the sample was buffered with 50 mM phosphate buffer. For black the TFA was removed by Sep-Pak column chromatography and the sample was measured in “neutral”  $\text{D}_2\text{O}$ .

## 2.6.15 NMR spectra Ln-DOTA-M8 (60)

La-DOTA-M8

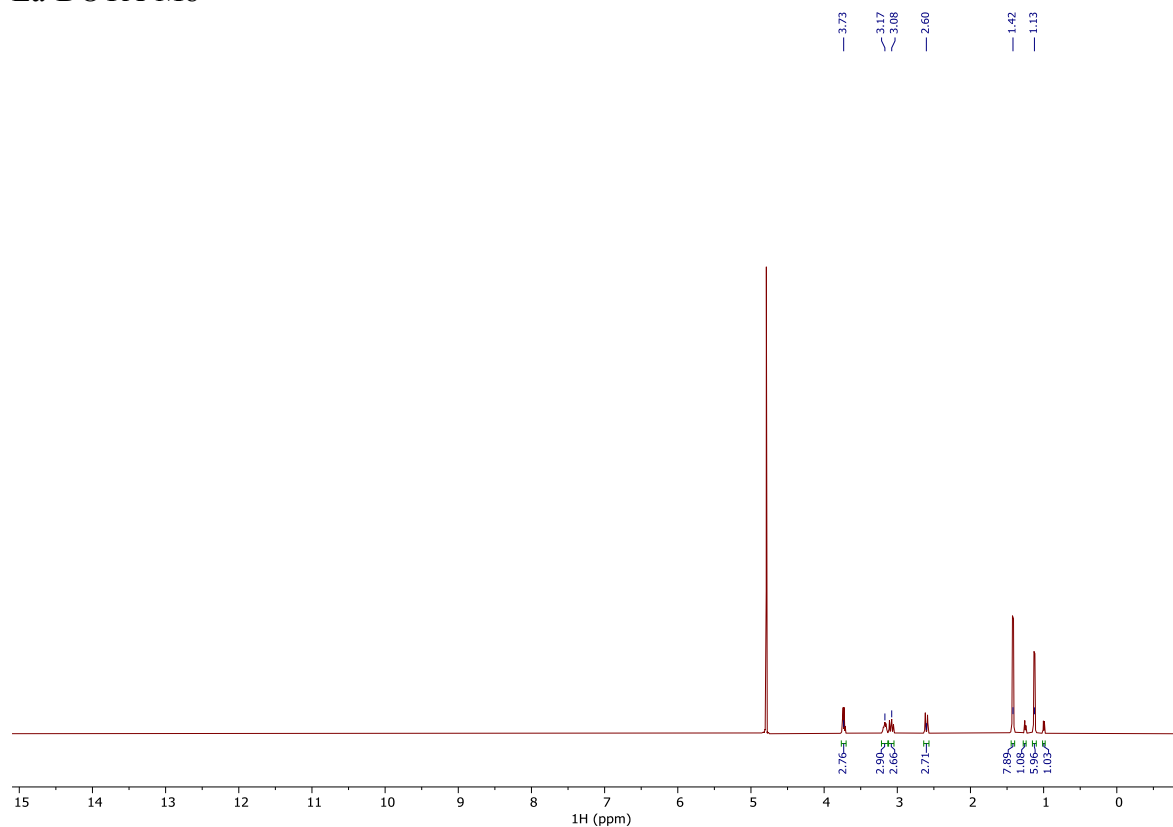


Figure S87:  $^1\text{H}$  NMR spectrum of La-DOTA-M8.

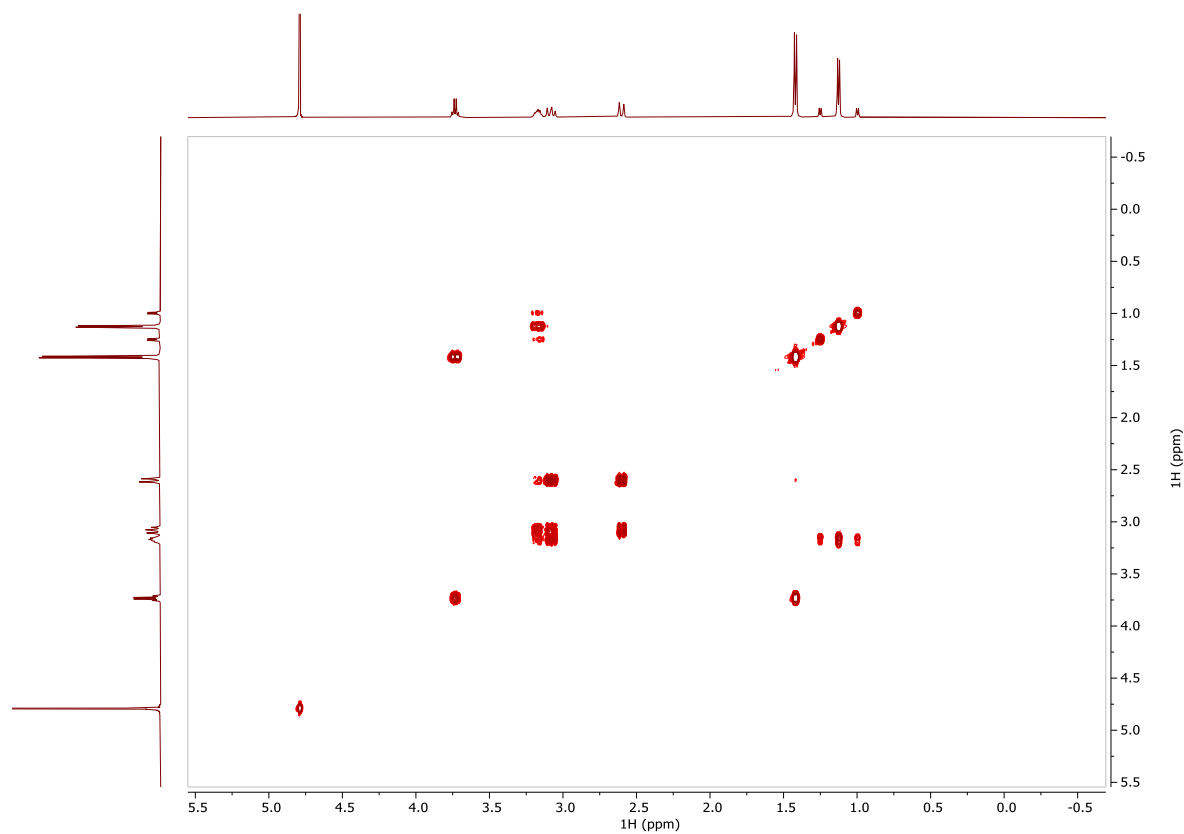


Figure S88:  $^1\text{H}$   $^1\text{H}$  COSY spectrum of La-DOTA-M8.

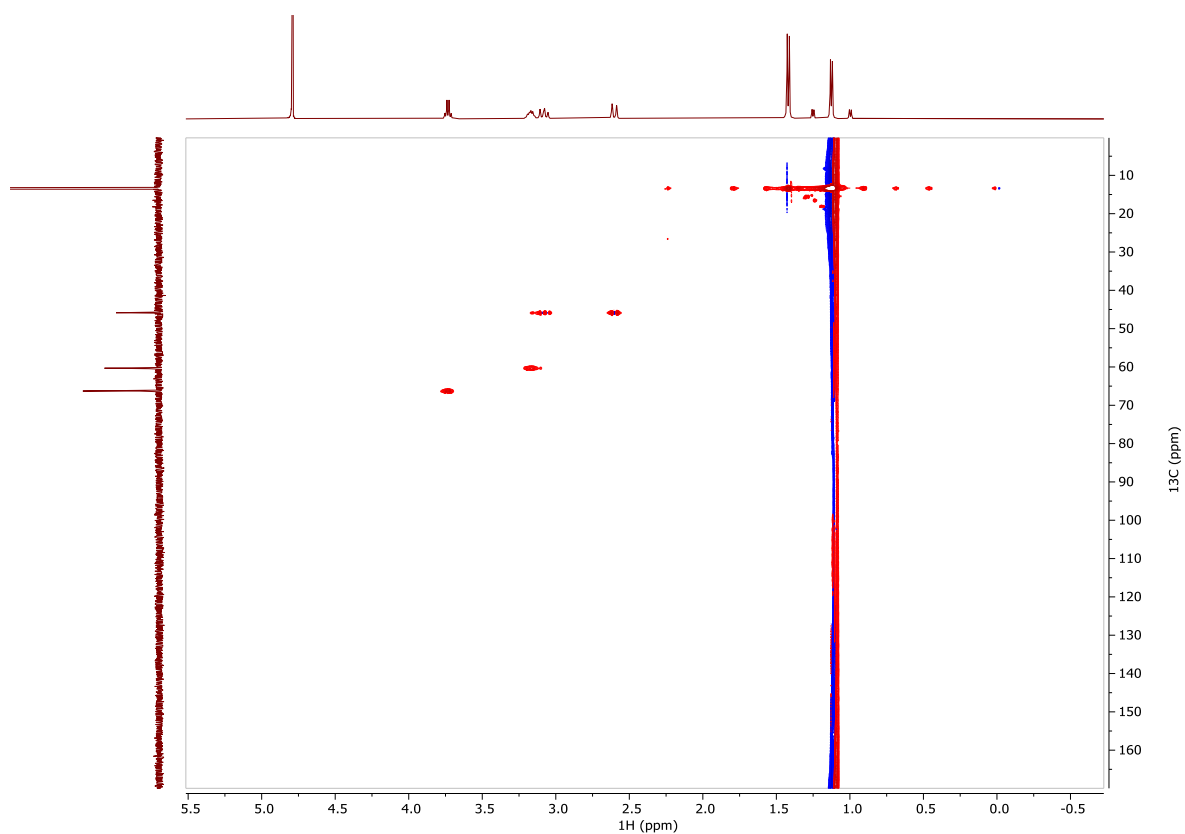


Figure S89:  $^1\text{H}$   $^{13}\text{C}$  HMQC spectrum of La-DOTA-M8.

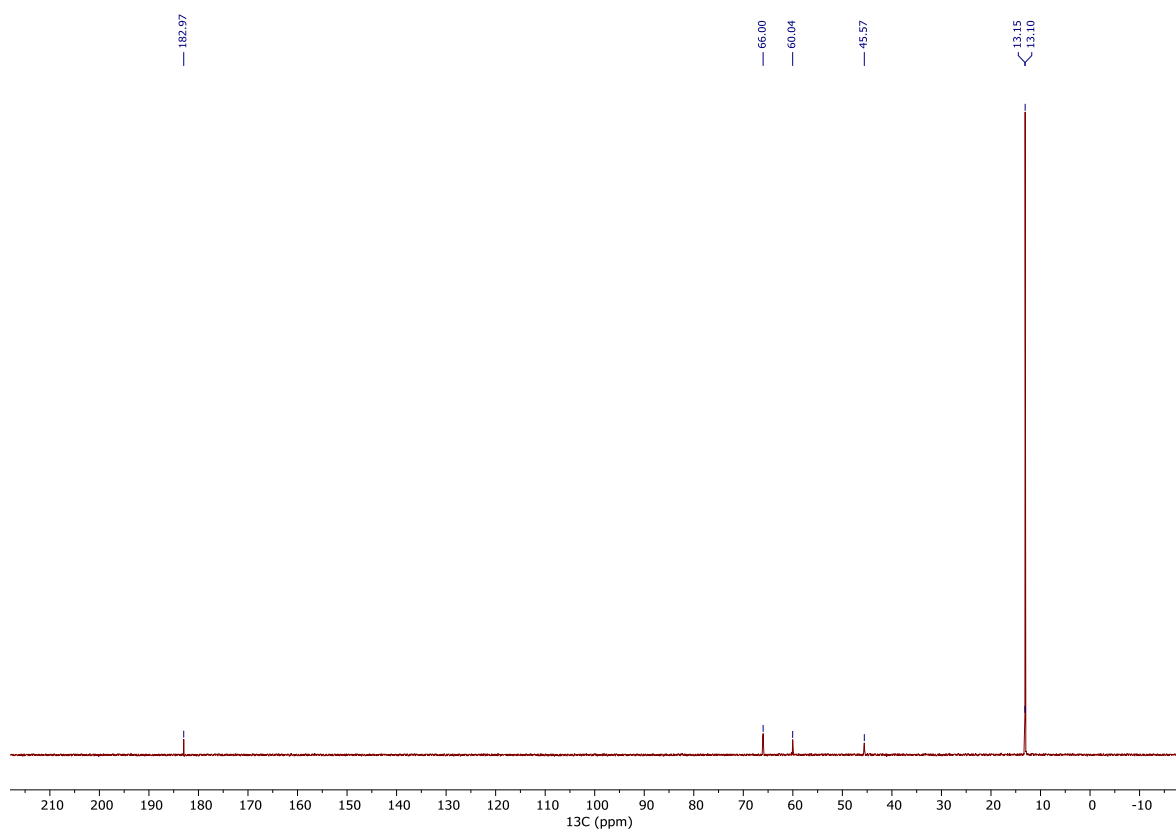
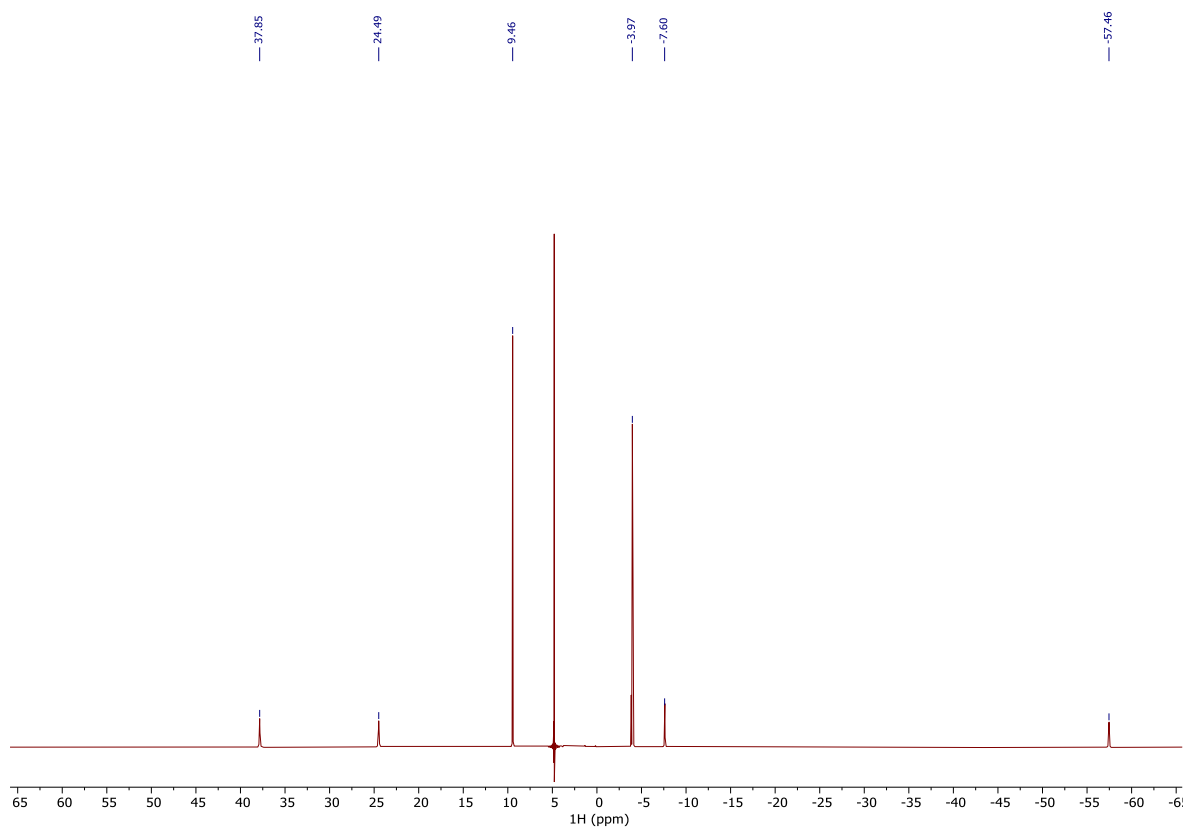
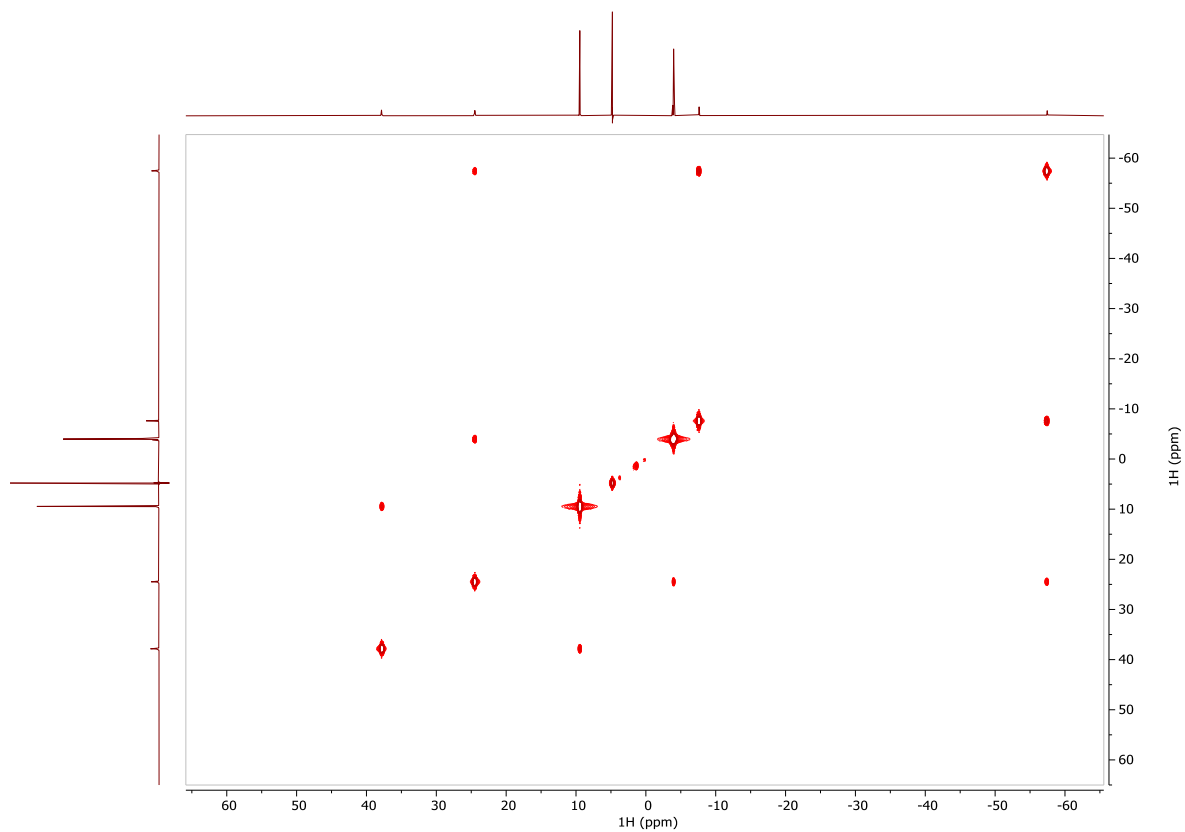


Figure S90:  $^{13}\text{C}\{^1\text{H}\}$  NMR spectrum of La-DOTA-M8.

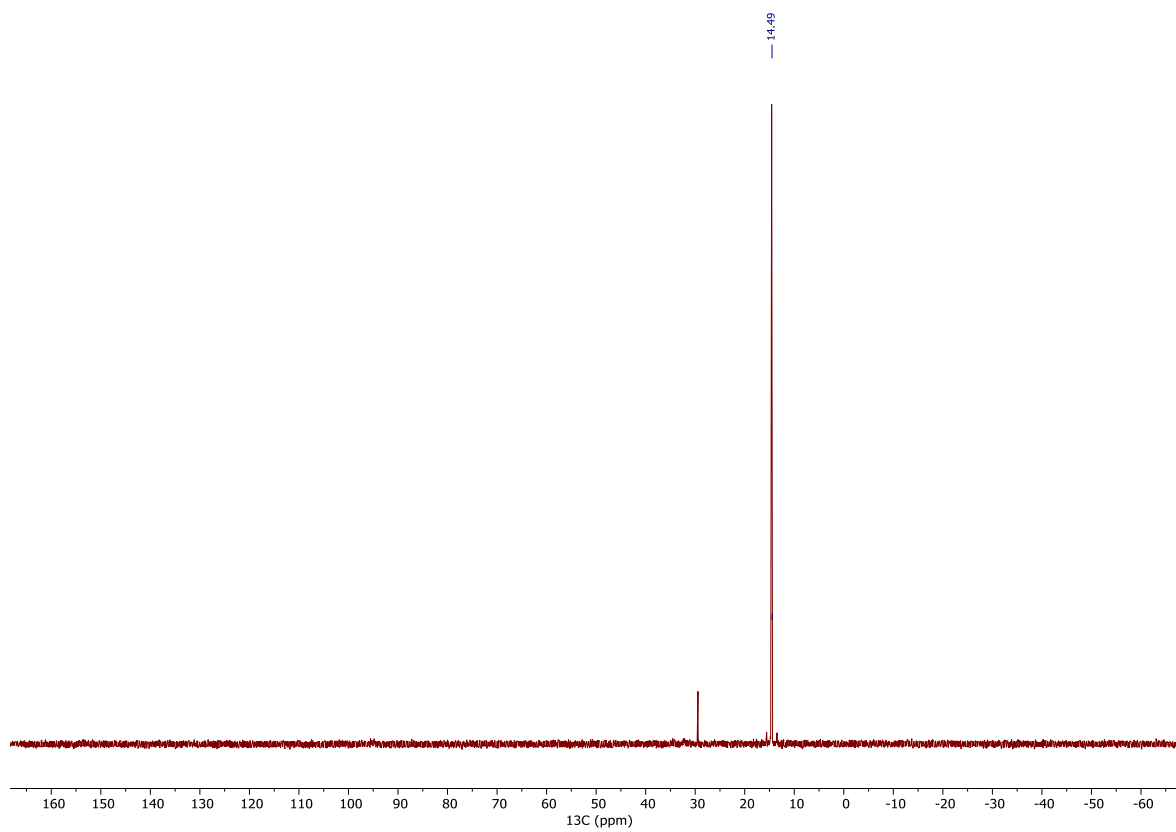
# Pr-DOTA-M8



**Figure S91:**  $^1\text{H}$  NMR spectrum of Pr-DOTA-M8.

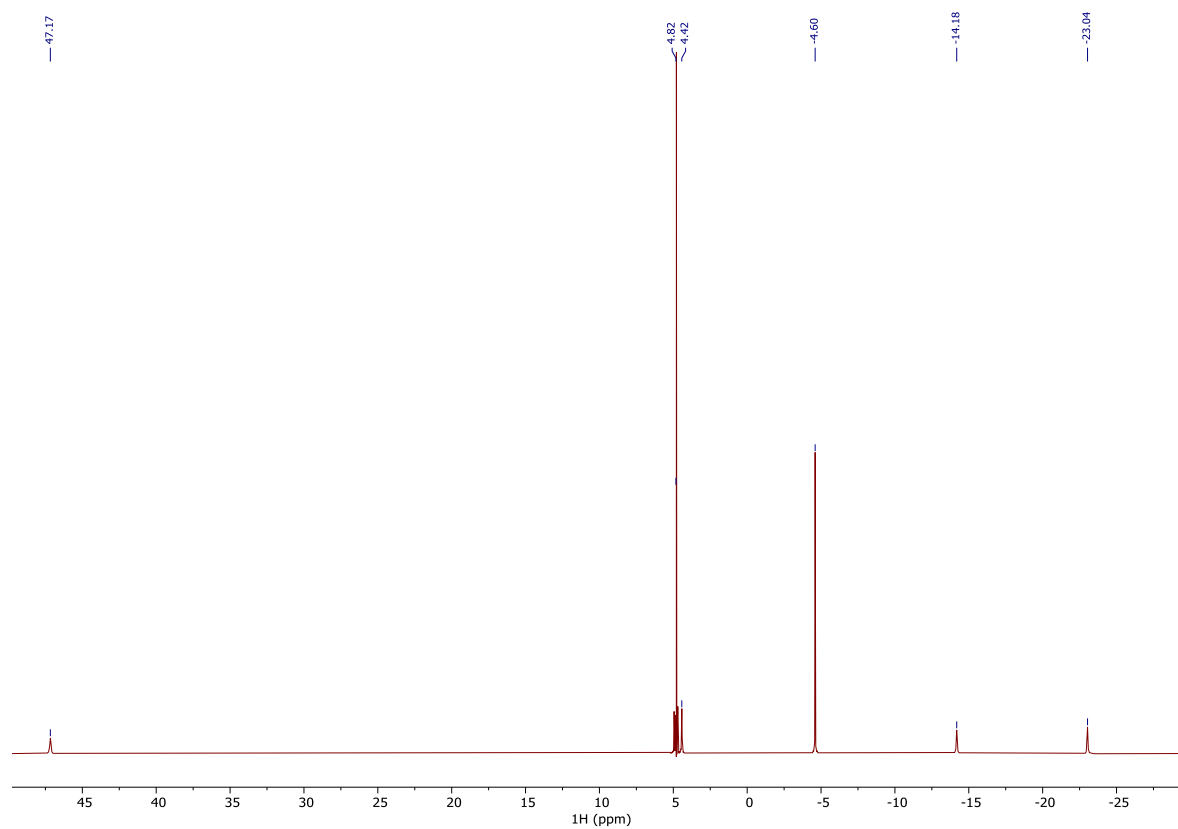


**Figure S92:**  $^1\text{H}$   $^1\text{H}$  COSY spectrum of Pr-DOTA-M8.

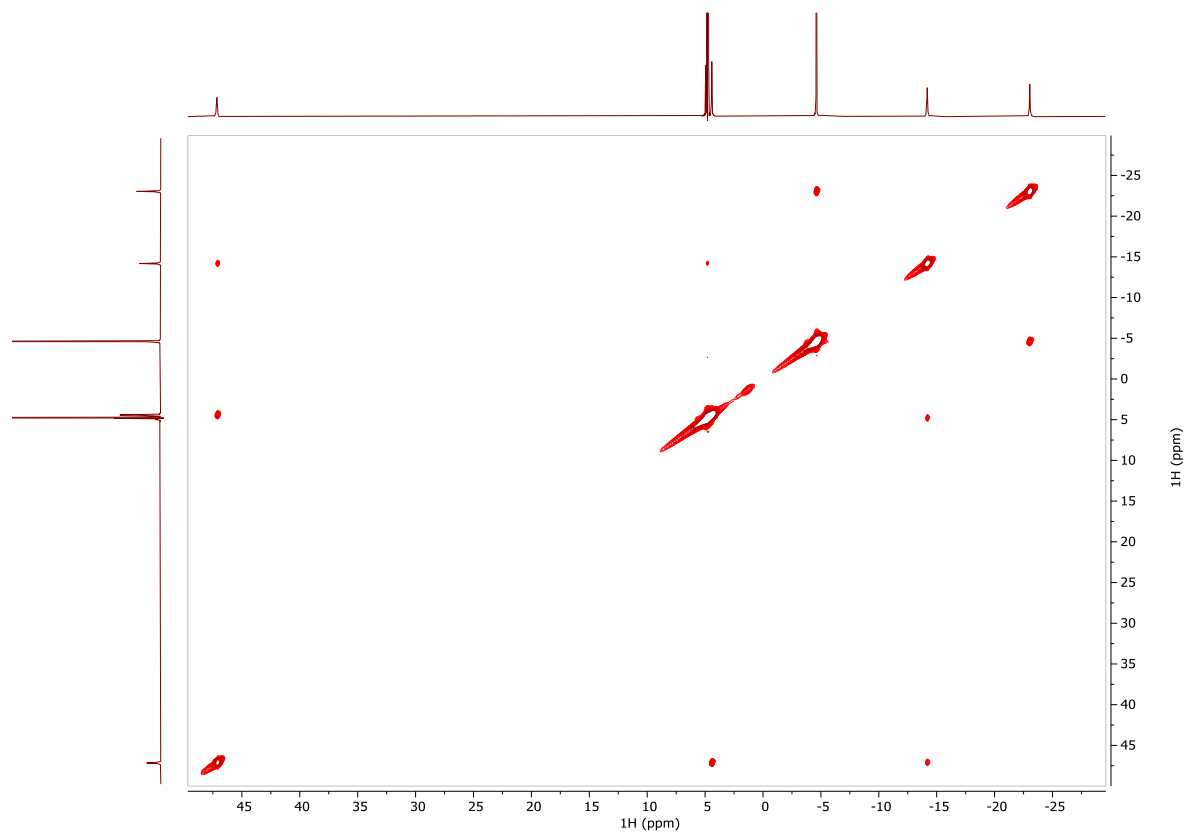


**Figure S93:**  $^{13}\text{C}\{^1\text{H}\}$  NMR spectrum of Pr-DOTA-M8.

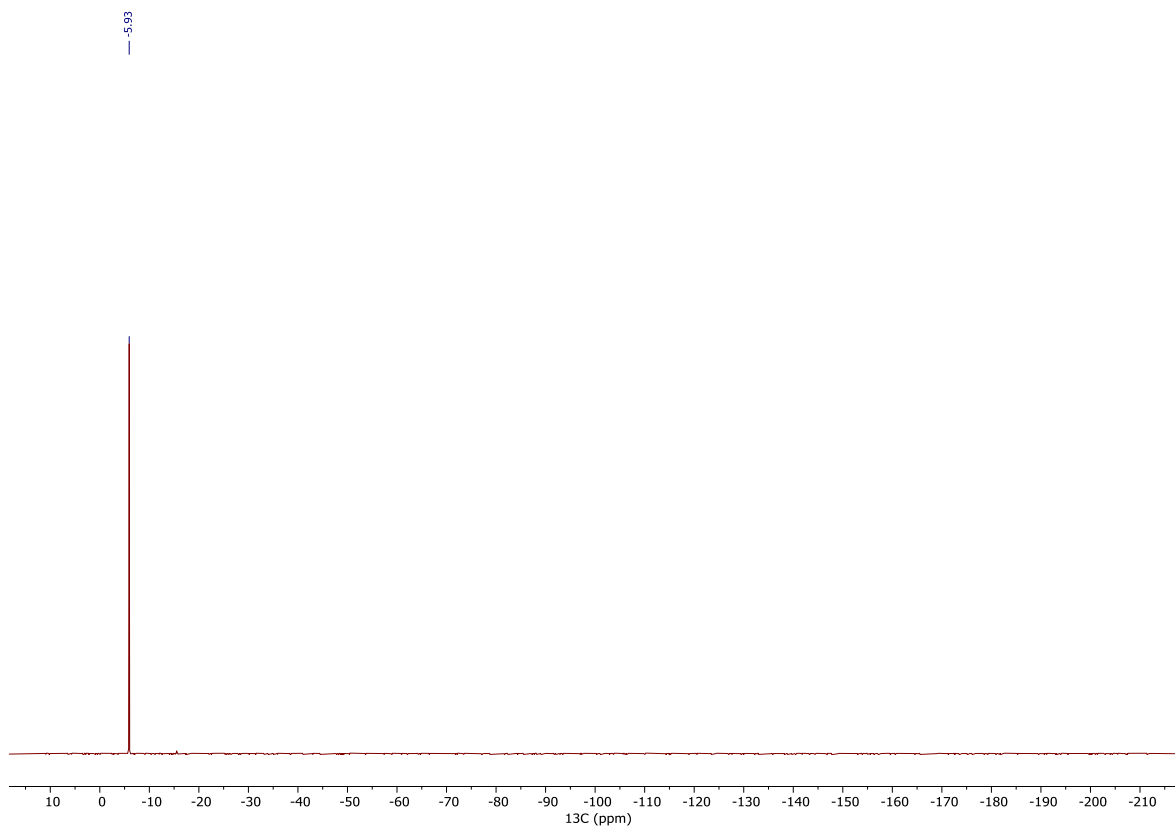
# Eu-DOTA-M8



**Figure S94:**  $^1\text{H}$  NMR spectrum of Eu-DOTA-M8.



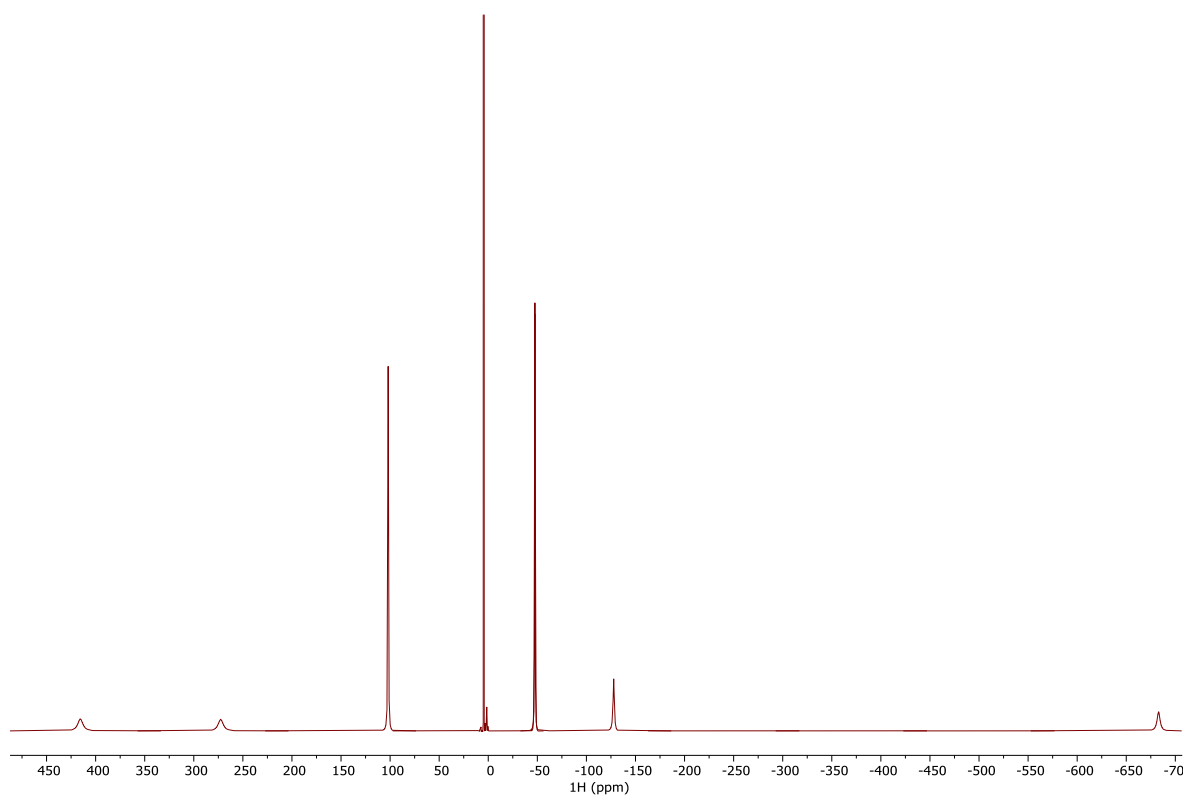
**Figure S95:**  $^1\text{H}$   $^1\text{H}$  COSY spectrum of Eu-DOTA-M8.



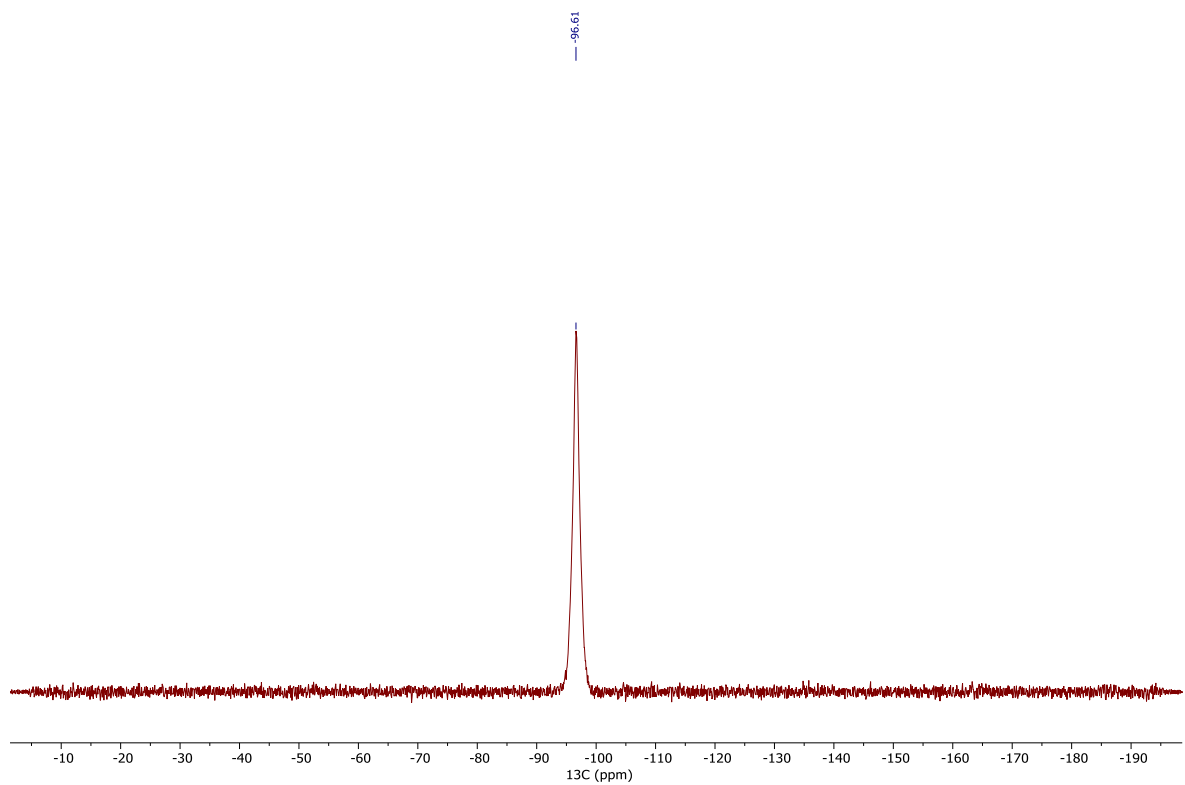
**Figure S96:**  $^{13}\text{C}\{^1\text{H}\}$  NMR spectrum of Eu-DOTA-M8.



# Dy-DOTA-M8

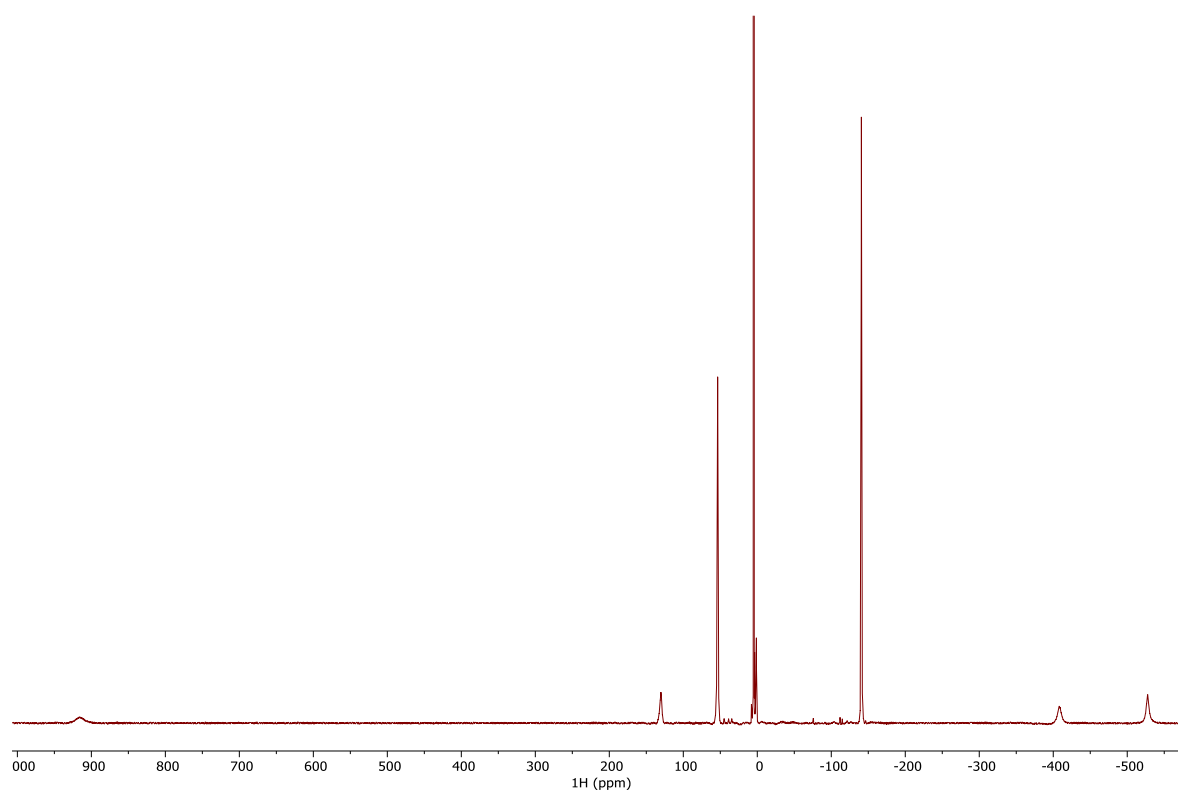


**Figure S97:**  $^1\text{H}$  NMR spectrum of Dy-DOTA-M8 pieced together from multiple spectra with a sweep width of 154 ppm.

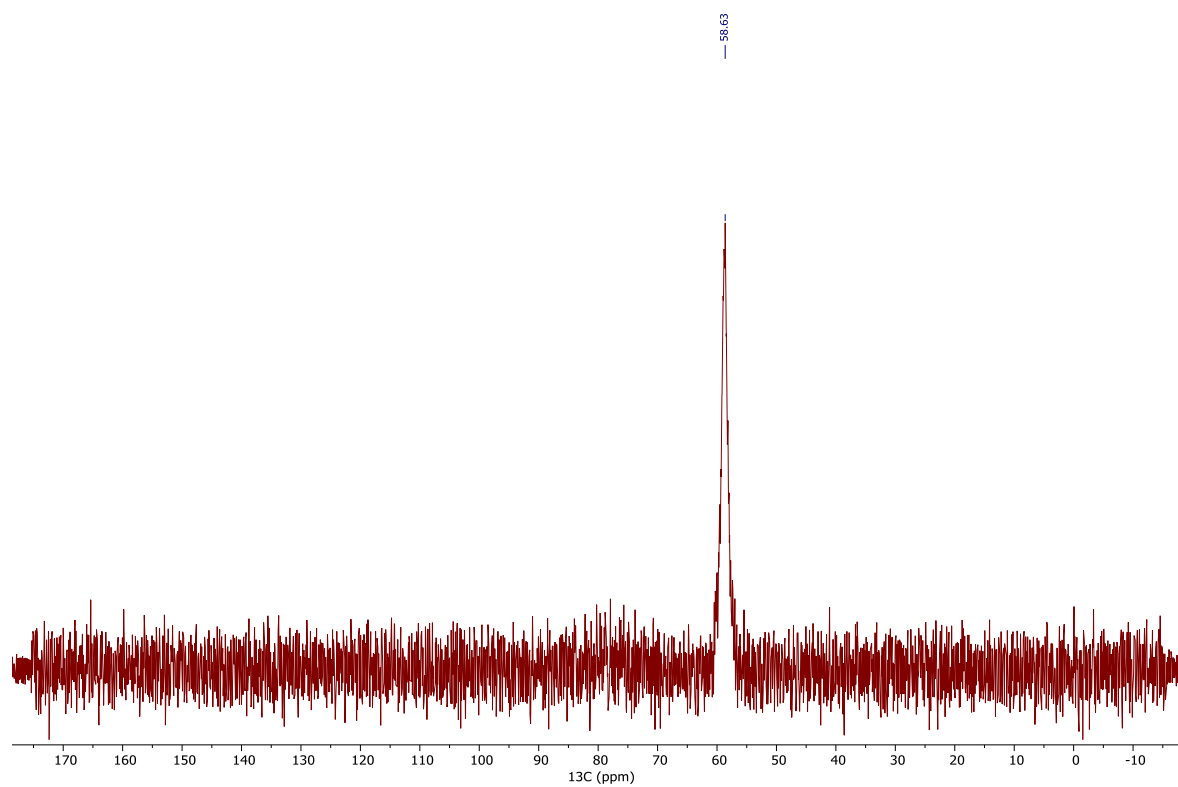


**Figure S98:**  $^{13}\text{C}\{^1\text{H}\}$  NMR spectrum of Dy-DOTA-M8.

Tm-DOTA-M8



**Figure S99:**  $^1\text{H}$  NMR spectrum of Tm-DOTA-M8 pieced together from multiple spectra with a sweep width of 154 ppm.



**Figure S100:**  $^{13}\text{C}\{^1\text{H}\}$  NMR spectrum of Tm-DOTA-M8.

Lu-DOTA-M8

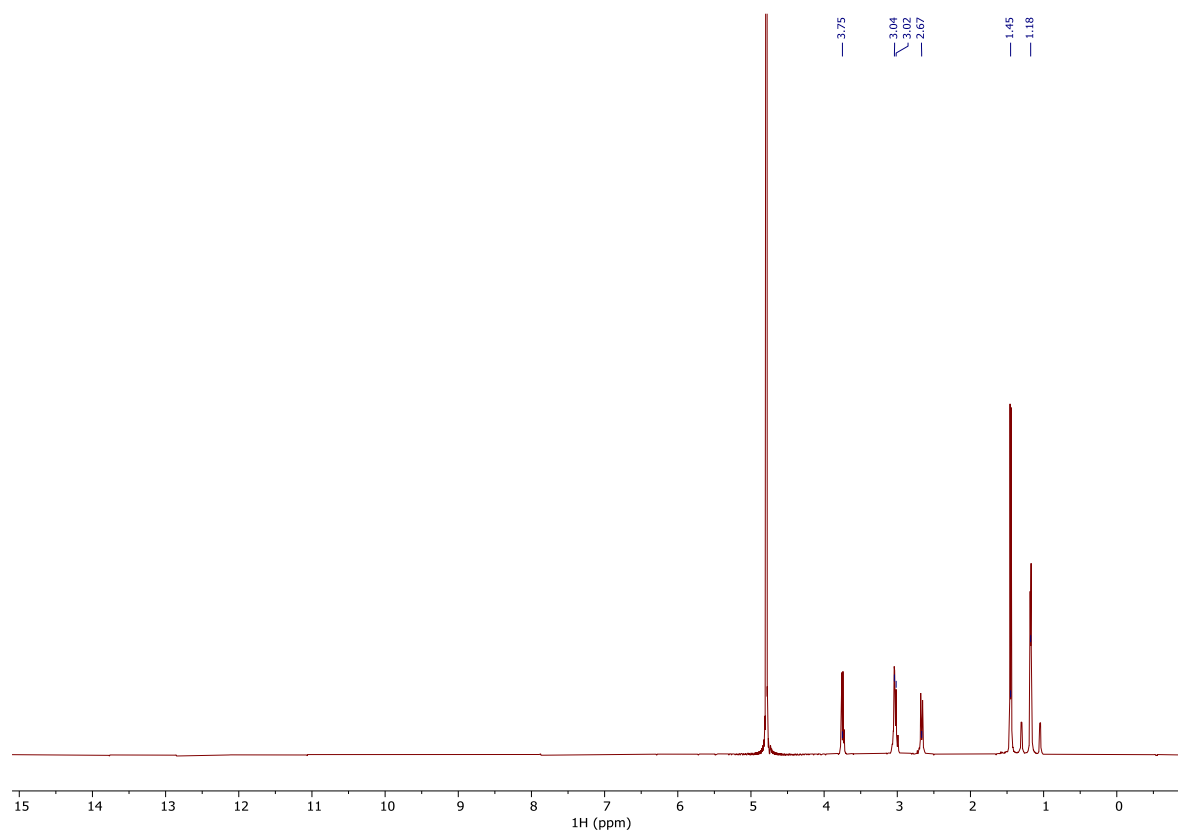


Figure S101:  $^1\text{H}$  NMR spectrum of Lu-DOTA-M8.

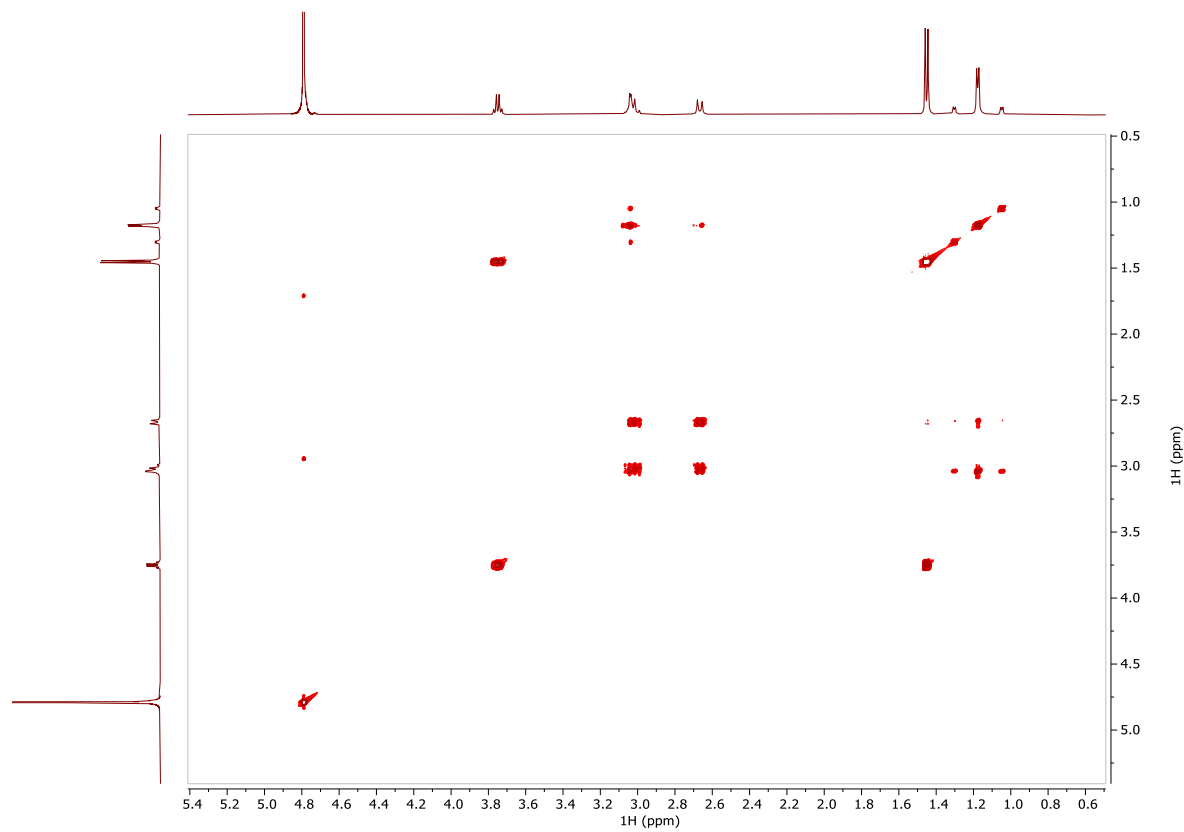


Figure S102:  $^1\text{H}$   $^1\text{H}$  COSY spectrum of Lu-DOTA-M8.

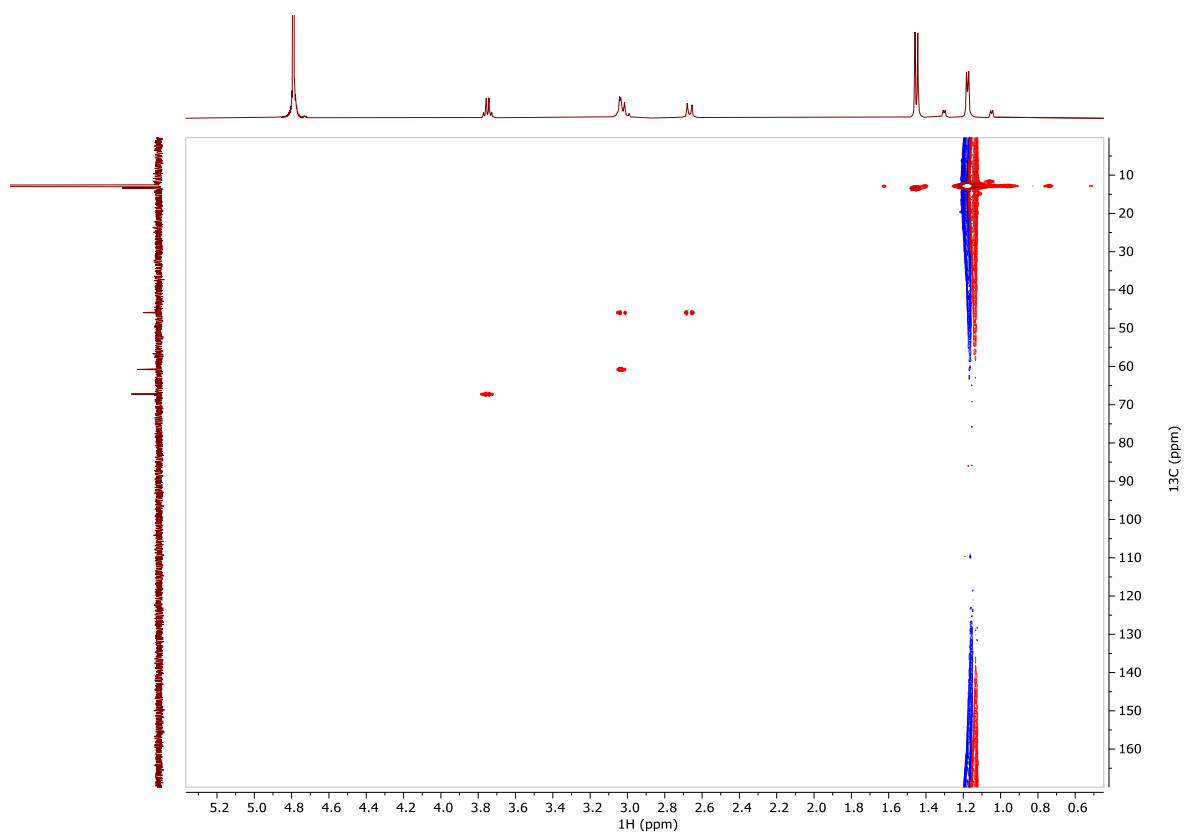


Figure S103:  $^1\text{H}$   $^{13}\text{C}$  HMQC spectrum of Lu-DOTA-M8.

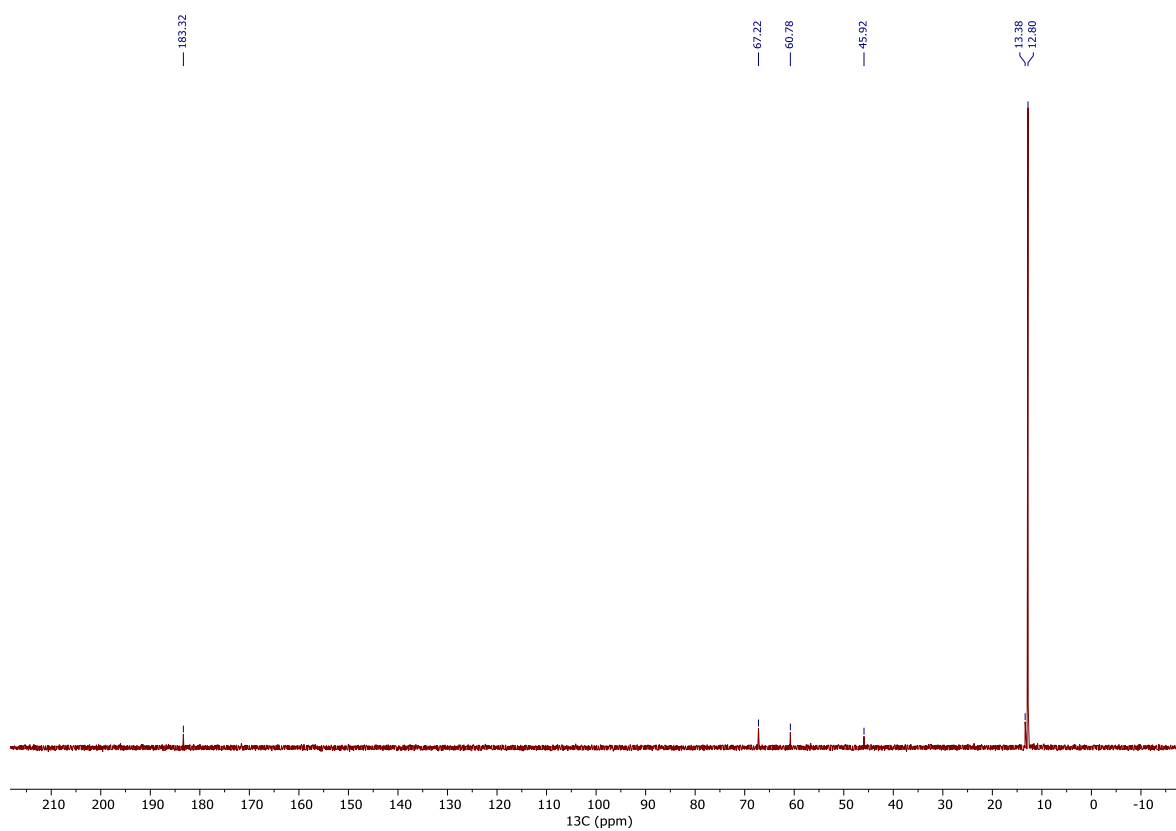
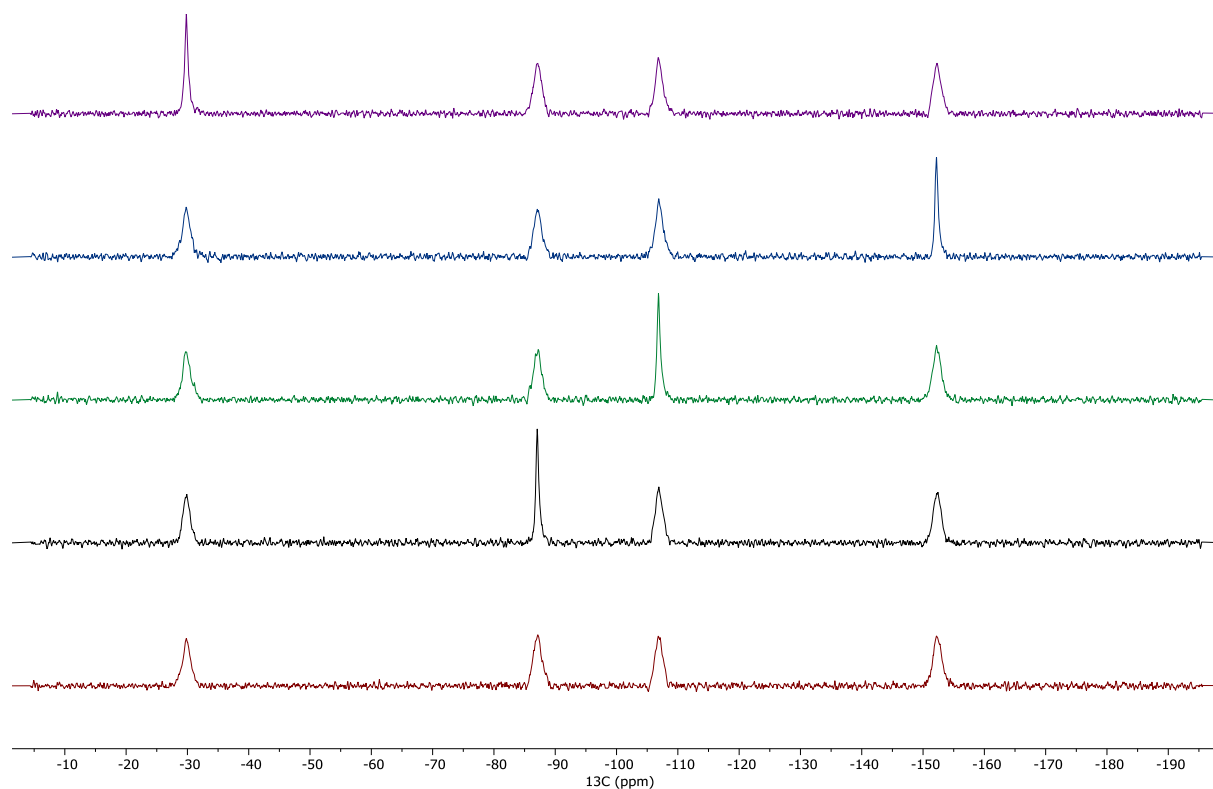


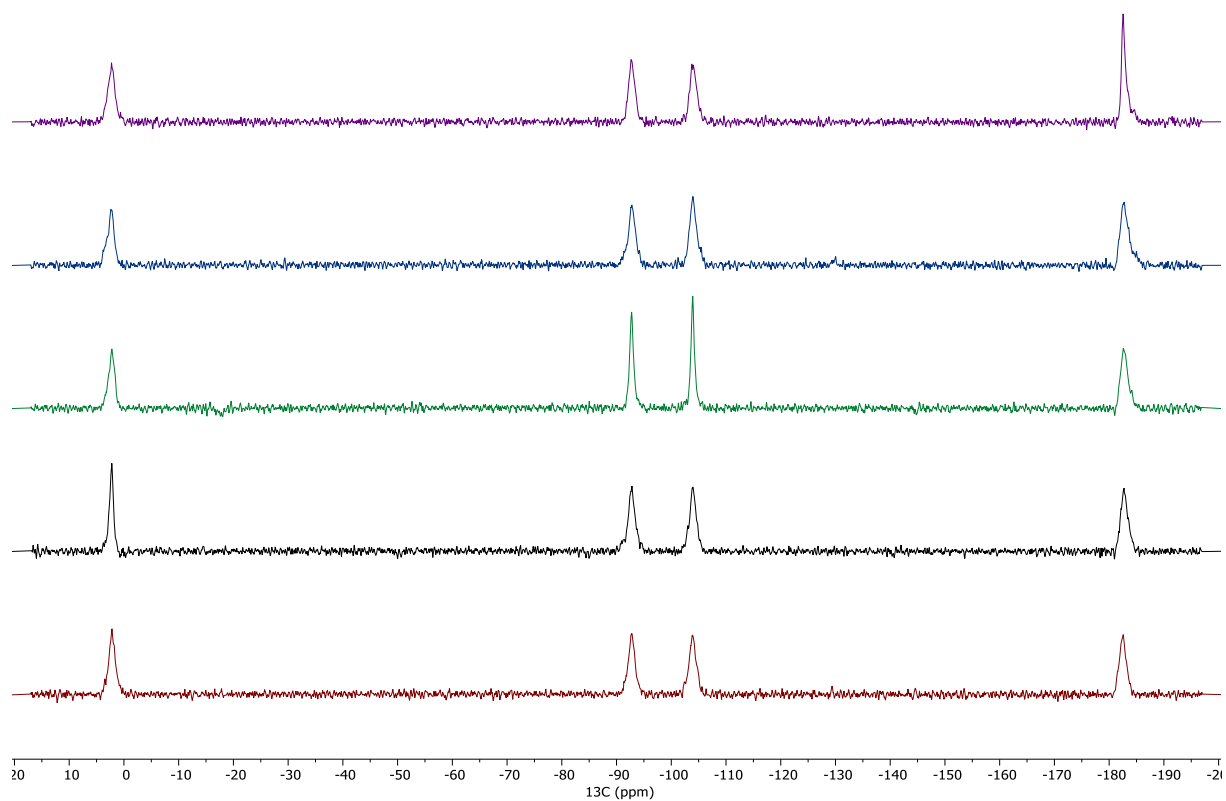
Figure S104:  $^{13}\text{C}\{^1\text{H}\}$  NMR spectrum of Lu-DOTA-M8.

## 2.6.16 Selectively $^1\text{H}$ decoupled $^{13}\text{C}$ spectra

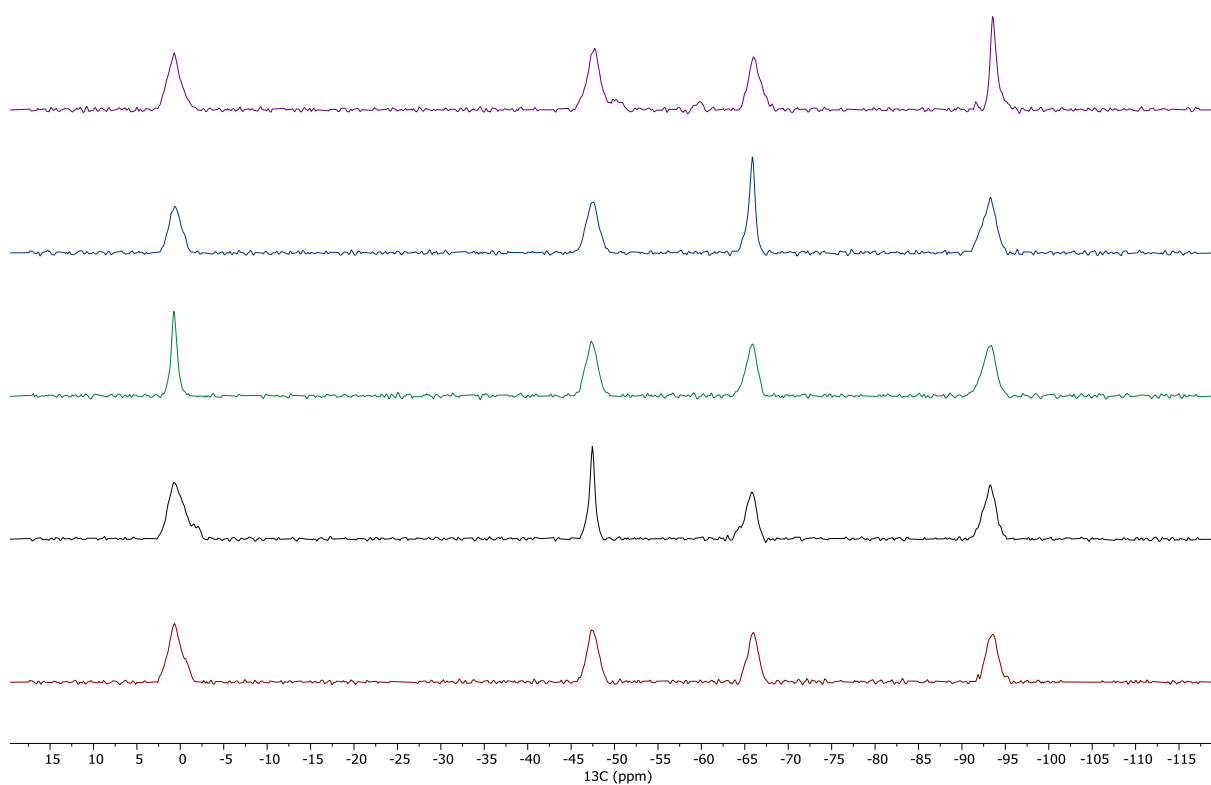
### 2.6.16.1 Ln-DOTA-M7FPy (1)



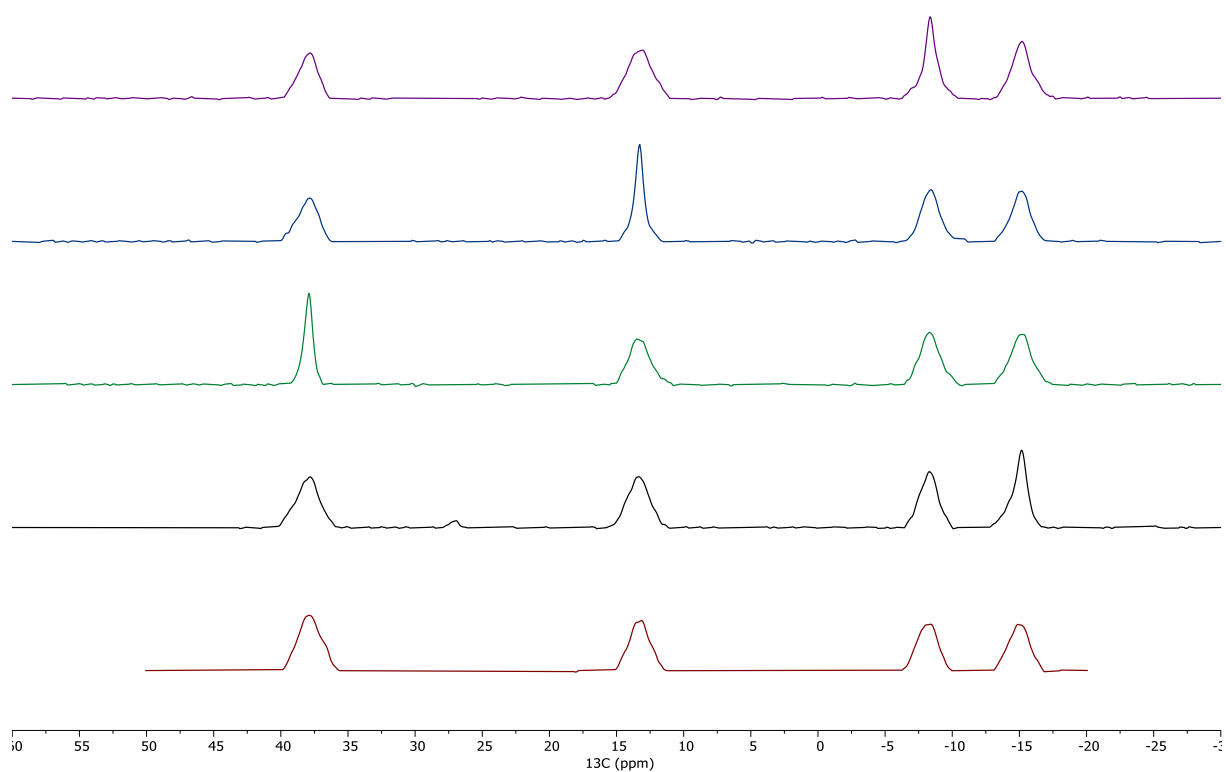
**Figure S105:** Selectively  $^1\text{H}$  decoupled  $^{13}\text{C}$  spectra of Tb-DOTA-M7FPy. The  $^1\text{H}$  decoupler offset has been set to the proton frequency of the following methyl resonances: 8.29 ppm (purple), -68.46 ppm (blue), -45.31 ppm (green) and -29.55 ppm (black). The red spectra with no decoupling was taken as a reference.



**Figure S106:** Selectively  $^1\text{H}$  decoupled  $^{13}\text{C}$  spectra of Dy-DOTA-M7FPy. The  $^1\text{H}$  decoupler offset has been set to the proton frequency of the following methyl resonances: -97.7 ppm (purple), -81.7 ppm (blue), -48.4 ppm (green) and 19.1 ppm (black). The red spectra with no decoupling was taken as a reference.

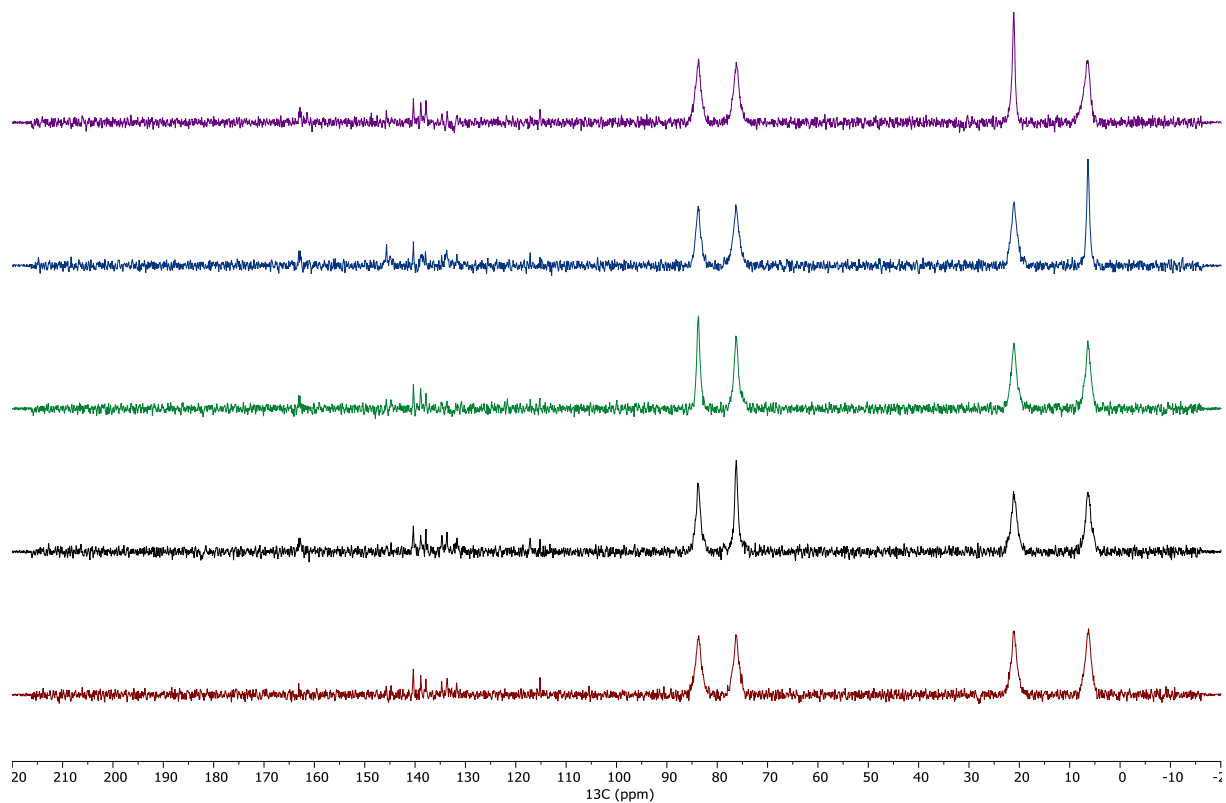


**Figure S107:** Selectively  $^1\text{H}$  decoupled  $^{13}\text{C}$  spectra of Ho-DOTA-M7FPy. The  $^1\text{H}$  decoupler offset has been set to the proton frequency of the following methyl resonances: -45.39 ppm (purple), -31.81 ppm (blue), 15.78 ppm (green) and -18.38 ppm (black). The red spectra with no decoupling was taken as a reference.



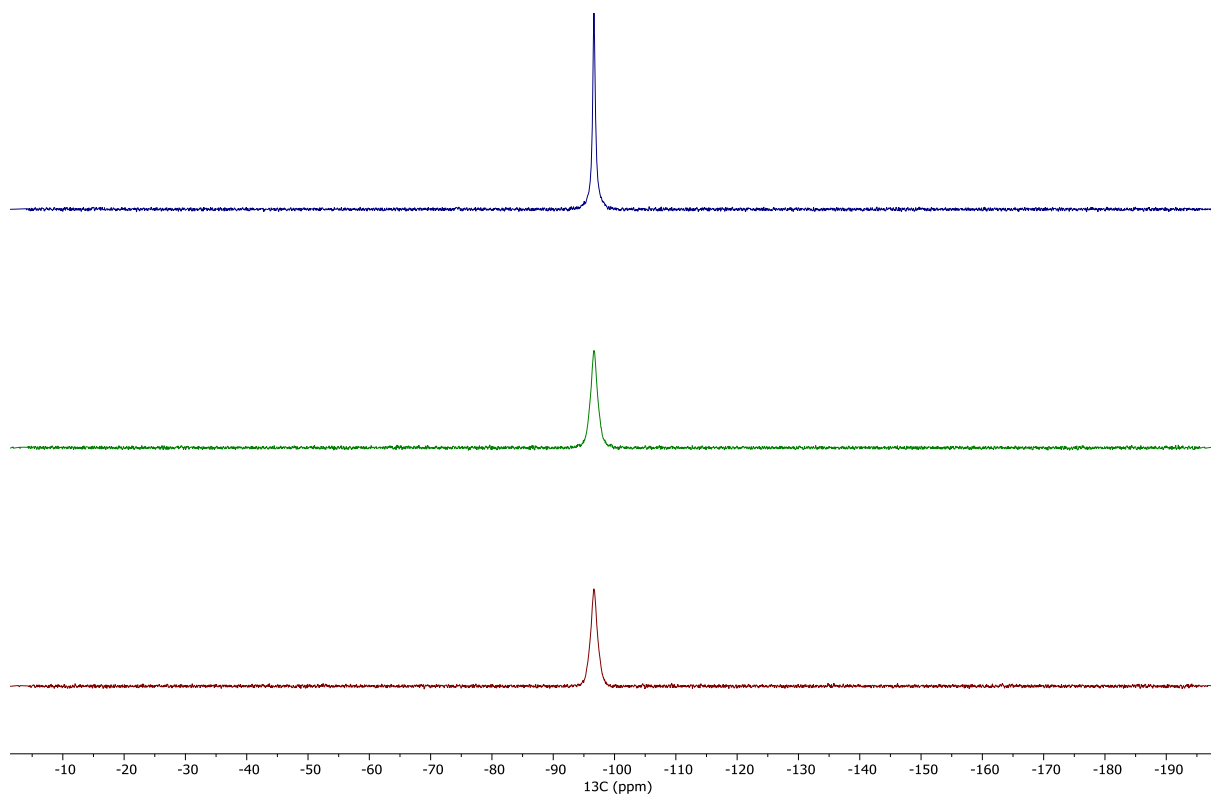
**Figure S108:** Selectively  $^1\text{H}$  decoupled  $^{13}\text{C}$  spectra of Er-DOTA-M7FPy. The  $^1\text{H}$  decoupler offset has been set to the proton frequency of the following methyl resonances: 5.5 ppm (purple), 25.34 ppm (blue), 40.06 ppm (green) and 2.0 ppm (black). The red spectra with no decoupling was taken as a reference.



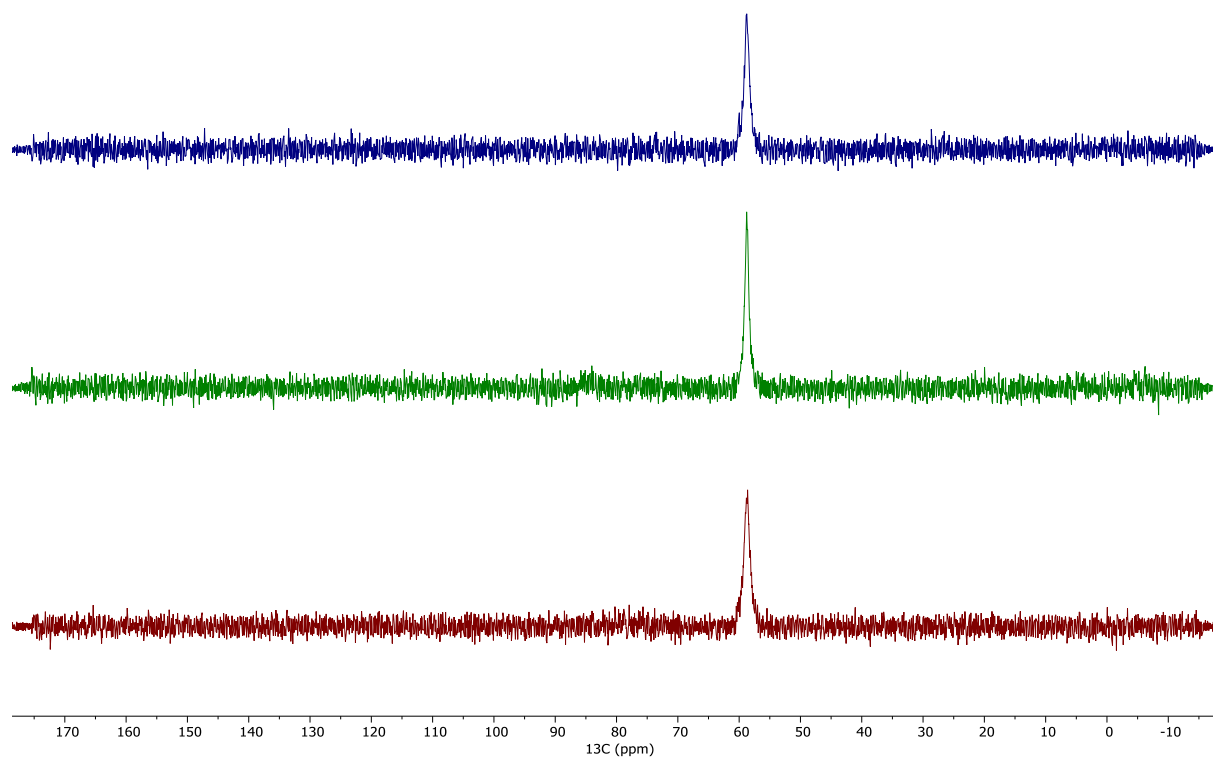


**Figure S109:** Selectively  $^1\text{H}$  decoupled  $^{13}\text{C}$  spectra of Tm-DOTA-M7FPy. The  $^1\text{H}$  decoupler offset has been set to the proton frequency of the following methyl resonances: 23.49 ppm (purple), 13.5 ppm (blue), 67.83 ppm (green) and 65.35 ppm (black). The red spectra with no decoupling was taken as a reference.

### 2.6.16.2 Ln-DOTA-M8 (60)

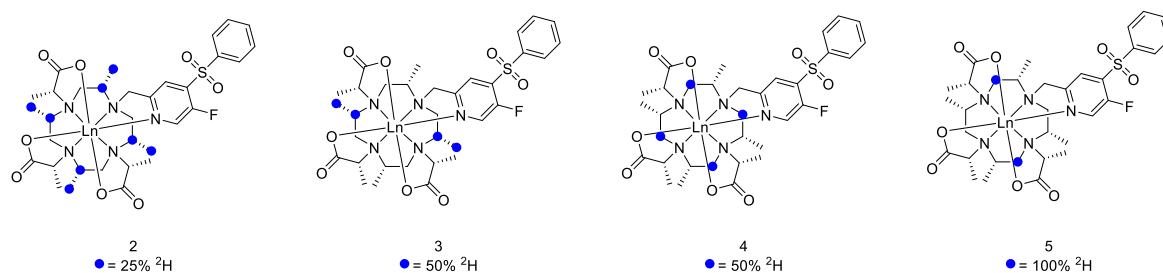


**Figure S110:** Selectively  $^1\text{H}$  decoupled  $^{13}\text{C}$  spectra of Dy-DOTA-M8. The  $^1\text{H}$  decoupler offset has been set to the proton frequency of the following methyl resonances: -47.5 ppm (blue) and 102.1 ppm (green). The red spectra with no decoupling was taken as a reference.



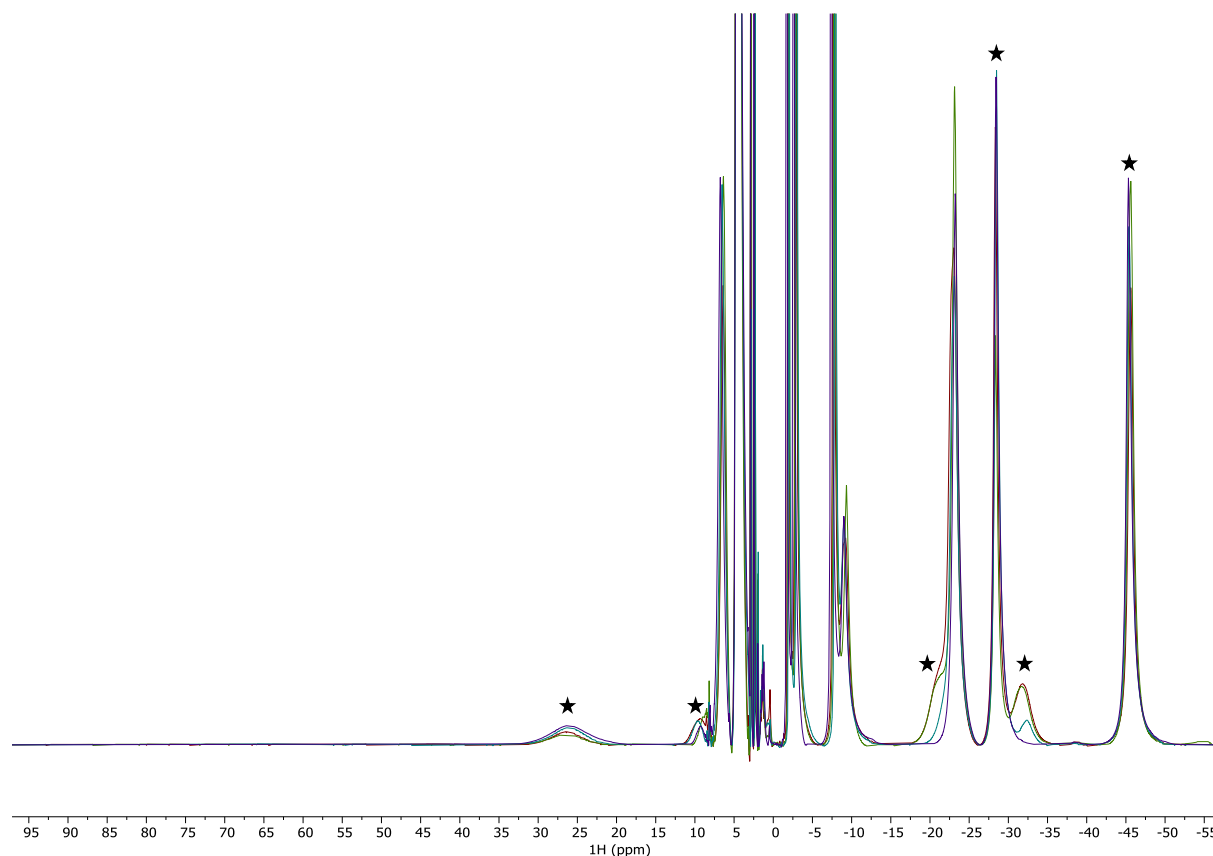
**Figure S111:** Selectively  $^1\text{H}$  decoupled  $^{13}\text{C}$  spectra of Tm-DOTA-M8. The  $^1\text{H}$  decoupler offset has been set to the proton frequency of the following methyl resonances: -140.7 ppm (blue) and 53.4 ppm (green). The red spectra with no decoupling was taken as a reference.

## 2.6.17 Overlaid spectra of the deuterium labelling schemes (2-5)

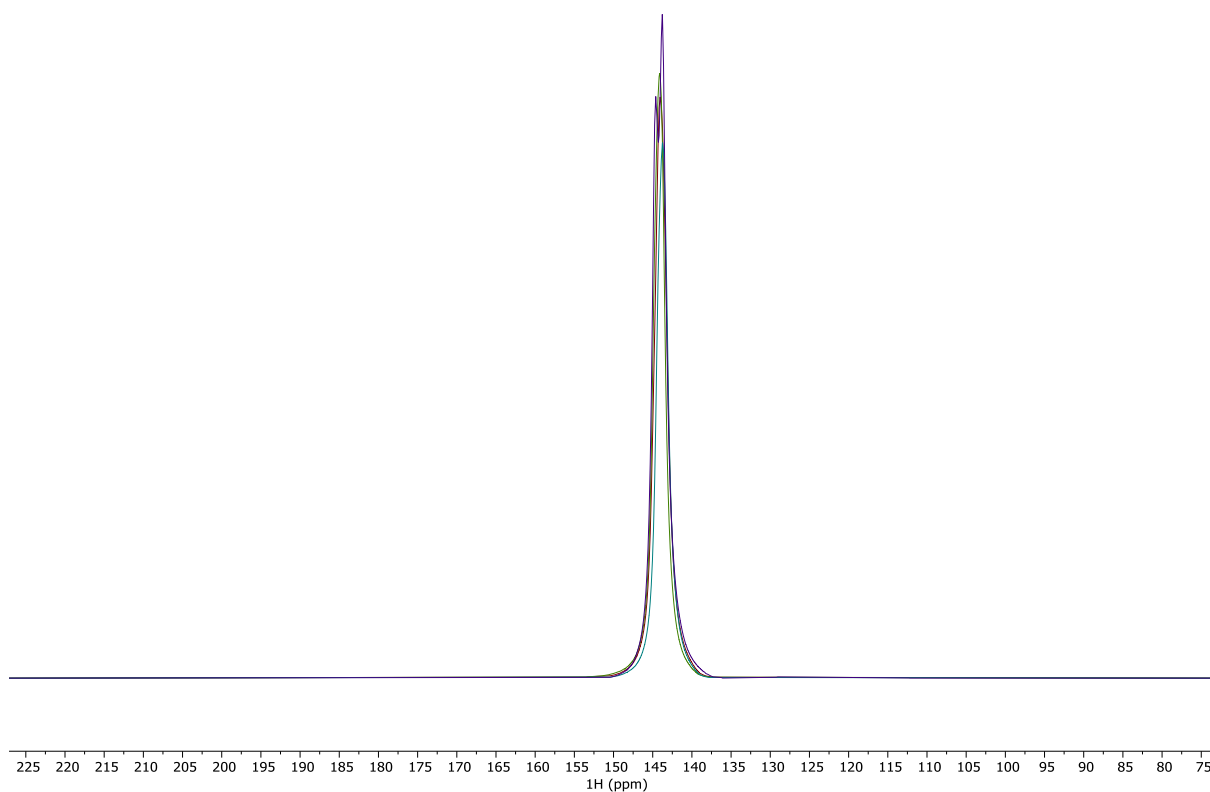


**Figure S112:** All four different deuterium labelling schemes of Ln-DOTA-M7FPy. On complex **2** and **3** the cyclen methyl and  $\text{H}_\alpha$  protons are labelled with 25% or 50% deuterium, respectively. On complex **4** and **5** the axial and equatorial cyclen methylene protons are labelled with 50% and 100% deuterium, respectively.

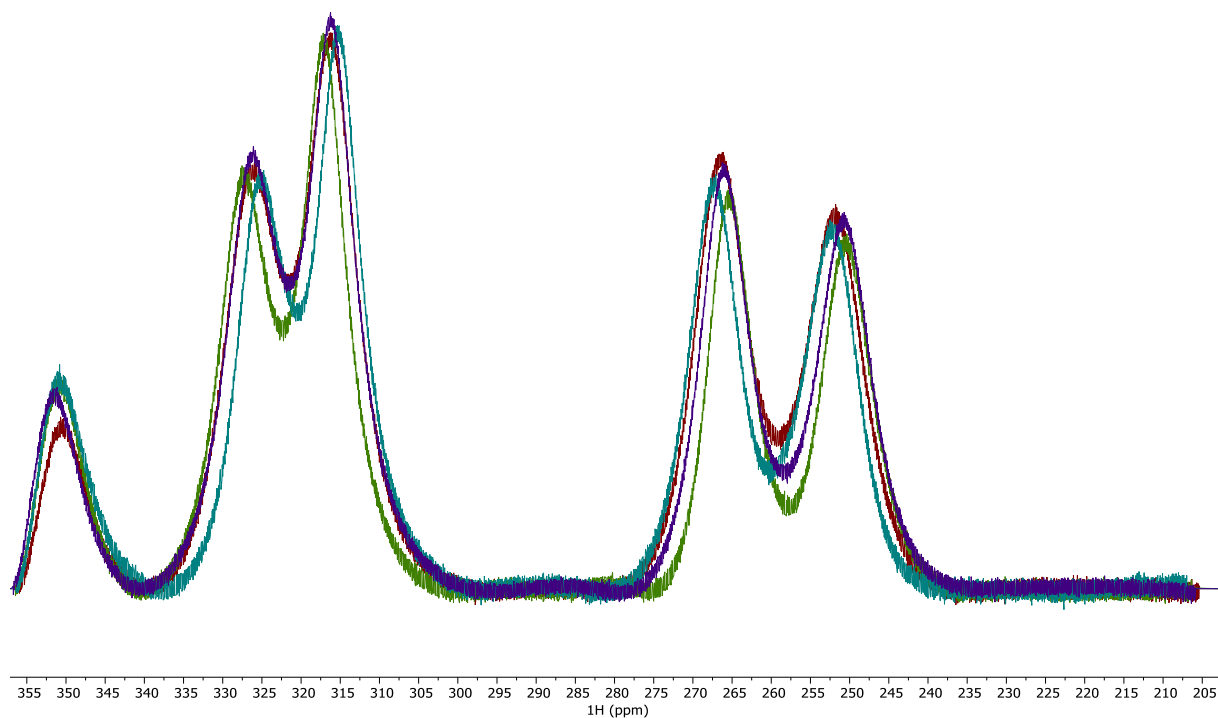
## Terbium



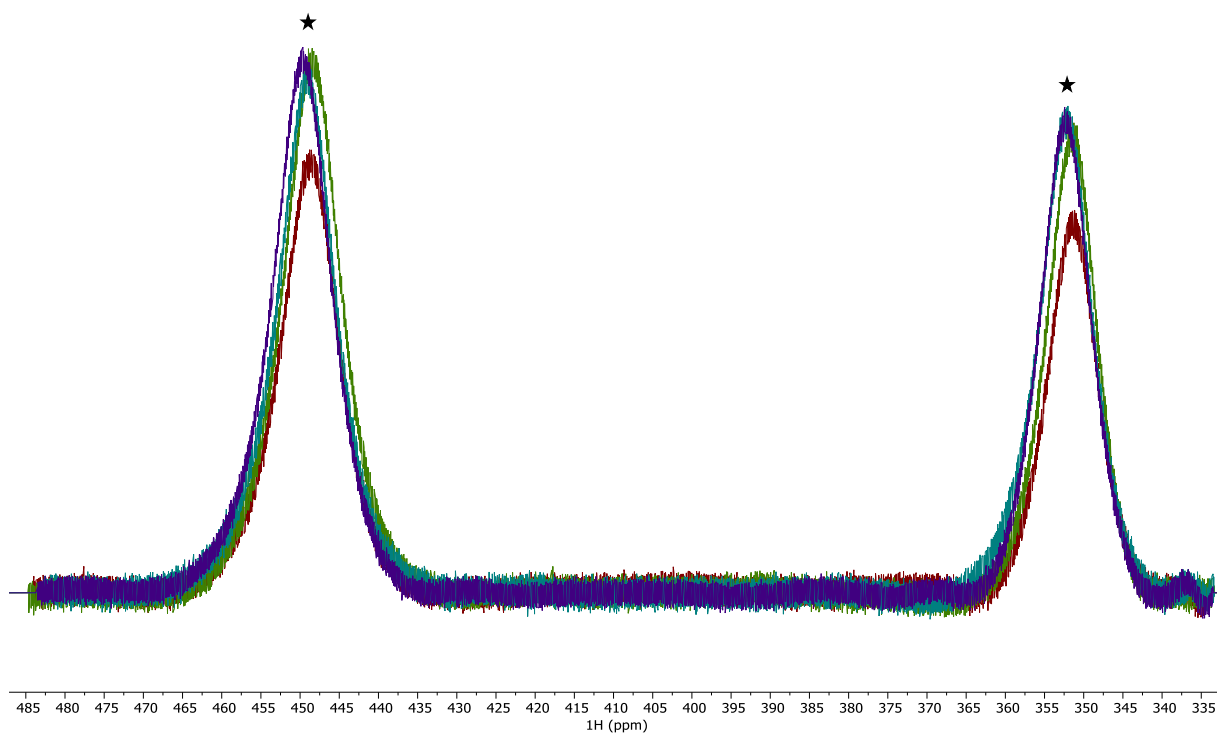
**Figure S113:** Superimposed  $^1\text{H}$  spectra of all four different deuterium labelling schemes of Tb-DOTA-M7FPy. The spectra are coloured as follows red (**2**), green (**3**), turquoise (**4**), purple (**5**). The numbers represent the labelling schemes and can be found in figure 2 in the main text or figure S111 in the SI. Signals which are affected by deuterium labelling are marked with a star.



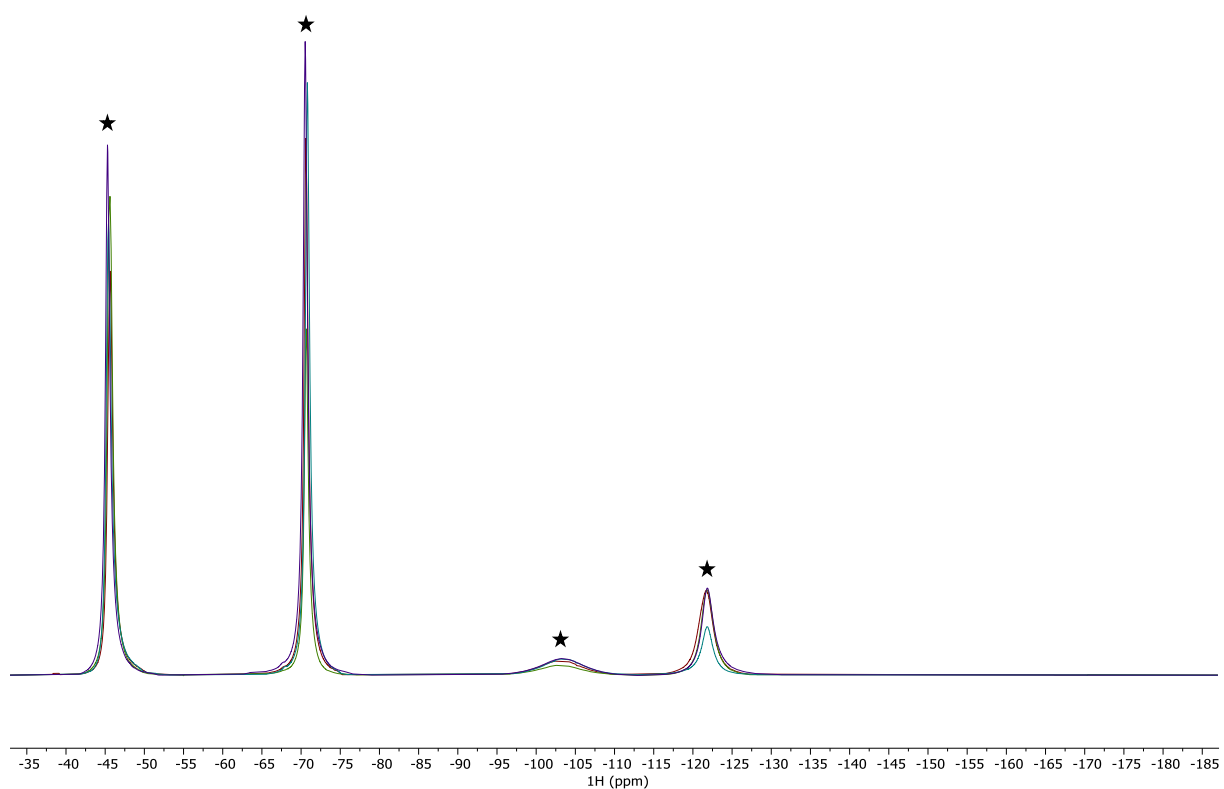
**Figure S114:** Superimposed <sup>1</sup>H spectra of all four different deuterium labelling schemes of Tb-DOTA-M7FPy. The spectra are coloured as follows red (2), green (3), turquoise (4), purple(5). The numbers represent the labelling schemes and can be found in figure 2 in the main text or figure S111 in the SI. Signals which are affected by deuterium labelling are marked with a star.



**Figure S115:** Superimposed <sup>1</sup>H spectra of all four different deuterium labelling schemes of Tb-DOTA-M7FPy. The spectra are coloured as follows red (2), green (3), turquoise (4), purple(5). The numbers represent the labelling schemes and can be found in figure 2 in the main text or figure S111 in the SI. Signals which are affected by deuterium labelling are marked with a star.

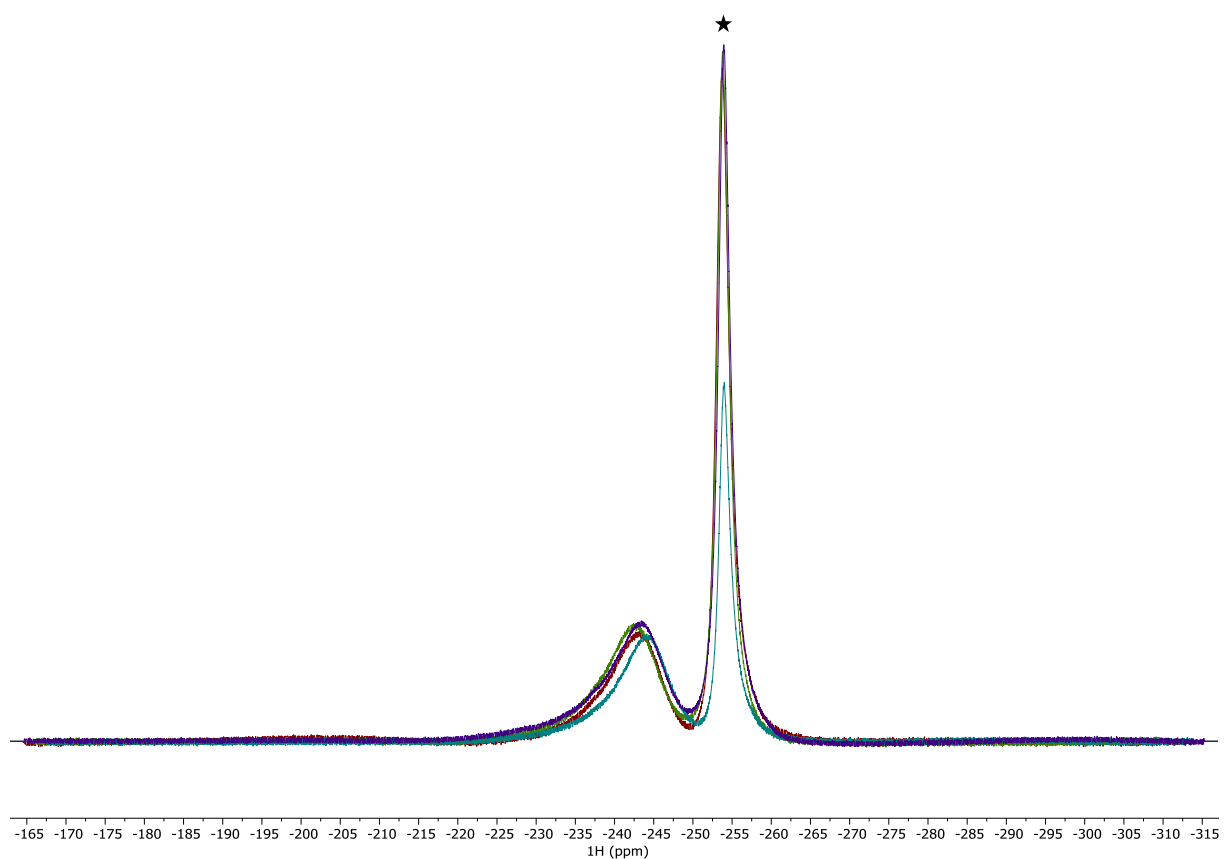


**Figure 116:** Superimposed  $^1\text{H}$  spectra of all four different deuterium labelling schemes of Tb-DOTA-M7FPy. The spectra are coloured as follows red (2), green (3), turquoise (4), purple(5). The numbers represent the labelling schemes and can be found in figure 2 in the main text or figure S111 in the SI. Signals which are affected by deuterium labelling are marked with a star.

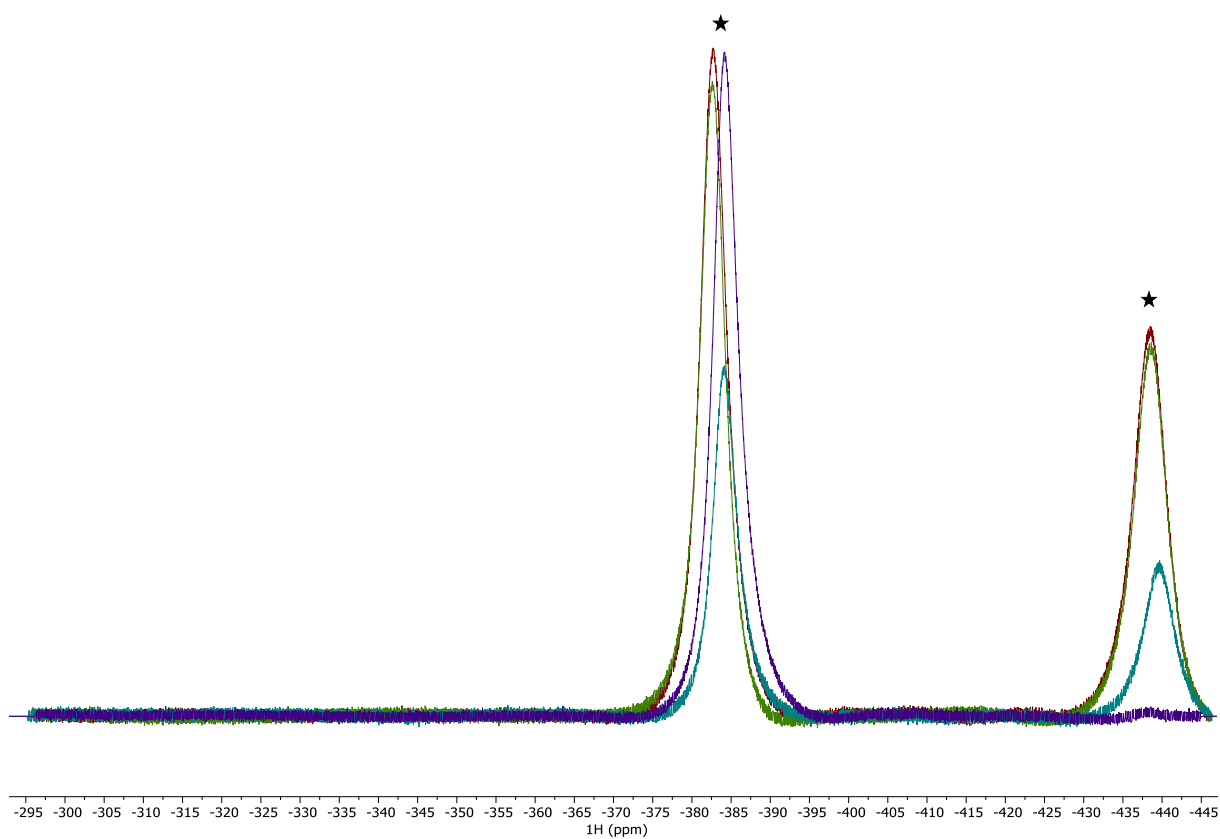


**Figure S117:** Superimposed <sup>1</sup>H spectra of all four different deuterium labelling schemes of Tb-DOTA-M7FPy. The spectra are coloured as follows red (2), green (3), turquoise (4), purple(5). The numbers represent the labelling schemes and can be found in figure 2 in the main text or figure S111 in the SI. Signals which are affected by deuterium labelling are marked with a star.

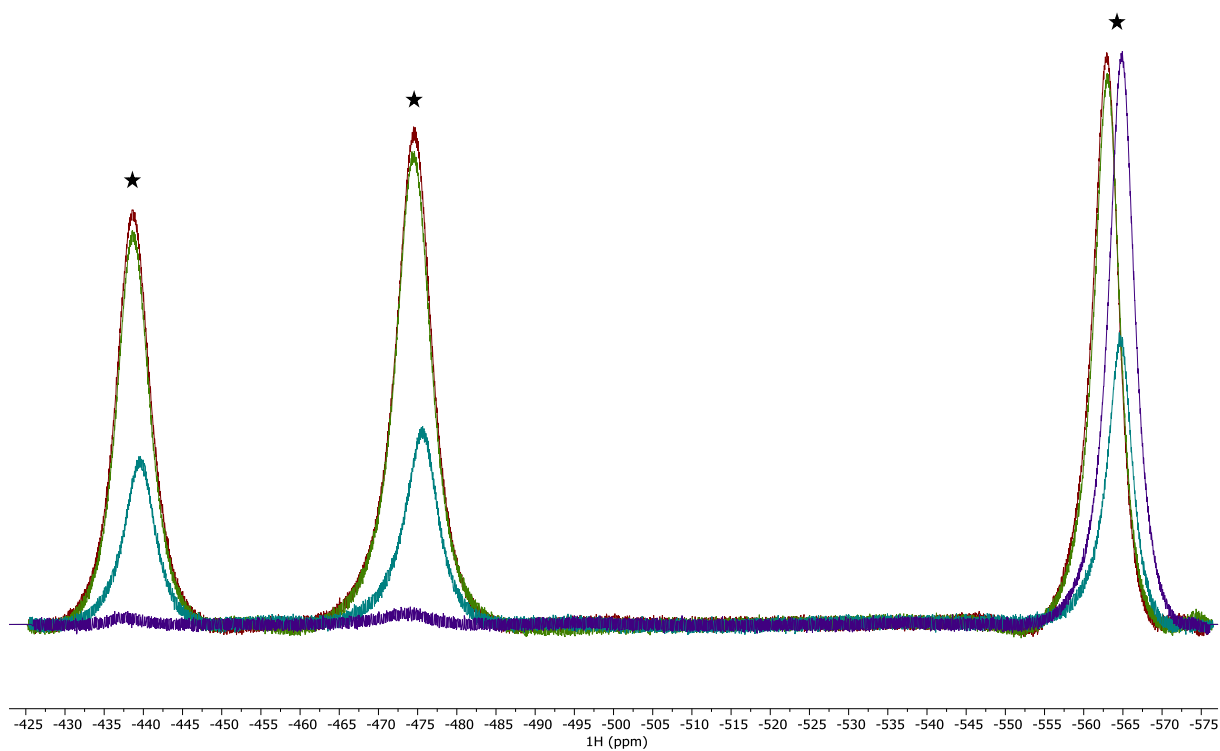




**Figure S118:** Superimposed <sup>1</sup>H spectra of all four different deuterium labelling schemes of Tb-DOTA-M7FPy. The spectra are coloured as follows red (2), green (3), turquoise (4), purple(5). The numbers represent the labelling schemes and can be found in figure 2 in the main text or figure S111 in the SI. Signals which are affected by deuterium labelling are marked with a star.

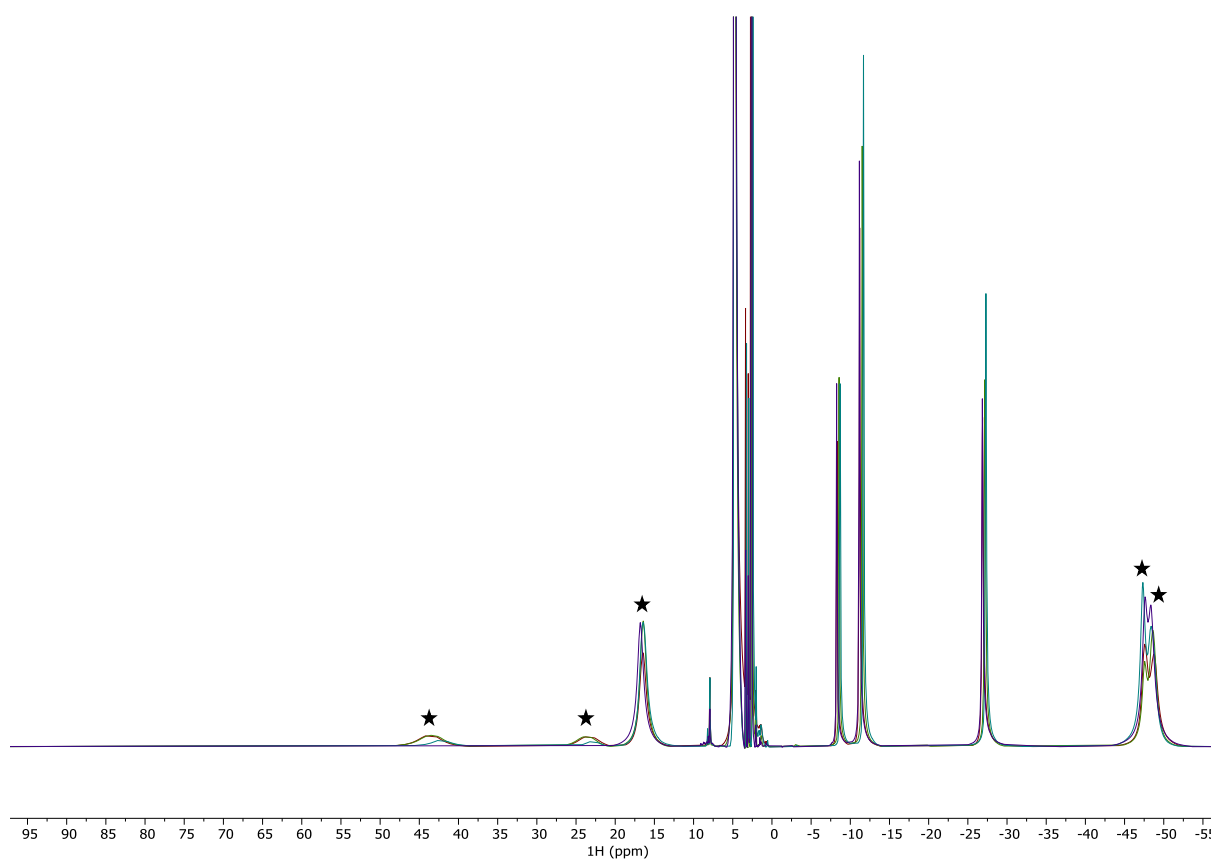


**Figure S119:** Superimposed <sup>1</sup>H spectra of all four different deuterium labelling schemes of Tb-DOTA-M7FPy. The spectra are coloured as follows red (2), green (3), turquoise (4), purple(5). The numbers represent the labelling schemes and can be found in figure 2 in the main text or figure S111 in the SI. Signals which are affected by deuterium labelling are marked with a star.

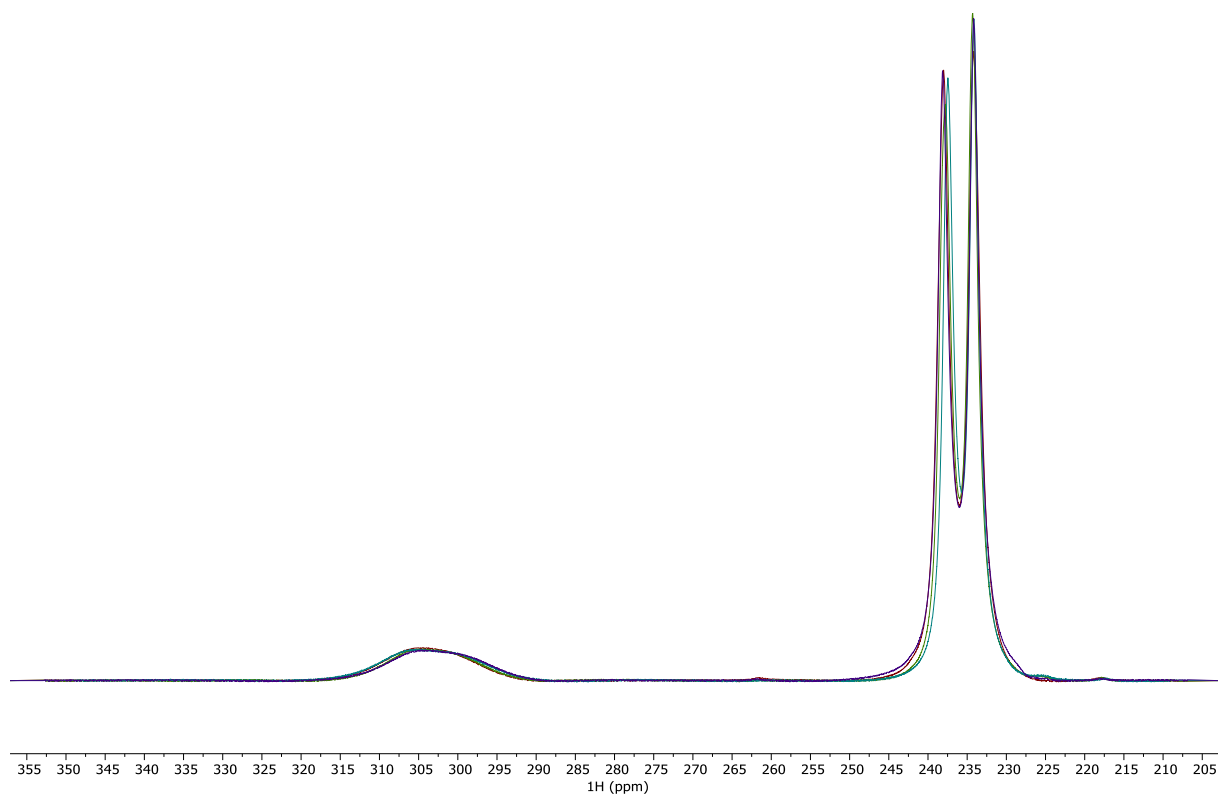


**Figure S120:** Superimposed <sup>1</sup>H spectra of all four different deuterium labelling schemes of Tb-DOTA-M7FPy. The spectra are coloured as follows red (2), green (3), turquoise (4), purple(5). The numbers represent the labelling schemes and can be found in figure 2 in the main text or figure S111 in the SI. Signals which are affected by deuterium labelling are marked with a star.

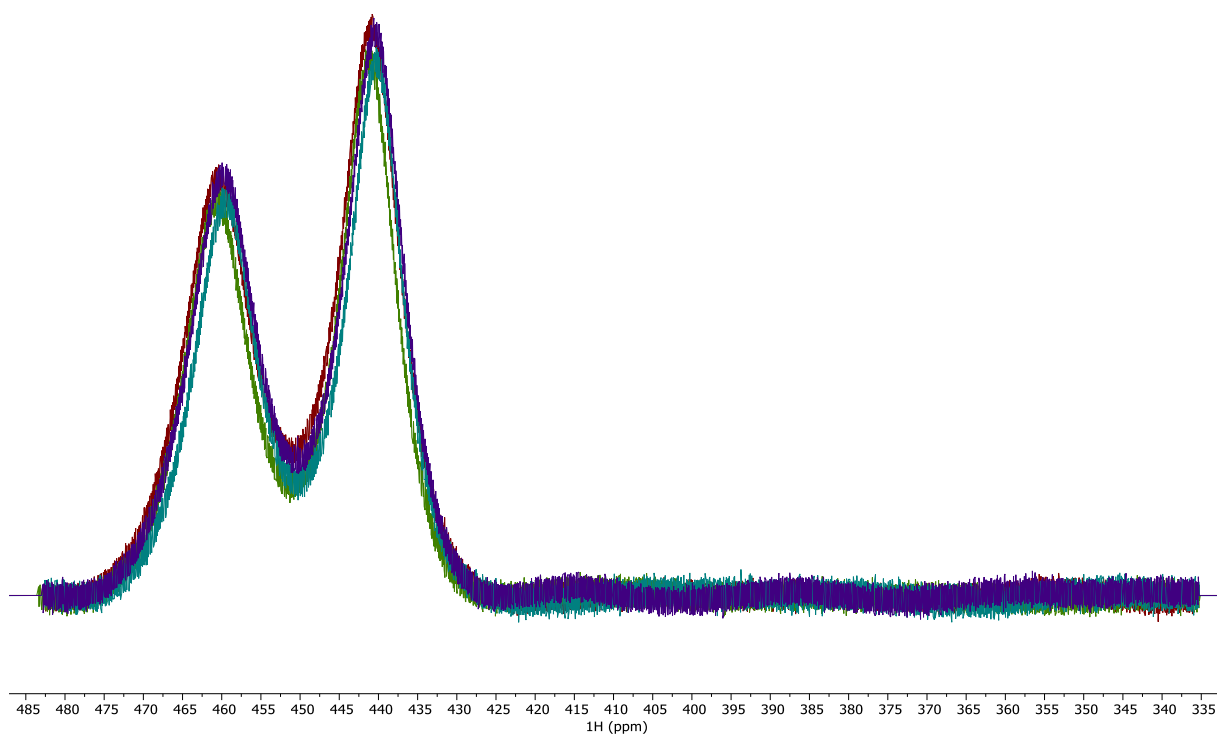
## Dysprosium



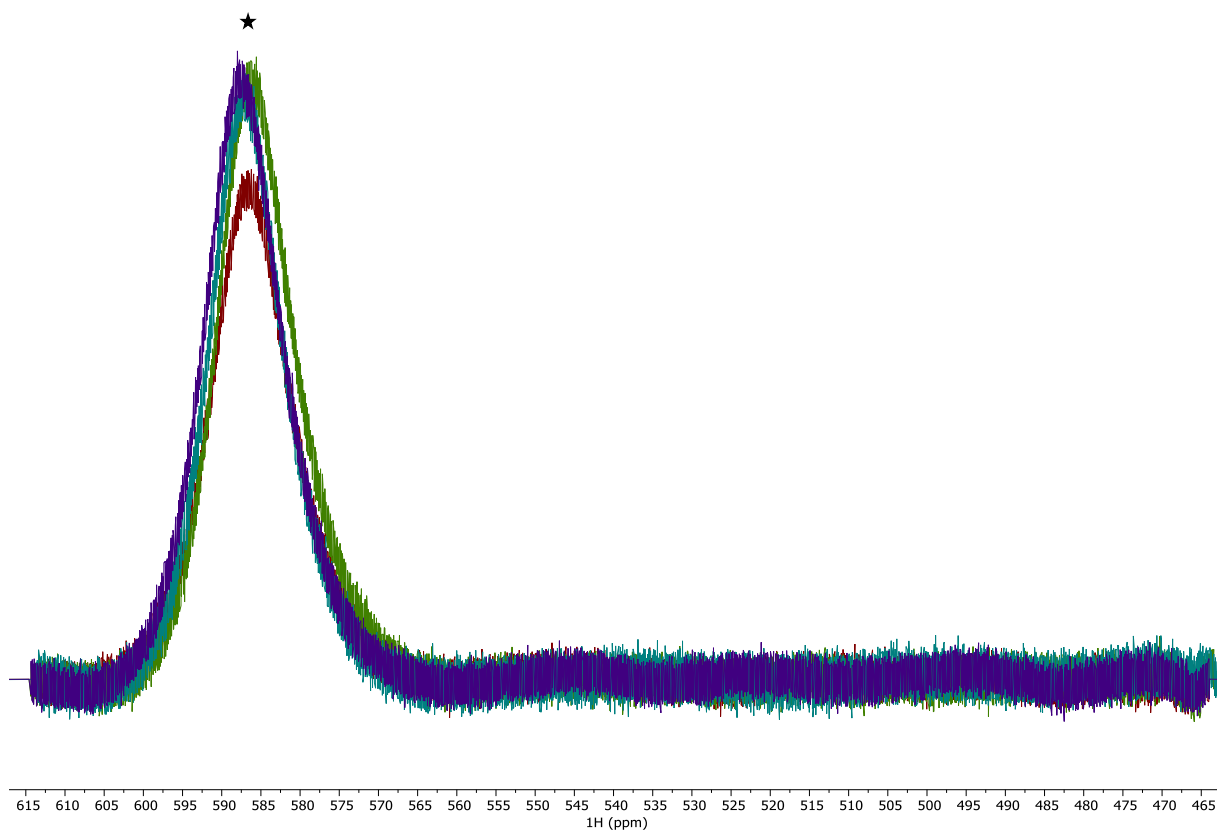
**Figure S121:** Superimposed <sup>1</sup>H spectra of all four different deuterium labelling schemes of Dy-DOTA-M7FPy. The spectra are coloured as follows red (2), green (3), turquoise (4), purple(5). The numbers represent the labelling schemes and can be found in figure 2 in the main text or figure S111 in the SI. Signals which are affected by deuterium labelling are marked with a star.



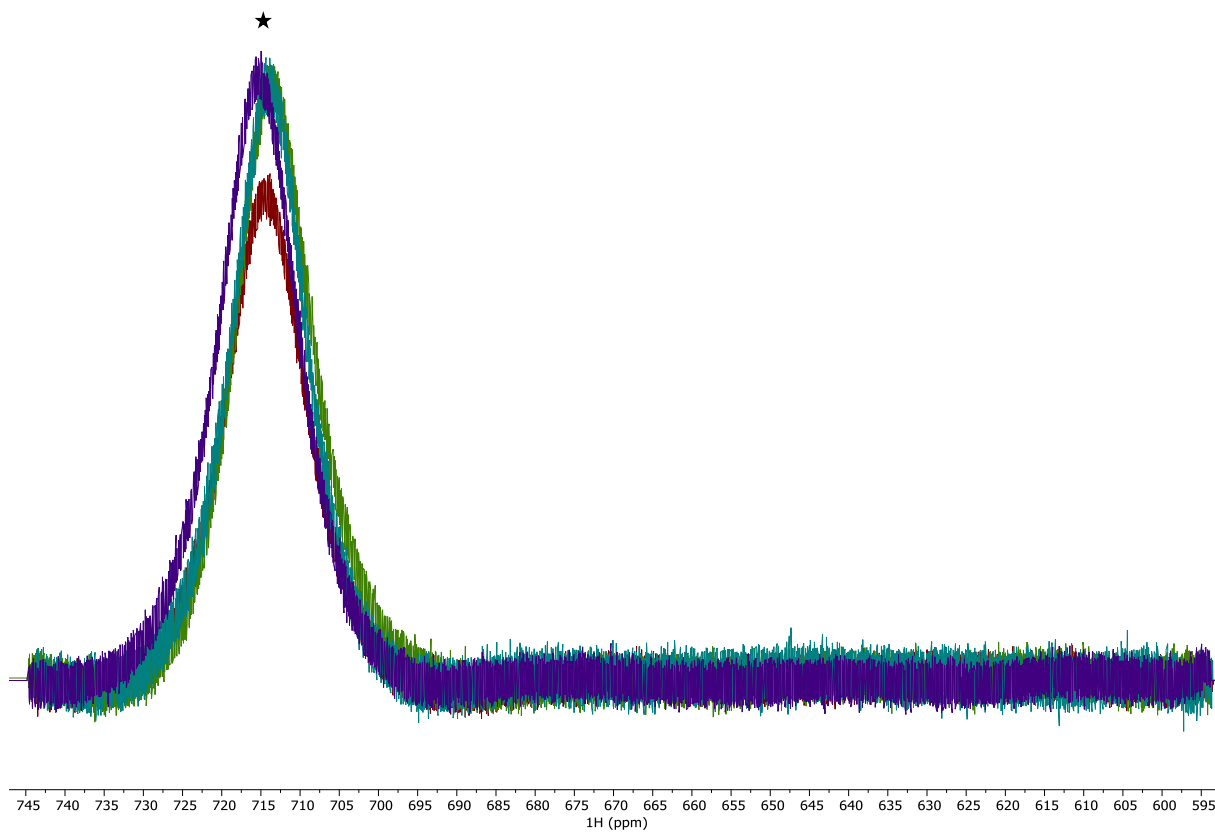
**Figure S122:** Superimposed  $^1\text{H}$  spectra of all four different deuterium labelling schemes of Dy-DOTA-M7FPy. The spectra are coloured as follows red (2), green (3), turquoise (4), purple(5). The numbers represent the labelling schemes and can be found in figure 2 in the main text or figure S111 in the SI. Signals which are affected by deuterium labelling are marked with a star.



**Figure S123:** Superimposed <sup>1</sup>H spectra of all four different deuterium labelling schemes of Dy-DOTA-M7FPy. The spectra are coloured as follows red (2), green (3), turquoise (4), purple(5). The numbers represent the labelling schemes and can be found in figure 2 in the main text or figure S111 in the SI. Signals which are affected by deuterium labelling are marked with a star.

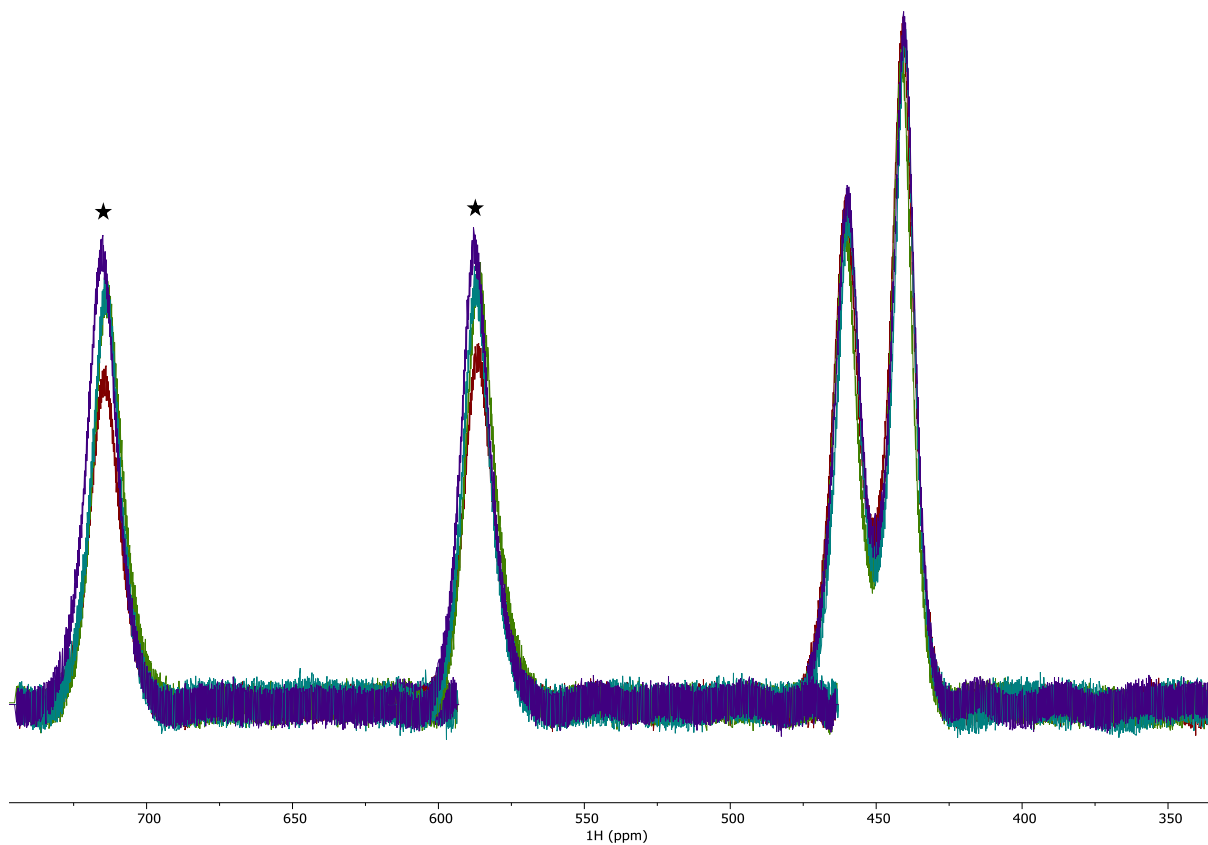


**Figure S124:** Superimposed  $^1\text{H}$  spectra of all four different deuterium labelling schemes of Dy-DOTA-M7FPy. The spectra are coloured as follows red (**2**), green (**3**), turquoise (**4**), purple(**5**). The numbers represent the labelling schemes and can be found in figure 2 in the main text or figure S111 in the SI. Signals which are affected by deuterium labelling are marked with a star.

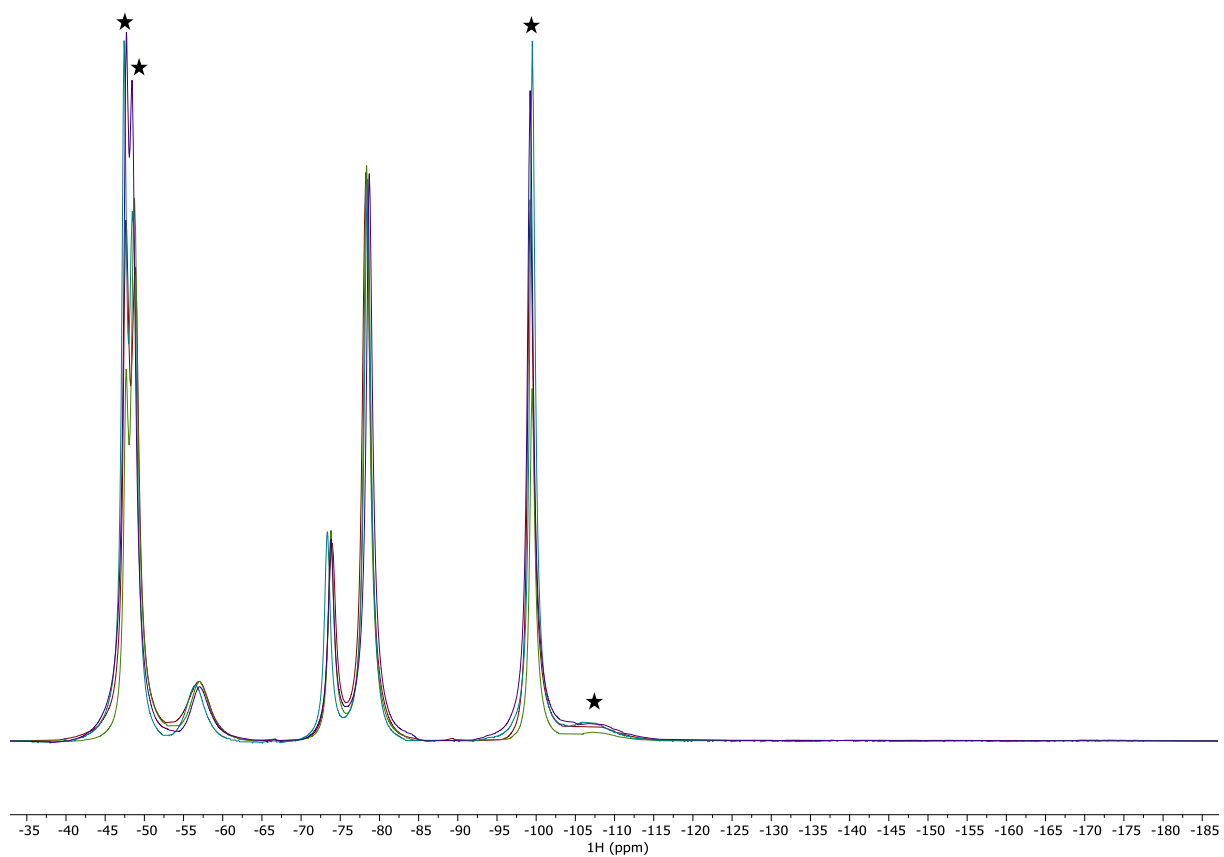


**Figure S125:** Superimposed <sup>1</sup>H spectra of all four different deuterium labelling schemes of Dy-DOTA-M7FPy. The spectra are coloured as follows red (2), green (3), turquoise (4), purple(5). The numbers represent the labelling schemes and can be found in figure 2 in the main text or figure S111 in the SI. Signals which are affected by deuterium labelling are marked with a star.

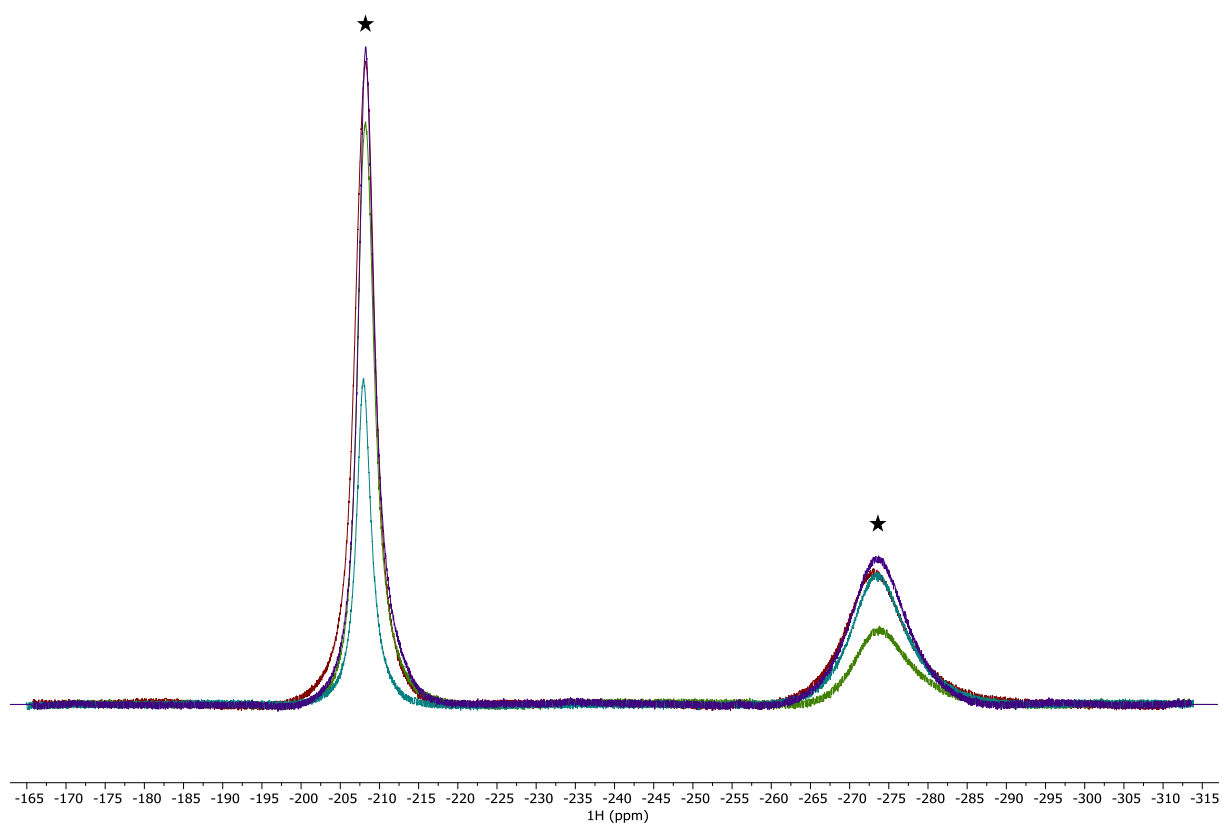




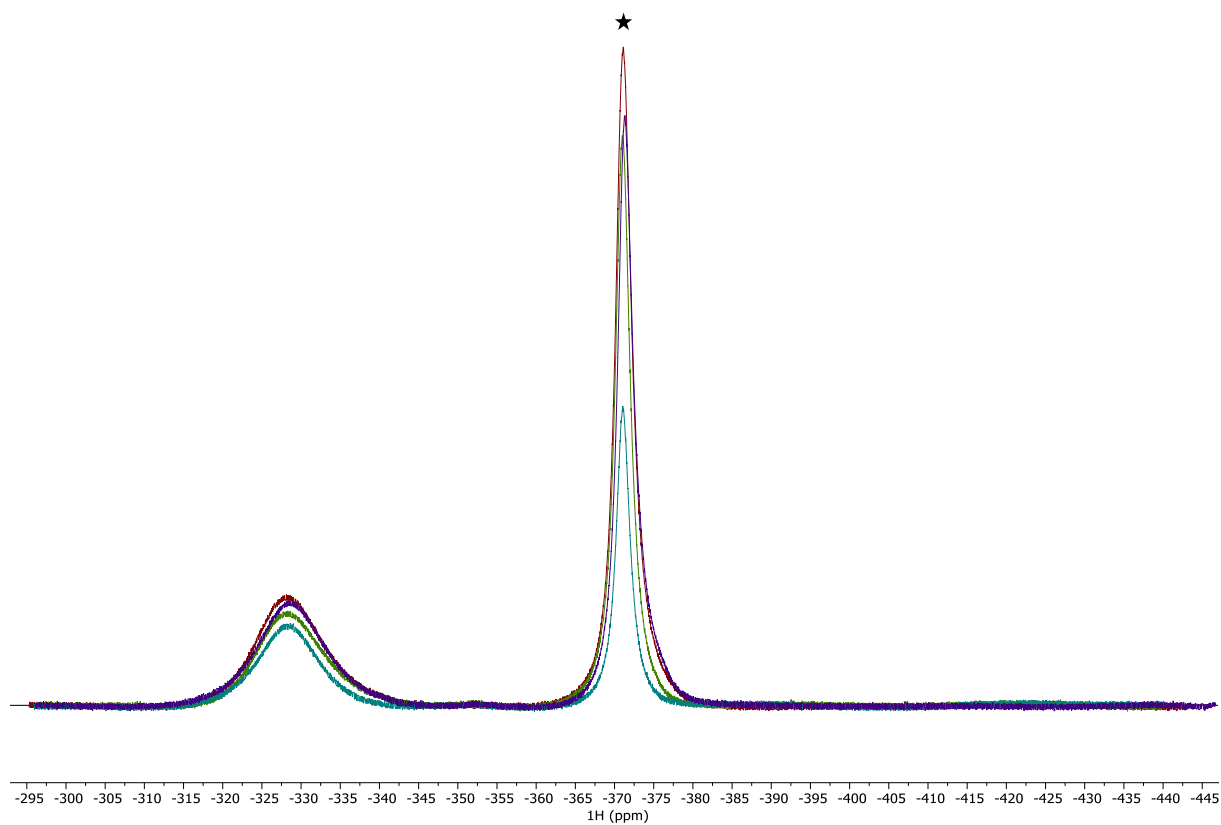
**Figure S126:** Superimposed <sup>1</sup>H spectra of all four different deuterium labelling schemes of Dy-DOTA-M7FPy. The spectra are coloured as follows red (2), green (3), turquoise (4), purple(5). The numbers represent the labelling schemes and can be found in figure 2 in the main text or figure S111 in the SI. Signals which are affected by deuterium labelling are marked with a star.



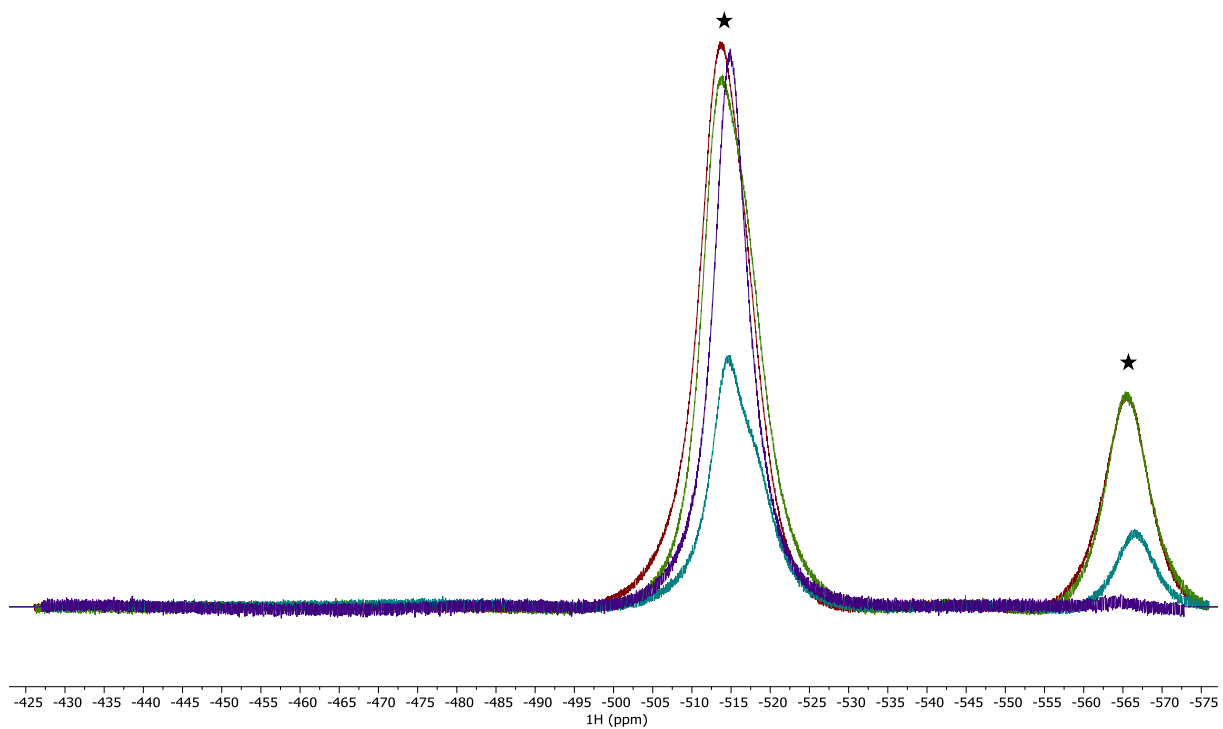
**Figure S127:** Superimposed <sup>1</sup>H spectra of all four different deuterium labelling schemes of Dy-DOTA-M7FPy. The spectra are coloured as follows red (2), green (3), turquoise (4), purple(5). The numbers represent the labelling schemes and can be found in figure 2 in the main text or figure S111 in the SI. Signals which are affected by deuterium labelling are marked with a star.



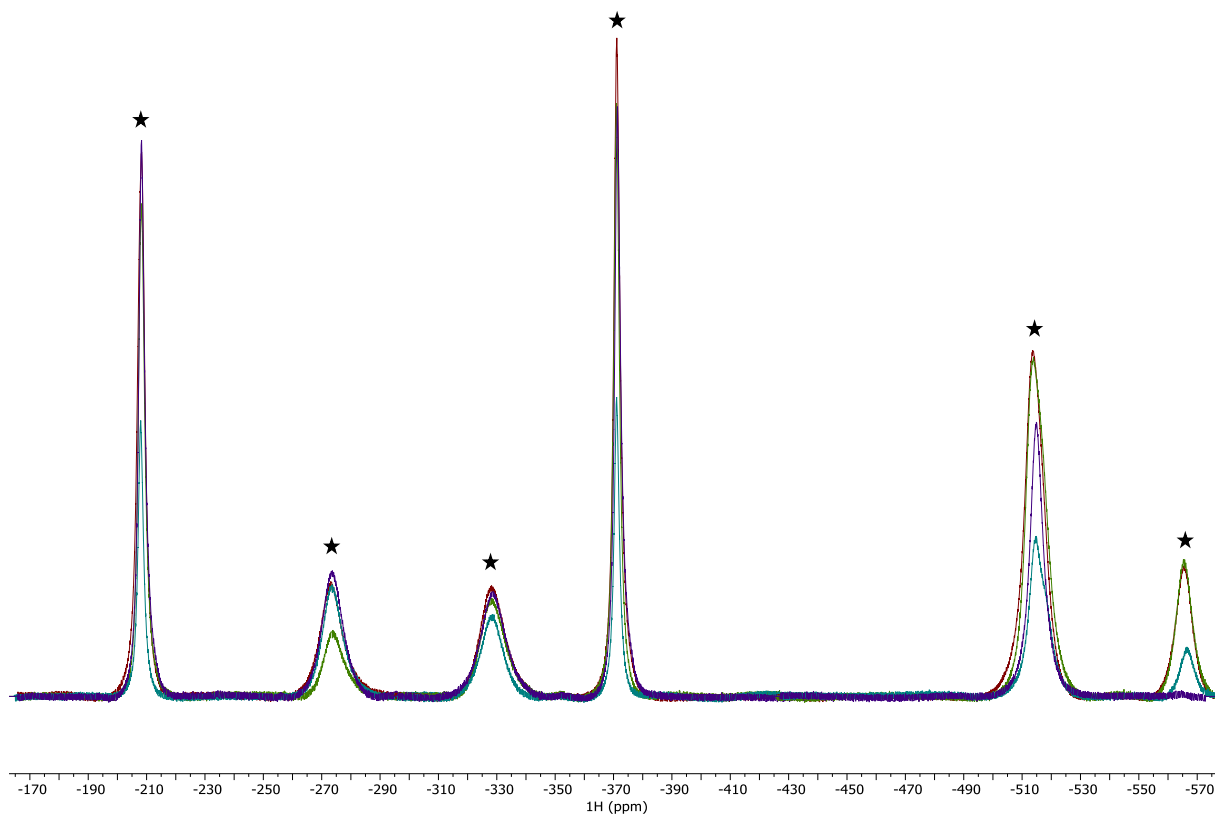
**Figure S128:** Superimposed <sup>1</sup>H spectra of all four different deuterium labelling schemes of Dy-DOTA-M7FPy. The spectra are coloured as follows red (2), green (3), turquoise (4), purple(5). The numbers represent the labelling schemes and can be found in figure 2 in the main text or figure S111 in the SI. Signals which are affected by deuterium labelling are marked with a star.



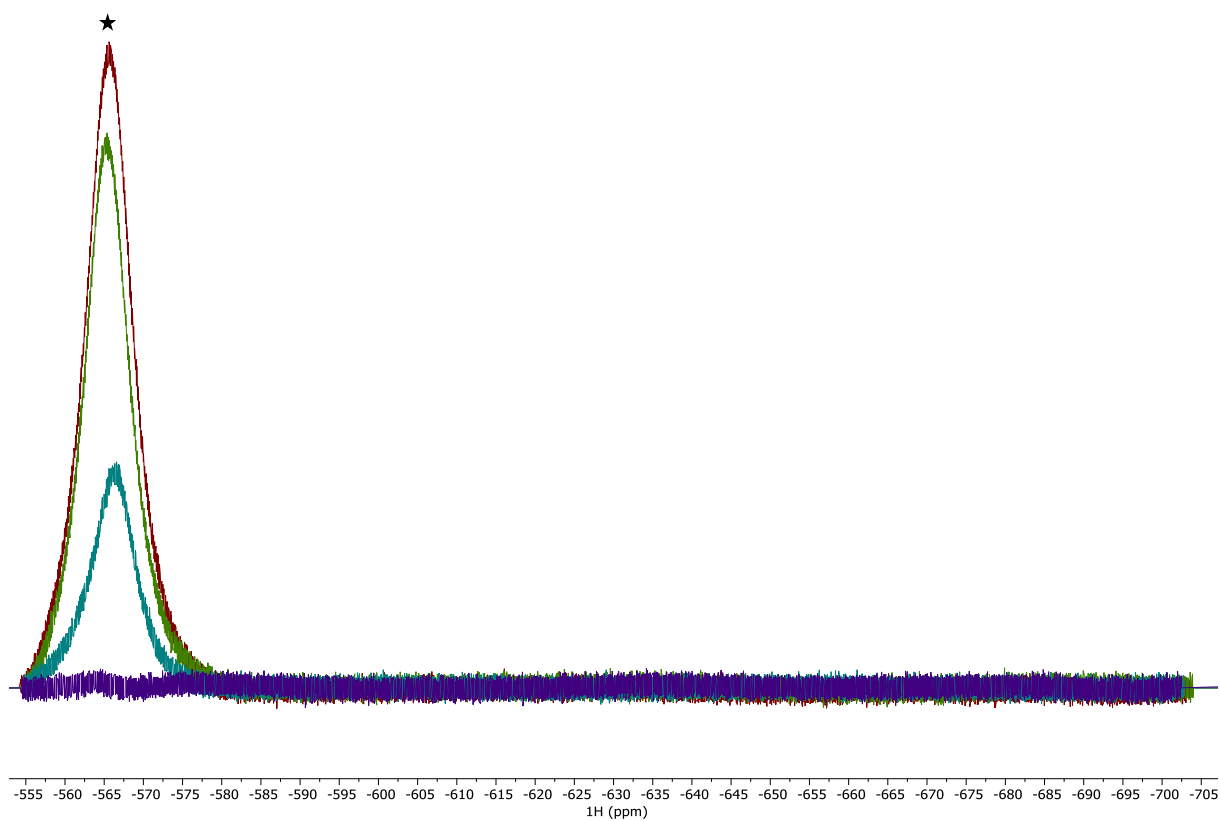
**Figure S129:** Superimposed <sup>1</sup>H spectra of all four different deuterium labelling schemes of Dy-DOTA-M7FPy. The spectra are coloured as follows red (2), green (3), turquoise (4), purple(5). The numbers represent the labelling schemes and can be found in figure 2 in the main text or figure S111 in the SI. Signals which are affected by deuterium labelling are marked with a star.



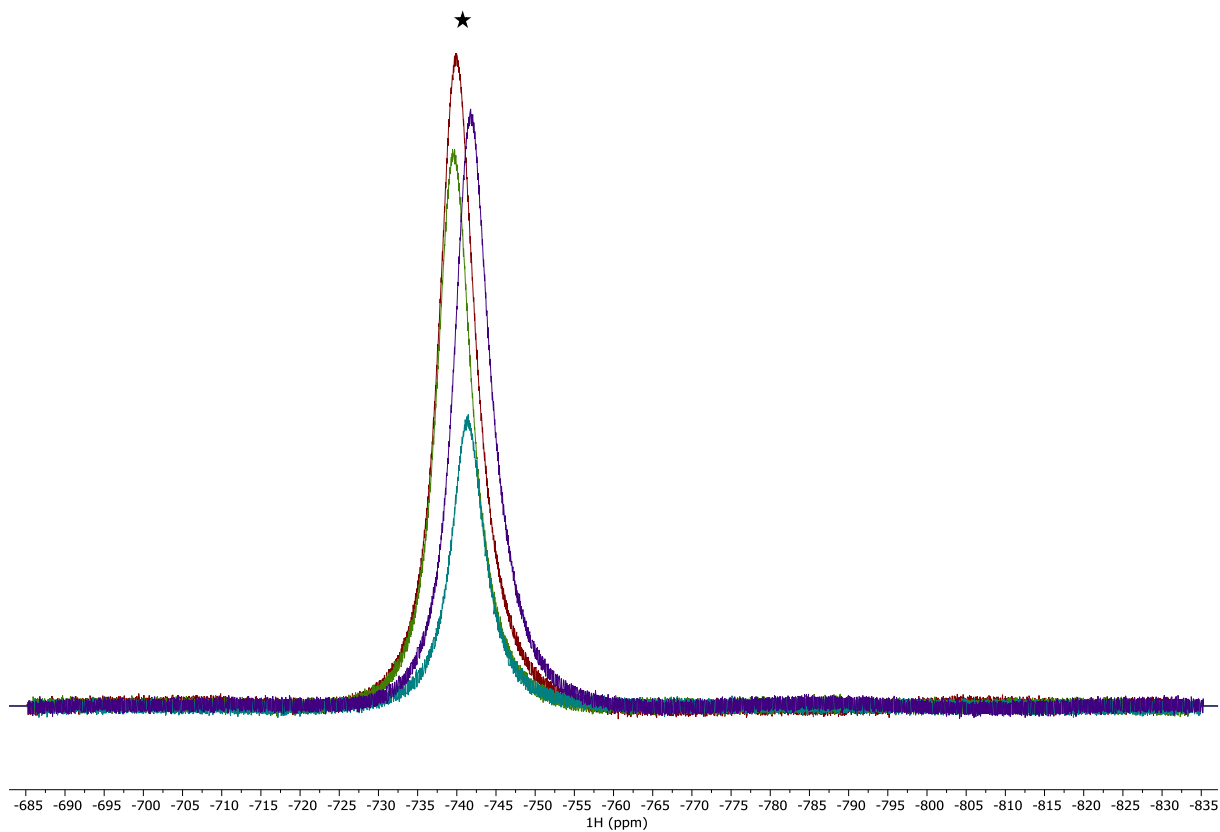
**Figure S130:** Superimposed <sup>1</sup>H spectra of all four different deuterium labelling schemes of Dy-DOTA-M7FPy. The spectra are coloured as follows red (2), green (3), turquoise (4), purple(5). The numbers represent the labelling schemes and can be found in figure 2 in the main text or figure S111 in the SI. Signals which are affected by deuterium labelling are marked with a star.



**Figure S131:** Superimposed <sup>1</sup>H spectra of all four different deuterium labelling schemes of Dy-DOTA-M7FPy. The spectra are coloured as follows red (2), green (3), turquoise (4), purple(5). The numbers represent the labelling schemes and can be found in figure 2 in the main text or figure S111 in the SI. Signals which are affected by deuterium labelling are marked with a star.



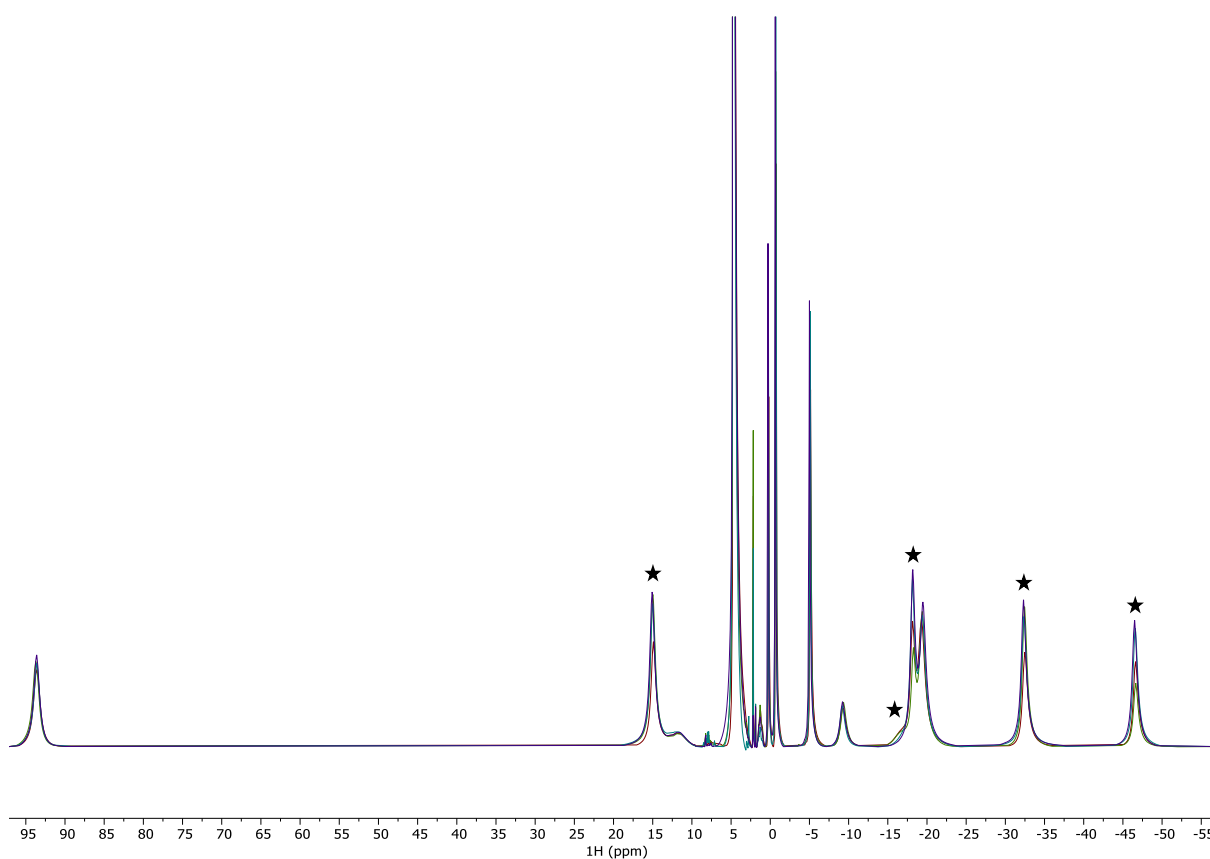
**Figure S132:** Superimposed <sup>1</sup>H spectra of all four different deuterium labelling schemes of Dy-DOTA-M7FPy. The spectra are coloured as follows red (2), green (3), turquoise (4), purple(5). The numbers represent the labelling schemes and can be found in figure 2 in the main text or figure S111 in the SI. Signals which are affected by deuterium labelling are marked with a star.



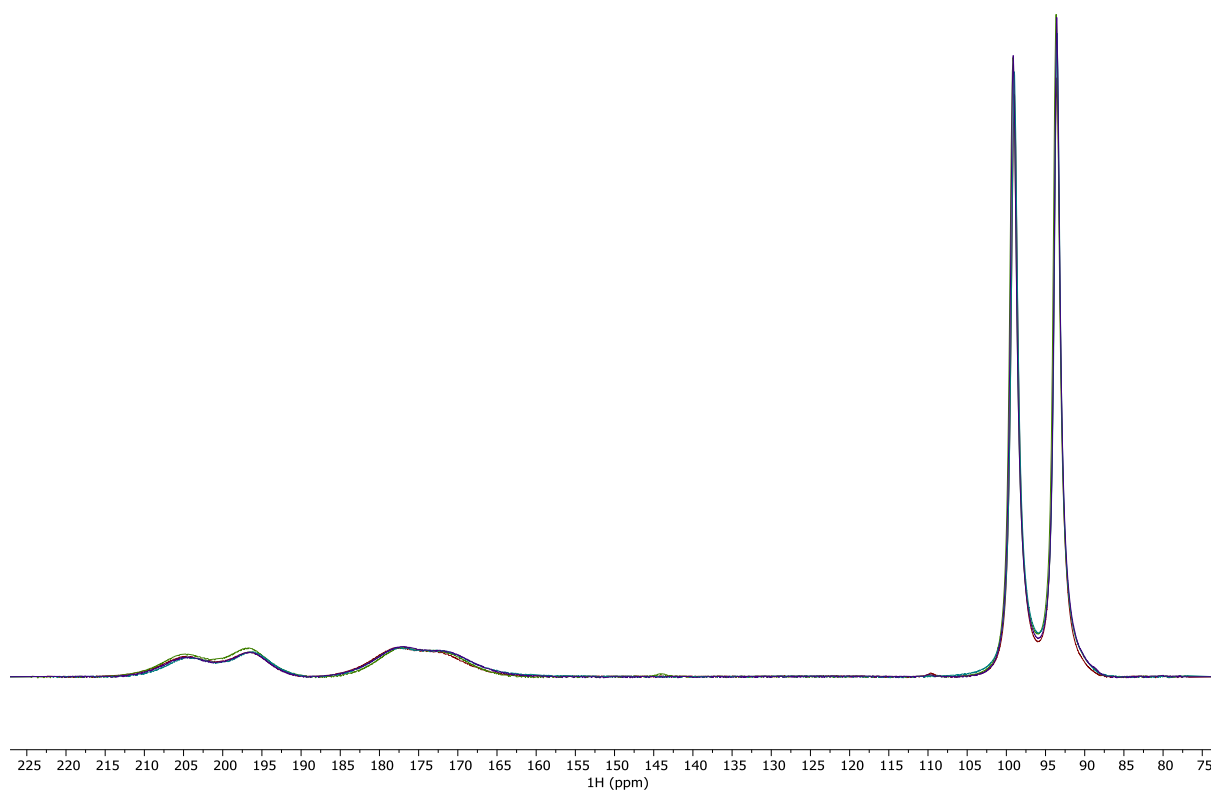
**Figure S133:** Superimposed <sup>1</sup>H spectra of all four different deuterium labelling schemes of Dy-DOTA-M7FPy. The spectra are coloured as follows red (2), green (3), turquoise (4), purple(5). The numbers represent the labelling schemes and can be found in figure 2 in the main text or figure S111 in the SI. Signals which are affected by deuterium labelling are marked with a star.



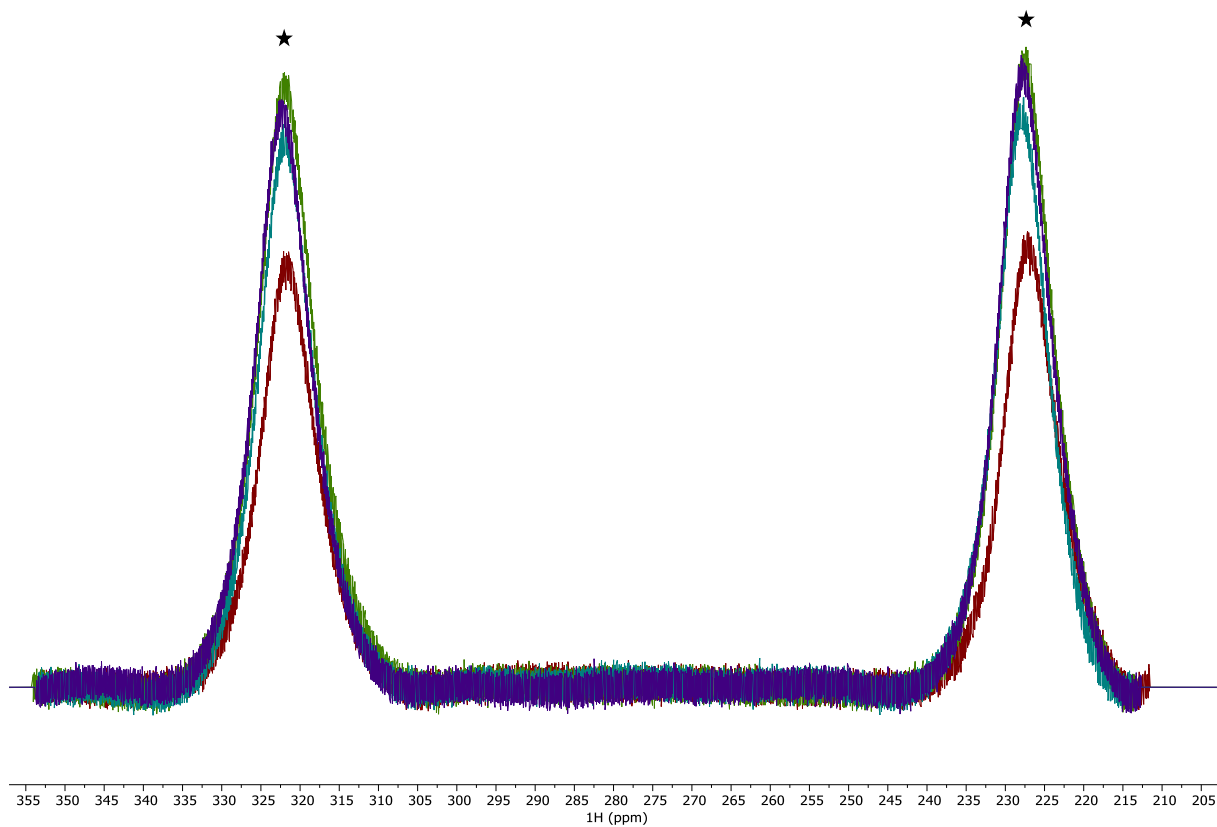
## Holmium



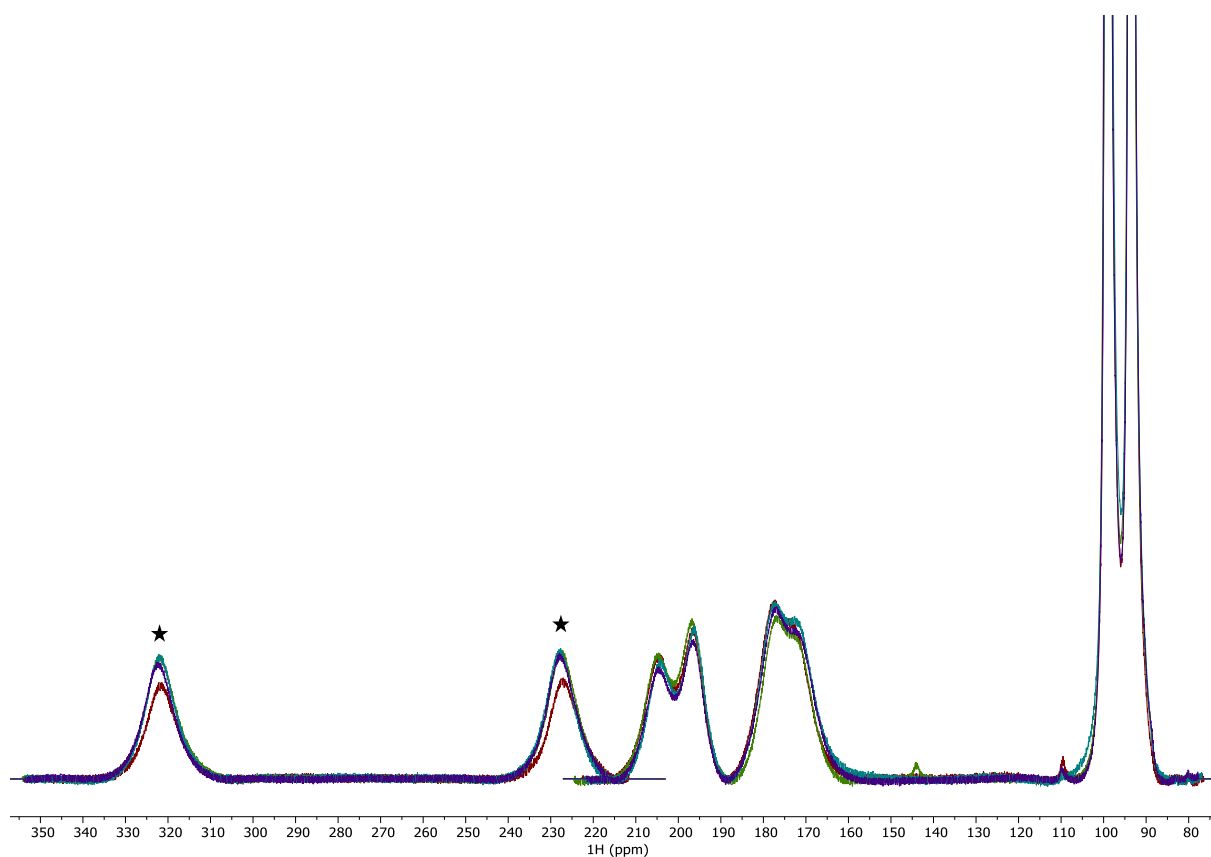
**Figure S134:** Superimposed  $^1\text{H}$  spectra of all four different deuterium labelling schemes of Ho-DOTA-M7FPy. The spectra are coloured as follows red (**2**), green (**3**), turquoise (**4**), purple(**5**). The numbers represent the labelling schemes and can be found in figure 2 in the main text or figure S111 in the SI. Signals which are affected by deuterium labelling are marked with a star.



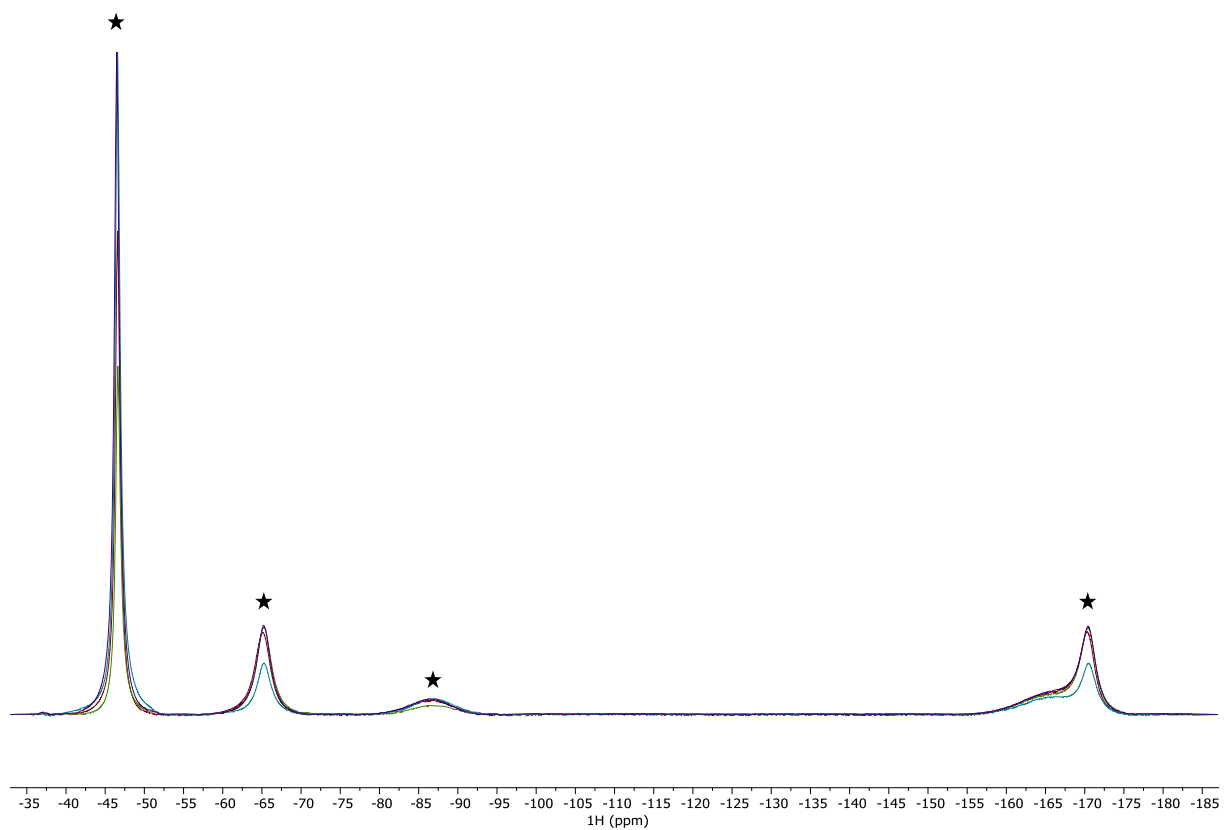
**Figure S135:** Superimposed <sup>1</sup>H spectra of all four different deuterium labelling schemes of Ho-DOTA-M7FPy. The spectra are coloured as follows red (**2**), green (**3**), turquoise (**4**), purple(**5**). The numbers represent the labelling schemes and can be found in figure 2 in the main text or figure S111 in the SI. Signals which are affected by deuterium labelling are marked with a star.



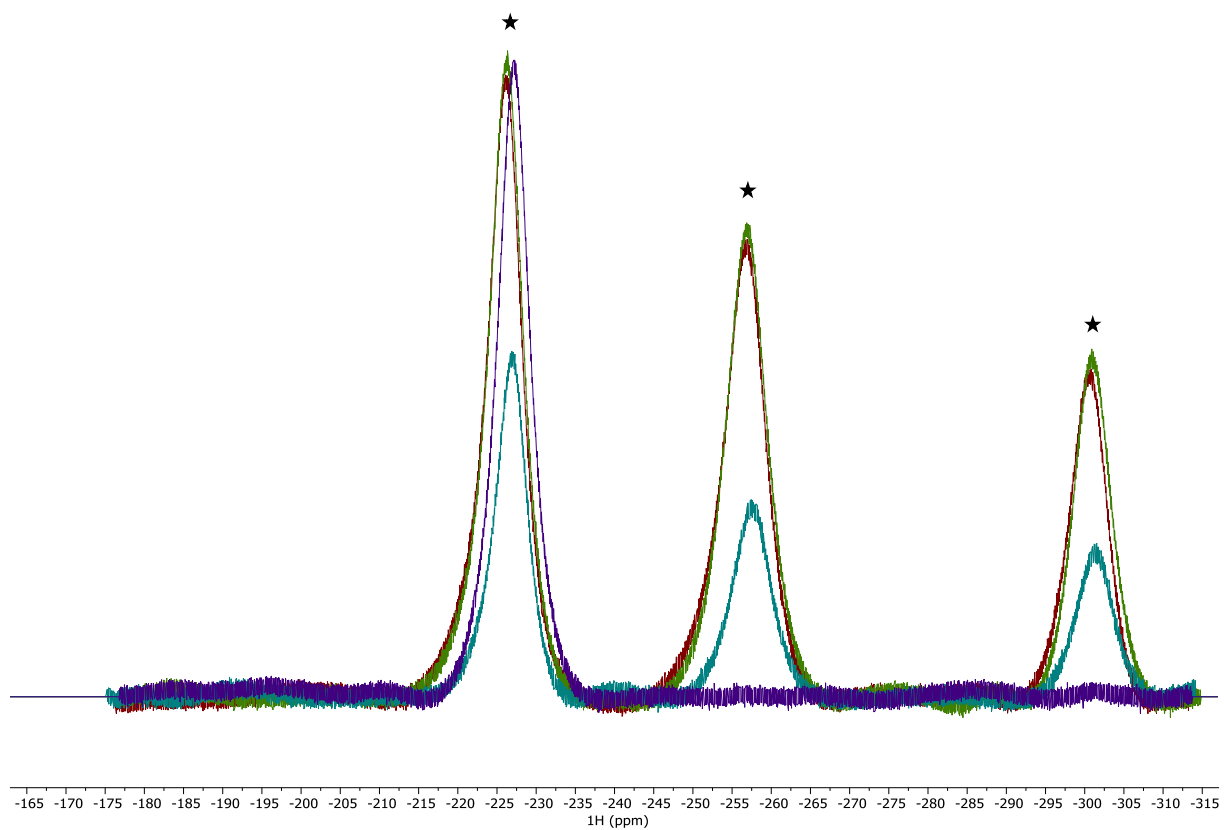
**Figure S136:** Superimposed <sup>1</sup>H spectra of all four different deuterium labelling schemes of Ho-DOTA-M7FPy. The spectra are coloured as follows red (2), green (3), turquoise (4), purple(5). The numbers represent the labelling schemes and can be found in figure 2 in the main text or figure S111 in the SI. Signals which are affected by deuterium labelling are marked with a star.



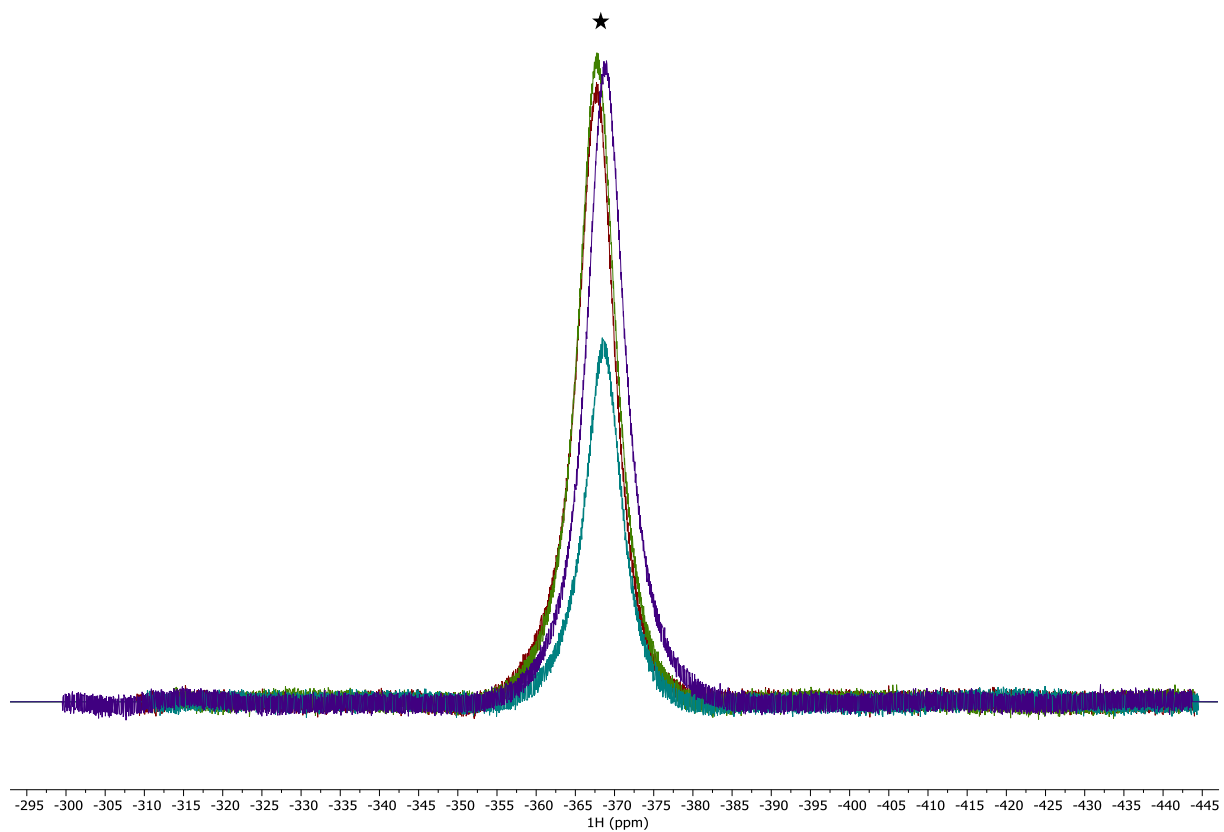
**Figure S137:** Superimposed <sup>1</sup>H spectra of all four different deuterium labelling schemes of Ho-DOTA-M7FPy. The spectra are coloured as follows red (2), green (3), turquoise (4), purple(5). The numbers represent the labelling schemes and can be found in figure 2 in the main text or figure S111 in the SI. Signals which are affected by deuterium labelling are marked with a star.



**Figure S138:** Superimposed <sup>1</sup>H spectra of all four different deuterium labelling schemes of Ho-DOTA-M7FPy. The spectra are coloured as follows red (2), green (3), turquoise (4), purple(5). The numbers represent the labelling schemes and can be found in figure 2 in the main text or figure S111 in the SI. Signals which are affected by deuterium labelling are marked with a star.

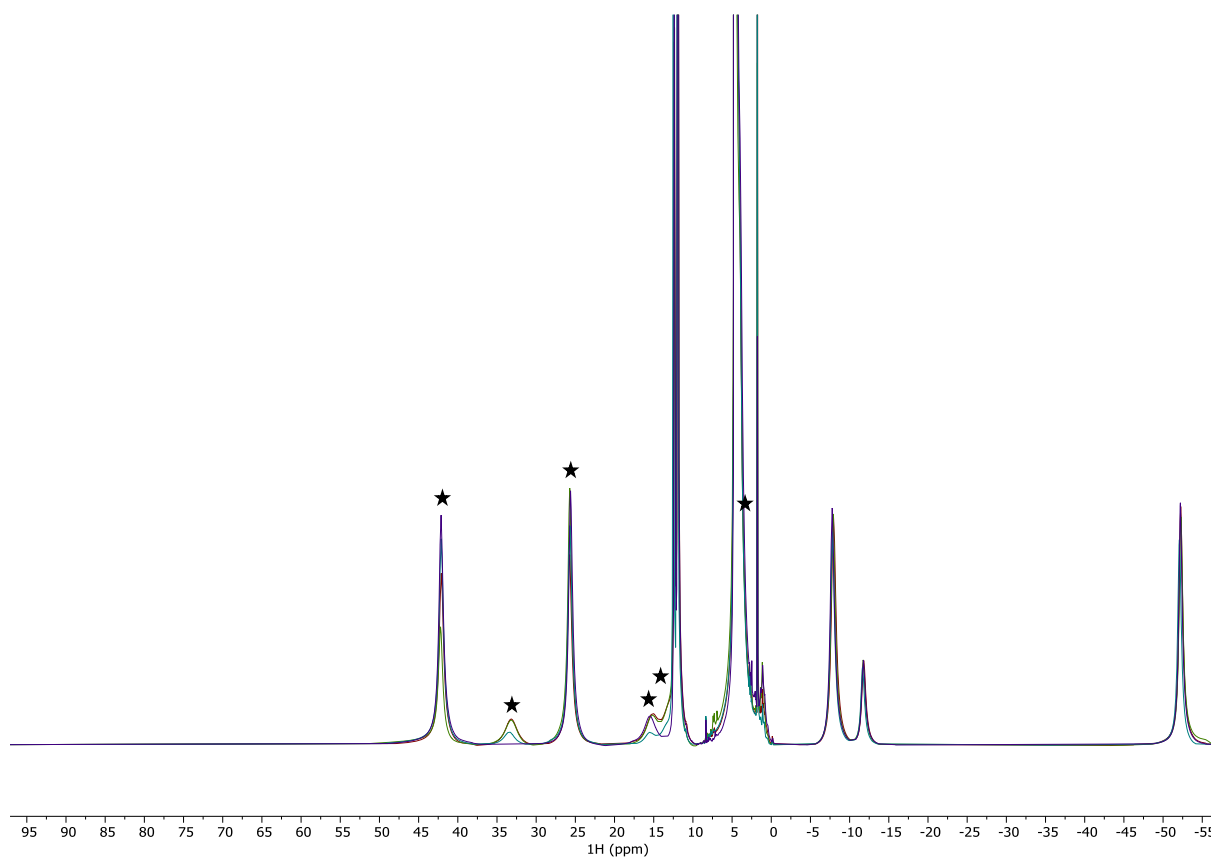


**Figure S139:** Superimposed <sup>1</sup>H spectra of all four different deuterium labelling schemes of Ho-DOTA-M7FPy. The spectra are coloured as follows red (2), green (3), turquoise (4), purple(5). The numbers represent the labelling schemes and can be found in figure 2 in the main text or figure S111 in the SI. Signals which are affected by deuterium labelling are marked with a star.



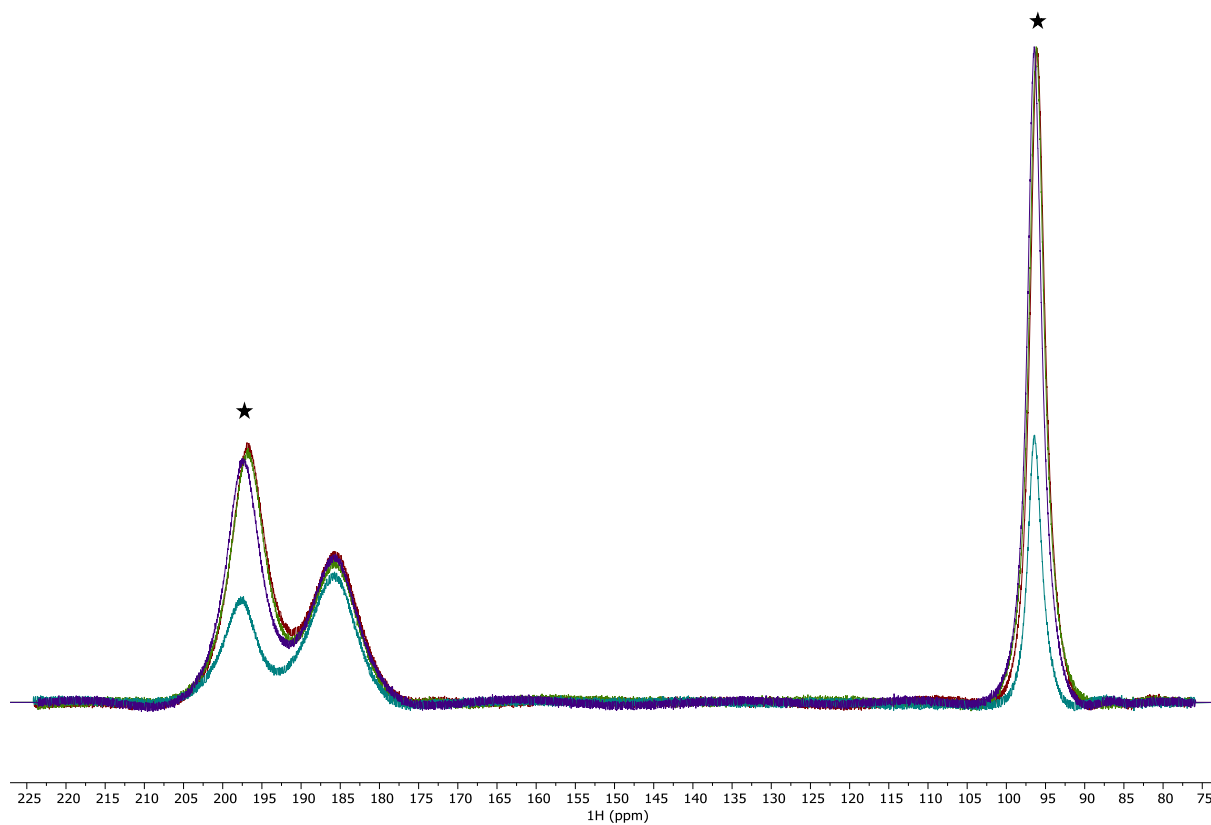
**Figure S140:** Superimposed <sup>1</sup>H spectra of all four different deuterium labelling schemes of Ho-DOTA-M7FPy. The spectra are coloured as follows red (2), green (3), turquoise (4), purple(5). The numbers represent the labelling schemes and can be found in figure 2 in the main text or figure S111 in the SI. Signals which are affected by deuterium labelling are marked with a star.

## Erbium

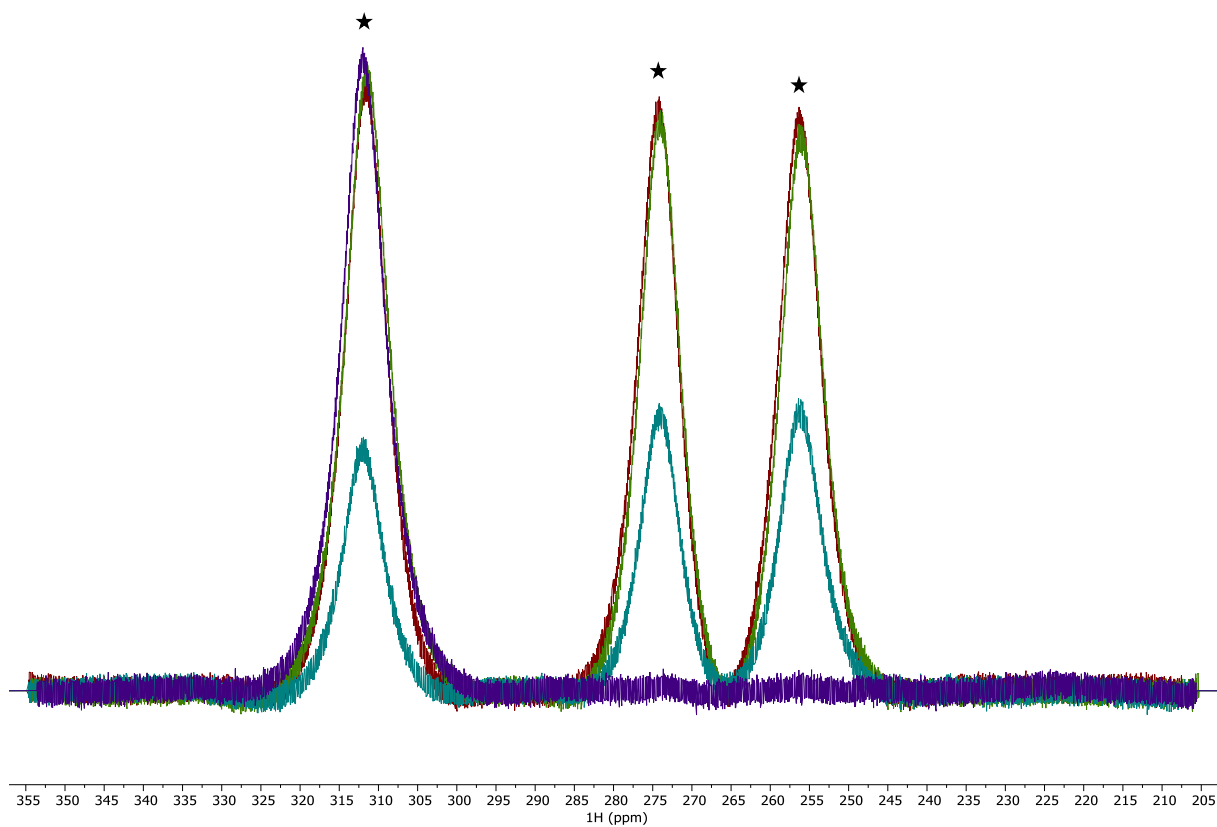


**Figure S141:** Superimposed  $^1\text{H}$  spectra of all four different deuterium labelling schemes of Er-DOTA-M7FPy. The spectra are coloured as follows red (2), green (3), turquoise (4), purple (5). The numbers represent the labelling schemes and can be found in figure 2 in the main text or figure S111 in the SI. Signals which are affected by deuterium labelling are marked with a star.

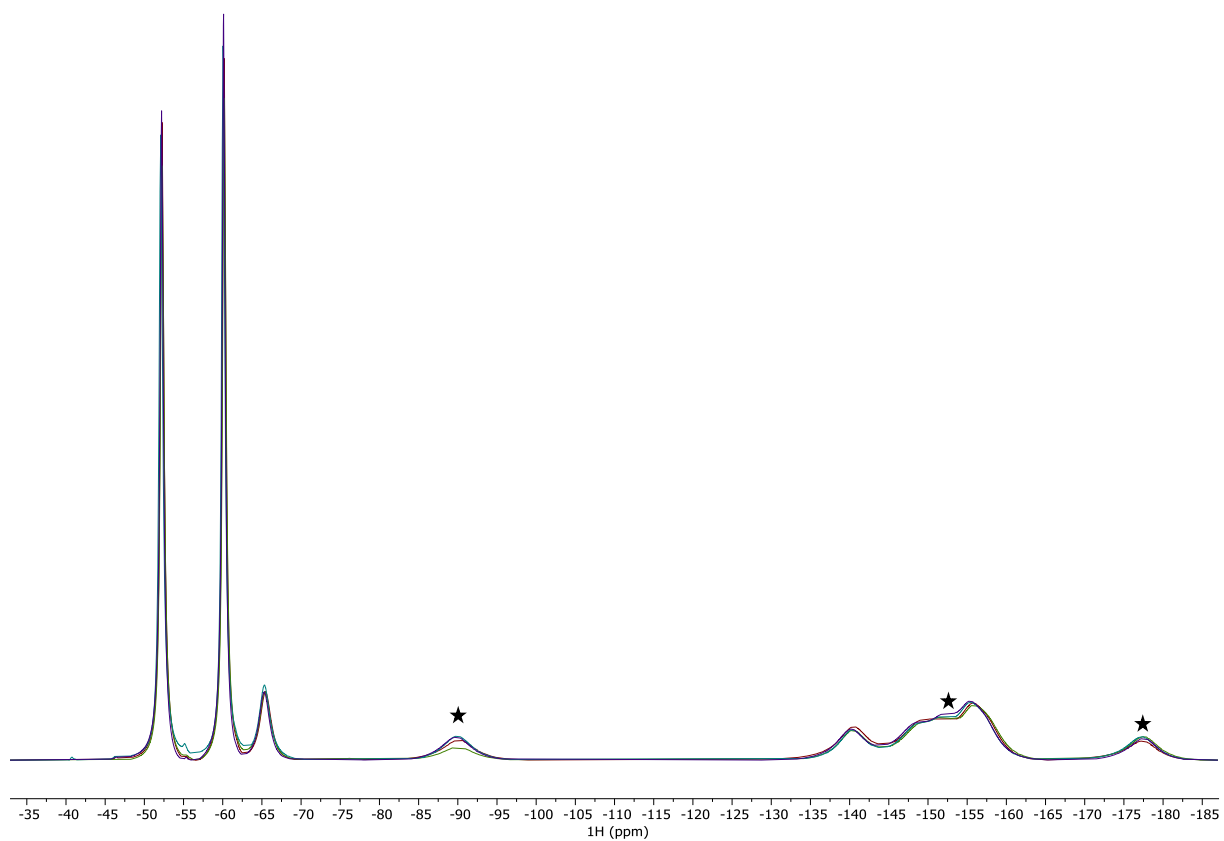




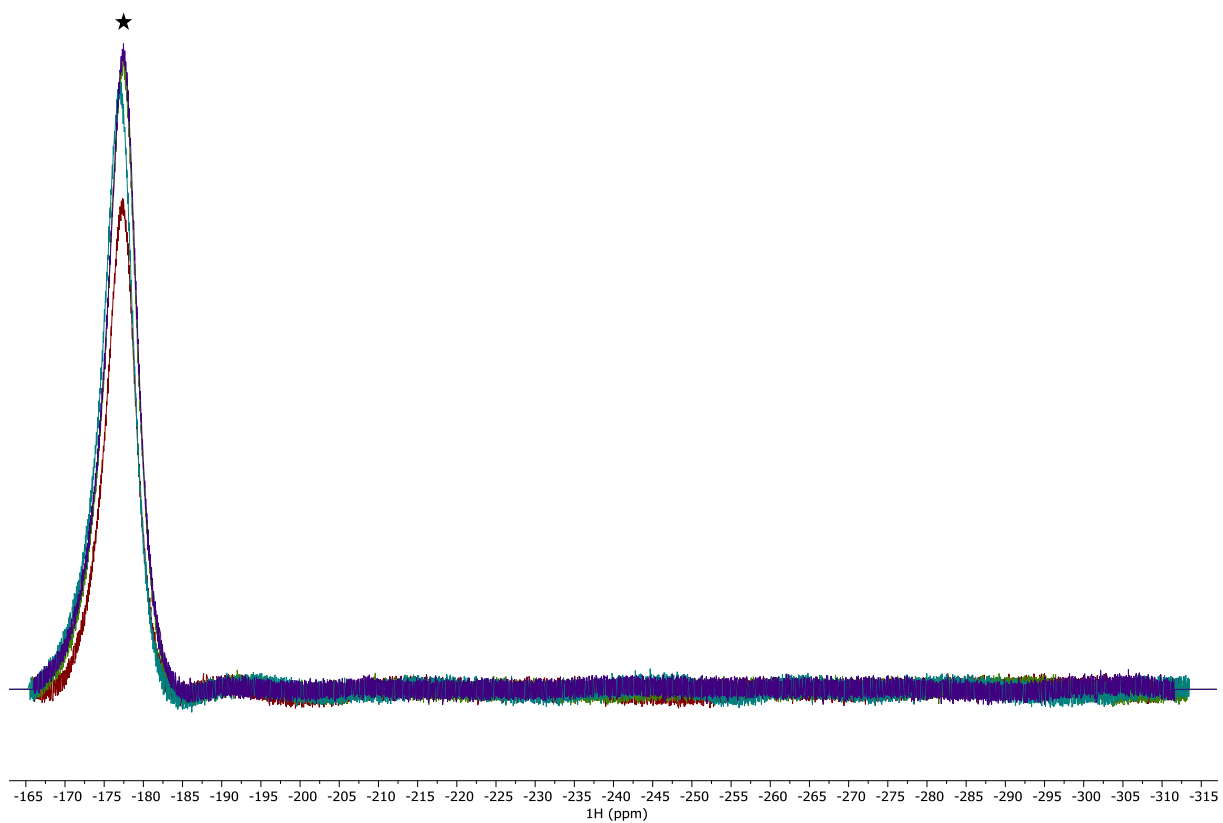
**Figure S142:** Superimposed <sup>1</sup>H spectra of all four different deuterium labelling schemes of Er-DOTA-M7FPy. The spectra are coloured as follows red (2), green (3), turquoise (4), purple(5). The numbers represent the labelling schemes and can be found in figure 2 in the main text or figure S111 in the SI. Signals which are affected by deuterium labelling are marked with a star.



**Figure S143:** Superimposed <sup>1</sup>H spectra of all four different deuterium labelling schemes of Er-DOTA-M7FPy. The spectra are coloured as follows red (2), green (3), turquoise (4), purple(5). The numbers represent the labelling schemes and can be found in figure 2 in the main text or figure S111 in the SI. Signals which are affected by deuterium labelling are marked with a star.

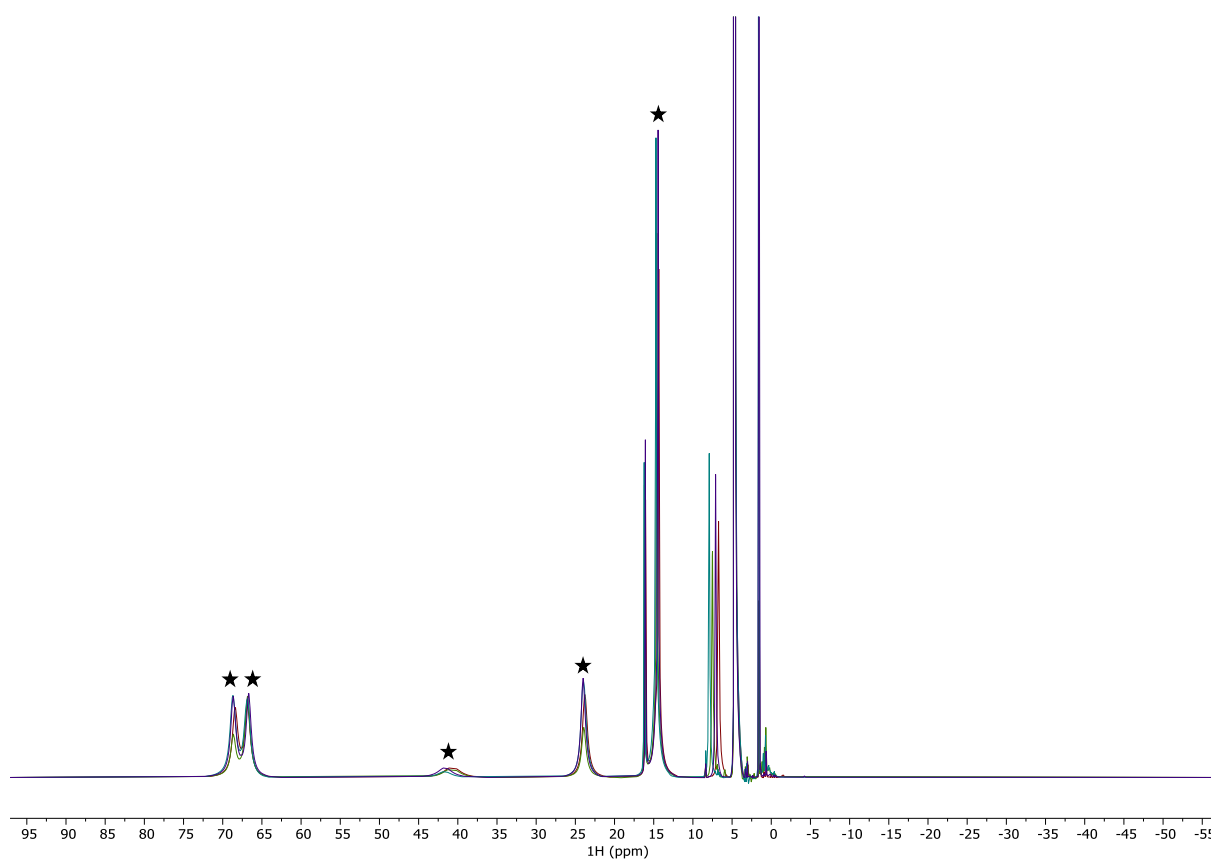


**Figure S144:** Superimposed <sup>1</sup>H spectra of all four different deuterium labelling schemes of Er-DOTA-M7FPy. The spectra are coloured as follows red (2), green (3), turquoise (4), purple(5). The numbers represent the labelling schemes and can be found in figure 2 in the main text or figure S111 in the SI. Signals which are affected by deuterium labelling are marked with a star.

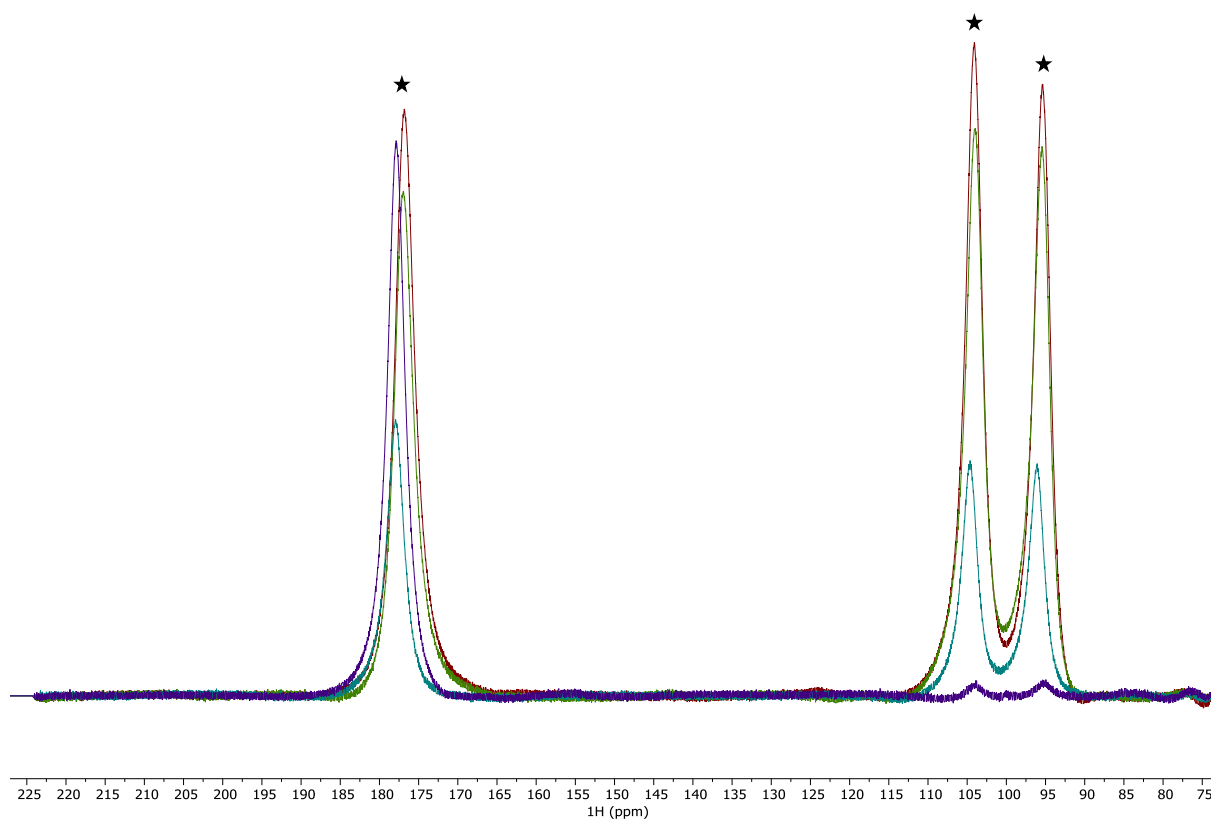


**Figure S145:** Superimposed <sup>1</sup>H spectra of all four different deuterium labelling schemes of Er-DOTA-M7FPy. The spectra are coloured as follows red (2), green (3), turquoise (4), purple(5). The numbers represent the labelling schemes and can be found in figure 2 in the main text or figure S111 in the SI. Signals which are affected by deuterium labelling are marked with a star.

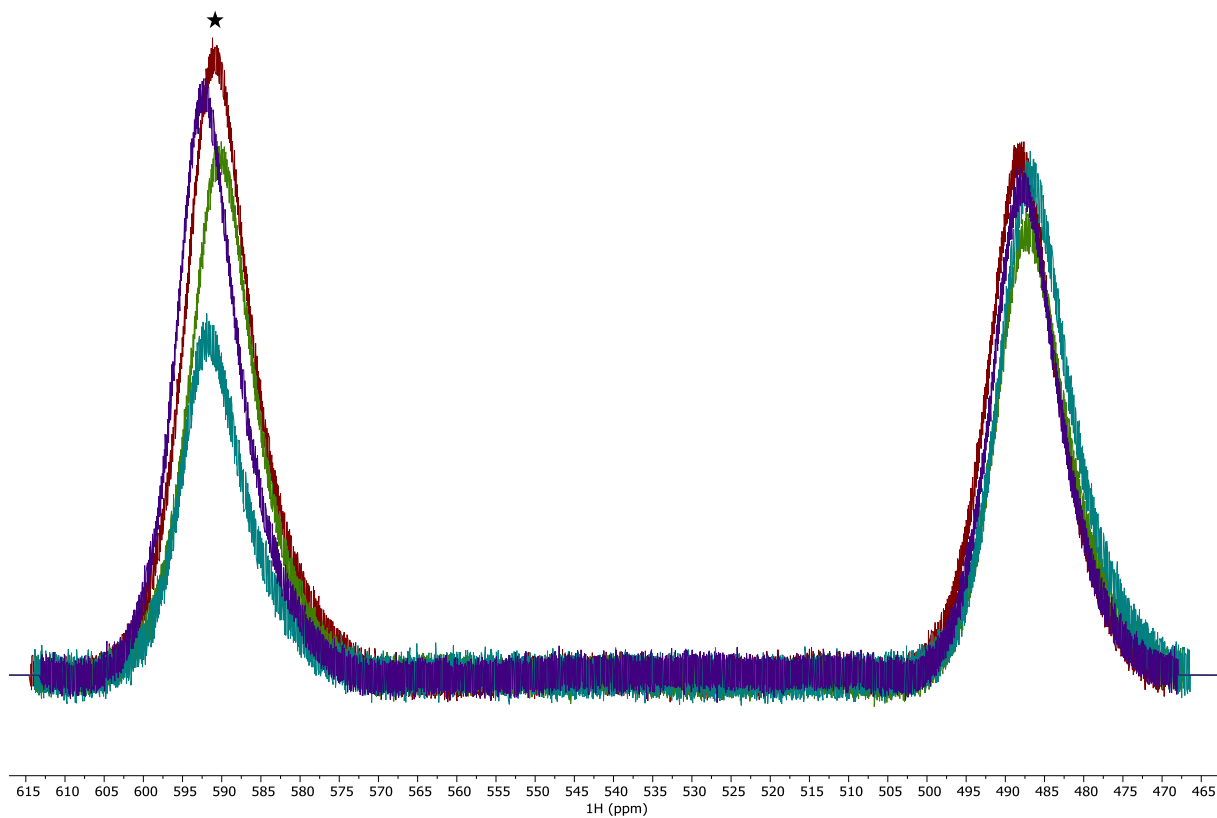
## Thulium



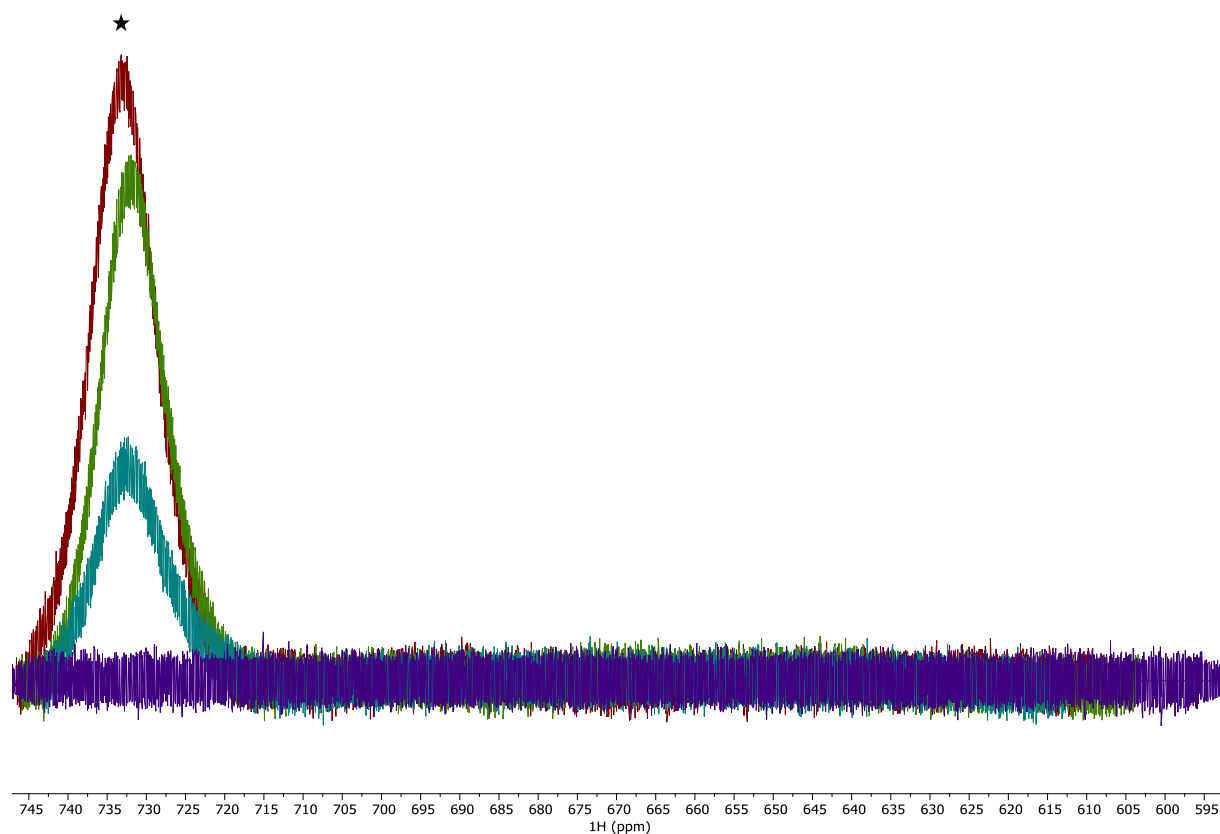
**Figure S146:** Superimposed <sup>1</sup>H spectra of all four different deuterium labelling schemes of Tm-DOTA-M7FPy. The spectra are coloured as follows red (2), green (3), turquoise (4), purple(5). The numbers represent the labelling schemes and can be found in figure 2 in the main text or figure S111 in the SI. Signals which are affected by deuterium labelling are marked with a star.



**Figure S147:** Superimposed <sup>1</sup>H spectra of all four different deuterium labelling schemes of Tm-DOTA-M7FPy. The spectra are coloured as follows red (2), green (3), turquoise (4), purple(5). The numbers represent the labelling schemes and can be found in figure 2 in the main text or figure S111 in the SI. Signals which are affected by deuterium labelling are marked with a star.

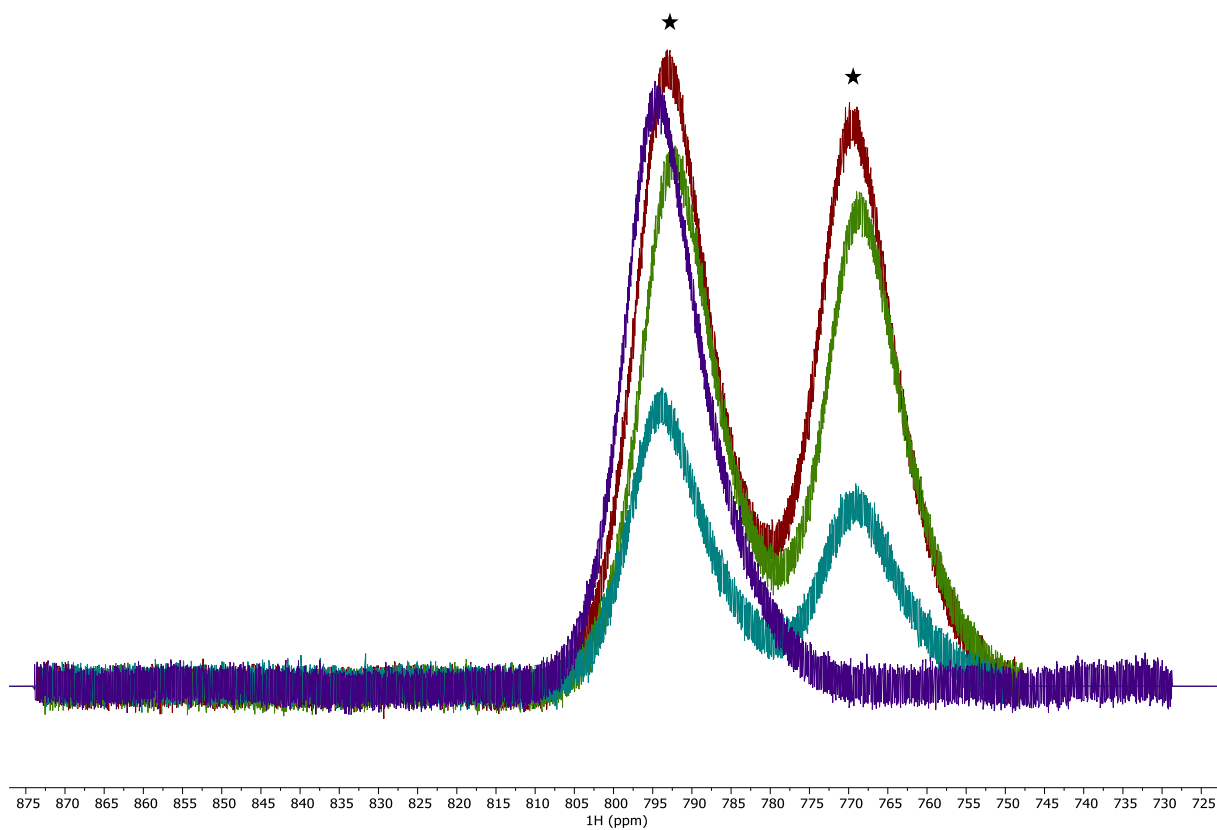


**Figure S148:** Superimposed <sup>1</sup>H spectra of all four different deuterium labelling schemes of Tm-DOTA-M7FPy. The spectra are coloured as follows red (2), green (3), turquoise (4), purple(5). The numbers represent the labelling schemes and can be found in figure 2 in the main text or figure S111 in the SI. Signals which are affected by deuterium labelling are marked with a star.

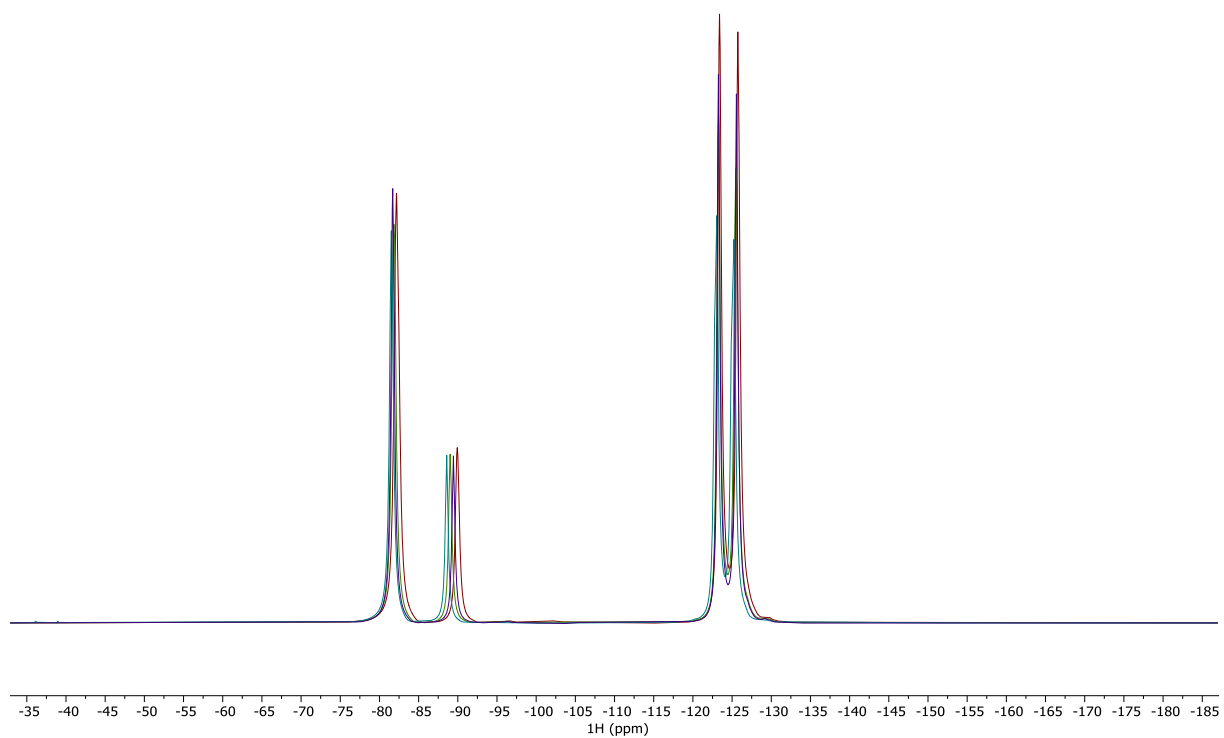


**Figure S149:** Superimposed <sup>1</sup>H spectra of all four different deuterium labelling schemes of Tm-DOTA-M7FPy. The spectra are coloured as follows red (2), green (3), turquoise (4), purple(5). The numbers represent the labelling schemes and can be found in figure 2 in the main text or figure S111 in the SI. Signals which are affected by deuterium labelling are marked with a star.

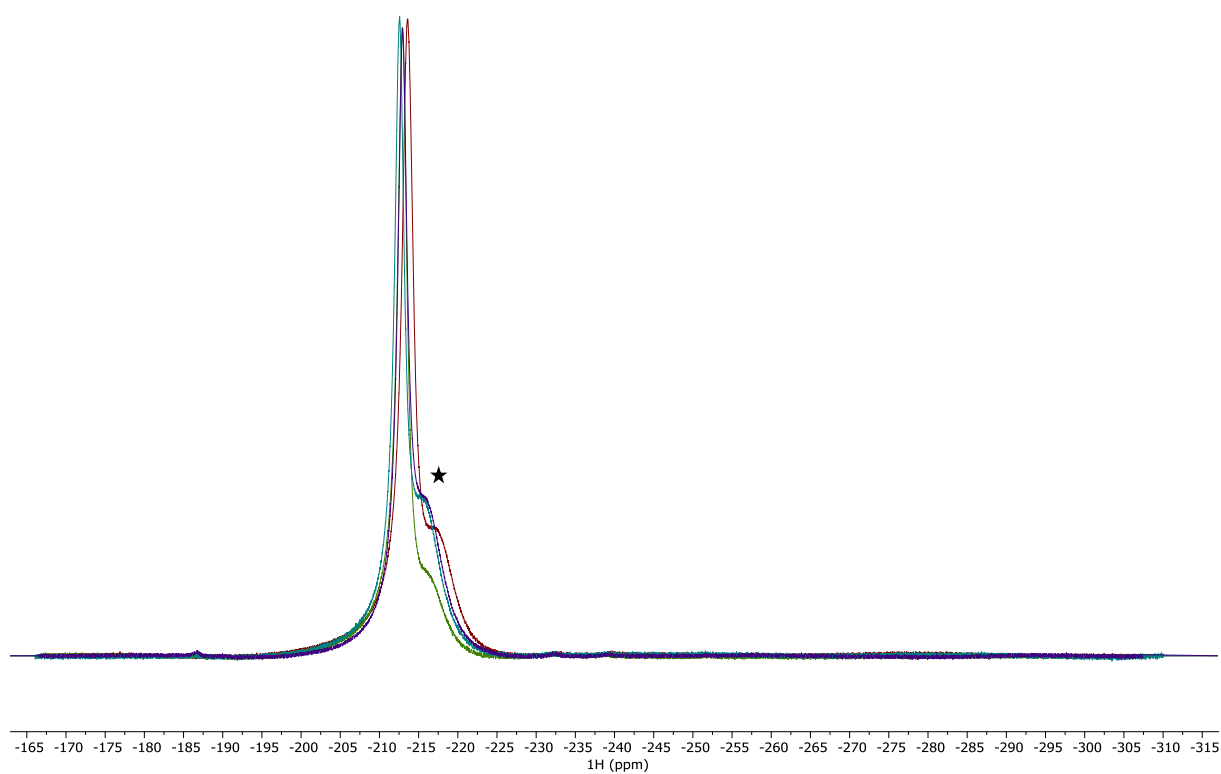




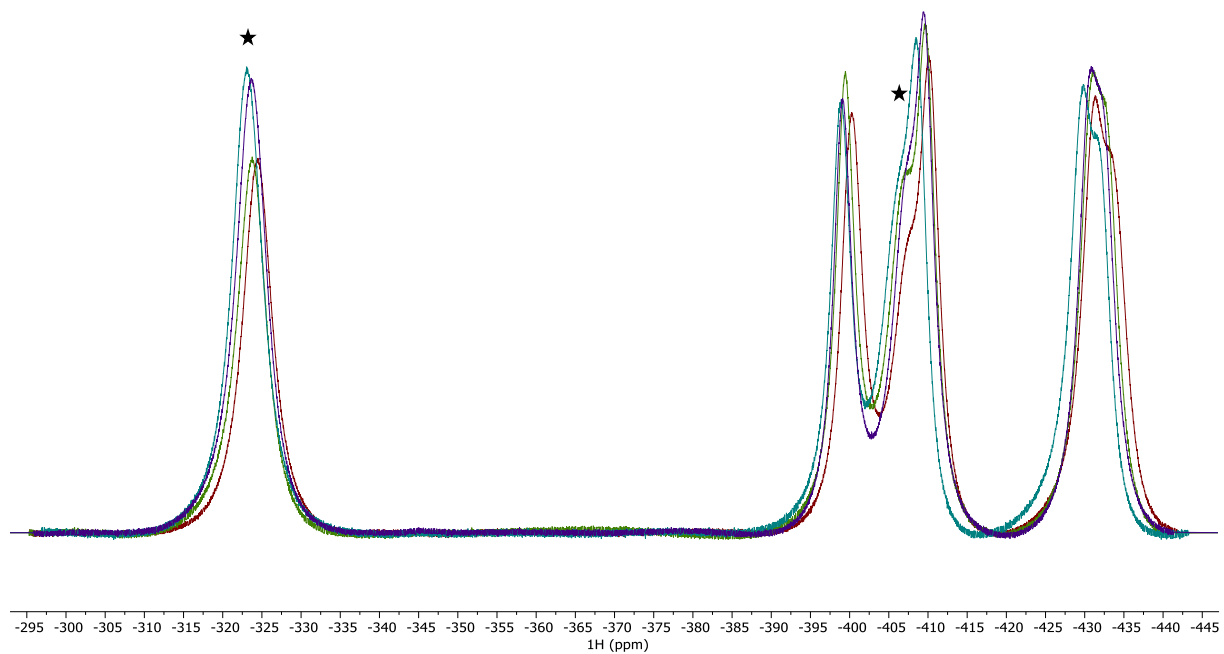
**Figure S150:** Superimposed  $^1\text{H}$  spectra of all four different deuterium labelling schemes of Tm-DOTA-M7FPy. The spectra are coloured as follows red (2), green (3), turquoise (4), purple(5). The numbers represent the labelling schemes and can be found in figure 2 in the main text or figure S111 in the SI. Signals which are affected by deuterium labelling are marked with a star.



**Figure S151:** Superimposed <sup>1</sup>H spectra of all four different deuterium labelling schemes of Tm-DOTA-M7FPy. The spectra are coloured as follows red (2), green (3), turquoise (4), purple(5). The numbers represent the labelling schemes and can be found in figure 2 in the main text or figure S111 in the SI. Signals which are affected by deuterium labelling are marked with a star.

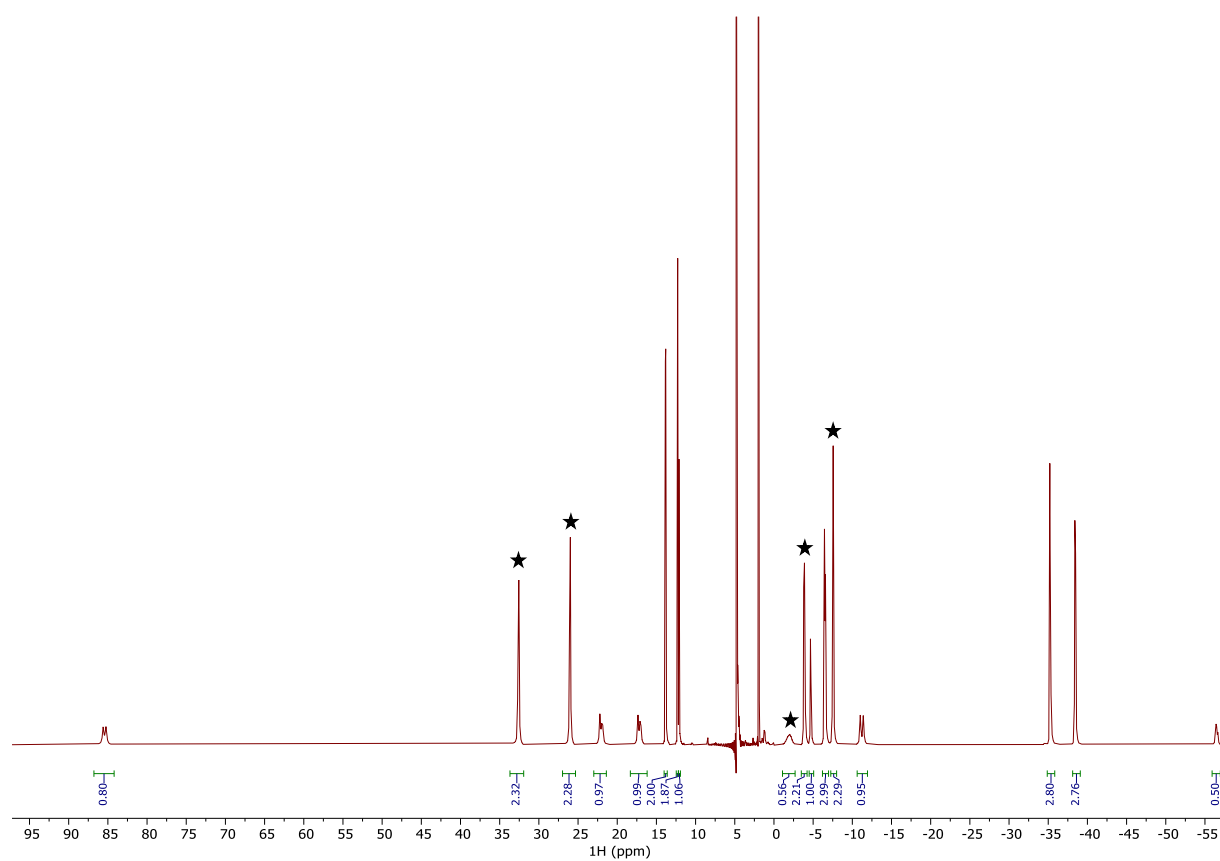


**Figure S152:** Superimposed  $^1\text{H}$  spectra of all four different deuterium labelling schemes of Tm-DOTA-M7FPy. The spectra are coloured as follows red (2), green (3), turquoise (4), purple(5). The numbers represent the labelling schemes and can be found in figure 2 in the main text or figure S111 in the SI. Signals which are affected by deuterium labelling are marked with a star.

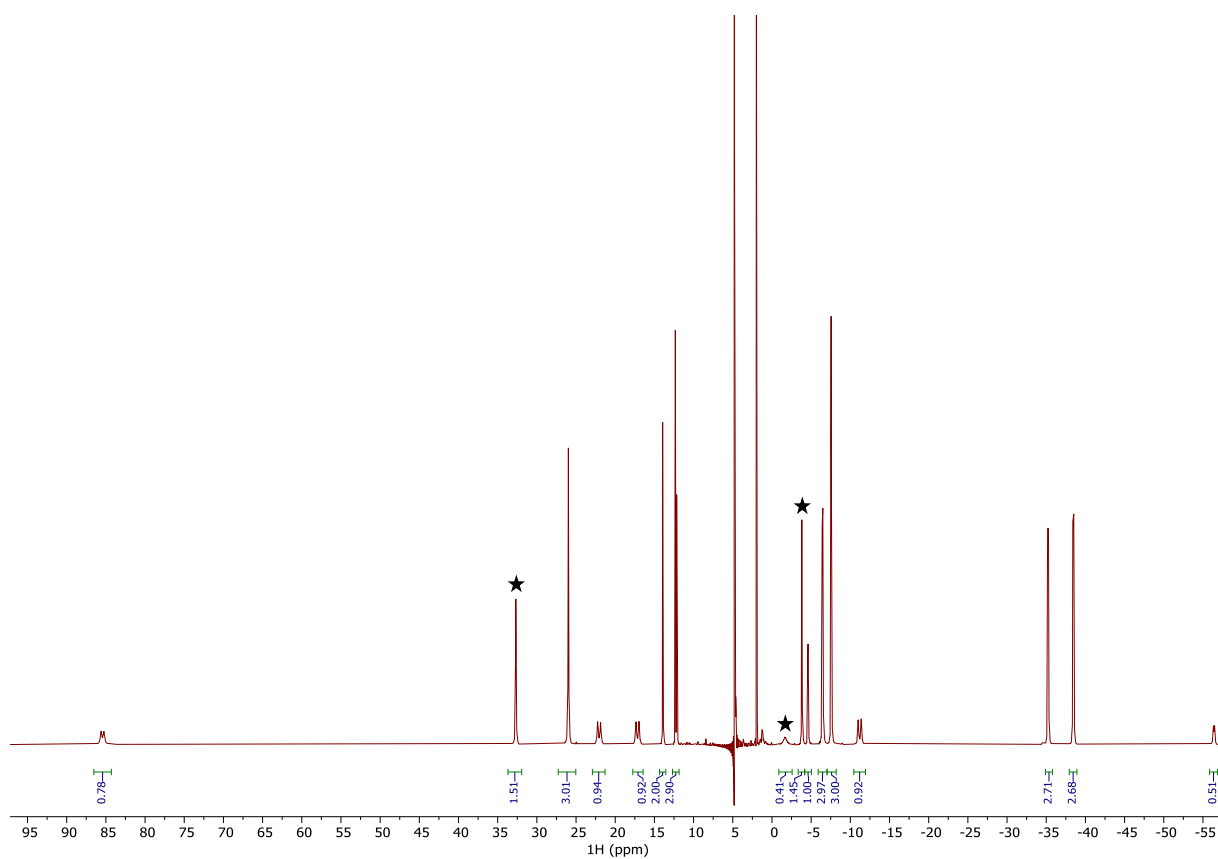


**Figure S153:** Superimposed <sup>1</sup>H spectra of all four different deuterium labelling schemes of Tm-DOTA-M7FPy. The spectra are coloured as follows red (2), green (3), turquoise (4), purple(5). The numbers represent the labelling schemes and can be found in figure 2 in the main text or figure S111 in the SI. Signals which are affected by deuterium labelling are marked with a star.

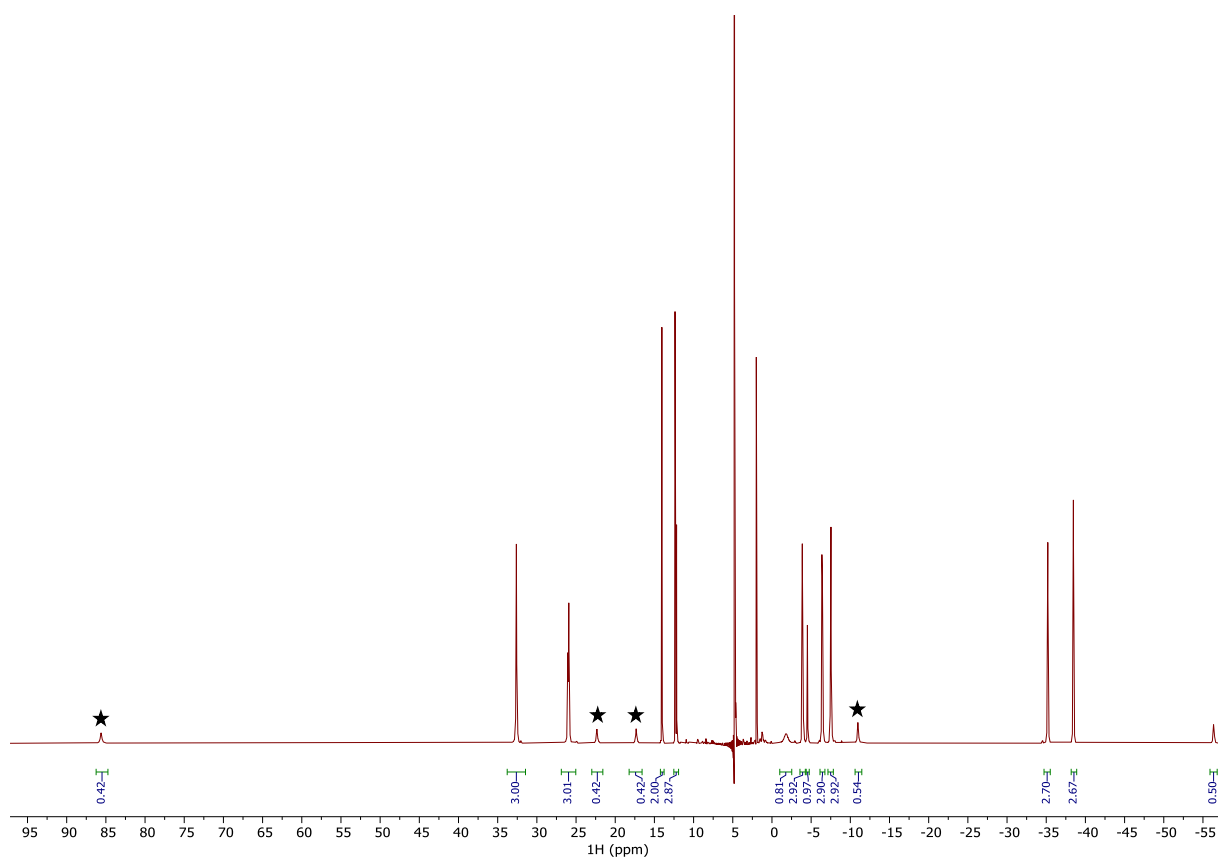
# Ytterbium



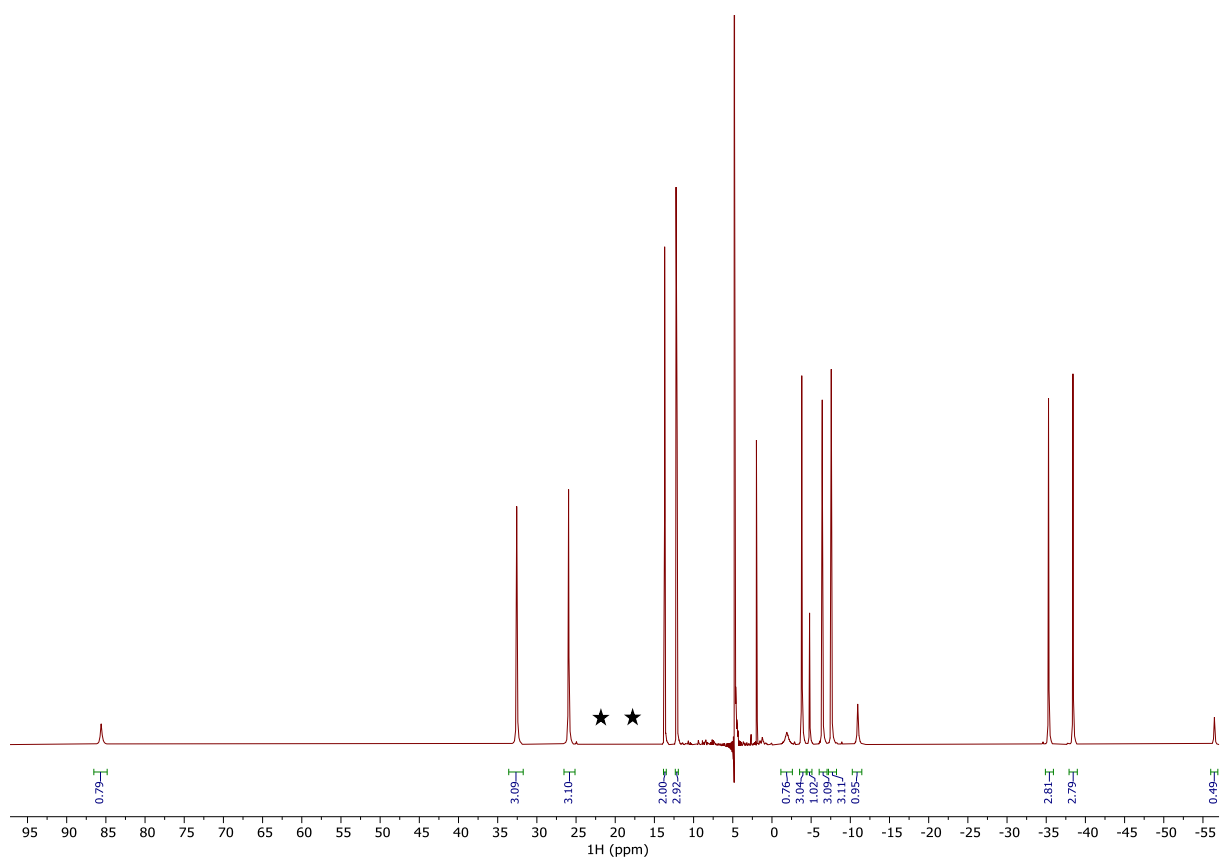
**Figure S154:** <sup>1</sup>H spectra of deuterium labelled Yb-DOTA-M7FPy complex (**2**). The number represent the labelling schemes and can be found in figure 2 in the main text or figure S111 in the SI. Signals which are affected by deuterium labelling are marked with a star.



**Figure S155:** <sup>1</sup>H spectra of deuterium labelled Yb-DOTA-M7FPy complex (**3**). The number represent the labelling schemes and can be found in figure 2 in the main text or figure S111 in the SI. Signals which are affected by deuterium labelling are marked with a star.

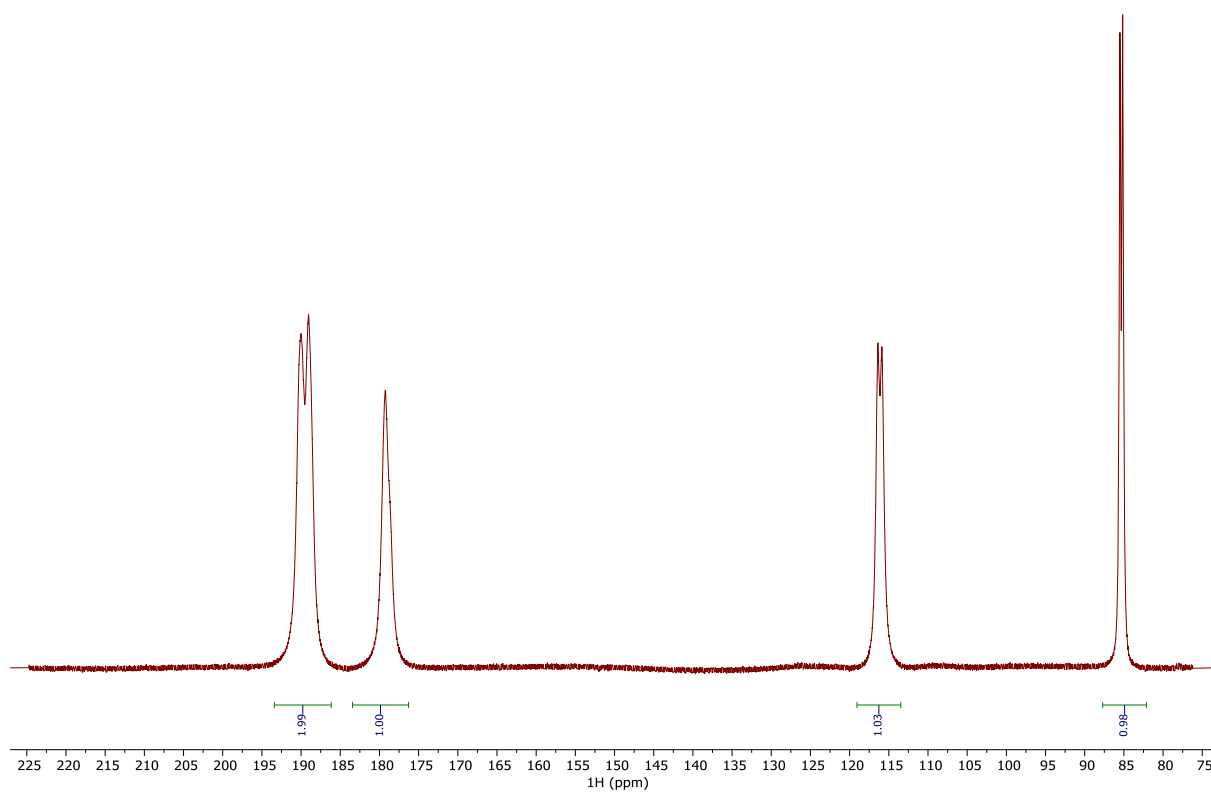


**Figure S156:**  $^1\text{H}$  spectra of deuterium labelled Yb-DOTA-M7FPy complex (**4**). The number represent the labelling schemes and can be found in figure 2 in the main text or figure S111 in the SI. Signals which are affected by deuterium labelling are marked with a star.

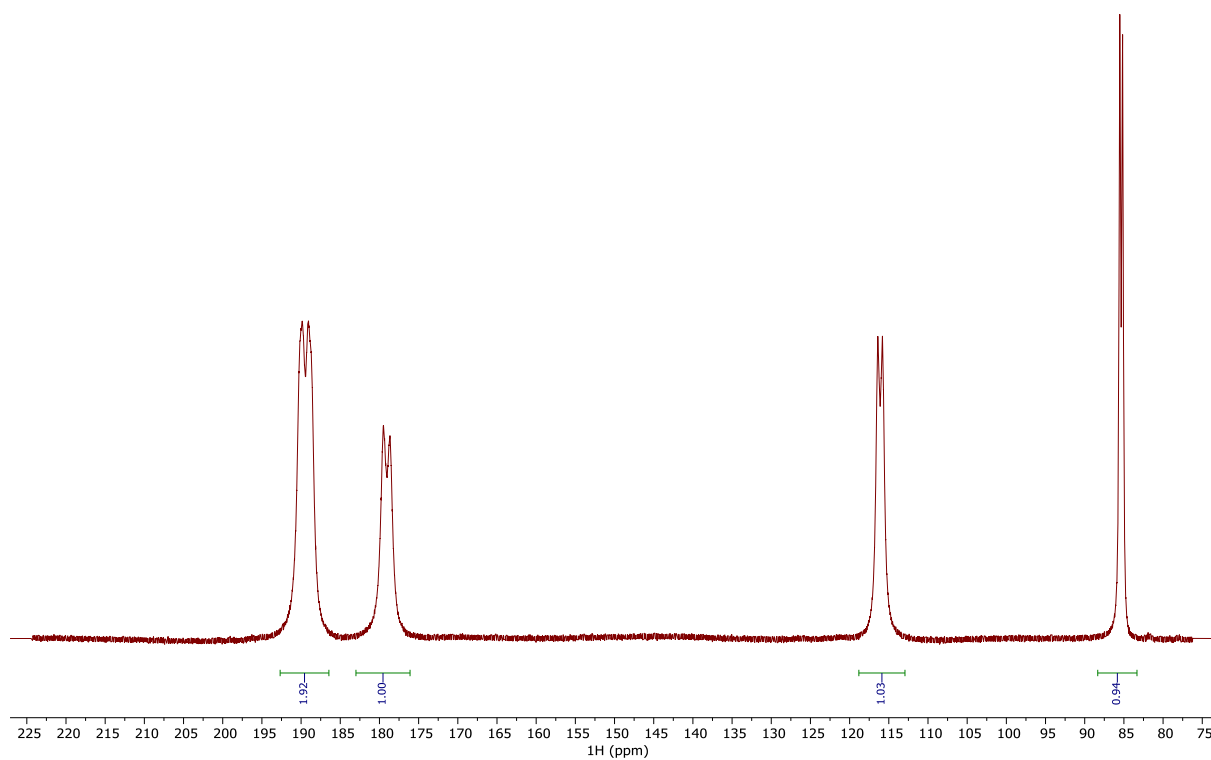


**Figure S157:**  $^1\text{H}$  spectra of deuterium labelled Yb-DOTA-M7FPy complex (**5**). The number represent the labelling schemes and can be found in figure 2 in the main text or figure S111 in the SI. Signals which are affected by deuterium labelling are marked with a star.

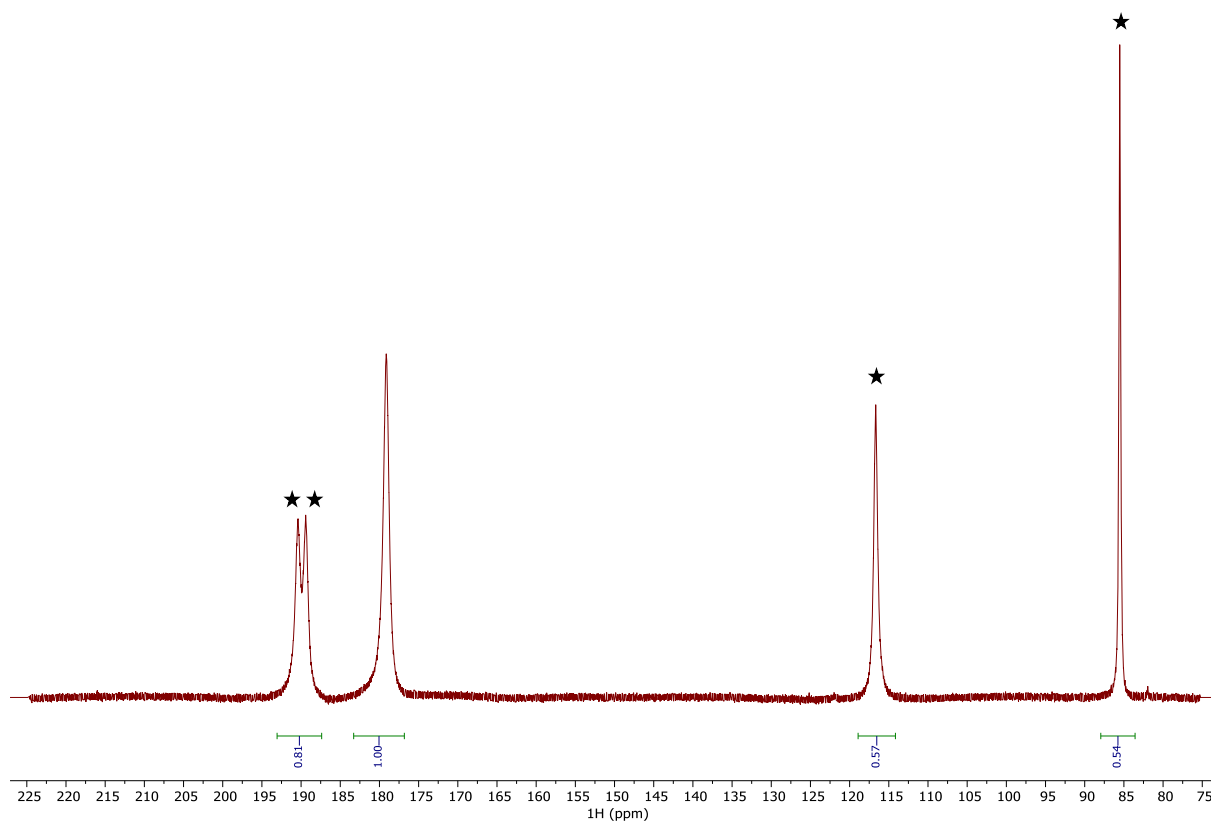




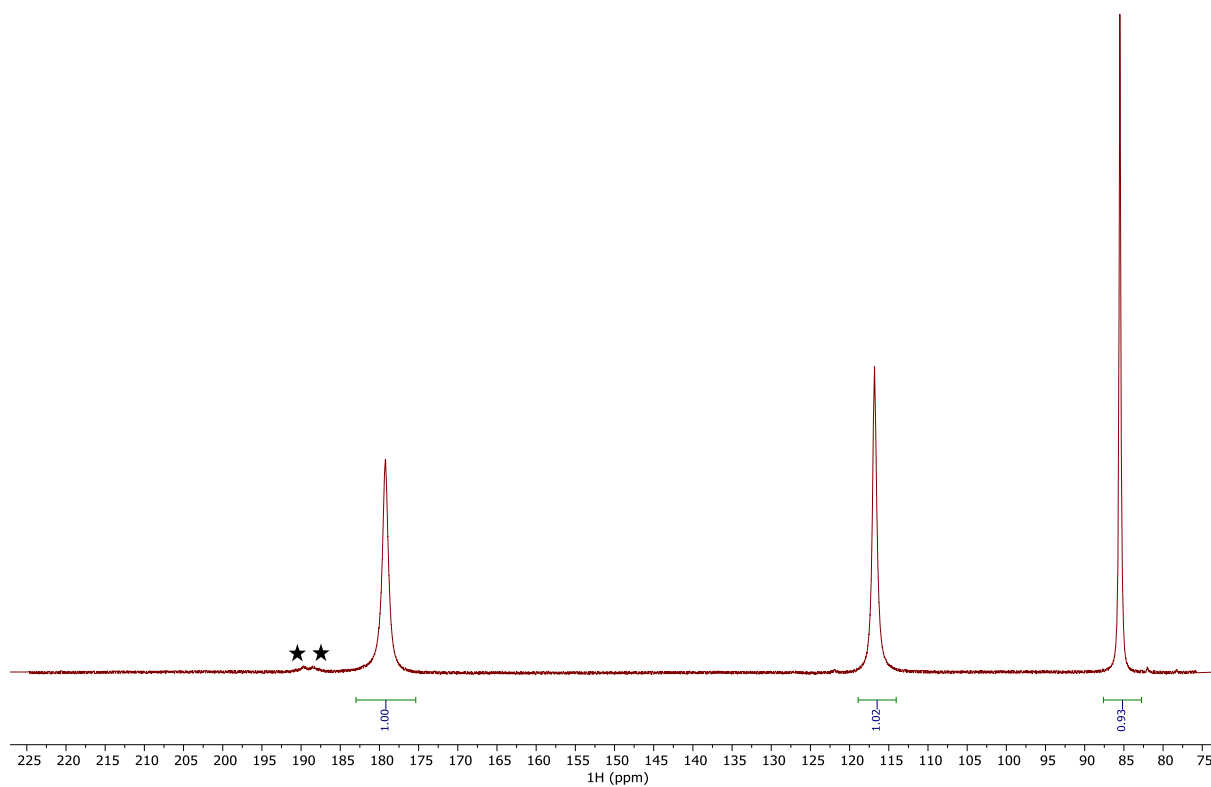
**Figure S158:**  $^1\text{H}$  spectra of deuterium labelled Yb-DOTA-M7FPy complex (**2**). The number represent the labelling schemes and can be found in figure 2 in the main text or figure S111 in the SI. Signals which are affected by deuterium labelling are marked with a star.



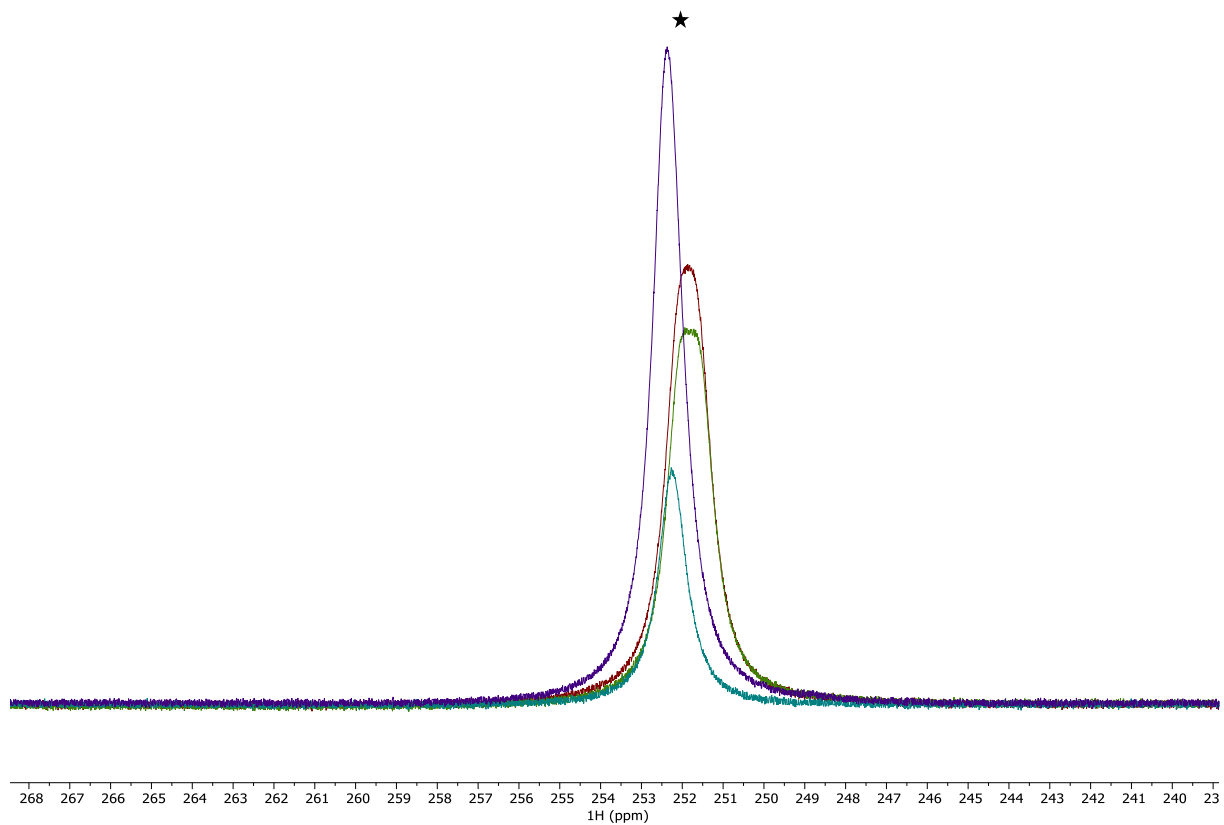
**Figure S159:**  $^1\text{H}$  spectra of deuterium labelled Yb-DOTA-M7FPy complex (**3**). The number represent the labelling schemes and can be found in figure 2 in the main text or figure S111 in the SI. Signals which are affected by deuterium labelling are marked with a star.



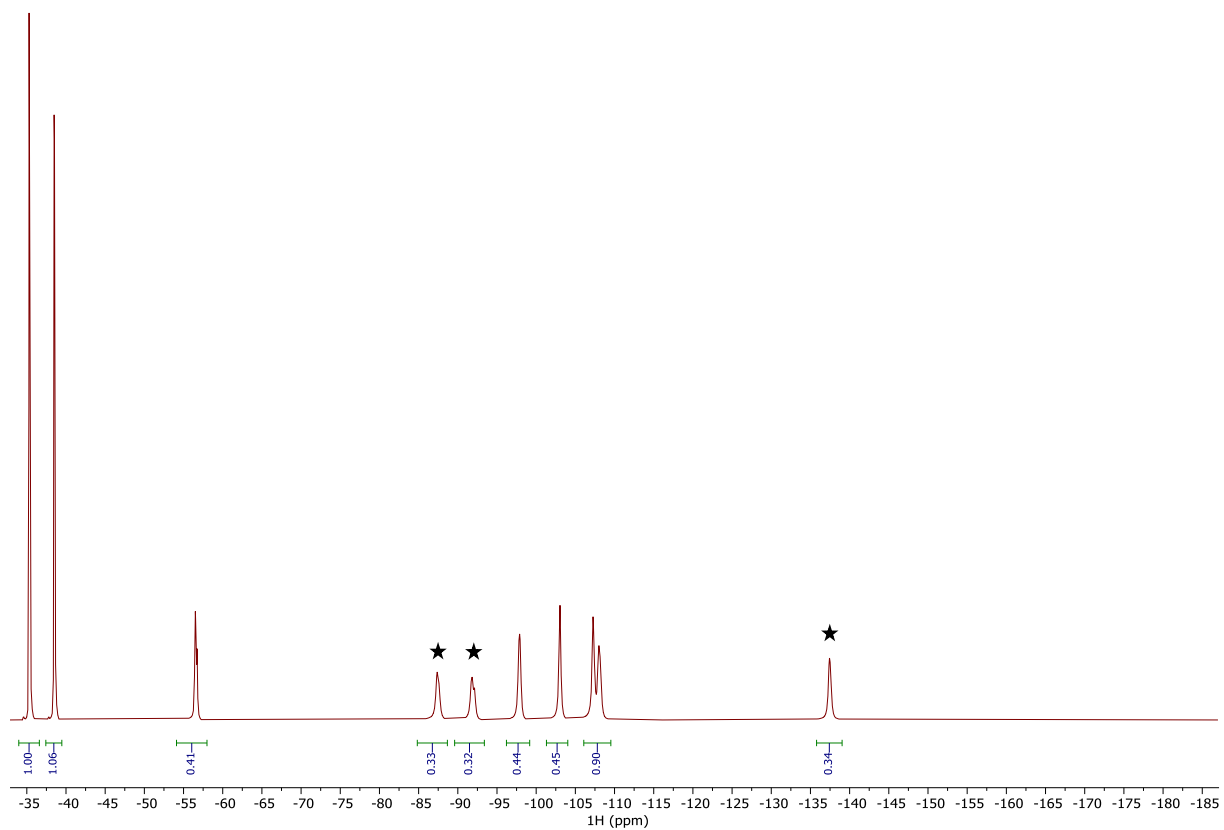
**Figure S160:**  $^1\text{H}$  spectra of deuterium labelled Yb-DOTA-M7FPy complex (**4**). The number represent the labelling schemes and can be found in figure 2 in the main text or figure S111 in the SI. Signals which are affected by deuterium labelling are marked with a star.



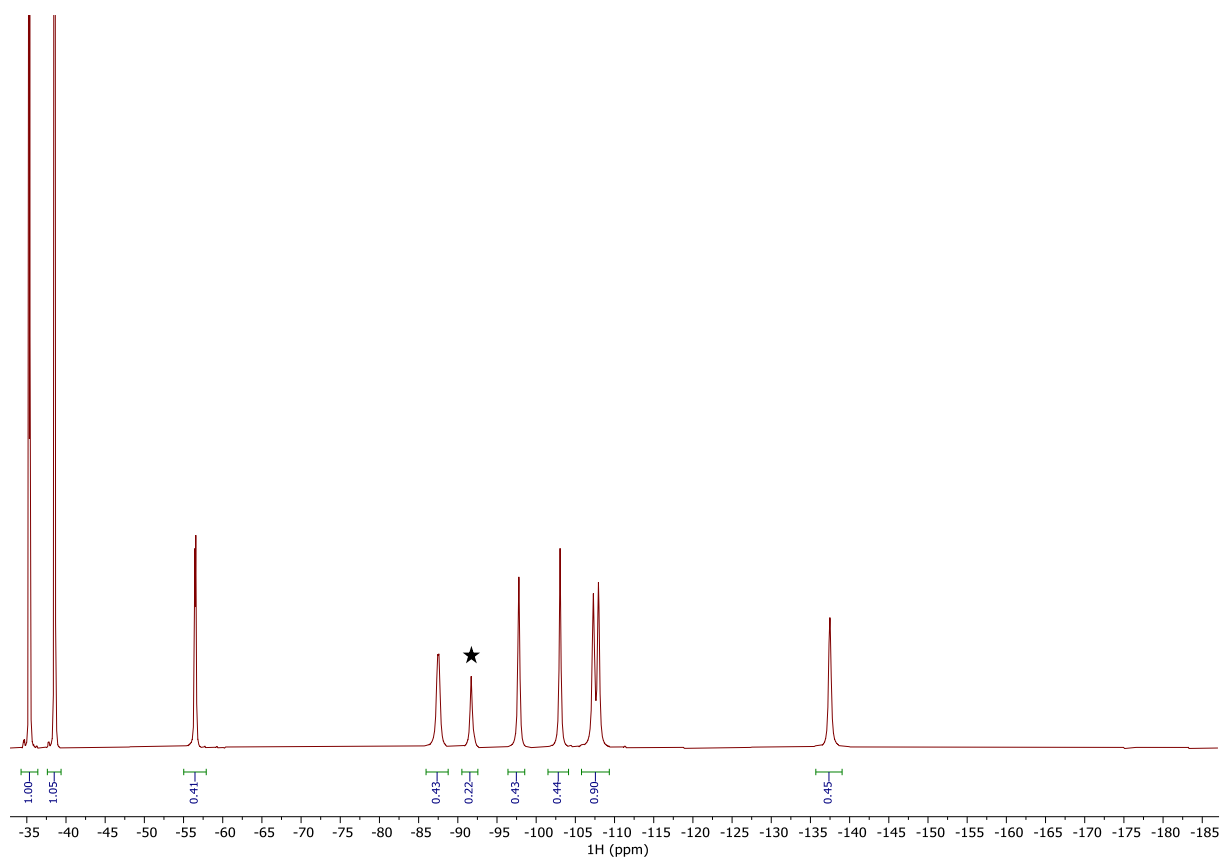
**Figure S161:**  $^1\text{H}$  spectra of deuterium labelled Yb-DOTA-M7FPy complex (**5**). The number represent the labelling schemes and can be found in figure 2 in the main text or figure S111 in the SI. Signals which are affected by deuterium labelling are marked with a star.



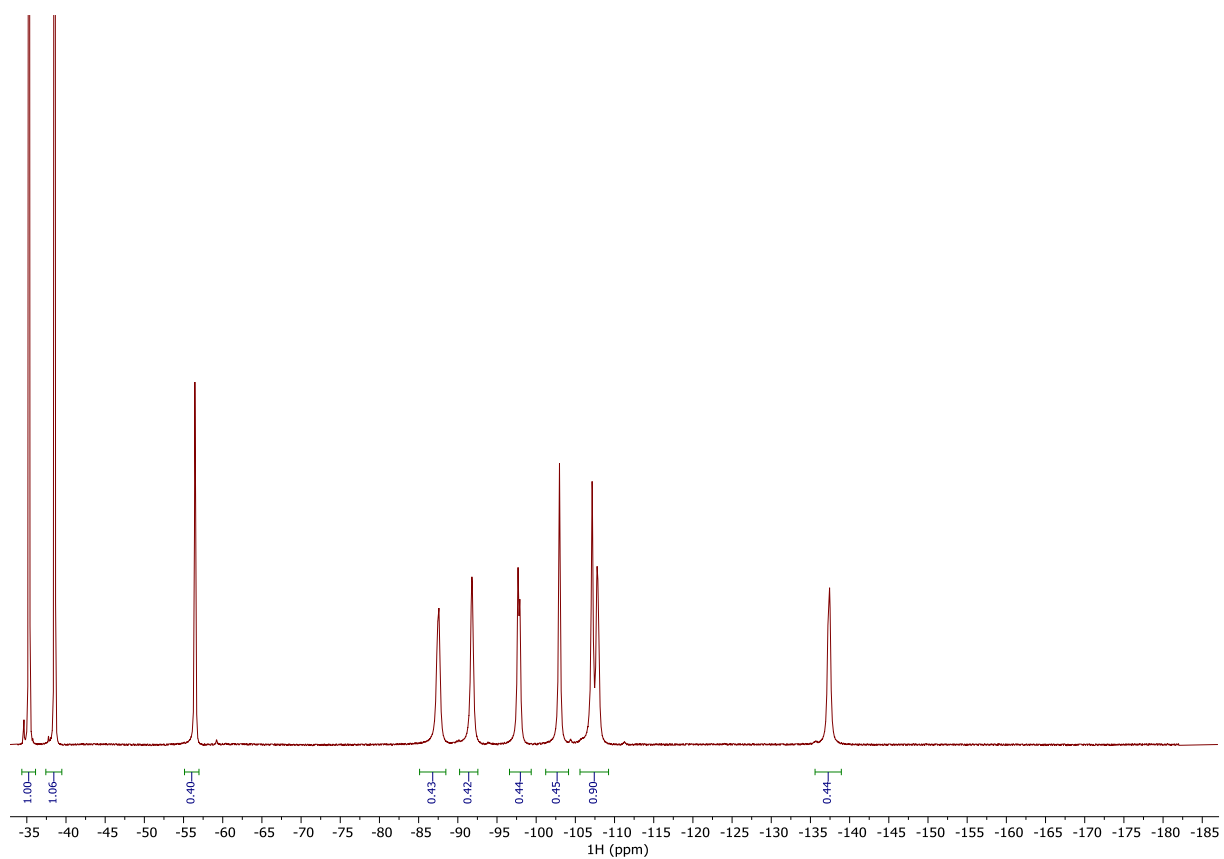
**Figure S162:** Superimposed <sup>1</sup>H spectra of all four different deuterium labelling schemes of TYb-DOTA-M7FPy. The spectra are coloured as follows red (2), green (3), turquoise (4), purple(5). The numbers represent the labelling schemes and can be found in figure 2 in the main text or figure S111 in the SI. Signals which are affected by deuterium labelling are marked with a star.



**Figure S163:** <sup>1</sup>H spectra of deuterium labelled Yb-DOTA-M7FPy complex (**2**). The number represent the labelling schemes and can be found in figure 2 in the main text or figure S111 in the SI. Signals which are affected by deuterium labelling are marked with a star.

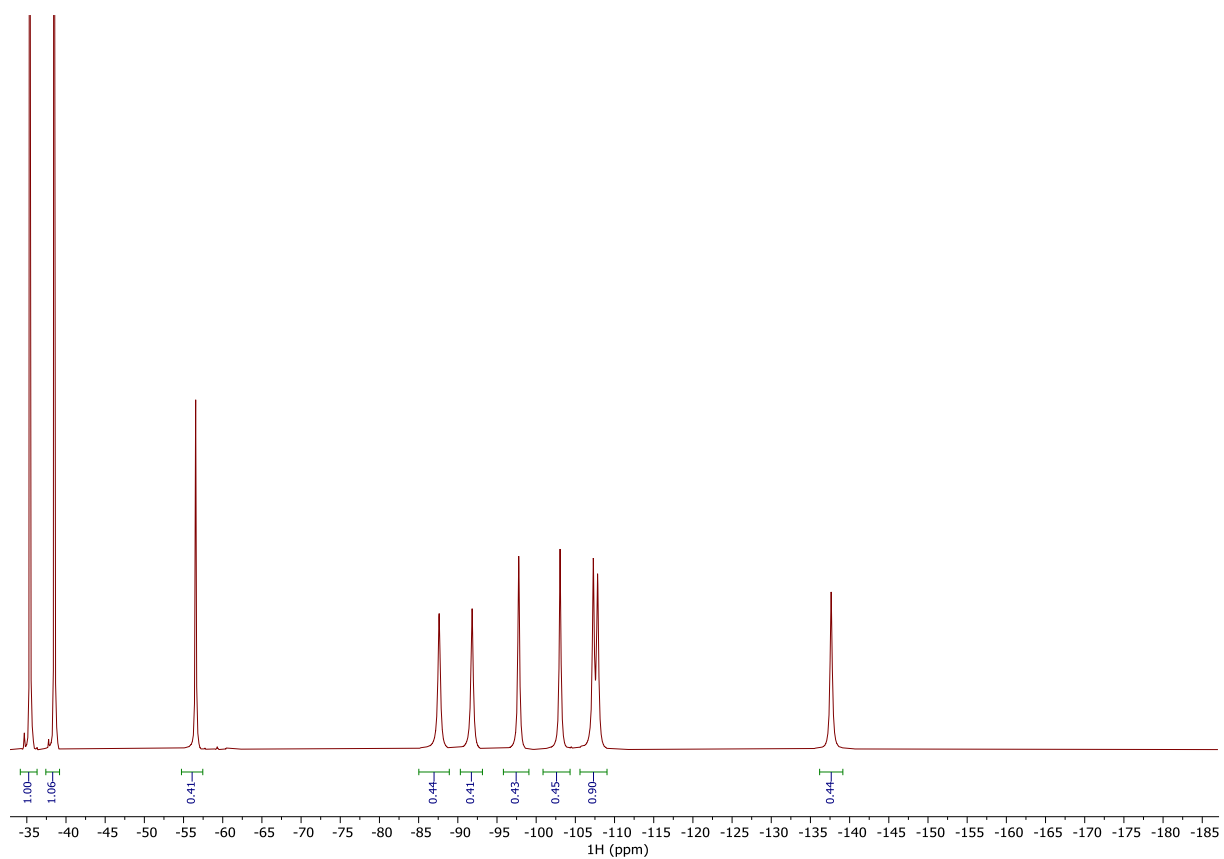


**Figure S164:** <sup>1</sup>H spectra of deuterium labelled Yb-DOTA-M7FPy complex (**3**). The number represent the labelling schemes and can be found in figure 2 in the main text or figure S111 in the SI. Signals which are affected by deuterium labelling are marked with a star.



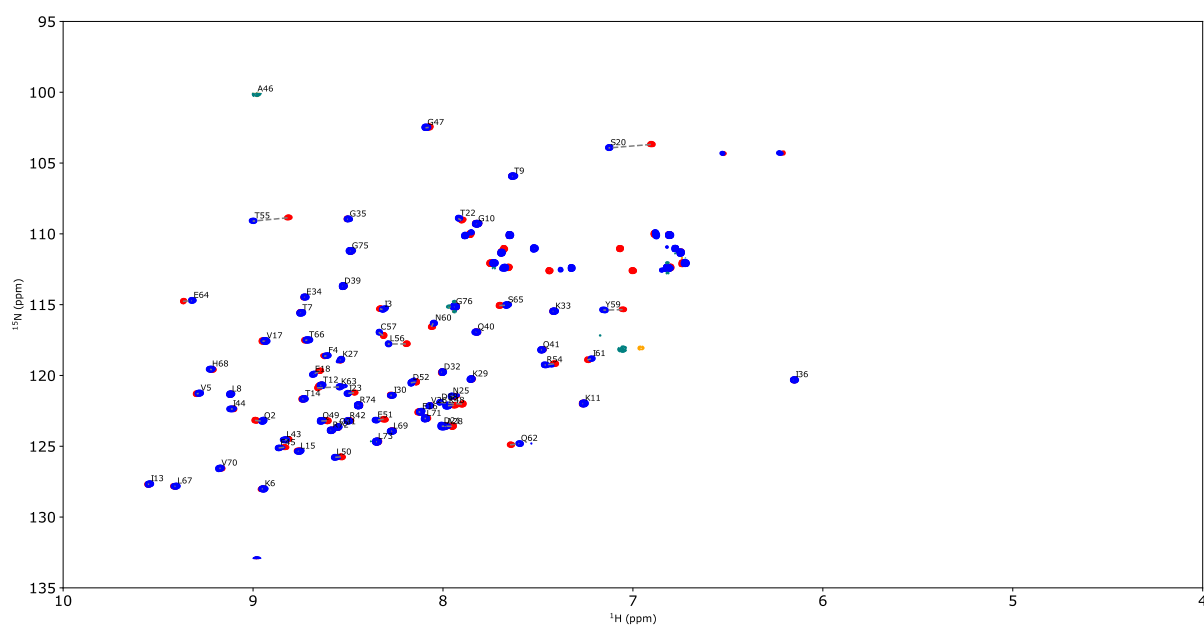
**Figure S165:**  $^1\text{H}$  spectra of deuterium labelled Yb-DOTA-M7FPy complex (**4**). The number represent the labelling schemes and can be found in figure 2 in the main text or figure S111 in the SI. Signals which are affected by deuterium labelling are marked with a star.



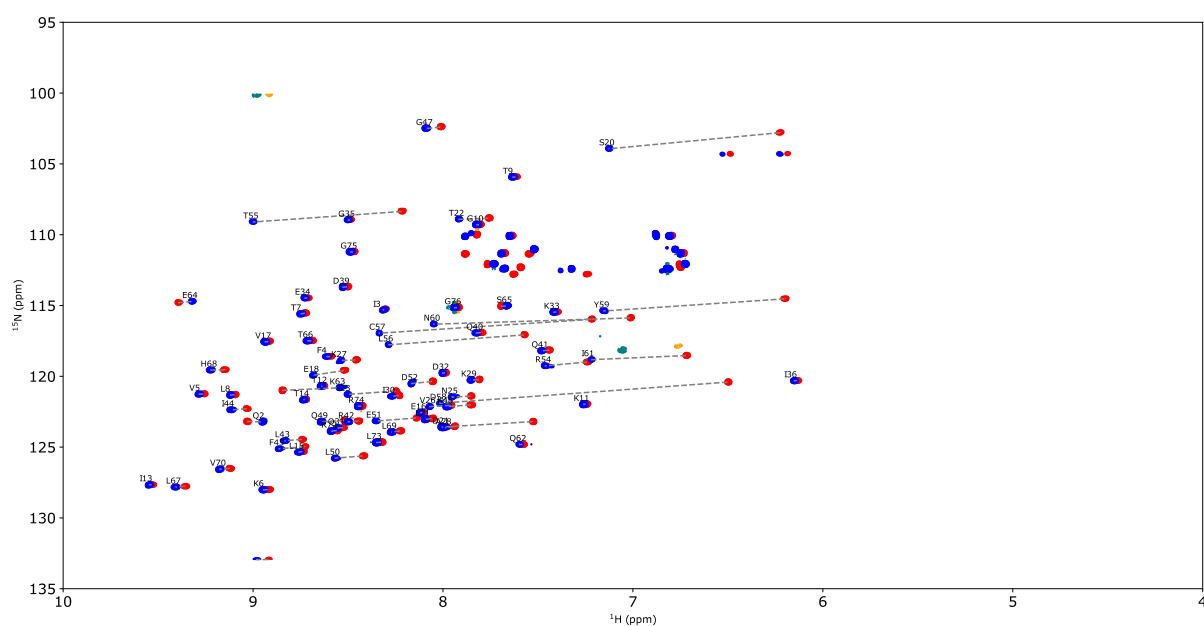


**Figure S166:**  $^1\text{H}$  spectra of deuterium labelled Yb-DOTA-M7FPy complex (**5**). The number represent the labelling schemes and can be found in figure 2 in the main text or figure S111 in the SI. Signals which are affected by deuterium labelling are marked with a star.

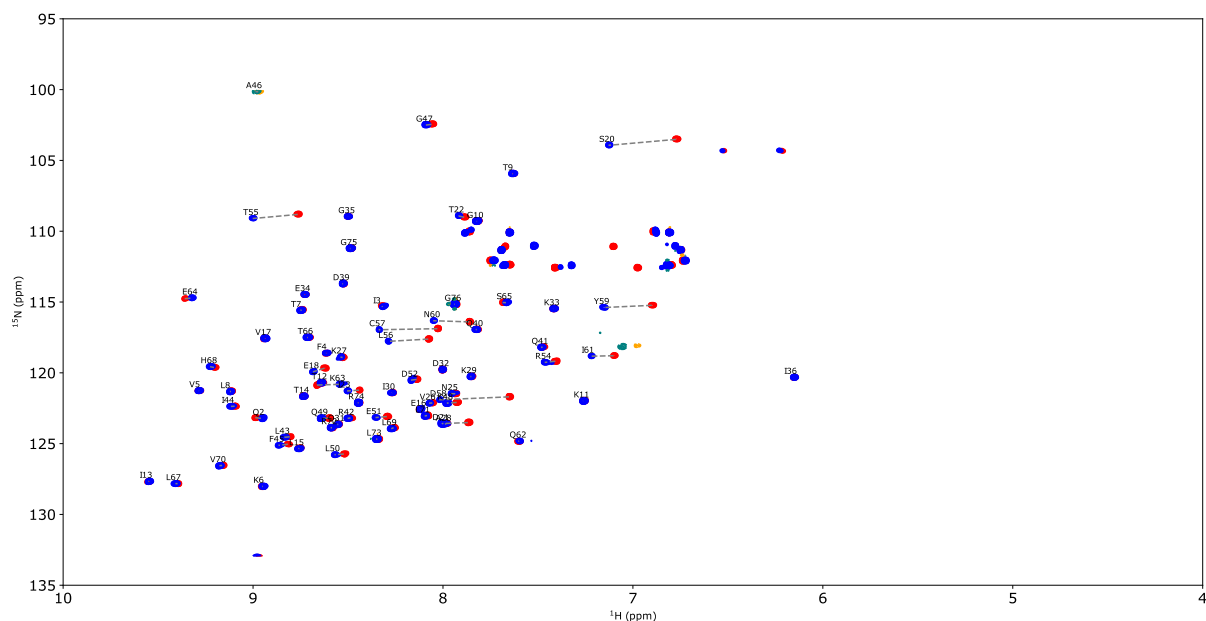
## 2.6.18 $^{15}\text{N}$ $^1\text{H}$ HSQC spectra of ubiquitin S57C



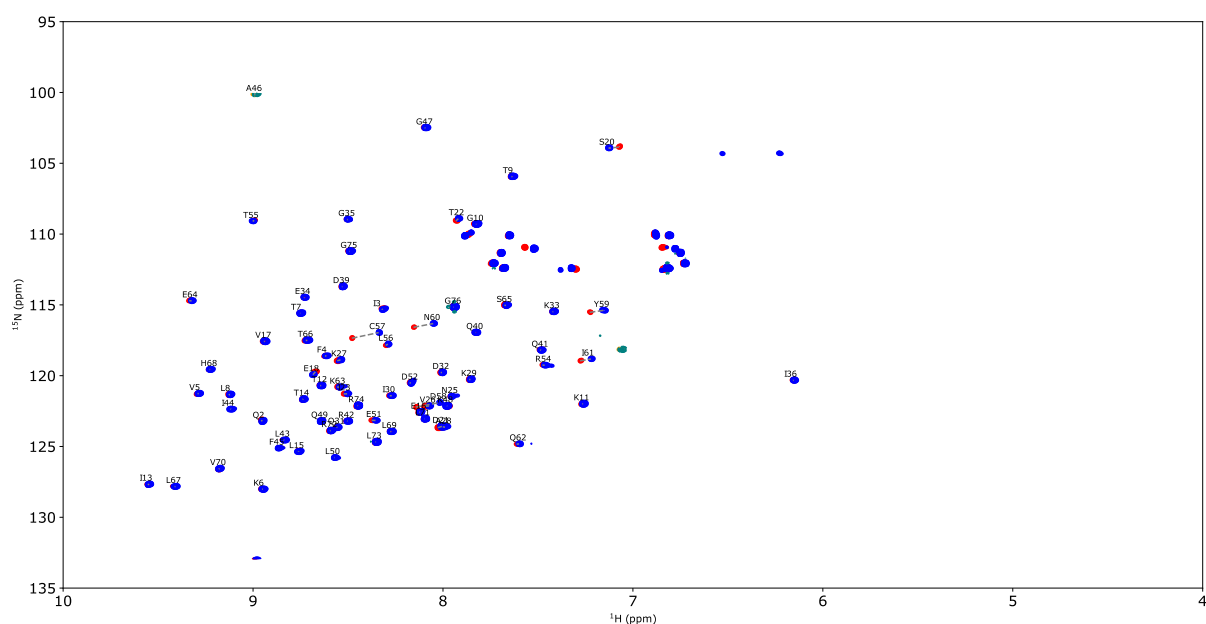
**Figure S167:** Superposition of 2D  $^{15}\text{N}$   $^1\text{H}$  HSQC spectra of ubiquitin S57C coupled to diamagnetic Lu-DOTA-M7FPy (blue) and paramagnetic Ce-DOTA-M7FPy (red) at 600 MHz and 298 K. The water signal was removed for clarity.



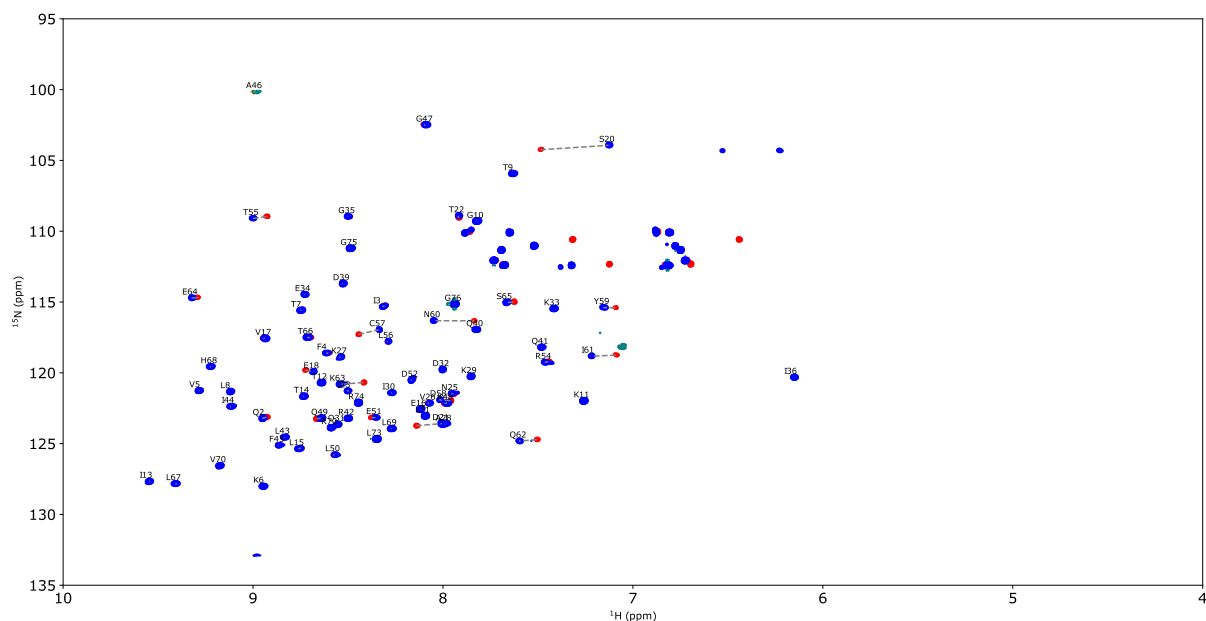
**Figure S168:** Superposition of 2D  $^{15}\text{N}$   $^1\text{H}$  HSQC spectra of ubiquitin S57C coupled to diamagnetic Lu-DOTA-M7FPy (blue) and paramagnetic Pr-DOTA-M7FPy (red) at 600 MHz and 298 K. The water signal was removed for clarity.



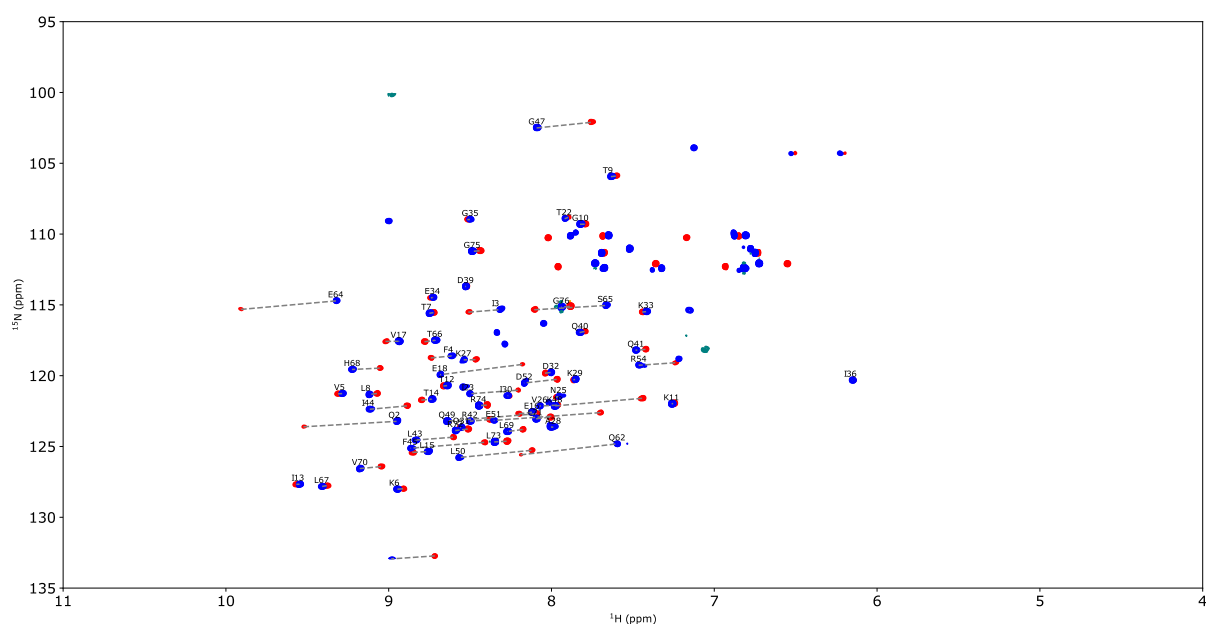
**Figure S169:** Superposition of 2D  $^{15}\text{N}$   $^1\text{H}$  HSQC spectra of ubiquitin S57C coupled to diamagnetic Lu-DOTA-M7FPy (blue) and paramagnetic Nd-DOTA-M7FPy (red) at 600 MHz and 298 K. The water signal was removed for clarity.



**Figure S170:** Superposition of 2D  $^{15}\text{N}$   $^1\text{H}$  HSQC spectra of ubiquitin S57C coupled to diamagnetic Lu-DOTA-M7FPy (blue) and paramagnetic Sm-DOTA-M7FPy (red) at 600 MHz and 298 K. The water signal was removed for clarity.

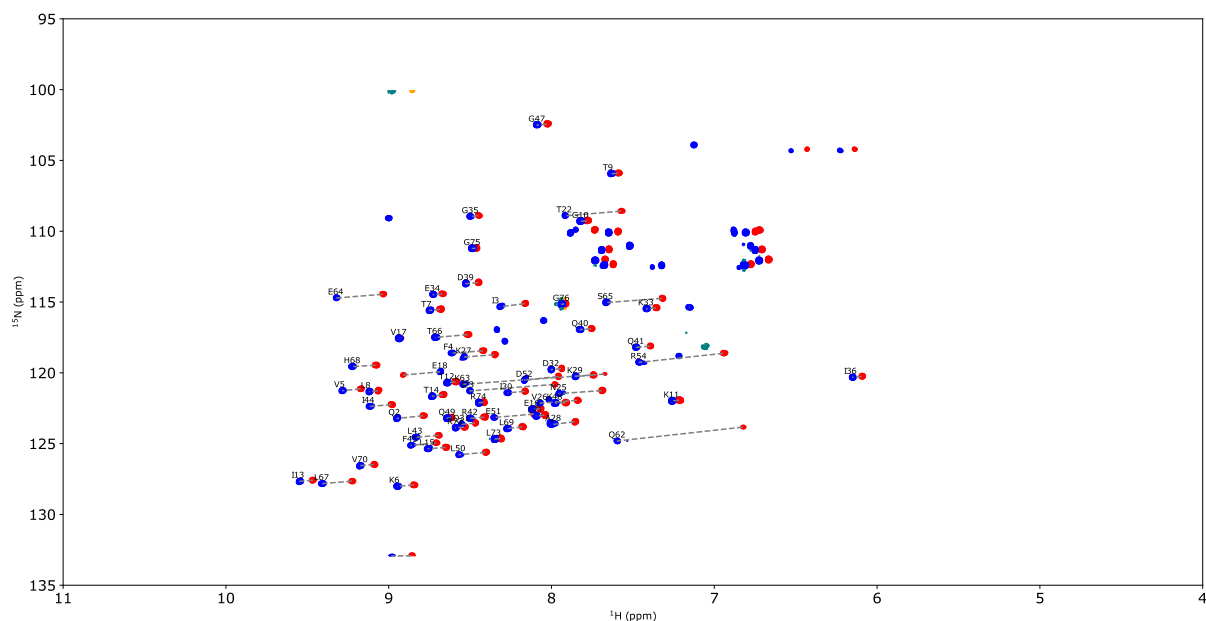


**Figure S171:** Superposition of 2D  $^{15}\text{N}$   $^1\text{H}$  HSQC spectra of ubiquitin S57C coupled to diamagnetic Lu-DOTA-M7FPy (blue) and paramagnetic Eu-DOTA-M7FPy (red) at 600 MHz and 298 K. The water signal was removed for clarity.

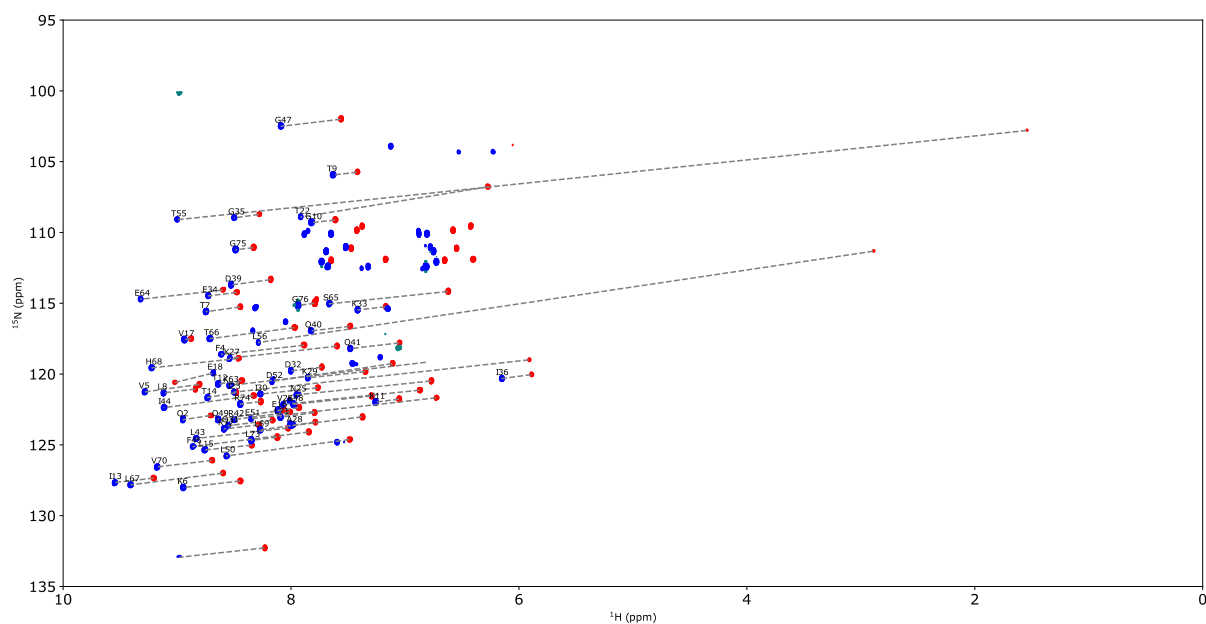


**Figure S172:** Superposition of 2D  $^{15}\text{N}$   $^1\text{H}$  HSQC spectra of ubiquitin S57C coupled to diamagnetic Lu-DOTA-M7FPy (blue) and paramagnetic Tb-DOTA-M7FPy (red) at 600 MHz and 298 K. The water signal was removed for clarity.

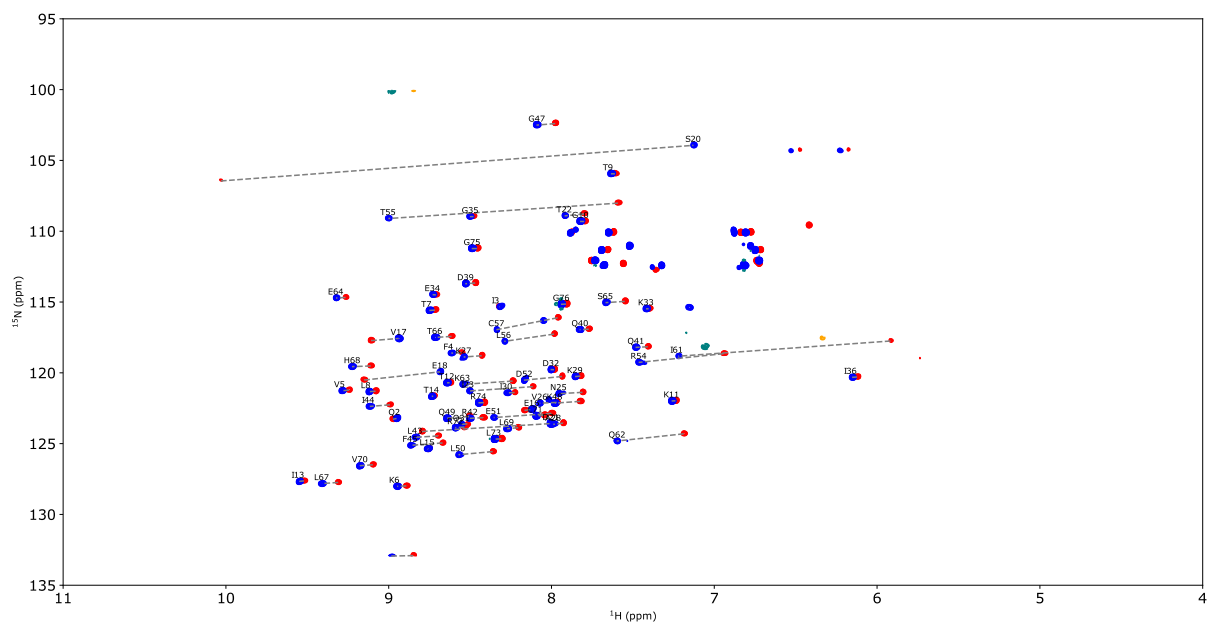




**Figure S175:** Superposition of 2D  $^{15}\text{N}$   $^1\text{H}$  HSQC spectra of ubiquitin S57C coupled to diamagnetic Lu-DOTA-M7FPy (blue) and paramagnetic Er-DOTA-M7FPy (red) at 600 MHz and 298 K. The water signal was removed for clarity.

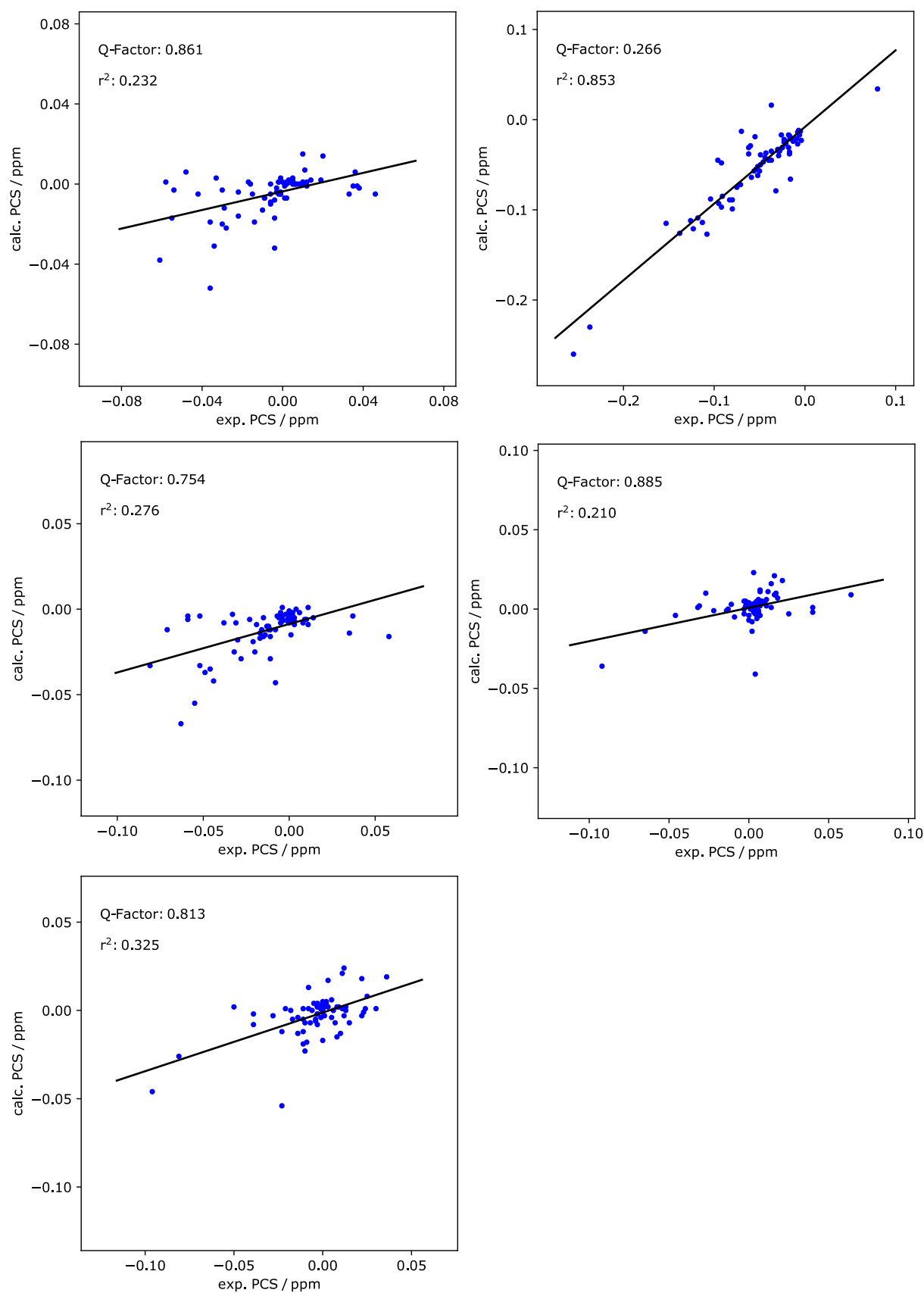


**Figure S176:** Superposition of 2D  $^{15}\text{N}$   $^1\text{H}$  HSQC spectra of ubiquitin S57C coupled to diamagnetic Lu-DOTA-M7FPy (blue) and paramagnetic Tm-DOTA-M7FPy (red) at 600 MHz and 298 K. The water signal was removed for clarity.



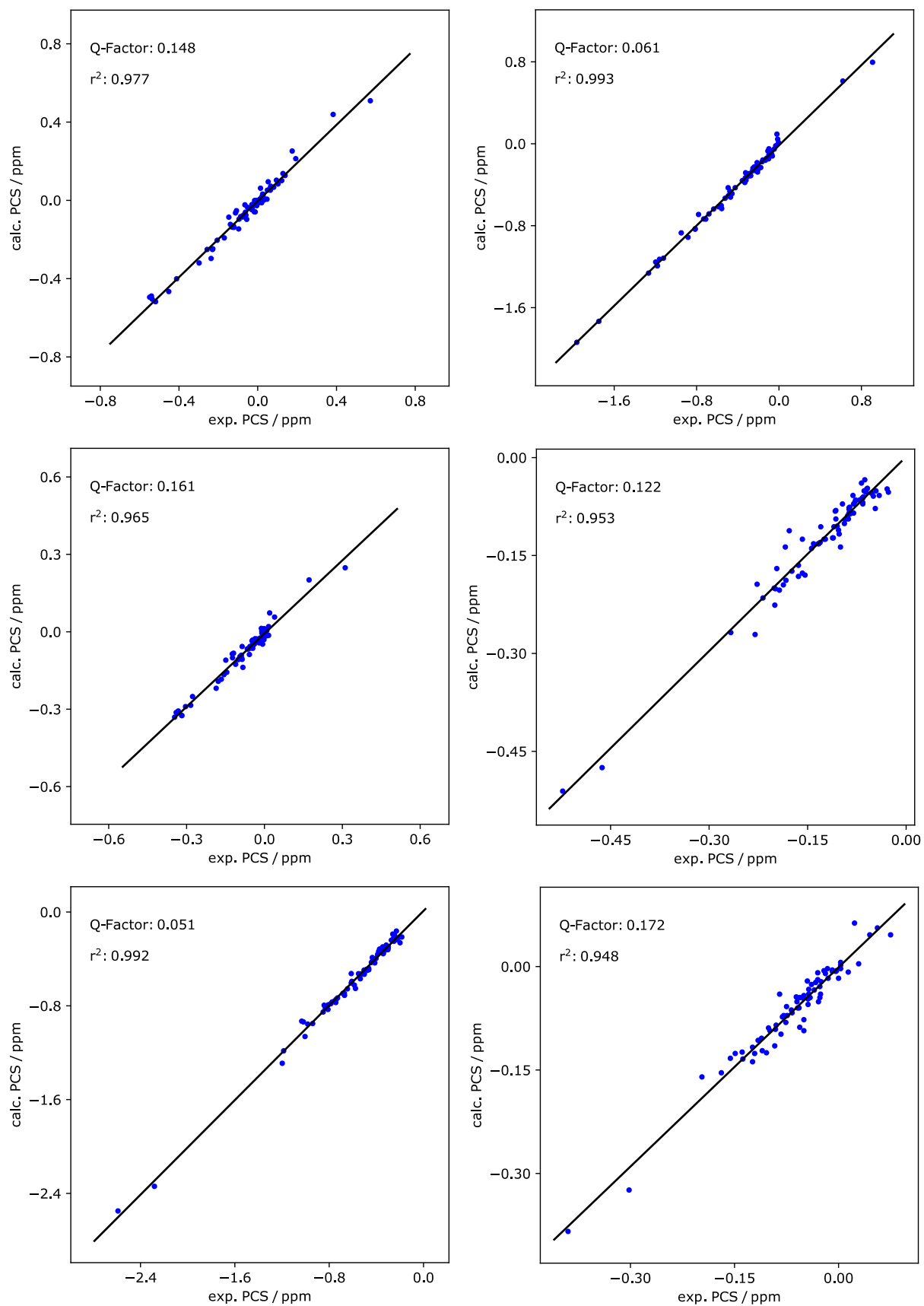
**Figure S177:** Superposition of 2D  $^{15}\text{N}$   $^1\text{H}$  HSQC spectra of ubiquitin S57C coupled to diamagnetic Lu-DOTA-M7FPy (blue) and paramagnetic Yb-DOTA-M7FPy (red) at 600 MHz and 298 K. The water signal was removed for clarity.

## 2.6.19 Correlation graphs ubiquitin S57C

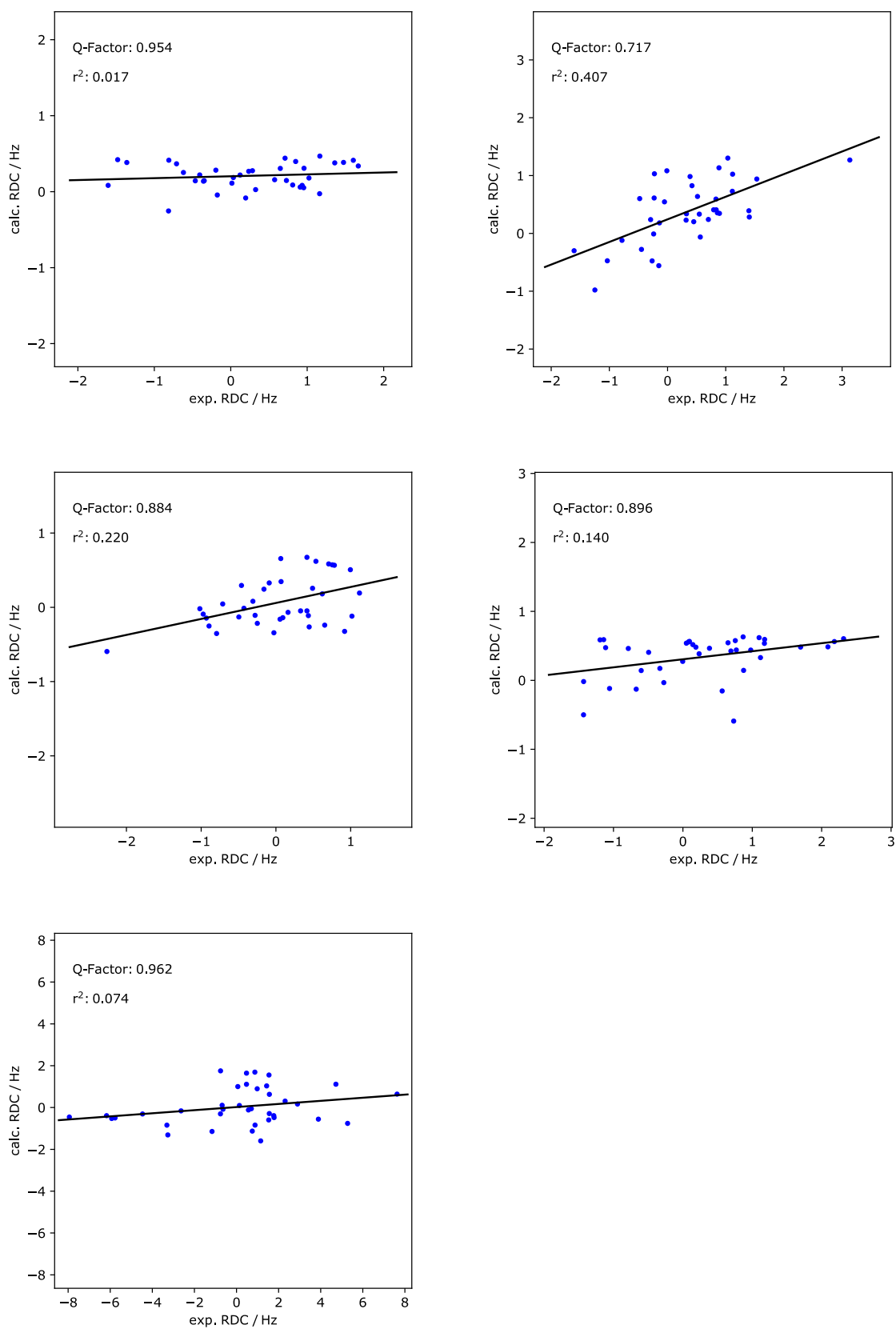


**Figure S178:** Correlation graphs between calculated PCS from the ubiquitin structure (1UBI) and experimental PCS. Only the PCS from residues residing within secondary structures are included. Top left Ce. Top right Pr. Middle left Nd. Middle right Sm. Bottom left Eu.

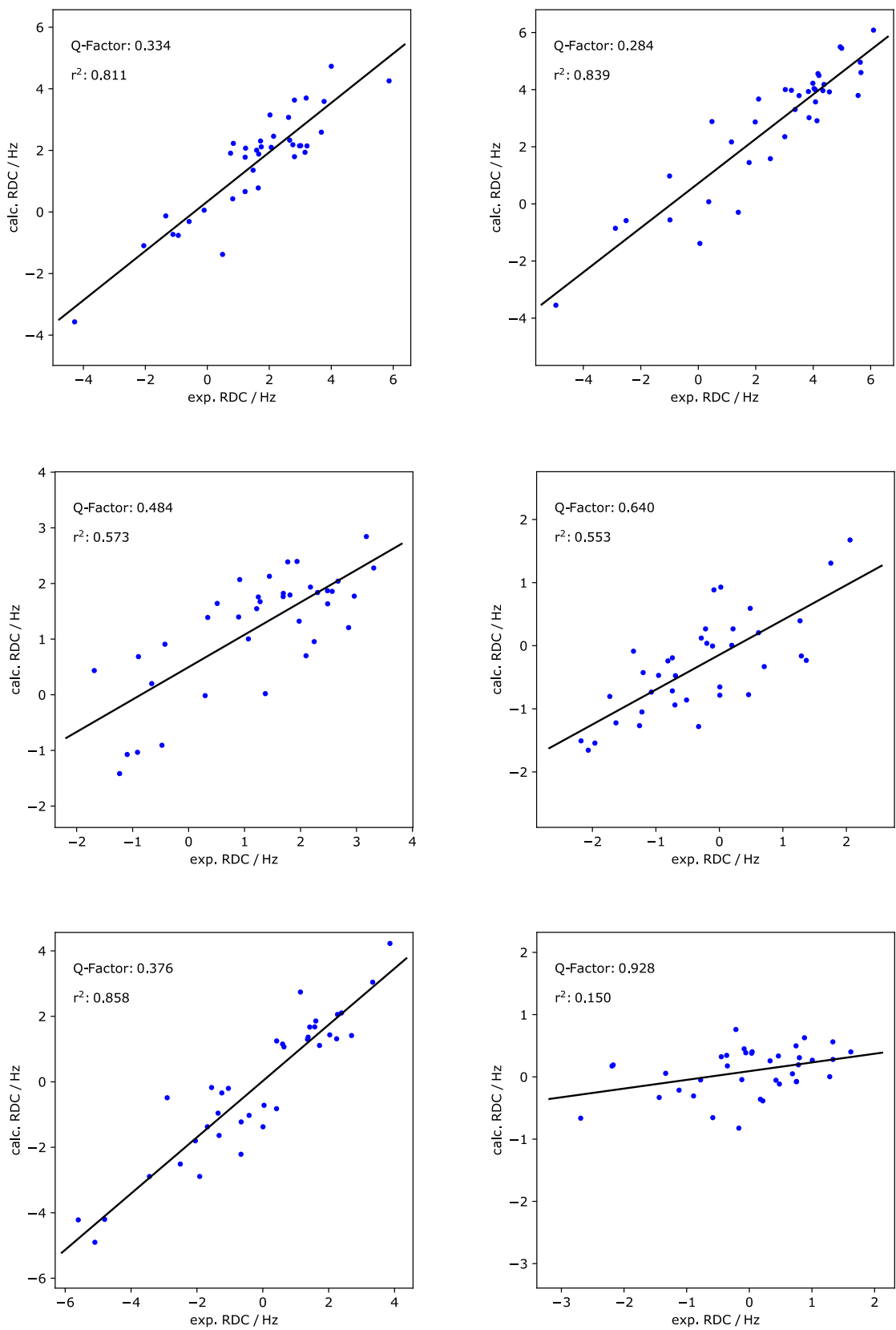




**Figure S179:** Correlation graphs between calculated PCS from the ubiquitin structure (1UBI) and experimental PCS. Only the PCS from residues residing within secondary structures are included. Top left Tb. Top right Dy. Middle left Ho. Middle right Er. Bottom left Tm. Bottom right Yb.



**Figure S180:** Correlation graphs between calculated RDC from the ubiquitin structure (1UBI) and experimental RDC. Only the RDC from residues residing within secondary structures are included. Top left Ce. Top right Pr. Middle left Nd. Middle right Sm. Bottom left Eu.



**Figure S181:** Correlation graphs between calculated RDC from the ubiquitin structure (1UBI) and experimental RDC. Only the RDC from residues residing within secondary structures are included Top right Tb. Top Left Dy. Middle left Ho. Middle right Er. Bottom left Tm. Bottom right Yb.

## 2.6.20 PCSs from DOTA-M7FPy on ubiquitin S57C

**Table S19:** PCS on ubiquitin S57C of the early lanthanoids in ppm measured at 600 MHz and 298 K.

Residue	Ce	Pr	Nd	Sm	Eu
2GlnH	0.03755	0.07995	0.03668	0.00445	-0.0226
2GlnN	-0.05352	-0.03749	-0.05878	-0.09244	-0.09568
3IleH	0.01405	-0.00887	0.00273	0.00221	-0.01033
3IleN	-0.04833	-0.07039	-0.05182	-0.06492	-0.08127
4PheH	0.0111	-0.02053	-3.79E-05	0.00696	-0.01051
4PheN	0.03551	-0.00773	0.01374	-0.00932	-1.62E-04
5ValH	0.01045	-0.0248	-7.80E-04	0.0061	-0.00334
5ValN	0.0354	-0.01683	0.01138	0.00427	0.01547
6LysH	0.00556	-0.0291	0.00341	0.00401	5.91E-04
6LysN	-0.00595	-0.0167	0.00765	-0.00311	0.00547
7ThrH	0.00113	-0.02296	-0.00555	0.00131	-0.00328
7ThrN	-0.02988	-0.05953	-0.03842	-0.01357	-0.02822
8LeuH	1.79E-04	-0.0251	-0.00523	0.00642	4.57E-04
8LeuN	-0.00266	-0.03216	-0.02278	0.01961	-0.01049
9ThrH	0.00175	-0.0168	-0.00256	0.00471	8.84E-05
9ThrN	0.00224	-0.0198	-3.95E-04	4.70E-04	0.00396
10GlyH	0.00196	-0.01407	-0.00166	0.00253	5.28E-04
10GlyN	-0.00417	-0.01027	0.00124	8.80E-05	0.00289
11LysH	0.00302	-0.01218	-6.60E-04	0.0041	7.36E-05
11LysN	-4.96E-04	-0.01257	-0.008	-6.17E-04	7.30E-04
12ThrH	0.00343	-0.00656	5.12E-04	0.00499	-8.68E-04
12ThrN	4.46E-04	-0.00511	-0.00237	0.00276	-0.01698
13IleH	0.00568	-0.0133	0.00267	0.00623	-0.00388
13IleN	0.03681	-0.00409	0.00943	0.04015	0.01161
14ThrH	0.0042	-0.00837	-3.23E-05	0.00404	-0.00423
14ThrN	0.01207	-0.02587	-0.00673	0.02473	-0.01027
15LeuH	0.00161	-0.02071	-0.00354	-4.26E-04	-0.01109
15LeuN	-0.0329	-0.05459	-0.03318	-0.04612	-0.03862
16GluH	0.00813	-0.01156	0.0014	0.0046	-6.12E-05
16GluN	0.00968	-0.01218	0.00984	0.00219	-0.01082
17ValH	0.01146	-0.01979	-2.90E-04	0.00447	0.00764
17ValN	0.01286	-0.03144	0.00265	0.02066	0.00695
18GluH	-0.03542	-0.1633	-0.06152	-0.01271	0.04033
18GluN	-0.2505	-0.34521	-0.26027	-0.20324	-0.1193
20SerH	-0.22251	-0.90107	-0.35492	-0.05506	0.35878
20SerN	-0.24846	-1.13852	-0.41991	-0.07794	0.3082
21AspH	-0.05405	-0.4779	-0.13682	0.02129	0.13562
21AspN	0.0072	-0.38568	-0.06905	0.08781	0.15463
22ThrH	-0.01562	-0.15946	-0.03093	0.01259	-0.00109
22ThrN	0.12897	-0.07928	0.0948	0.14893	0.15141

23IleH	-0.03614	-0.25545	-0.06277	0.01771	-0.00868
23IleN	-0.06148	-0.23696	-0.05538	0.00682	-0.02312
25AsnH	-0.01732	-0.10423	-0.02313	0.00271	-0.01368
25AsnN	0.01919	-0.07063	0.00207	0.01645	0.02269
26ValH	-5.19E-04	-0.11252	-0.01674	0.02121	0.00818
26ValN	-0.00307	-0.09534	-0.01576	0.01375	-8.87E-04
27LysH	0.00108	-0.08013	-0.01083	0.01712	0.00639
27LysN	0.04639	-0.03227	0.03492	0.06383	0.02434
28AlaH	-0.00169	-0.04852	-0.00538	0.01162	0.00138
28AlaN	-0.05849	-0.09602	-0.05872	-0.02731	-0.04975
29LysH	-0.001	-0.04369	-0.00484	0.00651	-2.98E-04
29LysN	0.00503	-0.02855	6.52E-04	0.01628	0.00209
30IleH	0.00669	-0.03741	-0.00117	0.01071	0.00344
30IleN	-0.01603	-0.06213	-0.01529	-0.00307	-0.02148
31GlnH	9.45E-04	-0.03009	-0.00429	0.00505	-7.68E-04
31GlnN	0.00978	-0.01849	-0.00465	0.0072	0.01298
32AspH	0.00254	-0.01634	2.74E-04	0.00628	-7.93E-04
32AspN	0.00533	-0.01722	0.00428	0.00827	-0.00299
33LysH	0.00263	-0.01609	1.14E-04	0.00415	-1.65E-04
33LysN	0.00523	-0.01848	0.00557	0.00674	-0.00257
34GluH	0.00212	-0.01586	-9.85E-04	0.00241	-0.00123
34GluN	-0.00223	-0.00645	0.00175	0.01139	0.01298
35GlyH	0.00315	-0.01145	4.11E-04	0.00423	0.00174
35GlyN	-0.00655	-0.0249	-0.00397	0.00634	-0.00165
36IleH	7.24E-04	-0.01745	2.34E-04	0.00372	4.01E-04
36IleN	0.00796	-0.01568	0.0037	0.01314	-0.01246
39AspH	-0.00139	-0.02542	-0.00366	0.00285	-0.00347
39AspN	-0.0012	-0.02781	2.36E-04	0.00503	-0.00844
40GlnH	-0.00219	-0.02833	-0.00478	0.00134	2.00E-04
40GlnN	-0.00894	-0.04257	-0.01327	0.00424	-0.00264
41GlnH	-0.00431	-0.04033	-0.00819	0.00424	-2.60E-04
41GlnN	-0.0147	-0.04905	-0.01897	-0.03058	-0.00562
42ArgH	-0.00643	-0.05555	-0.0145	0.00268	-0.00119
42ArgN	-0.02932	-0.05214	-0.02971	-0.02152	-0.01058
43LeuH	-0.01358	-0.09237	-0.02819	0.00505	0.00213
43LeuN	-0.02211	-0.09107	-0.03212	-0.01298	0.0303
44IleH	-0.00973	-0.0828	-0.01951	0.00271	0.00546
44IleN	-0.00359	-0.07992	-0.01126	-0.03161	0.02525
45PheH	-0.03048	-0.13826	-0.04946	-3.68E-04	0.00256
45PheN	-0.05523	-0.15306	-0.08057	-0.01071	-0.00764
46AlaH	-0.00279	-0.06746	-0.01399	0.00749	0.01136
46AlaN	0.00109	-0.2009	0.00802	0.0159	0.04297
47GlyH	-0.01661	-0.07892	-0.03192	0.00468	0.00834
47GlyN	-0.02219	-0.10351	-0.05085	-0.00664	-0.00114

48LysH	-0.03606	-0.12644	-0.05202	-0.00231	0.01214
48LysN	-0.02831	-0.11831	-0.04568	0.00406	0.0114
49GlnH	-0.03377	-0.1231	-0.0437	3.59E-04	0.02234
49GlnN	-0.00384	-0.10839	-0.00826	-0.00273	0.03609
50LeuH	-0.03349	-0.14855	-0.04909	0.00224	0.00685
50LeuN	-0.03276	-0.16142	-0.04839	-0.00165	0.01556
51GluH	-0.04252	-0.2139	-0.05965	0.0198	0.02318
51GluN	-0.06243	-0.21855	-0.0762	-0.00625	-0.00116
52AspH	-0.02541	-0.11248	-0.03075	0.00627	-0.00594
52AspN	-0.05833	-0.15748	-0.05817	-0.0199	-0.04333
54ArgH	-0.04821	-0.22343	-0.05666	0.01155	-0.01847
54ArgN	-0.08531	-0.27238	-0.07988	-0.01359	-0.05036
55ThrH	-0.18363	-0.78481	-0.23691	-0.00791	-0.07358
55ThrN	-0.23826	-0.74472	-0.29262	-0.07404	-0.14486
56LeuH	-0.09549	-0.71647	-0.21306	0.01149	0.0034
56LeuN	-0.00515	-0.70401	-0.16042	0.07749	0.05048
57CysH	-0.02243	-1.11943	-0.30917	0.1416	0.10737
57CysN	0.22725	-0.97835	-0.07009	0.39798	0.33172
58AspH	-0.11919	-1.51754	-0.36678	0.12338	-0.05784
58AspN	0.11837	-1.49186	-0.20608	0.31331	0.0573
59TyrH	-0.09973	-0.9536	-0.25452	0.07235	-0.06268
59TyrN	-0.0392	-0.85392	-0.1528	0.14155	0.02333
60AsnH	0.00926	-1.03648	-0.18956	0.10346	-0.21417
60AsnN	0.23953	-0.43918	0.08228	0.26767	0.0125
61IleH	0.01833	-0.50132	-0.12003	0.05684	-0.1309
61IleN	0.07888	-0.28971	-0.0358	0.12618	-0.07469
62GlnH	0.04602	-0.01704	0.00356	0.01263	-0.09381
62GlnN	0.08099	-0.00162	0.02491	0.02213	-0.10382
63LysH	0.11521	0.30028	0.11651	0.00996	-0.12856
63LysN	0.05965	0.17793	0.05122	-0.01992	-0.13037
64GluH	0.04585	0.07113	0.03631	0.01256	-0.02852
64GluN	0.04763	0.08402	0.04778	-0.01164	-0.02648
65SerH	0.03558	0.02754	0.01748	0.00808	-0.03997
65SerN	0.01989	0.00774	-0.00478	-0.0252	-0.0454
66ThrH	0.01036	-0.02255	-0.00366	0.00771	-0.01413
66ThrN	0.02041	-0.02077	0.01055	0.01044	0.00952
67LeuH	0.00479	-0.05035	-0.01138	0.0041	-0.00703
67LeuN	0.01196	-0.05878	0.00127	0.01384	0.02184
68HisH	-0.00936	-0.07474	-0.02058	0.00267	-0.00458
68HisN	0.03254	-0.01625	0.05834	-0.00225	0.01095
69LeuH	-0.00313	-0.04596	-0.0124	0.00491	-8.56E-04
69LeuN	-0.04199	-0.09186	-0.07062	0.00163	-0.03929
70ValH	-0.00583	-0.05433	-0.01405	0.00364	-7.71E-04
70ValN	0.00161	-0.05159	-0.01733	0.03965	0.00933

71LeuH	-0.00581	-0.03707	-0.01242	0.00157	-0.00128
71LeuN	-0.02222	-0.06177	-0.03147	0.00234	-0.01788
72ArgH	-0.00242	-0.03238	-0.00677	0.0042	0.00244
72ArgN	-0.00616	-0.04675	3.48E-06	0.00985	0.00824
73LeuH	-0.00376	-0.02668	-0.00644	0.00295	0.00117
73LeuN	-0.00502	-0.02536	-0.00127	-0.00212	0.01146
74ArgH	-0.00212	-0.01861	-0.00335	0.00243	0.00181
74ArgN	-0.01202	-0.02185	-7.08E-04	-0.00212	-0.00135
75GlyH	-0.00174	-0.01574	-0.00253	0.00229	0.00173
75GlyN	5.73E-04	-0.01405	-0.00249	-0.00203	0.00687
76GlyH	-0.00189	-0.01681	-0.00288	0.0024	0.00194
76GlyN	-0.00534	-0.01604	7.64E-04	5.99E-05	0.00565

**Table S20:** PCS on ubiquitin S57C of the late lanthanoids in ppm measured at 600 MHz and 298 K. Empty fields mean that the signal in the paramagnetic spectrum could not be detected.

Residue	Tb	Dy	Ho	Er	Tm	Yb
2GlnH	0.57201	0.90828	0.3114	-0.16407	-0.24578	0.02252
2GlnN	0.38337	0.61971	0.17155	-0.19693	-0.299	0.05606
3IleH	0.19314	-0.01304	0.03912	-0.15376	-0.53644	0.0026
3IleN	0.17514	-0.02043	0.02009	-0.22742	-0.60766	-0.00327
4PheH	0.12759	-0.21329	-8.95E-04	-0.19289	-0.72911	-0.05934
4PheN	0.13916	-0.15728	0.00689	-0.16385	-0.64512	-0.04061
5ValH	0.02542	-0.23974	-0.02945	-0.11238	-0.47841	-0.04294
5ValN	0.0176	-0.28814	-0.04543	-0.12268	-0.5293	-0.04361
6LysH	-0.03697	-0.35646	-0.06184	-0.10179	-0.50157	-0.05701
6LysN	-0.02995	-0.28752	-0.04479	-0.10294	-0.46362	-0.02948
7ThrH	-0.0248	-0.21161	-0.0393	-0.06626	-0.30247	-0.03473
7ThrN	-0.05241	-0.25267	-0.06088	-0.08011	-0.33663	-0.02634
8LeuH	-0.04981	-0.23621	-0.04723	-0.05474	-0.28031	-0.04125
8LeuN	-0.07133	-0.23836	-0.0612	-0.05958	-0.26938	-0.03343
9ThrH	-0.02957	-0.16919	-0.03294	-0.04209	-0.21343	-0.02427
9ThrN	-0.03866	-0.16238	-0.04798	-0.03323	-0.19853	0.00474
10GlyH	-0.02805	-0.16225	-0.0322	-0.04169	-0.2093	-0.0256
10GlyN	-0.00633	-0.11321	-0.0237	-0.04182	-0.18367	0.0095
11LysH	-0.00959	-0.13341	-0.02257	-0.04551	-0.20848	-0.02368
11LysN	-0.01812	-0.13399	-0.0351	-0.0532	-0.21787	-0.01167
12ThrH	0.02263	-0.08317	-0.00421	-0.05194	-0.206	-0.01524
12ThrN	0.02833	-0.08874	-0.00998	-0.06589	-0.22284	-3.20E-04
13IleH	0.01922	-0.16377	-0.01632	-0.07988	-0.34122	-0.02747
13IleN	0.01558	-0.13217	-0.02083	-0.07692	-0.31591	-0.03003
14ThrH	0.06389	-0.04611	0.0085	-0.06645	-0.25126	-0.0087
14ThrN	0.06242	-0.07143	-0.00999	-0.10651	-0.34563	-0.00935
15LeuH	0.0946	-0.10833	-7.31E-04	-0.11102	-0.41297	-0.00352
15LeuN	0.05308	-0.09778	-0.01214	-0.09399	-0.34189	0.02902
16GluH	0.08128	-0.03191	0.00559	-0.04968	-0.18425	0.04538
16GluN	0.12174	-0.00488	0.01628	-0.04739	-0.19942	0.0753
17ValH	0.08141	-0.09179	-0.04726	-0.00249	-0.05865	0.16944
17ValN	0.01028	-0.18988	-0.0864	-0.0047	-0.05899	0.15556
18GluH	-0.50344	-	-0.5159	0.22804	0.33753	0.46602
18GluN	-0.72397	-	-0.70971	0.22548	0.66585	0.57962
20SerH	-	-	-	-	-	2.90236
20SerN	-	-	-	-	-	2.51191
21AspH	-	-1.5334	-	-	-	0.79022
21AspN	-	-2.01576	-	-	-	0.56063
22ThrH	-0.02203	-1.0356	-0.11384	-0.34557	-1.64237	-0.11903
22ThrN	-0.09461	-1.63863	-0.16559	-0.33359	-2.13499	-0.13597



23IleH	-0.29777	-1.96251	-0.28399	-0.52297	-2.59091	-0.38961
23IleN	-0.25705	-1.74909	-0.27655	-0.46329	-2.282	-0.30195
25AsnH	0.01431	-0.63404	-0.03626	-0.26656	-1.1861	-0.14887
25AsnN	0.04945	-0.4705	-0.00343	-0.21753	-0.98155	-0.09104
26ValH	-0.10769	-0.9489	-0.14875	-0.22954	-1.19834	-0.1043
26ValN	-0.06489	-0.78145	-0.11883	-0.19962	-1.00461	-0.05623
27LysH	-0.07168	-0.68006	-0.09481	-0.18741	-0.93978	-0.11095
27LysN	-0.01307	-0.56138	-0.05776	-0.15772	-0.85133	-0.08983
28AlaH	0.01374	-0.3322	-0.0144	-0.13115	-0.61254	-0.05965
28AlaN	-0.01634	-0.32713	-0.04794	-0.17807	-0.61322	-0.08535
29LysH	0.00987	-0.29576	-0.02791	-0.10981	-0.50396	-0.03309
29LysN	0.03224	-0.20025	-0.00489	-0.10751	-0.43404	-0.03043
30IleH	-0.00372	-0.31993	-0.03768	-0.10462	-0.50218	-0.04293
30IleN	-0.00886	-0.25573	-0.03656	-0.10733	-0.44194	-0.02545
31GlnH	0.00524	-0.21764	-0.01521	-0.08625	-0.38964	-0.03933
31GlnN	0.01974	-0.19775	-0.04543	-0.09657	-0.38111	-0.04475
32AspH	0.03503	-0.10072	0.00683	-0.06442	-0.27292	-0.02094
32AspN	0.04726	-0.06459	0.01581	-0.06751	-0.2609	0.00299
33LysH	0.02388	-0.10319	-0.00173	-0.05911	-0.24695	-0.0161
33LysN	0.0322	-0.0724	0.00398	-0.06255	-0.22985	0.00344
34GluH	0.0109	-0.12061	-0.0057	-0.05956	-0.25266	-0.0193
34GluN	0.02524	-0.09785	0.00601	-0.04598	-0.24046	0.01374
35GlyH	0.01567	-0.09497	0.00114	-0.0504	-0.21915	-0.02199
35GlyN	0.01247	-0.13371	-0.00981	-0.06977	-0.23982	-0.00153
36IleH	-8.26E-04	-0.14258	-0.00837	-0.05906	-0.26143	-0.03074
36IleN	-0.00257	-0.13767	-0.00508	-0.06526	-0.27982	-0.02427
39AspH	-0.00479	-0.17683	-0.00189	-0.07824	-0.34894	-0.06099
39AspN	-0.01769	-0.20823	-0.00748	-0.0811	-0.37298	-0.05013
40GlnH	-0.03107	-0.22516	-0.01967	-0.07125	-0.3428	-0.05607
40GlnN	-0.07619	-0.27428	-0.051	-0.06132	-0.32212	-0.02708
41GlnH	-0.06041	-0.3201	-0.0448	-0.0875	-0.43201	-0.07524
41GlnN	-0.06336	-0.31436	-0.05633	-0.08682	-0.40344	-0.04419
42ArgH	-0.12283	-0.45616	-0.08798	-0.08919	-0.48842	-0.08138
42ArgN	-0.12104	-0.49256	-0.08607	-0.08783	-0.5288	-0.0495
43LeuH	-0.23004	-0.81432	-0.1664	-0.14079	-0.80666	-0.13902
43LeuN	-0.20571	-0.73134	-0.14531	-0.13266	-0.74168	-0.09186
44IleH	-0.22797	-0.81392	-0.17829	-0.13374	-0.7863	-0.12385
44IleN	-0.23717	-0.88289	-0.18558	-0.12521	-0.84319	-0.11013
45PheH	-0.45207	-1.26596	-0.31796	-0.1576	-1.019	-0.19674
45PheN	-0.41168	-1.19693	-0.30382	-0.18381	-1.03344	-0.16862
46AlaH	-0.26732	-0.8343	-0.21249	-0.12717	-0.75444	-0.13742
46AlaN	-0.41034	-2.01385	-0.34311	-0.22064	-0.87179	-0.23931
47GlyH	-0.33413	-0.80711	-0.23234	-0.06446	-0.5284	-0.11486
47GlyN	-0.39139	-0.86578	-0.26473	-0.05566	-0.50157	-0.10871

48LysH	-0.53621	-1.17971	-0.34606	-0.06496	-0.68398	-0.15584
48LysN	-0.53952	-1.12141	-0.33953	-0.02913	-0.58668	-0.1207
49GlnH	-0.54863	-1.15999	-0.33199	-0.02669	-0.57709	-0.13818
49GlnN	-0.51911	-1.18185	-0.31874	-0.0413	-0.67102	-0.12399
50LeuH	-0.4478	-1.29185	-0.30041	-0.16551	-1.08186	-0.20943
50LeuN	-0.50918	-1.4177	-0.33725	-0.1648	-1.15592	-0.21942
51GluH	-0.6536	-	-0.39239	-0.24601	-1.62535	-0.35453
51GluN	-0.5494	-	-0.32478	-0.24834	-1.48202	-0.29692
52AspH	-0.20102	-0.82702	-0.10489	-0.20939	-1.05666	-0.23356
52AspN	-0.25958	-1.01293	-0.14944	-0.25946	-1.25659	-0.26202
54ArgH	-0.22452	-1.49235	-0.10447	-0.52014	-	-0.52155
54ArgN	-0.17568	-1.52945	-0.0791	-0.63849	-	-0.61452
55ThrH	-	-	-	-	-7.45558	-1.40969
55ThrN	-	-	-	-	-6.30409	-1.0883
56LeuH	-	-	-	-	-5.39789	-0.30589
56LeuN	-	-	-	-	-6.45385	-0.51699
57CysH	-	-	-	-	-	-0.37585
57CysN	-	-	-	-	-	-0.84112
58AspH	-	-	-	-	-	-
58AspN	-	-	-	-	-	-
59TyrH	-	-	-	-	-	-
59TyrN	-	-	-	-	-	-
60AsnH	-	-	-	-	-	-
60AsnN	-	-	-	-	-	-
61IleH	-	-	-	-	-	-1.30337
61IleN	-	-	-	-	-	-1.07087
62GlnH	0.59029	-	0.0798	-0.77393	-	-0.4119
62GlnN	0.77263	-	0.14747	-0.98334	-	-0.51272
63LysH	-	-	-	-0.87331	-1.72943	-0.30818
63LysN	-	-	-	-0.72929	-1.64456	-0.23271
64GluH	0.58399	0.67797	0.27581	-0.28559	-0.72456	-0.05873
64GluN	0.60371	0.73945	0.26791	-0.26213	-0.65185	-0.03826
65SerH	0.43727	0.20731	0.14736	-0.34594	-1.04325	-0.11784
65SerN	0.30421	0.07794	0.0773	-0.29516	-0.87284	-0.08542
66ThrH	0.06569	-0.31726	-0.04419	-0.20059	-0.74428	-0.10077
66ThrN	0.10252	-0.28016	-0.02454	-0.19861	-0.77608	-0.07558
67LeuH	-0.02826	-0.523	-0.09423	-0.18281	-0.81002	-0.09862
67LeuN	-0.05596	-0.58685	-0.11072	-0.17381	-0.83333	-0.08312
68HisH	-0.17017	-0.71099	-0.15568	-0.14435	-0.76043	-0.11611
68HisN	-0.0968	-0.55567	-0.08293	-0.09981	-0.67049	-0.04988
69LeuH	-0.09502	-0.42504	-0.0892	-0.09301	-0.4828	-0.06791
69LeuN	-0.1473	-0.49361	-0.12431	-0.13038	-0.55112	-0.07397
70ValH	-0.12999	-0.47602	-0.10131	-0.08654	-0.48403	-0.07921
70ValN	-0.13868	-0.47718	-0.12282	-0.0853	-0.46512	-0.06701

71LeuH	-0.08682	-0.30222	-0.06567	-0.05287	-0.2989	-0.05146
71LeuN	-0.11268	-0.32404	-0.0858	-0.06717	-0.31996	-0.05145
72ArgH	-0.07688	-0.28198	-0.04178	-0.05456	-0.30632	-0.05645
72ArgN	-0.10589	-0.32144	-0.07055	-0.04059	-0.2828	-0.04838
73LeuH	-0.07636	-0.2403	-0.04848	-0.03709	-0.22824	-0.04385
73LeuN	-0.05102	-0.21686	-0.03222	-0.03465	-0.22201	-0.01271
74ArgH	-0.0509	-0.17465	-0.03104	-0.02977	-0.18014	-0.03366
74ArgN	-0.04322	-0.16971	-0.03066	-0.03422	-0.17489	-0.01322
75GlyH	-0.0479	-0.15963	-0.02728	-0.02483	-0.15864	-0.03132
75GlyN	-0.04227	-0.15789	-0.03314	-0.02537	-0.15286	-0.00195
76GlyH	-0.0544	-0.15962	-0.03006	-0.02106	-0.14715	-0.03032
76GlyN	-0.05628	-0.15482	-0.032	-0.01902	-0.15661	-0.01026

## 2.6.21 RDCs from DOTA-M7FPy on ubiquitin S57C

**Table S21:**  $^1\text{H}$ - $^{15}\text{N}$  Backbone amid RDC measured at 600 MHz and 298 K on ubiquitin S57C of the early lanthanoids in Hz of all residues used to fit the RDC tensor.

	Ce	Pr	Nd	Sm	Eu
2Gln	0.95	0.79	0.75	-0.27	-0.76
3Ile	0.93	0.88	0.54	1.70	0.47
4Phe	0.57	0.84	-0.31	0.05	2.90
5Val	0.73	0.86	0.65	0.87	-4.47
6Lys	0.28	-0.78	-0.50	0.87	5.28
7Thr	0.23	0.52	-1.02	-1.43	2.31
12Thr	-1.48	0.39	0.49	0.00	7.63
13Ile	-0.35	0.33	-0.89	-1.06	-2.64
14Thr	-0.19	0.45	-0.28	0.08	1.79
15Leu	-1.60	-0.01	0.71	2.09	1.54
16Glu	0.02	0.42	0.07	-0.79	0.87
23Ile	1.36	1.40	0.42	0.14	-6.18
25Asn	0.03	-1.03	-0.93	-1.19	-3.31
26Val	0.96	-0.29	0.43	0.65	-5.77
27Lys	0.85	0.32	-0.43	2.32	1.53
28Ala	-0.46	-1.25	-0.03	0.19	1.15
29Lys	-0.62	-0.24	-0.97	1.10	3.89
30Ile	-0.71	0.55	0.16	1.18	-7.94
31Gln	0.65	-0.45	0.09	-1.14	0.75
32Asp	0.12	-0.15	-0.25	1.18	-1.16
33Lys	-0.41	0.89	1.02	0.98	1.56
34Glu	0.71	-0.23	0.62	2.18	-0.64
39Asp	0.32	1.53	0.07	0.23	1.43
40Gln	-0.81	-1.61	-2.26	-1.43	0.88
41Gln	-0.18	1.12	1.00	-0.33	0.06
42Arg	-0.81	-0.48	-0.16	0.09	0.70
43Leu	1.67	3.13	0.42	-1.11	0.47
44Ile	1.60	0.83	-0.71	0.38	0.57
45Phe	-1.36	-0.23	-0.46	-0.60	0.98
48Lys	1.16	0.56	0.44	0.73	0.14
49Gln	0.81	0.70	0.92	0.57	-0.76
66Thr	0.91	1.11	1.12	-0.49	1.56
67Leu	0.20	-0.14	-0.79	-0.67	1.77
68His	1.48	1.40	0.33	0.75	-5.93
69Leu	1.16	1.04	0.78	0.77	4.72
70Val	1.02	-0.27	0.05	0.69	-3.26
71Leu	-0.36	-0.05	-0.09	1.12	-0.68

**Table S22:**  $^1\text{H}$ - $^{15}\text{N}$  Backbone amid RDC measured at 600 MHz and 298 K on ubiquitin S57C of the late lanthanoids in Hz of all residues used to fit the RDC tensor.

	Tb	Dy	Ho	Er	Tm	Yb
2Gln	-1.11	3.99	3.31	-1.26	-2.05	-1.12
3Ile	-2.05	4.94	1.94	-0.74	0.42	0.80
4Phe	3.77	4.17	1.44	-1.07	0.04	0.43
5Val	3.01	3.01	2.86	-0.28	1.36	1.01
6Lys	0.49	4.08	0.51	-0.33	-1.92	0.22
7Thr	1.59	3.86	1.22	-0.20	2.03	1.62
12Thr	-1.34	5.66	2.67	1.29	0.64	-0.08
13Ile	-0.59	2.51	2.24	-0.22	1.58	-0.36
14Thr	2.02	4.03	2.48	-0.52	-1.68	0.48
15Leu	2.14	4.99	1.77	1.37	1.72	1.34
16Glu	3.22	6.10	3.17	-1.22	-1.36	-0.78
23Ile	1.66	3.03	2.96	0.01	0.42	0.69
25Asn	-0.94	1.98	0.89	-2.07	-4.80	-2.69
26Val	-4.28	4.07	2.30	-1.73	-0.66	0.75
27Lys	2.06	3.37	1.98	0.46	-1.33	0.75
28Ala	2.66	0.36	1.37	-2.18	-5.10	-0.17
29Lys	2.81	3.24	2.56	-1.63	-2.50	-1.44
30Ile	1.48	4.34	1.69	-0.74	-0.42	1.28
31Gln	1.64	1.77	-1.69	-0.70	-3.44	0.18
32Asp	2.76	1.15	1.07	-1.96	-5.60	-0.58
33Lys	1.72	3.51	1.81	-0.96	-1.55	-1.33
34Glu	-0.10	2.10	0.34	-1.20	-2.90	-2.19
39Asp	3.15	4.56	1.28	0.22	2.27	-0.06
40Gln	1.74	-4.95	-1.23	1.76	3.34	-0.45
41Gln	0.75	-0.99	-0.48	2.06	3.86	-0.21
42Arg	0.84	0.48	-0.42	-0.81	-1.24	0.78
43Leu	4.00	4.13	2.10	0.49	2.39	0.88
44Ile	2.81	4.38	1.69	-0.69	-1.04	-2.17
45Phe	2.98	4.20	0.91	-1.35	2.69	0.75
48Lys	0.82	-2.51	-0.66	0.62	0.60	-0.35
49Gln	2.62	-1.00	-0.90	1.27	1.61	0.47
66Thr	1.22	3.83	1.25	0.19	2.24	0.33
67Leu	1.24	1.39	0.30	-0.09	1.14	0.04
68His	1.22	5.56	2.48	0.01	0.01	-0.12
69Leu	3.68	5.64	2.18	-0.11	1.38	1.33
70Val	3.19	0.05	-0.91	0.71	-0.66	-0.89
71Leu	5.87	-2.88	-1.10	0.02	1.43	0.05

## 2.6.22 References

1. Heiko, G. (2014). Combining NMR spectroscopy and organic synthesis : From small building blocks to large biomolecules.
2. Müntener, T., Kottelat, J., Huber, A., and Häussinger, D. (2018). New Lanthanide Chelating Tags for PCS NMR Spectroscopy with Reduction Stable, Rigid Linkers for Fast and Irreversible Conjugation to Proteins. *Bioconjug. Chem.* *29*, 3344–3351.
3. Suturina, E.A., Mason, K., Geraldès, C.F.G.C., Chilton, N.F., Parker, D., and Kuprov, I. (2018). Lanthanide-induced relaxation anisotropy. *Phys. Chem. Chem. Phys.* *20*, 17676–17686.

# Chapter II

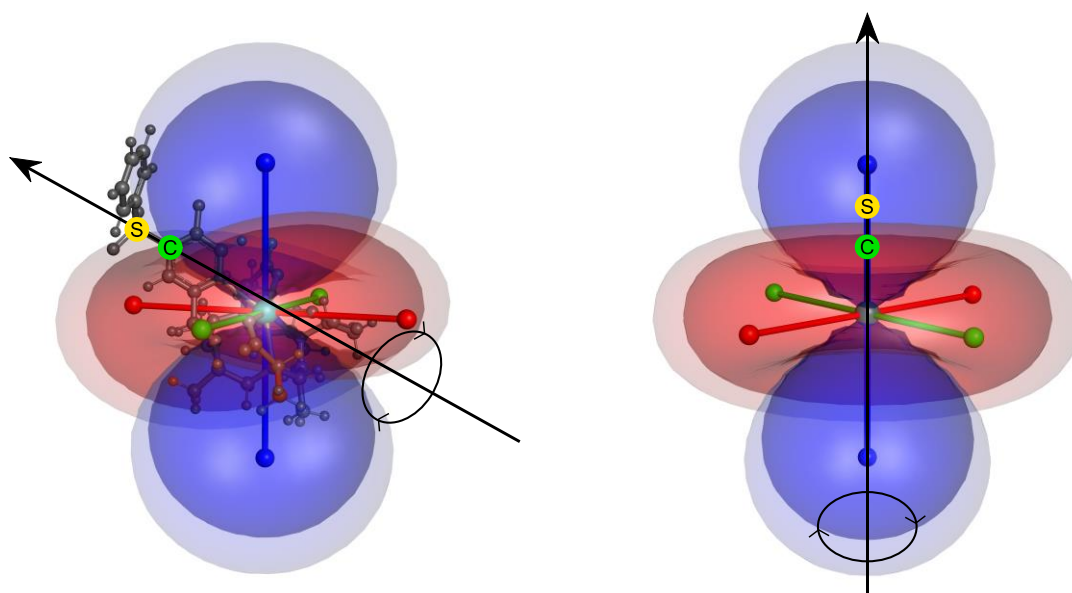
3. A new lanthanoid chelating tag – towards predictable anisotropy parameters





### 3.1 Aim of the Project

For the application of PCS NMR spectroscopy, it is usually necessary to know the anisotropy parameters observed on a protein conjugated to an LCT. For single-arm LCTs the observed anisotropy parameters are different for each protein as well as for each tagging site on the same protein. The convenient application of PCS NMR spectroscopy would profit greatly if the anisotropy parameters of an LCT would be predictable, which would eliminate the need to always redetermine them. Furthermore, the a priori knowledge of the anisotropy parameters would allow the choice of the best-suited tagging sites for a given application and facilitate the assignment of paramagnetic signals. To date, the only LCTs that provide predictable anisotropy parameters are the double-arm LCTs like CLaNP5 developed in the Ubbink lab.<sup>[1][2]</sup> The predictability of these LCTs originates from the fact that their rotational motion relative to the protein is nearly fully suppressed due to the two anchoring points on the protein. However, the need for a double cysteine mutation with a specific distance between the two cysteine residues complicates their application. The aim of this project was the development of a new lanthanoid chelating tag, which could provide predictable anisotropy parameters on a conjugated protein relying only on a single attachment point.



**Figure 1:** Rotational freedom for a single-armed thioether LCT. On the left a classical LCT (DOTA-M7FPy) is depicted where the rotation axis between the cysteine S and the LCT is oriented arbitrary with regard to the tensor frame. From the orientation of the rotation axis to the tensor frame it is clear that different degrees of rotational freedom will lead to vastly different averaging. On the right, the situation is depicted if the rotation axis is coaxial to the z-axis of the tensor frame. For the optimal depicted case of a fully axial tensor, it becomes apparent that the averaging would be independent of the rotational freedom.

For single-arm LCTs the observed anisotropy parameters on a conjugated protein depend strongly on the tagging site. The tagging site in combination with the bulkiness of the LCT and the rigidity of the linkage to the protein determines how much rotational freedom the LCT has. The idea behind this project was not to suppress the rotation, as this is impossible independent of the tagging site, but to control it. Since the isosurfaces describing the PCS are symmetrical ( $C_{2h}$  or  $C_{\infty h}$  for rhombic or fully axial anisotropy parameters, respectively) it was hypothesized that a rotation around the z-axis of the tensor frame would lead to predictable anisotropy parameters for different tagging sites (Fig. 1). To test this hypothesis a new single-armed LCT would have to be developed, which provides coaxiality between the rotation axis and the z-axis of the tensor frame. Rotation around the z-axis should occur if the rotation around the bond between the cysteine S (Fig. 1 yellow) and the carbon of the LCT (Fig. 1 green) is coaxial to the z-axis of the tensor frame.

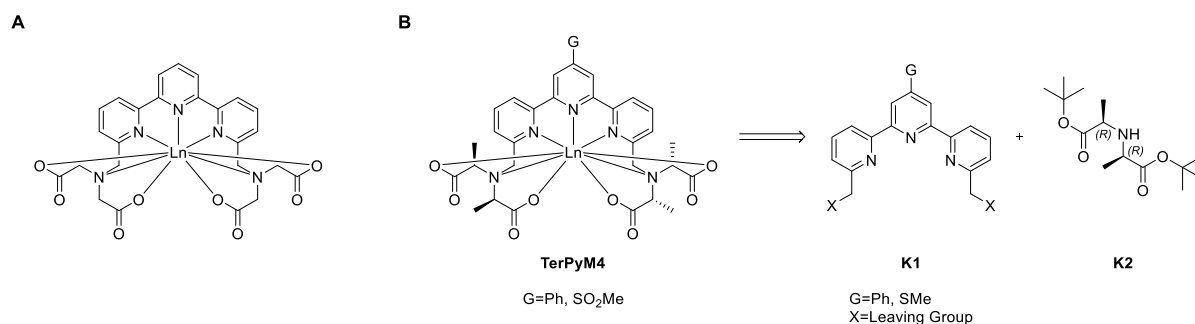
Coaxiality between the rotation axis and the z-axis of the tensor frame can be achieved by developing an LCT, which forms a symmetric lanthanoid complex. It should be noted that from a synthetic perspective symmetry above  $C_2$  is difficult to achieve but coaxiality between the  $C_n$ -symmetry-axis and the z-axis of the tensor frame is only guaranteed for  $C_n$  symmetry with  $n \geq 3$ .<sup>[3,4]</sup> While this might seem to be a problem, it could also be that coaxiality between the rotation axis and the x- or y-axis of the tensor frame is sufficient to obtain predictable anisotropy parameters. The linkage to the protein should allow the rotation around only one axis, which is given for a thioether linkage. Suitable candidates for a new LCT providing predictable anisotropy parameters would therefore have to fulfil two criteria: (i) the lanthanoid binding scaffold has to be symmetric and (ii) the LCT has to provide a thioether linkage to the protein. It must be possible to place the required leaving group and therefore also the attachment point to the protein onto the  $C_n$ -symmetry-axis in order to retain the symmetry of the lanthanoid binding scaffold. This additionally guarantees that one of the tensor frame axes is coaxial to the rotation axis.

## 3.2 Terpyridine based LCTs

### 3.2.1 Molecular design

In literature, several stable lanthanide complexes using the same terpyridine-based scaffold are described.<sup>[5–7]</sup> The terpyridine scaffold consists out of a central terpyridine unit that is equipped with four carboxylic acid side arms to form a nonadentate ligand (Fig. 2A). The symmetry as well as the possibility for a central attachment point makes such terpyridine based ligands good candidates for a new LCT that could possibly yield predictable anisotropy parameters. Since the complexes in literature are used as luminescence probes they do not necessarily adopt a single conformation as it is not a primary requirement for luminescence applications. Ligands that adopt a single conformation might be obtained by decorating the carboxylic acid side arms with stereospecific methyl groups (Fig. 2B) similarly to the stereospecific installation of methyl groups in DOTA M8 based tags.

The general synthetic strategy towards terpyridine-based LCTs was adapted from literature and is based on two key intermediates, the central terpyridine unit **K1** and the side arm **K2** (Fig. 2B).<sup>[5,7]</sup> The synthesis towards the lactic acid side arms should be straightforward to achieve even with the added methyl groups. 4' substituted terpyridines on the other hand can be more or less challenging to synthesize depending on the chosen substituent. For the purpose of the new LCT a thioether linkage to the protein is required as it provides the necessary single rotatable bond between the protein and the LCT. It is therefore necessary to install a leaving group at the 4' position, which will react with a cysteine in a nucleophilic aromatic substitution reaction. Based on previously developed LCTs a methyl sulfone leaving group was chosen. The methyl sulfone leaving group should provide the necessary reactivity and has the advantage compared to a phenyl sulfone leaving group that it does not promote the formation of protein dimers.<sup>[8]</sup> On the central terpyridine building block the precursor for the methylsulfone the

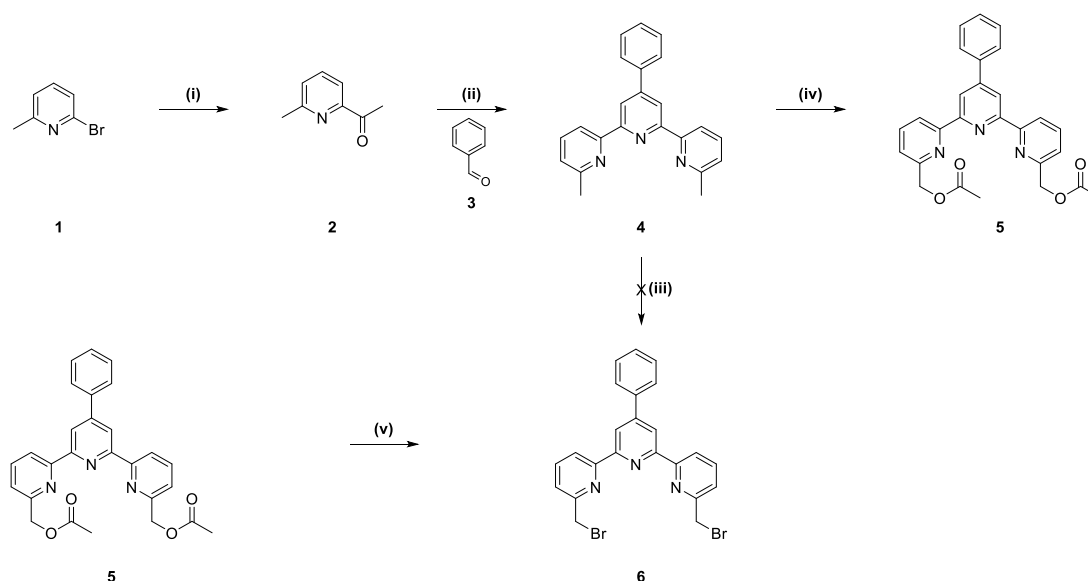


**Figure 2:** A: Structure of the terpyridine scaffold. B: The two key intermediates in the retrosynthesis towards the new TerPyM4 scaffold.

methyl thioether would have to be installed. Based on previously reported 4' substituted terpyridines<sup>[7,9,10]</sup> it was assumed that the synthesis towards the 4' methyl thioether substituted version of the central terpyridine building block (**K1**) will be challenging. Furthermore, it is unclear if the additional methyl groups are sufficient to lock the complex into a single conformation. Therefore, we decided to first synthesize a prototype complex with an easier accessible central terpyridine building block. As a simpler central terpyridine building block the 4' phenyl substituted terpyridine was chosen, which is accessible through the procedure reported by Wang and Hanan<sup>[11]</sup>. Based on the properties displayed by the prototype complex it will be assessed if it is reasonable to synthesize a LCT using the TerPyM4 scaffold.

### 3.2.2 Results and Discussion

#### 3.2.2.1 Synthesis of the Ln-TerPyM4-Prototype complex



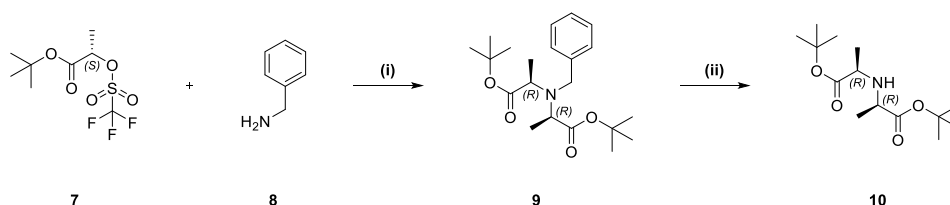
**Figure 3:** Synthesis of the central phenyl-terpyridine building block **6**. (i) *n*-BuLi, DMAC, THF, -78°C. (ii) NH<sub>4</sub>OH, KOH, EtOH, 20-25°C. (iii) NBS, AIBN, CCl<sub>4</sub>, 76°C. (iv) 1. *m*-CPBA, DCM, 20-25°C; 2. Ac<sub>2</sub>O, 130°C. (v) HBr 33% in AcOH, 70°C.

The synthesis for the central terpyridine building block **6** (Fig. 3) of the prototype complex **13** was started from the commercially available pyridine **1**. **1** was acylated using *n*-BuLi and *N,N'*-dimethylacetamide in tetrahydrofuran with a good yield of 70%. The formation of the 4' phenyl substituted terpyridine **4** was achieved by refluxing ketone **2** and benzaldehyde

(3) in the presence of ammonium hydroxide and potassium hydroxide according to the procedure from Wang and Hanan<sup>[11]</sup>.

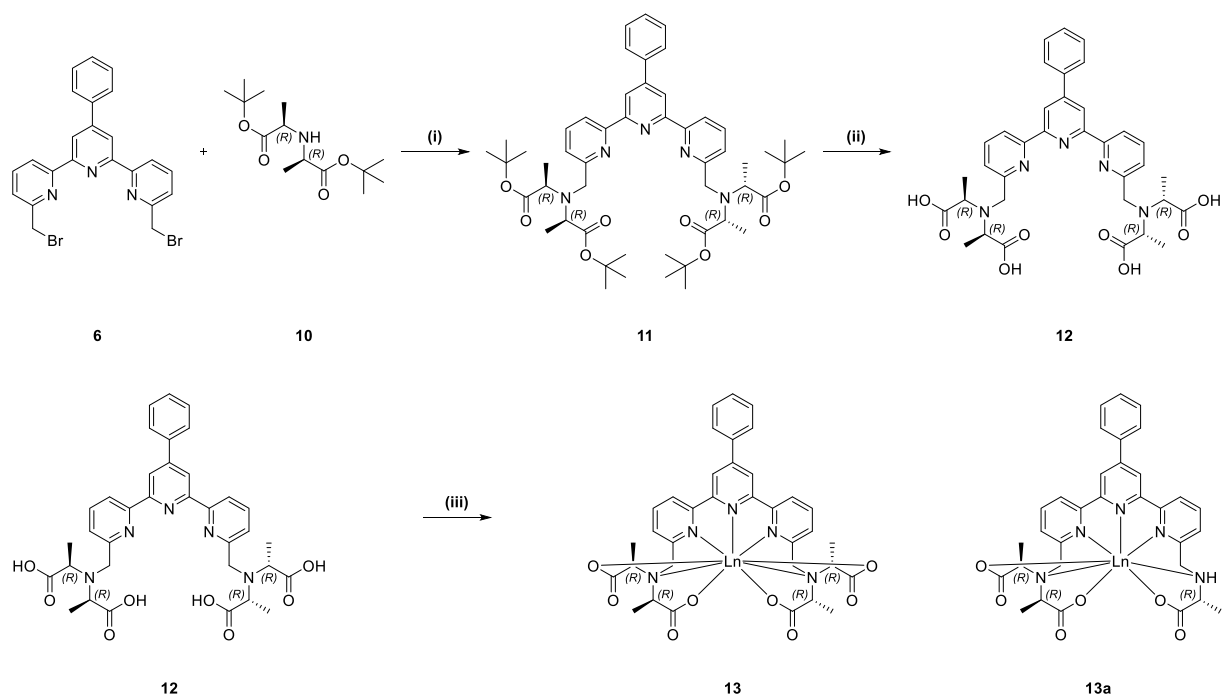
The desired product was obtained with a low yield of 33%. However, the product was easily purified by-recrystallization. The bromination at the benzylic positions of terpyridine **4** was initially attempted via a direct radical bromination with NBS and AIBN. The dibrominated species was observed but it was not possible to isolate it in a pure form. In a second attempt, the two terminal pyridine rings of **4** were oxidized with *m*-CPBA to the pyridine N-oxide and then rearranged by a Boekelheide reaction in acetic anhydride at 140°C to the di-acetate **5** with a yield of 45% over two steps. The two acetates were then transformed into two bromines with hydrogen bromide in acetic acid to conveniently provide the terpyridine building block **6** in 90% yield.

The synthesis towards the second key intermediate **10**, the side arm, is depicted in Figure 4. The lactic acid triflate **7** was synthesized according to literature.<sup>[12]</sup> The triflate **7** was then used to dialkylate benzylamine (**8**) with potassium carbonate in acetonitrile to yield the tertiary amine **9** in 66% yield. A subsequent debenzylation of the tertiary amine **9** with hydrogen and palladium on carbon in methanol provided the secondary amine **10** with an excellent yield of 96%.



**Figure 4:** Synthesis of the lactic acid side arm **10**. (i) K<sub>2</sub>CO<sub>3</sub>, MeCN, 20-25°C. (ii) H<sub>2</sub>, Pd/C, MeOH, 20-25°C.

The successfully synthesized central terpyridine building block **6** and the side arm **10** were combined to form the protected ligand **11**. The substitution reaction was carried out using potassium carbonate as base and potassium iodide to increase the reactivity of the leaving group via an *in-situ* Finkelstein reaction. Due to the steric hindrance, the reaction proceeded rather slowly. After a reaction time of 64 h the protected ligand **11** was obtained in a good yield of 74%. The deprotection of the carboxylic acids of **11** under acidic conditions yielded the free ligand **12** in 68% yield. Formation of the terpyridine prototype complex **13** was accomplished by the addition of the lanthanide(III) ion of choice to a solution of the free ligand **12** in aqueous ammonium acetate. The complexation was completed within hours at room temperature.



**Figure 5:** Synthesis of the terpyridine prototype complex **13**. (i)  $\text{K}_2\text{CO}_3$ , KI, MeCN, THF, DCM,  $80^\circ\text{C}$ . (ii) aq. HCl, MeCN,  $80^\circ\text{C}$ . (iii)  $\text{Ln(III)}$ , aq.  $\text{CH}_3\text{COONH}_4$ ,  $20\text{--}25^\circ\text{C}$ .

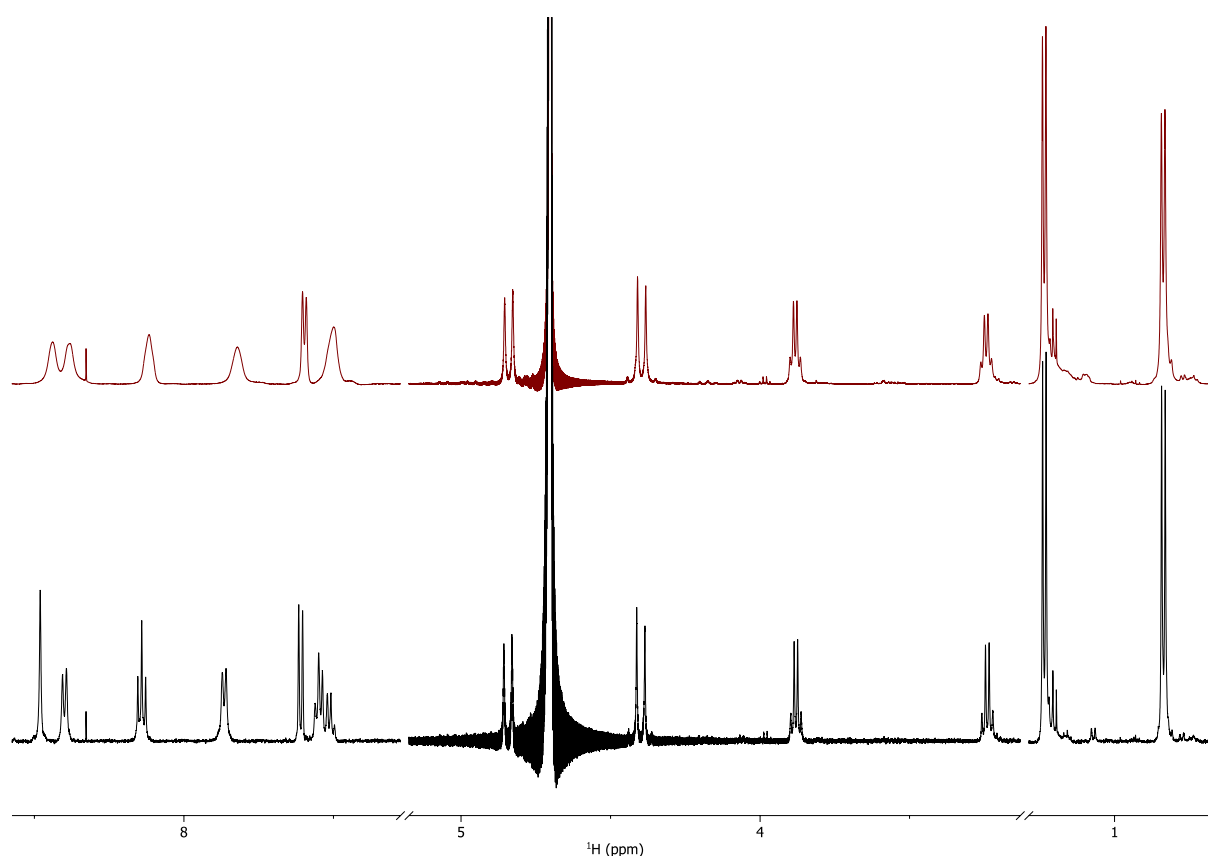
Interestingly, an increase of the reaction time leads to the formation of a complex missing one of the lactic acid side arms **13a**. To assess the suitability of the TerPyM4 scaffold for its use as an LCT the lutetium and thulium complexes were prepared. Reduction of the reaction time for the complexation from 5 h to 2 h going from lutetium to thulium increased the yield from 40% to 80%.

### 3.2.2.2 Properties of the Ln-TerPyM4-Prototype complex

In the proton NMR spectrum of the lutetium complex, a single set of peaks was observed, which was expected for a single conformation. However, the aromatic signals were rather broad (Fig. 6 top), pointing either at a fast exchange between two or more conformations or aggregation in solution due to  $\pi$ -stacking. Since  $\pi$ -stacking is concentration dependent a diluted sample of **13** was measured (Fig. 6 bottom). The sharp signals observed in the aromatic region in the diluted sample confirmed that the line broadening was caused by  $\pi$ -stacking. The complex could nonetheless be in the fast exchange regime between two conformations, as this would for a sufficiently fast exchange also lead to the observation of a single set of sharp signals. However, the large shift range observed for the thulium complex (791 ppm) was contradicting the fast exchange between two conformations because it was expected that this

would strongly diminish the observed paramagnetic shifts. Therefore, we assumed, based on the observation of a single set of sharp signals and the large chemical shift range observed for the thulium complex, that the complex adopts only a single conformation in solution.

From the proton spectrum of the thulium complex it was possible to estimate the size of the intrinsic anisotropy parameters. In chapter one, it was shown that it is possible to obtain a rough estimation of the anisotropy parameters from the shift range. For the Tm-TerPyM4-Prototype complex a shift range of 791 ppm was observed (See Fig. S8). This correlates approximately to a value of  $\Delta\chi_{ax}$  in the range of  $40\text{-}60 \times 10^{-32} \text{ m}^3$ . If the estimated intrinsic anisotropy can be transferred onto a protein, the new scaffold would rival previous high performance LCTs such as DOTA-M7PyThiazol<sup>[8]</sup>. Only  $\Delta\chi_{ax}$  was estimated as it correlates to the size of the induced PCS while  $\Delta\chi_{rh}$  is responsible for the different shape of the isosurfaces in UTR.<sup>[13]</sup>



**Figure 6:** <sup>1</sup>H-NMR spectra of the Lu-TerPyM4-Prototype complex in deuterium oxide at 298 K at higher (top) and lower (bottom) concentrations.

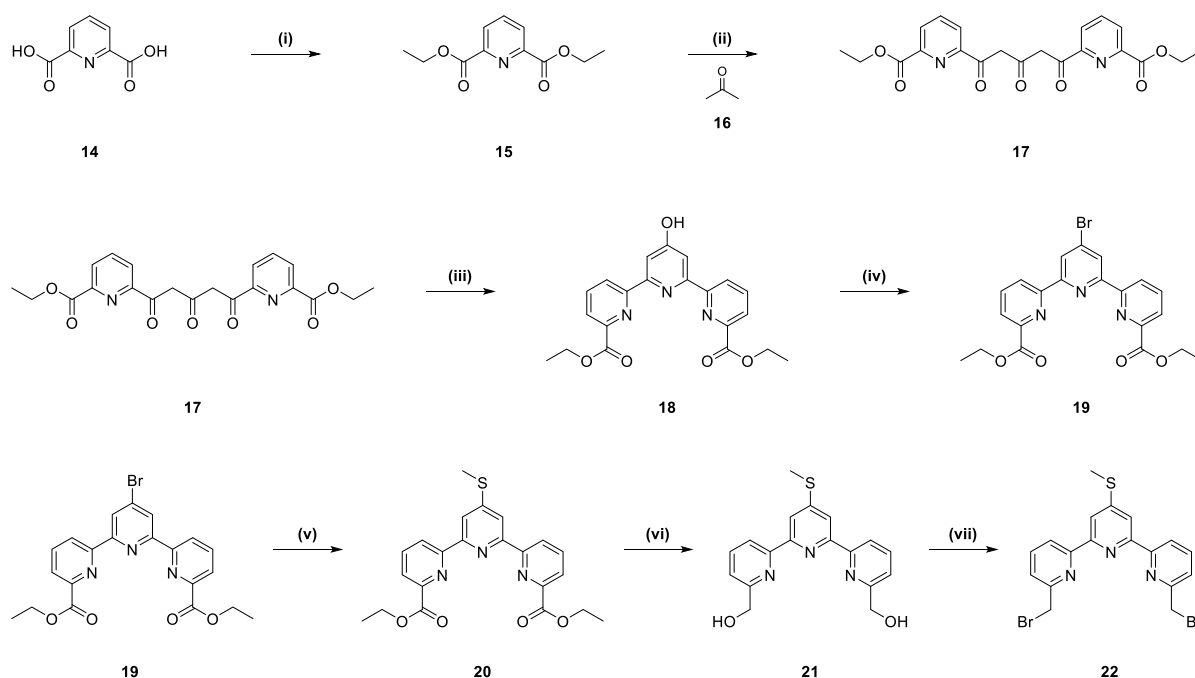
Additionally, the prototype complex showed high stability in water, which is favourable for LCTs. Even after months in the NMR tube no degradation in the spectra were observed. The presence of only a single conformation in solution in combination with the estimated

intrinsic anisotropy parameters and the high stability of the complex in water made this scaffold a promising candidate for the further development of a new lanthanoid chelating tag. Therefore, the synthesis towards an LCT based on the TerPyM4 scaffold was continued.

### 3.2.2.3 Synthesis of Ln-TerPyM4-SO<sub>2</sub>-Me

The synthesis of Ln-TerPyM4-SO<sub>2</sub>-Me was in large part executed by Mirko Markovic as part of his student internship under my supervision.

For the synthesis of Ln-TerPyM4-SO<sub>2</sub>-Me a different central terpyridine building block was required that contained at the 4' position a methyl thioether as a precursor for the methylsulfone leaving group. The synthesis towards the modified central terpyridine building block **22** was adapted from the synthesis reported by Kadjane *et al.*<sup>[7]</sup> and is shown in figure 7. Commercially available dipicolinic acid (**14**) was transformed into the di-ethyl-ester **15** with sulphuric acid in ethanol under reflux. The reaction worked well with a good yield of 78%. Triketone **17** was formed by a Claisen condensation between acetone (**16**) and di-ethyl-ester **15** in tetrahydrofuran with sodium hydride as a base. The reaction initially suffered from

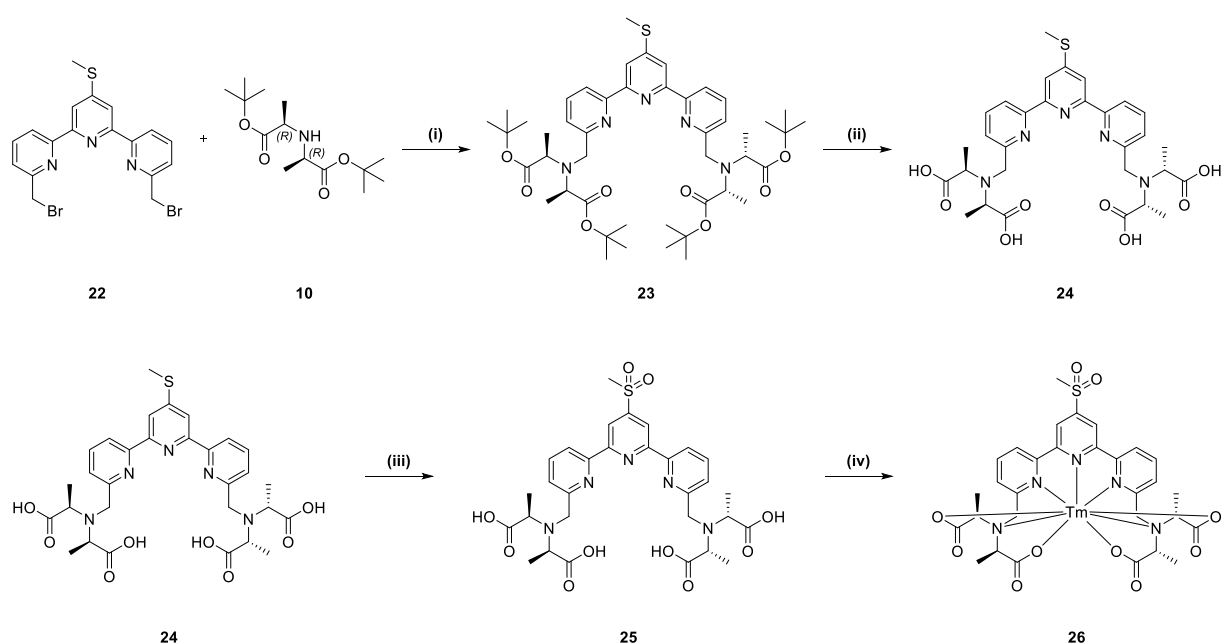


**Figure 7:** Synthesis of the central terpyridine building block **22**. (i) H<sub>2</sub>SO<sub>4</sub>, EtOH, 82°C. (ii) NaH, THF, 64°C. (iii) NH<sub>4</sub>OAc, EtOH, 82°C. (iv) PBr<sub>3</sub>, DMF, MeCN, 85°C. (v) SMT, Cs<sub>2</sub>CO<sub>3</sub>, DMSO. (vi) LiAlH<sub>4</sub>, THF, 0-5°C. (vii) PBr<sub>3</sub>, MeCN, 85°C.



polymerisation. Slow addition of acetone (**16**) to a refluxing mixture of **15** and sodium hydride in tetrahydrofuran mostly suppressed the polymerisation and allowed the isolation of **17** in acceptable purity and yield. Since purification on this step was not possible due to solubility issues, tri-ketone **17** was directly cyclized to the terpyridine **18** with ammonium acetate in refluxing ethanol. **18** was obtained pure with a yield of 32% over two steps. The 4' hydroxyl group was then brominated with phosphorus tribromide in acetonitrile. For the reaction to occur, the addition of *N,N'*-dimethylformamide was necessary. The reaction was carried out using 1.5 equivalents of *N,N'*-dimethylformamide. Subsequently, **19** was treated with *S*-methylisothiurea sulfate and caesium carbonate to obtain the methyl thioester in a good yield of 70%, according to a literature known procedure<sup>[14]</sup>. Following the incorporation of the leaving group precursor, the ethyl esters of **20** were reduced to the alcohol with lithium aluminium hydride and brominated with PBr<sub>3</sub> to afford the modified central terpyridine building block **22**. The low yield of 29% over two steps was attributed to the fact that during the reduction of **20**, a partial reduction of the pyridine rings to the dihydropyridine occurred. The whole synthesis was accompanied by solubility issues. They were most likely the reason why from **19** onwards the steps could only be carried out on small scale and all attempts to obtain **22** in larger amounts (>100 mg) were unsuccessful.

The benzylic bromines of **22** were substituted with the secondary amine **10**. The reactivity of the leaving group was again increased by an *in-situ* Finkelstein reaction. A



**Figure 8:** Synthesis of Ln-TerPyM4-SO<sub>2</sub>-Me (**26**). (i) K<sub>2</sub>CO<sub>3</sub>, KI, MeCN, THF, 80°C. (ii) aq. HCl, MeCN, 80°C. (iii) Na<sub>2</sub>WO<sub>4</sub>, H<sub>2</sub>O<sub>2</sub>, TFA, MeOH, 20-25°C. (iv) Tm(III), aq. CH<sub>3</sub>COONH<sub>4</sub>, 20-25°C.

prolonged reaction time of 120 h, compared to the prototype complex (section 3.2.2.1), provided the protected ligand with a yield of 54%. The lower yield after a longer reaction time was attributed to the lower solubility of **22**. The removal of the tert-butyl protecting groups was achieved with aqueous hydrochloric acid in acetonitrile at 80°C to provide the free ligand **24** with a yield of 69%. The thioether of the free ligand **24** was oxidized with sodium tungstate dihydrate, hydrogen peroxide and trifluoroacetic acid to the corresponding sulfone. The addition of trifluoroacetic acid was essential as it ensured full protonation of the pyridine nitrogen suppressing the formation of the pyridine *N*-oxide. The activated ligand **25** was obtained in a medium yield of 50%. Activation prior to the metalation had the advantage that the reaction had to be carried out only once for all lanthanoids. To test the reactivity of the new LCT and probe its anisotropy parameters on ubiquitin S57C Tm-TerPyM4-SO<sub>2</sub>-Me (**26**) was prepared. The metalation of **25** with thulium was carried out in aqueous ammonium acetate and provided the complex with a yield of 84%.

#### **3.2.2.4 Suitability of Ln-TerPyM4-SO<sub>2</sub>-Me as an LCT**

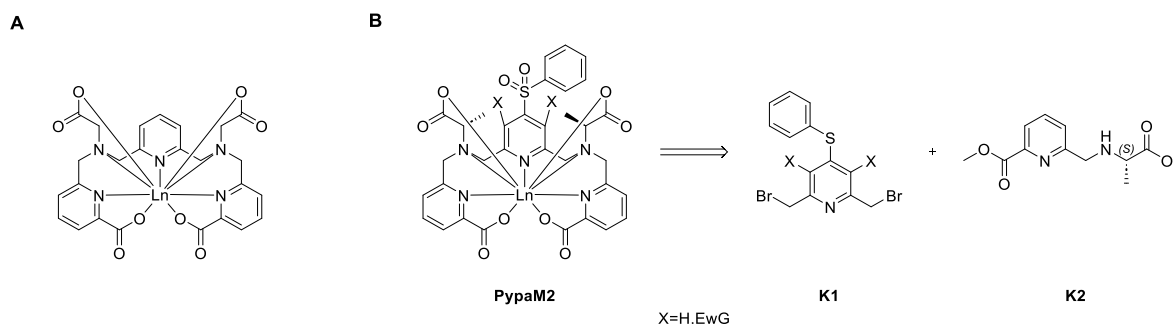
Unfortunately, Tm-TerPyM4-SO<sub>2</sub>-Me appeared to be, after its isolation, insoluble in water or polar organic solvents, which are miscible with water. To test the reactivity of the new complex it would be necessary to add it as a solution in water or a water miscible organic solvent to ubiquitin S57C. The observed insolubility in water or a water miscible organic solvent made the new LCT therefore rather unsuitable as an LCT. Due to the challenging synthesis of the modified central terpyridine building block **22** and the solubility issues of the final complex we decided to abandon the synthesis of a symmetric LCT based on the TerPyM4 scaffold at this point and turned our attention towards different ligands.

### 3.3 Pypa Based LCTs

#### 3.3.1 Molecular design

A second candidate for a symmetric LCT was the Pypa (6,6'-(((pyridine-2,6-diylbis(methylene)))bis((carboxymethyl)azanediyl))bis(methylene))dipicolinic acid) scaffold described in literature for its use as a ligand in radiotherapy.<sup>[15,16]</sup> Pypa is a nonadentate ligand built around a central pyridine unit (Fig. 9A). The complexes of the ligand with Ln(III) are reported to show high thermodynamic stability and to be water soluble. Like for the terpyridine scaffold the Pypa scaffold was not developed to exclusively adopt a single conformation as this is not required for its application in radiotherapy. Locking the complex into a single conformation might be possible by introducing two methyl groups, creating stereogenic centres of the same configuration on the side arms (Fig. 9B). Initially only two methyl groups were planned, to reduce the synthetic complexity of the molecule. The synthesis of PypaM2 (Fig. 9B) can be adapted from the synthesis of Pypa described in literature.<sup>[16]</sup> The synthesis relies like the synthesis of TerPyM4 on two key intermediates, the central pyridine building block **K1** and the side arm **K2**. On the pyridine the required sulfone for the formation of the thioether linkage to the protein will be installed. As a leaving group phenyl sulfone was chosen as it is simpler to synthesize and slightly more reactive towards cysteine than methyl sulfone.<sup>[8]</sup> Because both key intermediates (Fig. 9B) should be readily available in a few steps we decided to probe the conformation and the paramagnetic properties of the new complex directly with the new symmetric LCT.

In literature, a few LCTs are described that use a linker moiety, which is similar to the proposed pyridine phenyl sulfone.<sup>[8,17]</sup> They are reported to be reactive towards cysteine but with a low reactivity. We therefore expected that it should be possible to conjugate PypaM2-SO<sub>2</sub>-Ph to a stable protein such as ubiquitin. Conjugation of an LCT to a stable protein is simpler



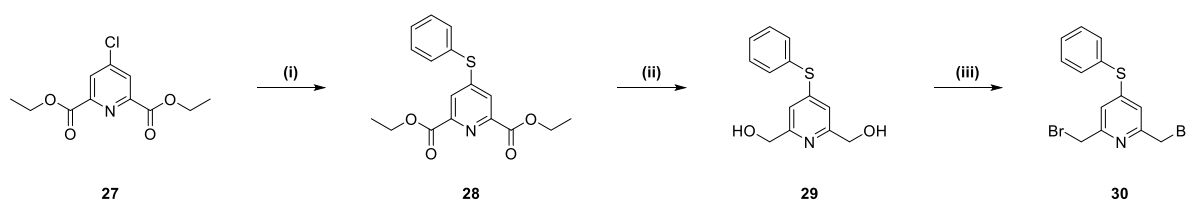
**Figure 9:** A: Structure of the Pypa scaffold. B: The two key intermediates in the retrosynthesis towards the new PypaM2 scaffold.

as the low reactivity of the linker moiety can in parts be compensated by applying harsher reactions conditions such as high pH (8-9) and elevated temperatures (40-60°C), which would damage most proteins. To test if the new LCT can provide predictable anisotropy parameters conjugation at multiple tagging sites on ubiquitin would be sufficient. For a broader application of the new LCT or if PypaM2-SO<sub>2</sub>-Ph does not react with ubiquitin the reactivity of the linker would have to be increased. The reactivity of the pyridine linker can be increased by the addition of electron withdrawing groups at the ortho positions of the central pyridine moiety. In order to retain C<sub>2</sub> symmetry of the resulting complex it is necessary to introduce two identical groups.

### 3.3.2 Results and Discussion

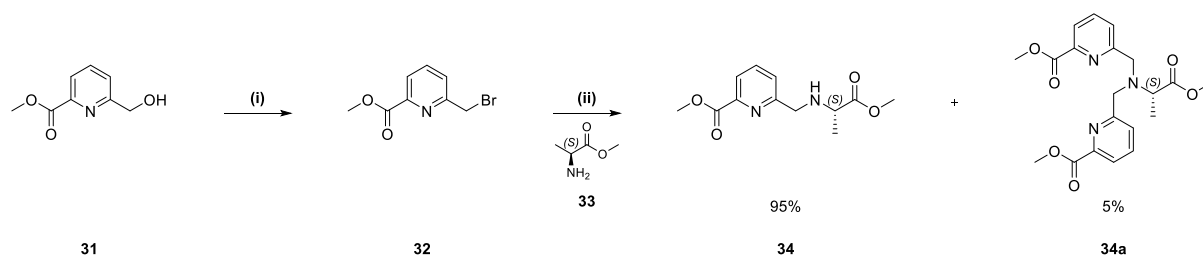
#### 3.3.2.1 Synthesis of Ln-PypaM2-SO<sub>2</sub>-Ph

The synthesis towards the central pyridine building block **30** (Fig. 10) started from chloropyridine **27**. A nucleophilic aromatic substitution of the chlorine by thiophenol with caesium carbonate as base afforded thioether **28**. Following the installation of the future leaving group was the reduction of the ethyl ester with sodium borohydride in ethanol to the di-alcohol **29**. Subsequent bromination of the di-alcohol **29** using phosphorus tribromide conveniently provided the first key intermediate **30** in an excellent overall yield of 56% over all three steps.



**Figure 10:** Synthesis of the central pyridine building block **30**. (i) PhSH, Cs<sub>2</sub>CO<sub>3</sub>, MeCN, 20-25°C. (ii) NaBH<sub>4</sub>, EtOH, 40°C. (iii) PBr<sub>3</sub>, MeCN, 85°C.

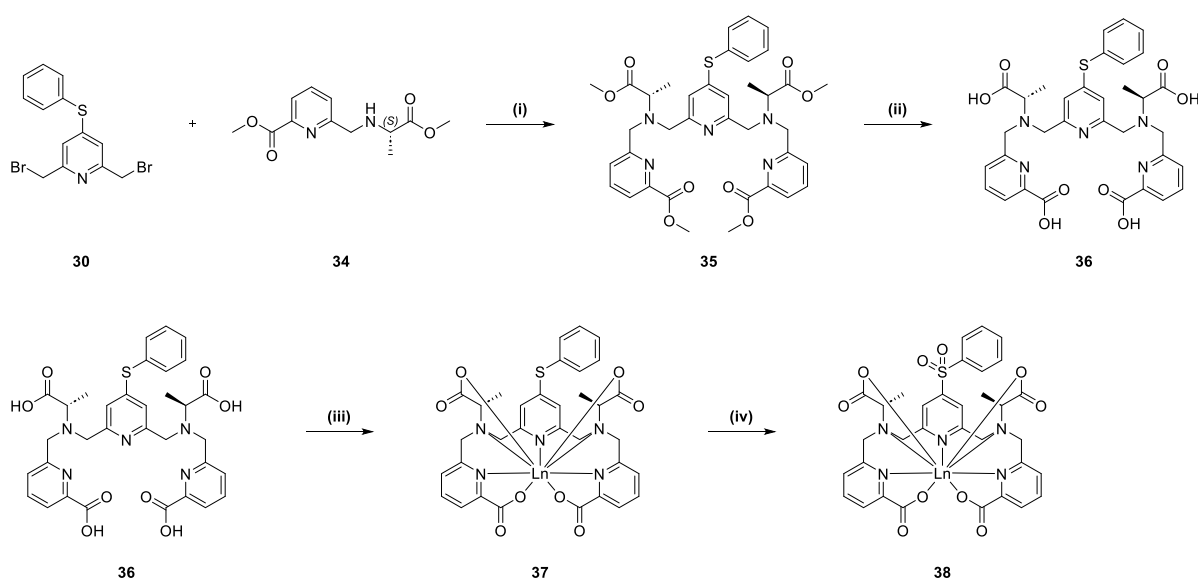
The methyl protected side arm **33** was readily afforded via a two-step synthesis (Fig. 11). First, the alcohol of the commercially available pyridine **31** was transformed into a bromine with phosphorus tribromide. The bromine was then substituted with L-alanine (**33**) to yield the second key intermediate **34**. The amine **34** was obtained as a mixture of the desired secondary amine and the tertiary amine **34a**. The tertiary amine **34a** was present due to an expected over alkylation of the primary amine and surprising difficulties to separate the tertiary and secondary amine from one another. The presence of the tertiary amine **34a** should not cause



**Figure 11:** Synthesis of the second key intermediate **34**. (i)  $\text{PBr}_3$ ,  $\text{CHCl}_3$ , 20–25°C. (ii)  $\text{K}_2\text{CO}_3$ , MeCN, 85°C.

any problems as the amine **34** was intended to be used as a nucleophile and **34a** is not nucleophilic. The second key intermediate **34** was therefore used as a mixture.

The synthesis of the final complex Ln-PypaM2-SO<sub>2</sub>-Ph (**38**) from the two key intermediates is depicted in figure 12. Substitution of the two benzylic bromine atoms, with the secondary amine **34** led to the formation of the methyl protected ligand **35** using potassium carbonate as base. Potassium iodide was added to increase the reactivity of the leaving group via an in-situ Finkelstein reaction. The reaction proceeded well with a good yield of 84%. As expected, no by-products were observed that could be derived from the presence of the tertiary amine **34a**. The deprotection of the methyl esters was carried out under basic conditions with aqueous sodium hydroxide and tetrahydrofuran to yield the free ligand **36** in an excellent yield of 90%. At this stage, oxidation of the thioether to the sulfone was attempted with sodium tungstate



**Figure 12:** Synthesis of Ln-PypaM2-SO<sub>2</sub>-Ph (**38**). (i)  $\text{K}_2\text{CO}_3$ , KI, MeCN, 40°C. (ii) aq. NaOH, THF, 20–25°C. (iii) Ln(III),  $\text{CH}_3\text{COONH}_4$ , 20–25°C. (iv)  $\text{Na}_2\text{WO}_4$ ,  $\text{H}_2\text{O}_2$ ,  $\text{H}_2\text{O}$ , 20–25°C.

dihydrate and hydrogen peroxide. An oxidation preceding the complexation would have been of great interest as then this step would have to be performed only once for different lanthanoid complexes. However, oxidation of one or more pyridine nitrogen to the pyridine N-oxide always occurred, even in the presence of trifluoroacetic acid, which prevented over oxidation during the synthesis of Ln-TerPyM4-SO<sub>2</sub>Me (section 2.2.2.3). Therefore, the methyl deprotection was followed by the complexation of the lanthanoid (III) ion of choice in aqueous ammonium acetate. As for the terpyridine ligands the complexation was completed rapidly at room temperature within an hour. The complexation was carried out with Tb, Tm, Yb and Lu. Activation of the leaving group was achieved by oxidation of the thioether to the sulfone with hydrogen peroxide and sodium tungstate dihydrate in water. The reaction took several days to reach full conversion but provided the activated complex **38** with a high yield of 90%.

### 3.3.2.2 Suitability of Ln-PypaM2-SO<sub>2</sub>-Ph as an LCT

*VT-NMR measurements of Lu-PypaM2-S-Ph were carried out by Annika Matt.*

The presence of only a single conformation was probed by proton NMR spectroscopy of the unactivated lutetium complex **37**. Initial results were inconclusive as the two diastereotopic CH<sub>2</sub> groups, showed two singlets instead of the expected four doublets. Changing the solvent from deuterium oxide to deuterated methanol gave rise to the expected signals indicating the presence of a single conformation. The appearance of the expected signals in methanol suggested that each proton in the diastereotopic methylene groups was accidentally isochronous in deuterium oxide. In order to confirm that the complex was not in the fast exchange regime on the NMR timescale, VT-NMR measurements were performed from 295 to 198 K (SI Fig. S15). During the cooling of the sample no splitting of the signals was observed, which was taken as proof that Ln-PypaM2 forms only a single conformation in solution and is not in fast exchange on the NMR time scale.

From the chemical shift range in the 1D proton spectra of the paramagnetic PypaM2-S-Ph complexes the intrinsic anisotropy parameters exhibited by Tb, Tm and Yb in the new scaffold were estimated. The chemical shift ranges of Ln-PypaM2-S-Ph and not Ln-PypaM2-SO<sub>2</sub>-Ph were used to estimate the intrinsic anisotropy parameters as the electronic structure of the thioether better represents the electronic structure of the LCT conjugated to the protein. The shift ranges observed for Tb (306 ppm), Tm (306 ppm) and Yb (133 ppm) show that the PypaM2 scaffold does neither provide a very good environment for either oblate (Tb) or prolate

lanthanoids (Tm, Yb). Based on the chemical shift ranges observed for Tb and Tm it can be expected that  $\Delta\chi_{ax}$  will not exceed  $25 \cdot 10^{-32} \text{ m}^3$  for any lanthanoid and will most likely be around  $20 \cdot 10^{-32} \text{ m}^3$  for the lanthanoids Tb and Tm. For Yb a lower value of  $10 \cdot 10^{-32} \text{ m}^3$  was estimated for  $\Delta\chi_{ax}$ . The estimated values of  $\Delta\chi_{ax}$  indicate that the new PypaM2 scaffold will not be able to challenge current high performance tags but could rival LCTs such as DOTA-M8SSPy (4R4S)<sup>[18]</sup> if the full anisotropy could be transferred onto a protein. The estimated intrinsic anisotropy parameters are certainly large enough to test if the new PypaM2 based LCT yields predictable anisotropy parameters.

The reactivity of Ln-PypaM2-SO<sub>2</sub>-Ph towards cysteine was tested directly with Ubiquitin S57C. Tagging was carried out in phosphate buffer in the presence of tris(2-carboxyethyl)phosphine (TCEP) to ensure that all disulphide bonds were reduced. A first tagging attempt was made at pH 7.6 as an LCT with a similar linker was conjugated at this pH to ubiquitin.<sup>[17]</sup> Unfortunately, no reaction between Ln-PypaM2-SO<sub>2</sub>-Ph and ubiquitin was observed. In order to increase the reactivity of the cysteine towards the sulfone the temperature (up to 60°C), reaction time (several days) and pH (up to pH 9.5) were increased. Under none of these conditions was any conversion observed. Partial conversion was observed at pH~9 and 45°C if ubiquitin S57C was replaced with *N*-acetylcysteine. From these results, it was concluded that Ln-PypaM2-SO<sub>2</sub>-Ph is not reactive enough for the reaction with a protein. As mentioned before the reactivity of the linker can be increased by the addition of electron withdrawing substituents ortho to the leaving group. In literature, a suitable building block containing two chlorines in ortho position to the linker for the synthesis of a Pypa-type LCT was reported.<sup>[19]</sup> We therefore decided to incorporate two chlorines in order to enhance the reactivity of the linker.

### 3.3.2.3 Ligand field like effects of Ln-PypaM2-SO<sub>2</sub>-Ph

While Ln-PypaM2-SO<sub>2</sub>-Ph could not be used to test if the coaxiality between the rotation axis and z-axis of the tensor frame would provide predictable anisotropy parameters it offered the possibility to gain some insights into the relation between the electronic structure and the anisotropy parameters. Based on the results obtained in chapter one we expected that the paramagnetic properties should change during the activation of the thioether as this reduces the electron density of the coordinating pyridine nitrogen and that the change would be different depending on the f-electron distribution of the lanthanoid. Ln-PypaM2-SO<sub>2</sub>-Ph was well suited as a study system for this, since the structure around the lanthanoid, going from the thioether to

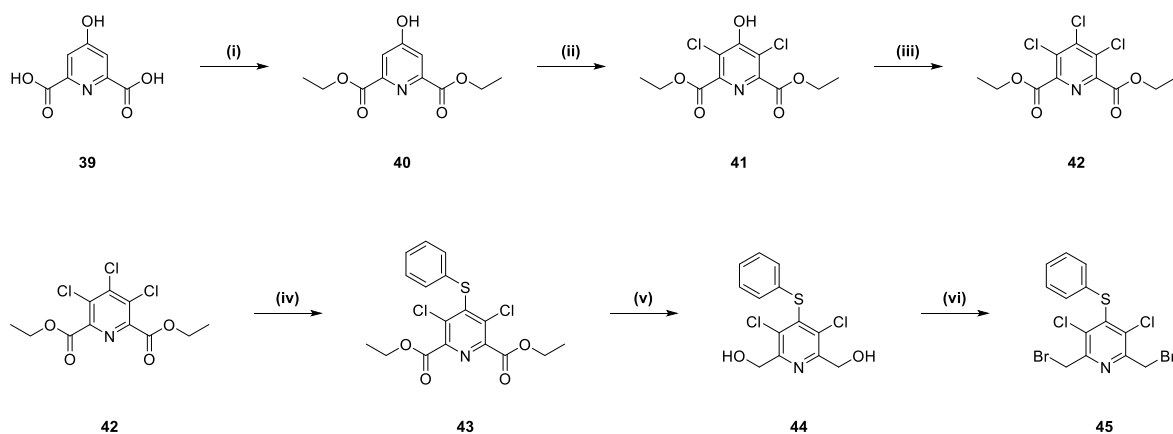
the sulfone, does not significantly change (Si Fig. S20). Therefore, any changes observed in the spectra going from the thioether to the sulfone can be attributed to the change in the electronic structure.

As expected, for all three lanthanoids slightly different spectra for Ln-PypaM2-S-Ph and Ln-PypaM2-SO<sub>2</sub>-Ph were observed (Si Fig. S21-S29). The shift ranges as well as the distribution of the signals were changed indicating that  $\Delta\chi_{ax}$  and  $\Delta\chi_{rh}$  are affected by changes in the electronic structure of the ligand. In order to excluded that the different pH of the samples is responsible for the observed changes all samples were re-measured at a pH around 6.5 (Si Fig. S30-S41). The spectra at the lower pH value were in regard of the shift range and the peak distribution identical to the ones at higher pH, which showed that the changes originate from the different electronic structure. As expected, the change in the chemical shift range, correlating to  $\Delta\chi_{ax}$  was different for Tb, Tm and Yb. For Tb and Tm an increase of the chemical shift range going from the thioether to the sulfone of 10 and 2 ppm was observed, respectively, while for Yb a decrease of 7 ppm was observed. Because the change in the chemical shift range is also different for Tm and Yb, which both show a prolate f-electron distribution, the effect cannot be directly correlated to the electron distribution. The observed effect was not huge but showed that a change in the electronic structure can affect the magnetic anisotropy and that the effect is slightly different for each lanthanoid.

#### 3.3.2.4 Synthesis of Ln-PypaM2Cl<sub>2</sub>-SO<sub>2</sub>-Ph

In general, PypaM2Cl<sub>2</sub>-SO<sub>2</sub>-Ph can be synthesized like PypaM2-SO<sub>2</sub>-Ph with the difference that a few additional steps are necessary to decorate the central pyridine building block with two chlorines. The synthesis towards the modified central pyridine building block **45** is depicted in figure 13. The steps towards trichloropyridine **42** were performed by analogy to literature methods.<sup>[19]</sup> The esterification of chelidamic acid (**39**) was done with thionylchloride in ethanol. Crystallization in this step was critical as some of the formed by-products lead later to impurities, which were no longer separable from the desired product. The resulting pyridone **40** was quantitatively chlorinated with *N*-chlorosuccinimide. Subsequently, with phosphoryl chloride the hydroxyl group was transformed into a chlorine. After the successful synthesis of **42** the same reaction sequence as for the central pyridine building block of PypaM2-SO<sub>2</sub>-Ph was applied (see section 3.3.2.1). For the reduction as well as the bromination the same reaction conditions were applied while for the nucleophilic aromatic substitution the reactions conditions were slightly adjusted by replacing caesium carbonate with

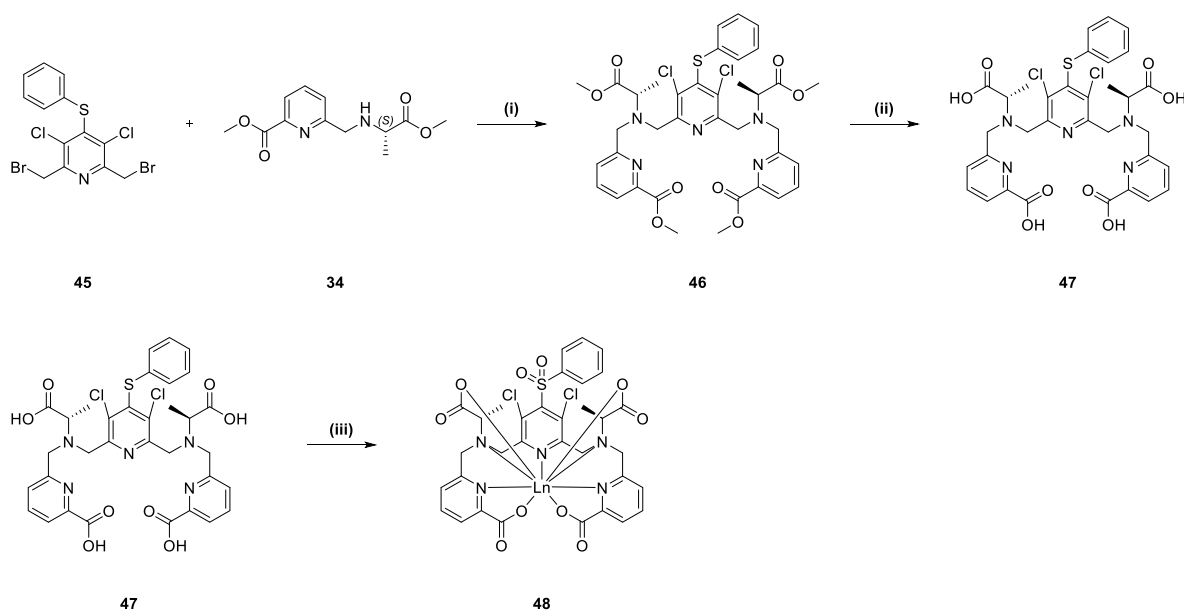




**Figure 13:** Synthesis of the central pyridine building block **45**. (i)  $\text{SOCl}_2$ , EtOH,  $80^\circ\text{C}$ . (ii) NCS, MeCN,  $70^\circ\text{C}$ . (iii)  $\text{POCl}_3$ , MeCN,  $70^\circ\text{C}$ . (iv) PhSH,  $\text{K}_2\text{CO}_3$ , MeCN,  $20\text{--}25^\circ\text{C}$ . (v)  $\text{NaBH}_4$ , EtOH,  $40^\circ\text{C}$ . (vi)  $\text{PBr}_3$ , MeCN  $85^\circ\text{C}$ .

potassium carbonate. Potassium carbonate was used instead of caesium carbonate due to the higher reactivity of the trichloropyridine **42** compared to the chloropyridine **27**. The yield over the three steps was with 31% significantly lower for **45** than for **30** because the bromination worked only with a moderate yield of 41%.

The synthesis starting from the two key intermediates **45** and **34** to the final complex **48** is depicted in figure 14. The substitution of the two benzylic bromines of **45** with the secondary amine **34** was carried out under the same conditions as for the unchlorinated ligand (see section 3.3.2.1). A very good yield of 88% comparable to the previous reaction was obtained. The free ligand **47** was obtained in 81% yield after a deprotection of the methyl esters with aqueous sodium hydroxide in tetrahydrofuran. Surprisingly, the free ligand **47** was unstable towards organic solvents. In organic solvents, the free ligand decomposed over time by losing one of the chlorine atoms. It was possible to purify the free ligand by preparative HPLC. However, a quick isolation was required as prolonged exposure to acetonitrile led to the loss of a chlorine atom. The same was observed if the NMR spectrum of **47** was recorded in acetonitrile. The following complexation and oxidation proved to be rather difficult. At first, it was tried, as for PypaM2- $\text{SO}_2\text{-Ph}$ , to form and isolate the complex and subsequently oxidize the thioester to the corresponding sulfone. However, due to the ominous instability of the chlorine pyridine bond this strategy was unsuccessful. During the isolation of the unactivated complex a significant amount of the monochlorinated by product formed, which could not be separated. Isolation of the final complex **48** was possible if the complexation and oxidation were carried out in the same solution without isolating the unactivated complex. The oxidation had to be carried out under slightly acidic conditions, which was achieved by adding acetic acid to the reaction



**Figure 14:** Synthesis of Ln-PypaM2Cl<sub>2</sub>-SO<sub>2</sub>-Ph (**48**). (i) K<sub>2</sub>CO<sub>3</sub>, KI, MeCN, 40°C. (ii), aq. NaOH, THF, 20-25°C. (iii) Ln(III), CH<sub>3</sub>COONH<sub>4</sub>, Na<sub>2</sub>WO<sub>4</sub>, AcOH, H<sub>2</sub>O, 20-25°C.

solution after the complexation was complete. The addition of acetic acid was required because **48** was susceptible to hydrolysis at neutral pH. Interestingly, the addition of a stronger acid like formic acid lead again to partial hydrolysis of the product. The oxidation proceeded slowly and full conversion was never reached. With the addition, in several portions, of a large excess of hydrogen peroxide the activated complex was isolated in yields ranging from 20-50% after reaction times between six to nine days. The slow oxidation was attributed to either the electron poor nature of the pyridine or the steric hindrance from the two adjacent chlorines. Due to the tedious synthesis **48** was only prepared with lutetium and thulium.

### 3.3.2.5 Suitability of Ln-PypaM2Cl<sub>2</sub>-SO<sub>2</sub>-Ph as an LCT

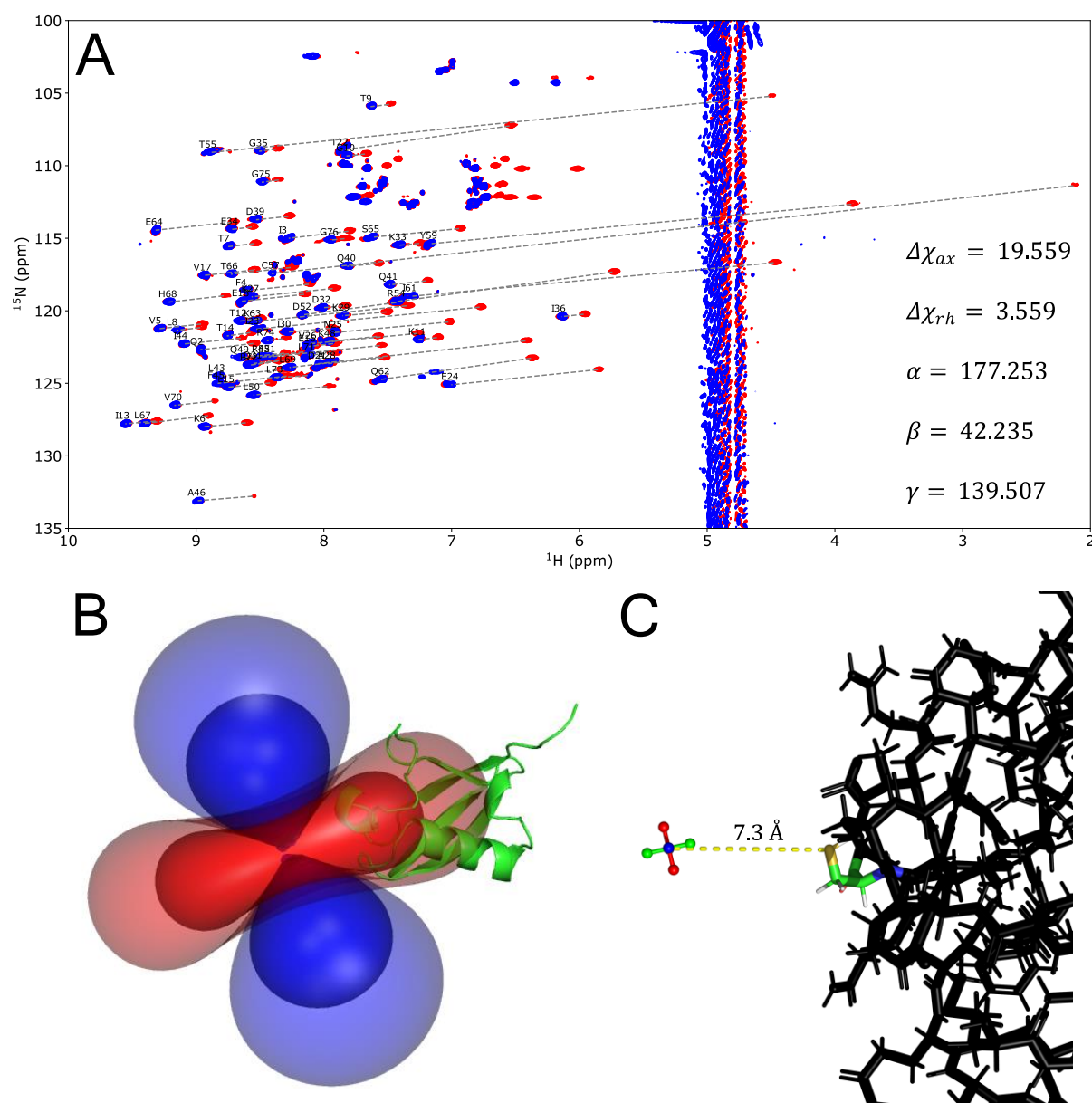
Because the chemical structure of Ln-PypaM2Cl<sub>2</sub>-SO<sub>2</sub>-Ph provides in principle the same coordination environment as Ln-PypaM2-SO<sub>2</sub>-Ph we assumed that the new complex would also adopt only a single conformation in solution. Therefore, no 1D spectra of Ln-PypaM2Cl<sub>2</sub>-SO<sub>2</sub>-Ph were recorded. The intrinsic anisotropy parameters of Tm-PypaM2Cl<sub>2</sub>-SO<sub>2</sub>-Ph should be the same as for Tm-PypaM2-SO<sub>2</sub>-Ph as the ligand field like effects showed that a decrease in the electron density of the central pyridine is not strongly affecting the chemical shift range and hence not  $\Delta\chi_{ax}$ .

Tagging of ubiquitin S57C was tested at pH 7 in aqueous phosphate buffer in the presence of TCEP at 25°C with Lu-PypaM2Cl<sub>2</sub>-SO<sub>2</sub>-Ph. Because of the observed hydrolysis

during the oxidation of the thioether it was expected that the complex would either hydrolyse or react rapidly with the protein. Surprisingly neither was the case. Ligation of Lu-PypaM2Cl<sub>2</sub>-SO<sub>2</sub>-Ph to ubiquitin S57C was observed but the reaction was rather slow and full ligation of ubiquitin was not reached. After several days a conversion of around 50% was reached. Increasing the temperature did not further increase the conversion. After several attempts to increase the tagging rate it was noticed that a higher concentration of ubiquitin and LCT was beneficial for the tagging rate and reliability of the conjugation. With a protein concentration of 0.4 mM and 48 h reaction time a tagging rate of 70%-80% was obtained. Using these conditions ubiquitin S57C was tagged with lutetium and thulium loaded PypaM2Cl<sub>2</sub>-SO<sub>2</sub>-Ph. The slow conversion and the incomplete tagging were attributed to steric clashes between the two chlorine atoms and the protein. The slow conversion observed during the tagging reaction also strongly indicates that the slow oxidation is a result of the steric hindrance. For the further development of Pypa-type LCTs it would therefore be advisable to introduce sterically less demanding substituents to further increase the reactivity such as fluorine atoms.

To determine the PCS and subsequently the anisotropy parameters 2D <sup>1</sup>H-<sup>15</sup>N HSQC spectra were recorded of the lutetium and thulium spin labelled ubiquitin S57C (Fig. 15A). The signals in the protein spectra were assigned using CcpNMR<sup>[20]</sup>. The assignment of the lutetium spectra was transferred from the spectrum of unlabelled ubiquitin S57C. Comparison between the spectrum of unlabelled and Lu-PypaM2Cl<sub>2</sub> labelled ubiquitin S57C revealed significant shifts in the vicinity of the tagging site. This could indicate that the presence of Ln-PypaM2Cl<sub>2</sub> is locally affecting the protein structure. For the thulium labelled ubiquitin large PCS up to 6 ppm were observed. Out of the 71 NH amide resonances 66 were assigned in the paramagnetic spectrum. The assignments of the diamagnetic and paramagnetic spectra can be found in the supporting information (Si Table S1). All available PCS (Si Table S1) were used to determine the anisotropy parameters (Fig 15A) not only those resulting from residues in secondary structure elements as for previous LCTs<sup>[8,18]</sup>. The anisotropy parameters were fitted using numbat<sup>[13]</sup>. An excellent correlation between the calculated and experimental PCS of  $r^2 = 0.998$  was obtained (Si Fig. S42). Because of the high correlation coefficient, it is unlikely that Ln-PypaM2Cl<sub>2</sub> is locally affecting the protein structure. A more likely explanation for the observed shifts in the lutetium spectrum are shift perturbations caused by the presence of the two chlorine atoms. Besides the correlation coefficient, the distance between the cysteine S and the paramagnetic centre gives an indication on the quality of the fit. For Tm-PypaM2Cl<sub>2</sub> the distance between the cysteine S and the metal centre matches with 7.3 Å (Fig. 15C) excellent

to the expected value of 7.14 Å obtained from a DFT geometry optimization of the complex. The excellent correlation and the well matching metal to cysteine S distance, even though PCS from more flexible residues were included, could indicate that the new design is positively affecting the correlation between the calculated and experimental data. A possible explanation for this could be that the rotational flexibility of the LCT is not affecting the metal position.



**Figure 15:** **A** Superimposed 2D  $^1\text{H}$ - $^{15}\text{N}$  HSQC spectra of Tm-PypaM2Cl<sub>2</sub> (red) and Lu-PypaM2Cl<sub>2</sub> (blue) labelled ubiquitin S57C and the anisotropy parameters, reported in UTR<sup>[13]</sup>, determined from the PCS observed on ubiquitin S57C. The anisotropy parameters  $\Delta\chi_{ax}$  and  $\Delta\chi_{rh}$  are reported in  $10^{-32} \text{ m}^3$ . The Euler angles are reported in degree. **B** Isosurfaces obtained from the PCS observed on ubiquitin S57C. Red isosurfaces indicate a negative shift, blue isosurfaces indicate the corresponding positive shift. The isosurfaces indicate a positive or negative shift of 1.0/0.3 ppm (inner sphere/ outer sphere). **C** Distance between the paramagnetic centre and ubiquitin S57C obtained from fitting the anisotropy parameters. The tensor frame axes are coloured in blue (z-axis), green (y-axis) and red (x-axis).

Another positive feature of the new design is that the signals from all protein residues are shifted in one direction, at least for small proteins such as ubiquitin, facilitating the assignment of the paramagnetic signals.

Unfortunately, the determination of the anisotropy parameters revealed that the rotation axis is not coaxial to the z-axis of the tensor frame but to the y-axis (Fig. 15C). Changing the lanthanoid from thulium to dysprosium or terbium might lead to the same reorientation of the tensor frame as observed for DOTA-M7FPy (chapter one) providing the sought coaxiality between the z-axis of the tensor frame and the rotation axis.

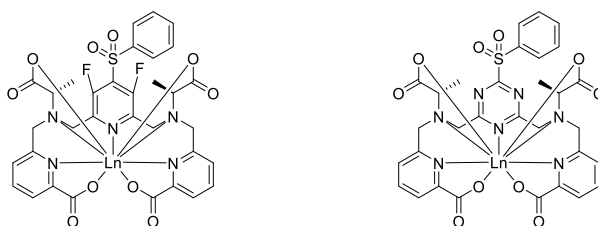
For Tm-PypaM2-SO<sub>2</sub>-Ph a maximum value of  $20\text{-}25 \cdot 10^{-32} \text{ m}^3$  for  $\Delta\chi_{ax}$  was estimated (see section 3.3.2.2). Based on the ligand field effects observed for Ln-PypaM2-SO<sub>2</sub>-Ph we assumed that the intrinsic anisotropy for Tm-PypaM2Cl<sub>2</sub>-SO<sub>2</sub>-Ph would be similar. The value of  $19.5 \cdot 10^{-32} \text{ m}^3$  for  $\Delta\chi_{ax}$  observed on ubiquitin S57C (Fig. 15A) tagged with Tm-PypaM2Cl<sub>2</sub>-SO<sub>2</sub>-Ph therefore suggests that the PCS observed on ubiquitin S57C suffers little from averaging. The marginal averaging of the PCS could indicate that they are barely affected by rotation around the y-axis. However, it could also indicate that the rotation of Tm-PypaM2Cl<sub>2</sub> is suppressed due to the presence of the two chlorines. If the marginal averaging of the PCS would originate from a suppression of the rotation the observed anisotropy parameters would not be independent of the tagging site and therefore not predictable. At the present stage, it is not possible to differentiate between the two possibilities. Attachment of the new LCT to other preferably more solvent exposed tagging sites could provide the necessary information.

### 3.4 Conclusion and Outlook

In order to find a symmetric LCT two known scaffolds were tested for their suitability as LCTs. The first tested TerPyM4 scaffold showed promising properties but solubility issues prevented the successful development of a new LCT. Based on the second tested scaffold, PypaM2, on the other hand a new symmetric LCT, Ln-PypaM2Cl<sub>2</sub>-SO<sub>2</sub>-Ph was successfully synthesised. The new LCT was tethered to ubiquitin S57C via a thioether, providing only one rotatable bond between the lanthanoid complex and the protein. The determination of the anisotropy parameters revealed that unfortunately, the rotation axis was not coaxial to the z-axis of the tensor frame but to the y-axis. By replacing the now-tested thulium with dysprosium it should be possible to reorient the tensor axis to achieve the preferred coaxiality with the z-axis. Nonetheless, comparison between the anisotropy parameters observed on the protein and the ones estimated on the LCT showed that nearly the full anisotropy of the LCT was transferred

onto the protein. The nearly full transfer of the anisotropy leaves two possible explanations. (i) the LCT is not able to rotate due to the steric hindrance of the two chlorines or (ii) the rotation around the y-axis of the tensor frame is not greatly affecting the anisotropy. To be able to differentiate between the two possibilities it is necessary to conjugate the LCT to additional tagging sites and compare the obtained anisotropy parameters. From the current data it can be gathered that, even if the coaxiality between a tensor frame axis and the rotation axis does not provide predictable anisotropy parameters, the coaxiality might lead to a better correlation between the calculated and experimental data and facilitates the assignment of the paramagnetic signals.

While the new LCT already provided promising results the presence of the two chlorines seems to be an issue. The main problem appears to be the steric bulk introduced by the two chlorine atoms. In order to increase the reactivity of the linker the chlorines could be replaced by two fluorines or instead of a pyridine core, a more reactive triazine could be used as the central building block (Fig. 16). The triazine would cause the least steric hindrance but the synthesis towards a triazine based Pypa scaffold is expected to be difficult. In literature, no compounds are known that could be readily incorporated into the existing synthesis. Introduction of the fluorine on the other hand should be possible by substituting *N*-chlorosuccinimide with a fluorinating agent such as selectfluor in the reaction sequence presented in figure 13 (section 3.3.2.4).



**Figure 16:** PypaM2 based ligands, which should cause less steric hindrance.

### 3.5 References

- [1] W. Liu, S. P. Skinner, M. Timmer, A. Blok, M. A. S. Hass, D. V. Filippov, M. Overhand, M. Ubbink, **2014**, 6256–6258.
- [2] P. H. J. Keizers, A. Saragliadis, Y. Hiruma, M. Overhand, M. Ubbink, *J. Am. Chem. Soc.* **2008**, *130*, 14802–14812.
- [3] A. Rodríguez-Rodríguez, D. Esteban-Gómez, A. De Blas, T. Rodríguez-Blas, M. Botta, R. Tripier, C. Platas-Iglesias, *Inorg. Chem.* **2012**, *51*, 13419–13429.
- [4] G. Castro, M. Regueiro-Figueroa, D. Esteban-Gómez, P. Pérez-Lourido, C. Platas-Iglesias, L. Valencia, *Inorg. Chem.* **2016**, *55*, 3490–3497.
- [5] B. Song, G. Wang, M. Tan, J. Yuan, *J. Am. Chem. Soc.* **2006**, *128*, 13442–13450.
- [6] V.-M. Mukkala, M. Helenius, I. Hemmilä, *Helv. Chim. Acta* **1993**, *76*, 1361–1378.
- [7] P. Kadjane, C. Platas-Iglesias, R. Ziessel, L. J. Charbonnière, *Dalt. Trans.* **2009**, 5688–5700.
- [8] T. Müntener, J. Kottelat, A. Huber, D. Häussinger, *Bioconjug. Chem.* **2018**, *29*, 3344–3351.
- [9] K. T. Potts, M. J. Cipullo, P. Ralli, G. Theodoridis, **1981**, 3585–3586.
- [10] K. T. Potts, D. A. Usifer, A. Guadalupe, H. D. Abruna, *J. Am. Chem. Soc.* **1987**, *109*, 3961–3967.
- [11] J. Wang, G. S. Hanan, *Synlett* **2005**, *8*, 1251–1254.
- [12] G. Heiko, Combining NMR spectroscopy and organic synthesis : From small building blocks to large biomolecules, Doctoral dissertation, University of Basel, **2014**.
- [13] C. Schmitz, M. J. Stanton-Cook, X. C. Su, G. Otting, T. Huber, *J. Biomol. NMR* **2008**, *41*, 179–189.
- [14] C. Zhang, Y. Zhou, J. Huang, C. Tu, X. Zhou, G. Yin, **2018**, 6316–6321.
- [15] L. Li, M. de Guadalupe Jaraquemada-Peláez, E. Aluicio-Sarduy, X. Wang, T. E. Barnhart, W. Cai, V. Radchenko, P. Schaffer, J. W. Engle, C. Orvig, *Dalt. Trans.* **2020**, *49*, 5547–5562.
- [16] L. Li, M. D. G. Jaraquemada-Peláez, H. T. Kuo, H. Merkens, N. Choudhary, K. Gitschtaler, U. Jermilova, N. Colpo, C. Uribe-Munoz, V. Radchenko, et al., *Bioconjug. Chem.* **2019**, *30*, 1539–1553.
- [17] F. Yang, X. Wang, B. Pan, X. Su, *Chem. Commun.* **2016**, *52*, 11535–11538.
- [18] D. Joss, R. M. Walliser, K. Zimmermann, D. Häussinger, *J. Biomol. NMR* **2018**, *72*, 29–38.
- [19] H. Wang, G. Zhang, Y. Guo, B. Ren, Z. Wang, C. Zhou, *5 or 8-Substituted Imidazo[1,*

*5-AJ Pyridines as Indoleamine and/or Tryptophane 2, 3-Dioxygenases*, **2019**, US 10,280,163 B2.

- [20] W. F. Vranken, W. Boucher, T. J. Stevens, R. H. Fogh, A. Pajon, M. Llinas, E. L. Ulrich, J. L. Markley, J. Ionides, E. D. Laue, *Proteins Struct. Funct. Genet.* **2005**, *59*, 687–696.



## 3.6 Supporting information

### 3.6.1 Materials and Methods

All chemicals were used as purchased without further purification if not stated otherwise.

All 400 MHz and 500 MHz NMR spectra were recorded on a Bruker Avance III NMR spectrometer operating at 400.13 MHz or 500.13 MHz proton frequency, respectively. The instruments were equipped with a direct observe 5-mm BBFO smart probe. All spectra were recorded at 298 K. All 600 MHz spectra were recorded either on a Bruker Avance III NMR spectrometer operating at 600.13 MHz proton frequency equipped with a direct observe 5-mm BBFO smart probe or indirect 5-mm BBI probe or a Bruker Avance III HD NMR spectrometer operating at 600.13 MHz proton frequency equipped with a cryogenic 5mm four-channel QCI probe (H/C/N/F).

HR-ESI-MS spectra were measured on a Bruker MaXis 4G HiRes ESI Mass Spectrometer.

Analytical and preparative HPLC were performed on a Shimadzu LC20 HPLC-system equipped with a prominence UV/VIS detector, a FRC-10A fraction collector and a Shimadzu 2020 ESI-MS detector. For analytical HPLC a ReprosilPur120 ODS-3, 3  $\mu\text{m}$  150x3 mm column was used. For preparative HPLC a Reprosil-Pur 120 ODS-3, 5  $\mu\text{m}$  150x20 mm column was used.

The methods use a binary gradient:

Solvent A: Water + 0.1% TFA.

Solvent B: 90% Acetonitrile + 10% water + 0.085% TFA.

For purification of Ln-PypaM<sub>2</sub>Cl<sub>2</sub>-SO<sub>2</sub>-Ph

Solvent A: Water + 0.1% formic Acid.

Solvent B: 90% Acetonitrile + 10% water + 0.085% formic Acid.

Analytical method: Flow rate: 1.0 ml/min, oven temperature 40°C, UV set to 254 and 280 nm, gradient: 2 minutes at 5% B followed by a gradient over 4 min from 5% B to 100% B. These

conditions were kept for 8 min followed by a gradient from 100% B to 5% B over 1 min. These conditions were kept constant for another 7 min, ESI-MS: positive mode 100-1500 m/z.

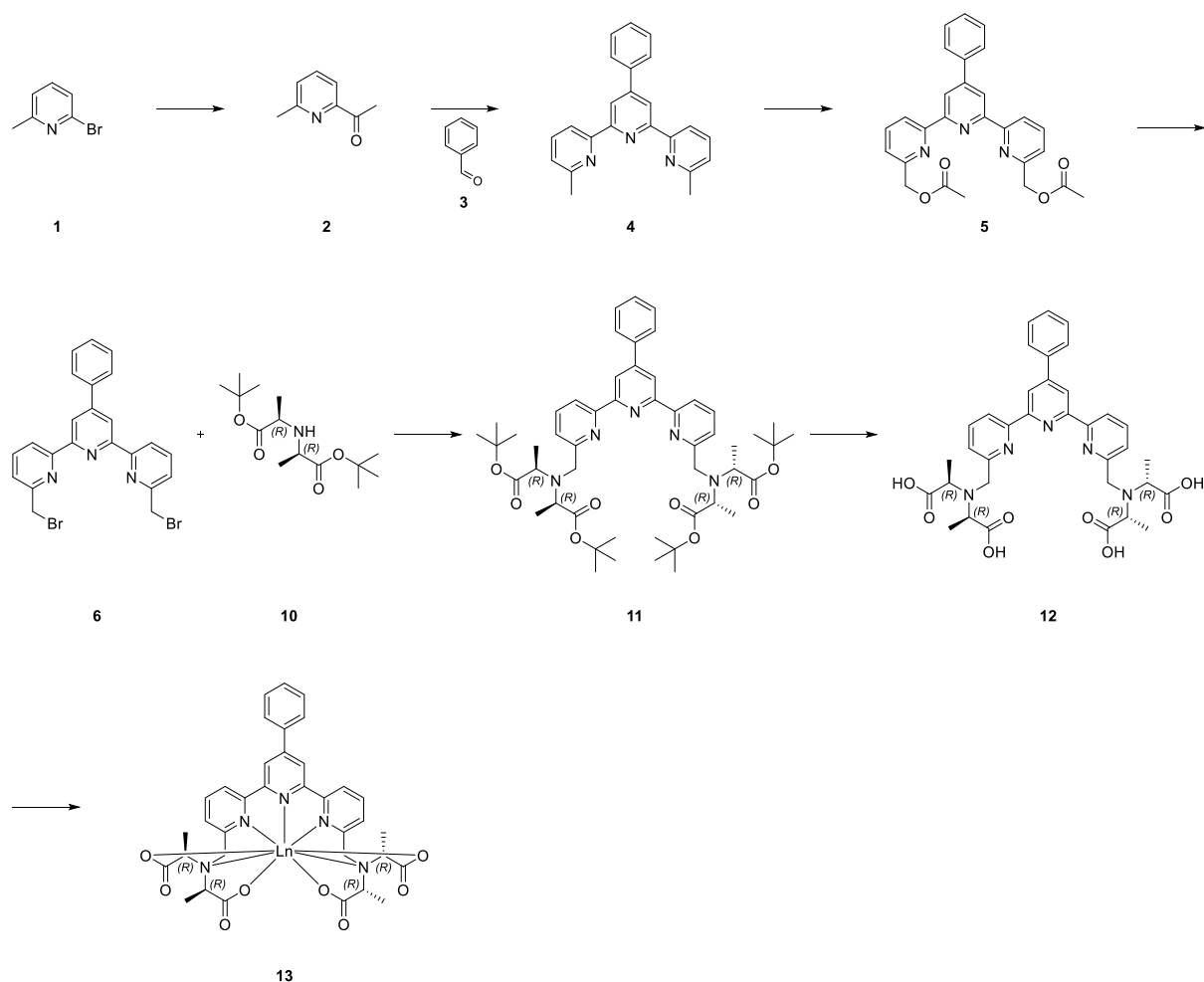
Preparative method: Flow rate: 9.0 ml/min, oven temperature 40°C, UV set to 254 and 280 nm, gradient: 2 min at 5% B followed by a gradient over 13 min from 5% B to 100% B. These conditions were kept for 7 min followed by a gradient from 100% B to 5% B over 1 min. These conditions were kept constant for another 2 min, ESI-MS: positive mode 100-1500 m/z. Fraction collector was set to the compound mass and a sample volume of 5-10 ml per fraction was collected.

For the Sep-Pak column chromatography Sep-Pak® Vac RC (500 mg) C18 cartridges were used. The Sep-Pak cartridges were used in combination with a Bio-Rad Econo Pump equipped with a Bio-Rad Econo UV-Monitor. The Sep-Pak column was wetted with acetonitrile (20 ml) and then equilibrated with water (20 ml). Afterwards the product was loaded onto the column and washed with aq. phosphate buffer (pH = 7, 20 ml) and water (20 ml). The product was eluted with acetonitrile : water (1:1, 10 ml) and collected according to the UV signal.

For buffer exchange of proteins a Hettich Universal 320 R centrifuge at 6750 G in combination with Amicon Ultra-4 Centrifugal Filters Ultracel-3K from Merck Millipore were used.

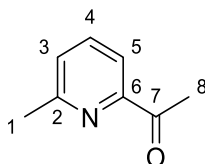
The structure of ubiquitin for the calculation of the anisotropy parameters was obtained from the PDB library (PDB: 1UBI).

### 3.6.2 Experimental Procedures and Characterization



**Figure S1:** Synthesis towards Ln-TerPyM4-Prototype complex (**13**).

**1-(6-Methylpyridin-2-yl)ethan-1-one (2):** 2-Bromo-6-methylpyridine (500 mg, 0.331 ml, 2.91 mmol, 1.0 eq) was dissolved in dry tetrahydrofuran (10 ml). The solution was cooled to  $-78^{\circ}\text{C}$ . Then *n*-butyllithium (1.6 M in hexane, 2.2 ml, 3.52 mmol, 1.2 eq.) was added slowly. The solution was stirred for 10 min. at  $-78^{\circ}\text{C}$ . Afterwards *N,N*-dimethylacetamide (359 mg, 0.38 ml, 4.07 mmol, 1.4 eq.) was added and the solution was stirred for 10 min. Then the solution was allowed to warm to  $0$ - $5^{\circ}\text{C}$  for 35 min. Water (5 ml) was added and the solution was extracted with ethyl acetate (3\*15 ml). The combined organic layers were washed with brine (20 ml) and dried over sodium sulphate. The solvent was evaporated and the crude product was purified by flash column chromatography ( $\text{SiO}_2$ , cyclohexane : ethyl acetate (9:1), liquid deposit in eluent) to yield 1-(6-methylpyridin-2-yl)ethan-1-one (287 mg, 2.91 mmol, 71%) as a colourless oil.

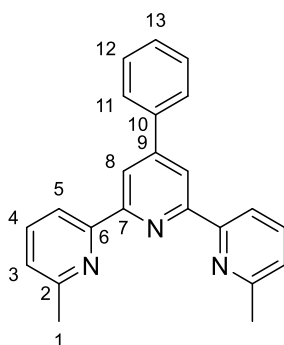


**$^1\text{H}$  NMR (500 MHz, Chloroform-*d*)**  $\delta$ : 7.83 (m, 1H, H<sub>5</sub>), 7.69 (dd,  $^3J_{\text{HH}} = 7.59$  Hz,  $^3J_{\text{HH}} = 7.59$  Hz, 1H, H<sub>4</sub>), 7.30 (m, 1H, H<sub>3</sub>), 2.71 (s, 3H, H<sub>8</sub>), 2.61 (s, 3H, H<sub>1</sub>) ppm.

**$^{13}\text{C}$  NMR (126 MHz, Chloroform-*d*)**  $\delta$ : 200.77 (C<sub>7</sub>), 158.15 (C<sub>2</sub>), 153.33 (C<sub>6</sub>), 136.97 (C<sub>4</sub>), 126.80 (C<sub>3</sub>), 118.81 (C<sub>5</sub>), 25.86 (C<sub>8</sub>), 24.57 (C<sub>1</sub>) ppm.

**HR-ESI-MS**: calcd. for  $[\text{M}+\text{H}]^+$  C<sub>8</sub>H<sub>10</sub>NO  $m/z = 136.0757$  found 136.0757.

**6,6''-Dimethyl-4'-phenyl-2,2':6',2''-terpyridine (4)**: Benzaldehyde (656 mg, 0.631 ml, 6.18 mmol, 1.0 eq) and 1-(6-methylpyridin-2-yl)ethan-1-one (1.67 g, 12.4 mmol, 2.0 eq) were dissolved in ethanol (27 ml). Then potassium hydroxide (724 mg, 12.9 mmol, 2.1 eq.) and ammonium hydroxide (25% w/w, 21 ml, 143 mmol, 23 eq.) were added. The solution was stirred at 20-25°C for 5.5 h. The colour changed from yellow to red orange and a white precipitate formed. The solvent was evaporated. The resulting heterogeneous oil was dissolved in chloroform (2 ml) and methanol (20 ml). The emulsion was heated to 65°C for 20 min. Then the solution was cooled to 20-25°C and stored at 5°C for 5 days. The suspension was filtered and the solid was washed with cold methanol. The solid was suspended in methylene chloride and filtered. The solvent was evaporated to yield the product 6,6''-dimethyl-4'-phenyl-2,2':6',2''-terpyridine (696 mg, 2.06 mmol, 33%) as a yellow-white solid.

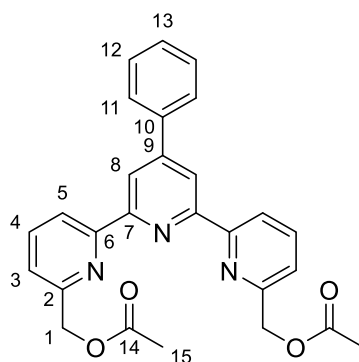


**<sup>1</sup>H NMR (500 MHz, Chloroform-*d*)**  $\delta$ : 8.72 (s, 2H, H<sub>8</sub>), 8.45 (d, <sup>3</sup>*J*<sub>HH</sub> = 7.73 Hz, 2H, H<sub>5</sub>), 7.89 (m, 2H, H<sub>11</sub>), 7.75 (dd, <sup>3</sup>*J*<sub>HH</sub> = 7.73 Hz, <sup>3</sup>*J*<sub>HH</sub> = 7.73 Hz, 2H, H<sub>4</sub>), 7.53 (m, 2H, H<sub>12</sub>), 7.46 (m, 1H, H<sub>13</sub>), 7.20 (d, <sup>3</sup>*J*<sub>HH</sub> = 7.73 Hz, 2H, H<sub>3</sub>), 2.67 (s, 6H, H<sub>1</sub>) ppm.

**<sup>13</sup>C NMR (126 MHz, Chloroform-*d*)**  $\delta$ : 158.02 (C<sub>2</sub>), 156.35 (C<sub>7</sub>), 155.93 (C<sub>6</sub>), 150.39 (C<sub>9</sub>), 139.16 (C<sub>10</sub>), 137.12 (C<sub>4</sub>), 129.02 (C<sub>12</sub>), 128.95 (C<sub>13</sub>), 127.52 (C<sub>11</sub>), 123.42 (C<sub>3</sub>), 119.05 (C<sub>8</sub>), 118.51 (C<sub>5</sub>), 24.85 (C<sub>1</sub>) ppm.

**HR-ESI-MS:** calcd. for [M+H]<sup>+</sup> C<sub>23</sub>H<sub>20</sub>N<sub>3</sub> m/z = 338.1652 found 338.1656.

**(4'-Phenyl-[2,2':6',2''-terpyridine]-6,6''-diyl) bis (methylene) diacetate (5):** 6,6''-Dimethyl-4'-phenyl-2,2':6',2''-terpyridine (410 mg, 1.22 mmol, 1.0 eq.) and *m*CPBA (832 mg, 4.82 mmol, 4.0 eq.) were dissolved in methylene chloride (30 ml). The yellow solution was stirred for 5 h. Then methylene chloride (20 ml) and sat. aq. NaHCO<sub>3</sub> (40 ml) were added. The layers were separated and the aqueous layer was extracted with methylene chloride (40 ml). The combined organic layers were dried over sodium sulphate and the solvent evaporated. The resulting yellow solid (780 mg) was suspended in acetic anhydride (20 ml). The suspension was heated to 130°C for 2.5 h. All solid dissolved at 130°C giving a clear brown solution. Then the solution was cooled to 0-5°C and sat. aq. NaHCO<sub>3</sub> (260 ml) was added carefully (strong gas evolution in the beginning). The solution was extracted with methylene chloride (3\*120 ml). The combined organic layers were dried over sodium sulphate and the solvent was evaporated. The crude product was purified by flash column chromatography (Al<sub>2</sub>O<sub>3</sub> neutral Brockmann activity I, cyclohexane : ethyl acetate (8.5:1.5), liquid deposit in methylene chloride) to yield (4'-phenyl-[2,2':6',2''-terpyridine]-6,6''-diyl)bis(methylene) diacetate (252 mg, 0.555 mmol, 45%) as a white solid.

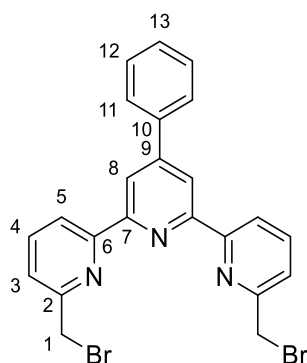


**<sup>1</sup>H NMR (500 MHz, Chloroform-*d*)**  $\delta$ : 8.75 (s, 2H, H<sub>8</sub>), 8.60 (d, <sup>3</sup>*J*<sub>HH</sub> = 7.74 Hz, 2H, H<sub>5</sub>), 7.89 (m, 4H, H<sub>11,4</sub>), 7.55 (m, 2H, H<sub>12</sub>), 7.48 (m, 1H, H<sub>13</sub>), 7.41 (d, <sup>3</sup>*J*<sub>HH</sub> = 7.74 Hz, 2H, H<sub>3</sub>), 5.36 (s, 4H, H<sub>1</sub>), 2.21 (s, 6H, H<sub>15</sub>) ppm.

**<sup>13</sup>C NMR (126 MHz, Chloroform-*d*)**  $\delta$ : 170.88 (C<sub>14</sub>) 155.99 (C<sub>7</sub>), 155.74 (C<sub>6</sub>), 155.45 (C<sub>2</sub>), 150.50 (C<sub>9</sub>), 138.80 (C<sub>10</sub>), 137.74 (C<sub>4</sub>), 129.18 (C<sub>12,13</sub>), 127.46 (C<sub>11</sub>), 121.77 (C<sub>3</sub>), 120.53 (C<sub>5</sub>), 119.47 (C<sub>8</sub>), 67.21 (C<sub>1</sub>), 21.17 (C<sub>15</sub>) ppm.

**HR-ESI-MS**: calcd. for [M+H]<sup>+</sup> C<sub>27</sub>H<sub>24</sub>N<sub>3</sub>O<sub>4</sub> m/z = 454.1761 found 454.1758.

**6,6''-Bis(bromomethyl)-4'-phenyl-2,2':6',2''-terpyridine (6):** (4'-Phenyl-[2,2':6',2''-terpyridine]-6,6''-diyl) bis(methylene) diacetate (59.0 mg, 0.130 mmol, 1.0 eq.) was dissolved in hydrobromic acid in acetic acid (33%, 2.5 ml). The solution was heated to 70°C for 6 h. Then the solution was cooled to 20-25°C and water (15 ml) and methylene chloride (10 ml) were added. Afterwards sat. aq. NaHCO<sub>3</sub> (45 ml) was added slowly to adjust the pH to approx. 7-8. The layers were separated, the aqueous layer was extracted with methylene chloride (3\*15 ml) and the combined organic layer was dried over sodium sulphate. The solvent was evaporated and the crude product was purified by flash column chromatography (SiO<sub>2</sub>, methylene chloride : methanol (95:5) +1 % acetic acid, liquid deposit in methylene chloride) to yield 6,6''-bis(bromomethyl)-4'-phenyl-2,2':6',2''-terpyridine (42.5 mg, 0.0858 mmol, 66%) as a white solid.

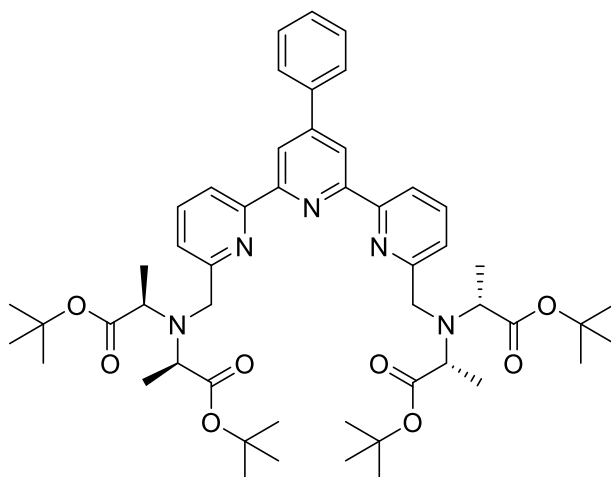


**<sup>1</sup>H NMR (500 MHz, Chloroform-*d*)**  $\delta$ : 8.77 (s, 2H, H<sub>8</sub>), 8.58 (dd, <sup>3</sup>J<sub>HH</sub> = 7.87 Hz, <sup>4</sup>J<sub>HH</sub> = 0.92 Hz, 2H, H<sub>5</sub>), 7.92-7.85 (m, 4H, H<sub>11,4</sub>), 7.56 (m, 2H, H<sub>12</sub>), 7.52 (dd, <sup>3</sup>J<sub>HH</sub> = 7.70 Hz, <sup>4</sup>J<sub>HH</sub> = 0.92 Hz, 2H, H<sub>3</sub>), 7.48 (m, 1H, H<sub>13</sub>), 4.68 (s, 4H, H<sub>1</sub>) ppm.

**<sup>13</sup>C NMR (126 MHz, Chloroform-*d*)**  $\delta$ : 156.44 (C<sub>2</sub>), 156.11 (C<sub>6</sub>), 155.62 (C<sub>7</sub>), 150.61 (C<sub>9</sub>), 138.89 (C<sub>10</sub>), 138.00 (C<sub>4</sub>), 129.17 (C<sub>12,13</sub>), 127.52 (C<sub>11</sub>), 123.69 (C<sub>3</sub>), 120.65 (C<sub>5</sub>), 119.57 (C<sub>8</sub>), 34.34 (C<sub>1</sub>) ppm.

**HR-ESI-MS:** calcd. for [M+Na]<sup>+</sup> C<sub>23</sub>H<sub>17</sub>Br<sub>2</sub>N<sub>3</sub>Na m/z = 515.9681 found 515.9673.

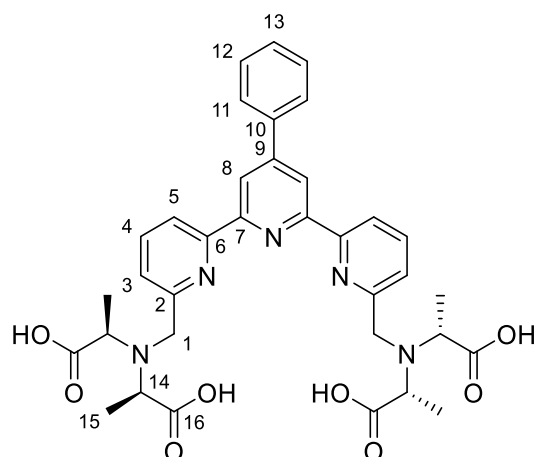
**Tetra-*tert*-butyl 2,2',2'',2'''- ((( 4'-phenyl-[2,2':6',2''-terpyridine] -6,6''-diyl) bis (methylene))bis (azanetriyl))(2*R*,2'*R*,2''*R*,2'''*R*)-tetrapropionate (11):** 6,6''-Bis(bromomethyl)-4'-phenyl-2,2':6',2''-terpyridine (29.7 mg, 0.0600 mmol, 1.0 eq.) was dissolved in dry tetrahydrofuran (1.5 ml) and dry methylene chloride (5 ml). Then di-*tert*-butyl 2,2'-(benzylazanediy)l(2*R*,2'*R*)-dipropionate (41.0 mg, 0.150 mmol, 2.5 eq.) dissolved in dry acetonitrile (0.75 ml), potassium carbonate (496 mg, 3.59 mmol, 60 eq.) and potassium iodide (7.6 mg, 0.0458 mmol, 0.76 eq.) were added. The suspension was stirred at 20-25°C for 16 h and then heated to 80°C for 48 h. Afterwards the suspension was cooled to 20-25°C and filtered. The solvent was evaporated and the crude product was purified by prep. HPLC to yield tetra-*tert*-butyl 2,2',2'',2'''- (((4'-phenyl-[2,2':6',2''-terpyridine] -6,6''-diyl)bis(methylene)) bis (azanetriyl)) (2*R*,2'*R*,2''*R*,2'''*R*)-tetrapropionate (39.3 mg, 0.0447 mmol, 74%) as a colourless oil.



**HR-ESI-MS:** calcd. for  $[M+Ag]^+$   $C_{51}H_{69}N_5O_8Ag$   $m/z = 986.4192$  found 986.4184.

**(2*R*,2'*R*,2''*R*,2'''*R*) -2,2',2'',2'''- (((4'-Phenyl-[2,2':6',2''-terpyridine]-6,6''-diyl) bis (methylene)) bis (azanetriyl)) tetrapropionic acid (12):** Tetra-*tert*-butyl 2,2',2'',2'''- (((4'-phenyl-[2,2':6',2''-terpyridine] -6,6''-diyl)bis(methylene)) bis (azanetriyl)) (2*R*,2'*R*,2''*R*,2'''*R*)-tetrapropionate (40.0 mg, 0.0454 mmol, 1.0 eq.) was dissolved in acetonitrile (5 ml) and aq. hydrochloric acid (1 M, 10 ml). The solution was heated to 80°C for 8 h. Then the solvent was evaporated and the crude product was purified by prep. HPLC to yield (2*R*,2'*R*,2''*R*,2'''*R*) -2,2',2'',2'''- (((4'-phenyl-[2,2':6',2''-terpyridine]-6,6''-diyl) bis (methylene))bis(azanetriyl)) tetrapropionic acid (20.3 mg, 0.0310 mmol, 68%) as a yellow solid.



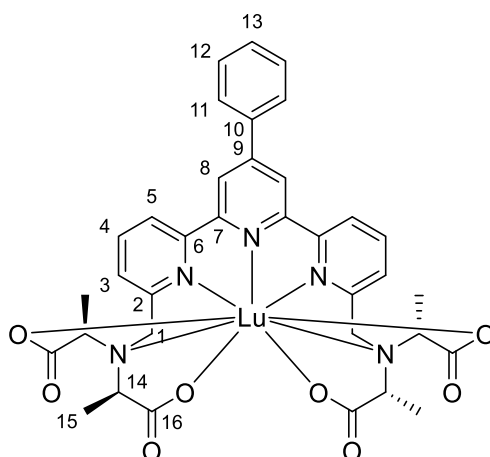


**$^1\text{H}$  NMR (500 MHz, Chloroform-*d*)**  $\delta$ : 8.92 (s, 2H, H<sub>8</sub>), 8.81 (m, 2H, H<sub>5</sub>), 8.41 (m, 2H, H<sub>4</sub>), 8.13 (m, 2H, H<sub>11</sub>), 7.79 (m, 2H, H<sub>3</sub>), 7.66 (m, 2H, H<sub>12</sub>), 7.64 (m, 1H, H<sub>13</sub>), 4.59 (s, 4H, H<sub>1</sub>), 4.20 (q,  $^3J_{\text{HH}} = 7.10$  Hz, 4H, H<sub>14</sub>), 1.60 (d,  $^3J_{\text{HH}} = 7.10$  Hz, 12H, H<sub>15</sub>) ppm.

**$^{13}\text{C}$  NMR (126 MHz, Chloroform-*d*)**  $\delta$ : 173.64 (C<sub>16</sub>), 153.45 (C<sub>2</sub>), 153.23 (C<sub>9</sub>), 151.79 (C<sub>7</sub>), 151.15 (C<sub>6</sub>), 144.54 (C<sub>4</sub>), 137.30 (C<sub>10</sub>), 131.40 (C<sub>13</sub>), 130.44 (C<sub>12</sub>), 128.76 (C<sub>11</sub>), 126.22 (C<sub>3</sub>), 124.16 (C<sub>5</sub>), 122.36 (C<sub>8</sub>), 60.53 (C<sub>14</sub>), 51.41 (C<sub>1</sub>), 14.16 (C<sub>15</sub>) ppm.

**HR-ESI-MS**: calcd. for  $[\text{M}+\text{H}]^+$  C<sub>35</sub>H<sub>38</sub>N<sub>5</sub>O<sub>8</sub>  $m/z = 656.2715$  found 656.2706.

**Lu-TerPyM4-Prototype complex (13):** (*2R,2'R,2''R,2'''R*)-2,2',2'',2'''-(((4'-Phenyl-[2,2':6',2''-terpyridine]-6,6''-diyl) bis (methylene))bis(azanetriyl))tetrapropionic acid (4.0 mg, 0.00610 mmol, 1.0 eq.) was dissolved in aq. ammonium acetate (100 mM, 5 ml). Then lutetium(III)trifluoromethanesulfonate (15.2 mg, 0.0244 mmol, 4.0 eq.) was added. The solution was stirred for 5 h at 20-25°C. Afterwards the crude product was directly purified by Sep-Pak column chromatography to yield Lu-TerPyM4-Prototype complex (1.9 mg, 0.00230 mmol, 38%) as a slightly yellow solid.



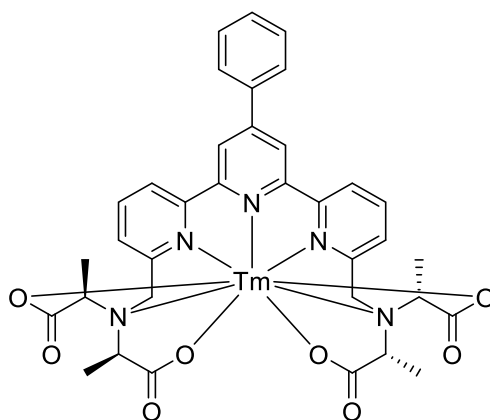
**<sup>1</sup>H NMR (500 MHz, D<sub>2</sub>O) δ:** 8.57 (s, 2H, H<sub>8</sub>), 8.49 (d, <sup>3</sup>J<sub>HH</sub> = 8.06 Hz, 2H, H<sub>5</sub>), 8.23 (dd, <sup>3</sup>J<sub>HH</sub> = 8.06 Hz, <sup>3</sup>J<sub>HH</sub> = 7.76 Hz, 2H, H<sub>4</sub>), 7.95 (d, <sup>3</sup>J<sub>HH</sub> = 7.49 Hz, 2H, H<sub>11</sub>), 7.70 (d, <sup>3</sup>J<sub>HH</sub> = 7.76 Hz, 2H, H<sub>3</sub>), 7.64 (m, 2H, H<sub>12</sub>), 7.60 (m, 1H, H<sub>13</sub>), 4.93 (d, <sup>2</sup>J<sub>HH</sub> = 16.34 Hz, 2H, H<sub>1a</sub>), 4.49 (d, <sup>2</sup>J<sub>HH</sub> = 16.34 Hz, 2H, H<sub>1b</sub>), 3.97 (q, <sup>3</sup>J<sub>HH</sub> = 7.03 Hz, 2H, H<sub>14b</sub>), 3.33 (q, <sup>3</sup>J<sub>HH</sub> = 7.03 Hz, 2H, H<sub>14a</sub>), 1.32 (d, <sup>3</sup>J<sub>HH</sub> = 7.03 Hz, 6H, H<sub>15a</sub>), 0.92 (d, <sup>3</sup>J<sub>HH</sub> = 7.03 Hz, 6H, H<sub>15b</sub>) ppm.

Due to severe  $\pi$ -stacking the <sup>13</sup>C shifts were not determined.

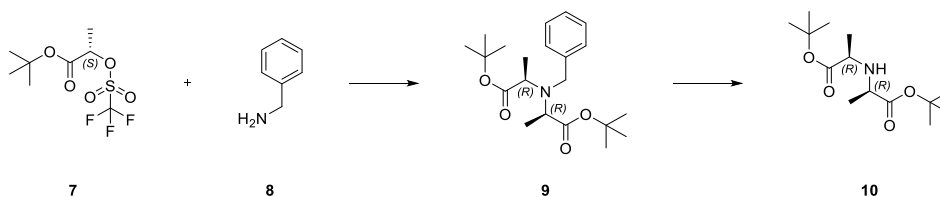
**HR-ESI-MS:** calcd. for [M+2H]<sup>+</sup> C<sub>35</sub>H<sub>35</sub>LuN<sub>5</sub>O<sub>8</sub> m/z = 828.1888 found 828.1886.

**Tm-TerPyM4-Prototype complex (13):** (*2R,2'R,2''R,2'''R*)-2,2',2'',2'''-(((4'-Phenyl-[2,2':6',2''-terpyridine]-6,6''-diyl) bis (methylene))bis(azanetriyl))tetrapropionic acid (2.5 mg, 0.00381 mmol, 1.0 eq.) was dissolved in aq. ammonium acetate (100 mM, 4 ml). Then thulium(III)trifluoromethanesulfonate (7.04 mg, 0.0114 mmol, 3.0 eq.) dissolved in aq. ammonium acetate (100 mM, 0.460 ml) was added. The solution was stirred for 2 h at 20-25°C.

Afterwards the crude product was directly purified by Sep-Pak column chromatography to yield Tm-TerPyM4-Prototype complex (2.7 mg, 0.00329 mmol, 86%) as a slightly yellow solid.

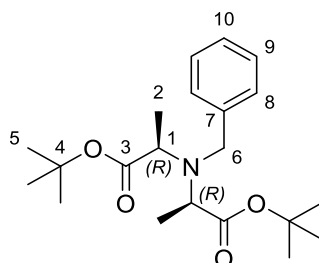


**HR-ESI-MS:** calcd. for  $[M+2H]^+$   $C_{35}H_{35}TmN_5O_8$   $m/z = 822.1822$  found 822.1810.



**Figure S2:** Synthesis towards lactic acid side arm **10**.

**Di-tert-butyl 2,2'-(benzylazanediyl)(2*R*,2'*R*)-dipropionate (9):** Benzylamine (245 mg, 0.25 ml, 2.29 mmol, 1.0 eq.) was dissolved in dry acetonitrile (10 ml). Then potassium carbonate (1.33 g, 9.62 mmol, 4.2 eq) and *tert*-butyl (*S*)-2-(((trifluoromethyl)sulfonyl)oxy)propanoate (1.29 g, 4.64 mmol, 2.0 eq.) dissolved in dry acetonitrile (5 ml) were added. The suspension was stirred at 20-25°C for 17 h. Afterwards the suspension was filtered and the solvent was evaporated. The crude product was purified by column chromatography (SiO<sub>2</sub>, cyclohexane : ethyl acetate (9:1), liquid deposit in ethyl acetate) to yield di-*tert*-butyl 2,2'-(benzylazanediyl)(2*R*,2'*R*)-dipropionate (552 mg, 1.52 mmol, 66%) as a colourless oil.

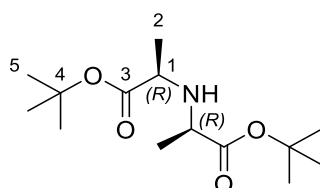


**<sup>1</sup>H NMR (500 MHz, Chloroform-*d*)**  $\delta$ : 7.40 (m, 2H, H<sub>8</sub>), 7.30 (m, 2H, H<sub>9</sub>), 7.21 (m, 1H, H<sub>10</sub>), 4.12 (m, 2H, H<sub>6</sub>), 3.55 (q, <sup>3</sup>*J*<sub>HH</sub> = 7.17 Hz, 2H, H<sub>1</sub>), 1.46 (s, 18H, H<sub>5</sub>), 1.26 (d, <sup>3</sup>*J*<sub>HH</sub> = 7.17 Hz, 6H, H<sub>2</sub>) ppm.

**<sup>13</sup>C NMR (126 MHz, Chloroform-*d*)**  $\delta$ : 173.75 (C<sub>3</sub>), 141.92 (C<sub>7</sub>), 128.23 (C<sub>8</sub>), 128.03 (C<sub>9</sub>), 126.63 (C<sub>10</sub>), 80.51 (C<sub>4</sub>), 56.92 (C<sub>1</sub>), 50.93 (C<sub>6</sub>), 28.35 (C<sub>5</sub>), 17.19 (C<sub>2</sub>), ppm.

**HR-ESI-MS:** calcd. for [M+H]<sup>+</sup> C<sub>21</sub>H<sub>34</sub>NO<sub>4</sub> m/z = 364.2482 found 364.2483.

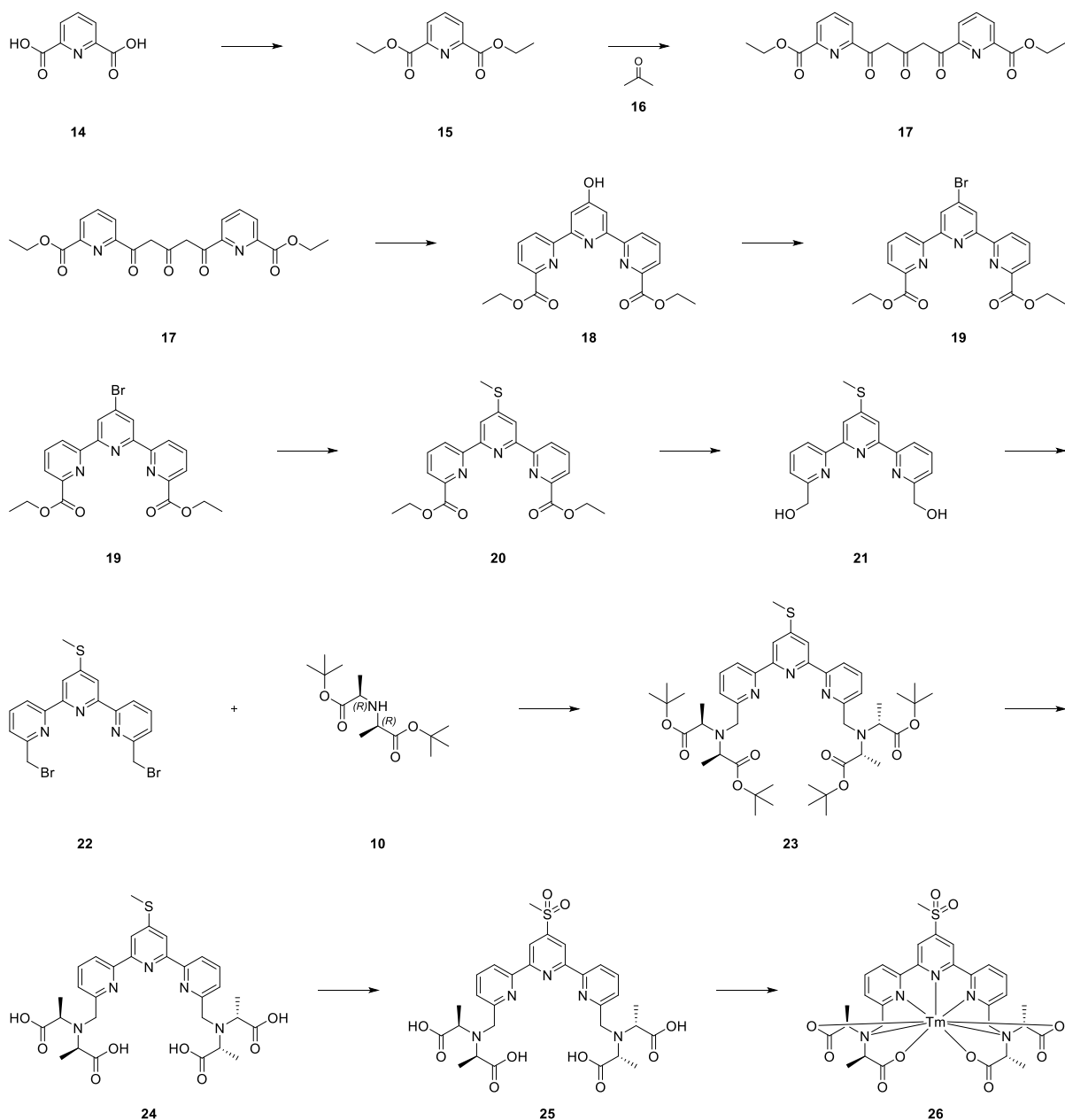
**Di-*tert*-butyl 2,2'-azanediyl(2*R*,2'*R*)-dipropionate (10):** Di-*tert*-butyl 2,2'-(benzylazanediyl)(2*R*,2'*R*)-dipropionate (550 mg, 1.51 mmol, 1.0 eq.) was dissolved in methanol (28 ml). Then palladium on carbon (10%, 32.1 mg, 0.302 mmol, 0.2 eq.) was added and hydrogen (one balloon) was bubbled through the solution. The suspension was stirred under a hydrogen atmosphere for 20 h. Then the suspension was filtered over celite and the solvent was evaporated to yield di-*tert*-butyl 2,2'-azanediyl(2*R*,2'*R*)-dipropionate (395 mg, 1.44 mmol, 96%) as a colourless oil.



**<sup>1</sup>H NMR (500 MHz, Chloroform-*d*)**  $\delta$ : 3.37 (q,  $^3J_{\text{HH}} = 7.03$  Hz, 2H, H<sub>1</sub>), 1.47 (s, 18H, H<sub>5</sub>), 1.34 (d,  $^3J_{\text{HH}} = 7.03$  Hz, 6H, H<sub>2</sub>) ppm.

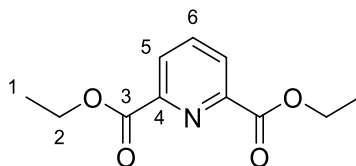
**<sup>13</sup>C NMR (126 MHz, Chloroform-*d*)**  $\delta$ : 173.63 (C<sub>3</sub>), 81.83 (C<sub>4</sub>), 55.93 (C<sub>1</sub>), 28.18 (C<sub>5</sub>), 19.01 (C<sub>2</sub>) ppm.

**HR-ESI-MS:** calcd. for [M+H]<sup>+</sup> C<sub>14</sub>H<sub>28</sub>NO<sub>4</sub> m/z = 274.2013 found 274.2017.



**Figure S3:** Synthesis towards Ln-TerPyM4-SO<sub>2</sub>-Me (**26**).

**Diethyl pyridine-2,6-dicarboxylate (15):** Pyridine-2,6-dicarboxylic acid (5.00 g, 29.9 mmol, 1.0 eq.) was suspended in dry ethanol (45 ml). Then sulphuric acid (2 ml, 3.66 g, 35.5mmol, 1.2 eq.) was added and the suspension was heated to 82°C for 22 h. The solution was allowed to cool to 20-25°C and the solvent was evaporated. The residue was dissolved in methylene chloride (50 ml). The organic layer was washed with sat. aq. NaHCO<sub>3</sub> (50 ml) and water (50 ml). The solvent was evaporated to yield diethyl pyridine-2,6-dicarboxylate (5.17 g, 23.2 mmol, 78%) as white crystals.

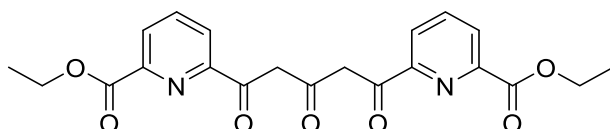


**<sup>1</sup>H NMR (500 MHz, Chloroform-*d*)**  $\delta$ : 8.28 (d,  $^3J_{\text{HH}} = 7.66$  Hz, 2H, H<sub>5</sub>), 8.00 (t,  $^3J_{\text{HH}} = 7.66$  Hz, 1H, H<sub>6</sub>), 4.49 (q,  $^3J_{\text{HH}} = 7.14$  Hz, 4H, H<sub>2</sub>), 1.46 (t,  $^3J_{\text{HH}} = 7.14$  Hz, 6H, H<sub>1</sub>) ppm.

**<sup>13</sup>C NMR (126 MHz, Chloroform-*d*)**  $\delta$ : 164.81 (C<sub>3</sub>), 148.81 (C<sub>4</sub>), 138.33 (C<sub>6</sub>), 127.96 (C<sub>5</sub>), 62.50 (C<sub>2</sub>), 14.37 (C<sub>1</sub>) ppm.

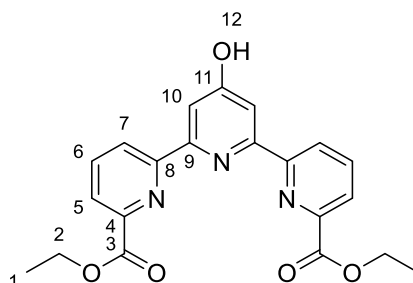
**HR-ESI-MS**: calcd. for [M+H]<sup>+</sup> C<sub>11</sub>H<sub>14</sub>NO<sub>4</sub> m/z = 224.0917 found 224.0915.

**Diethyl 6,6'-(3-oxopentanedioyl)dipicolinate (17)**: Sodium hydride (55-65%, 1.60 g, 39.9 mmol, 3.0 eq.) was suspended in dry tetrahydrofuran (35 ml) and heated to 64°C. When the suspension started to reflux diethyl pyridine-2,6-dicarboxylate (8.91 g, 39.9 mmol, 3.0 eq.) dissolved in dry tetrahydrofuran (24 ml) was added. Then acetone (0.98 ml, 0.772 g, 13.3 mmol, 1.0 eq.) dissolved in dry tetrahydrofuran (12 ml) was added to the suspension using a syringe pump (flow speed 16ml/h). Afterwards the suspension was stirred at 64°C for 5.5 h. The suspension was filtered and washed with cold tetrahydrofuran (200 ml). The solid was transferred to a round bottom flask and stirred overnight in a mixture of methylene chloride (350 ml), water (70 ml) and aq. acetic acid (5%, 45 ml). The layers were separated and the organic layer was washed with water (2\*250 ml) and brine (250 ml) and dried over sodium sulphate. The solvent was evaporated to yield diethyl 6,6'-(3-oxopentanedioyl)dipicolinate (4.65 g, 11.3 mmol, 85%) as a yellow solid. The product was used in the next step without further purification.



**HR-ESI-MS**: calcd. for [M+H]<sup>+</sup> C<sub>21</sub>H<sub>21</sub>N<sub>2</sub>O<sub>7</sub> m/z = 413.1343 found 413.1343.

**Diethyl 4'-hydroxy-[2,2':6',2''-terpyridine]-6,6''-dicarboxylate (18):** Diethyl 6,6'-(3-oxopentanedioyl) dipicolinate (4.66 g, 11.3 mmol, 1.0 eq.) was suspended in ethanol (70 ml) and heated to 82°C. Then ammonium acetate (6.10 g, 79.1 mmol, 7.0 eq.) was added. The solution was stirred at 82°C for 2.5 h. Afterwards the solution was allowed to cool to 20-25°C and the solvent was evaporated. The residue was dissolved in methylene chloride (400 ml) and water (150 ml). The layers were separated and the organic layer was washed with water (2\*150 ml) and brine (100 ml) and dried over sodium sulphate. The solvent was evaporated and the crude product was purified by flash column chromatography (SiO<sub>2</sub>, tetrahydrofuran : methylene chloride (1:1) → tetrahydrofuran) to yield diethyl 4'-hydroxy-[2,2':6',2''-terpyridine]-6,6''-dicarboxylate (1.65 g, 4.19 mmol, 32% (over two steps)) as an off white solid.



**<sup>1</sup>H NMR (500 MHz, Chloroform-*d*)** δ: 8.22 (dd, <sup>3</sup>*J*<sub>HH</sub> = 7.31 Hz, <sup>4</sup>*J*<sub>HH</sub> = 1.31 Hz, 2H, H<sub>5</sub>), 8.08 (dd, <sup>3</sup>*J*<sub>HH</sub> = 8.08 Hz, <sup>4</sup>*J*<sub>HH</sub> = 1.31 Hz, 2H, H<sub>7</sub>), 8.22 (dd, <sup>3</sup>*J*<sub>HH</sub> = 7.31 Hz, <sup>3</sup>*J*<sub>HH</sub> = 8.08 Hz, 2H, H<sub>6</sub>), 7.12 (s, 2H, H<sub>10</sub>), 4.59 (q, <sup>3</sup>*J*<sub>HH</sub> = 7.14 Hz, 4H, H<sub>2</sub>), 1.48 (t, <sup>3</sup>*J*<sub>HH</sub> = 7.14 Hz, 6H, H<sub>1</sub>) ppm.

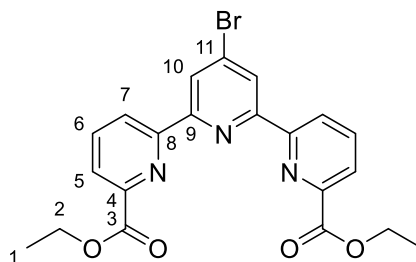
**<sup>13</sup>C NMR (126 MHz, Chloroform-*d*)** δ: 181.35 (C<sub>11</sub>), 164.32 (C<sub>3</sub>), 149.23 (C<sub>8</sub>), 148.44 (C<sub>4</sub>), 143.87 (C<sub>9</sub>), 138.95 (C<sub>6</sub>), 126.20 (C<sub>5</sub>), 123.23 (C<sub>7</sub>), 114.87 (C<sub>10</sub>), 62.35 (C<sub>2</sub>), 14.45 (C<sub>1</sub>) ppm.

**HR-ESI-MS:** calcd. for [M+Na]<sup>+</sup> C<sub>21</sub>H<sub>19</sub>N<sub>3</sub>NaO<sub>5</sub> m/z = 416.1217 found 416.1215.

**Diethyl 4'-bromo-[2,2':6',2''-terpyridine]-6,6''-dicarboxylate (19):** Diethyl 4'-hydroxy-[2,2':6',2''-terpyridine]-6,6''-dicarboxylate (1.65 g, 4.19 mmol, 1.0 eq.) was dissolved in dry acetonitrile (60 ml). Then *N,N*-dimethylformamide (0.486 ml, 495 mg, 6.29 mmol, 1.5 eq.) and phosphorous tribromide (1.18 ml, 3.40 g, 12.6 mmol, 3.0 eq.) were added and the solution was heated to 80°C for 2 h. Afterwards the solution was cooled to 20-25°C and the solvent was evaporated. The residue was dissolved in water (50 ml) and neutralized with sat. aq. NaHCO<sub>3</sub>



(approx. 70 ml). The aqueous layer was extracted with methylene chloride (2\*175 ml). The combined organic layers were washed with water (2\*175 ml) and brine (175 ml) and dried over sodium sulphate. The solvent was evaporated and the crude product was purified by flash column chromatography (SiO<sub>2</sub>, methylene chloride : ethanol (97.5:2.5)) to yield diethyl 4'-bromo-[2,2':6',2''-terpyridine]-6,6''-dicarboxylate (1.34 g, 2.95 mmol, 70%) as a beige solid.



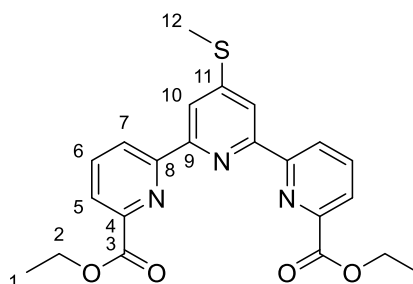
**<sup>1</sup>H NMR (500 MHz, Chloroform-*d*)**  $\delta$ : 8.80 (s, 2H, H<sub>10</sub>), 8.76 (dd, <sup>3</sup>*J*<sub>HH</sub> = 7.86 Hz, <sup>4</sup>*J*<sub>HH</sub> = 0.98 Hz, 2H, H<sub>7</sub>), 8.18 (dd, <sup>3</sup>*J*<sub>HH</sub> = 7.63 Hz, <sup>4</sup>*J*<sub>HH</sub> = 0.98 Hz, 2H, H<sub>5</sub>), 8.01 (dd, <sup>3</sup>*J*<sub>HH</sub> = 7.86 Hz, <sup>3</sup>*J*<sub>HH</sub> = 7.63 Hz, 2H, H<sub>6</sub>), 4.53 (q, <sup>3</sup>*J*<sub>HH</sub> = 7.19 Hz, 4H, H<sub>2</sub>), 1.50 (t, <sup>3</sup>*J*<sub>HH</sub> = 7.19 Hz, 6H, H<sub>1</sub>) ppm.

**<sup>13</sup>C NMR (126 MHz, Chloroform-*d*)**  $\delta$ : 165.32 (C<sub>3</sub>), 155.76 (C<sub>9</sub>), 155.20 (C<sub>8</sub>), 148.18 (C<sub>4</sub>), 138.09 (C<sub>6</sub>), 135.59 (C<sub>11</sub>), 125.64 (C<sub>5</sub>), 125.36 (C<sub>10</sub>), 124.56 (C<sub>7</sub>), 62.19 (C<sub>2</sub>), 14.49 (C<sub>1</sub>) ppm.

**HR-ESI-MS:** calcd. for [M+H]<sup>+</sup> C<sub>21</sub>H<sub>19</sub>BrN<sub>3</sub>O<sub>4</sub> m/z = 456.0553 found 456.0545.

**Diethyl 4'-(methylthio)-[2,2':6',2''-terpyridine]-6,6''-dicarboxylate (20):** Diethyl 4'-bromo-[2,2':6',2''-ter-pyridine]-6,6''-dicarboxylate (100 mg, 0.219 mmol, 1.0 eq.) was suspended in dry dimethylsulfide (10 ml). Then S-methylisothiourea sulphate (124 mg, 0.438 mmol, 2.0 eq) and caesium carbonate (571 mg, 1.75 mmol, 8.0 eq) were added. The suspension was heated to 80°C for 3 h. Then the suspension was allowed to cool to 20-25°C. The suspension was diluted with methylene chloride (40 ml) and water (40 ml). The layers were separated. The organic layer was washed with water (2\*40 ml) and brine (80 ml) and dried over sodium sulphate. The solvent was evaporated and the crude product was purified by flash column chromatography (SiO<sub>2</sub>, methylene chloride : tetrahydrofuran (95:5), liquid deposit in methylene chloride) to

yield diethyl 4'-(methylthio)-[2,2':6',2''-terpyridine]-6,6''-dicarboxylate (63.5 mg, 0.150 mmol, 69%) as a white solid.

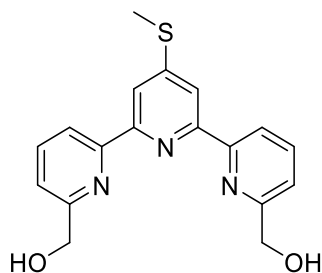


**<sup>1</sup>H NMR (500 MHz, Chloroform-*d*)**  $\delta$ : 8.78 (dd,  $^3J_{\text{HH}} = 7.91$  Hz,  $^4J_{\text{HH}} = 1.11$  Hz, 2H, H<sub>7</sub>), 8.47 (s, 2H, H<sub>10</sub>), 8.15 (dd,  $^3J_{\text{HH}} = 7.70$  Hz,  $^4J_{\text{HH}} = 1.11$  Hz, 2H, H<sub>5</sub>), 8.00 (dd,  $^3J_{\text{HH}} = 7.91$  Hz,  $^3J_{\text{HH}} = 7.70$  Hz, 2H, H<sub>6</sub>), 4.52 (q,  $^3J_{\text{HH}} = 7.14$  Hz, 4H, H<sub>2</sub>), 2.69 (s, 3H, H<sub>12</sub>), 1.49 (t,  $^3J_{\text{HH}} = 7.14$  Hz, 6H, H<sub>1</sub>) ppm.

**<sup>13</sup>C NMR (126 MHz, Chloroform-*d*)**  $\delta$ : 165.45 (C<sub>3</sub>), 156.21 (C<sub>8</sub>), 154.19 (C<sub>9</sub>), 153.05 (C<sub>11</sub>), 147.95 (C<sub>4</sub>), 137.94 (C<sub>6</sub>), 125.24 (C<sub>5</sub>), 124.59 (C<sub>7</sub>), 118.03 (C<sub>10</sub>), 62.05 (C<sub>2</sub>), 14.47 (C<sub>1</sub>), 14.08 (C<sub>12</sub>) ppm.

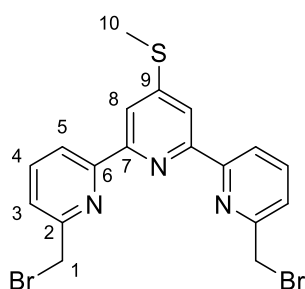
**HR-ESI-MS**: calcd. for [M+Ag]<sup>+</sup> C<sub>22</sub>H<sub>21</sub>AgN<sub>3</sub>O<sub>4</sub>S m/z = 530.0298 found 530.0301.

**(4'-(Methylthio)-[2,2':6',2''-terpyridine]-6,6''-diyl)dimethanol (21)**: Diethyl 4'-(methylthio)-[2,2':6',2''-ter-pyridine]-6,6''-dicarboxylate (126 mg, 0.298 mmol, 1.0 eq.) was dissolved in dry tetrahydrofuran (20 ml). The solution was cooled to 0-5°C and lithium aluminium hydride (2.4 M, 0.62 ml, 1.49 mmol, 5.0 eq.) was added dropwise. The solution was stirred at 0-5°C for 20 min. Afterwards water (0.6 ml) was added and the solution was filtered. The solvent was evaporated to yield (4'-(methylthio)-[2,2':6',2''-terpyridine]-6,6''-diyl)dimethanol (99.6 mg, 0.293 mmol, 98%) as a yellow-orange solid. The product was used in the next step without further purification.



**HR-ESI-MS:** calcd. for  $[M+Ag]^+$   $C_{18}H_{17}N_3NaO_2S$   $m/z = 362.0934$  found 362.0935.

**6,6''-Bis(bromomethyl) -4'-(methylthio) -2,2':6',2''- terpyridine (22):** (4'-(methylthio) - [2,2':6',2''-ter-pyridine]-6,6''-diyl)dimethanol (101 mg, 0.298 mmol, 1.0 eq.) was suspended in dry acetonitrile. Then phosphorous tribromide (85  $\mu$ l, 243 mg, 0.897 mmol, 3.0 eq.) was added and the suspension was heated to 85°C for 30 min. Afterwards the suspension was allowed to cool to 20-25°C and the solvent was evaporated. The residue was suspended in water (40 ml) and neutralized with sat. aq.  $NaHCO_3$  (4.5 ml). The suspension was diluted with water (40 ml) and extracted with methylene chloride (3\*40 ml). The combined organic layers were washed with brine (60 ml) and dried over sodium sulphate. The solvent was evaporated to yield 6,6''-bis(bromomethyl) -4'-(methylthio)-2,2':6',2''-terpyridine (41.0 mg, 0.0881 mmol, 30%) as a white solid

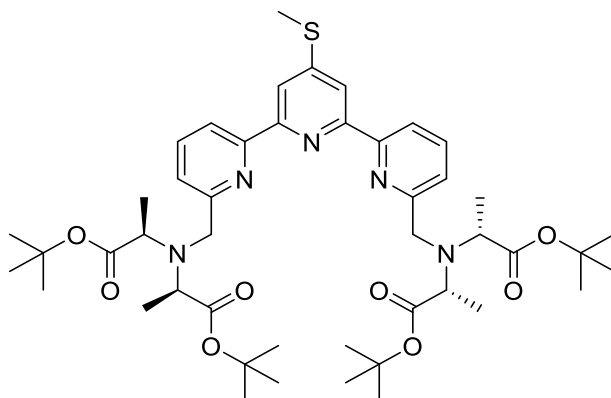


**$^1H$  NMR (500 MHz, Chloroform-*d*)  $\delta$ :** 8.51 (dd,  $^3J_{HH} = 7.91$  Hz,  $^4J_{HH} = 0.86$  Hz, 2H,  $H_5$ ), 8.36 (s, 2H,  $H_8$ ), 7.85 (dd,  $^3J_{HH} = 7.91$  Hz,  $^3J_{HH} = 7.65$  Hz, 2H,  $H_4$ ), 7.50 (dd,  $^3J_{HH} = 7.65$  Hz,  $^4J_{HH} = 1.11$  Hz, 2H,  $H_3$ ), 4.66 (s, 4H,  $H_1$ ), 2.68 (s, 3H,  $H_{10}$ ) ppm.

**$^{13}C$  NMR (126 MHz, Chloroform-*d*)  $\delta$ :** 156.36 ( $C_2$ ), 155.78 ( $C_6$ ), 154.57 ( $C_7$ ), 152.55 ( $C_9$ ), 138.00 ( $C_4$ ), 123.74 ( $C_3$ ), 120.73 ( $C_5$ ), 117.47 ( $C_8$ ), 34.28 ( $C_1$ ), 14.20 ( $C_{10}$ ) ppm.

**HR-ESI-MS:** calcd. for  $[M+H]^+$   $C_{18}H_{16}Br_2N_3S$   $m/z = 463.9426$  found 463.9429.

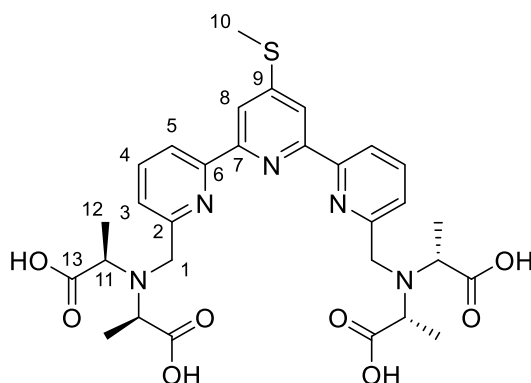
**Tetra-*tert*-butyl 2,2',2'',2'''- (((4'-(methylthio) - [2,2':6',2''-terpyridine] - 6,6''-diyl) bis(methylene)) bis (azanetriyl))(2*R*,2'*R*,2''*R*,2'''*R*)-tetrapropionate (23):** 6,6''-Bis(bromomethyl) -4'-(methylthio)-2,2':6',2''- terpyridine (41.0 mg, 0.0881 mmol, 1.0 eq.) was dissolved in dry tetrahydrofuran (2 ml) and dry acetonitrile (8 ml). Then di-*tert*-butyl 2,2'-azanediyl(2*R*,2'*R*)-dipropionate (59.3 mg, 0.217 mmol, 2.5 eq.) dissolved in dry acetonitrile (1.5 ml), dry potassium carbonate (622 mg, 4.50 mmol, 51 eq.) and dry potassium iodide (15.1 mg, 0.0910 mmol, 1.0eq.) were added. The suspension was stirred at 80°C for five days. Then the suspension was allowed to cool to 20-25°C. Afterwards the suspension was filtered and the solvent was evaporated. The crude product was purified by prep. HPLC to yield tetra-*tert*-butyl 2,2',2'',2'''- (((4'-(methylthio) - [2,2':6',2''-terpyridine] - 6,6''-diyl) bis(methylene)) bis (azanetriyl))(2*R*,2'*R*,2''*R*,2'''*R*)-tetrapropionate (40.7 mg, 0.0479 mmol, 54%) as a yellow oil.



**HR-ESI-MS:** calcd. for  $[M+H]^+$   $C_{46}H_{68}N_5O_8S$   $m/z = 850.4783$  found 850.4774.

**(2*R*,2'*R*,2''*R*,2'''*R*)-2,2',2'',2''' - (((4'-(methylthio) - [2,2':6',2''-terpyridine]-6,6''-diyl) bis (methylene)) bis (azanetriyl))tetrapropionic acid (24):** Tetra-*tert*-butyl 2,2',2'',2'''- (((4'-(methylthio) - [2,2':6',2''-terpyridine] - 6,6''-diyl) bis(methylene)) bis (azanetriyl))(2*R*,2'*R*,2''*R*,2'''*R*)-tetrapropionate (40.7 mg, 0.0479 mmol, 1.0 eq.) was dissolved in methylene chloride (10 ml). Then trifluoroacetic acid (7.5 ml) was added and the solution was heated to 40°C for 48 h. Afterwards the solution was allowed to cool to 20-25°C, diluted with methylene chloride (10 ml) and the solvent was evaporated. The crude product was purified by prep. HPLC to yield (2*R*,2'*R*,2''*R*,2'''*R*)-2,2',2'',2''' - (((4'-(methylthio) - [2,2':6',2''-

terpyridine]-6,6''-diyl) bis (methylene)) bis (azanetriyl))tetrapropionic acid (20.0 mg, 0.0320 mmol, 69%) as a yellow solid.



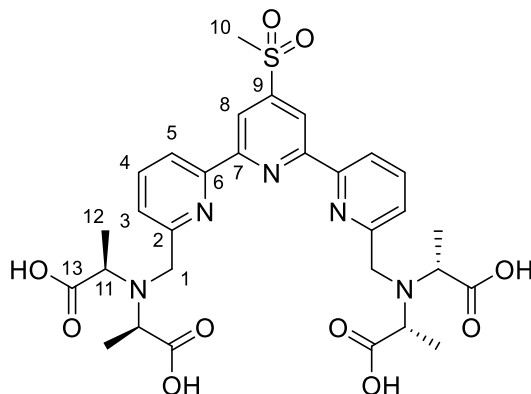
**<sup>1</sup>H NMR (500 MHz, Acetonitrile-*d*<sub>3</sub>)**  $\delta$ : 8.67 (d, <sup>3</sup>*J*<sub>HH</sub> = 8.07 Hz, 2H, H<sub>5</sub>), 8.43 (s, 2H, H<sub>8</sub>), 8.35 (dd, <sup>3</sup>*J*<sub>HH</sub> = 8.07 Hz, <sup>3</sup>*J*<sub>HH</sub> = 7.78 Hz, 2H, H<sub>4</sub>), 7.75 (d, <sup>3</sup>*J*<sub>HH</sub> = 7.78 Hz, 2H, H<sub>3</sub>), 4.56 (m, 4H, H<sub>1</sub>), 4.13 (q, <sup>3</sup>*J*<sub>HH</sub> = 7.29 Hz, 4H, H<sub>11</sub>), 2.77 (s, 3H, H<sub>10</sub>), 1.59 (d, <sup>3</sup>*J*<sub>HH</sub> = 7.29 Hz, 12H, H<sub>12</sub>) ppm.

**<sup>13</sup>C NMR (126 MHz, Acetonitrile-*d*<sub>3</sub>)**  $\delta$ : 173.54 (C<sub>13</sub>), 158.23 (C<sub>9</sub>), 153.25 (C<sub>2</sub>), 150.84 (C<sub>6</sub>), 150.57 (C<sub>7</sub>), 144.25 (C<sub>4</sub>), 126.37 (C<sub>3</sub>), 123.98 (C<sub>5</sub>), 120.32 (C<sub>8</sub>), 60.62 (C<sub>11</sub>), 51.38 (C<sub>1</sub>), 14.43 (C<sub>10</sub>), 14.01 (C<sub>12</sub>) ppm.

**HR-ESI-MS:** calcd. for [M-H]<sup>-</sup> C<sub>30</sub>H<sub>34</sub>N<sub>5</sub>O<sub>8</sub>S *m/z* = 624.2134 found 624.2137.

**(2*R*,2'*R*,2''*R*,2'''*R*) - 2,2',2'',2''' - (((4'-(methylsulfonyl) - [2,2':6',2''-terpyridine]-6,6''-diyl) bis(methylene)) bis (azanetriyl))tetrapropionic acid (25):** (2*R*,2'*R*,2''*R*,2'''*R*)-2,2',2'',2''' - (((4'-(Methylthio) - [2,2':6',2''-terpyridine]-6,6''-diyl) bis (methylene)) bis (azanetriyl))tetrapropionic acid (5.0 mg, 0.00799 mmol, 1.0 eq.) was dissolved in methanol. Then trifluoroacetic acid (2.47  $\mu$ l, 3.65 mg, 0.0320 mmol, 4.0 eq.), sodium tungstate dihydrate (2.30 mg, 0.00697 mmol, 0.87 eq.) and hydrogen peroxide (30%, 3.78  $\mu$ l, 0.0400 mmol, 5.0 eq.) were added. The solution was stirred at 20-25°C for 5 h. Then manganese dioxide (4.00 mg, 0.0460 mmol, 5.8 eq.) was added and the suspension was stirred for 15 min. The suspension was filtered and the solvent was evaporated. The crude product was purified by prep. HPLC to yield (2*R*,2'*R*,2''*R*,2'''*R*) -

2,2',2'',2'''- (((4'-(methylsulfonyl)- [2,2':6',2''-terpyridine]-6,6''-diyl)bis (methylene)) bis (azanetriyl))tetrapropionic acid (2.6 mg, 0.00395 mmol, 50%) as a yellow solid.

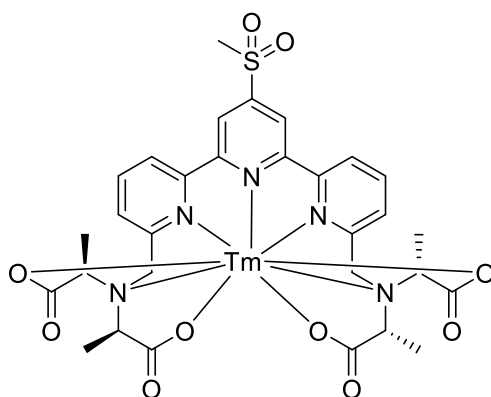


**<sup>1</sup>H NMR (500 MHz, Acetonitrile-*d*<sub>3</sub>)**  $\delta$ : 8.98 (s, 2H, H<sub>8</sub>), 8.77 (d, <sup>3</sup>*J*<sub>HH</sub> = 7.86 Hz, 2H, H<sub>5</sub>), 8.32 (dd, <sup>3</sup>*J*<sub>HH</sub> = 7.86 Hz, <sup>3</sup>*J*<sub>HH</sub> = 7.89 Hz, 2H, H<sub>4</sub>), 7.73 (d, <sup>3</sup>*J*<sub>HH</sub> = 7.65 Hz, 2H, H<sub>3</sub>), 4.63 (m, 4H, H<sub>1</sub>), 4.26 (q, <sup>3</sup>*J*<sub>HH</sub> = 7.30 Hz, 4H, H<sub>11</sub>), 3.38 (s, 3H, H<sub>10</sub>), 1.64 (d, <sup>3</sup>*J*<sub>HH</sub> = 7.30 Hz, 12H, H<sub>12</sub>) ppm.

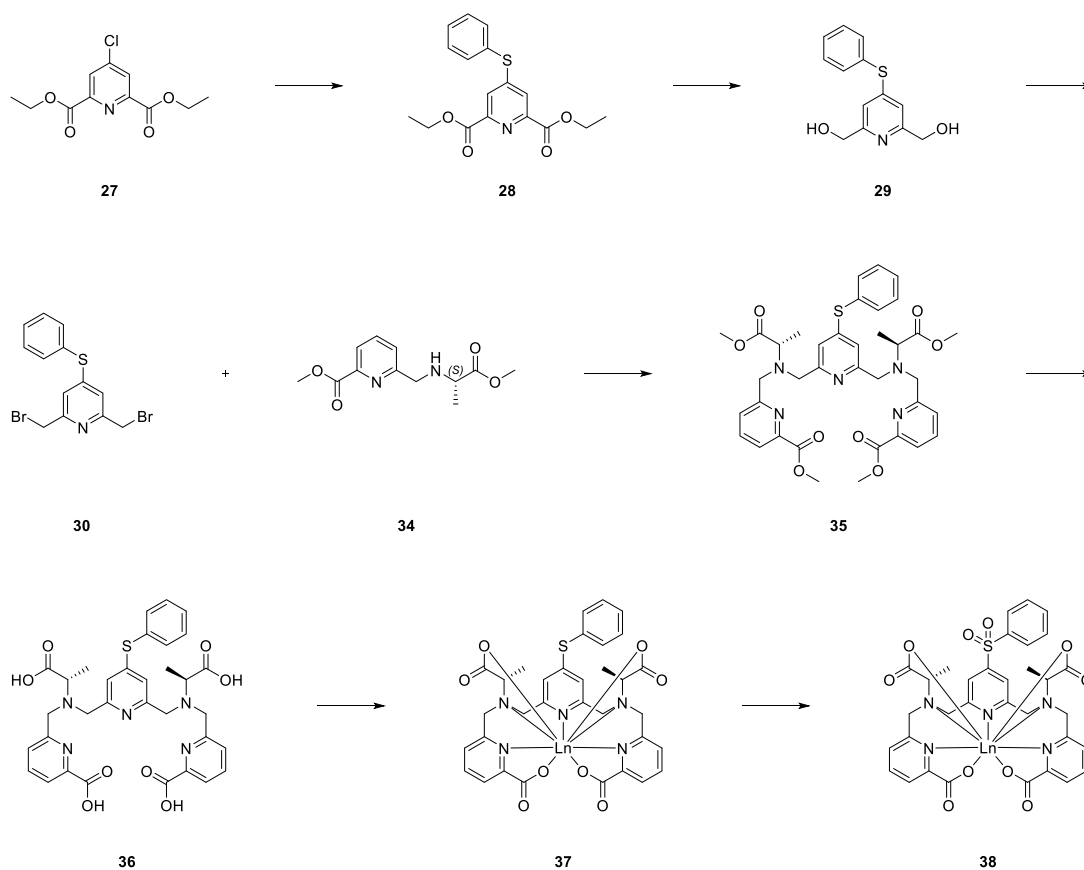
**<sup>13</sup>C NMR (126 MHz, Acetonitrile-*d*<sub>3</sub>)**  $\delta$ : 172.68 (C<sub>13</sub>), 154.76 (C<sub>7</sub>), 153.57 (C<sub>9</sub>), 152.53 (C<sub>2</sub>), 151.66 (C<sub>6</sub>), 143.39 (C<sub>4</sub>), 126.36 (C<sub>3</sub>), 123.95 (C<sub>5</sub>), 120.66 (C<sub>8</sub>), 61.13 (C<sub>11</sub>), 51.77 (C<sub>1</sub>), 43.39 (C<sub>10</sub>), 13.57 (C<sub>12</sub>) ppm.

**HR-ESI-MS**: calcd. for [M+H]<sup>+</sup> C<sub>30</sub>H<sub>36</sub>N<sub>5</sub>O<sub>10</sub>S m/z = 658.2177 found 658.2170.

**Tm-TerPyM4-SO<sub>2</sub>-Me (26)**: (2*R*,2'*R*,2''*R*,2'''*R*)-2,2',2'',2'''-(((4'-(Methylsulfonyl)-[2,2':6',2''-terpyridine]-6,6''-diyl)bis (methylene)) bis (azanetriyl))tetrapropionic acid (1.9 mg, 0.00289 mmol, 1.0 eq.) was dissolved in aq. ammonium acetate (100 mM, 4 ml). Then thulium(III)trifluoromethanesulfonate (6.4 mg, 0.0104 mmol, 3.6 eq.) was added and the solution was stirred for 1.5 h. Then the solvent was evaporated and the crude product was purified by prep HPLC (dissolved in aq. ammonium acetate (10 mM, 2 ml), eluent: water Milli-Q : acetonitrile 95:5 10 mM ammonium acetate, isocratic, otherwise the same setup as described in the Materials and Methods section was used) to yield Tm-TerPyM4-SO<sub>2</sub>-Me (2.0 mg, 0.00243 mmol, 84%) as a white solid.

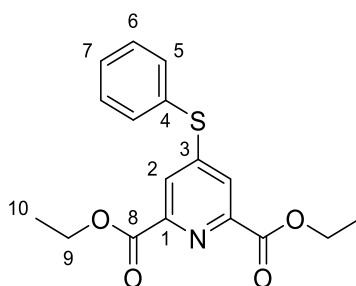


**HR-ESI-MS:** calcd. for  $[M+2H]^+$   $C_{30}H_{33}N_5O_{10}STm$   $m/z = 824.1285$  found 824.1272.



**Figure S4:** Synthesis towards Ln-PypaM2-SO<sub>2</sub>-Ph (**38**).

**Diethyl 4-(phenylthio)pyridine-2,6-dicarboxylate (28):** Diethyl 4-chloropyridine-2,6-dicarboxylate (510 mg, 1.98 mmol, 1.0 eq) was dissolved in acetonitrile (10 ml). Then thiophenol (207 mg, 0.192 ml, 1.88 mmol, 0.95 eq.) and caesium carbonate (1.32 g, 4.05 mmol, 2.0 eq.) were added. The suspension was stirred at 20-25°C for 6 h. Then the suspension was filtered and the solvent was evaporated. The crude product was purified by flash column chromatography (SiO<sub>2</sub>, cyclohexane : ethyl acetate (7:3), liquid deposit in ethyl acetate) to yield diethyl 4-(phenylthio)pyridine-2,6-dicarboxylate (517 mg, 1.56 mmol, 79%) as a colourless oil.



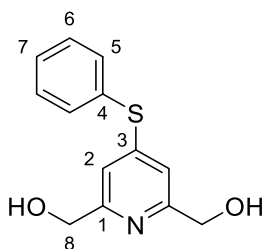


**<sup>1</sup>H NMR (500 MHz, Chloroform-*d*)**  $\delta$ : 7.86 (s, 2H, H<sub>2</sub>), 7.61-7.48 (m, 5H, H<sub>5,6,7</sub>), 4.42 (q, <sup>3</sup>J<sub>HH</sub> = 7.29 Hz, 4H, H<sub>9</sub>), 1.41 (t, <sup>3</sup>J<sub>HH</sub> = 7.29 Hz, 6H, H<sub>10</sub>) ppm.

**<sup>13</sup>C NMR (126 MHz, Chloroform-*d*)**  $\delta$ : 164.67 (C<sub>8</sub>), 154.49 (C<sub>3</sub>), 148.56 (C<sub>1</sub>), 135.52 (C<sub>5/6/7</sub>), 130.63 (C<sub>5/6/7</sub>), 130.50 (C<sub>5/6/7</sub>), 128.01 (C<sub>4</sub>), 124.21 (C<sub>2</sub>), 62.55 (C<sub>9</sub>), 14.30 (C<sub>10</sub>) ppm.

**HR-ESI-MS**: calcd. for [M+H]<sup>+</sup> C<sub>17</sub>H<sub>18</sub>NO<sub>4</sub>S m/z = 332.0951 found 332.0951.

**(4-(Phenylthio)pyridine-2,6-diyl)dimethanol (29)**: Diethyl 4-(phenylthio)pyridine-2,6-dicarboxylate (252 mg, 0.760 mmol, 1.0 eq) was dissolved in dry ethanol (15 ml). Then sodium borohydride (201 mg, 5.31 mmol, 7.0 eq.) was added. The suspension was stirred at 40°C for 16.5 h. Then the suspension was allowed to cool to 20-25°C. Afterwards water (25 ml) was added. The solution was extracted with ethyl acetate (3\*40 ml). The combined organic layers were washed with brine (30 ml) and dried over sodium sulphate. The solvent was evaporated to yield (4-(phenylthio)pyridine-2,6-diyl)dimethanol (186 mg, 0.752 mmol, 99%) as a white solid.

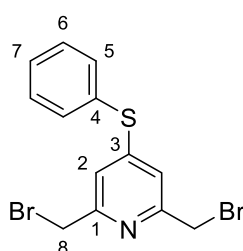


**<sup>1</sup>H NMR (500 MHz, Methanol-*d*<sub>4</sub>)**  $\delta$ : 7.61-7.48 (m, 5H, H<sub>5,6,7</sub>), 7.09 (s, 2H, H<sub>2</sub>), 4.55 (s, 4H, H<sub>8</sub>), ppm.

**<sup>13</sup>C NMR (126 MHz, Methanol-*d*<sub>4</sub>)**  $\delta$ : 161.82 (C<sub>1</sub>), 154.20 (C<sub>3</sub>), 136.40 (C<sub>5/6/7</sub>), 131.16 (C<sub>5/6/7</sub>), 131.00 (C<sub>5/6/7</sub>), 130.55 (C<sub>4</sub>), 116.79 (C<sub>2</sub>), 65.17 (C<sub>8</sub>) ppm.

**HR-ESI-MS**: calcd. for [M+H]<sup>+</sup> C<sub>13</sub>H<sub>14</sub>NO<sub>2</sub>S m/z = 248.0740 found 248.0744.

**2,6-Bis(bromomethyl)-4-(phenylthio)pyridine (30):** (4-(Phenylthio) pyridine-2,6-diyl) dimethanol (117 mg, 0.760 mmol, 1.0 eq) was dissolved in dry acetonitrile (10 ml). Then phosphorous tribromide (0.18 ml, 512 mg, 1.89 mmol, 4.0 eq.) was added. The suspension was stirred at 85°C for 6 h. Then the suspension was allowed to cool to 20-25°C and the solvent was evaporated. The residue was suspended in water (20 ml) and sat. aq. NaHCO<sub>3</sub> (5 ml) was added. The aqueous layer was extracted with methylene chloride (3\*20 ml). The combined organic layers were washed with brine (20 ml) and dried over sodium sulphate. The solvent was evaporated to yield 2,6-bis(bromomethyl)-4-(phenylthio)pyridine (127 mg, 0.752 mmol, 72%) as a white solid.



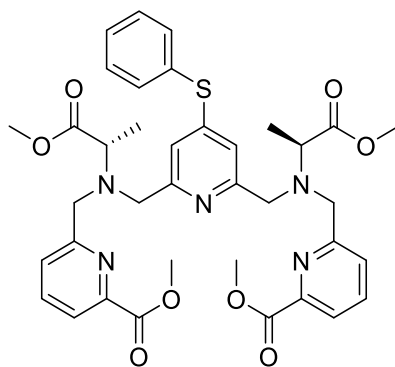
**<sup>1</sup>H NMR (500 MHz, Chloroform-*d*)**  $\delta$ : 7.58-7.46 (m, 5H, H<sub>5,6,7</sub>), 6.98 (s, 2H, H<sub>2</sub>), 4.40 (s, 4H, H<sub>8</sub>) ppm.

**<sup>13</sup>C NMR (126 MHz, Chloroform-*d*)**  $\delta$ : 156.72 (C<sub>1</sub>), 153.16 (C<sub>3</sub>), 135.37 (C<sub>5/6/7</sub>), 130.25 (C<sub>5/6/7</sub>), 130.20 (C<sub>5/6/7</sub>), 128.75 (C<sub>4</sub>), 119.61 (C<sub>2</sub>), 33.41 (C<sub>8</sub>) ppm.

**HR-ESI-MS:** calcd. for [M+H]<sup>+</sup> C<sub>13</sub>H<sub>12</sub>NBr<sub>2</sub>S  $m/z$  = 371.9052 found 371.9056.

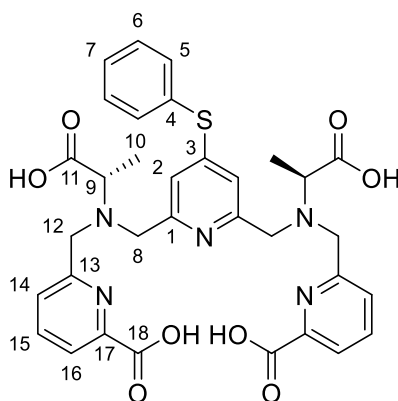
**Dimethyl 6,6'-((((4-(phenylthio)pyridine-2,6-diyl)bis(methylene))bis(((*S*)-1-methoxy-1-oxopropan-2-yl)azanediyl)) bis (methylene)) dipicolinate (35):** Methyl (*S*)-6-(((1-methoxy-1-oxopropan-2-yl)amino) methyl)picolinate (380 mg, 1.51 mmol, 2.2 eq) was dissolved in dry acetonitrile (10 ml). Then 2,6-bis(bromomethyl)-4-(phenylthio)pyridine (252 mg, 0.675 mmol, 1.0 eq.), dry potassium carbonate (508 mg, 3.68 mmol, 5.4 eq) and dry potassium iodide (61.2 mg, 0.369 mmol, 0.55 eq.) were added and the suspension was heated to 40°C for 48 h. Additional methyl (*S*)-6-(((1-methoxy-1-oxopropan-2-yl)amino) methyl)picolinate (100 mg, 0.396 mmol, 0.59 eq.) dissolved in dry acetonitrile (2.5 ml) was added and the suspension was heated to 40°C for 16 h. Then potassium carbonate (202 mg, 1.46 mmol, 2.2 eq.) was added

and the suspension was heated to 40°C for 7 h. The suspension was allowed to cool to 20-25°C. Then the suspension was filtered and the solvent was evaporated. The crude product was purified by prep. HPLC to yield dimethyl 6,6'-(((4-(phenylthio)pyridine-2,6-diyl)bis(methylene))bis(((S)-1-methoxy-1-oxopropan-2-yl)azanediyl)) bis(methylene)) dipicolinate (507 mg, 0.568 mmol, 83%) as a yellow oil.



**HR-ESI-MS:** calcd. for  $[M+H]^+$   $C_{37}H_{42}N_5O_8S$   $m/z = 716.2749$  found 716.2746.

**3,3'-(((4-(Phenylthio) pyridine-2,6-diyl) bis(methylene)) bis (((S)-1-carboxyethyl)azanediyl)) bis (methylene)dibenzoic acid (36):** Dimethyl 6,6'-(((4-(phenylthio)pyridine-2,6-diyl)bis (methylene))bis (((S)-1-methoxy-1-oxopropan-2-yl)azanediyl)) bis (methylene)) dipicolinate (73.7 mg, 0.103 mmol, 1.0 eq) was dissolved in tetrahydrofuran (5 ml) and water (2.5 ml). Then aq. sodium hydroxide (4 M, 0.26 ml) was added. The suspension was stirred vigorously at 20-25°C for 3 h. The tetrahydrofuran was evaporated. The remaining liquid was diluted with acetonitrile:water (1:1+1% TFA) to a total volume of 4 ml. The resulting solution was purified by prep HPLC to yield 3,3'-(((4-(phenylthio) pyridine-2,6-diyl) bis (methylene)) bis (((S)-1-carboxyethyl)azanediyl)) bis (methylene) dibenzoic acid (60.8 mg, 0.114 mmol, 90%) as a white solid.

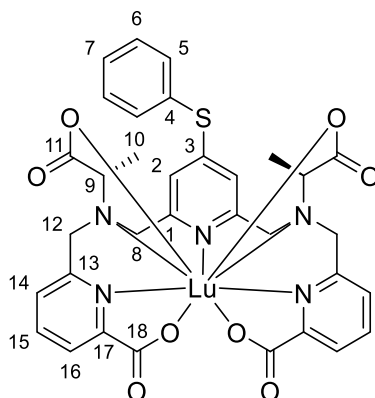


**<sup>1</sup>H NMR (500 MHz, Acetonitrile-*d*<sub>3</sub>) δ:** 8.02 (dd, <sup>3</sup>*J*<sub>HH</sub> = 7.72 Hz, <sup>4</sup>*J*<sub>HH</sub> = 0.81 Hz, 2H, H<sub>16</sub>), 7.97 (dd, <sup>3</sup>*J*<sub>HH</sub> = 7.72 Hz, <sup>3</sup>*J*<sub>HH</sub> = 7.72 Hz, 2H, H<sub>15</sub>), 7.61-7.49 (m, 7H, H<sub>5,6,7,14</sub>), 6.83 (s, 2H, H<sub>2</sub>), 4.52 (d, <sup>2</sup>*J*<sub>HH</sub> = 15.58 Hz, 2H, H<sub>12a</sub>), 4.48 (d, <sup>2</sup>*J*<sub>HH</sub> = 15.58 Hz, 2H, H<sub>12b</sub>), 4.31 (d, <sup>2</sup>*J*<sub>HH</sub> = 15.34 Hz, 2H, H<sub>8a</sub>), 4.27 (d, <sup>2</sup>*J*<sub>HH</sub> = 15.34 Hz, 2H, H<sub>8b</sub>), 4.23 (q, <sup>3</sup>*J*<sub>HH</sub> = 7.22 Hz, 2H, H<sub>9</sub>), 1.57 (d, <sup>3</sup>*J*<sub>HH</sub> = 7.22 Hz, 6H, H<sub>10</sub>) ppm.

**<sup>13</sup>C NMR (126 MHz, Acetonitrile-*d*<sub>3</sub>) δ:** 172.53 (C<sub>11</sub>), 165.06 (C<sub>18</sub>), 158.27 (C<sub>3</sub>), 152.89 (C<sub>13</sub>), 152.11 (C<sub>1</sub>), 146.99 (C<sub>17</sub>), 141.00 (C<sub>15</sub>), 136.31 (C<sub>5/6</sub>), 131.73 (C<sub>7</sub>), 131.47 (C<sub>5/6</sub>), 128.37 (C<sub>14</sub>), 127.63 (C<sub>4</sub>), 125.28 (C<sub>16</sub>), 120.73 (C<sub>2</sub>), 62.30 (C<sub>9</sub>), 56.27 (C<sub>12</sub>), 55.87 (C<sub>8</sub>), 12.25 (C<sub>10</sub>) ppm.

**HR-ESI-MS:** calcd. for [M+Ag]<sup>+</sup> C<sub>33</sub>H<sub>33</sub>N<sub>5</sub>O<sub>8</sub>S m/z = 766.1095 found 766.1093.

**Lu-PypaM2-S-Ph (37):** 3,3'-((((4-(Phenylthio) pyridine-2,6-diyl) bis (methylene)) bis (((S)-1-carboxyethyl)azanediyl)) bis (methylene)) dibenzoic acid (16.2 mg, 0.0246 mmol, 1.0 eq) was dissolved in water (4 ml). Then ammonium acetate (25.6 mg, 0.332 mmol, 14 eq.) and lutetium(III)trifluoromethanesulfonate (19.0 mg, 0.0305 mmol, 1.2 eq) were added. The solution was stirred at 20-25°C for 1 h. Afterwards the crude product was directly purified by Sep-Pak column chromatography to yield Lu-PypaM2-S-Ph (13.4 mg, 0.0161 mmol, 66%) as a white solid.



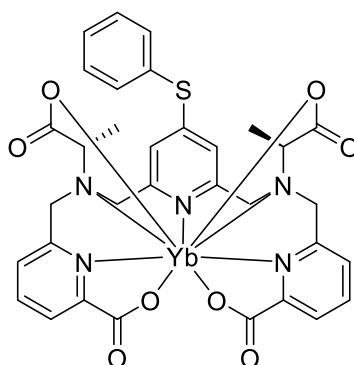
**<sup>1</sup>H NMR (500 MHz, Methanol-*d*4) δ:** 8.05 (dd, <sup>3</sup>J<sub>HH</sub> = 7.60 Hz, <sup>3</sup>J<sub>HH</sub> = 7.60 Hz, 2H, H<sub>15</sub>), 7.98 (d, <sup>3</sup>J<sub>HH</sub> = 7.60 Hz, 2H, H<sub>16</sub>), 7.63 (d, <sup>3</sup>J<sub>HH</sub> = 7.60 Hz, 2H, H<sub>14</sub>), 7.54-7.47 (m, 5H, H<sub>5,6,7</sub>), 6.89 (s, 2H, H<sub>2</sub>), 4.61 (d, <sup>2</sup>J<sub>HH</sub> = 15.88 Hz, 2H, H<sub>12a</sub>), 4.45 (d, <sup>2</sup>J<sub>HH</sub> = 15.88 Hz, 2H, H<sub>12b</sub>), 4.18 (d, <sup>2</sup>J<sub>HH</sub> = 14.76 Hz, 2H, H<sub>8a</sub>), 3.96 (d, <sup>2</sup>J<sub>HH</sub> = 14.76 Hz, 2H, H<sub>8b</sub>), 3.88 (q, <sup>3</sup>J<sub>HH</sub> = 7.24 Hz, 2H, H<sub>9</sub>), 1.26 (d, <sup>3</sup>J<sub>HH</sub> = 7.24 Hz, 6H, H<sub>10</sub>) ppm.

**<sup>13</sup>C NMR (126 MHz, Methanol-*d*4) δ:** 179.70 (C<sub>11</sub>), 173.04 (C<sub>18</sub>), 157.78 (C<sub>13</sub>), 155.32 (C<sub>3</sub>), 153.50 (C<sub>17</sub>), 153.44 (C<sub>1</sub>), 141.40 (C<sub>15</sub>), 136.19 (C<sub>5/6/7</sub>), 131.33 (C<sub>5/6/7</sub>), 131.24 (C<sub>5/6/7</sub>), 125.41 (C<sub>4</sub>), 124.50 (C<sub>16</sub>), 119.40 (C<sub>2</sub>), 67.33 (C<sub>9</sub>), 65.43 (C<sub>12</sub>), 56.75 (C<sub>8</sub>), 10.36 (C<sub>12</sub>) ppm.

**HR-ESI-MS:** calcd. for [M+2H]<sup>+</sup> C<sub>33</sub>H<sub>31</sub>LuN<sub>5</sub>O<sub>8</sub>S m/z = 832.1296 found 832.1291.

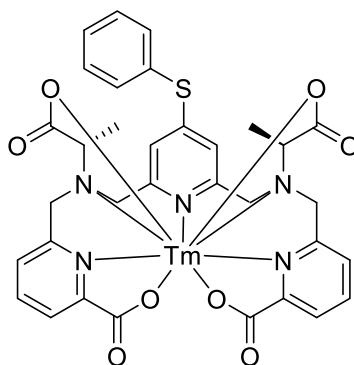
**Yb-PypaM2-S-Ph (37):** 3,3'-((((4-(Phenylthio) pyridine-2,6-diyl) bis (methylene)) bis (((S)-1-carboxyethyl)azanediyl)) bis (methylene)) dibenzoic acid (16.8 mg, 0.0255 mmol, 1.0 eq) was dissolved in water (4 ml). Then ammonium acetate (46.0 mg, 0.597 mmol, 23 eq.) and ytterbium(III) nitrate pentahydrate (16.2 mg, 0.0361 mmol, 1.4 eq) were added. The solution was stirred at 20-25°C for 2 h. Afterwards the crude product was directly purified by Sep-Pak

column chromatography to yield Yb-PypaM2-S-Ph (11.6 mg, 0.0140 mmol, 55%) as a white solid.



**HR-ESI-MS:** calcd. for  $[M+2H]^+$   $C_{33}H_{31}YbN_5O_8S$   $m/z = 831.1280$  found 831.1274.

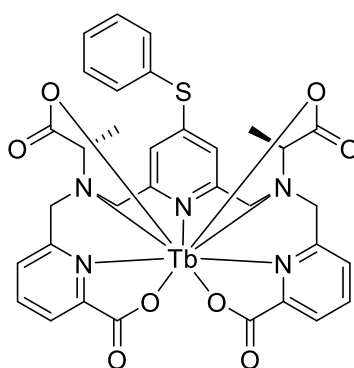
**Tm-PypaM2-S-Ph (37):** 3,3'-((((4-(Phenylthio) pyridine-2,6-diyl) bis (methylene)) bis (((S)-1-carboxyethyl)azanediyl)) bis (methylene)) dibenzoic acid (13.4 mg, 0.0203 mmol, 1.0 eq) was dissolved in aq. ammonium acetate (100 mM, 4 ml). Then thulium(III) trifluoromethanesulfonate (12.5 mg, 0.0203 mmol, 1.0 eq) was added. The solution was stirred at 20-25°C for 2 h. Afterwards the crude product was directly purified by Sep-Pak column chromatography to yield Tm-PypaM2-S-Ph (16.3 mg, 0.0198 mmol, 97%) as a colourless solid.



**HR-ESI-MS:** calcd. for  $[M+2H]^+$   $C_{33}H_{31}N_5O_8STm$   $m/z = 826.1230$  found 826.1225.

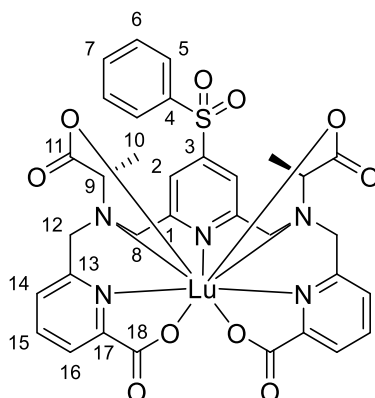
**Tb-PypaM2-S-Ph (37):** 3,3'-((((4-(Phenylthio) pyridine-2,6-diyl) bis (methylene)) bis (((S)-1-carboxyethyl)azanediyl)) bis (methylene)) dibenzoic acid (16.8 mg, 0.0255 mmol, 1.0 eq) was

dissolved in water (8 ml). Then ammonium acetate (42.0 mg, 0.545 mmol, 21 eq.) and terbium(III) chloride hexahydrate (9.52 mg, 0.0255 mmol, 1.0 eq) were added. The solution was stirred at 20-25°C for 2 h. Afterwards the crude product was directly purified by Sep-Pak column chromatography to yield Tb-PypaM2-S-Ph (12.7 mg, 0.0156 mmol, 61%) as a white solid.



**HR-ESI-MS:** calcd. for  $[M+2H]^+$   $C_{33}H_{31}N_5O_8STb$   $m/z = 816.1141$  found 816.1135.

**Lu-PypaM2-SO<sub>2</sub>-Ph (38):** Lu-PypaM2-S-Ph (3.0 mg, 0.00361 mmol, 1.0 eq) was dissolved in water (3 ml). Then sodium tungstate dihydrate (1.6 mg, 0.00485 mmol, 1.3 eq) and hydrogen peroxide (30%, 1  $\mu$ l, 0.00997 mmol, 2.8 eq.) were added. The suspension was stirred at 20-25°C for 96 h. During this time hydrogen peroxide (30%, 1.5  $\mu$ l, 0.0149 mmol, 4.1 eq) was added five times at irregular intervals. Then manganese dioxide (0.5 mg, 0.00575 mmol, 1.6 eq.) was added and the suspension was stirred for 15 min. Afterwards the crude product was directly purified by Sep-Pak column chromatography to yield Lu-PypaM2-SO<sub>2</sub>-Ph (3.1 mg, 0.00359 mmol, 99%) as a white solid.

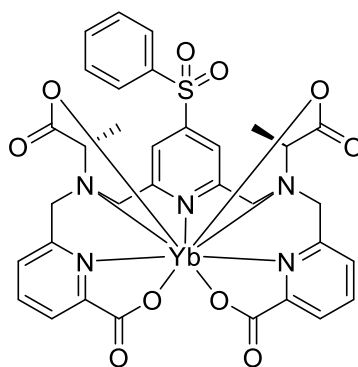


**<sup>1</sup>H NMR (500 MHz, Deuterium Oxide) δ:** 8.19 (dd, <sup>3</sup>J<sub>HH</sub> = 7.84 Hz, <sup>3</sup>J<sub>HH</sub> = 7.84 Hz, 2H, H<sub>15</sub>), 8.02 (dd, <sup>3</sup>J<sub>HH</sub> = 7.84 Hz, <sup>4</sup>J<sub>HH</sub> = 0.79 Hz, 2H, H<sub>16</sub>), 7.99 (m, 2H, H<sub>5</sub>), 7.96 (s, 2H, H<sub>2</sub>), 7.78 (m, 3H, H<sub>7,14</sub>), 7.66 (m, 2H, H<sub>6</sub>), 4.64 (d, <sup>3</sup>J<sub>HH</sub> = 16.46 Hz, 2H, H<sub>12a</sub>), 4.60 (d, <sup>3</sup>J<sub>HH</sub> = 16.46 Hz, 2H, H<sub>12b</sub>), 4.36 (d, <sup>3</sup>J<sub>HH</sub> = 15.84 Hz, 2H, H<sub>8a</sub>), 4.20 (d, <sup>3</sup>J<sub>HH</sub> = 15.84 Hz, 2H, H<sub>8b</sub>), 3.96 (q, <sup>3</sup>J<sub>HH</sub> = 7.24 Hz, 2H, H<sub>9</sub>), 1.28 (d, <sup>3</sup>J<sub>HH</sub> = 7.24 Hz, 6H, H<sub>10</sub>) ppm.

**<sup>13</sup>C NMR (126 MHz, Deuterium Oxide) δ:** 179.75 (C<sub>11</sub>), 172.93 (C<sub>18</sub>), 156.26 (C<sub>13</sub>), 154.13 (C<sub>1</sub>), 151.17 (C<sub>3</sub>), 150.37 (C<sub>17</sub>), 141.46 (C<sub>15</sub>), 136.86 (C<sub>4</sub>), 135.42 (C<sub>7</sub>), 130.03 (C<sub>6</sub>), 128.23 (C<sub>5</sub>), 125.64 (C<sub>14</sub>), 124.03 (C<sub>16</sub>), 119.85 (C<sub>2</sub>), 65.75 (C<sub>9</sub>), 63.90 (C<sub>12</sub>), 55.20 (C<sub>8</sub>), 9.38 (C<sub>10</sub>) ppm.

**HR-ESI-MS:** calcd. for [M+2H]<sup>+</sup> C<sub>33</sub>H<sub>31</sub>LuN<sub>5</sub>O<sub>10</sub>S m/z = 864.1194 found 864.1191.

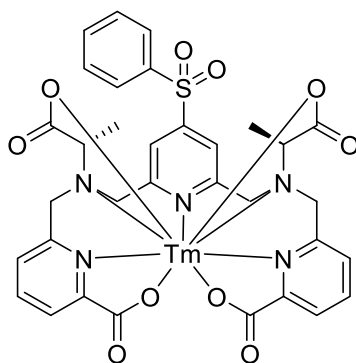
**Yb-PypaM2-SO<sub>2</sub>-Ph (38):** Yb-PypaM2-S-Ph (9.0 mg, 0.0109 mmol, 1.0 eq) was dissolved in water (5 ml). Then sodium tungstate dihydrate (3.0 mg, 0.00909 mmol, 0.8 eq) and hydrogen peroxide (30%, 10 μl, 0.0997 mmol, 9.1 eq.) were added. The suspension was stirred at 20-25°C for 100 h. During this time hydrogen peroxide (30%, 10 μl, 0.0997 mmol, 9.1 eq) was added four times approximately every 24 h. Then manganese dioxide (1.5 mg, 0.0173 mmol, 1.6 eq.) was added and the suspension was stirred for 15 min. Afterwards the crude product was directly purified by Sep-Pak column chromatography to yield Yb-PypaM2-SO<sub>2</sub>-Ph (8.4 mg, 0.00976 mmol, 90%) as a white solid.



**HR-ESI-MS:** calcd. for [M+2H]<sup>+</sup> C<sub>33</sub>H<sub>31</sub>N<sub>5</sub>O<sub>10</sub>SYb m/z = 863.1178 found 863.1183.

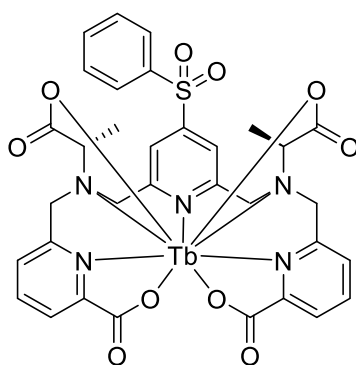


**Tm-PypaM2-SO<sub>2</sub>-Ph (38):** Tm-PypaM2-S-Ph (10 mg, 0.0121 mmol, 1.0 eq) was dissolved in water (4 ml). Then sodium tungstate dihydrate (8.3 mg, 0.0252 mmol, 2.1 eq) and hydrogen peroxide (30%, 12.2  $\mu$ l, 0.121 mmol, 10 eq.) were added. The suspension was stirred at 20-25°C for 140 h. After 48 h additional hydrogen peroxide (30%, 12.2  $\mu$ l, 0.121 mmol, 10 eq) was added. Then manganese dioxide (3.7 mg, 0.0426 mmol, 3.5 eq.) was added and the suspension was stirred for 30 min. Afterwards the crude product was directly purified by Sep-Pak column chromatography to yield Tm-PypaM2-SO<sub>2</sub>-Ph (9.6 mg, 0.0112 mmol, 92%) as a white solid.

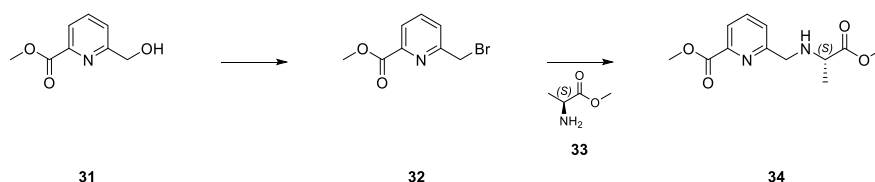


**HR-ESI-MS:** calcd. for  $[M+2H]^+$  C<sub>33</sub>H<sub>31</sub>N<sub>5</sub>O<sub>10</sub>STm m/z = 858.1128 found 858.1134.

**Tb-PypaM2-SO<sub>2</sub>-Ph (38):** Tb-PypaM2-S-Ph (5.0 mg, 0.00614 mmol, 1.0 eq) was dissolved in water (3 ml). Then sodium tungstate dihydrate (3.7 mg, 0.0112 mmol, 1.8 eq) and hydrogen peroxide (30%, 7  $\mu$ l, 0.0698 mmol, 11 eq.) were added. The suspension was stirred at 20-25°C for 77 h. During this time hydrogen peroxide (30%, 7  $\mu$ l, 0.0698 mmol, 1.0 eq) was added three times approximately every 24 h. Then manganese dioxide (3.5 mg, 0.0403 mmol, 6.6 eq.) was added and the suspension was stirred for 30 min. Afterwards the crude product was directly purified by Sep-Pak column chromatography to yield Tb-PypaM2-SO<sub>2</sub>-Ph (4.7 mg, 0.00555 mmol, 90%) as a white solid.

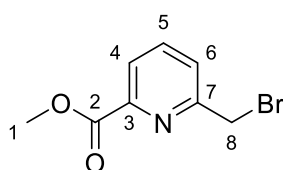


**HR-ESI-MS:** calcd. for  $[M+2H]^+$  C<sub>33</sub>H<sub>31</sub>N<sub>5</sub>O<sub>10</sub>STb m/z = 848.1040 found 848.1037.



**Figure S5:** Synthesis towards side arm **34**.

**Methyl 6-(bromomethyl)picolinate (32):** Methyl 6-(hydroxymethyl)picolinate (1.00 g, 5.98 mmol, 1.0 eq) was dissolved in dry chloroform (20 ml) and the solution was cooled to 0-5°C. Then phosphorous tribromide (0.87 ml, 2.43 g, 8.97 mmol, 1.5 eq.) was added slowly. The suspension was allowed to warm to 20-25°C and stirred for 23 h. Then the solution was cooled to 0-5°C and sat. aq. NaHCO<sub>3</sub> (50 ml) was added slowly to neutralize the solution. The layers were separated and the aqueous layer was extracted with methylene chloride (2\*20 ml). The combined organic layers were washed with brine (30 ml) and dried over sodium sulphate. The solvent was evaporated to yield methyl 6-(bromomethyl)picolinate (1.20 g, 5.22 mmol, 87%) as a white solid.



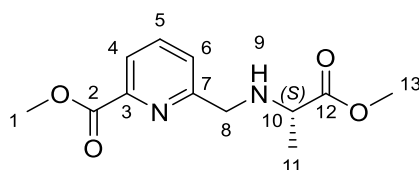
**<sup>1</sup>H NMR (500 MHz, Chloroform-*d*)**  $\delta$ : 8.06 (dd, <sup>3</sup>*J*<sub>HH</sub> = 7.77 Hz, <sup>4</sup>*J*<sub>HH</sub> = 1.04 Hz, 1H, H<sub>4</sub>), 7.87 (dd, <sup>3</sup>*J*<sub>HH</sub> = 7.77 Hz, 1H, H<sub>5</sub>), 8.06 (dd, <sup>3</sup>*J*<sub>HH</sub> = 7.77 Hz, <sup>4</sup>*J*<sub>HH</sub> = 1.04 Hz 1H, H<sub>6</sub>), 4.65 (s, 2H, H<sub>8</sub>), 4.02 (s, 3H, H<sub>1</sub>), ppm.

**<sup>13</sup>C NMR (126 MHz, Chloroform-*d*)**  $\delta$ : 165.51 (C<sub>2</sub>), 157.57 (C<sub>7</sub>), 147.78 (C<sub>3</sub>), 138.32 (C<sub>5</sub>), 127.27 (C<sub>6</sub>), 124.60 (C<sub>4</sub>), 53.25 (C<sub>1</sub>), 33.29 (C<sub>8</sub>) ppm.

**HR-ESI-MS:** calcd. for [M+H]<sup>+</sup> C<sub>8</sub>H<sub>9</sub>NBrO<sub>2</sub> *m/z* = 229.9811 found 229.9811.

**Methyl (S)-6-(((1-methoxy-1-oxopropan-2-yl)amino)methyl)picolinate (34):** Methyl 6-(bromomethyl) picolinate (600 mg, 2.61 mmol, 1.0 eq) was dissolved in dry acetonitrile (30 ml). Then L-alanine methyl ester hydrochloride (1.18 g, 8.45 mmol, 3.2 eq.) and potassium carbonate (2.48 g, 17.9 mmol, 6.9 eq.) was added. The suspension was stirred at 85°C for 18 h.

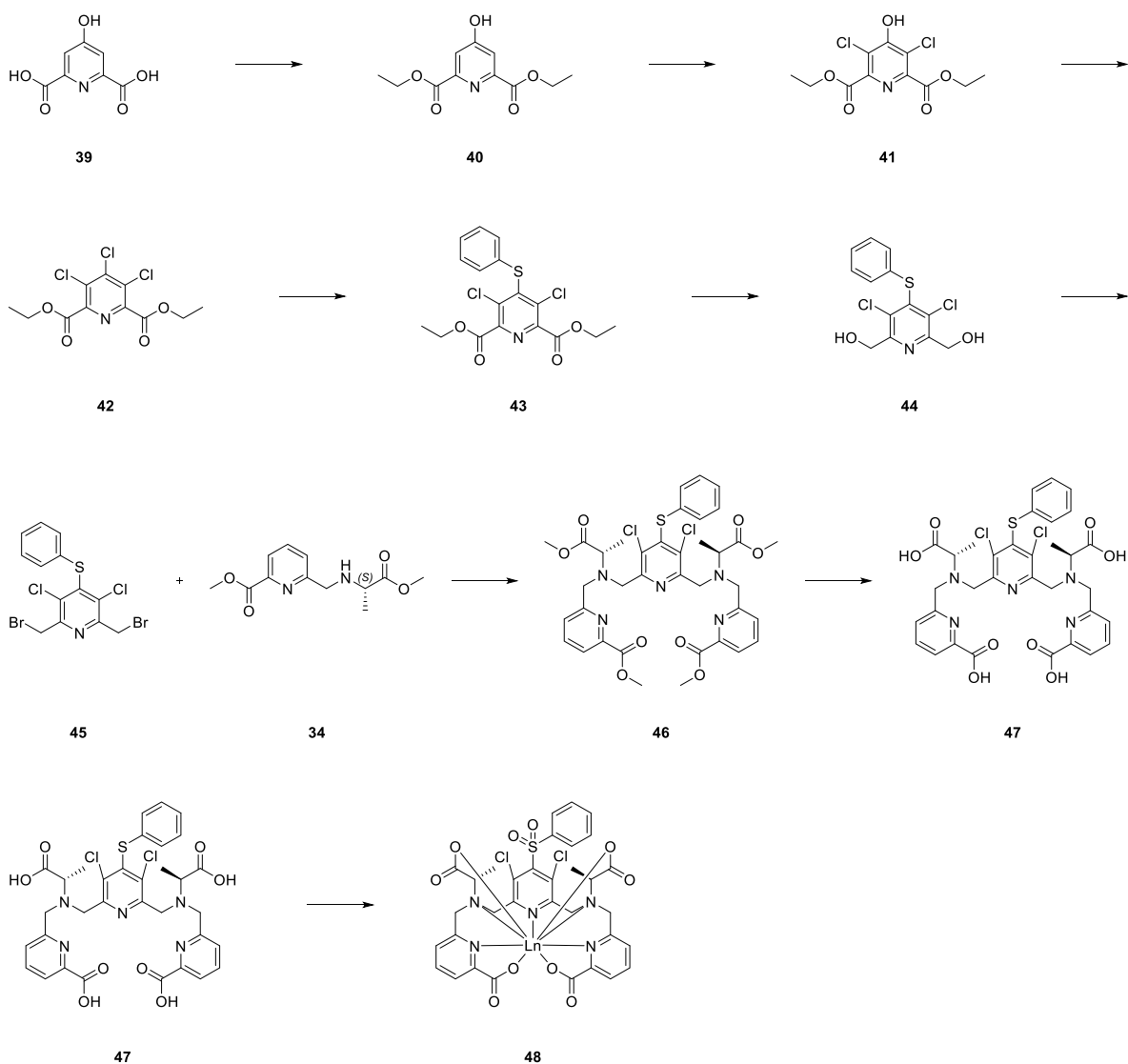
Then the suspension was allowed to cool to 20-25°C. Water (50 ml) and ethyl acetate (40 ml) were added and the layers were separated. The aqueous layer was extracted with ethyl acetate (2\*40 ml). The combined organic layers were washed with brine (50 ml) and dried over sodium sulphate. The solvent was evaporated and the crude product was purified by flash column chromatography (SiO<sub>2</sub>, methylene chloride : methanol (95:5), liquid deposit in methylene chloride) to yield methyl (*S*)-6-(((1-methoxy-1-oxopropan-2-yl)amino)methyl)picolinate (476 mg, 1.79 mmol, 69%) as a yellow oil.



**<sup>1</sup>H NMR (500 MHz, Chloroform-*d*)**  $\delta$ : 8.00 (m, 1H, H<sub>4</sub>), 7.81 (dd, <sup>3</sup>*J*<sub>HH</sub> = 7.70 Hz, <sup>3</sup>*J*<sub>HH</sub> = 7.70 Hz, 1H, H<sub>5</sub>), 7.64 (m, 1H, H<sub>6</sub>), 4.08 (d, <sup>2</sup>*J*<sub>HH</sub> = 14.89 Hz, 1H, H<sub>8a</sub>), 3.99 (s, 3H, H<sub>1</sub>), 3.93 (d, <sup>2</sup>*J*<sub>HH</sub> = 14.89 Hz, 1H, H<sub>8b</sub>), 3.72 (s, 3H, H<sub>13</sub>), 3.44 (q, <sup>3</sup>*J*<sub>HH</sub> = 6.99 Hz, 1H, H<sub>10</sub>), 1.36 (d, <sup>3</sup>*J*<sub>HH</sub> = 6.99 Hz, 3H, H<sub>11</sub>) ppm.

**<sup>13</sup>C NMR (126 MHz, Chloroform-*d*)**  $\delta$ : 175.89 (C<sub>12</sub>), 166.00 (C<sub>2</sub>), 160.55 (C<sub>7</sub>), 147.65 (C<sub>3</sub>), 137.61 (C<sub>5</sub>), 125.54 (C<sub>6</sub>), 123.73 (C<sub>4</sub>), 56.50 (C<sub>10</sub>), 53.35 (C<sub>8</sub>), 53.03 (C<sub>1</sub>), 52.06 (C<sub>13</sub>), 19.24 (C<sub>11</sub>) ppm.

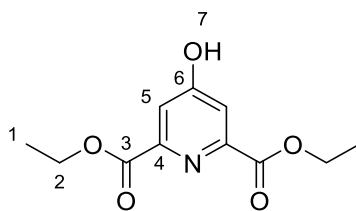
**HR-ESI-MS**: calcd. for [M+H]<sup>+</sup> C<sub>12</sub>H<sub>17</sub>N<sub>2</sub>O<sub>4</sub> *m/z* = 253.1183 found 253.1185.



**Figure S6:** Synthesis towards Ln-PypaM<sub>2</sub>Cl<sub>2</sub>-SO<sub>2</sub>-Ph (**48**).

**Diethyl 4-hydroxypyridine-2,6-dicarboxylate (40):** Thionyl chloride (4.8 ml, 7.80 g, 65.6 mmol, 4.0 eq) was dissolved in dry ethanol (30 ml). The solution was cooled to 0-5°C. Then chelidamic acid (3.00 g, 16.4 mmol, 1.0 eq.) was added in one portion and the solution was allowed to warm to 20-25°C for 5 h. Then the solution was heated to 80°C for 3 h. Afterwards the solution was cooled to 0-5°C. Water (20 ml) was added and the solution was neutralized with sat. aq. NaHCO<sub>3</sub> (ca. 150 ml). The aqueous layer was extracted with methylene chloride (3\*100 ml). The combined organic layers were washed with brine (100 ml) and dried over sodium sulphate. The solvent was evaporated until only a brown oil remained and taken off the rotary evaporator before it solidified. Then the oil was suspended in diethyl ether (10 ml). The resulting precipitate (might require some cooling to start the precipitation) was

filtered off and washed with diethyl ether to yield diethyl 4-hydroxypyridine-2,6-dicarboxylate (3.01 g, 12.6 mmol, 77%) as a brown solid.

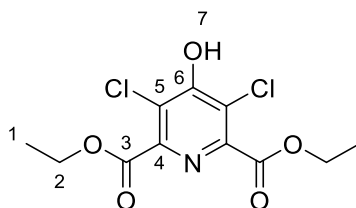


**<sup>1</sup>H NMR (500 MHz, Chloroform-*d* + K<sub>2</sub>CO<sub>3</sub>)**  $\delta$ : 7.41 (bs, 2H, H<sub>5</sub>), 4.42 (q, <sup>3</sup>*J*<sub>HH</sub> = 7.18 Hz, 4H, H<sub>2</sub>), 1.39 (t, <sup>3</sup>*J*<sub>HH</sub> = 7.18 Hz, 6H, H<sub>1</sub>) ppm.

**<sup>13</sup>C NMR (126 MHz, Chloroform- *d* + K<sub>2</sub>CO<sub>3</sub>)**  $\delta$ : 175.57 (C<sub>3</sub>), 163.37 (C<sub>4</sub>), 142.74 (C<sub>6</sub>), 118.91 (C<sub>5</sub>), 62.86 (C<sub>2</sub>), 14.09 (C<sub>1</sub>) ppm.

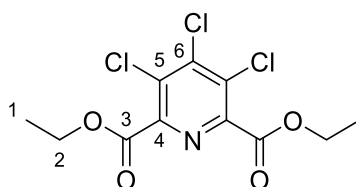
**HR-ESI-MS:** calcd. for [M+H]<sup>+</sup> C<sub>11</sub>H<sub>14</sub>NO<sub>5</sub> m/z = 240.0866 found 240.0867.

**Diethyl 3,5-dichloro-4-hydroxy pyridine-2,6-dicarboxylate (41):** Diethyl 4-hydroxypyridine-2,6-dicarboxylate (840 mg, 3.51 mmol, 1.0 eq) was dissolved in dry acetonitrile (20 ml). Then *N*-chlorosuccinimide (1.17 g, 8.76 mmol, 2.5 eq.) was added and the solution was heated to 70°C for 17 h. Then the solution was allowed to cool to 20-25°C and water (20 ml) was added. The solution was extracted with ethyl acetate (3\*20 ml). The combined organic layers were washed with water (20 ml) and brine (20 ml) and dried over sodium sulphate. The solvent was evaporated to yield diethyl 3,5-dichloro-4-hydroxypyridine-2,6-dicarboxylate (1.07 g, 3.48 mmol, 99%) as a brown solid which was used in the next step without further purification.



**HR-ESI-MS:** calcd. for [M+H]<sup>+</sup> C<sub>11</sub>H<sub>12</sub>Cl<sub>2</sub>NO<sub>5</sub> m/z = 308.0087 found 308.0081.

**Diethyl 3,4,5-trichloropyridine-2,6-dicarboxylate (42):** Diethyl 3,5-dichloro-4-hydroxypyridine-2,6-dicarboxylate (1.07 g, 3.48 mmol, 1.0 eq) was dissolved in dry acetonitrile (20 ml). Then phosphorus oxychloride (0.8 ml, 1.34 g, 8.74 mmol, 2.5 eq.) was added. The suspension was heated to 70°C for 16 h. Then the solution was cooled to 0-5°C and water (1 ml) was added. Afterwards the solution was allowed to warm to 20-25°C for 10 min. Then water (20 ml) and aq. sodium hydroxide (4 M, 10 ml) were added. The aqueous layer was extracted with ethyl acetate (2\*20 ml). The combined organic layers were washed with sat. aq. NaHCO<sub>3</sub> (30 ml), brine (30 ml) and dried over sodium sulphate. The solvent was evaporated and the crude product was purified by flash column chromatography (SiO<sub>2</sub>, cyclohexane : ethyl acetate (9:1), liquid deposit in ethyl acetate) to yield diethyl 3,4,5-trichloropyridine-2,6-dicarboxylate (704 mg, 2.16 mmol, 62%) as a white solid.

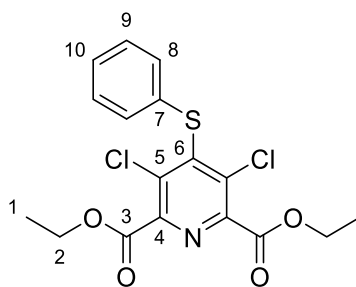


**<sup>1</sup>H NMR (500 MHz, Chloroform-*d*)**  $\delta$ : 4.48 (q, <sup>3</sup>*J*<sub>HH</sub> = 7.16 Hz, 4H, H<sub>2</sub>), 1.42 (t, <sup>3</sup>*J*<sub>HH</sub> = 7.16 Hz, 6H, H<sub>1</sub>) ppm.

**<sup>13</sup>C NMR (126 MHz, Chloroform-*d*)**  $\delta$ : 163.28 (C<sub>3</sub>), 147.56 (C<sub>4</sub>), 144.43 (C<sub>6</sub>), 131.38 (C<sub>5</sub>), 63.10 (C<sub>2</sub>), 14.19 (C<sub>1</sub>) ppm.

**HR-ESI-MS:** calcd. for [M+H]<sup>+</sup> C<sub>11</sub>H<sub>11</sub>Cl<sub>3</sub>NO<sub>4</sub> m/z = 325.9748 found 325.9744.

**Diethyl 3,5-dichloro-4-(phenylthio)pyridine-2,6-dicarboxylate (43):** Diethyl 3,4,5-trichloropyridine-2,6-dicarboxylate (209 mg, 0.640 mmol, 1.0 eq) was dissolved in dry acetonitrile (20 ml). Then thiophenol (64  $\mu$ l, 69.0 mg, 0.626 mmol, 0.98 eq.) and potassium carbonate (176 mg, 1.28 mmol, 2.0 eq.) were added. The suspension was stirred at 20-25°C for 5 h. Then the suspension was filtered and the solvent was evaporated. The crude product was purified by flash column chromatography (SiO<sub>2</sub>, pentane : methyl *tert*-butyl ether (9:1), liquid deposit in pentane : methyl *tert*-butyl ether (1:1)) to yield diethyl 3,5-dichloro-4-(phenylthio)pyridine-2,6-dicarboxylate (195 mg, 0.487 mmol, 76%) as a white oil.

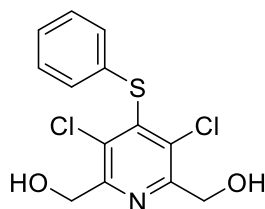


**<sup>1</sup>H NMR (500 MHz, Chloroform-*d*)**  $\delta$ : 7.34-7.24 (m, 5H, H<sub>8,9,10</sub>), 4.45 (q, <sup>3</sup>J<sub>HH</sub> = 7.12 Hz, 4H, H<sub>2</sub>), 1.40 (t, <sup>3</sup>J<sub>HH</sub> = 7.12 Hz, 6H, H<sub>1</sub>) ppm.

**<sup>13</sup>C NMR (126 MHz, Chloroform-*d*)**  $\delta$ : 163.89 (C<sub>3</sub>), 147.95 (C<sub>4</sub>), 146.54 (C<sub>6</sub>), 135.59 (C<sub>6</sub>), 132.26 (C<sub>7</sub>), 130.55 (C<sub>8/9</sub>), 129.73 (C<sub>8/9</sub>), 128.21 (C<sub>10</sub>), 62.95 (C<sub>2</sub>), 14.18 (C<sub>1</sub>) ppm.

**HR-ESI-MS**: calcd. for [M+H]<sup>+</sup> C<sub>17</sub>H<sub>16</sub>Cl<sub>2</sub>NO<sub>4</sub>S m/z = 400.0172 found 400.0172.

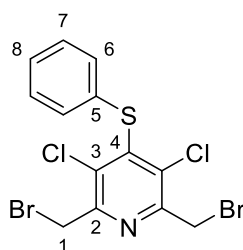
**(3,5-Dichloro-4-(phenylthio)pyridine-2,6-diyl)dimethanol (44)**: Diethyl 3,5-dichloro-4-(phenylthio)pyridine-2,6-dicarboxylate (174 mg, 0.435 mmol, 1.0 eq) was dissolved in dry ethanol (15 ml). Then sodium borohydride (100 mg, 2.64 mmol, 6.1 eq.) was added. The suspension was heated to 40°C for 15 h. Then the solution was allowed to cool to 20-25°C and water (25 ml) was added. The aqueous layer was extracted with ethyl acetate (3\*30 ml). The combined organic layers were washed with brine (25 ml) and dried over sodium sulphate. The solvent was evaporated to yield (3,5-dichloro-4-(phenylthio)pyridine-2,6-diyl)dimethanol (139 mg, 0.435 mmol, quant.) as a white solid. The product was used in the next step without further purification.



**HR-ESI-MS**: calcd. for [M+H]<sup>+</sup> C<sub>13</sub>H<sub>12</sub>Cl<sub>2</sub>NO<sub>2</sub>S m/z = 315.9960 found 315.9958.



**2,6-Bis(bromomethyl)-3,5-dichloro-4-(phenylthio)pyridine (45):** Diethyl 3,5-dichloro-4-(phenylthio) pyridine-2,6-dicarboxylate (137 mg, 0.433 mmol, 1.0 eq) was dissolved in dry acetonitrile (20 ml). Then phosphorous tribromide (163  $\mu$ l, 469 mg, 1.73 mmol, 4.0 eq.) was added. The solution was heated to 40°C for 75 min. Then the solution was allowed to cool to 20-25°C and the solvent was evaporated. The residue was suspended in water (30 ml) and sat. aq. NaHCO<sub>3</sub> (20 ml) was added. The aqueous layer was extracted with methylene chloride (3\*30 ml). The combined organic layers were washed with brine (50 ml) and dried over sodium sulphate. The solvent was evaporated and the crude product was purified by flash column chromatography (SiO<sub>2</sub>, cyclohexane : toluene (5:5), liquid deposit in eluent) to yield 2,6-bis(bromomethyl)-3,5-dichloro-4-(phenylthio)pyridine (78.5 mg, 0.178 mmol, 41%) as a white oil.



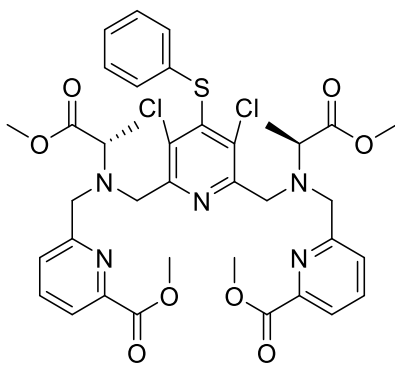
**<sup>1</sup>H NMR (500 MHz, Chloroform-*d*)  $\delta$ :** 7.33-7.20 (m, 5H, H<sub>6,7,8</sub>), 4.67 (s, 4H, H<sub>1</sub>), ppm.

**<sup>13</sup>C NMR (126 MHz, Chloroform-*d*)  $\delta$ :** 153.24 (C<sub>2</sub>), 145.15 (C<sub>4</sub>), 136.43 (C<sub>3</sub>), 133.24 (C<sub>5</sub>), 130.31 (C<sub>6/7</sub>), 129.85 (C<sub>6/7</sub>), 128.04 (C<sub>8</sub>), 31.84 (C<sub>1</sub>) ppm.

**HR-ESI-MS:** calcd. for [M+H]<sup>+</sup> C<sub>13</sub>H<sub>10</sub>Br<sub>2</sub>Cl<sub>2</sub>NS m/z = 439.8272 found 439.8270.

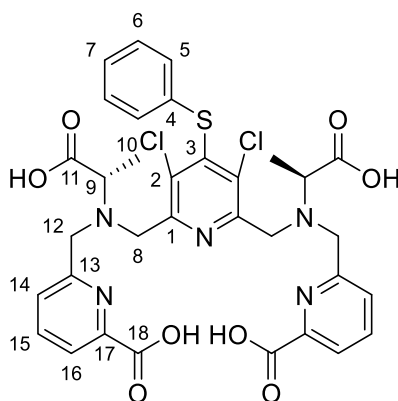
**Dimethyl 6,6'-((((3,5-dichloro-4-(phenylthio)pyridine-2,6-diyl)bis(methylene))bis(((S)-1-methoxy-1-oxopropan-2-yl)azanediyl))bis(methylene))dipicolinate (46):** 2,6-Bis (bromomethyl) -3,5- dichloro -4 -(phenylthio)pyridine (75.1 mg, 0.170 mmol, 1.0 eq) was dissolved in dry acetonitrile (9 ml) and dry methylene chloride (1 ml). Then methyl (*S*)-6-(((1-methoxy-1-oxopropan-2-yl)amino) methyl)picolinate (107 mg, 0.425 mmol, 2.5 eq.) dissolved in dry acetonitrile (3.2 ml), dry potassium carbonate (76.3 mg, 0.552 mmol, 3.2 eq) and dry potassium iodide (8.2 mg, 0.0494 mmol, 0.30 eq.) were added and the suspension was heated

to 85°C for 16 h. Afterwards the suspension was allowed to cool to 20-25°C. Then the suspension was filtered and the solvent was evaporated. The crude product was purified by prep. HPLC to yield dimethyl 6,6'-((((3,5-dichloro-4-(phenylthio)pyridine-2,6-diyl)bis(methylene)) bis (((S)-1-methoxy-1-oxopropan-2-yl)azanediyl)) bis (methylene)) dipicolinate (118 mg, 0.150 mmol, 88%) as a yellow oil.



**HR-ESI-MS:** calcd. for  $[M+H]^+$   $C_{37}H_{40}Cl_2N_5O_8S$   $m/z = 784.1969$  found 784.1970.

**6,6'-((((3,5-Dichloro-4- (phenylthio) pyridine -2,6- diyl) bis (methylene)) bis(((S)-1-carboxyethyl) azanediyl))bis(methylene))dipicolinic acid (47):** Dimethyl 6,6'-((((3,5-dichloro-4-(phenylthio)pyridine-2,6-diyl)bis(methylene)) bis (((S)-1-methoxy-1-oxopropan-2-yl) azanediyl)) bis (methylene)) dipicolinate (136 mg, 0.173 mmol, 1.0 eq) was dissolved in tetrahydrofuran (8 ml) and water (4 ml). Then aq. sodium hydroxide (4M, 346  $\mu$ l) was added. The solution was stirred vigorously at 20-25°C for 4 h. Then acetonitrile (20 ml) and trifluoroacetic acid (0.1 ml) were added. The solvent was evaporated and the crude product was purified by prep HPLC to yield 6,6'-((((3,5-dichloro-4- (phenylthio) pyridine -2,6- diyl) bis (methylene)) bis(((S)-1-carboxyethyl) azanediyl))bis(methylene))dipicolinic acid (102.5 mg, 0.141 mmol, 81%) as a colourless solid.



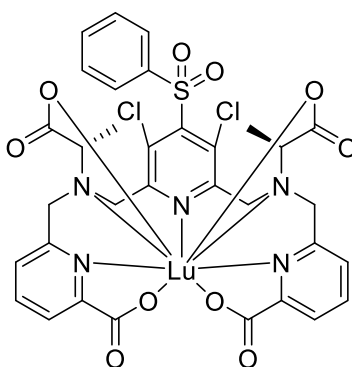
**$^1\text{H}$  NMR (500 MHz, Acetonitrile- $d_3$ )  $\delta$ :** 8.01-7.94 (m, 4H,  $\text{H}_{15,16}$ ), 7.65-7.60 (m, 2H,  $\text{H}_{14}$ ), 7.33-7.26 (m, 3H,  $\text{H}_{5/6,7}$ ), 7.15-7.10 (m, 2H,  $\text{H}_{5/6}$ ), 4.68-4.53 (m, 6H,  $\text{H}_{8a,12a,12b}$ ), 4.48 (d,  $^2J_{\text{HH}} = 15.66$  Hz, 2H,  $\text{H}_{8b}$ ), 4.32 (q,  $^3J_{\text{HH}} = 7.19$  Hz, 2H,  $\text{H}_9$ ), 1.61 (d,  $^3J_{\text{HH}} = 7.19$  Hz, 6H,  $\text{H}_{10}$ ) ppm.

**$^{13}\text{C}$  NMR (126 MHz, Acetonitrile- $d_3$ )  $\delta$ :** 172.66 ( $\text{C}_{11}$ ), 164.96 ( $\text{C}_{18}$ ), 152.70 ( $\text{C}_{13}$ ), 149.04 ( $\text{C}_1$ ), 147.09 ( $\text{C}_{17}$ ), 145.74 ( $\text{C}_3$ ), 141.10 ( $\text{C}_{15}$ ), 136.39 ( $\text{C}_2$ ), 133.00 ( $\text{C}_4$ ), 130.55 ( $\text{C}_{5/6}$ ), 130.45 ( $\text{C}_{5/6}$ ), 128.77 ( $\text{C}_7$ ), 128.05 ( $\text{C}_{14}$ ), 125.44 ( $\text{C}_{16}$ ), 63.12 ( $\text{C}_9$ ), 55.82 ( $\text{C}_{8,12}$ ), 12.09 ( $\text{C}_{10}$ ) ppm.

**HR-ESI-MS:** calcd. for  $[\text{M}+\text{H}]^+$   $\text{C}_{33}\text{H}_{32}\text{Cl}_2\text{N}_5\text{O}_8\text{S}$   $m/z = 728.1343$  found 728.1336.

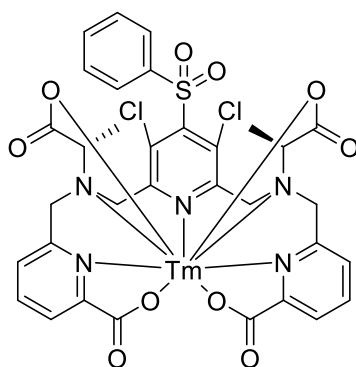
**Lu-PypaM2Cl<sub>2</sub>-SO<sub>2</sub>-Ph (48):** 6,6'-((((3,5-Dichloro-4- (phenylthio) pyridine -2,6- diyl) bis (methylene)) bis(((S)-1-carboxyethyl) azanediyl))bis(methylene))dipicolinic acid (3.3 mg, 0.00453 mmol, 1.0 eq.) was dissolved in aq. ammonium acetate (100 mM, 2 ml). Then

lutetium(III)trifluoromethanesulfonate (2.82 mg, 0.00453 mmol, 1.0 eq) dissolved in aq. ammonium acetate (100 mM, 90  $\mu$ l) was added. The solution was stirred at 20-25°C for 2 h. Afterwards glacial acetic acid (31  $\mu$ l, 32.5 mg, 0.542 mmol, 120 eq.), sodium tungstate dihydrate (18.2 mg, 0.0552 mmol, 12 eq.) and hydrogen peroxide (30%, 550  $\mu$ l, 18.3 mmol, 4040 eq) were added. The solution was stirred at 20-25°C for 6 days. Then the solvent was removed by lyophilisation and the crude product was purified by prep. HPLC (formic acid was used as an additive. The complex is unstable if TFA is used as an additive. The solvent was removed by lyophilisation) to yield Lu-PypaM2Cl<sub>2</sub>-SO<sub>2</sub>-Ph (1.2 mg, 0.00129 mmol, 28%) as a white solid.



**HR-ESI-MS:** calcd. for  $[M+2Na]^+$  C<sub>33</sub>H<sub>27</sub>Cl<sub>2</sub>LuN<sub>5</sub>Na<sub>2</sub>O<sub>10</sub>S m/z = 976.0053 found 976.0038.

**Tm-PypaM2Cl<sub>2</sub>-SO<sub>2</sub>-Ph (48):** 6,6'-((((3,5-Dichloro-4-(phenylthio)pyridine-2,6-diyl)bis(methylene))bis(((S)-1-carboxyethyl)azanediyl))bis(methylene))dipicolinic acid (3.3 mg, 0.00453 mmol, 1.0 eq.) was dissolved in aq. ammonium acetate (100 mM, 2 ml). Then thulium(III)trifluoromethanesulfonate (2.93 mg, 0.00476 mmol, 1.1 eq) dissolved in aq. ammonium acetate (100 mM, 89  $\mu$ l) was added. The solution was stirred at 20-25°C for 2 h. Afterwards glacial acetic acid (31  $\mu$ l, 32.5 mg, 0.542 mmol, 120 eq.), sodium tungstate dihydrate (21.8 mg, 0.0661 mmol, 15 eq.) and hydrogen peroxide (30%, 550  $\mu$ l, 18.3 mmol, 4040 eq) were added. The solution was stirred at 20-25°C for 9 days. Then the solvent was removed by lyophilisation and the crude product was purified by prep. HPLC (formic acid was used as an additive. The complex is unstable if TFA is used as an additive. The solvent was removed by lyophilisation) to yield Tm-PypaM2Cl<sub>2</sub>-SO<sub>2</sub>-Ph (2.3 mg, 0.00249 mmol, 55%) as a white solid.



**HR-ESI-MS:** calcd. for  $[M+2H]^+$   $C_{33}H_{29}Cl_2N_5O_{10}STm$   $m/z = 926.0349$  found 926.0332.

**Protein Tagging:** To a solution of Ubiquitin S57C (60  $\mu$ l, 1 mM in 10 mM phosphate, pH = 7.00) a phosphate buffer (440  $\mu$ l, 10 mM phosphate, 3.5 mM TCEP, pH = 7.00) was added. The solution was incubated in the fridge for 24 h to reduce disulphides. The buffer was exchanged by ultrafiltration (4x) (Amicon Ultra-4 Centrifugal Filters Ultracel-3K, Millipore) to a phosphate buffer (10 mM phosphate, 500  $\mu$ M TCEP, pH = 7.00). The Ubiquitin S57C concentration was adjusted to 0.400 mM (150  $\mu$ l). To the two samples a 6-fold excess of Ln-PypaM2Cl<sub>2</sub>-SO<sub>2</sub>Ph (**48**) loaded with either Lu or Tm was added and the sample was shaken for 65 h at 25°C. The reaction progress was monitored by HPLC-MS. The buffer was exchanged by ultrafiltration (4x) (Amicon Ultra-4 Centrifugal Filters Ultracel-3K, Millipore) to a phosphate buffer (10 mM phosphate, pH = 6.00). The final solution was concentrated to 250  $\mu$ l, the filter unit was washed with 40  $\mu$ l phosphate buffer (10 mM phosphate, pH = 6.00) and deuterium oxide (15  $\mu$ l) was added.

### 3.6.3 NMR Spectra TerPyM4

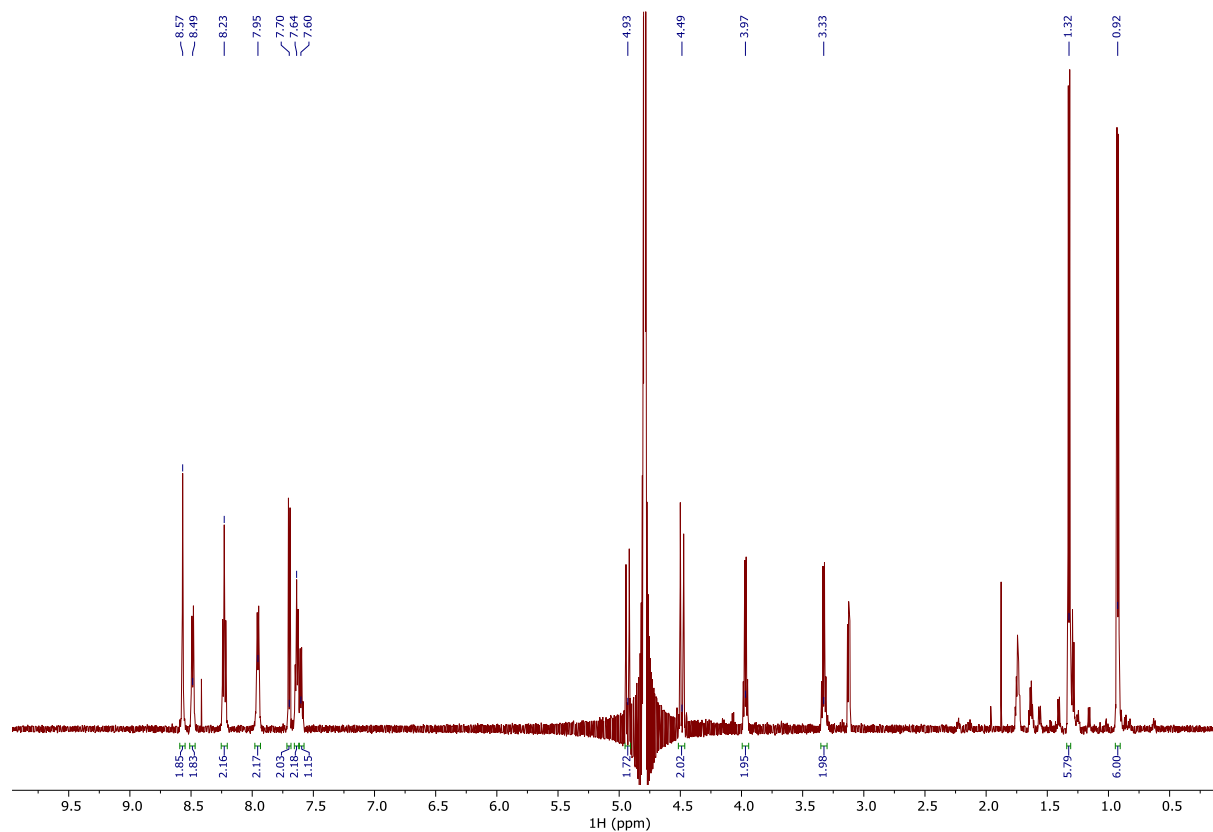


Figure S7:  $^1\text{H}$  NMR spectrum of Lu-TerPyM4-prototype complex in  $\text{D}_2\text{O}$ .

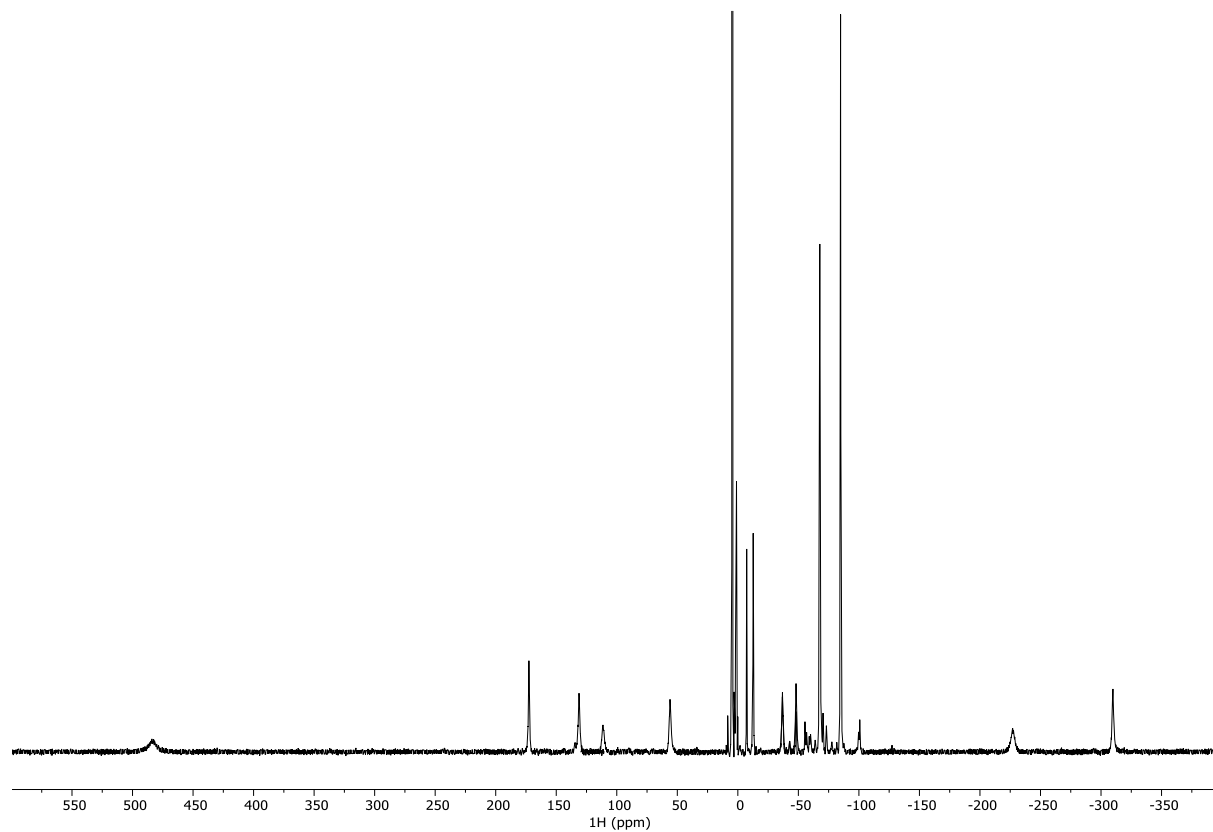
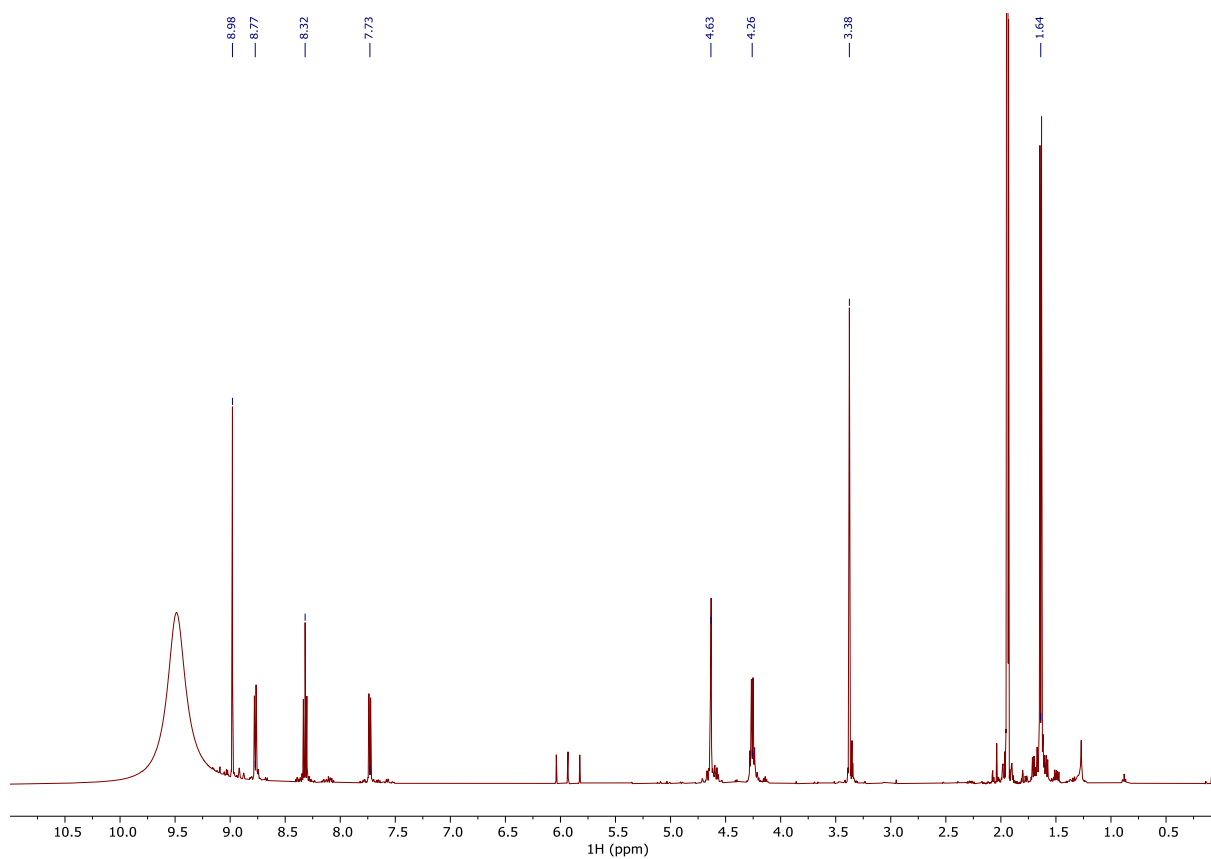
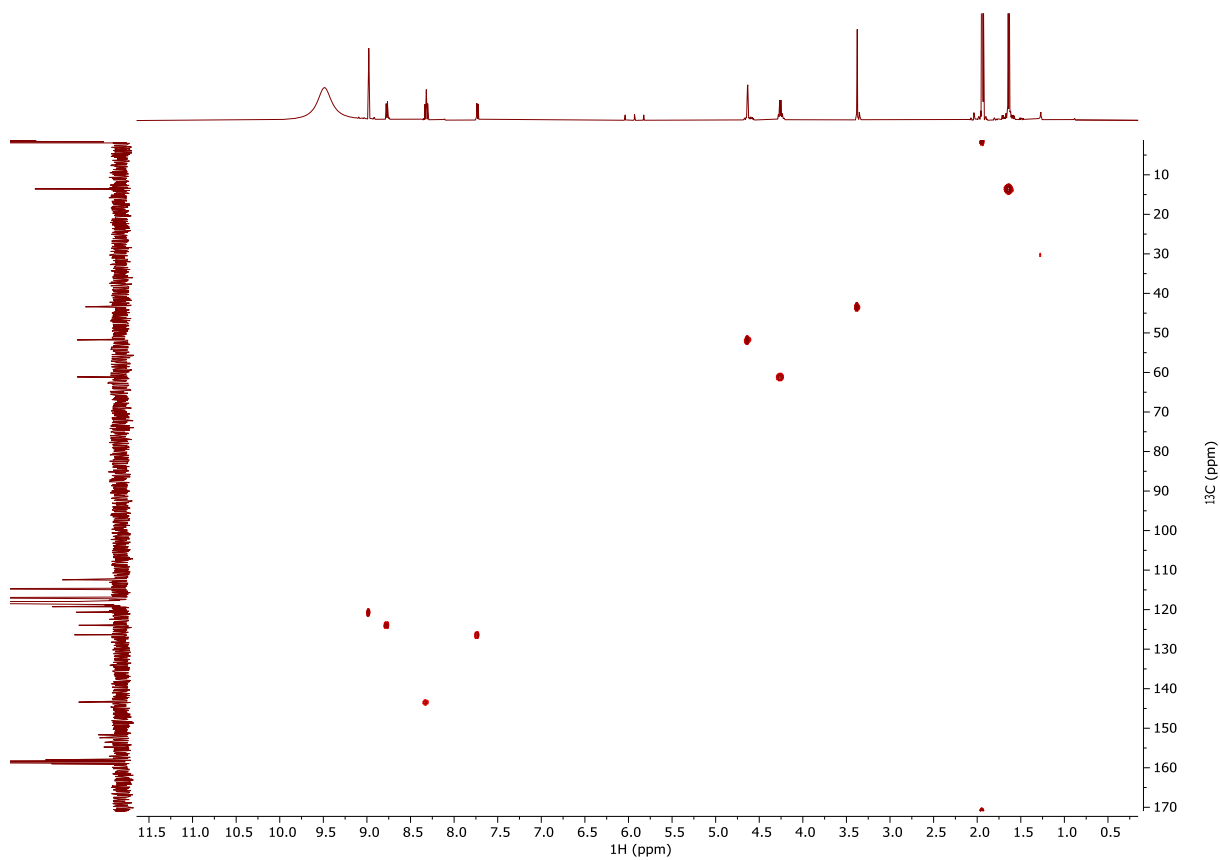


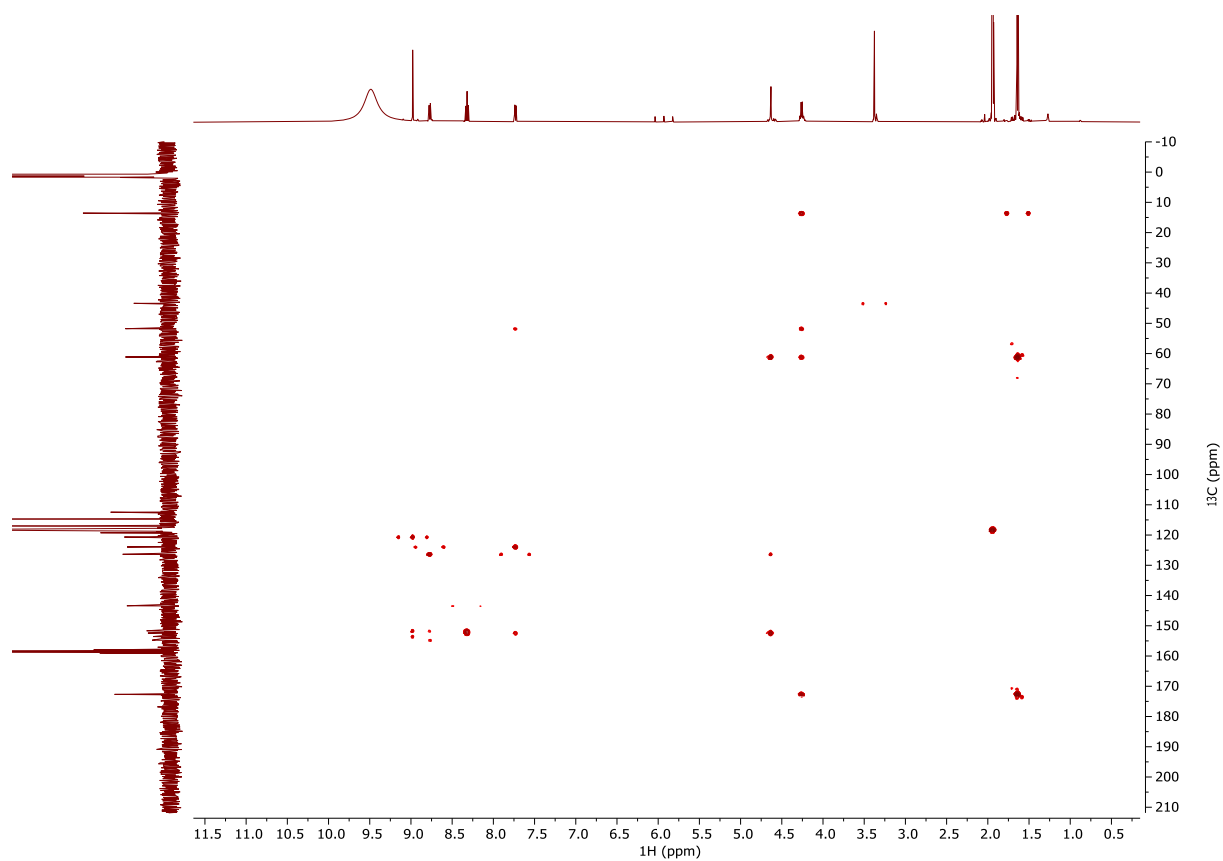
Figure S8:  $^1\text{H}$  NMR spectrum of Tm-TerPyM4-prototype complex in  $\text{D}_2\text{O}$ .



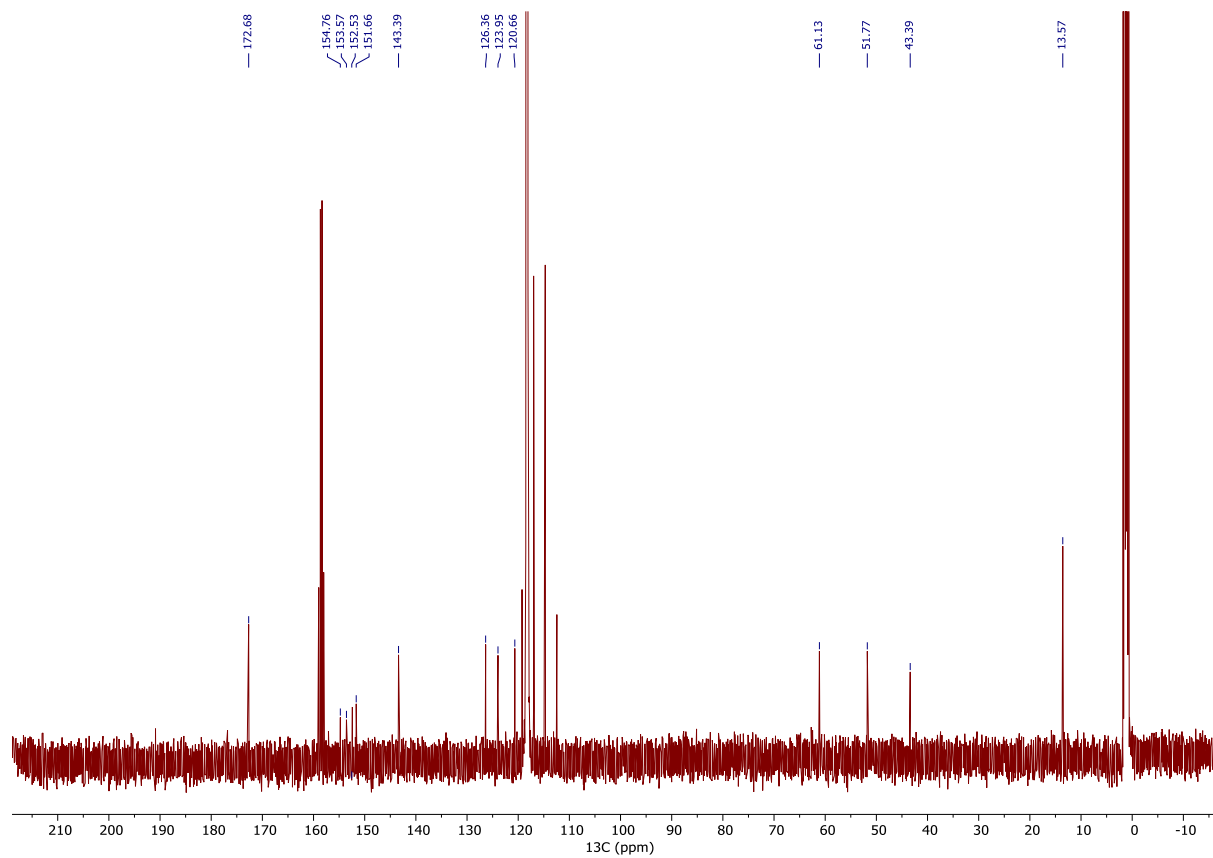
**Figure S9:**  $^1\text{H}$  NMR spectrum of TerPyM4-SO<sub>2</sub>-Me in CD<sub>3</sub>CN.



**Figure S10:**  $^1\text{H}$   $^{13}\text{C}$  HMQC spectrum of TerPyM4-SO<sub>2</sub>-Me in CD<sub>3</sub>CN.



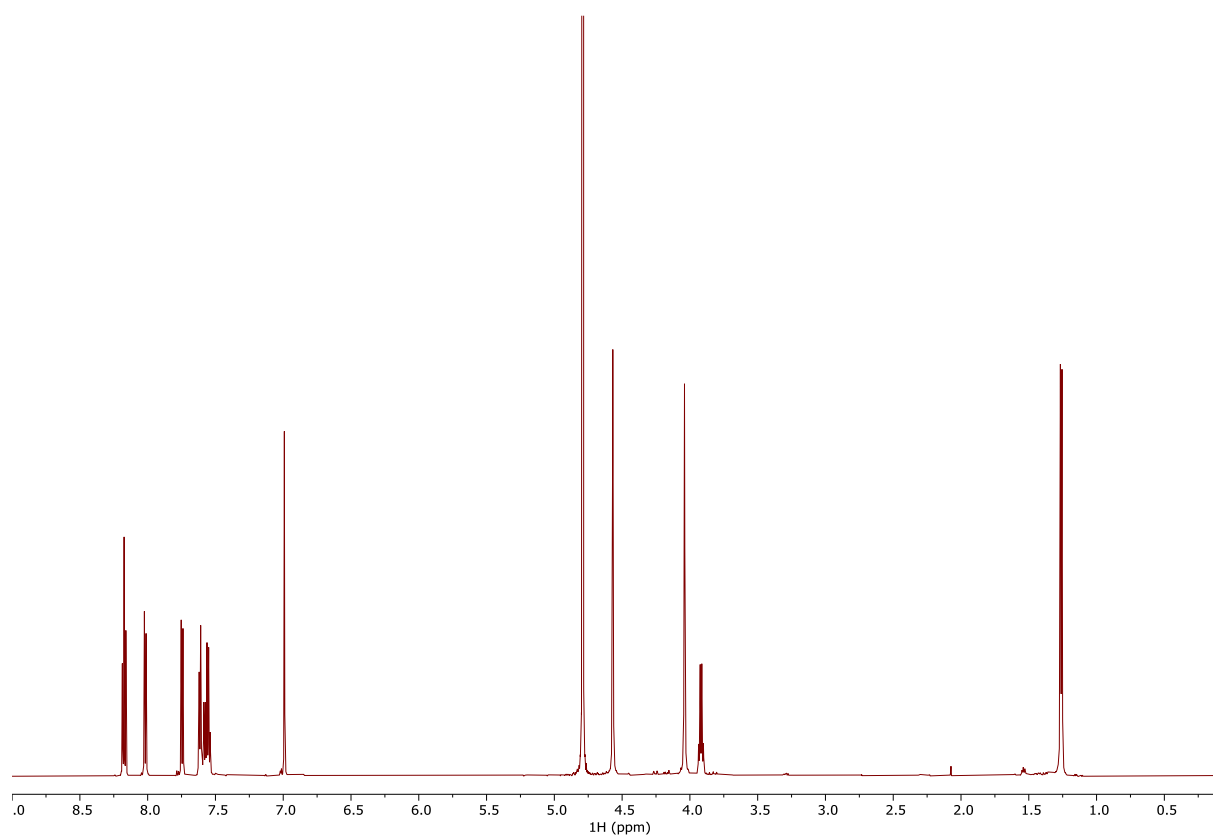
**Figure S11:**  $^1\text{H}$   $^{13}\text{C}$  HMBC spectrum of TerPyM4-SO<sub>2</sub>-Me in CD<sub>3</sub>CN.



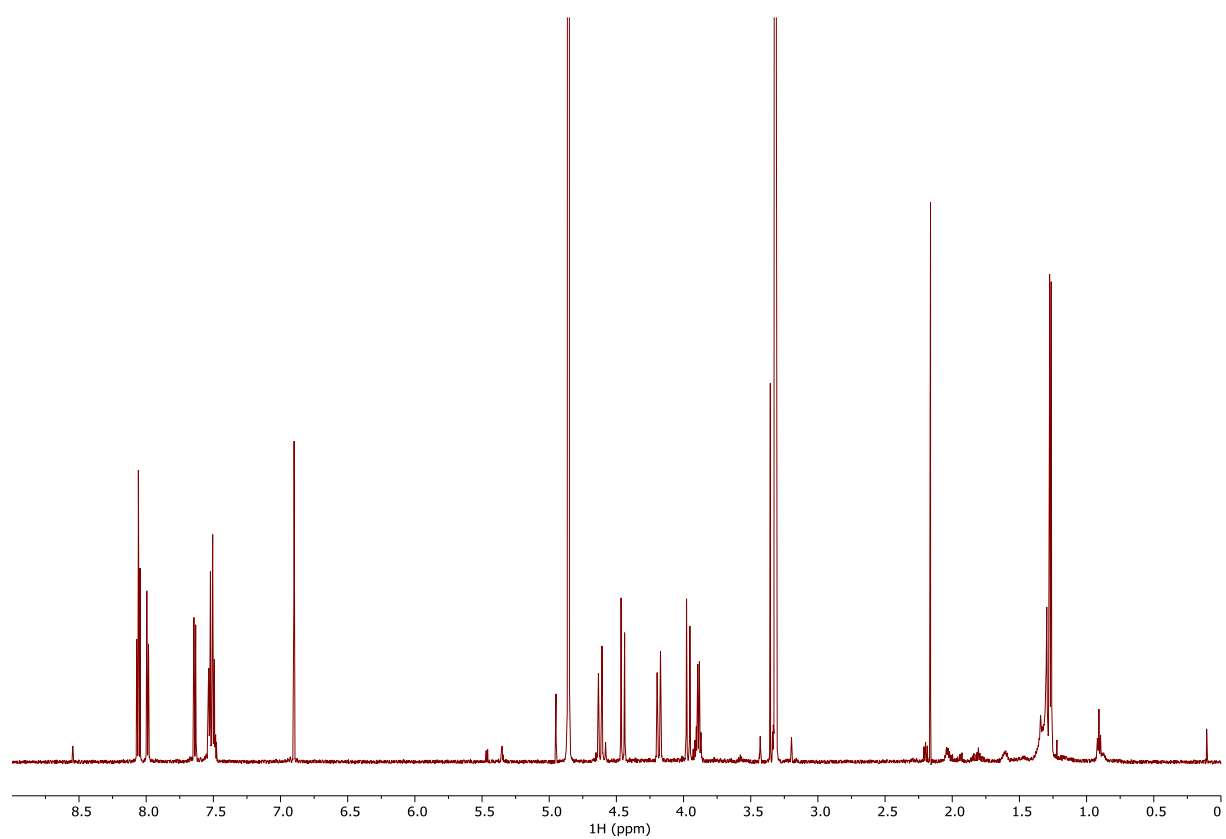
**Figure S12:**  $^{13}\text{C}\{^1\text{H}\}$  NMR spectrum of TerPyM4-SO<sub>2</sub>-Me in CD<sub>3</sub>CN.



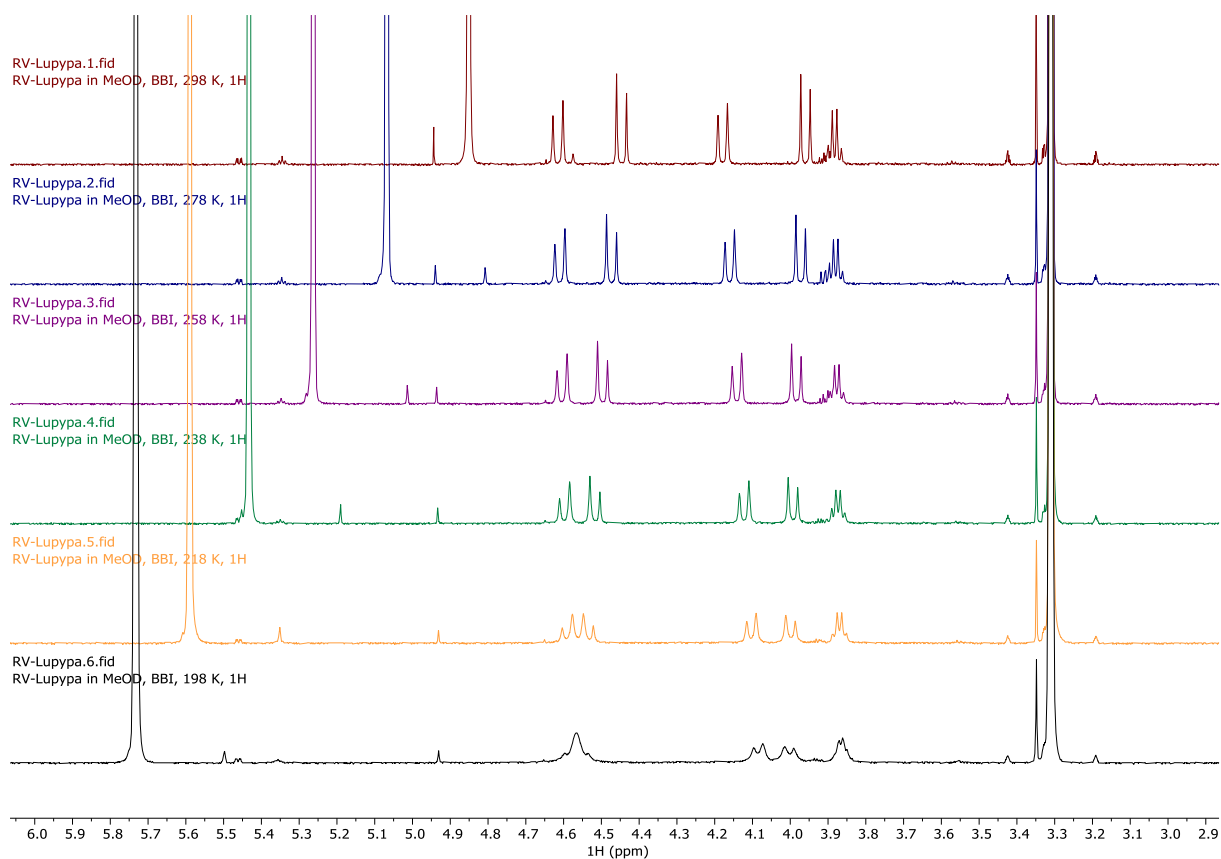
### 3.6.4 NMR Spectra PypaM2



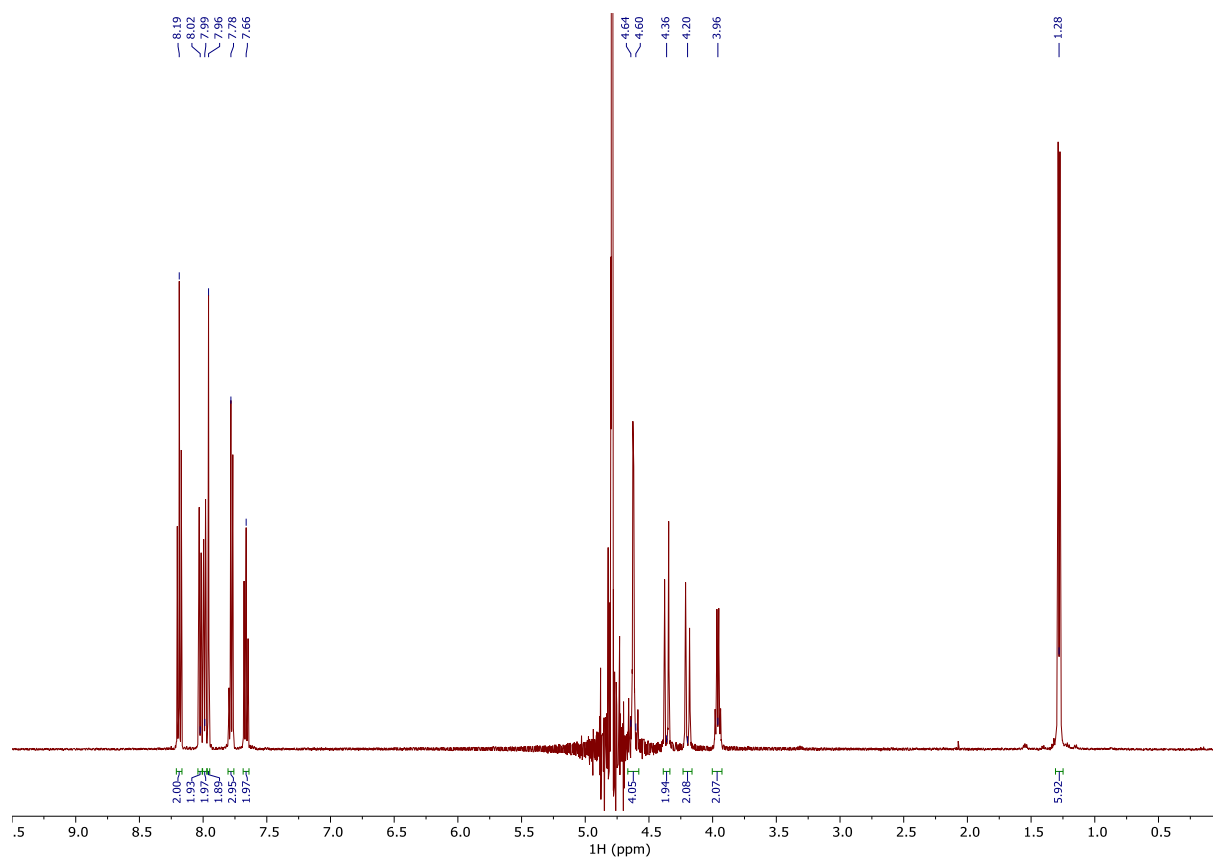
**Figure S13:** <sup>1</sup>H NMR spectrum of Lu-PypaM2-S-Ph in D<sub>2</sub>O.



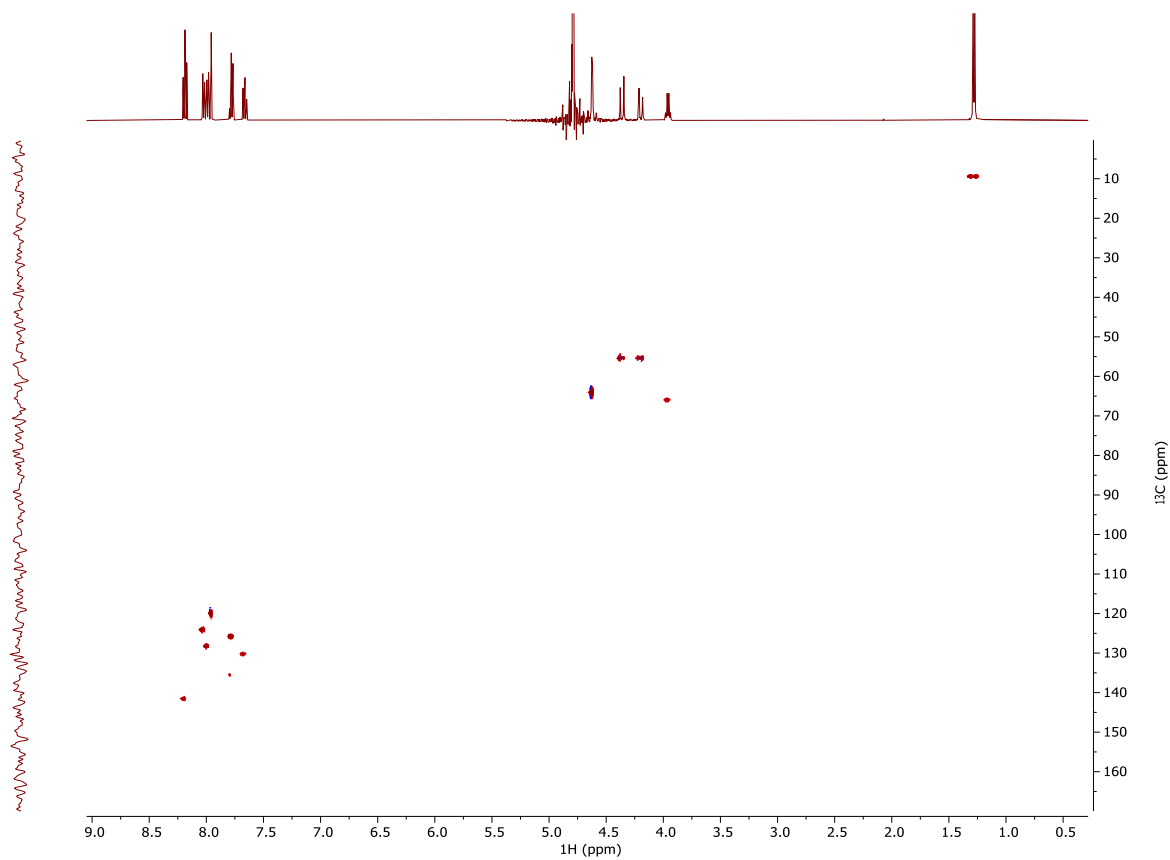
**Figure S14:** <sup>1</sup>H NMR spectrum of Lu-PypaM2-S-Ph in MeOD.



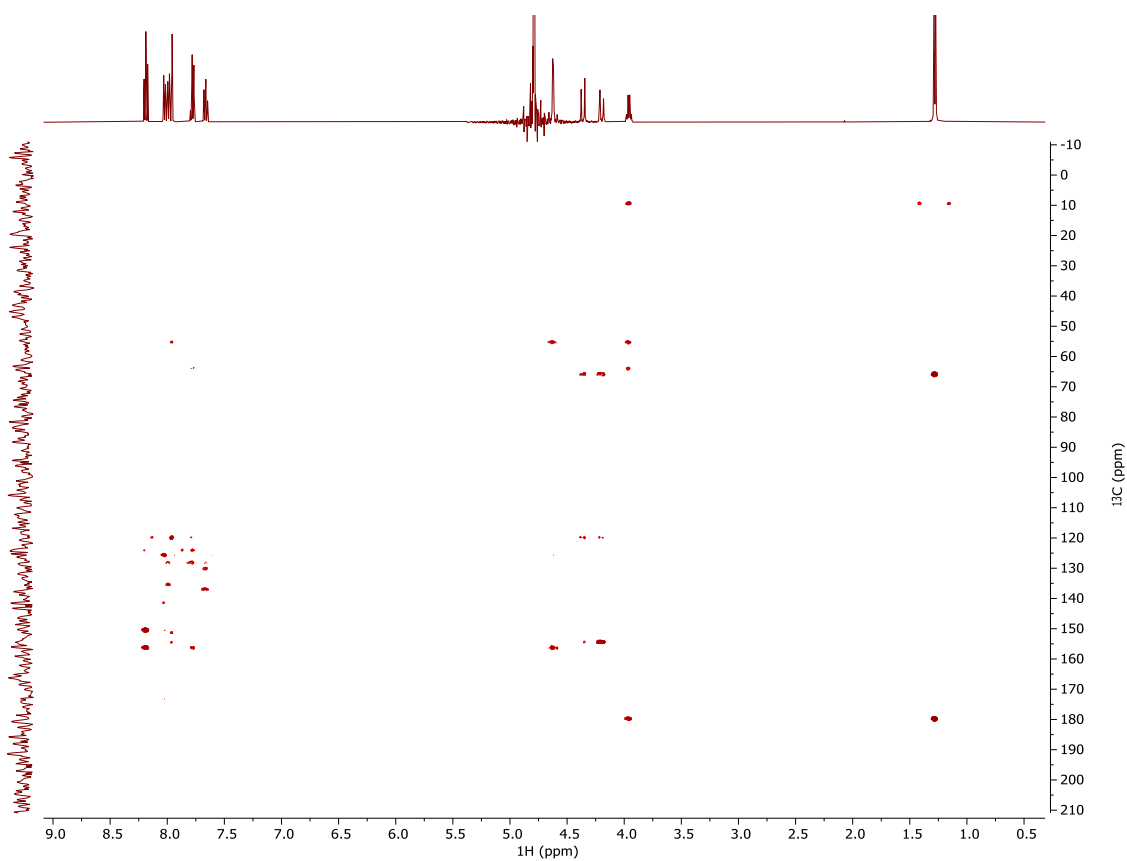
**Figure S15:** Stacked CH<sub>2</sub> regions of the <sup>1</sup>H NMR spectrum of Lu-PypaM2-S-Ph at different temperatures in MeOD. The spectra were recorded at 298 K (red), 278 K, (blue), 258 K (purple), 238 K (green), 218 K (orange) and 198 K (black). At 198 K the lines start to broaden due the increasing viscosity of methanol at low temperatures.



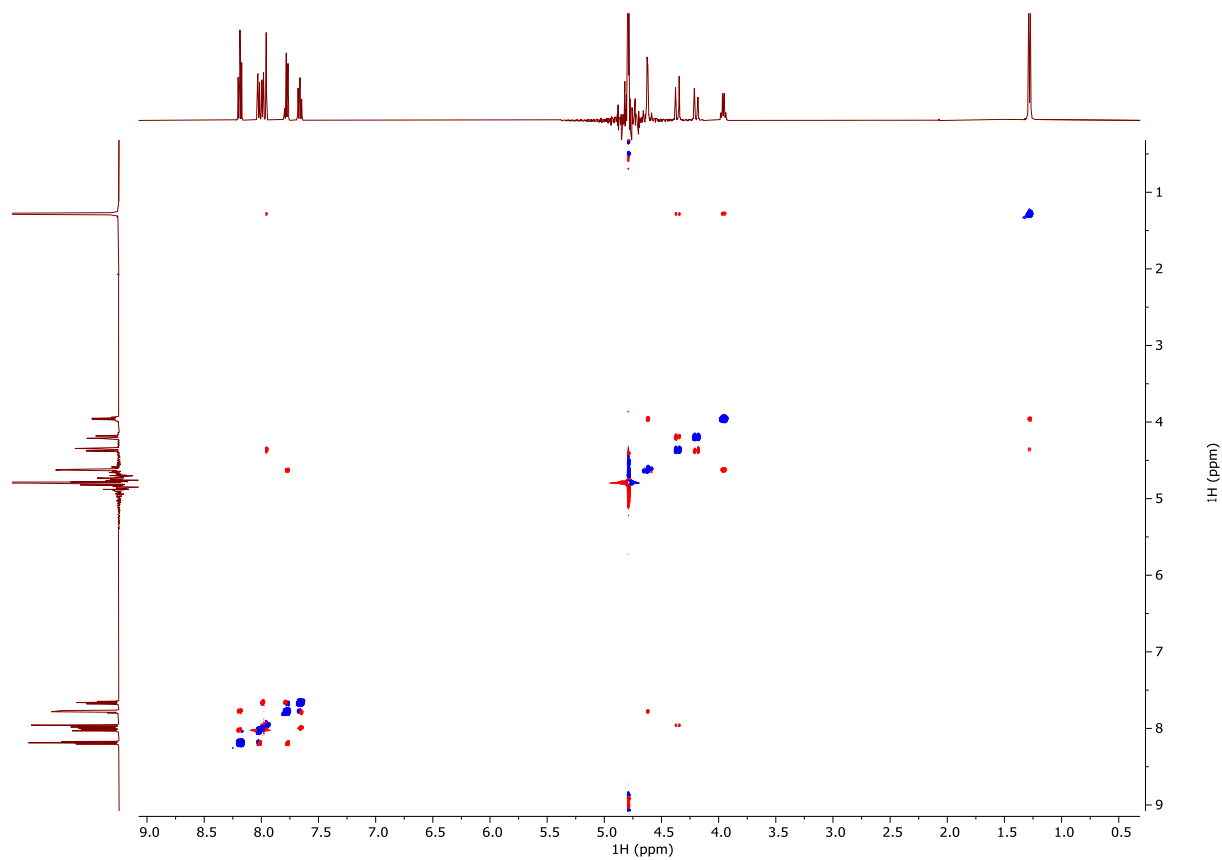
**Figure S16:**  $^1\text{H}$  NMR spectrum of Lu-PypaM2-SO<sub>2</sub>-Ph in D<sub>2</sub>O.



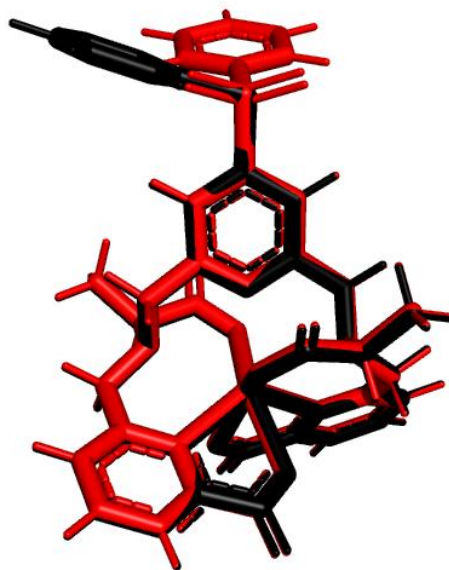
**Figure S17:**  $^1\text{H}$   $^{13}\text{C}$  HMQC spectrum of Lu-PypaM2-SO<sub>2</sub>-Ph in D<sub>2</sub>O.



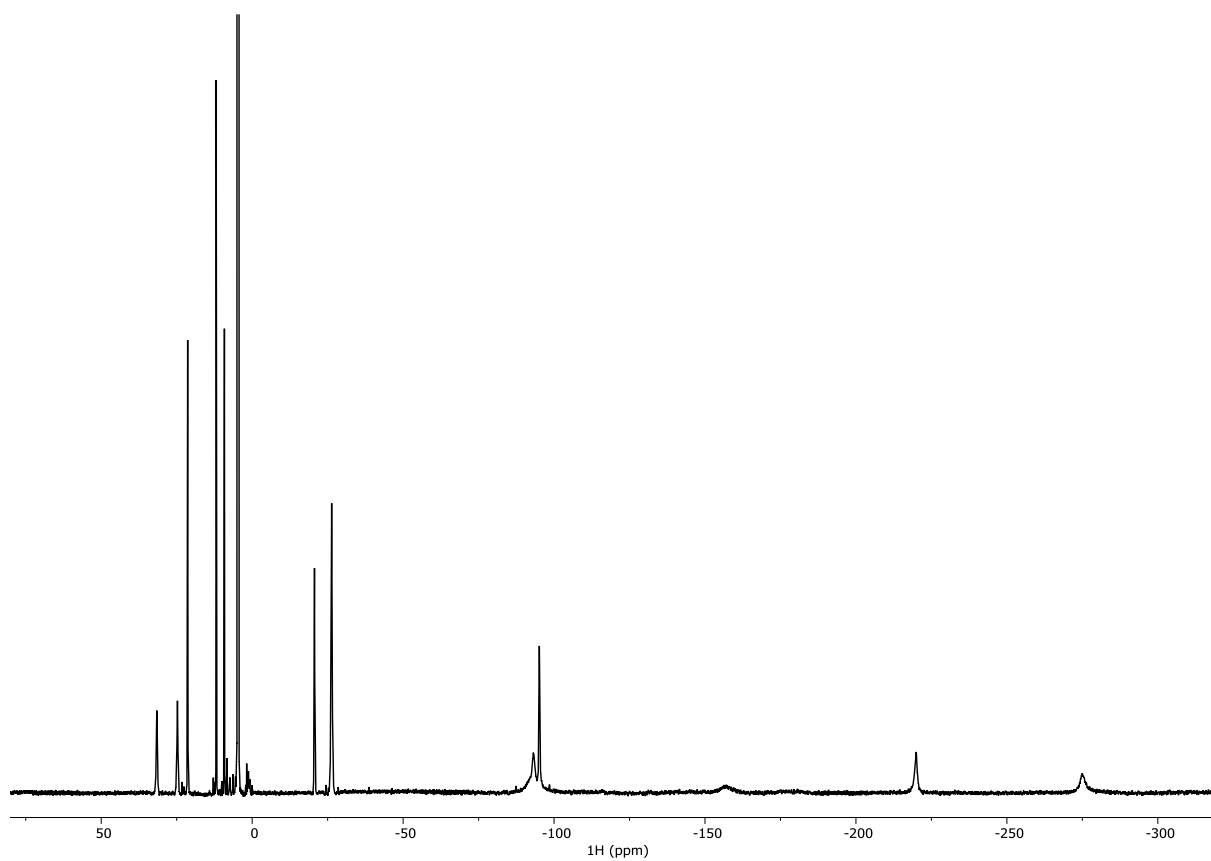
**Figure S18:** <sup>1</sup>H <sup>13</sup>C HMBC spectrum of Lu-PypaM2-SO<sub>2</sub>-Ph in D<sub>2</sub>O.



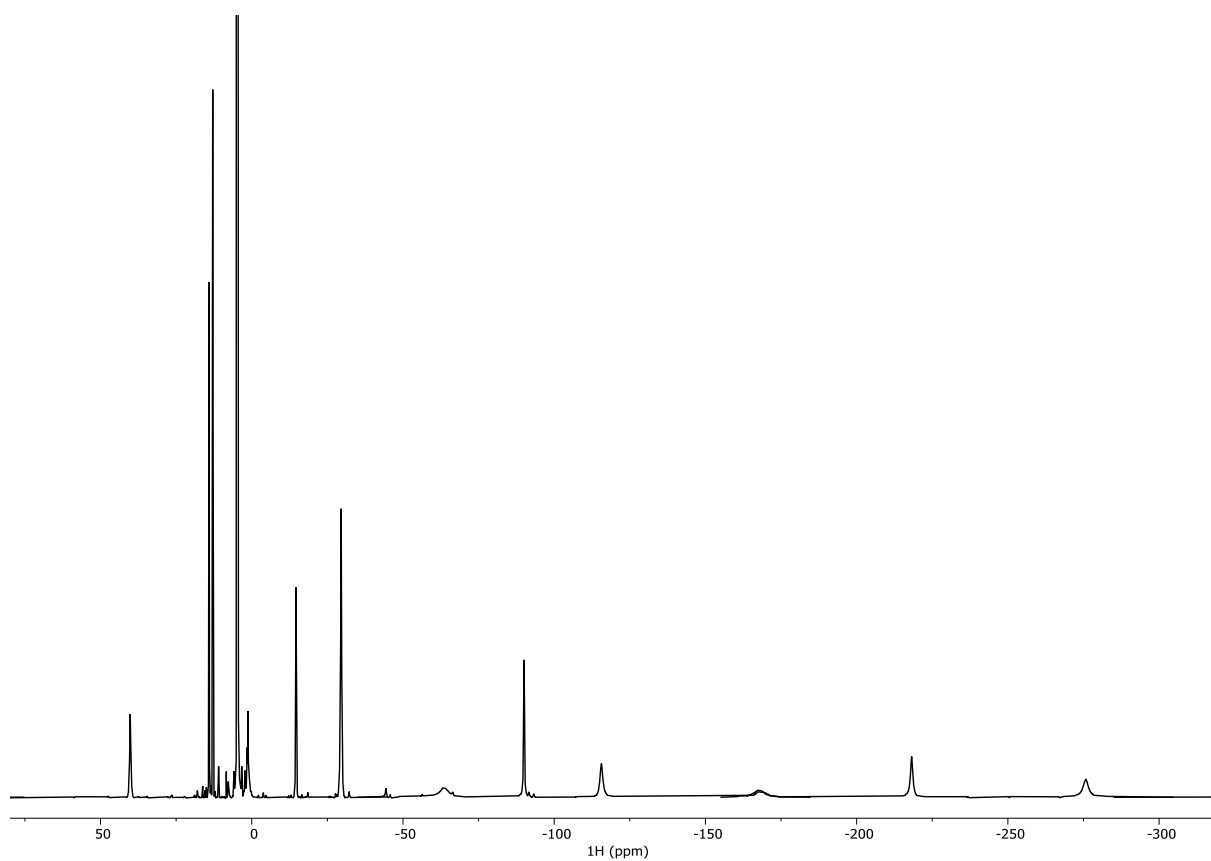
**Figure S19:** <sup>1</sup>H <sup>1</sup>H NOESY spectrum of Lu-PypaM2-SO<sub>2</sub>-Ph in D<sub>2</sub>O.



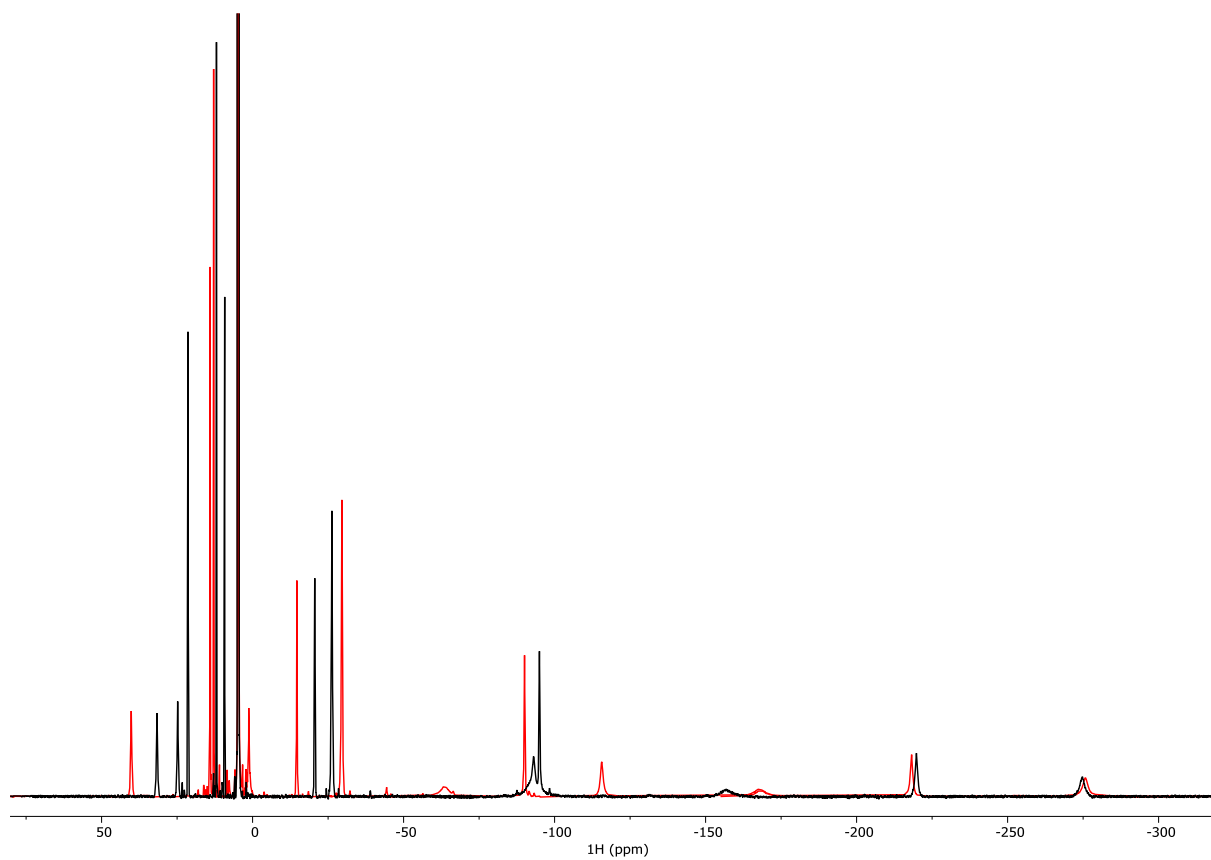
**Figure S20:** Superimposed DFT structures of Yb-PypaM2-S-Ph (black) and Yb-PypaM2-SO<sub>2</sub>-Ph (red).



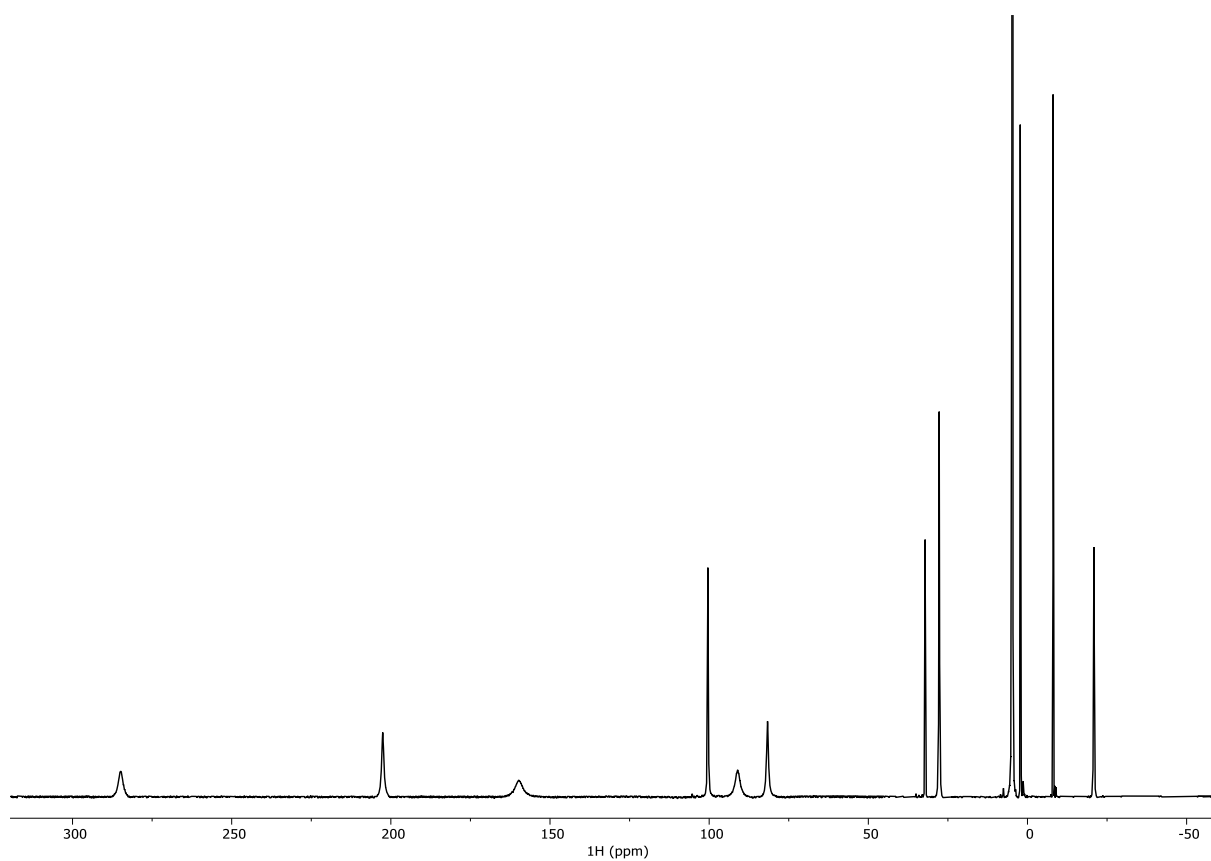
**Figure S21:** <sup>1</sup>H NMR spectrum of Tb-PypaM2-S-Ph in D<sub>2</sub>O at pH=8.85.



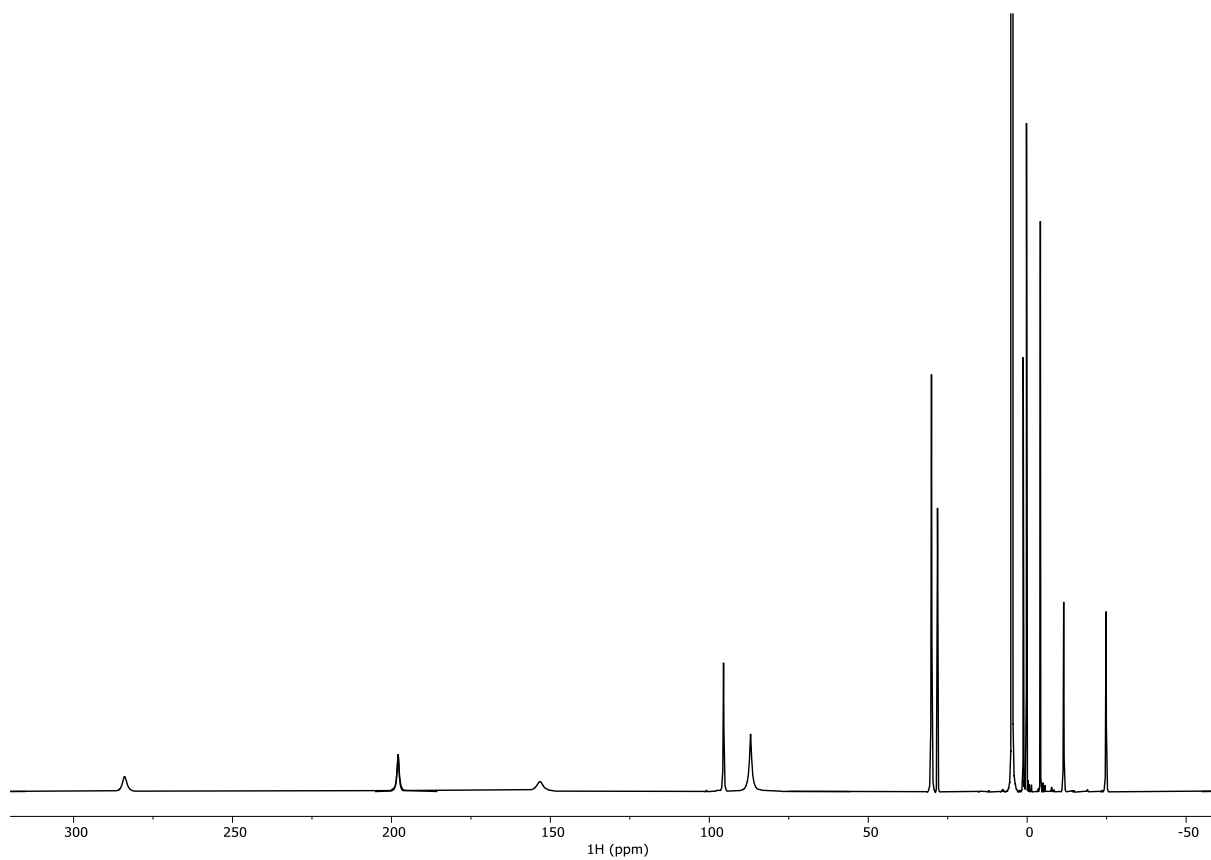
**Figure S22:** <sup>1</sup>H NMR spectrum of Tb-PypaM2-SO<sub>2</sub>-Ph in D<sub>2</sub>O at pH=7.62.



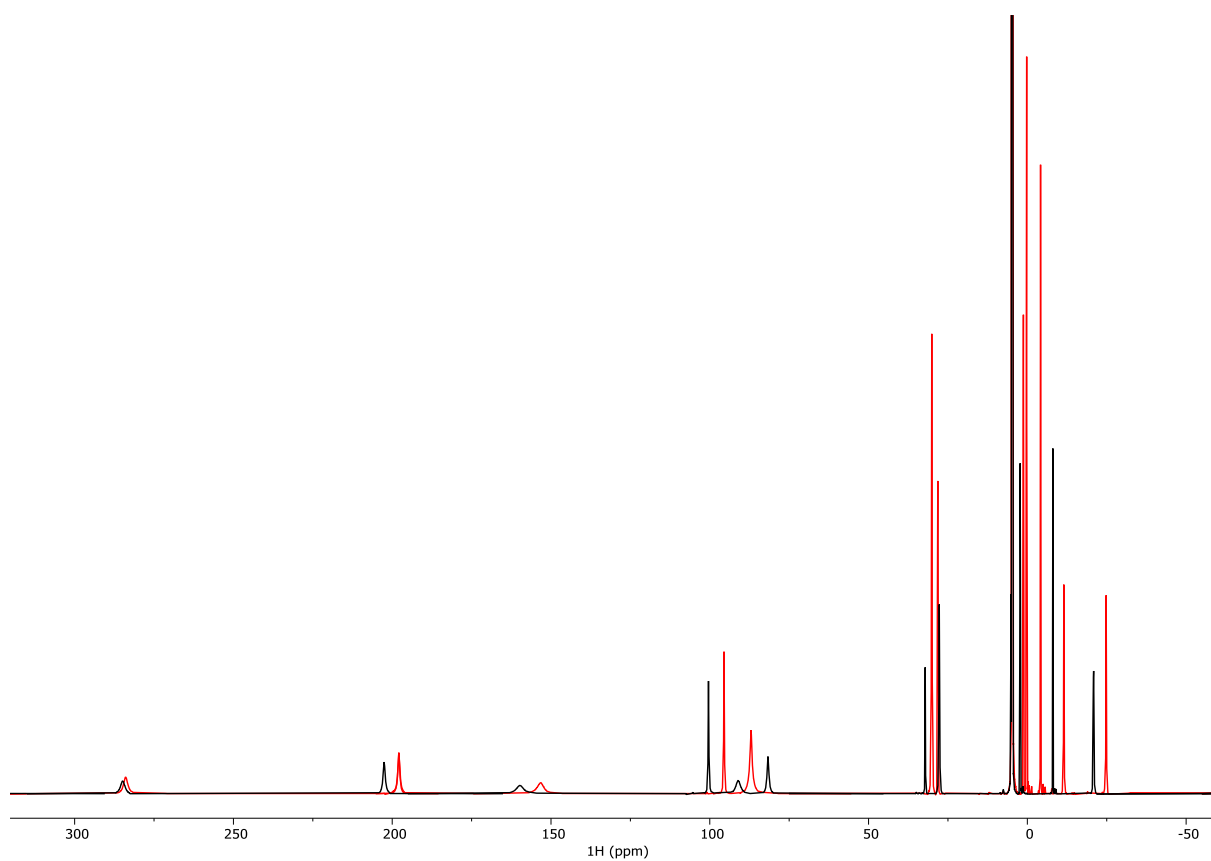
**Figure S23:** Superimposed <sup>1</sup>H NMR spectra of Tb-PypaM2-S-Ph (black) and Tb-PypaM2-SO<sub>2</sub>-Ph (red).



**Figure S24:**  $^1\text{H}$  NMR spectrum of Tm-PypaM2-S-Ph in  $\text{D}_2\text{O}$  at  $\text{pH}=8.10$ .

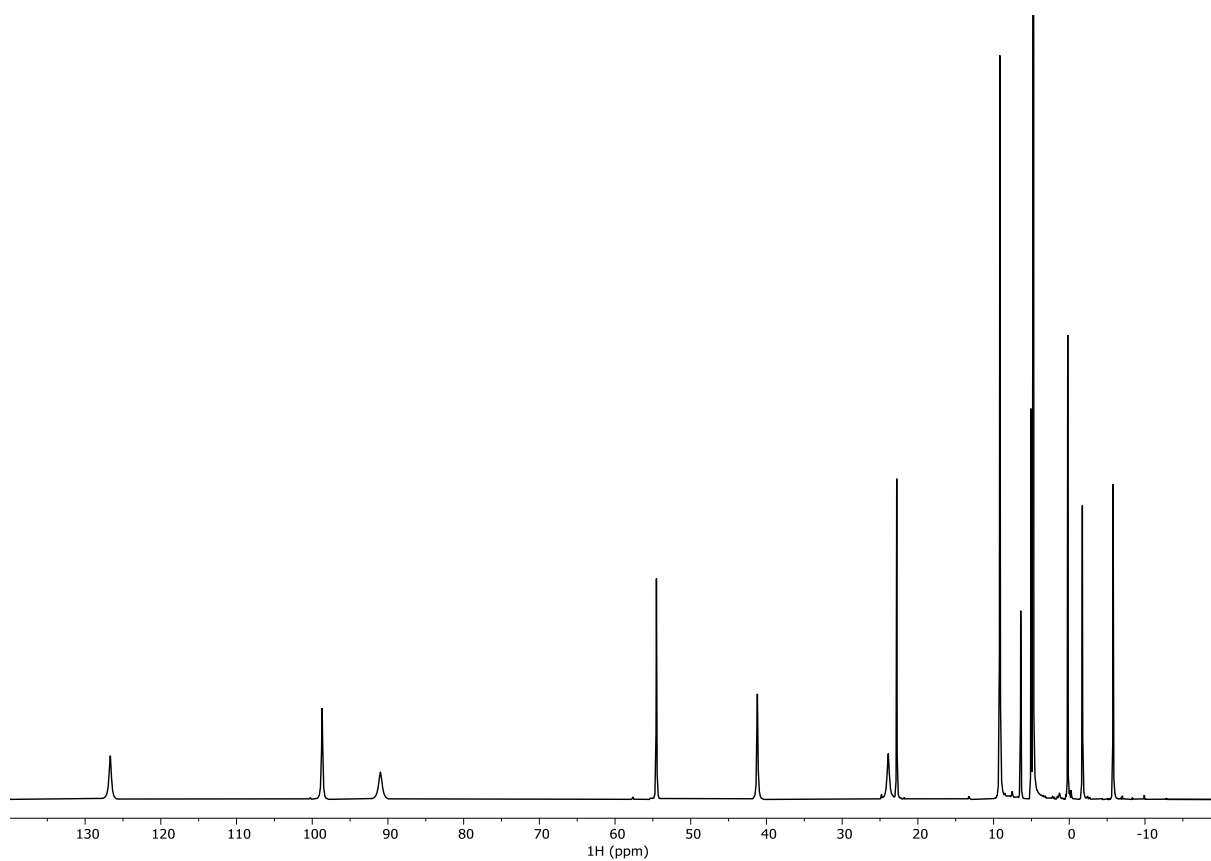


**Figure S25:**  $^1\text{H}$  NMR spectrum of Tm-PypaM2-SO<sub>2</sub>-Ph in  $\text{D}_2\text{O}$  at  $\text{pH}=7.56$ .

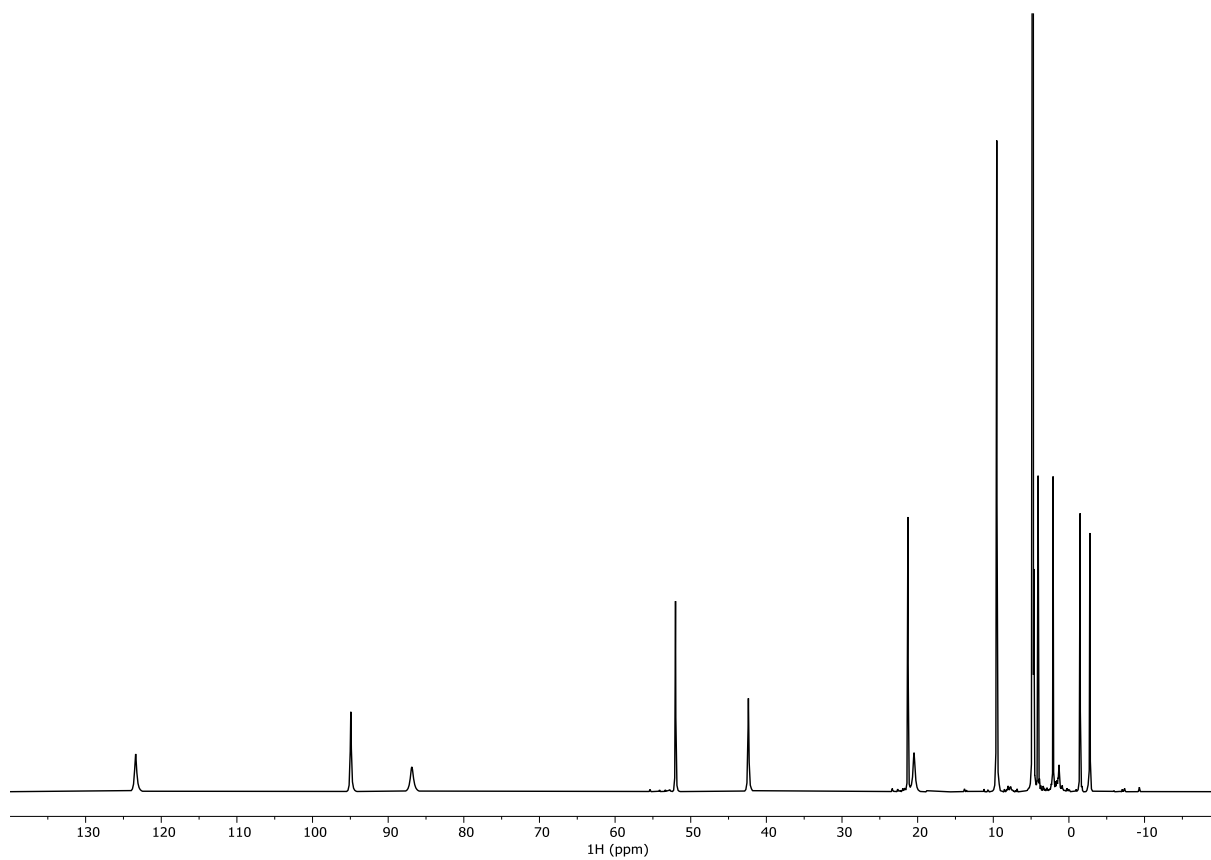


**Figure S26:** Superimposed <sup>1</sup>H NMR spectra of Tm-PypaM2-S-Ph (black) and Tm-PypaM2-SO<sub>2</sub>-Ph (red).

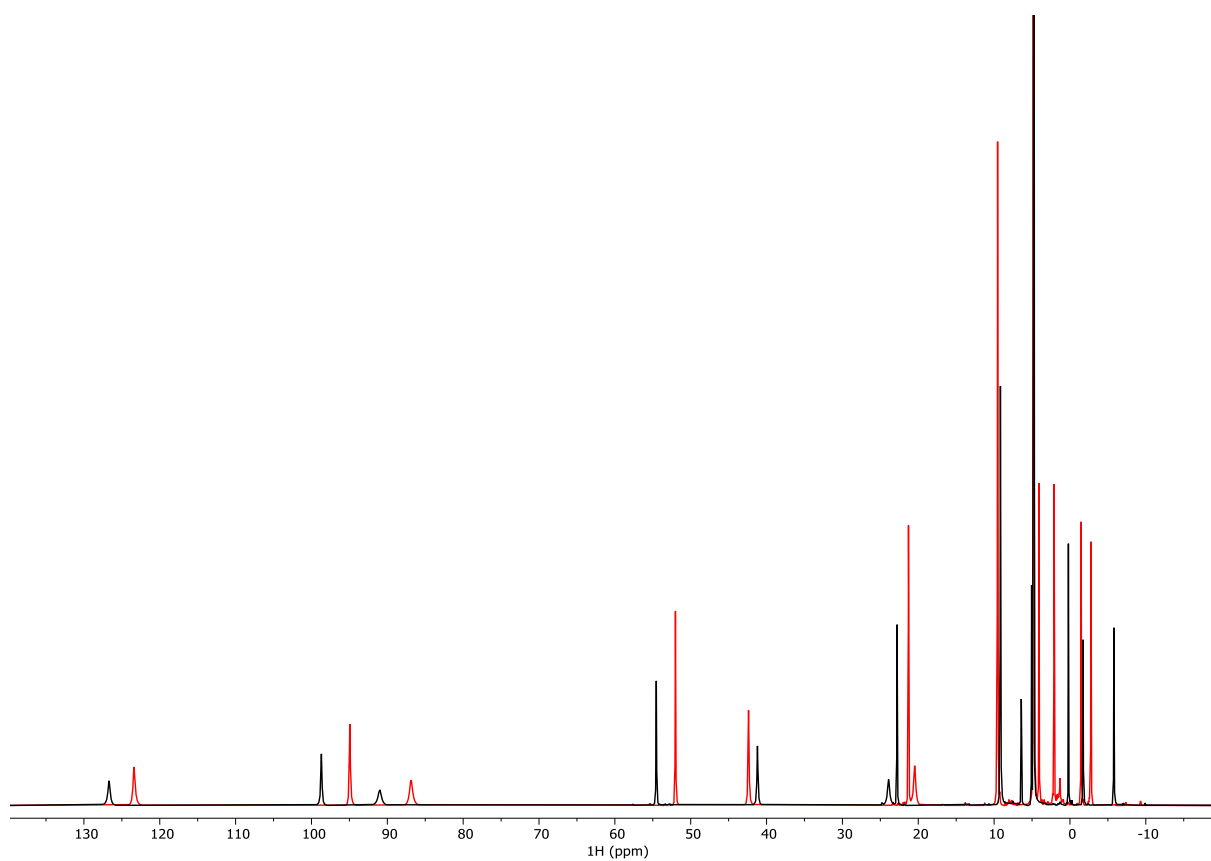




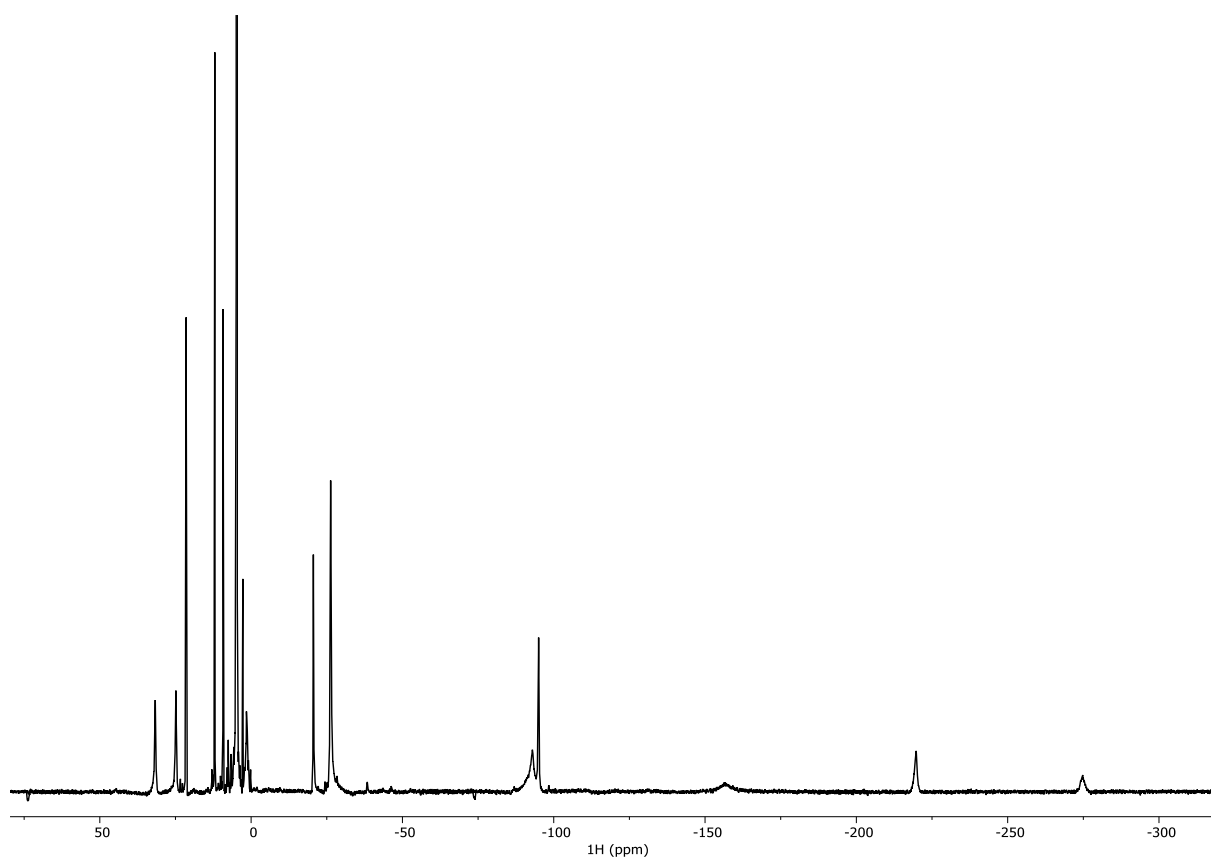
**Figure S27:**  $^1\text{H}$  NMR spectrum of Yb-PypaM2-S-Ph in  $\text{D}_2\text{O}$  at pH=7.69.



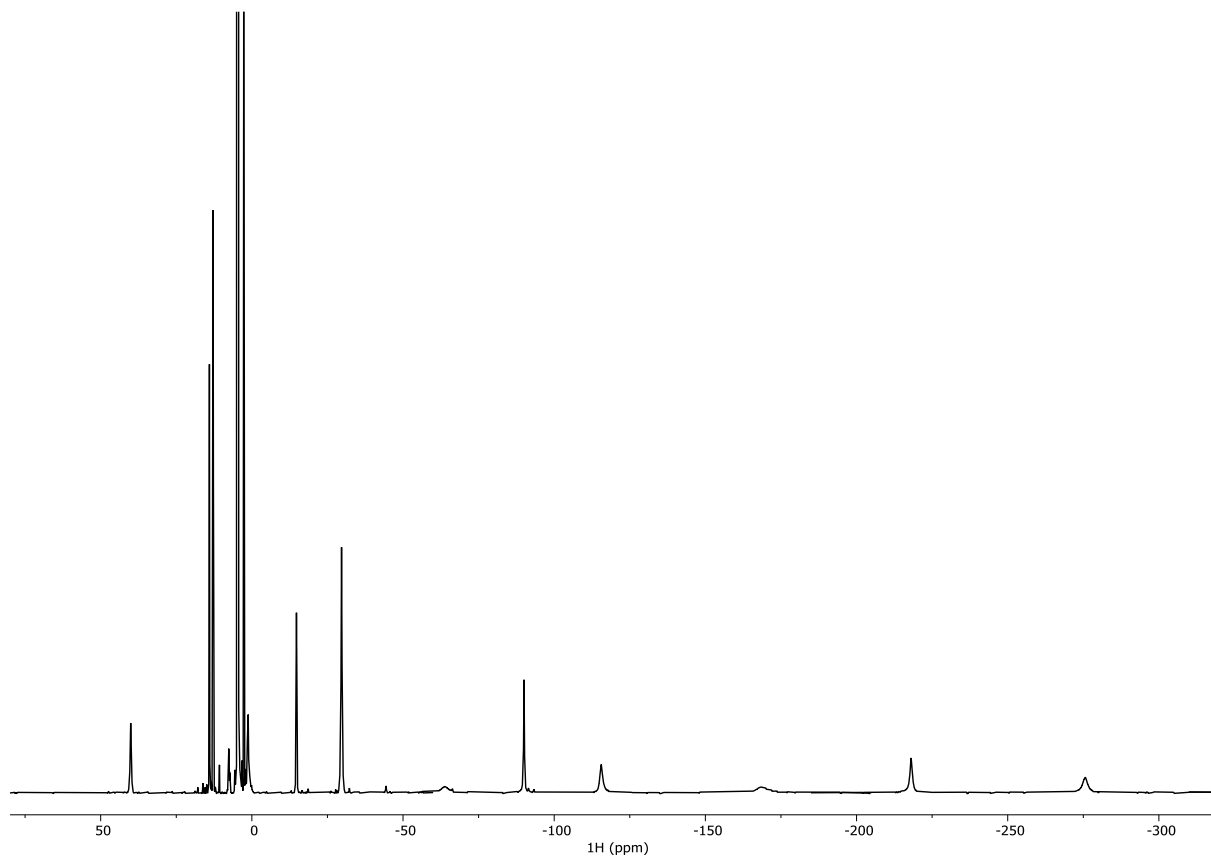
**Figure S28:**  $^1\text{H}$  NMR spectrum of Yb-PypaM2-SO<sub>2</sub>-Ph in  $\text{D}_2\text{O}$  at pH=7.21.



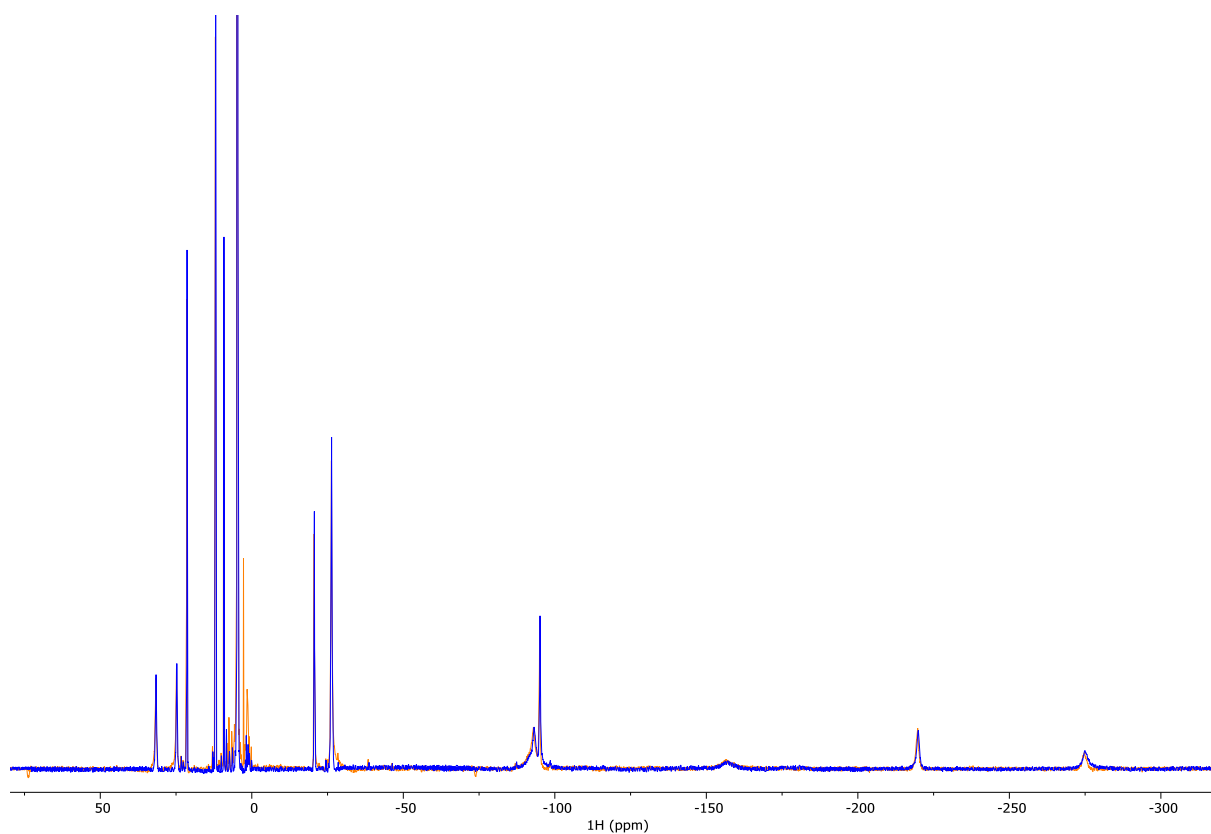
**Figure S29:** Superimposed <sup>1</sup>H NMR spectra of Yb-PypaM2-S-Ph (black) and Yb-PypaM2-SO<sub>2</sub>-Ph (red).



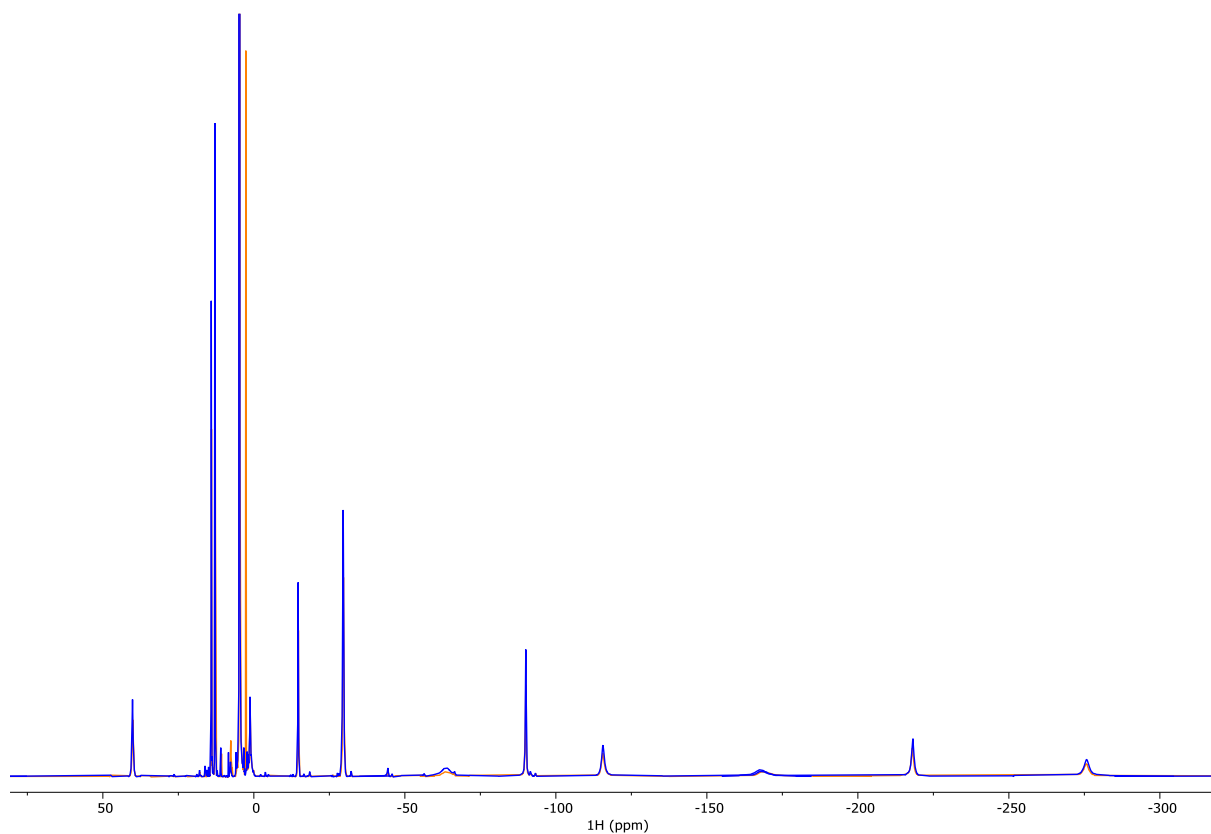
**Figure S30:**  $^1\text{H}$  NMR spectrum of Tb-PypaM2-S-Ph in deuterated phosphate buffer (10 mM) at pH=6.27.



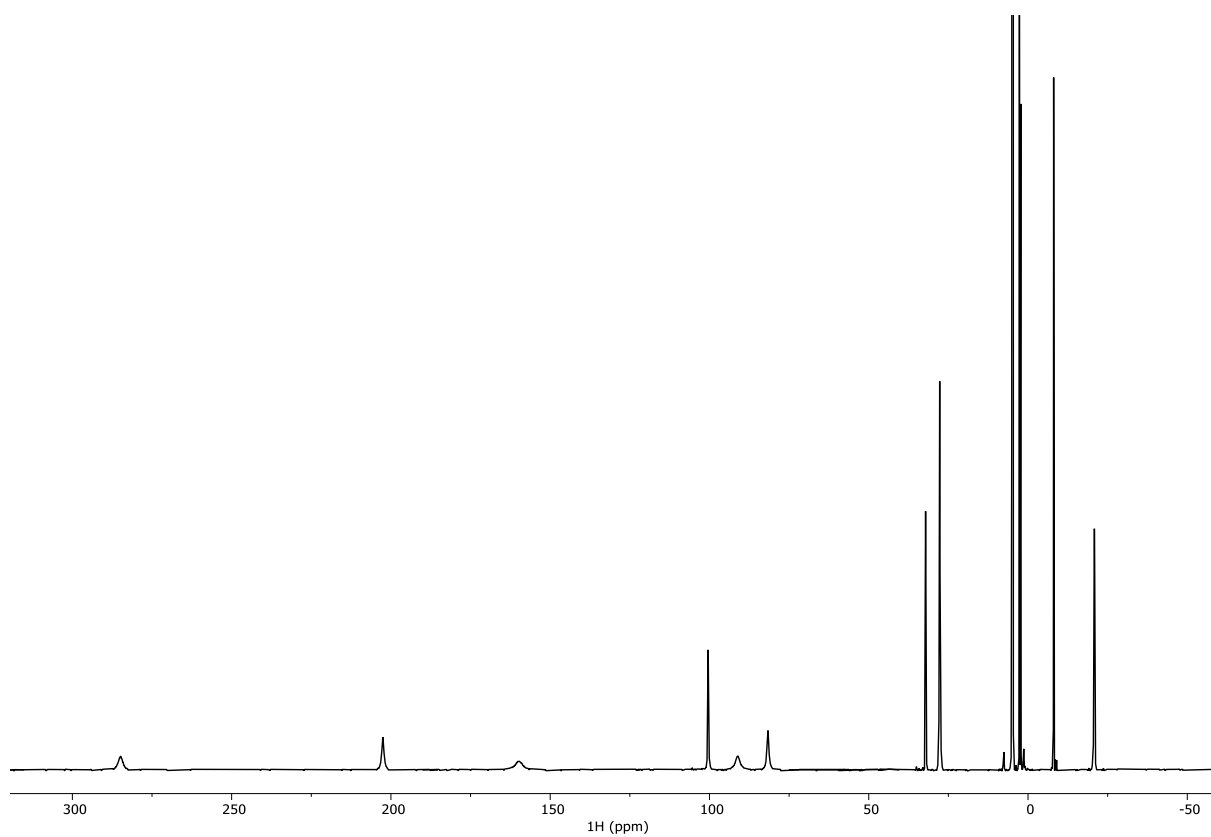
**Figure S31:**  $^1\text{H}$  NMR spectrum of Tb-PypaM2-SO<sub>2</sub>-Ph in deuterated phosphate buffer (10 mM) at pH=6.27.



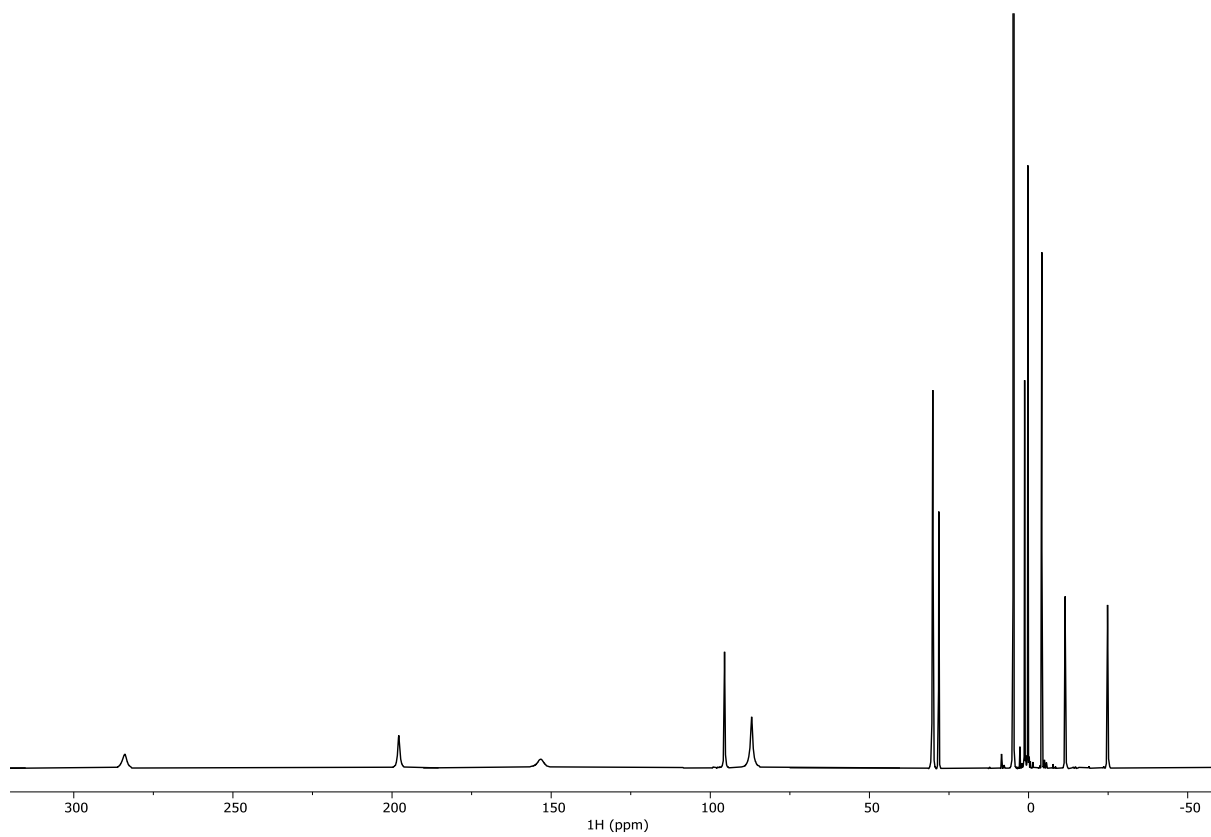
**Figure S32:** Superimposed  $^1\text{H}$  NMR spectrum of Tb-PypaM2-S-Ph in  $\text{D}_2\text{O}$  at  $\text{pH}=8.85$  (blue) and Tb-PypaM2-SO<sub>2</sub>-Ph in deuterated phosphate buffer (10 mM) at  $\text{pH}=6.27$  (orange).



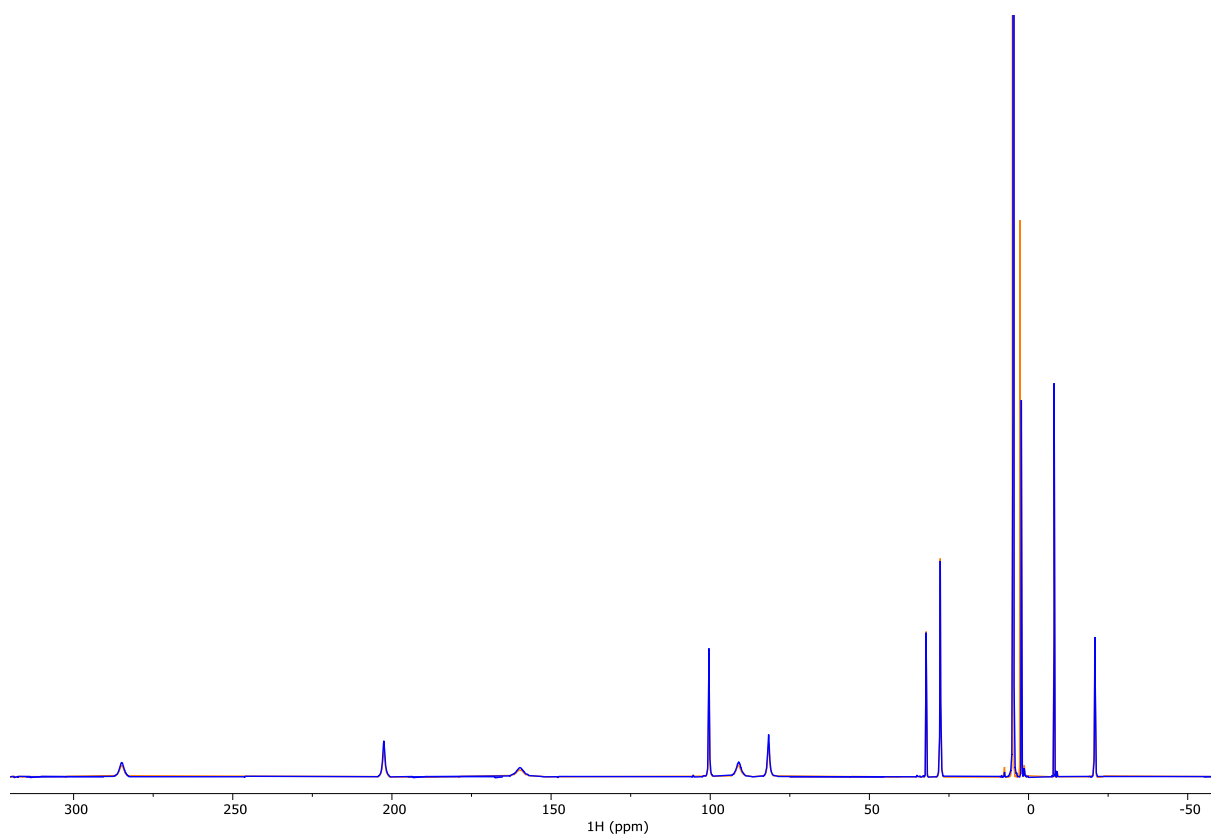
**Figure S33:** Superimposed  $^1\text{H}$  NMR spectrum of Tb-PypaM2-SO<sub>2</sub>-Ph in  $\text{D}_2\text{O}$  at  $\text{pH}=7.62$  (blue) and Tb-PypaM2-SO<sub>2</sub>-Ph in deuterated phosphate buffer (10 mM) at  $\text{pH}=6.27$  (orange).



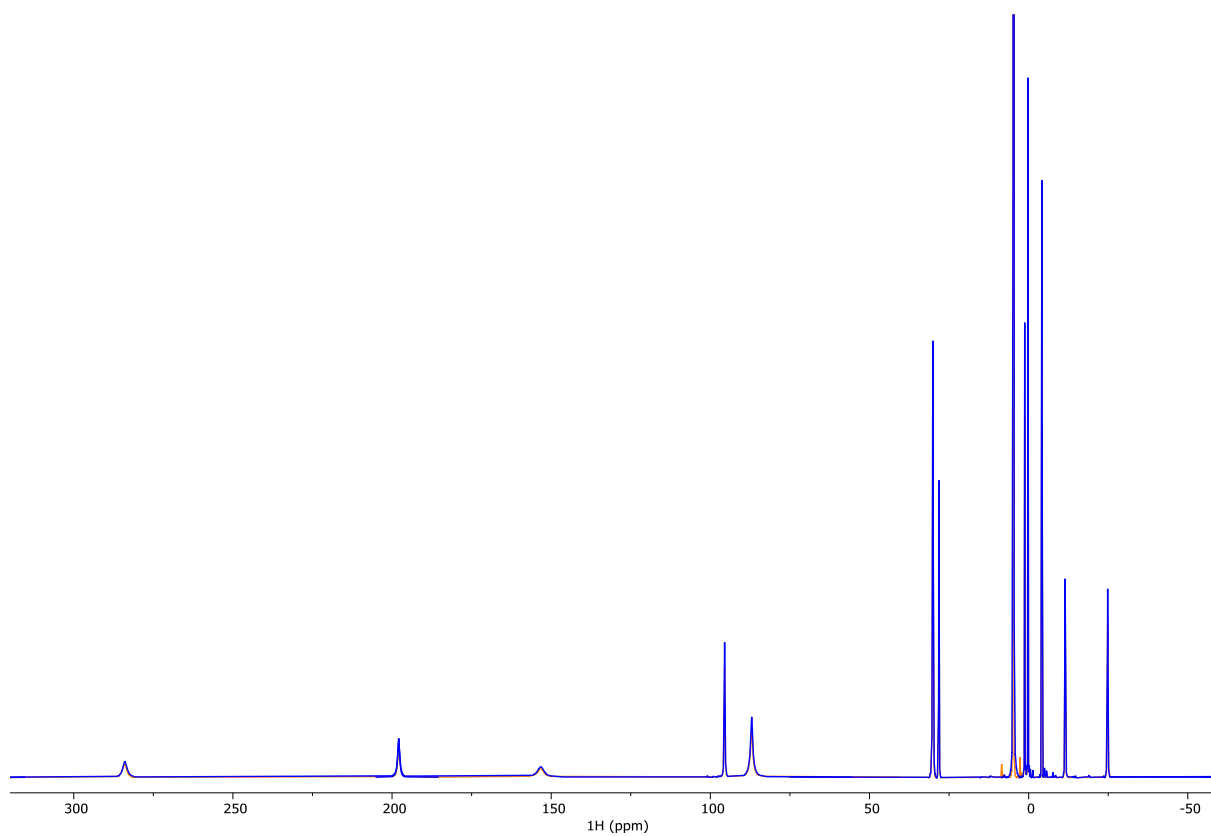
**Figure S34:**  $^1\text{H}$  NMR spectrum of Tm-PypaM2-S-Ph in deuterated phosphate buffer (10 mM) at pH=6.33.



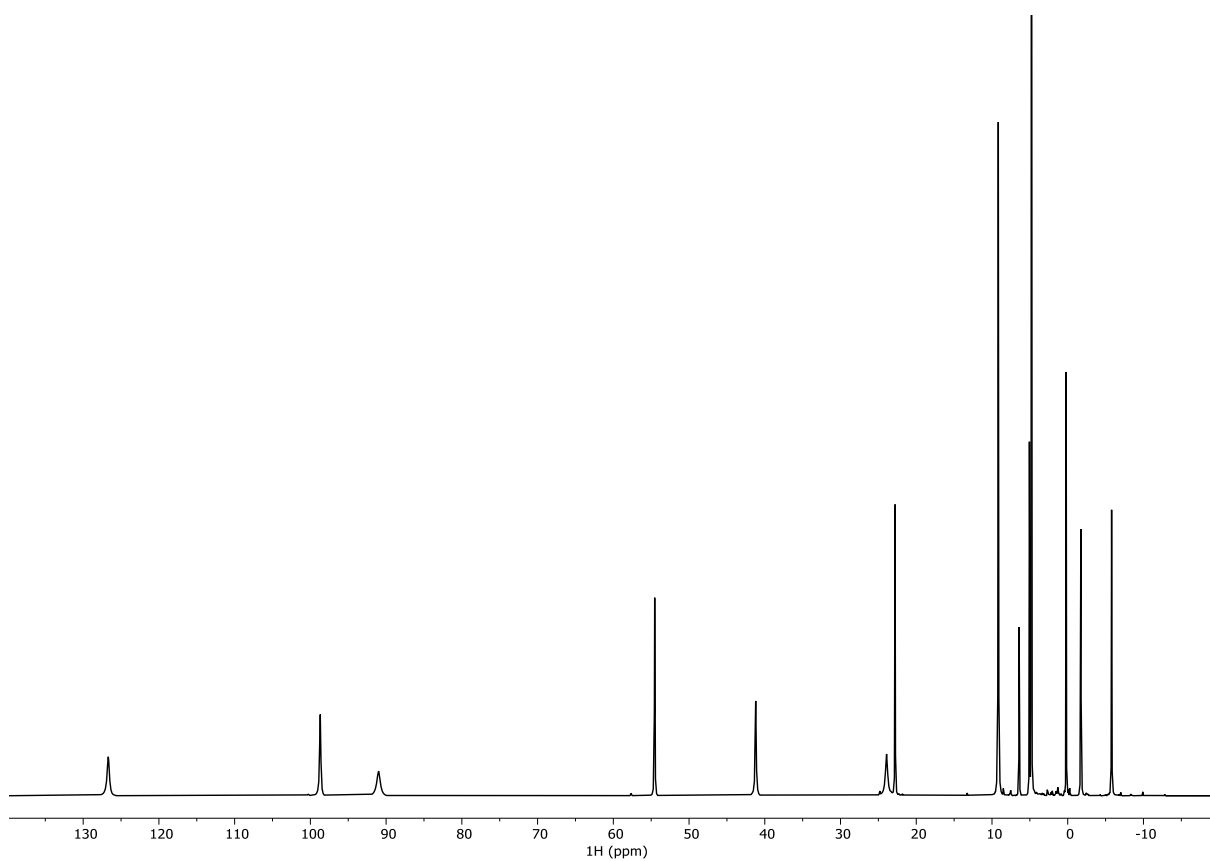
**Figure S35:**  $^1\text{H}$  NMR spectrum of Tm-PypaM2-SO<sub>2</sub>-Ph in deuterated phosphate buffer (10 mM) at pH=6.36.



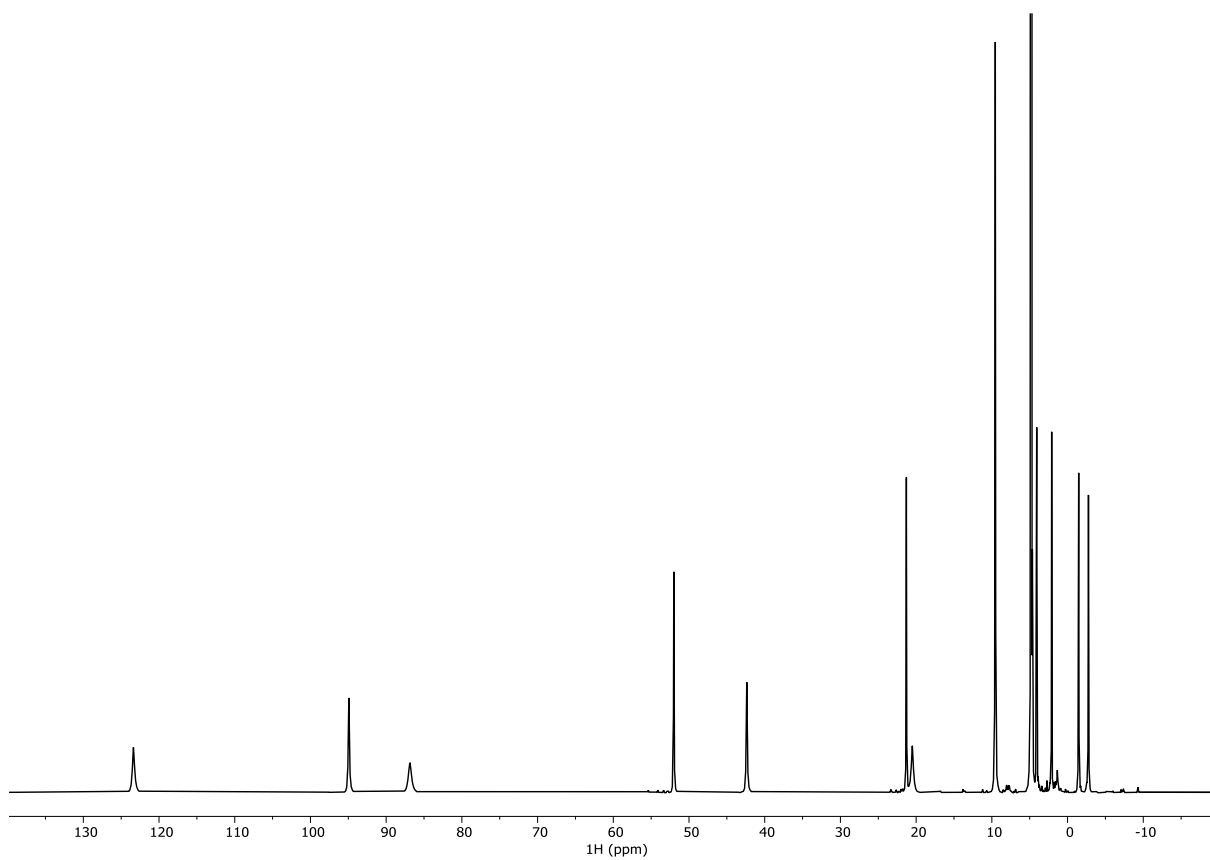
**Figure S36:** Superimposed  $^1\text{H}$  NMR spectrum of Tm-PypaM2-S-Ph in  $\text{D}_2\text{O}$  at pH=8.1 (blue) and Tm-PypaM2-S-Ph in deuterated phosphate buffer (10 mM) at pH=6.33 (orange).



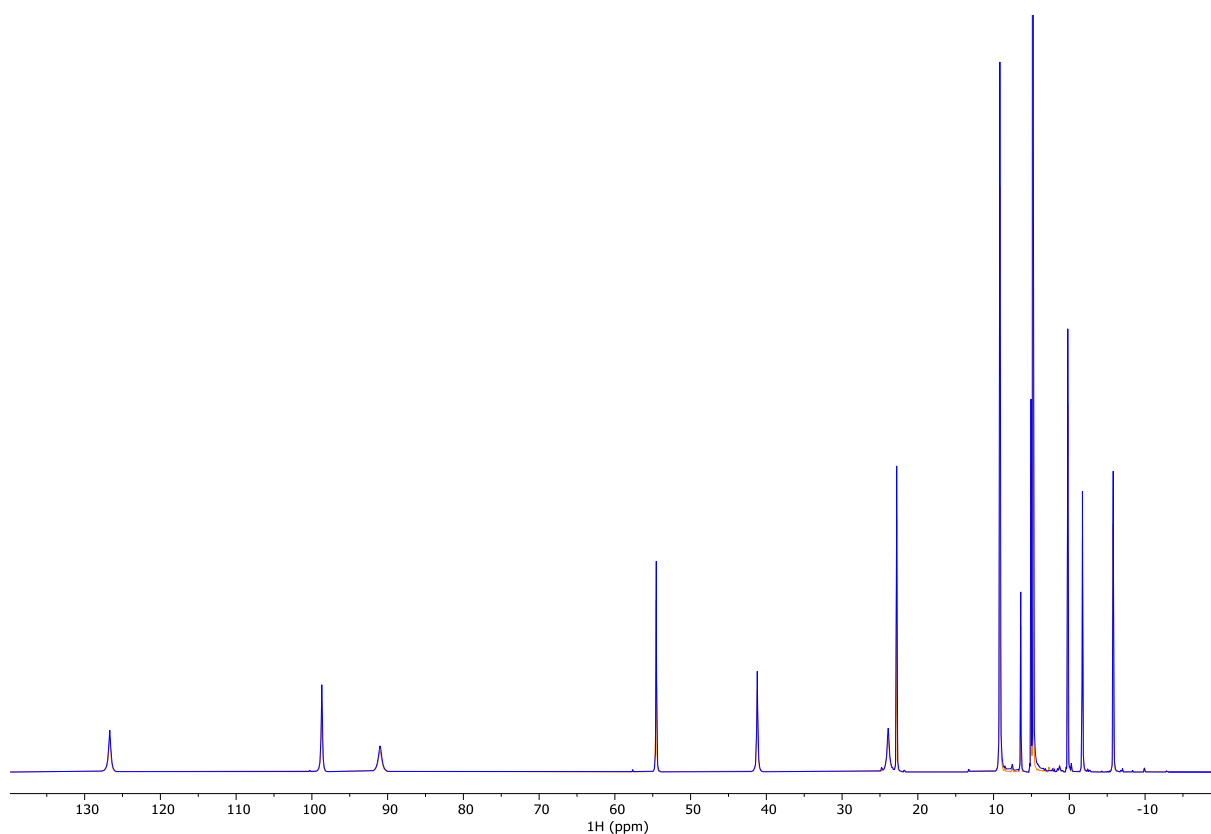
**Figure S37:** Superimposed  $^1\text{H}$  NMR spectrum of Tm-PypaM2-SO<sub>2</sub>-Ph in  $\text{D}_2\text{O}$  at pH=7.56 (blue) and Tm-PypaM2-S-Ph in deuterated phosphate buffer (10 mM) at pH=6.36 (orange).



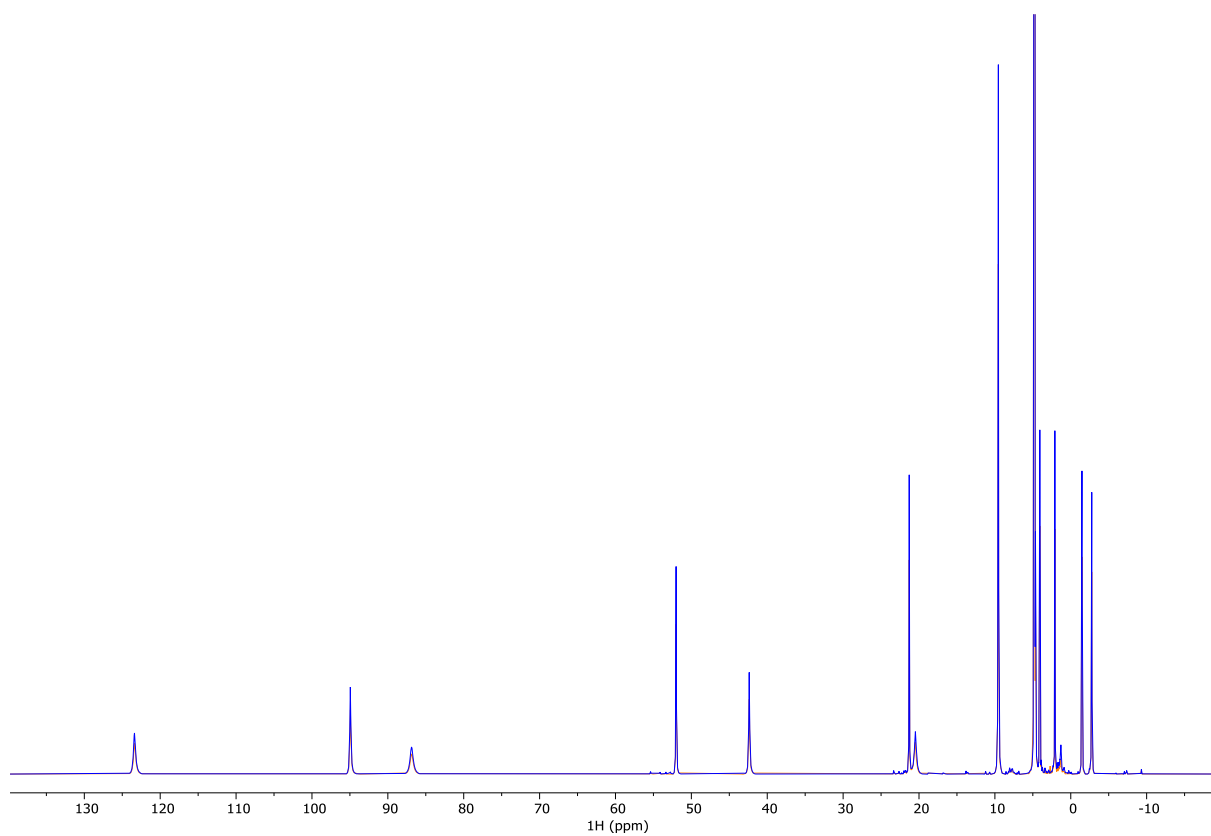
**Figure S38:**  $^1\text{H}$  NMR spectrum of Yb-PypaM2-S-Ph in deuterated phosphate buffer (10 mM) at pH=6.78.



**Figure S39:**  $^1\text{H}$  NMR spectrum of Yb-PypaM2-SO<sub>2</sub>-Ph in deuterated phosphate buffer (10 mM) at pH=6.50.



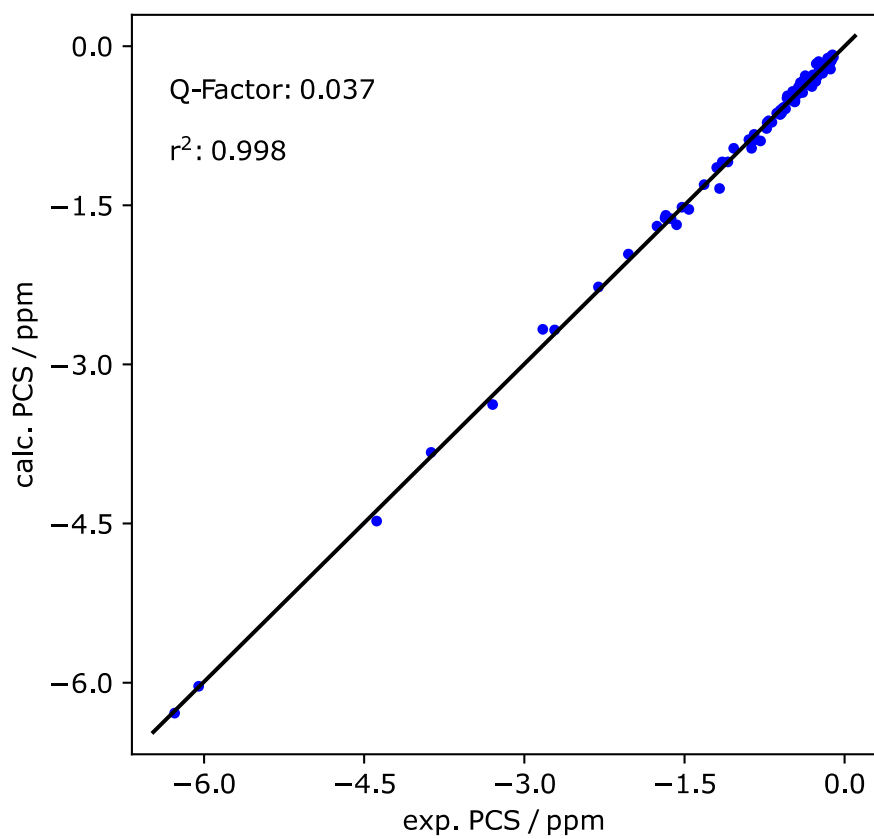
**Figure S40:** Superimposed  $^1\text{H}$  NMR spectrum of Yb-PypaM2-S-Ph in  $\text{D}_2\text{O}$  at pH=7.69 (blue) and Yb-PypaM2-S-Ph in deuterated phosphate buffer (10 mM) at pH=6.78 (orange).



**Figure S41:** Superimposed  $^1\text{H}$  NMR spectrum of Yb-PypaM2-SO<sub>2</sub>-Ph in  $\text{D}_2\text{O}$  at pH=7.21 (blue) and Yb-PypaM2-SO<sub>2</sub>-Ph in deuterated phosphate buffer (10 mM) at pH=6.50 (orange).



### 3.6.5 Correlation graph



**Figure S42:** Correlation graph between calculated PCS from the ubiquitin structure (1UBI) and experimental PCS.

### 3.6.6 Assignments and PCS on ubiquitin S57C

Table S1: Assignment and PCS from Tm and Lu- PypaM2Cl<sub>2</sub> tagged ubiquitin S57C.

Residue	Lu-PypaM2Cl <sub>2</sub>	Tm-PypaM2Cl <sub>2</sub>	PCS
2GlnH	8.96734	8.55265	-0.41469
2GlnN	122.68832	122.25585	-0.43248
3IleH	8.27603	7.80875	-0.46728
3IleN	115.00397	114.51658	-0.48739
4PheH	8.61249	8.1189	-0.49359
4PheN	118.61336	118.16893	-0.44443
5ValH	9.28807	8.96187	-0.3262
5ValN	121.23709	120.91647	-0.32061
6LysH	8.94001	8.61072	-0.32929
6LysN	127.99241	127.72284	-0.26958
7ThrH	8.74891	8.54313	-0.20577
7ThrN	115.57663	115.36183	-0.2148
8LeuH	9.1511	8.96785	-0.18324
8LeuN	121.34887	121.16568	-0.18319
9ThrH	7.63401	7.48962	-0.14439
9ThrN	105.93533	105.78165	-0.15368
10GlyH	7.82357	7.67844	-0.14513
10GlyN	109.3304	109.19697	-0.13342
11LysH	7.26063	7.1152	-0.14543
11LysN	122.00202	121.84632	-0.1557
12ThrH	8.6589	8.50294	-0.15596
12ThrN	120.71515	120.5419	-0.17326
13IleH	9.55432	9.31703	-0.23729
13IleN	127.79041	127.60538	-0.18503
14ThrH	8.75896	8.57452	-0.18445
14ThrN	121.73204	121.50251	-0.22953
15LeuH	8.75186	8.422	-0.32986
15LeuN	125.27203	124.97682	-0.2952
16GluH	8.12037	7.92642	-0.19395
16GluN	122.4657	122.25979	-0.2059
17ValH	8.94152	8.54971	-0.39181
17ValN	117.56479	117.19581	-0.36898
18GluH	8.64154	8.15453	-0.48701
18GluN	119.34225	118.86776	-0.4745
20SerH	7.10614	-	-
20SerN	103.57088	-	-
21AspH	8.04633	6.42178	-1.62455
21AspN	123.64608	122.07226	-1.57382
22ThrH	7.86367	6.54748	-1.31619
22ThrN	108.93654	107.26201	-1.67453
23IleH	8.5391	6.7815	-1.75761

23IleN	121.27565	119.75202	-1.52362
24GluH	7.00263	5.85699	-1.14564
24GluN	125.09847	124.05946	-1.03902
25AsnH	7.92219	7.02498	-0.89721
25AsnN	121.50294	120.77695	-0.72599
26ValH	8.11797	7.26998	-0.84798
26ValN	122.27488	121.56271	-0.71217
27LysH	8.56639	7.9306	-0.63579
27LysN	119.03586	118.46786	-0.568
28AlaH	7.96801	7.53593	-0.43208
28AlaN	123.6403	123.22238	-0.41792
29LysH	7.85599	7.50951	-0.34649
29LysN	120.33848	120.08004	-0.25844
30IleH	8.2896	7.94827	-0.34133
30IleN	121.47362	121.20182	-0.2718
31GlnH	8.55112	8.29387	-0.25725
31GlnN	123.63071	123.38064	-0.25007
32AspH	8.01381	7.84416	-0.16965
32AspN	119.79243	119.65657	-0.13586
33LysH	7.41221	7.25424	-0.15797
33LysN	115.48209	115.36045	-0.12164
34GluH	8.72816	8.56458	-0.16358
34GluN	114.40175	114.22742	-0.17433
35GlyH	8.50708	8.37182	-0.13526
35GlyN	109.00471	108.84696	-0.15776
36IleH	6.13983	5.96659	-0.17324
36IleN	120.40605	120.23793	-0.16813
39AspH	8.53055	8.27873	-0.25182
39AspN	113.7277	113.4901	-0.2376
40GlnH	7.81821	7.57695	-0.24126
40GlnN	116.93071	116.74747	-0.18324
41GlnH	7.48983	7.19686	-0.29298
41GlnN	118.21137	117.93463	-0.27674
42ArgH	8.48537	8.16053	-0.32484
42ArgN	123.18828	122.83751	-0.35077
43LeuH	8.82556	8.30879	-0.51677
43LeuN	124.50485	124.03683	-0.46803
44IleH	9.09948	8.65054	-0.44893
44IleN	122.29022	121.89693	-0.39329
45PheH	8.83132	8.29132	-0.54
45PheN	125.00345	124.50229	-0.50116
46AlaH	8.98627	8.55661	-0.42966
46AlaN	133.09115	132.78404	-0.30711
47GlyH	8.09692	-	-
47GlyN	102.51406	-	-
48LysH	7.9661	7.58404	-0.38207

48LysN	122.1319	121.76275	-0.36914
49GlnH	8.65474	8.31064	-0.3441
49GlnN	123.23694	122.92769	-0.30925
50LeuH	8.55263	7.97501	-0.57761
50LeuN	125.81435	125.21028	-0.60406
51GluH	8.43426	7.56192	-0.87234
51GluN	123.18388	122.39551	-0.78837
52AspH	8.16506	7.43361	-0.73146
52AspN	120.27879	119.42908	-0.84971
54ArgH	7.42473	5.74128	-1.68345
54ArgN	119.35752	117.33293	-2.02458
55ThrH	8.89689	4.51345	-4.38344
55ThrN	109.09701	105.22451	-3.87251
56LeuH	8.14435	-	-
56LeuN	117.54997	-	-
57CysH	8.40926	2.13459	-6.27467
57CysN	117.4336	111.3834	-6.0502
58AspH	7.96801	-	-
58AspN	123.54356	-	-
59TyrH	7.16765	3.87076	-3.29689
59TyrN	115.37661	112.66101	-2.7156
60AsnH	8.21332	-	-
60AsnN	116.59125	-	-
61IleH	7.30669	4.47932	-2.82737
61IleN	118.99263	116.68671	-2.30592
62GlnH	7.55206	6.37967	-1.17239
62GlnN	124.73086	123.27233	-1.45853
63LysH	8.55037	7.35281	-1.19756
63LysN	120.75197	119.65832	-1.09366
64GluH	9.31771	8.71614	-0.60157
64GluN	114.44429	113.89089	-0.55339
65SerH	7.62258	6.94158	-0.681
65SerN	114.92981	114.34059	-0.58922
66ThrH	8.72844	8.25997	-0.46847
66ThrN	117.48402	117.01899	-0.46503
67LeuH	9.40509	8.9074	-0.49769
67LeuN	127.76948	127.23374	-0.53574
68HisH	9.21513	8.78507	-0.43006
68HisN	119.4059	118.96814	-0.43776
69LeuH	8.26923	7.97473	-0.2945
69LeuN	123.91246	123.60167	-0.31079
70ValH	9.17076	8.87272	-0.29805
70ValN	126.52254	126.23822	-0.28432
71LeuH	8.12216	7.93046	-0.1917
71LeuN	123.05318	122.92046	-0.13272
72ArgH	8.57788	8.36161	-0.21627

72ArgN	123.74452	123.47845	-0.26607
73LeuH	8.372	8.12759	-0.24442
73LeuN	124.61038	124.46402	-0.14636
74ArgH	8.44661	8.318	-0.12861
74ArgN	122.06062	121.93146	-0.12916
75GlyH	8.48689	8.35358	-0.1333
75GlyN	111.1417	110.98228	-0.15942
76GlyH	7.95201	7.83816	-0.11385
76GlyN	115.13084	115.02579	-0.10505



# Chapter III

4. Synthesis of a new cyclen building block for  
DOTA-based LCTs

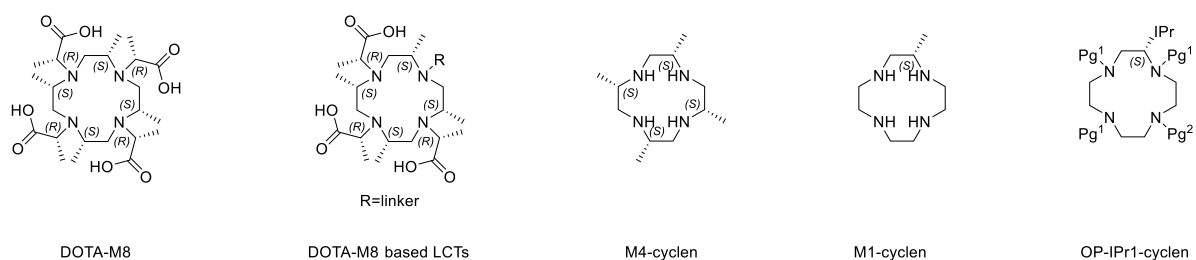




## 4.1 Aim of the project

Based on the DOTA-M8 (Fig. 1) framework<sup>[1]</sup> a series of high performing LCTs has been developed.<sup>[2-6]</sup> The DOTA-M8 framework provides a single conformation and large intrinsic anisotropy parameters, which makes it an excellent scaffold for the development of LCTs. The inherent problem of DOTA-M8 based LCTs is that they are difficult to synthesise and therefore are not available in larger quantities. For the widespread application of paramagnetic NMR spectroscopy it would be of great interest to have a LCT which could combine the favourable properties of the DOTA-M8 framework with a simpler synthesis. The main synthetic challenge towards DOTA-M8 based LCTs is the synthesis of M4-cyclen (Fig. 1). M4 cyclen contains four methyl groups to suppress the ring flip observed for unsubstituted cyclen. This ensures that the final LCT adopts only a single conformation. Ranganathan *et al.* showed that already one methyl group would be sufficient to lock the cyclen ring into a single conformation.<sup>[1]</sup> Therefore, a substantially easier to synthesis version of the DOTA-M8 framework could be obtained by replacing the M4 cyclen with a mono substituted cyclen (M1-cyclen) (Fig. 1). With this approach, the favourable properties of the DOTA-M8 framework should be conserved as the remaining substituent still ensures a single conformation and the intrinsic anisotropy parameters should not be significantly affected. The only downside is that the steric bulk of a LCT based on a mono substituted cyclen is reduced, which could potentially lead to more flexibility of the LCT relative to the protein and hence reduce the observed anisotropy parameters. The loss of steric bulk can in part be compensated by replacing the methyl group with a bulkier group like an isopropyl or a benzyl.

The  $C_4$ -symmetry of M4 cyclen allows a statistical alkylation of its amines while for M1 cyclen this is no longer possible because the amines are no longer chemically identical. A statistical alkylation of a mono substituted cyclen would lead to a complex mixture of diastereomers. For the convenient synthesis of a LCT from mono substituted cyclen it would be necessary to obtain the cyclen with protecting groups that allow the installation of the



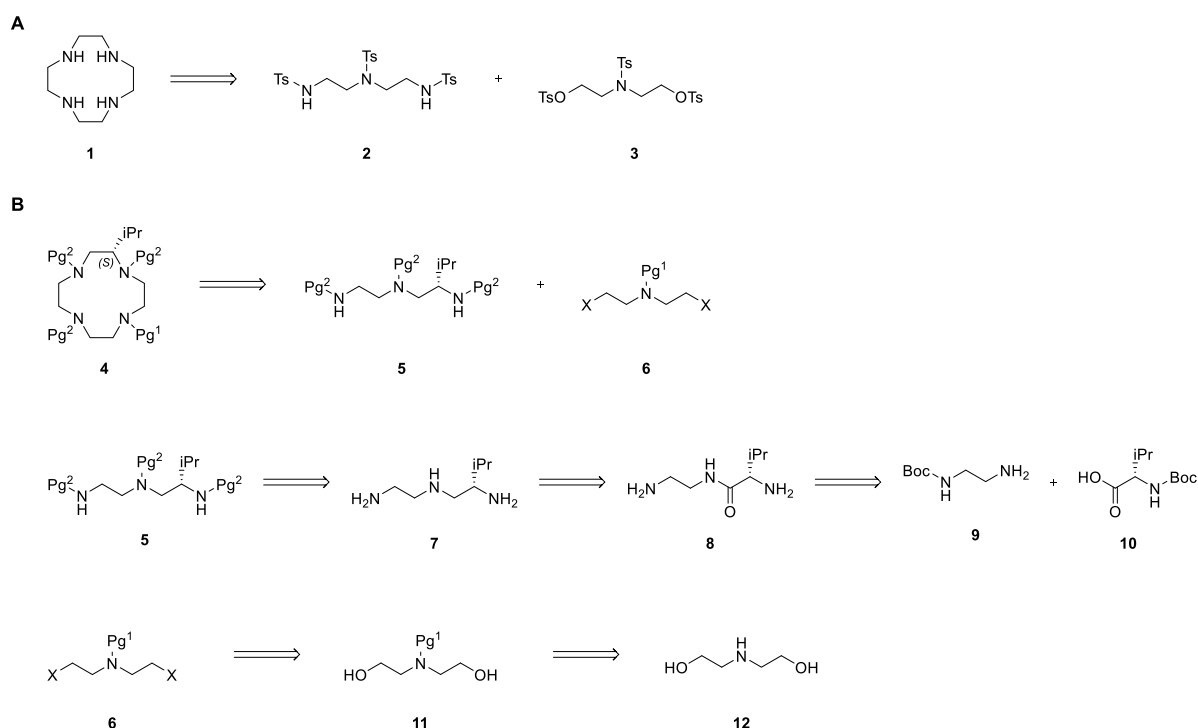
**Figure 1:** Chemical structures of DOTA-M8, DOTA-M8-based LCTs, M4-cyclen, M1-cyclen and OP-IPr1-cyclen from left to right.

necessary pendant arms without having to rely on a statistical alkylation. This is possible by installing orthogonal protecting groups on the nitrogen of which three and one can be removed at the same time. The use of protecting groups would additionally have the advantage that the tedious separation of the differently alkylated cyclen species could be circumvented providing the possibility to further simplify the synthesis towards a new LCT. The goal of this project was to find a convenient synthesis for an orthogonal protected mono isopropyl substituted cyclen (OP-IPr1-cyclen) (Fig 1).

## 4.2 Retrosynthetic analysis

Richman and Atkins reported<sup>[7]</sup> the convenient synthesis of cyclen (**1**) from tri-tosylated diethylenetriamine **2** and tri tosylated ethanol diamine **3** (Fig. 2). While M4 cyclen cannot be synthesized using this simple approach, the synthesis of a mono substituted cyclen can be achieved by this method as shown by Garrity *et al.*<sup>[8]</sup> This approach has additionally the advantage that on the formed cyclen ring three protecting groups originate from one key indeterminate (**5**) and one from the other (**6**). Therefore, if orthogonal protecting groups are installed on the two building blocks the desired three to one ration of the protecting groups will be obtained. (Fig. 2).

The first key intermediate for the cyclization, the protected triamine **5** was envisioned to be synthesized starting from a boc protected valine (**10**) and boc-protected ethylenediamine (**9**). The two starting materials can be connected with an amide coupling. After removal of the boc protecting group and reduction of the amide **8** the desired orthogonal protecting groups can be installed giving the first key intermediate **5**. Incorporation of the protecting group at a late

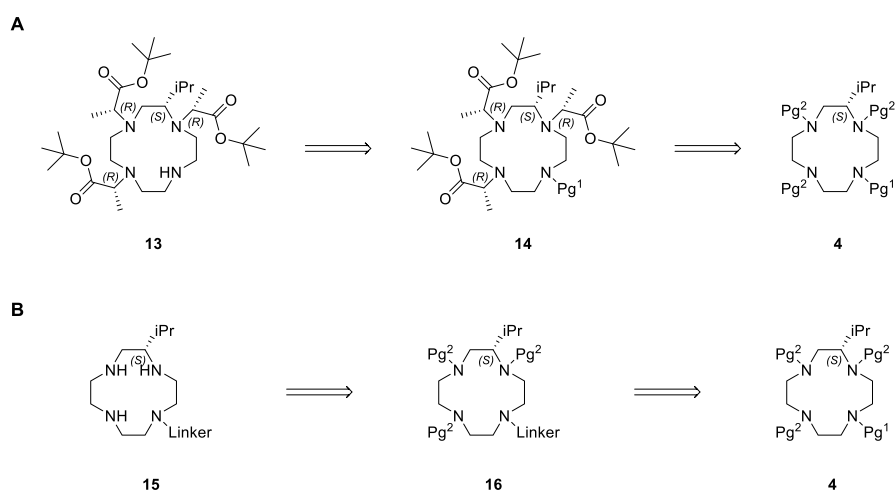


**Figure 2:** A: retrosynthesis of cyclen. B: Retrosynthetic analysis of orthogonal protected mono isopropyl substituted cyclen (OP-IPr1-cyclen).

stage has the advantage that it simplifies the testing of different protecting groups. The second key intermediate **6** should be readily available from diethanolamine (**12**). Due to the higher nucleophilicity of the nitrogen compared to oxygen atoms the selective protection of the amine

should be possible in the presence of two unprotected alcohols. Subsequent transformation of the hydroxyl into a leaving group would in a short two step synthesis provide the second key intermediate **6**.

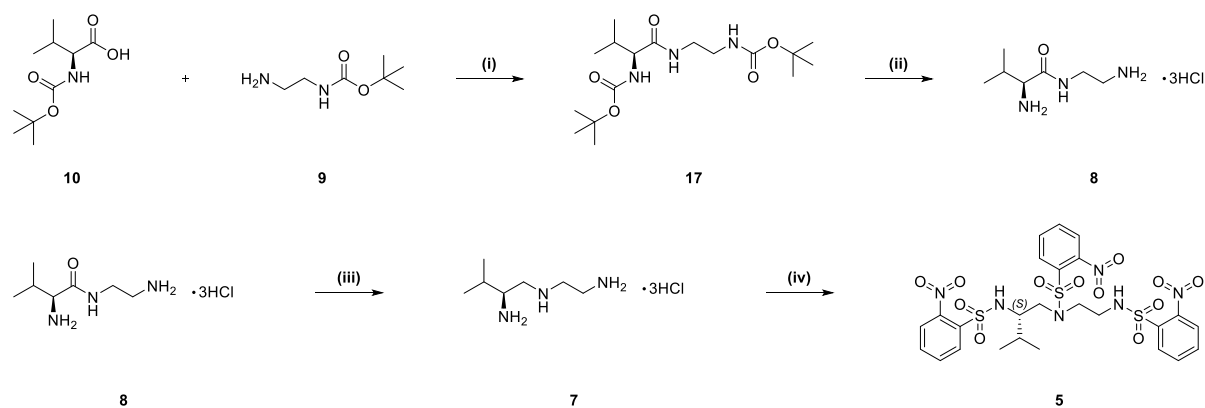
The choice of the protecting groups is not only crucial for the resulting cyclen but also for the cyclization step. The protecting groups on the triamine **5** have to prevent overalkylation of the nitrogen but have to provide the necessary nucleophilicity for the cyclization. For this purpose, sulphonamides were used in the classical cyclen synthesis. We decided to also install sulphonamide protecting groups on the triamine **5** to ensure that the cyclization will not cause any problems. As a sulphonamide protecting group the nosyl group was chosen since it can be deprotected under mild conditions. Removal of the nosyl group is possible with the addition of a thiol nucleophile.<sup>[9]</sup> As an orthogonal protecting group on the second key intermediate **6** a benzyl protecting group was chosen. In order to avoid a complex mixture of diastereomers two options exist to continue the synthesis from OP-IPr1-cyclen towards an LCT (Fig. 3). (i) Three protection groups are removed and the three pendant arms are installed (**14**). Then the remaining protecting group is removed to make room for the linker (**13**). This strategy requires that the remaining protecting group can be removed without harming the already installed pendant arms (Fig. 3A). (ii) One protecting group is removed and the linker is installed in its place (**16**). This is followed by the removal of the three protecting groups to replace them with the pendant arms (**15**). In this case, the linker has to be stable under the deprotection conditions required for the removal of the sulfonamide (Fig. 3B). The benzyl group is optimally suited for the first strategy (Fig. 3 A) as we know from the synthesis of the isotope labelled complexes in chapter one that the benzyl protecting group can be removed in the presence of the t-Bu protected lactic acid side arms.



**Figure 3:** Retrosynthesis of the two options to continue from OP-IPr1-cyclen towards an LCT.

### 4.3 Results and Discussion

The synthesis towards the nosyl protected triamine **5** starting from the commercially available boc-protected L-valine **10** and boc-protected ethylenediamine **9** is depicted in figure 4. An amide coupling using HATU as a coupling reagent afforded the protected amide **17** with a good yield of 80%. **17** was purified by a simple recrystallization from ethyl acetate. The boc protecting groups were removed under acidic conditions yielding the hydrochloride salt **8** in an excellent yield of 90%, **8** was used directly in the next step without further purification. Due to its ionic nature **8** was not soluble in any organic solvents. Since the reduction to compound **7** has to be carried out in dry organic solvents it was attempted to transform the hydrochloride salt **8** into the corresponding free base. However, any attempts to obtain the free base resulted in a significant loss of material. Therefore, the reduction was performed with a suspension of the hydrochloride salt **8** in dry tetrahydrofuran using borane dimethylsulfide as a reducing agent. Full conversion of the starting material was achieved after refluxing the reaction for three days. The resulting triamine **7** was recrystallized as its hydrochloride salt from ethanol yielding the desired compound in 65% yield. According to a previously published protocol, it should be possible to increase the reactivity of borane dimethylsulfide by distilling the dimethylsulfide off, which could significantly speed up the reaction. A convenient side effect of this is the

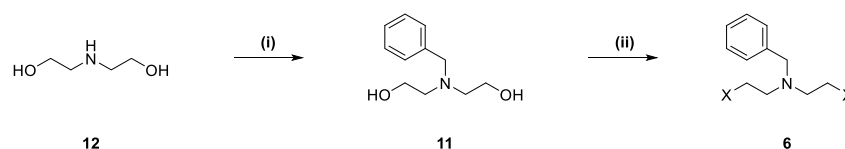


**Figure 4:** Synthesis towards the nosyl protected triamine **5**. (i) HATU, DIPEA, MeCN, 20-25°C. (ii) aq. HCl, MeOH, 20-25°C. (iii) BMS, THF, 66°C. (iv) NsCl, Et<sub>3</sub>N, DCM, 20-25°C.

possibility to quench the distilled dimethylsulfide during the reaction and therefore drastically reducing the olfactory pollution. After the successful synthesis of the free triamine **7** the nosyl protecting group was installed. The installation of the nosyl protecting group proved to be unexpectedly difficult. With nosyl chloride and triethylamine in methylene chloride the protected triamine **5** was obtained in a medium yield of 50%. As the main side product the two

times nosyl protected amine was obtained. Additionally to the mediocre yield, purification of **5** was not possible without column chromatography. The use of column chromatography is mainly problematic for large scale synthesis. Further optimisation of the reaction conditions and the work-up procedure might increase the yield and ease the purification of **5**. Another possibility to increase the conversion would be the use of a sterically less demanding protecting group.

The two step sequence towards the second key intermediate is depicted in figure 5. Commercially available diethanolamine (**12**) was *N*-benzylated using benzyl bromide. Diethanolamine (**12**) was used in small excess to avoid the formation of large amounts of di- and tri-benzylated by-products. Benzyl protected diethanolamine **11** was obtained in 64% after purification by an acid-base extraction. Subsequently it was attempted to transform the alcohol into a leaving group. Transformations of the alcohol into either a tosyl, mesyl or bromine leaving group were all unsuccessful. From the transformation of the alcohol into a tosylate with tosyl chloride the di-chlorinated version of **6** was isolated. At this point, it was realised that the second building block is a nitrogen mustard derivative, which can form a highly reactive intramolecular aziridinium ion. The formation of the intramolecular aziridinium ion explains the inability to isolate any of the compounds with a leaving group more reactive than a chlorine. We decided that for the purpose of a simple and scalable synthesis the use of a nitrogen mustard derivative was not suitable. The reactivity of the second key intermediate can be reduced if the benzyl-protecting group is replaced with a carbamate protecting group. With the presence of a carbamate, the lone pair of the nitrogen should no longer be able to intramolecularly attack the leaving group. This should in principal prevent the formation of the aziridinium ion leading to a more controllable reactivity. As a carbamate protecting group the most straightforward choice is the Cbz group as it should provide similar properties as the benzyl group.

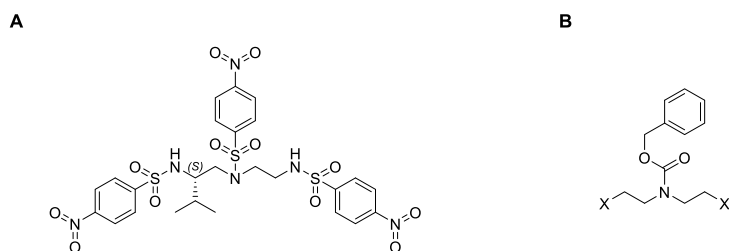


**Figure 5:** Synthesis towards the second key intermediate **6**. (i) BnBr, K<sub>2</sub>CO<sub>3</sub>, MeCN, 78°C. (ii) a. TsCl, Et<sub>3</sub>N, DCM, 0-5°C; b. PBr<sub>3</sub>, MeCN, 0-5°C; c. Ms<sub>2</sub>O, Et<sub>3</sub>N, DCM, 0-5°C.

## 4.4 Conclusion and Outlook

In summary, a convenient synthesis towards OP-IPr1-cyclen relying on two key intermediates was tested. The synthesis of the first key intermediate, the nosyl protected triamine **5** was successful. If the last step can be optimized, **5** would be readily available even on gram scale to further test the cyclization and the following deprotection. In case the nosyl protecting group proves to be sterically too demanding it can be replaced with a less bulky protecting group. A viable alternative to the employed ortho substituted nosyl group would be the para substituted version (Fig. 6A).

The second key intermediate **6** on the other hand turned out to be too reactive for the designated purpose. In addition, the current design is highly similar to existing nitrogen mustards. Replacement of the benzyl-protecting group with a carbamate protecting group should reduce the reactivity as it prevents the formation of the intramolecular aziridinium ion. An obvious choice for the carbamate is Cbz as it can be removed under the same conditions as the benzyl group (Fig. 6B).



**Figure 6:** Alternative key intermediates for the proposed synthetic strategy.

## 4.5 References

- [1] R. S. Ranganathan, N. Raju, H. Fan, X. Zhang, M. F. Tweedle, J. F. Desreux, V. Jacques, *Inorg. Chem.* **2002**, *41*, 6856–6866.
- [2] D. Häussinger, J. R. Huang, S. Grzesiek, *J. Am. Chem. Soc.* **2009**, *131*, 14761–14767.
- [3] D. Joss, D. Häussinger, *Chem. Commun.* **2019**, *55*, 10543–10546.
- [4] D. Joss, M. Bertrams, D. Häussinger, *Chem. – A Eur. J.* **2019**, *25*, 11910–11917.
- [5] D. Joss, R. M. Walliser, K. Zimmermann, D. Häussinger, *J. Biomol. NMR* **2018**, *72*, 29–38.
- [6] T. Müntener, J. Kottelat, A. Huber, D. Häussinger, *Bioconjug. Chem.* **2018**, *29*, 3344–3351.
- [7] J. E. Richman, T. J. Atkins, *J. Am. Chem. Soc.* **1974**, *96*, 2268–2270.
- [8] M. L. Garrity, G. M. Brown, J. E. Elbert, R. A. Sachleben, **1993**, *34*, 5531–5534.
- [9] T. Kan, T. Fukuyama, *Chem. Commun.* **2004**, *4*, 353–359.



## 4.6 Supporting information

### 4.6.1 Materials and Methods

All chemicals were used as purchased without further purification if not stated otherwise.

All 400 MHz and 500 MHz NMR spectra were recorded on a Bruker Avance III NMR spectrometer operating at 400.13 MHz or 500.13 MHz proton frequency, respectively. The instruments were equipped with a direct observe 5-mm BBFO smart probe. All spectra were recorded at 298 K.

HR-ESI-MS spectra were measured on a Bruker MaXis 4G HiRes ESI Mass Spectrometer.

Analytical HPLC was performed on a Shimadzu LC20 HPLC-system equipped with a prominence UV/VIS detector, and a Shimadzu 2020 ESI-MS detector. A ReprosilPur120 ODS-3, 3  $\mu\text{m}$  150x3 mm column was used.

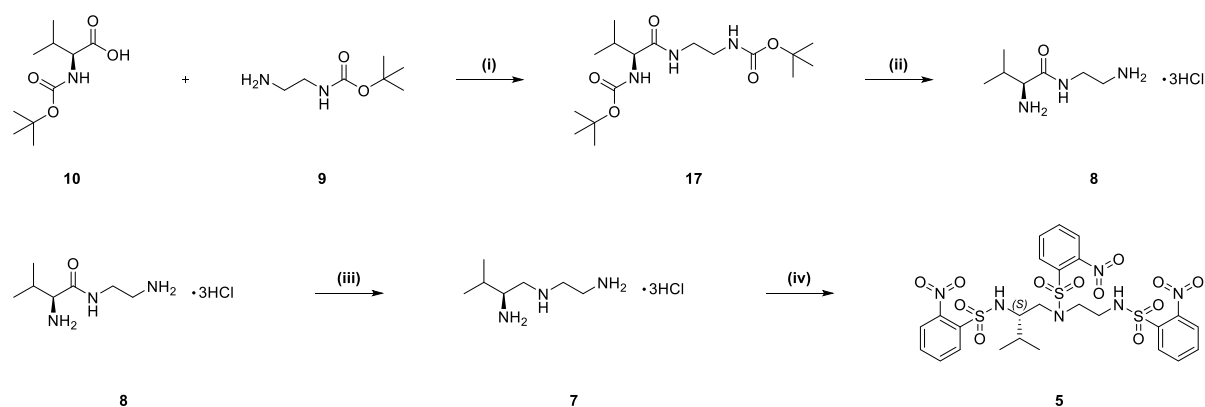
The method uses a binary gradient:

Solvent A: Water + 0.1% TFA.

Solvent B: 90% Acetonitrile + 10% water + 0.085% TFA.

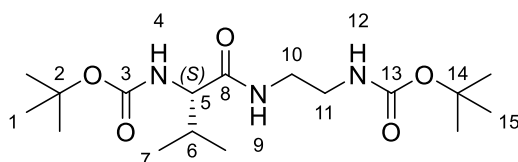
Analytical method: Flow rate: 1.0 ml/min, oven temperature 40°C, UV set to 254 and 280 nm, gradient: 2 minutes at 5% B followed by a gradient over 4 min from 5% B to 100% B. These conditions were kept for 8 min followed by a gradient from 100% B to 5% B over 1 min. These conditions were kept constant for another 7 min, ESI-MS: positive mode 100-1500 m/z.

## 4.6.2 Experimental Procedures and Characterization



**Figure S1:** Synthesis towards the nosyl protected triamine **5**.

**tert-Butyl (S)-2-(2-((tert-butoxycarbonyl)amino)-3-methylbutanamido)ethyl carbamate (17):** (*tert*-Butoxycarbonyl)-L-valine (10.3 g, 47.4 mmol, 1.0 eq.) was dissolved in acetonitrile (100 ml). Then *N,N*-diisopropylethylamine (18.2 ml, 13.5 g, 104 mmol, 2.2 eq.) and HATU (19.8 g, 52.1 mmol, 1.1 eq.) were added and the solution was cooled to 0-5°C. Afterwards *tert*-butyl (2-aminoethyl)carbamate (7.5 ml, 7.59 g, 47.4 mmol, 1.0 eq.) was added and the solution was allowed to warm to 20-25°C for 20 min. Then the solution was diluted with water (200 ml) and ethyl acetate (500 ml) and the layers were separated. The organic layer was washed with sat. aq. sodium hydrogen carbonate (200 ml), water (200 ml) and brine (200 ml) and dried over sodium sulphate. The solvent was evaporated. The remaining solid was suspended in cold ethyl acetate (25 ml) and put in an ice bath for 5 min. The solid was filtered off and washed with cold ethyl acetate (2\*20 ml) to yield *tert*-butyl (*S*)-2-(2-((*tert*-butoxycarbonyl)amino)-3-methylbutanamido)ethyl carbamate (13.6 g, 37.8 mmol, 80%) as a white solid.

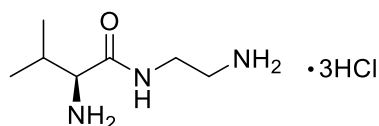


**<sup>1</sup>H NMR (500 MHz, Chloroform-*d*)**  $\delta$ : 6.71 (m, 1H, H<sub>9</sub>), 5.13 (m, 1H, H<sub>4</sub>), 5.08 (m, 1H, H<sub>12</sub>), 3.88 (t, <sup>3</sup>J<sub>HH</sub> = 6.69 Hz, 1H, H<sub>5</sub>), 3.35 (m, 2H, H<sub>10</sub>), 3.26 (m, 2H, H<sub>11</sub>), 2.11 (m, 1H, H<sub>6</sub>), 1.43 (s, 9H, H<sub>1/15</sub>), 1.42 (s, 9H, H<sub>1/15</sub>), 0.94 (d, <sup>3</sup>J<sub>HH</sub> = 6.71 Hz, 3H, H<sub>7a</sub>), 0.89 (d, <sup>3</sup>J<sub>HH</sub> = 6.82 Hz, 3H, H<sub>7b</sub>) ppm.

$^{13}\text{C}$  NMR (126 MHz, Chloroform-*d*)  $\delta$ : 172.44 (C<sub>8</sub>), 156.79 (C<sub>13</sub>), 156.08 (C<sub>3</sub>), 79.99 (C<sub>2/14</sub>), 79.71 (C<sub>2/14</sub>), 60.28 (C<sub>5</sub>), 40.46 (C<sub>10</sub>), 40.41 (C<sub>11</sub>), 30.96 (C<sub>6</sub>), 28.51 (C<sub>1/15</sub>), 28.47 (C<sub>1/15</sub>), 19.40 (C<sub>7a</sub>) 17.92 (C<sub>7b</sub>) ppm.

**HR-ESI-MS**: calcd. for  $[\text{M}+\text{H}]^+$  C<sub>17</sub>H<sub>34</sub>N<sub>3</sub>O<sub>5</sub>  $m/z$  = 360.2493 found 360.2488.

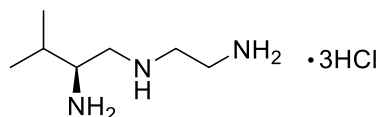
**(*S*)-1-((2-Ammonioethyl)amino)-3-methyl-1-oxobutan-2-aminium chloride (8)**: *tert*-Butyl (*S*)-(2- (2- ((*tert*-butoxycarbonyl)amino) -3- methylbutanamido)ethyl) carbamate (3.00 g, 8.35 mmol, 1.0 eq.) was dissolved in methanol (30 ml) and the solution was cooled to 0-5°C. Then aq. hydrochloric acid (12 M, 15 ml) was added and the solution was allowed to warm to 20-25°C for 5.5 h. Afterwards the solution was diluted with methanol (80 ml) and the solvent was evaporated. The residue was dissolved in methanol (60 ml) and filtered. The solvent was evaporated to yield (*S*)-1-((2-ammonioethyl)amino)-3-methyl-1-oxobutan-2-aminium chloride (1.98 g, 7.46 mmol, 90%) as a white foam. The product was used without further purification.



**HR-ESI-MS**: calcd. for  $[\text{M}+\text{H}]^+$  C<sub>7</sub>H<sub>18</sub>N<sub>3</sub>O  $m/z$  = 160.1444 found 160.1443.

**(*S*)-*N*<sup>1</sup>-(2-Ammonioethyl)-3-methylbutane-1,2-diaminium chloride (7)**: (*S*)-1-((2-Ammonioethyl)amino)-3-methyl-1-oxobutan-2-aminium chloride (1.50 g, 5.65 mmol, 1.0 eq.) was suspended in dry tetrahydrofuran (30 ml). The suspension was cooled to 0-5°C. Then borane dimethylsulfide (2.2 ml, 1.76 g, 23.2 mmol, 4.1 eq.) was added. The suspension was heated to 70°C for 72 h. Then the suspension was allowed to cool to 20-25°C for 20 min. and methanol (8 ml) was added slowly. Afterwards the suspension was heated to 70°C for 3 h. The suspension was allowed to cool to 20-25°C and the solvent was evaporated. The residue was dissolved in aq. hydrochloric acid (4 M, 8.5 ml) and methanol (40 ml). The solution was heated to 70°C for 25 min. Then the solution was allowed to cool to 20-25°C. The solution was filtered and the solvent evaporated. The residue was dissolved in methanol (30 ml) and the solvent was evaporated. This was repeated once. The crude product was dried under high vacuum. The

resulting oil was suspended in dry ethanol (10 ml) and heated to 85°C for 30 min. Then the suspension was cooled to 0-5°C. The solid was filtered off and washed with cold dry ethanol (5 ml) to yield (*S*)-*N*<sup>1</sup>-(2-ammonioethyl)-3-methylbutane-1,2-diaminium chloride (915 mg, 3.64 mmol, 65%) as a white solid.

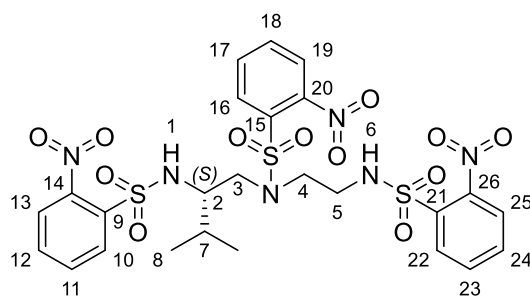


**<sup>1</sup>H NMR (500 MHz, Methanol-*d*)**  $\delta$ : 3.60 (m, 1H, H<sub>2</sub>), 3.58-3.43 (m, 5H, H<sub>6a,6b,5a,5b,3a</sub>), 3.39 (dd, <sup>2</sup>*J*<sub>HH</sub> = 13.89 Hz, <sup>3</sup>*J*<sub>HH</sub> = 8.01 Hz, 1H, H<sub>3b</sub>), 2.16 (m, 1H, H<sub>8</sub>), 1.11 (d, <sup>3</sup>*J*<sub>HH</sub> = 6.88 Hz, 3H, H<sub>9a</sub>), 1.10 (d, <sup>3</sup>*J*<sub>HH</sub> = 6.88 Hz, 3H, H<sub>9b</sub>) ppm.

**<sup>13</sup>C NMR (126 MHz, Methanol-*d*)**  $\delta$ : 55.48 (C<sub>2</sub>), 49.08 (C<sub>3</sub>), 46.43 (C<sub>5</sub>), 36.97 (C<sub>6</sub>), 30.76 (C<sub>8</sub>), 18.21 (C<sub>9a</sub>), 17.84 (C<sub>9b</sub>) ppm.

**HR-ESI-MS:** calcd. for [M+H]<sup>+</sup> C<sub>7</sub>H<sub>20</sub>N<sub>3</sub> *m/z* = 146.1652 found 146.1652.

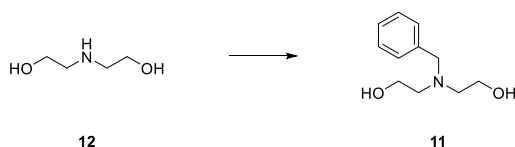
**(*S*)-*N*-(3-Methyl-2-((2-nitrophenyl) sulfonamido) butyl) -2-nitro-*N*-(2-((2-nitrophenyl) sulfonamido) ethyl)benzenesulfonamide (5):** (*S*)-*N*<sup>1</sup>-(2-Ammonioethyl)-3-methylbutane-1,2-diaminium chloride (111 mg, 0.440 mmol, 1.0 eq.) was suspended in dry methylene chloride (10 ml). The suspension was cooled to 0-5°C. Then 2-nitrobenzenesulfonyl chloride (295 mg, 1.33 mmol, 3.0 eq.) and triethylamine (0.37 ml, 269 mg, 2.66 mmol, 6.0 eq.) were added. The solution was allowed to warm to 20-25°C and stirred for 16 h. Then water (20 ml) and methylene chloride (30 ml) were added and the layers were separated. The organic layer was washed with sat. aq. NaHCO<sub>3</sub> (25 ml) and dried over sodium sulphate. The solvent was evaporated and the crude product was purified by flash column chromatography (SiO<sub>2</sub>, cyclohexane : ethyl acetate (3:7)) to yield (*S*)-*N*-(3-methyl-2-((2-nitrophenyl) sulfonamido) butyl) -2-nitro-*N*-(2-((2-nitrophenyl)sulfonamido) ethyl)benzenesulfonamide (159 mg, 0.227 mmol, 52%) as a colourless oil.



**<sup>1</sup>H NMR (500 MHz, Chloroform-*d*)**  $\delta$ : 8.16 (dd,  $^3J_{\text{HH}} = 6.69$  Hz,  $^4J_{\text{HH}} = 1.59$  Hz, 1H, H<sub>10</sub>), 8.12 (m, 1H, H<sub>22</sub>), 7.98 (m, 1H, H<sub>16</sub>), 7.86 (m, 1H, H<sub>25</sub>), 7.85 (dd,  $^3J_{\text{HH}} = 7.81$  Hz,  $^4J_{\text{HH}} = 1.52$  Hz, 1H, H<sub>13</sub>), 7.78-7.69 (m, 6H, H<sub>12,11,17,18,23,24</sub>), 7.62 (m, 1H, H<sub>19</sub>), 5.74 (t,  $^3J_{\text{HH}} = 6.22$  Hz, 1H, H<sub>6</sub>), 5.59 (d,  $^3J_{\text{HH}} = 8.18$  Hz, 1H, H<sub>1</sub>), 3.72 (dtd,  $^3J_{\text{HH}} = 7.51$  Hz,  $^3J_{\text{HH}} = 7.51$  Hz,  $^3J_{\text{HH}} = 3.43$  Hz, 1H, H<sub>2</sub>), 3.67-3.43 (m, 4H, H<sub>3a,3b,4a,4b</sub>), 3.35 (m, 2H, H<sub>5</sub>), 1.95 (septd,  $^3J_{\text{HH}} = 6.87$  Hz,  $^3J_{\text{HH}} = 3.43$  Hz, 1H, H<sub>7</sub>), 0.98 (d,  $^3J_{\text{HH}} = 6.87$  Hz, 3H, H<sub>8a</sub>), 0.71 (d,  $^3J_{\text{HH}} = 6.87$  Hz, 3H, H<sub>8b</sub>) ppm.

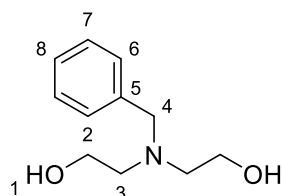
**<sup>13</sup>C NMR (126 MHz, Chloroform-*d*)**  $\delta$ : 148.23 (C<sub>20</sub>), 148.14 (C<sub>26</sub>), 156.08 (C<sub>3</sub>), 147.67 (C<sub>14</sub>), 134.57 (C<sub>9</sub>), 134.30 (C<sub>18</sub>), 134.01 (C<sub>24</sub>), 133.72 (C<sub>12</sub>), 133.43 (C<sub>11</sub>), 133.28 (C<sub>21</sub>), 133.15 (C<sub>23</sub>), 132.24 (C<sub>17</sub>), 132.18 (C<sub>15</sub>), 131.10 (C<sub>22</sub>), 130.92 (C<sub>16</sub>), 130.71 (C<sub>10</sub>), 125.67 (C<sub>25</sub>), 125.45 (C<sub>13</sub>), 124.51 (C<sub>19</sub>), 57.92 (C<sub>2</sub>), 50.89 (C<sub>3</sub>), 48.15 (C<sub>4</sub>), 42.16 (C<sub>5</sub>), 29.10 (C<sub>7</sub>), 19.23 (C<sub>8b</sub>), 16.34 (C<sub>8a</sub>) ppm.

**HR-ESI-MS**: calcd. for [M+Na]<sup>+</sup> C<sub>25</sub>H<sub>28</sub>N<sub>6</sub>NaO<sub>12</sub>S<sub>3</sub> m/z = 723.0820 found 723.0816.



**Figure S2:** Synthesis of benzyl protected diethanolamine **11**.

**2,2'-(Benzylazanediyl)bis(ethan-1-ol) (11):** 2,2'-Azanediylbis(ethan-1-ol) (27.1 g, 258 mmol, 1.2 eq.) was dissolved in acetonitrile (200 ml). Then potassium carbonate (73.9 g, 535 mmol, 2.6 eq.) and benzyl bromide (24.6 ml, 35.2 g, 206 mmol, 1.0 eq.) were added and the suspension was heated to 78°C for 22 h. Afterwards the suspension was allowed to cool to 20-25°C. The suspension was filtered and the solvent evaporated. The remaining oil was dissolved in water (250 ml) and ethyl acetate (200 ml). The layers were separated and the aqueous layer was extracted with ethyl acetate (2\*200 ml). The combined organic layers were extracted with aq. hydrochloric acid (1 M, 2\*200 ml). The combined acidic aqueous layers were neutralized with aq. sodium hydroxide (4 M, approx. 80 ml) till pH~8. Then sat. aq. sodium hydrogen carbonate (150 ml) was added. The aqueous layer was extracted with methylene chloride (3\*200 ml). The combined organic layers were washed with brine (200 ml) and dried over sodium sulfate. The solvent was evaporated to yield 2,2'-(benzylazanediyl)bis(ethan-1-ol) (25.9 g, 133 mmol, 64%) as a colourless oil.

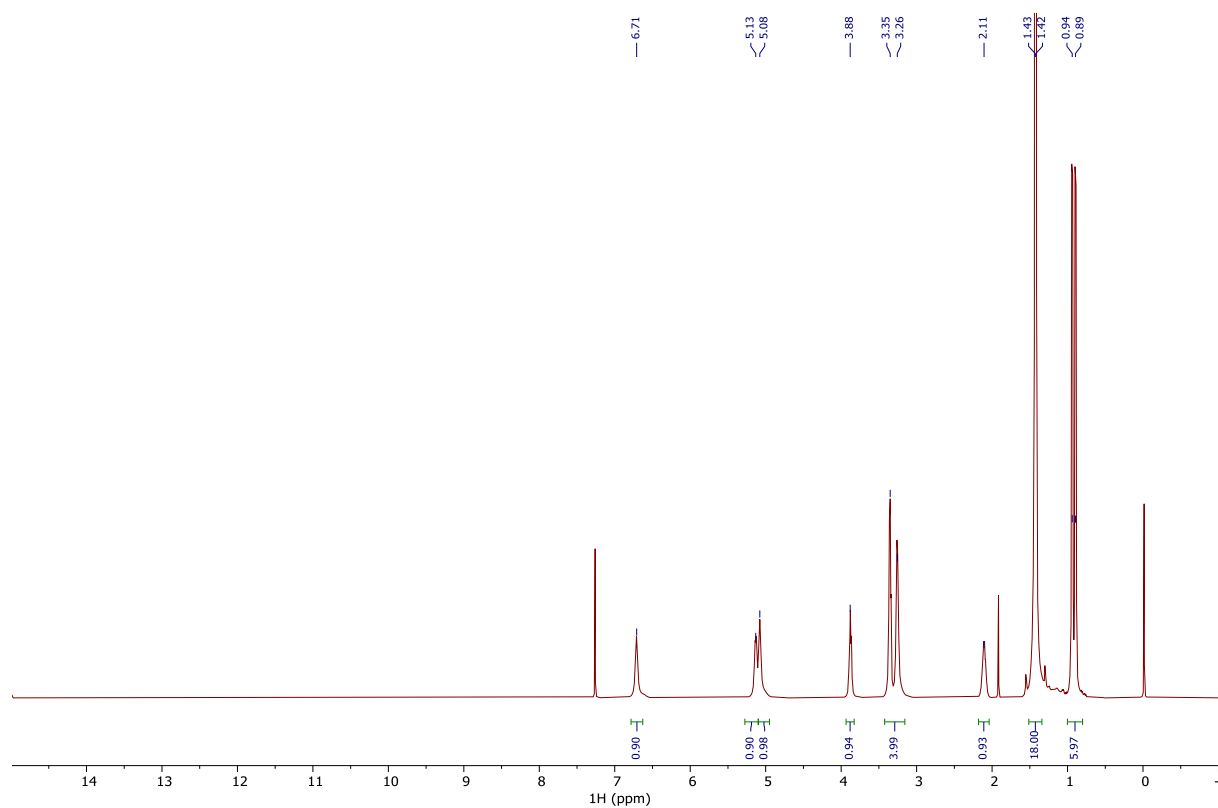


**<sup>1</sup>H NMR (500 MHz, Chloroform-*d*)**  $\delta$ : 7.35-7.29 (m, 4H, H<sub>7,6</sub>), 7.28-7.24 (m, 1H, H<sub>8</sub>), 3.71 (s, 2H, H<sub>4</sub>), 3.63 (m, 4H, H<sub>2</sub>), 2.72 (m, 4H, H<sub>3</sub>) ppm.

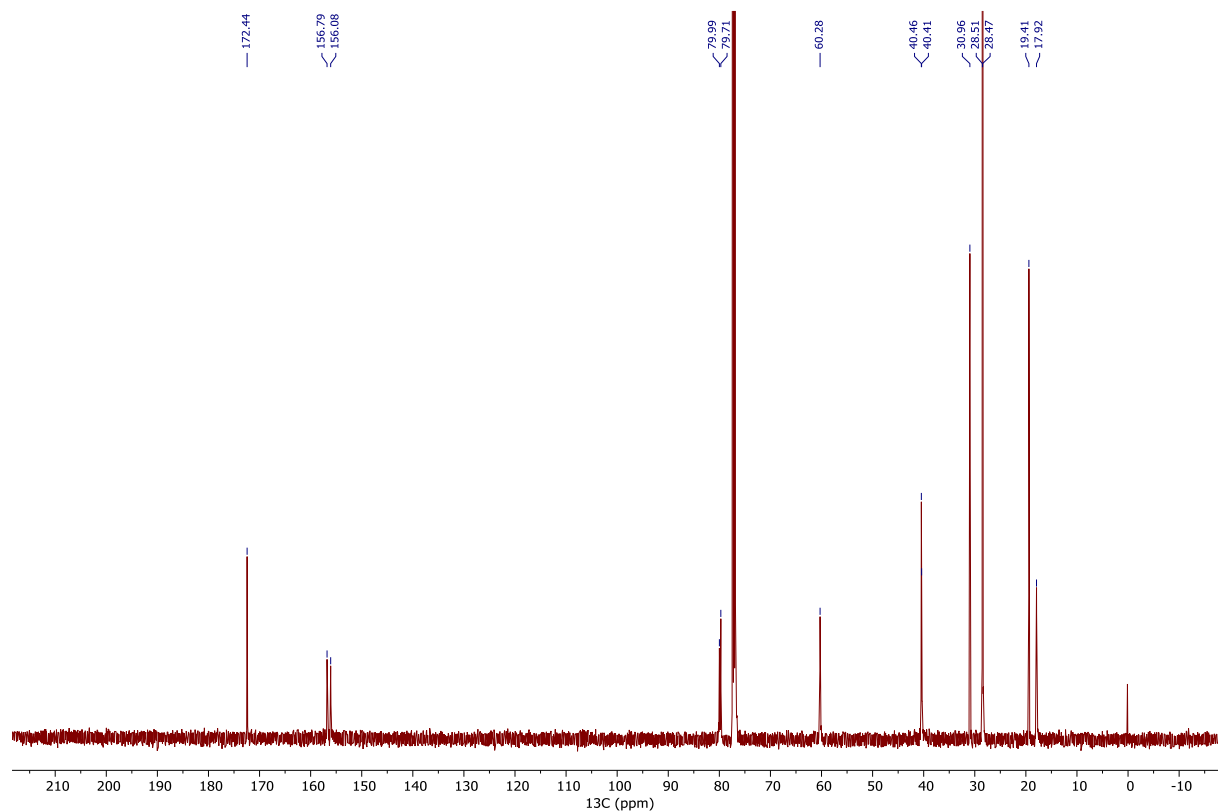
**<sup>13</sup>C NMR (126 MHz, Chloroform-*d*)**  $\delta$ : 138.91 (C<sub>5</sub>), 129.05 (C<sub>7/6</sub>), 128.67 (C<sub>7/6</sub>), 127.50 (C<sub>8</sub>), 59.85 (C<sub>2</sub>), 59.44 (C<sub>4</sub>), 55.99 (C<sub>3</sub>) ppm.

**HR-ESI-MS:** calcd. for [M+H]<sup>+</sup> C<sub>11</sub>H<sub>18</sub>NO<sub>2</sub> m/z = 196.1332 found 196.1334.

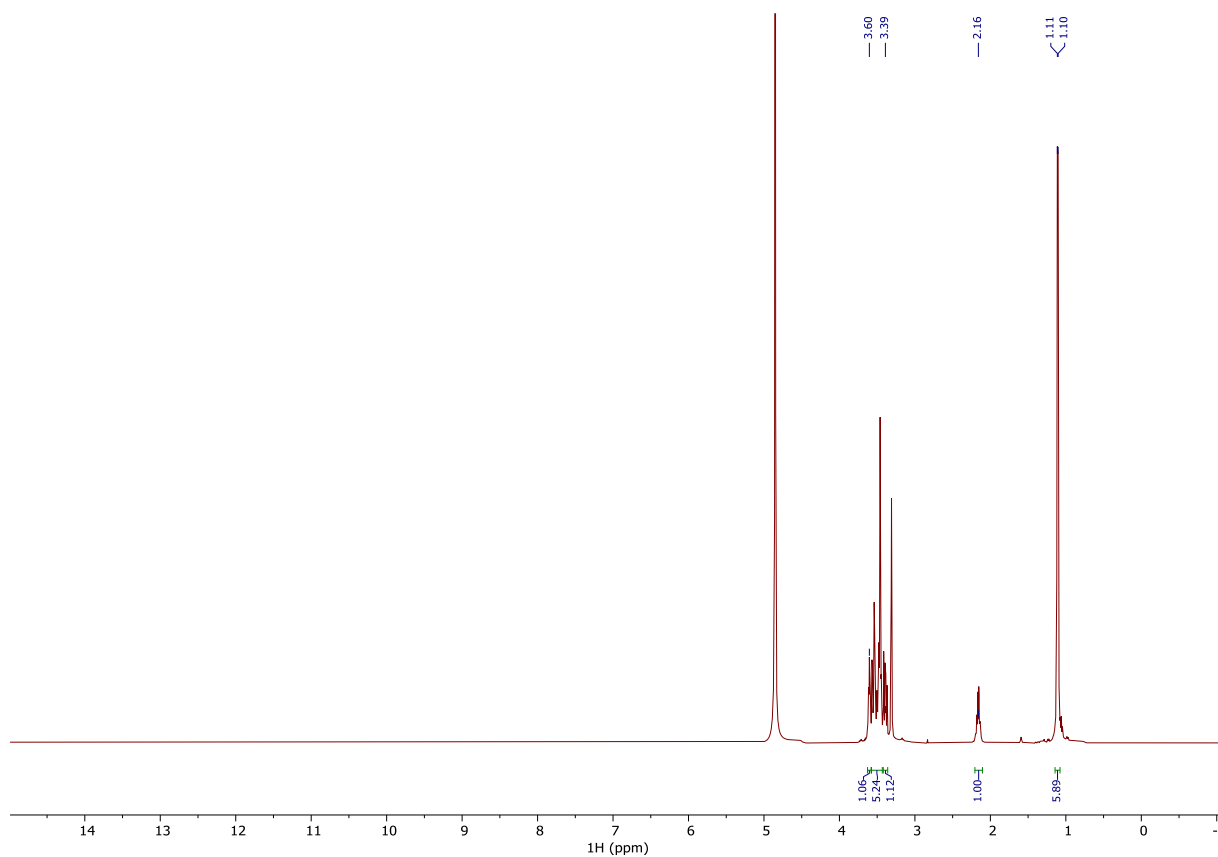
### 4.6.3 $^1\text{H}$ and $^{13}\text{C}$ NMR Spectra



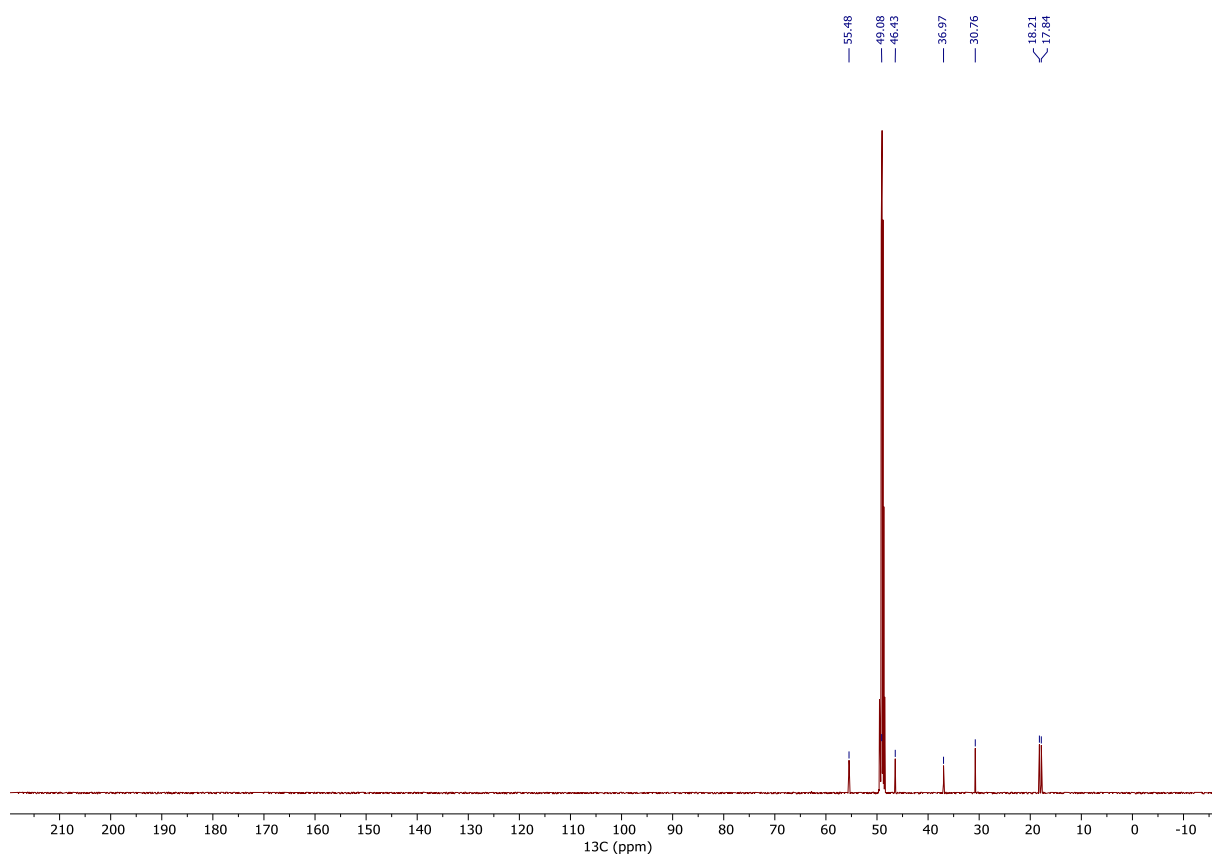
**Figure S3:**  $^1\text{H}$  NMR spectrum of *tert*-butyl (S)-(2-(2-((*tert*-butoxycarbonyl)amino)-3-methylbutanamido) ethyl) carbamate (**17**).



**Figure S4:**  $^{13}\text{C}\{^1\text{H}\}$  NMR spectrum of *tert*-butyl (S)-(2-(2-((*tert*-butoxycarbonyl)amino)-3-methylbutanamido) ethyl) carbamate (**17**).

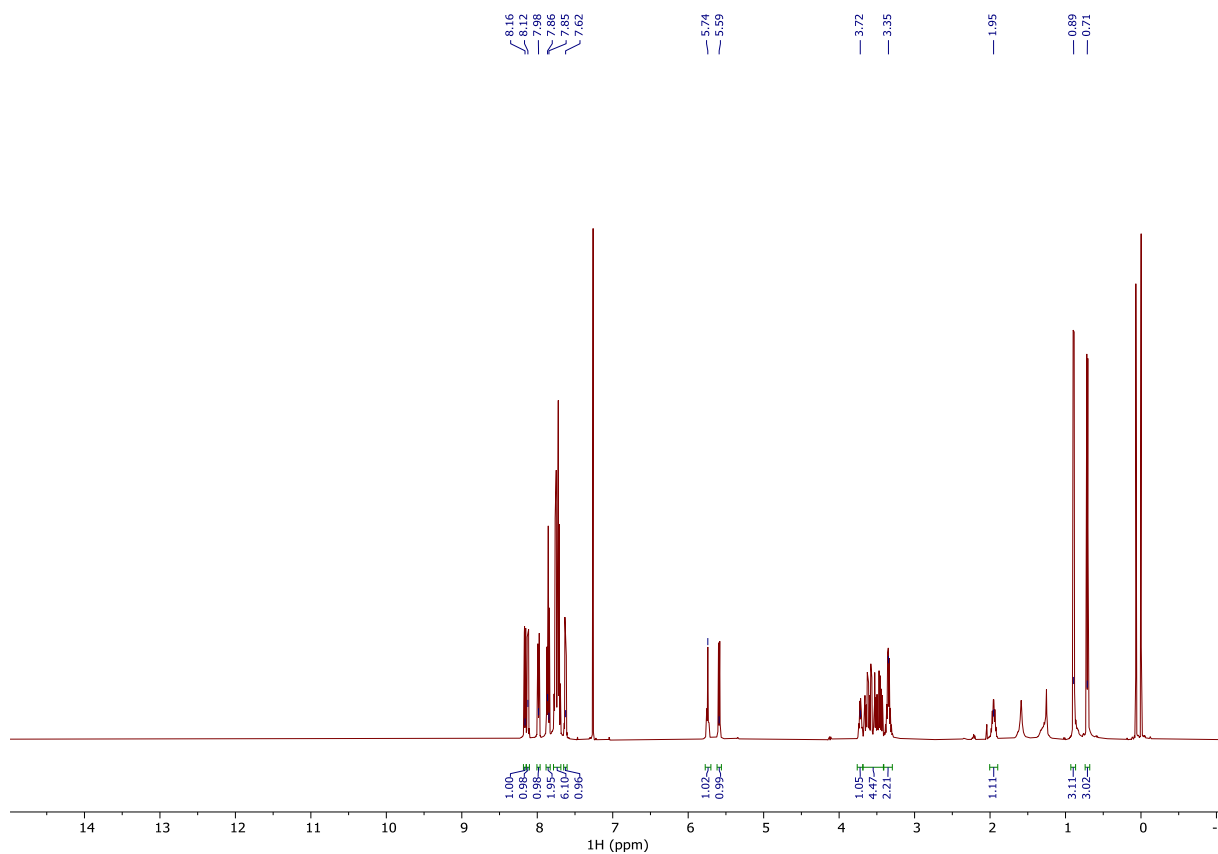


**Figure S5:**  $^1\text{H}$  NMR spectrum of (S)- $N^1$ -(2-ammonioethyl)-3-methylbutane-1,2-diaminium chloride (7).

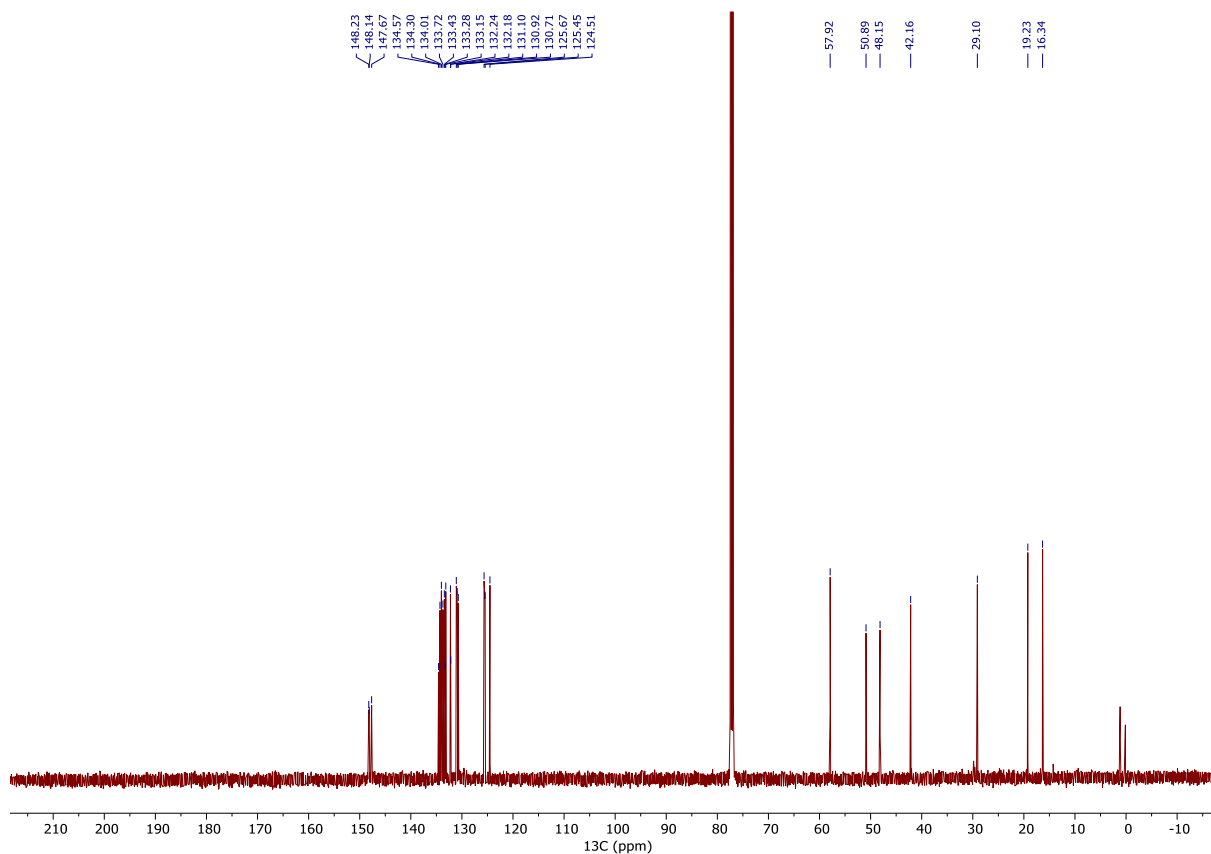


**Figure S6:**  $^{13}\text{C}\{^1\text{H}\}$  NMR spectrum of (S)- $N^1$ -(2-ammonioethyl)-3-methylbutane-1,2-diaminium chloride (7).

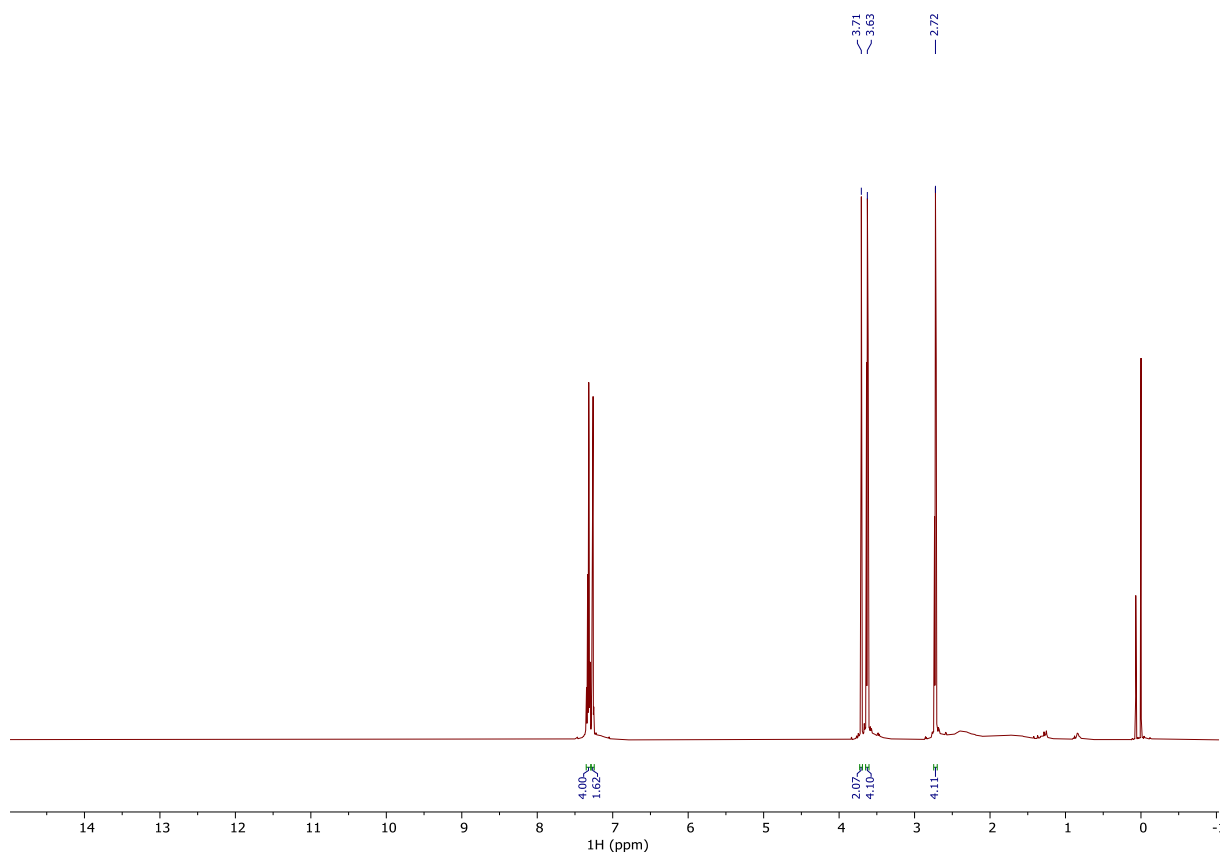




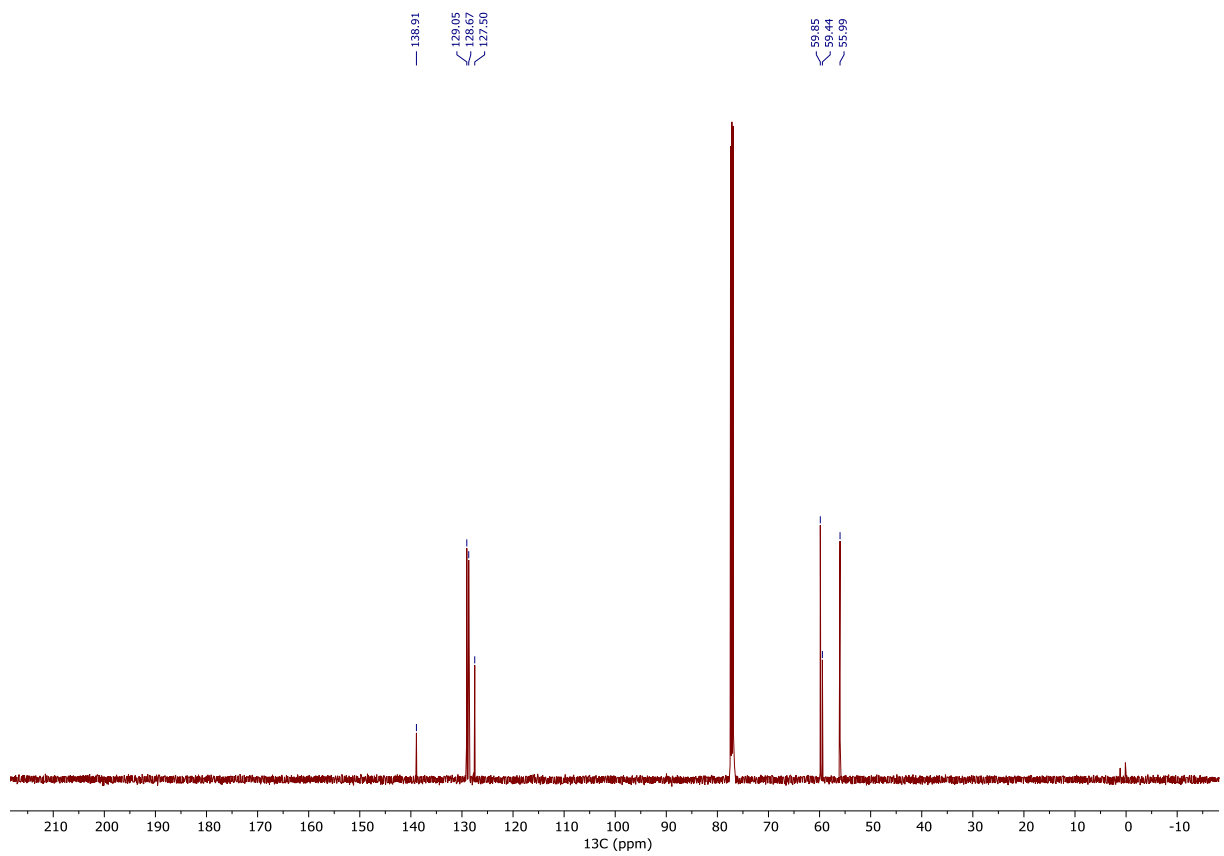
**Figure S7:**  $^1\text{H}$  NMR spectrum of (*S*)-*N*-(3-methyl-2-(2-nitrophenyl)sulfonamido)butyl)-2-nitro-*N*-(2-(2-nitrophenyl)sulfonamido)ethyl)benzenesulfonamide (**5**).



**Figure S8:**  $^{13}\text{C}\{^1\text{H}\}$  NMR spectrum of (*S*)-*N*-(3-methyl-2-(2-nitrophenyl)sulfonamido)butyl)-2-nitro-*N*-(2-(2-nitrophenyl)sulfonamido)ethyl)benzenesulfonamide (**5**).



**Figure S9:**  $^1\text{H}$  NMR spectrum of 2,2'-(benzylazanediy)bis(ethan-1-ol) (**11**).



**Figure S10:**  $^{13}\text{C}\{^1\text{H}\}$  NMR spectrum of 2,2'-(benzylazanediy)bis(ethan-1-ol) (**11**).